GL011860

JAB-99-81
UC-35

THE SPECTRAL MATRIX METHOD OF PREDICTING DAMAGE FROM GROUND MOTION

by

John A. Blume
and
Robert E. Monroe

John A. Blume & Associates
Research Division
San Francisco, California

September, 1971

Prepared under Contract AT(26-1)-99
for the Nevada Operations Office,
United States Atomic Energy Commission

ABSTRACT

Many factors influence structure damage caused by ground motion generated by underground nuclear detonations or earthquakes; such factors include the number and type of structures exposed, the level of ground motion, and the capacity of structures to resist the motion. On a large scale it is necessary to express the variables statistically and to predict damage levels based upon the joint statistical distribution of the individual variables. The Spectral Matrix Method (SMM) was devised to incorporate all relevant parameters in a unified prediction scheme which takes into account statistical variations of the individual factors. A discussion is presented of the SMM and its application in relation to past and current programs of the U. S. Atomic Energy Commission, Nevada Operations Office.

THE SPECTRAL MATRIX METHOD OF PREDICTING DAMAGE FROM GROUND MOTION

CONTENTS

CONTENTS (continued)

TABLES

CONTENTS (continued)

FIGURES

NOMENCLATURE

C = Capacity; $\overline{C}$ = Mean capacity; $\breve{C}$ = Median capacity

C_b = Base shear coefficient

C_v = Coefficient of variation of capacity

C_y = Base shear coefficient causing yield stress; dimensionless

C_z = Structural condition factor for zone Z

D = Demand; $\breve{D}$ = Median demand

D_A = Dollar damage for area A

D_u = Dollar damage for unit U

D_z = Dollar damage for zone Z

D_{zk} = Dollar damage for building class k in zone Z

E_{zk} = Estimated total dollar value or exposure for zone Z and building class k

F = Damage factor; $F = 1$ is total damage

F_A = Damage factor for area A

F_k = Damage factor for building class k

F_o = A specified damage factor

F_u = Damage factor for unit U

F_z = Damage factor for zone Z

M = Geometric standard deviation for capacity

N = Geometric standard deviation for demand

$N(0,1)$ = Normally distributed random variable with mean = 0, standard deviation = 1

P_{ult} = Force causing ultimate stress; kips

P_y = Force causing yield; kips

Q = $\rho(\mu_{ult} - 1)$

S = Stiffness or P_y/Δ_y

S_a = Absolute spectral acceleration; g units

S_{a_y} = Mean spectral acceleration that causes yield level stresses; g units

S_d = Relative spectral displacement; cm

S_v = Relative spectral response velocity; cm/sec

S_{v_y} = Mean spectral velocity that causes yield level stresses; g units

S_z = Soil condition factor for zone Z

T = Period; sec

U = Unit or locality subjected to essentially the same response spectrum

U_Δ = Area under a force-deformation plot to distortion, Δ

V_{iz} = Shear from mode i, story z

V_y = Base shear causing yield stress; kips

W = Total seismic weight; kips

Y_c = Normally distributed random variable for capacity with zero mean and standard deviation = 1

Y_d = Normally distributed random variable for demand with zero mean and standard deviation = 1 (used to model noncoherent portion of demand)

Y_s = Normally distributed random variable for demand with zero mean and standard deviation = 1

Z = Zone, or part of a unit having essentially the same soil and building conditions

Z_d = Normally distributed random variable for demand with zero mean and standard deviation = 1 (used to model coherent part of demand)

g = Acceleration of gravity

m = Story mass; kip sec^2 cm^{-1}

n = Number of stories; also number of buildings in a class

nk = Number of classes of buildings in a zone

nu = Number of units in an area

nz = Number of zones in a unit

α = A factor as defined in Equation 17; dimensionless

β_F = See Appendix A

γ_i = Participation factor as per Equation 14

Δ = Deflection; Δ_y = Yield point deflection

λ = A factor to reduce the yield-value capacity based on fundamental mode response for the effects of multi-modal response; dimensionless

μ = Ductility factor, Δ/Δ_y; dimensionless

μ_{ult} = Ductility factor at ultimate load or stress; dimensionless

ν = Coherence coefficient

ρ = $(P_{ult} - P_y)/P_y$

σ_c = Standard deviation for capacity

Ψ = A factor to modify S_v; $\Psi = 1.00$ for 5% damping

$\emptyset$ = Mode shape normalized to top story deformation; dimensionless

ω = Natural circular frequency; radians/sec

i = Subscript for row or intensity in spectral matrix; also mode number subscript

j = Subscript for period band in spectral matrix; also for story numbers

k = Subscript for building class k

y, z = Story number subscripts

INTRODUCTION

The prediction of damage is a very important subject in the consideration of natural phenomena such as earthquakes, tornados, hurricanes, and floods, and also in connection with proposed man-made events such as nuclear explosions and blasting. The damage problem is usually approached empirically, and often with very limited or inapplicable data.

A comprehensive method was devised by the senior author in and for the structural response phase of the Atomic Energy Commission's effects evaluation program relating to the explosion of underground nuclear devices in Nevada and elsewhere. The Spectral Matrix Method (SMM), which has been used in connection with predictions of the effects of nuclear explosion induced ground motion, involves important structural and dynamic considerations, inelastic response characteristics, and joint probabilities of statistical variations in ground motion and structural resistance. SMM is used both for prediction purposes and as a research tool in categorizing and isolating important parameters in the problem. It has direct application to natural earthquakes as well as to nuclear explosion induced ground motion, and it has been applied to the problem of air blast. It may also be adapted to other potential causes of structure damage.

SMM has been in development and in use over a period of several years. It was presented in an early form at a U. S. Department of Commerce Meeting on Seismology and Engineering Seismology, at Rockville, Maryland, in January 1967.[1] A report was issued in March 1968 which presented an early simplified version of SMM.[2] Since then the method has been refined and extended, adapted to rapid computer execution, and used for several studies of proposed nuclear detonations including interoceanic canal construction by nuclear explosive means. There is a companion subject, an Engineering Intensity Scale,[3] that can be used to predict

whether more detailed analyses of structural response and damage potential are required.

The basic Spectral Matrix Method is an orderly, standardized procedure for the prediction of damage, if any, to a wide variety of structures subjected to ground motion. It includes consideration of: the frequency distribution of ground motion and of the natural frequencies of the structures exposed to the motion, the resulting response, the foundation conditions, the structure conditions, the inelastic reserve capacity to absorb excess energy, and the probabilistic evaluation of random variables inherent in the prediction problem. The method is especially adaptable to computer processing.

BASIC PHILOSOPHY

A basic philosophy of SMM is that the onset of damage in a given area can be related to the spectral response diagram for that area; that the extent of damage can be related to the extent to which the spectral response exceeds the damage threshold of the structure, and also to the inelastic properties of the structure; and that in dealing with large populations of structures there will be considerable variation in properties of interest including strength, natural periods, inelastic properties, age and condition, foundation materials, and ground motion. Further, it is recognized that most of the parameters in the damage problem are random variables, and that these as well as their combinations may be described with the aid of appropriate laws of probability.

It is fully recognized that theory alone cannot solve such problems, and that the results are dependent upon the accuracy of the input data and the success with which numbers can be provided to represent real values and their probability distributions. Much more is to be learned about many of the properties under consideration. However, much has been learned with SMM as a tool to improve and accelerate the acquisition and logical treatment of data. Input constants are simply to be changed if and as new facts make this step desirable.

Large areas -- in fact whole countries -- have been analyzed using SMM. This analysis involves breaking the area of interest into subareas that are assumed to have common values of such parameters as spectral response, soil conditions, etc. There is also the capacity in developed SMM programs to consider not one but several disturbances in an area: perhaps several nuclear detonations, or perhaps a swarm of earthquakes. Thus the method, with computer aid, is applicable to very large areas, multiple disturbances, and any range of conditions. SMM is not only very useful in estimating damage but is also valuable

in data acquisition, parameter studies, and research activities. The balance of the report is devoted to SMM as used in estimating damage from ground motion.

GENERAL DESCRIPTION OF THE SPECTRAL MATRIX METHOD (SMM)

There are several items -- theory, techniques, methods, assumptions, empirical data, etc. -- which are combined in SMM for the basic objective of estimating damage from ground motion. Because several disciplines are involved, nomenclature may in some cases depart from the more usual notation in certain disciplines. Although some components of SMM could be approached in any one of several alternative ways, in each case the selected approach or technique has been that offering the optimum combination of adequacy for the intended purpose, acceptance in contemporary technology, simplicity, and availability of input data. It is recognized, of course, that in some cases more rigorous or academic avenues could be taken. It is believed, however, that the results obtained would not be improved in any significant degree, nor would such further complication of an already complex problem be justified.

Spectral Response, or Demand

The concept of spectral response, or the peak response of a simple one-degree-of-freedom elastic damped oscillator to a time history of ground motion, is adopted as the best single index of damage potential. The spectral response diagram and its determination has been described many times in the literature[4,5,6,7,8] and will not be repeated here. Under the generally acceptable assumption that for structures the peak motion is generally harmonic in nature, there is a simple relationship between peak relative response velocity, S_v, peak relative response displacement, S_d, and peak absolute response acceleration, S_a.[8] For convenience, especially with four-way log plot spectra, S_v is used in SMM as the basic parameter for the ground motion "demand" on the structure. A standard damping value of 5% of critical damping is used but an adjustment factor is introduced for cases where 5% would not be a reasonable value.

Yield Value, or Capacity

The "capacity" of the structure to resist a particular response spectrum at its fundamental mode period without exceeding its yield value is developed in consideration of the materials, strength, and characteristics of the structure; its relationship to the simple oscillator of the spectrum development; the probable effect of simultaneous motion in more than the fundamental mode; and other considerations. Capacity is indicated in terms of velocity units as is demand, but in the determination of capacity one may work in more conventional acceleration or displacement terms; the values are simply converted to velocity units by the use of the harmonic assumption and proper factors. If the demand should exceed capacity there would be damage, and if it should not there would not be damage, by definition. The amount and the type of damage would depend upon the inelastic characteristics of the structure and other parameters, all of which constitute another step in SMM to be described subsequently. A complication that may occur in the damage criterion noted above is related to how capacity and damage are defined. For example, the conventional method of using only structural elements in determining yield value may underestimate the capacity, or, conversely, there may be nonstructural elements subject to damage or failure before the structural yield capacity is reached. It is thus desirable either to consider all the building elements in analysis or to use empirical data which automatically embraces all the elements.

The determination of capacity is one of the most difficult and important aspects of the problem. Another is the relationship of damage to deformation beyond the yield point.

Random Variables and Probability Considerations

The discussion thus far has implicitly considered demand and capacity to be definite or to have deterministic values. In addition, the natural fundamental mode period is needed in the comparison of demand

and capacity and thus, implicitly at least, has been a deterministic value. The facts are, however, that the problem embraces countless random variables and uncertainties because of their probabilistic distributions and also because of errors or unknowns in available data. There would be some uncertainty in dealing with only one ground motion and one structure. In dealing with a whole large area and hundreds or thousands of structures, the uncertainties and variations from the expected average or median conditions are expanded. Thus SMM employs probabilistic models rather than finite values for demand, capacity, and period. The problem is to obtain appropriate models and to evaluate properly the model parameters, often with only limited data.

It is known that response spectra amplitude distributions are generally rather highly skewed with most of the values on the low side bounded by zero, and with low probabilities of high or extreme values with bounds which mathematically extend to infinity but which in a more practical sense are limited by physical constraints not yet fully evaluated. The lognormal distribution has been used in SMM but any appropriate probabilistic model can be employed.

Capacity also has limits on both the low and high side but it is not generally expected to be skewed very much, if at all, according to available test data of materials and structural elements. Thus, if the coefficient of variation is not so large as to lead to a significant number of negative values, a Gaussian distribution may be acceptable. Sometimes a lognormal or other zero-bounded distribution can be used with parameters so as to cause minor skew characteristics.

Period is often quite uncertain but is not usually too sensitive a variable in the process if smoothed spectra are used. A uniform distribution has been used successfully.

The mathematics in combining these various distributions can become difficult and costly. The Monte Carlo technique with random numbers has been used in SMM computer runs with good results where sufficient trials are made.

Units, Zones, and Categories

The above consideration of SMM with regard to demand, capacity, and random variables would apply in general to one demand and to one class of structure. The real problem, however, is that for a natural earthquake or an underground nuclear explosion there are countless levels and types of ground motion to be considered and perhaps hundreds of types of structures. In SMM the predicted (or actual) ground motion is discretized into convenient and representative spectra based upon typical soil conditions. For example, a small town at some distance from the energy source may be represented by one spectrum. Correction factors are introduced for significant soil variations and for structure variations from the typical. Structures are classified into as many types and categories as may be deemed necessary.

Output

A whole region, state, or country can be analyzed for damage in one computer run. The output, for each area of interest, is the estimated damage and the probability of that estimate being exceeded. Thus there is a damage estimate for any desired confidence level.

UNITS, ZONES, SOIL FACTORS, CONDITION FACTORS

The first step is to break the area of interest -- that area to be subjected to the ground motion -- into units. A unit is defined as a convenient part of the overall area that will be subjected to essentially the same response spectrum. A city or a town at some distance from the energy source would be a typical unit providing there is no reason to predict a significant variation in the motion over the area of the city. However, if part of the city should be on rock and part on soft alluvium, there may well be two different ground motion predictions. In such cases there would be two units for the city.

Each unit is subject to division into zones. There may be one or more reasons for this, but the controlling ones would normally be soil conditions and conditions of the structures. For example, there may be only one ground motion prediction for a city, but soil conditions may vary sufficiently within the city to warrant separate zones -- for example, firm, dry alluvium and soft, saturated alluvium. Or one portion of the city may be old, with buildings in very poor condition, while another portion may have contemporary buildings designed to an earthquake code and in good condition. Each zone has an assigned factor for soil conditions, S_z, and for general structural condition, C_z.

If the soil conditions under and about the buildings and other structures in a zone are typical of the soil conditions contemplated in the ground motion prediction, S_z is simply unity. If the soil is particularly better or worse than contemplated, S_z is changed to values below or above unity, respectively. S_z is a local soil factor intended to express the variations in damage due to variations in soil from the overall (average) condition assumed. For example, if firm, dry alluvium is the basis for the ground motion prediction but a certain zone has soft, saturated

material, S_z for that zone might be assigned a value greater than unity. The important point is that the factor is for relative soil conditions. Data are being accumulated on these factors. Currently they must be largely subjective. The values of S_z would rarely, if ever, fall outside the range of 0.5 to 3.0.

C_z would normally be unity. However, this factor is provided for use in special cases where condition is obviously very poor and more than average damage (a high percentage of total damage, or collapse) is expected. Old buildings, in poor condition and with no lateral force provisions in their design, would rate a factor greater than unity. A zone with exceptionally resistant buildings would be assigned a factor less than one. C_z will vary from unity only where the structures vary from assumptions made in assigning the factors to be described subsequently. C_z might vary from as low as 0.3 to 4 or more.

Figure 1 indicates a hypothetical unit, such as a city, situated so far from the source of energy that the ground motion will not vary significantly over the unit because of variations in radial or epicentral distance. The ground motion has been predicted for the normal soil conditions in the area, as for example in zones 1 and 2. Because of the combination of soil conditions and building conditions in this unit, it would be divided into four zones, as shown. As an example, the soil and condition factors might be assigned as shown in Table 1.

TABLE 1

HYPOTHETICAL SOIL AND CONDITION FACTORS

Zone, Z	Soil Factor, S_z	Condition Factor, C_z	S_zC_z
1	1.00	1.00	1.00
2	1.00	1.20	1.20
3	1.30	1.00	1.30
4	1.30	1.20	1.56

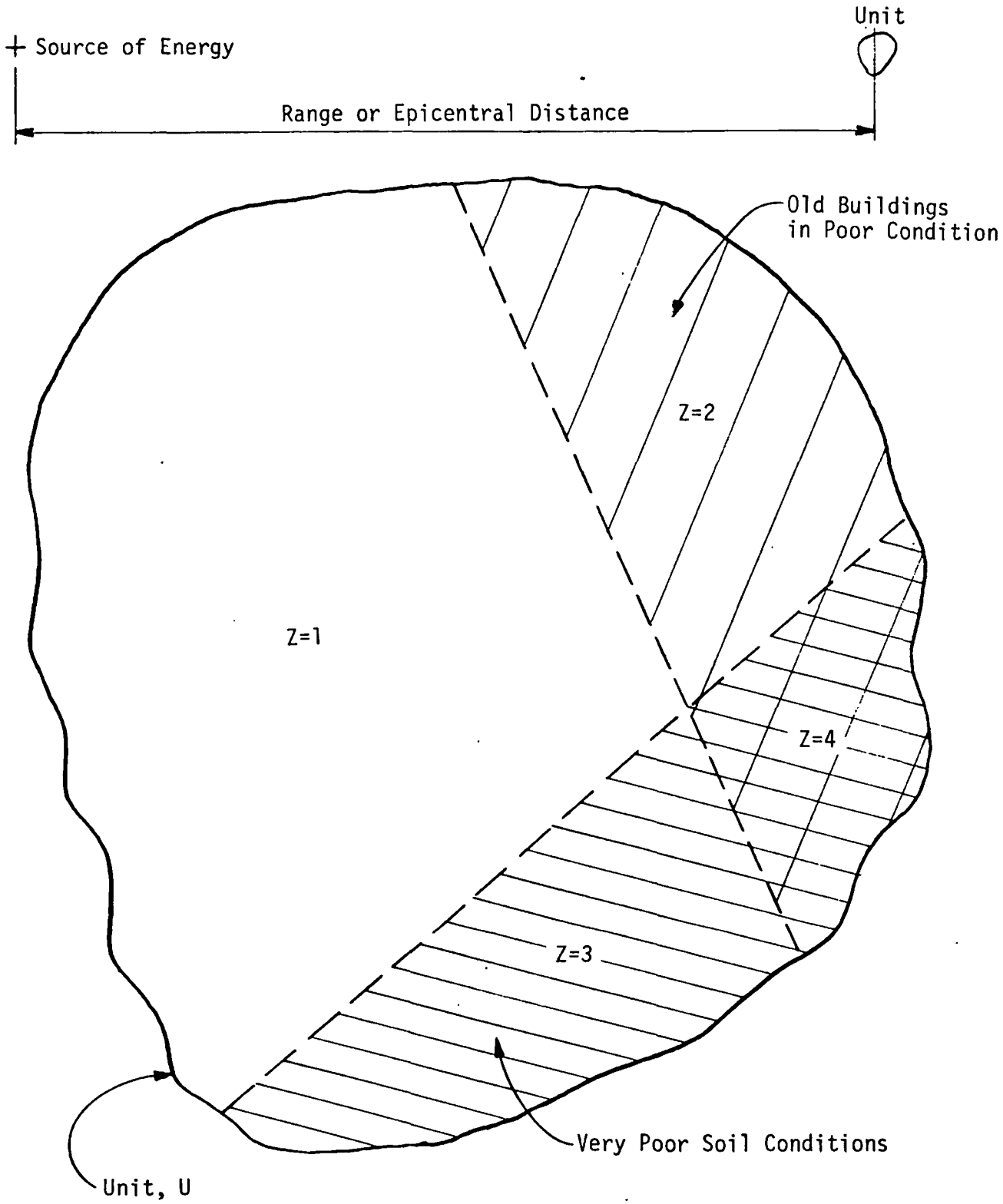

FIGURE 1 - A HYPOTHETICAL UNIT

STRUCTURE CLASSIFICATIONS

The buildings in each unit are divided into classifications or types, based upon such parameters as the number of stories, type of occupancy, type of framing, natural fundamental period, materials, strength, and inelastic properties. There are, of course, many possible categories, and these may vary from place to place. A tentative tabulation and terminology used in Nevada has been developed, based upon results of structure studies thus far. It will be extended as more data become available. In other areas or countries where construction is different, other categories have been used.

Table 2 shows building classes currently used for damage estimates in Nevada. The last column shows the range of fundamental periods for each category.

Table 3 shows mean capacity values for the various building classes in terms of displacement, velocity, and acceleration ranges. The capacity is defined as that demand value which reaches the first yield point stress of any material in the structure. The capacities shown have been obtained from estimates of base shear capacities in terms of a fraction of gravity, which have then been converted under the assumption of simple harmonic motion at maximum response to corresponding velocity and displacement ranges. Data developed in the AEC structural response program, indicate that there is little error associated with these assumptions, at least in light of the overall problem of damage estimation.[8,12] Several of the capacities have also been modified using data from known nondamaging response levels in Nevada and from estimates of the possible statistical variations. They are tentative since further modifications are expected with additional empirical data.

TABLE 2

BUILDING CLASSES FOR NEVADA TEST SITE
UNDERGROUND NUCLEAR DETONATIONS

Building Class	Description	Fundamental Period Range, sec.
1	Adobe buildings, 1-story	0.05 - 0.15
2	Adobe buildings, 2-story	0.15 - 0.20
3	Brick and stone buildings, 1-story	0.05 - 0.15
4	Brick and stone buildings, 2-story	0.15 - 0.20
5	Wood frame, 1-story	0.05 - 0.15
6	Wood frame, 2-story	0.15 - 0.20
7	3- to 5-story commercial	0.20 - 0.40
8	6- to 8-story commercial	0.30 - 0.50
9	6- to 8-story commercial	0.51 - 0.80
10	6- to 8-story commercial	0.81 - 1.00
11	Las Vegas high-rise	0.65 - 0.90
12	Las Vegas high-rise	0.91 - 1.30
13	Las Vegas high-rise	1.31 - 2.00
14	Salt Lake City high-rise	0.65 - 1.80
15	Reno high-rise	0.65 - 1.80

TABLE 3

ESTIMATED BUILDING CLASS MEAN CAPACITIES

Building Class*	Displacement, cm	Velocity, cm/sec	Acceleration, g's
1	0.04 - 0.12	5	0.21 - 0.64
2	0.17 - 0.22	7	0.22 - 0.30
3	0.06 - 0.19	8	0.34 - 1.02
4	0.29 - 0.38	12	0.38 - 0.51
5	0.10 - 0.29	20	0.51 - 1.54
6	0.48 - 0.64	25	0.64 - 0.85
7	0.80 - 1.60	25	0.40 - 0.80
8	1.30 - 2.00	25	0.32 - 0.53
9	2.40 - 3.82	30	0.24 - 0.38
10	5.10 - 6.35	40	0.26 - 0.32
11	4.37 - 5.10	35	0.25 - 0.34
12	6.08 - 9.30	45	0.22 - 0.34
13	9.30 - 12.88	45	0.16 - 0.22
14	5.20 - 14.30	50	0.18 - 0.49
15	5.68 - 15.74	55	0.20 - 0.54

* As in Table 2

DOLLAR EXPOSURE, E_{zk}

For each unit, zone, and building class there is a dollar exposure, E_{zk}. This is defined as the cost in dollars in each unit should all structures in building class k zone Z be completely destroyed, or if damage should be so great as to make replacement as economical as repairs. Various considerations may be involved that would indicate other than fair replacement cost. For example an original $10,000 house may have appreciated to a current value of $20,000, but if destroyed it would cost $30,000 to replace it with a new structure. The owner may not be able or want to pay the difference in cost between a new house and the current value of the old house. This question involves legal, moral, appraisal, and policy factors. The value of E_{zk} to be used should be that which most closely represents the anticipated cost if damage should be total.

There may be tax assessment or other official data that would be useful in assigning E_{zk} values. On the other hand there may be a sparsity of useful information, and a survey combined with typical cost estimates may be employed. If all else fails, factors may be employed to estimate the number and value of various classifications according to population. For example, there may be 1 residence to every 4 persons, 1 church to every 1000 persons, etc. Another method is to use one representative city or town as a model for others in determining ratios and costs. When little damage is expected, such approximate methods may be satisfactory.

THE SPECTRAL MATRIX SYSTEM

The spectral matrix is superimposed on four-way logarithmic graph paper as shown in Figure 2. There are nine columns or period bands, which correspond to those of the proposed Engineering Intensity Scale.[3] Many classes of structures would fall into one period band, based upon the periods of their estimated fundamental modes. However if a category has periods which extend into two or more bands, its total value, E_{zk}, is simply prorated to those bands by a period vector, as will be shown.

The horizontal rows represent intensity levels based upon predicted or actual 5%-damped pseudo relative velocity, S_v. The rows shown in Figure 2 correspond with those for the Engineering Intensity Scale. Table 4 gives the S_v values for the lower bounds of the rows. There are actually ten rows or intensity levels, although the lowest row is not shown in Figure 2. Some changes for standardization purposes have been made in the row spacing from that used in earlier versions of SMM. For high speed computer operations the rows are not used. Instead, the computer programs operate directly with S_v values and their probabilistic variations.

In the matrices, period bands are given the subscript j (from 1 through 9) and intensity levels if used as such are given the subscript i (from 0 through 9).

The spectral grid provides a convenient classification scheme for correlating observed damage with observed ground motion. It can be used for damage prediction directly if a deterministic estimate of the response spectrum can be provided. Of interest is the relative value of S_v or demand, and yield strength or capacity; in the same units, of course. From these and the inelastic properties, the damage factor F is obtained. It is assumed that damping is 5% of critical. Data available show that this is a reasonable average value. Special variations are provided for with a correction factor.

It is to be noted that the yield value represents the point up to which there would be no damage; thus it is a damage threshold.

Another assumption is that maximum building response is largely in the fundamental mode and is harmonic in nature. Conversions can then readily be made between acceleration, velocity, and displacement in terms of the fundamental mode period. Adjustment factors (subsequently introduced) provide for the effects of other modes than the fundamental and for other conditions.

TABLE 4

LOWER BOUND S_v VALUES FOR THE MATRIX ROWS
(FOR 5% OF CRITICAL DAMPING)

Matrix Row*	S_v Values		
	cm/sec	in./sec	ft/sec
9	300	118	9.84
8	100	39.4	3.28
7	60	23.6	1.97
6	30	11.8	0.984
5	10	3.94	0.328
4	4	1.57	0.131
3	1	0.034	0.0328
2	0.1	0.039	0.0033
1	0.01	0.0039	0.00033
0	0	0	0

* Also EI Scale intensity level

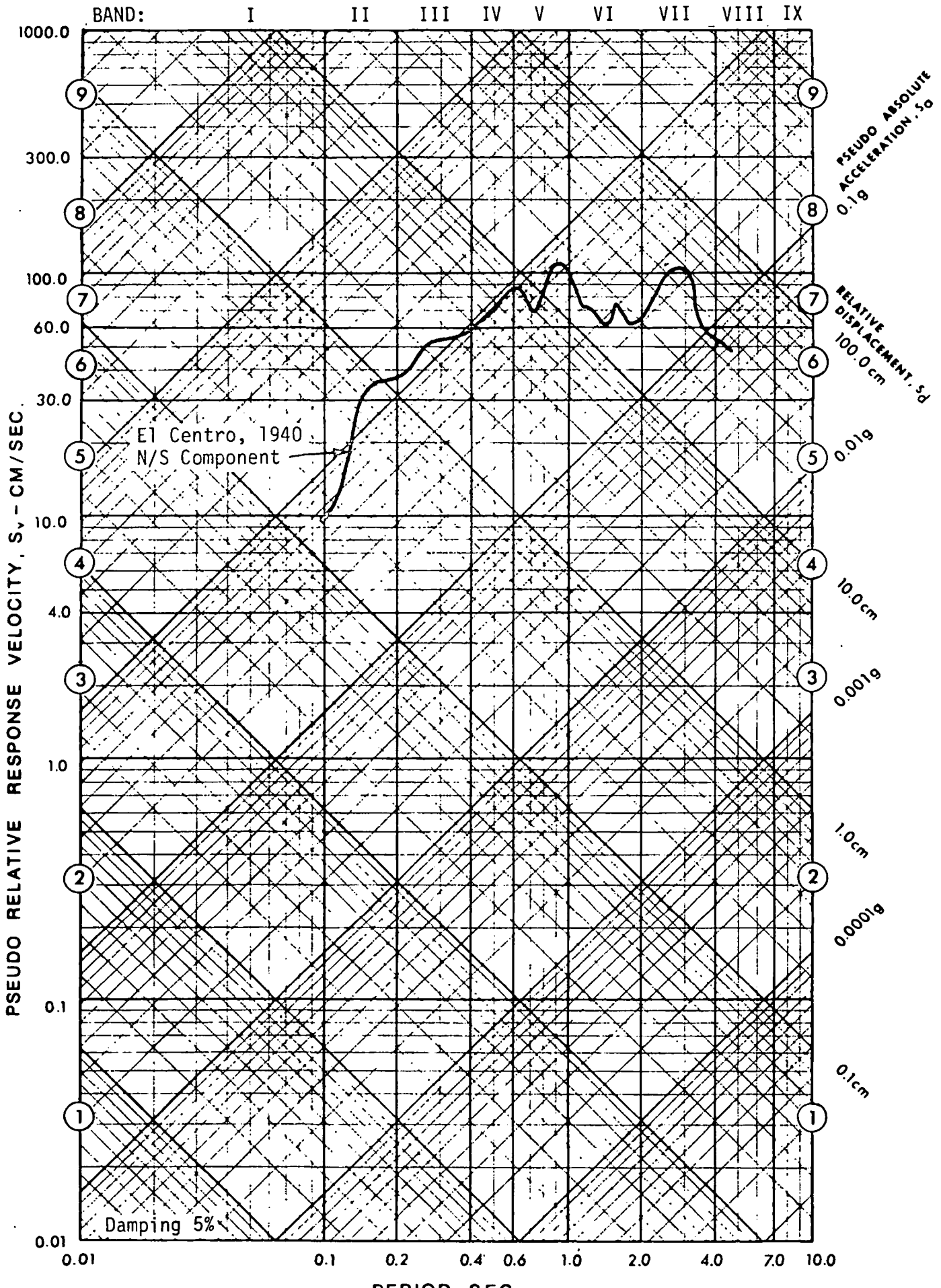

FIGURE 2 - SPECTRAL MATRIX WITH EXAMPLE SPECTRUM

DEMAND

It has been concluded after much study that the best single parameter for demand is the spectral response of simple oscillators to a time history of ground motion. Each oscillator is a single-degree-of-freedom elastic system with viscous damping. For convenience the response is considered in terms of relative response velocity, S_v. A standard damping value of 5% of critical damping is used, with a factor Ψ as shown in Figure 3 to provide for any necessary adjustments in demand due to other damping values. The curves in Figure 3 were obtained from a study of response spectra from events JORUM and BOXCAR as recorded in the Las Vegas area. Thus demand is $S_v\Psi$ where S_v is for 5% damping at the period of interest.

Demand is in the familiar terms of spectral response velocity which can be computed from a time history of ground motion.[8] Demand can also be predicted directly from results of studies of past ground motion,[12] using parameters such as energy at the source,[11] the conditions at the source and at the point of reception, the depth of the source, the distance from the source to the recording station, etc.

There is no commitment necessary, or intended, that velocity is more meaningful than acceleration or displacement. Under the assumption of harmonic motion of the structure, the relative response velocity can be readily transformed to acceleration or to relative displacement using the following equations:

$$S_v = \omega S_d = \frac{S_a g}{\omega} \qquad (1)$$

$$S_a = \frac{\omega^2 S_d}{g} = \frac{\omega S_v}{g} \qquad (2)$$

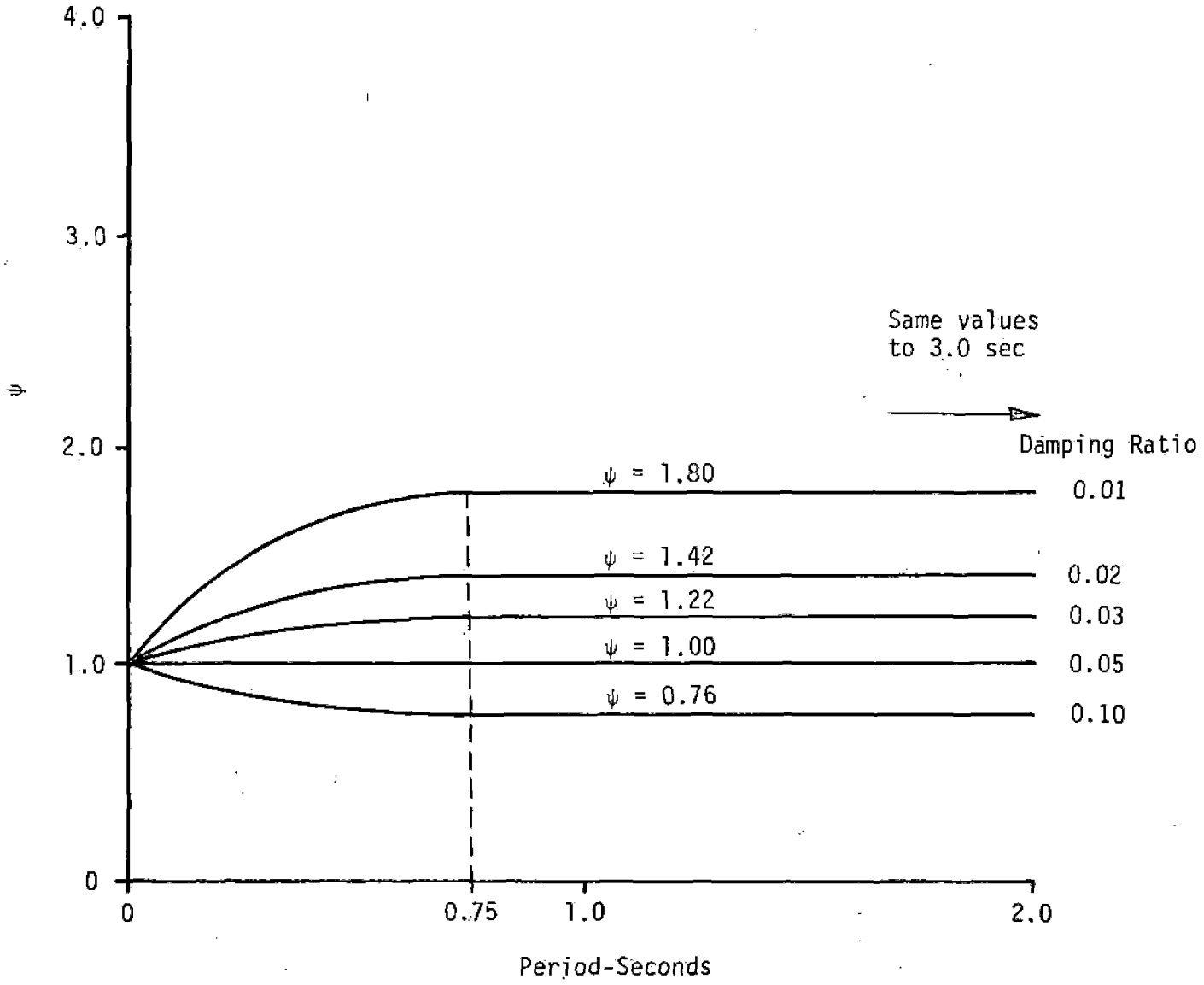

FIGURE 3 - ψ FACTORS FOR SEVERAL DAMPING RATIOS

in which

S_v = spectral value of response velocity relative to the ground; cm/sec

S_a = spectral value of the absolute acceleration as a fraction of gravity; dimensionless

S_d = maximum displacement relative to the ground during the time history of acceleration; cm

ω = undamped natural circular frequency; radians/sec

g = acceleration of gravity; cm/sec^2

The ground motion parameters and spectral response velocity are random variables with highly skewed probabilistic distributions. Studies are being conducted on the most appropriate models and parameter values. SMM is able to operate under any probabilistic distribution. However, thus far only the lognormal form has been utilized. It will therefore be used herein as an example to explain the procedure.

Let the median or most probable value of S_v taken from the spectral diagram be designated $\tilde{S}_v$; N be the geometric standard deviation; Y_s be a normally distributed random variable with mean equal to 0 and standard deviation equal to 1.

Then,

$$\text{Demand} = D = \tilde{S}_v \Psi N^{Y_s} \qquad (3)$$

Values of N may vary from period band to period band and are based upon data samples and other considerations. The values employed have ranged from 1.2 to 3.0. It can be demonstrated that the above expression is in lognormal form.

CAPACITY

Capacity is arbitrarily defined herein as the level of demand at which the yield point of the real structure is first exceeded. The yield point may be considered as the threshold of damage at which initial distress such as cracking or stretching would start to occur in any material or element.* This involves many important factors such as the elastic strength, the response amplification to ground motion relative to that of a simple oscillator, modal contributions, damping, and probabilistic variations from the mean or median value. The response in the inelastic range is considered separately under the determination of the damage factor, F.

It is convenient to use base shear value as a basis for determining capacity. The shear applied to the base of the building by the ground motion can be related to the ground motion characteristics coupled with those of the building. Approximate methods are used in SMM to decrease the labor and cost and because on a broad basis involving many structures the results are satisfactory. Critical buildings should have individual analyses by more rigorous methods. The base shear that causes yield somewhere in the building (the capacity) can in turn be converted into the spectral velocity that would lead to that base shear, and thus have a capacity value in the same units as demand. It is important to note that no building is a simple oscillator and thus adjustments are required.

---

* NOTE: The definition applies to any material or element. If it can be established or modeled that some nonstructural element would reach its yield value prior to the main structural system or element, that element under further distortion would offer some resistance, even though perhaps minor, and it would show the initial distress. However, in many cases and in the present state of knowledge, the structural system is often considered as the control for capacity.

First it will be assumed that the problem is deterministic and that the structure is a single-degree-of-freedom system for which

$$V_y = C_y W \tag{4}$$

in which

V_y = the base shear causing yield stress; kips (a kip is 1000 pounds)

C_y = the base shear coefficient causing yield stress; dimensionless

W = the total seismic weight of the structure, or all dead weight and attached or confined live load above the base; kips

It can be shown from Equation 4 and Newton's second law that $C_y = S_{a_y}$.

But $S_{a_y} = \omega S_{v_y}/g$ by harmonic motion (Equation 2), and therefore since $C_y = S_{a_y}$,

$$S_{v_y} = \frac{C_y g}{\omega} \tag{5}$$

The real building is not an idealized single-degree-of-freedom system and it may be subject to other simultaneous responses than that of the fundamental mode. These increase stresses and lead to yield at lower values of C_y and S_{v_y} than if only the fundamental mode is considered. A factor, λ, will be introduced to reduce the fundamental mode yield value velocity, S_{v_y}, to account for these effects of multi-modal activity.

Another important consideration is that a multi-degree-of-freedom system has different responses than a single-degree-of-freedom system and it thus has a different base shear capacity than such a

simple system. This is a somewhat complex consideration involving so-called participation factors in each mode of interest. These participation factors are based on the distribution of mass and stiffness throughout the building, mode shapes, and the distribution of forces and shears throughout the height relative to the capacity at various height levels. Although rigorous solutions can be reached for specific models, only simple approximations and adjustments are made in SMM to allow for these multi-degree-of-freedom responses. This is considered adequate and well within the basic objectives of SMM since SMM is of general application to groups of buildings rather than to individual structures. A factor, α, will be introduced for these considerations.

The median yield point capacity of each class of building is thus determined in velocity units (to correspond to the demand units), as follows:

$$\widetilde{C} = \frac{C_y g}{\omega} \alpha\lambda \qquad (6)$$

also

$$\widetilde{C} = S_{v_y} \alpha\lambda \qquad (7)$$

But capacity is also a random variable and variations from the median are expected. Tests of various materials and structural elements indicated that for a large population of structures capacity at yield varies in a reasonably symmetrical manner from the median value. If the coefficient of variation is not too large (say less than 0.25 or 0.30), the probability distribution can be considered Gaussian. In such case the median would equal the mean value ($\widetilde{C} = \overline{C}$) and the standard deviation, σ_c, can be defined as

$$\sigma_c = \overline{C}\, C_v \qquad (8)$$

wherein

C_v = the coefficient of variation of capacity

Let

Y_c = the standardized normal variate with mean = 0 and standard deviation = 1

Then,

$$C = \overline{C} + Y_c \sigma_c \tag{9}$$

or,

$$C = S_{v_y} \alpha\lambda + Y_c \sigma_c \tag{10}$$

or,

$$C = \frac{C_y g \alpha \lambda}{\omega} + Y_c \sigma_c \tag{11}$$

Table 3 provides sample values of S_{v_y} for certain classes of buildings in the velocity column. The last column provides C_y values because C_y equals S_a when S_a is in g units. The range of values is due to period, or ω variations.

The values of σ_c may be obtained with Equation 8 if C_v and $\overline{C}$ are known. The coefficient of variation C_v may be estimated by analogy to material and member tests. Much more is to be learned about the value for real buildings. To date C_v values of 0.20 to 0.40 have been used. The determination of α and λ will be discussed in the following sections.

The Factor α

Few structures can properly be modeled as one-degree-of-freedom systems, as was assumed -- for preliminary computations only -- in determining C_y. Factor α is intended to provide a partial correction (for the fundamental mode) for the fact that the real building has different properties than the simple oscillator assumed for the purpose of

obtaining C_y. Factor λ provides correction for higher mode participation.

Most buildings can be modeled as lumped-mass systems with one mass for each story. The fundamental mode response (which is pertinent to factor α) may be more or less than the spectral response, S_v or S_a, depending upon the mass distribution, the mode shape, and the story under consideration. Equations 12 and 13 show relationships for story shear for any mode i.

$$V_{iz} = \gamma_i \omega_i S_{v_i} \left(\sum_{y=n}^{z} m_y \phi_{iy} \right) \tag{12}$$

$$V_{iz} = \gamma_i S_{a_i} g \left(\sum_{y=n}^{z} m_y \phi_{iy} \right) \tag{13}$$

in which

V_{iz} = the shear from mode i response, in the story between level z and z - 1, with z numbered from the base up; kips

γ_i = the participation factor for mode i, with ϕ_{in} equal to unity; dimensionless

m_y = the mass of story y; kip cm^{-1} sec^2

ϕ_{iy} = the modal deformation of story y in mode i relative to the top story deformation; dimensionless

Subscripts:

i = mode number

y, z = mass or floor number, starting with the first floor above the base as 1

n = number of masses or floors; value of y or z for top mass

$$\gamma_i = \frac{\sum_y m_y \phi_{iy}}{\sum_y m_y \phi_{iy}^2} \qquad (14)$$

If the masses and mode shapes are known the story shears can be determined for any given response spectrum value. In many cases they may not be known or there may be too many buildings for specific analyses. It is desirable therefore to consider the lateral inertia forces on a hypothetical basis for the purpose of making damage estimates on a broad scale.

Figure 4 shows six idealized fundamental mode shapes. Some buildings have mode shapes like cases (a), (b), or (c). Case (d) represents a system with one effective degree of freedom. Case (e) represents a typical shear system and case (f) a flexural or cantilever-type system.

There will be different patterns of inertial forces, story shears, and moments along the height of a building depending upon the mode shapes and the modal superimpositions existing at any instant. This becomes a very complex problem which can only be approached probabilistically or by specific solution for each structure and ground-motion time history. Insofar as α is concerned, there are two considerations: (1) the base shear adjustment for the multi-mass system, and (2) a possible further reduction of the base shear value due to some higher story being more critical than the first story under a reasonable assumption of mode shapes and modal combinations.

Figure 5 shows how the base shear coefficient C_b varies relative to S_a for the various idealized fundamental mode shapes of Figure 4. With the exception of model f, the ratio of C_b/S_a is close to unity. Figure 5 was plotted under the assumption that the story masses are equal, so that the general equation, 15, for the fundamental mode,

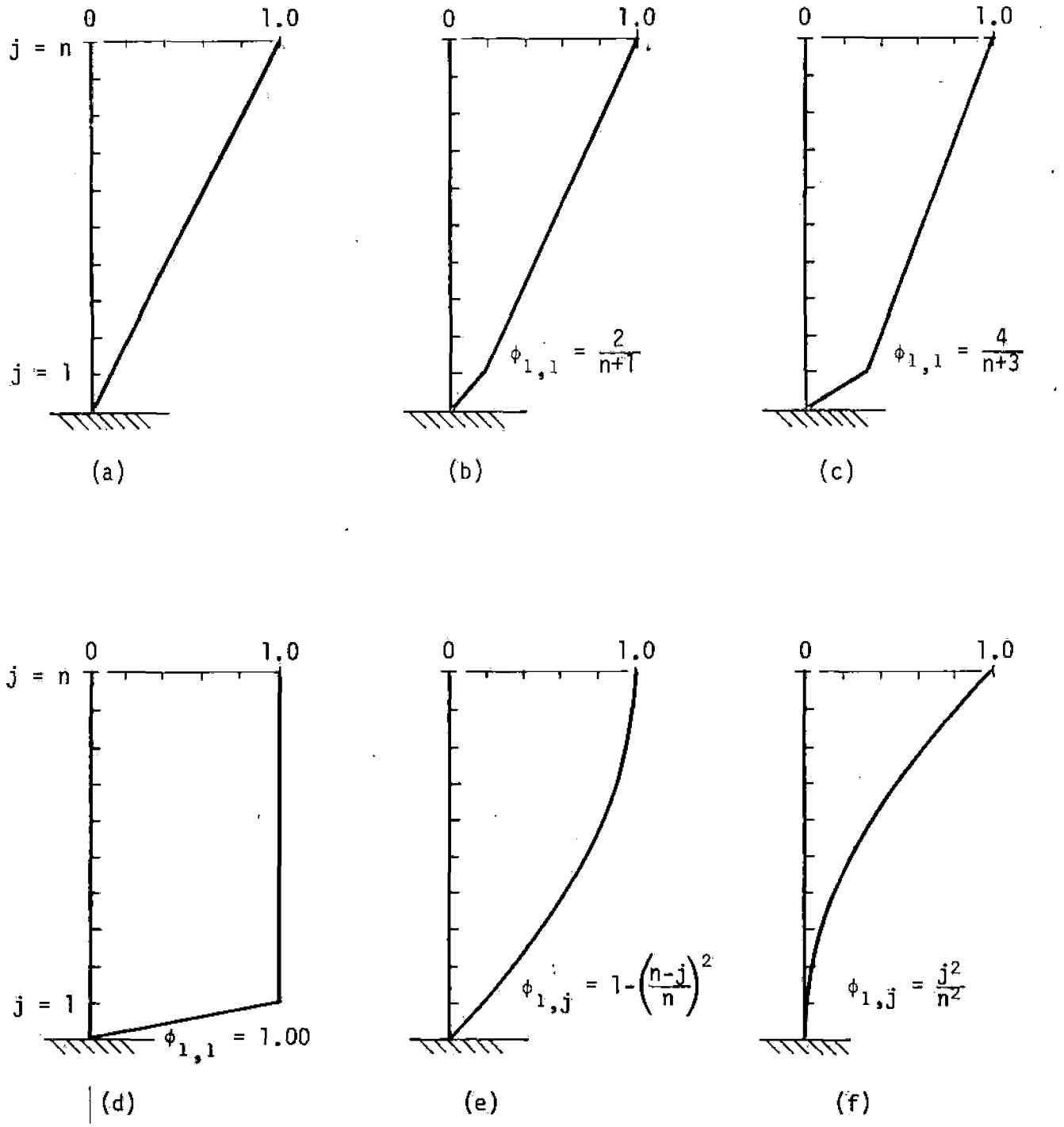

NOTE: Scale Applies Only To Special Case of n = 10

FIGURE 4 - IDEALIZED FUNDAMENTAL MODE SHAPES

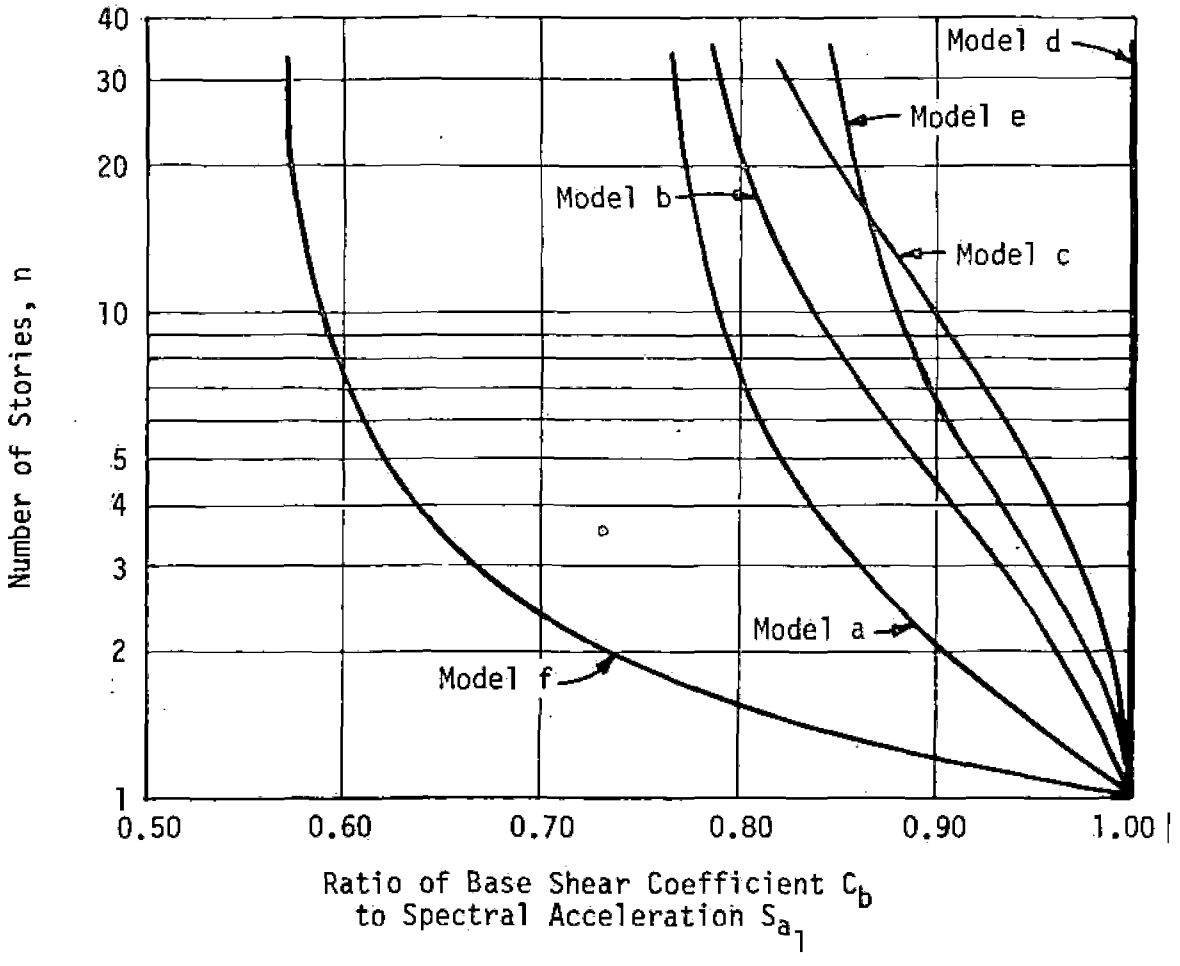

FIGURE 5 - FUNDAMENTAL MODE BASE SHEAR RATIOS FOR MODELS WITH UNIFORM STORY HEIGHTS AND MASSES

$$\frac{C_b}{S_{a_1}} = \frac{\left(\sum_{y=n}^{1} m_y \phi_{1y}\right)^2}{\left(\sum_{y=n}^{1} m_y\right)\left(\sum_{y=n}^{1} m_y \phi_{1y}^2\right)} \qquad (15)$$

reduces to the simpler form of Equation 16,

$$\frac{C_b}{S_{a_1}} = \frac{\left(\sum_{y=n}^{1} \phi_{1y}\right)^2}{n\left(\sum_{y=n}^{1} \phi_{1y}^2\right)} \qquad (16)$$

The Uniform Building Code[13] seismic design requirements are based upon the assumption of inverted triangular inertial forces. This idealization implies a straight-line modal deformation as in Figure 4(a). The same assumption is used in SMM unless other more pertinent data should be available. Thus the value of C_b/S_a may be taken from curve a of Figure 5.

The next phase of determining α is locating where in the building the story shear first becomes critical. Buildings designed for only wind forces often have a critical story or stories at a high level rather than in the base story. The base story value would then be decreased proportionally to the overstress at the higher level in order that "capacity" just be reached.

Figure 6 shows the seismic forces and story shears for a ten-story building with assumed equal masses and story heights. It also shows the forces and story shears for an assumed uniform wind force design requirement with the wind base shear normalized to the seismic value. In this case, if the structure were designed only and exactly to the wind requirements, the seismic base shear value of 550 kips would have to be reduced to avoid overstress at the upper levels. The seismic capacity would only be 0.55 × 550 or 302 kips allowable base shear.

The apparent base shear must be corrected by the minimum ratio of provided story shear value to the apparent value from C_b and the inverted triangular force distribution, called the seismic shear demand. Thus, we come to the definition of α as in Equation 17,

$$\alpha = \left(\frac{S_{a_1}}{C_b}\right)\left(\frac{\text{Provided Shear Value}_y}{\text{Seismic Shear Demand}_y}\right)_{min} \qquad (17)$$

For example, in the building of Figure 6 and with $C_b/S_{a_1} = 0.79$ from Figure 5 for 10 stories and model (a),

$$\alpha = \left(\frac{1}{0.79}\right)\left(0.55\right) = 0.70$$

The Factor λ

There is an infinite variety of modal superimpositions, especially in tall, slender buildings. Up to this point it has been assumed that only the fundamental mode contributed to stress. There is no easy solution to the question of how much higher modes will add to the fundamental mode stresses, or whether the higher mode stresses will dominate in some parts of the structure. However, some knowledge is available as an aid to judgment in approaching this problem.[8] Where buildings are situated at considerable distances from the energy source, the fundamental mode seems to dominate the response at least under the maximum or controlling conditions. Reference 8 provides data on fundamental, second mode, and third mode contributions to maximum top-level accelerations under response to nuclear event ground motion. On the average the fundamental mode contributed 87% of the maximum top-level acceleration, although in one case the value was only 55%. If the former figure were used, λ would be 0.87; and with the latter value it would be 0.55, to reduce the capacity based only upon assumed fundamental loading. Consideration should be given to the location of critical stresses in the building. In general if the upper levels are critical λ should be smaller. If the base is critical λ could be close to unity since

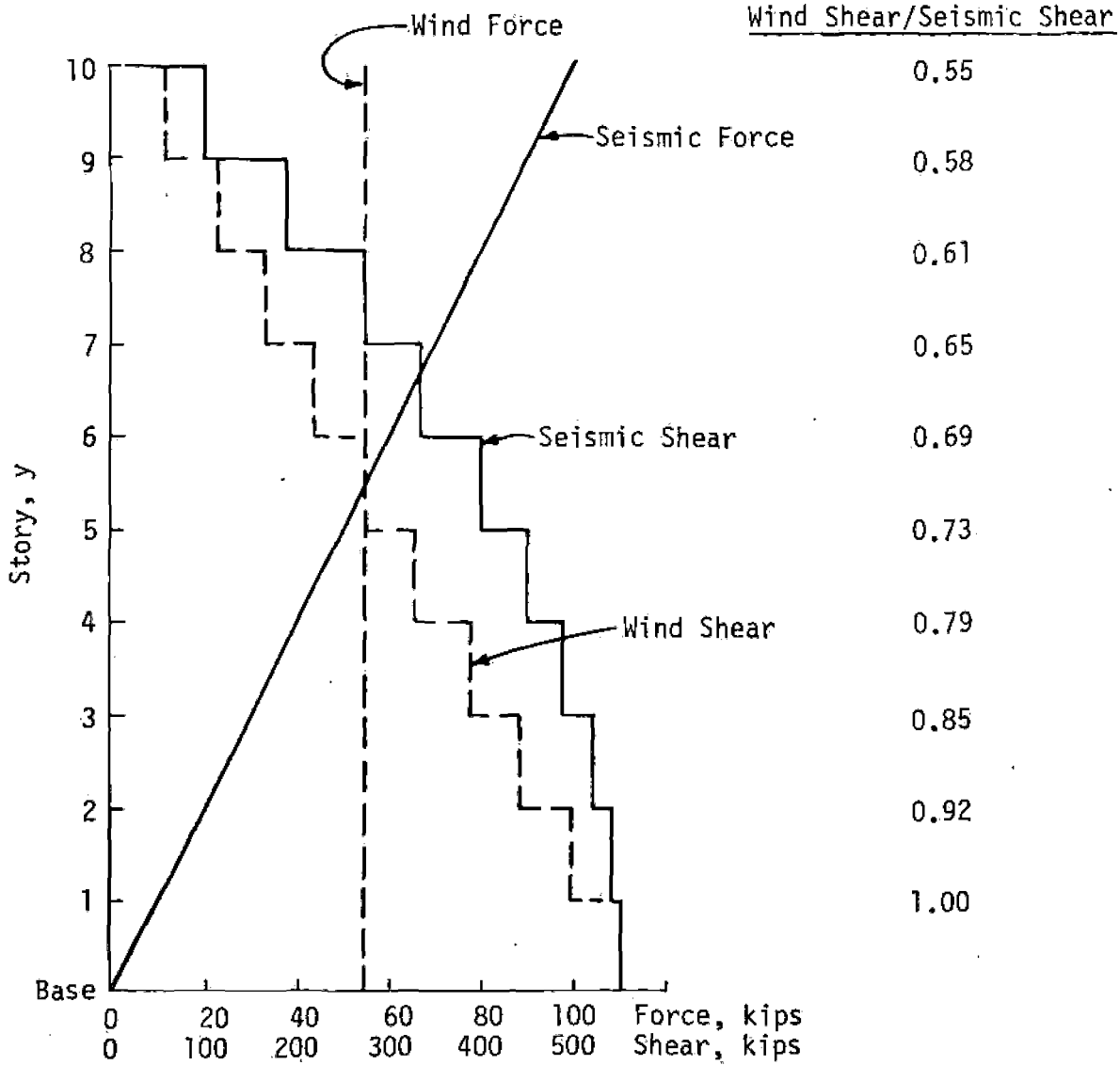

FIGURE 6 - FORCES AND SHEARS ON AN IDEALIZED BUILDING

the fundamental mode tends to dominate base stresses. Since biaxial loading may also be possible in some degree,[9] a λ value of 0.90 seems to be a reasonable maximum for tall buildings. If the building is small and the fundamental mode period is short λ may be close to unity. Good judgment is essential in this determination.

INELASTIC EFFECTS

In the preceding section it was assumed that the building response was elastic. If this were always true there would be no damage since the capacity is related to the yield point. In this section behavior in the inelastic range beyond the yield point is considered. One way to approach inelastic behavior is to develop spectral response curves for inelastic rather than elastic models. Because of the many possible sets of characteristics in the inelastic range this becomes very complex in a procedure such as SMM that is concerned with many types of structures. A much more convenient and apparently reliable approach is to utilize the Reserve Energy Technique[14] with various idealized inelastic models. The following development will be on the basis of assumed one-mass systems as in the initial development of the yield base shear coefficient C_y but with the correction factors α and λ for certain multi-mass effects. For each case within the population there will be real values of demand capacity D and C, regardless of the probabilistic aspects of arriving at D and C. There may be a strong value of D (well above $\tilde{D}$) associated with a weak value of C (well below $\bar{C}$), or any other combination. The joint probabilities of each set occurring are computed in SMM. For the present discussion, it matters only that the sets D, C exist. The objective is to determine the extent of damage given D, C sets for various inelastic models.

Figure 7 shows seven types of inelastic models in terms of their force-deformation characteristics. Three basic types are shown; brittle (Model I), elastoplastic (Models II and III), and bilinear softening (Models IV, V, VI, and VII). General equations will be developed for each of these types with which other values of the parameters μ_{ult} and ρ can be used. Most structures can be idealized with the models in Figure 7. Other models can, of course, be developed if needed.

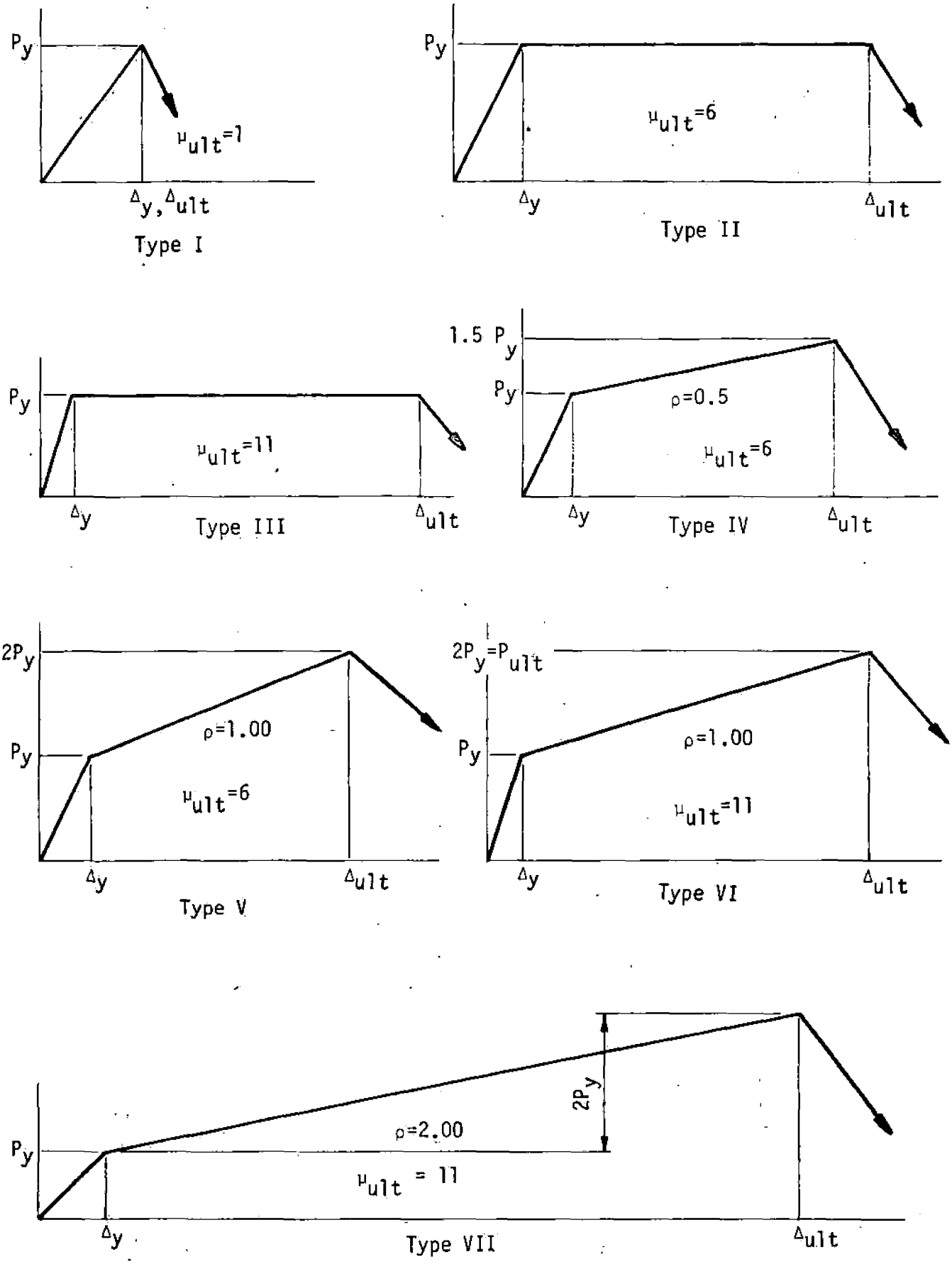

Note: Scale And Values Vary From Model To Model

FIGURE 7 - INELASTIC MODELS OF ASSUMED ONE MASS SYSTEMS

Assuming deterioration and period changes[7,14] are negligible for broad-scale SMM uses, common equations for all the models of Figure 7 are as follows:

$$S = \frac{P_y}{\Delta_y} \tag{18}$$

$$T = 2\pi\sqrt{W/gS} \tag{19}$$

$$P_y = C_y \alpha \lambda W \tag{20}$$

$$\Delta_y = \frac{C_y g T^2}{4\pi^2} \tag{21}$$

$$\mu = \frac{\Delta}{\Delta_y} \; ; \; \mu_{ult} = \frac{\Delta_{ult}}{\Delta_y} \tag{22}$$

$$\rho = \left(P_{ult} - P_y\right)/P_y \tag{23}$$

wherein

S = the stiffness in the elastic state; kips/cm

P_y = the force (or story shear) that causes yield in the one-mass model, modified for the multi-story α and λ effects; kips

P_{ult} = the ultimate force (or story shear); kips

W = the seismic weight; kips

T = the period in the elastic state; sec

Δ_y = the yield point distortion; cm

Δ = the total distortion; cm

μ = the ductility factor; dimensionless

ρ = as defined in Equation 23

If the oscillator remains elastic throughout the response period, the peak kinetic energy of the system can be taken as $\frac{1}{2}\frac{W}{g}\left(S_v\Psi\right)^2$. As an approximation to the real conditions, the peak response of a conservative system is obtained in the Reserve Energy Technique by setting the peak kinetic energy of the equivalent elastic system equal to the area under the force-deformation diagram of the inelastic system as follows:

$$\frac{1}{2}\frac{W}{g}\left(S_v\Psi\right)^2 = U_\Delta$$

where

U_Δ = the total of the energy stored and absorbed to deformation Δ

It can be shown that for the elastoplastic conditions of Models II and III,

$$U_\Delta = P_y\Delta_y\left(\mu - \frac{1}{2}\right) \tag{24}$$

and

$$\mu = \frac{1}{2}\left[\left(\frac{D}{C}\right)^2 \alpha\lambda + 1\right] \tag{25}$$

For the bilinear softening Models IV, V, VI, and VII,

$$U_\Delta = P_y\Delta_y\left[\mu - \frac{1}{2} + \left(\mu - 1\right)^2\frac{Q}{2}\right] \tag{26}$$

and

$$\mu = 1 - \frac{1}{Q} \pm \sqrt{\frac{1}{Q^2} - \frac{1}{Q} + \frac{\alpha\lambda}{Q}\left(\frac{D}{C}\right)^2} \tag{27}$$

in which

$$Q = \frac{\rho}{\mu_{ult} - 1}$$

for convenience.

D and C are from Equations 3 and 10, respectively. The above four equations are for μ values from μ_y to μ_{ult}. Note that if the product $\alpha\lambda$ is made equal to unity, then a D/C ratio of 1 corresponds to a μ-value of 1 as it should. This situation would apply to an idealized one-degree-of-freedom system.

RELATIONSHIP BETWEEN DUCTILITY AND DAMAGE

In this section, the ratio D/C is used. This actually represents demand and capacity sets D,C obtained from any combination of variations from actual central values. If the set should be the median values $\breve{D}$, $\breve{C}$ the results would be the same as deterministic. If probabilistic values are to be used on a large scale the procedures of the following sections are more practical, especially with computer support.

When the ductility ratio $\mu = 1.0$ the structure is at its yield point and damage is assumed to be zero. When $\mu = \mu_{ult}$, where μ_{ult} is defined as the point at which the structure deformation increases with decreasing force or shear (as indicated by the arrows in Figure 7), the damage is assumed to be total. The assessment of damage for intermediate values of μ is of necessity somewhat subjective and dependent on a great many factors not amenable to analytical treatment. It will be assumed that damage varies linearly between $\mu = 1$ and $\mu = \mu_{ult}$ for all models. Let F equal the ratio of damage to total damage. Then,

$$F = \frac{\mu - 1}{\mu_{ult} - 1} \quad \text{for} \quad \left(1 \leq \mu \leq \mu_{ult}\right) \tag{28a}$$

$$F = 0 \quad \text{for} \quad \left(\mu \leq 1\right) \tag{28b}$$

The assigned constant values of μ_{ult} are shown in Figure 7. From Equation 28,

$$\mu = F\left(\mu_{ult} - 1\right) + 1 \quad \text{for} \quad \left(1 \leq \mu \leq \mu_{ult}\right) \tag{29}$$

Equating Equations 29 and 25, there is obtained for any elastoplastic

model an expression for F,

$$F = \frac{\frac{1}{2}\left[\left(\frac{D}{C}\right)^2 \alpha\lambda - .1\right]}{\mu_{ult} - 1} \tag{30}$$

Using Equation 30, the data in Figure 7, and subscripts for the model number, there is obtained,

$$F_{II} = \frac{\alpha\lambda}{10}\left(\frac{D}{C}\right)^2 - \frac{1}{10} \tag{31}$$

and

$$F_{III} = \frac{\alpha\lambda}{20}\left(\frac{D}{C}\right)^2 - \frac{1}{20} \tag{32}$$

Likewise, using Equation 27 there is obtained,

$$F_{IV} = -2 + 0.632\sqrt{9 + \alpha\lambda\left(\frac{D}{C}\right)^2} \tag{33}$$

$$F_{V} = -1 + 0.448\sqrt{4 + \alpha\lambda\left(\frac{D}{C}\right)^2} \tag{34}$$

$$F_{VI} = -1 + 0.316\sqrt{9 + \alpha\lambda\left(\frac{D}{C}\right)^2} \tag{35}$$

$$F_{VII} = -0.5 + 0.224\sqrt{4 + \alpha\lambda\left(\frac{D}{C}\right)^2} \tag{36}$$

Damage would be total (F = 1) when the following values are reached:

Model	Value of $(D/C)(\alpha\lambda)^{1/2}$ when F = 1
I	1.00
II	3.32
III	4.58
IV	3.69
V	4.00
VI	5.56
VII	6.39

Figure 8 shows damage factors, F, plotted against $(D/C)(\alpha\lambda)^{1/2}$ for the seven model types. It is obvious that ductility is very beneficial in reducing damage.

Table 5 provides formulas for obtaining damage factors and damage estimates for zones, units, and areas in SMM.

In the following section, the joint probability relationships of various ratios of D/C are considered.

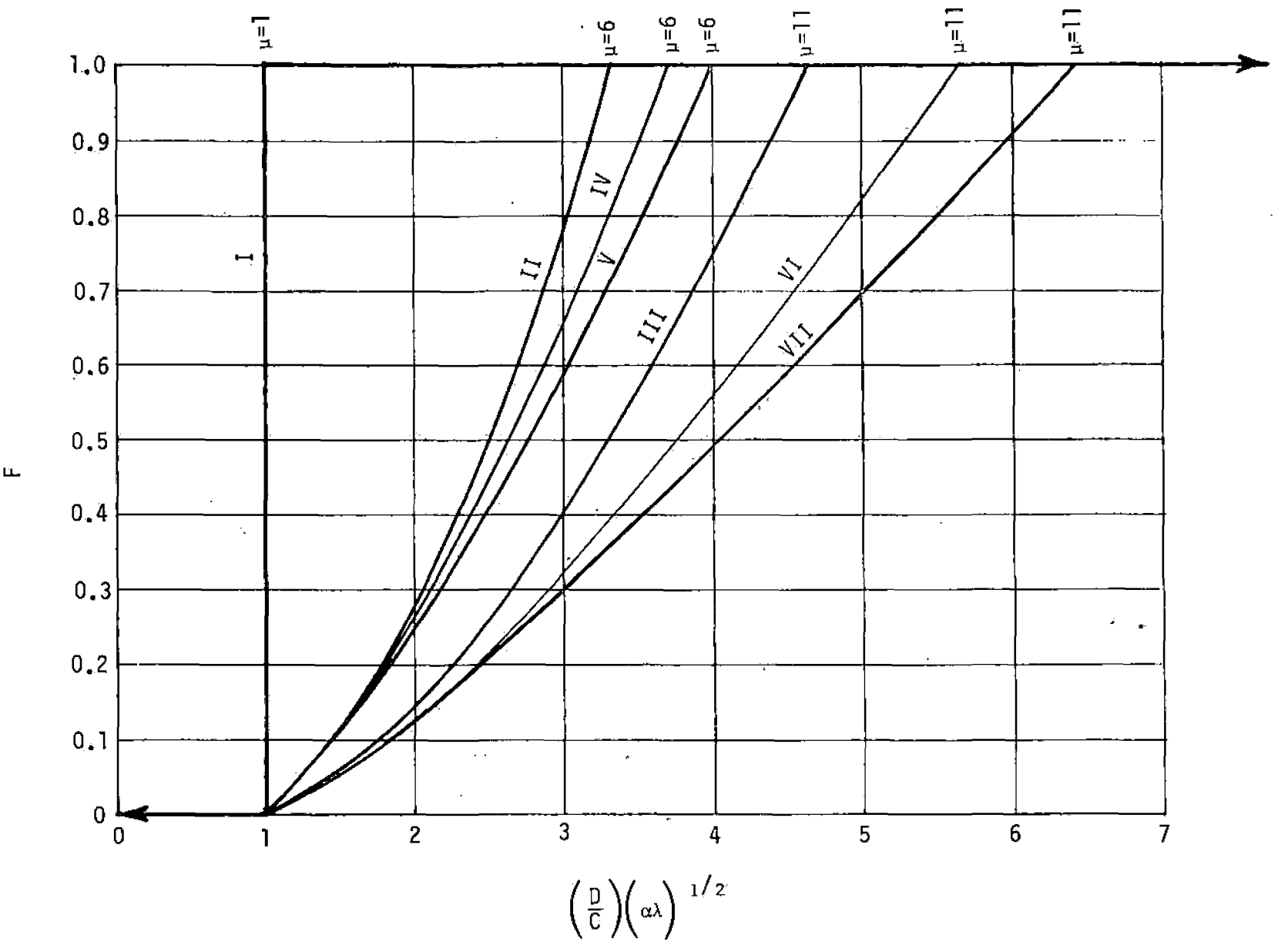

FIGURE 8 - DAMAGE FACTORS FOR VARIOUS MODELS

TABLE 5

SUMMARY OF FORMULAS USED IN DAMAGE PREDICTION

Item	Damage Factor	Dollar Damage
Individual Building Damage Factor	See Equations 31 - 36 and 42 - 46 inclusive	
Building Class	$F_k = \frac{1}{n} \sum_{i=1}^{n} F_i$	$D_{zk} = F_k E_{zk}$
Zone*	$F_z = \sum_{k=1}^{nk} \frac{D_{zk}}{E_{zk}}$	$D_z = C_z S_z \sum_{k=1}^{nk} D_{zk}$
Unit	$F_u = \sum_{z=1}^{nz} \frac{D_z}{E_z}$	$D_u = \sum_{z=1}^{nz} D_z$
Area	$F_A = \sum_{u=1}^{nu} \frac{D_u}{E_u}$	$D_A = \sum_{u=1}^{nu} D_u$

* The maximum value of D_z is $\sum_{k=1}^{nk} E_{zk}$

Much more remains to be learned about the actual distributions, the central tendencies, and the variations from the medians of both demand and capacity. There is currently not adequate data to reach firm determinations for various conceivable conditions. Certain characteristics of the distributions have been discussed in prior sections, namely the skewed nature of ground motion amplitude probabilities and the fairly symmetrical nature of structural values, barring any bias. Negative values of any significance are, of course, inadmissible on a physical basis for both demand and capacity. One other item worth noting is that, in general, structural central tendency values may exceed specified values by an appreciable amount. As an example, specified concrete strength may be obtained in a modern project by designing a mix that would provide a central or mean value well above the specified value. By this means, the tests below the specified level are hopefully kept few. In estimating damage, realistic values should be used.

The presentation that follows is intended as an example procedure and for clarification purposes. The distributions, and the distribution parameters are not intended to be the final ones for SMM which can operate under any form of distribution, but instead they represent operations that have been conducted thus far in the AEC structural response program.

Equation 3 for demand is repeated here for convenience,

$$D = \tilde{S}_v \Psi N^{Y_s} \tag{3}$$

By taking logarithms to the base e, it can be shown that

$$Y_s = \frac{\log_e D - \log_e \left(\tilde{S}_v \Psi \right)}{\log_e N} \tag{37}$$

Y_s is a normally distributed random variable with mean equal to zero and standard deviation equal to one. S_v and N are functions of the natural period of the oscillator and Ψ of its damping. As stated previously, there is still uncertainty about the proper value of N, but depending on the prediction technique, values from 1.2 to 3.0 have been used.

The expressions for capacity (Equations 9, 10, or 11) are in Gaussian form, and may be used as such in SMM by the Monte Carlo technique with tables of random numbers or with a digital computer and random number generation. If a closed form solution for the joint probabilities is desired, it is convenient to approximate the capacity distribution as a lognormal form closely resembling the Gaussian for small coefficients of variation, say below 0.30. Alternatively, it may be the case that lognormal or other distributions with a zero lower bound may best represent the data when more sample points are available. Since the damage factor F is a function of μ (Equation 28) and since μ is a function of the two random variables D and C (Equations 25 and 27), then F is also a random variable.

Appendix A provides a means of approximating the Gaussian or normal distribution and of obtaining closed-form joint-probability solutions of the two lognormal distributions for D and C. In lieu of Equation 9, let C be approximated by Equation 38,

$$C = \breve{C} M^{Y_C} \tag{38}$$

in which

$$M = \log_e^{-1} C_v$$

Then,

$$\frac{D}{C} = \frac{S_v \Psi \cdot N^{Y_s}}{\breve{C} M^{Y_C}} = \frac{\breve{D} N^{Y_s}}{\breve{C} M^{Y_C}} \tag{39}$$

or,

$$\frac{D}{C} = \left(\frac{D}{C}\right) \cdot \beta^{Y} \tag{40}$$

where

$$Y,\ Y_s,\ Y_c = N(0,1)$$

and,

$$\left(\frac{D}{C}\right)^2 = \left(\frac{D}{C}\right)^2 \beta_F^{Y} \tag{41}$$

in which, per Appendix A,

$$\beta_F = \log_e^{-1}\left\{2\left[\left(\log_e N\right)^2 + \left(\log_e M\right)^2\right]^{1/2}\right\}$$

Letting $\alpha\lambda = 1.0$ for convenience (this is often a good approximation), and substituting into Equation 31 for Model II (as an example),

$$F_{II} = 0.10\left(\frac{D}{C}\right)^2 \beta_F^{Y} - 0.10 \tag{42}$$

The probability that the damage factor F is less than some specified level F_o ($0 \leq F_o \leq 1$) can be found by evaluating the following expression:

$$P\left(F \leq F_o\right) = \frac{1}{\sqrt{2\pi}} \int_{-\infty}^{Y} e^{k^2/2}\, dk \tag{43}$$

The value of Y is obtained by taking base e logs of both sides of Equation 42, substituting for β_F, and solving for Y. The right-hand side of Equation 44 is the standardized normal probability

integral. Tabulations of the integral as a function of Y can be found in a handbook of statistical tables.

$$Y = \frac{\log_e \left(F_o + 0.10\right) - 2.30259 - 2\log_e \left(\frac{\bar{D}}{\bar{C}}\right)}{2\left[\left(\log_e N\right)^{1/2} + \left(C_v\right)^2\right]^{1/2}} \tag{44}$$

Since F = 0 for $\mu \leq 1$, P (F = 0) = P ($F \leq 0$) and the probability that the structure is not damaged is given by

$$P\ (F = 0) = \frac{1}{\sqrt{2\pi}} \int_{-\infty}^{Y} e^{-k^2/2}\, dk \tag{45}$$

where

$$Y = \frac{\log_e \left(\frac{\bar{D}}{\bar{C}}\right)}{\left[\left(\log_e N\right)^2 + \left(C_v\right)^2\right]^{1/2}} \tag{46}$$

Figure 9 shows the results of the closed form approximation using Model II and the above equations with the following numerical values:

$$\bar{D} = 0.8 \text{ cm/sec}, \quad N = 3.0$$

$$\bar{C} = 1.0 \text{ cm/sec}, \quad C_v = 0.25$$

The figure also shows comparative results from the use of the Monte Carlo technique with 50 samples to obtain the cumulative probability curve. The Monte Carlo solution in this case gives probabilities about 10% lower than the closed form solution. This is due to the approximation of the normal distribution C values with the equivalent lognormal distribution.

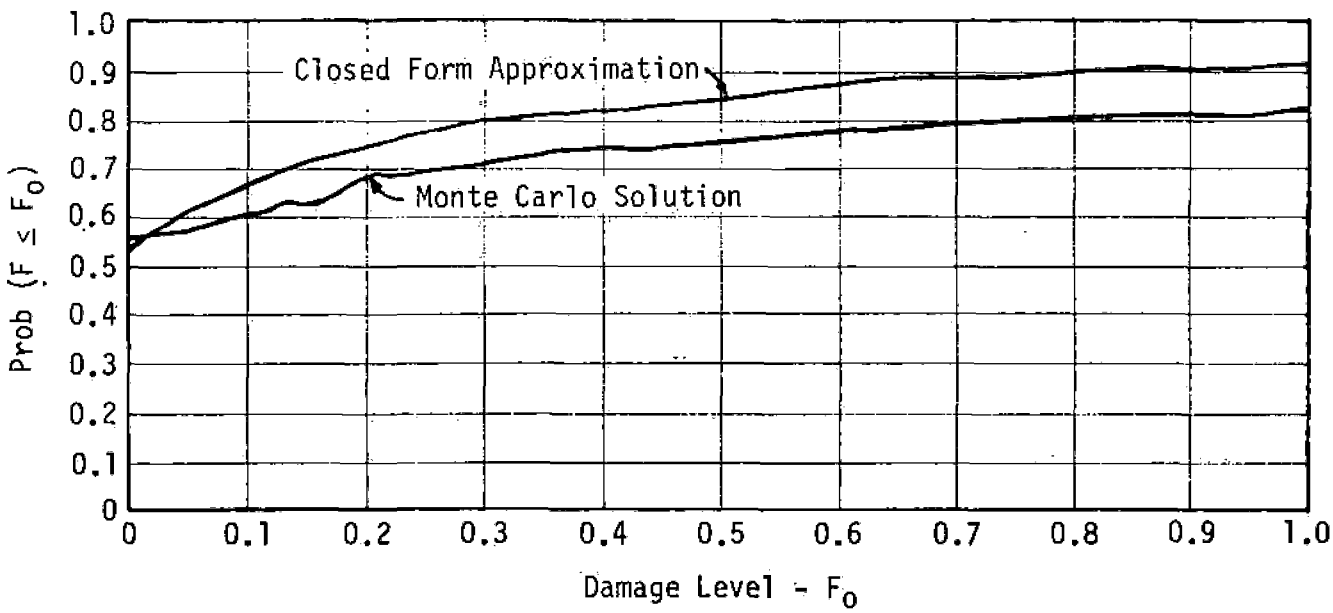

FIGURE 9 - COMPARISON OF MONTE CARLO AND CLOSED FORM SOLUTIONS

It is important to note that Figure 8 shows damage levels on the basis of deterministic quantities while Figure 9 shows the probabilities of exceeding various damage levels when the response parameters are specified by the statistical distributions given above. SMM usually involves the type of output illustrated in Figure 9.

Consider now what happens when there are a large number of similar structures such as in a typical subdivision, and it is desired to obtain a cumulative probability curve similar to Figure 9 which describes the cumulative damage for the entire group of structures.

Let

$$F_k = \frac{1}{n} \sum_{i=1}^{n} F_i \qquad (47)$$

in which

F_i = the damage factor for the i<u>th</u> building ($0 \leq F_i \leq 1$)

n = the total number of buildings

F_k = the damage factor for the entire group of structures ($0 \leq F_k \leq 1$)

F_k is a random variable which is the sum of n random variables. It has a cumulative probability curve which is a function of the random variables D and C and of the number of buildings, n. Mathematical determination of probability distributions for functions of a random variable such as this is very cumbersome and except in the simplest cases no closed form solution exists.

The great advantage of the Monte Carlo technique is that it can be readily extended to generate probability distributions for random variables such as F_k for which no closed form solution exists. In this case we form <u>one</u> sample of F_k by first generating n samples of

the random variable F and by then finding the average as indicated in Equation 47. Figure 10 shows the cumulative probability curves for various values of n, the number of buildings. For $n = 1$, F_k is of course the same as in Figure 9.

The curves derived in Figure 10 were based upon the assumption that D and C values for each individual building were <u>independent</u> random variables. This is probably not the best assumption when all buildings are located in a geographically compact area such as a typical subdivision. In this case it could be assumed that all houses in the subdivision might experience substantially the same ground motion and implicitly the same D level.* In this case D values for each individual building would be <u>dependent</u> random variables. The distinction between independent or dependent random variables has an important bearing on the question of predicting damage and adds one more vexatious problem to the already complex issue of predicting damage namely the spatial relationships of the structures.

In order to account for possible dependence of D values for contiguous structures, the expression of D is modified as follows:

$$\tilde{D} = \tilde{D} \cdot N^{[(1 - \nu)Y_d + \nu Z_d]} \qquad (48)$$

in which

ν = coherence coefficient ($0 \leq \nu \leq 1$)

and

Z_d, Y_d = standardized normal variate

The coherence coefficient, ν, is a measure of relative dependence of the random variables. If $\nu = 1$ the D values are completely dependent, and if $\nu = 0$ there is independence.

---

* There is some evidence, however, that even in one general area there may be much randomness of ground motion from place to place.

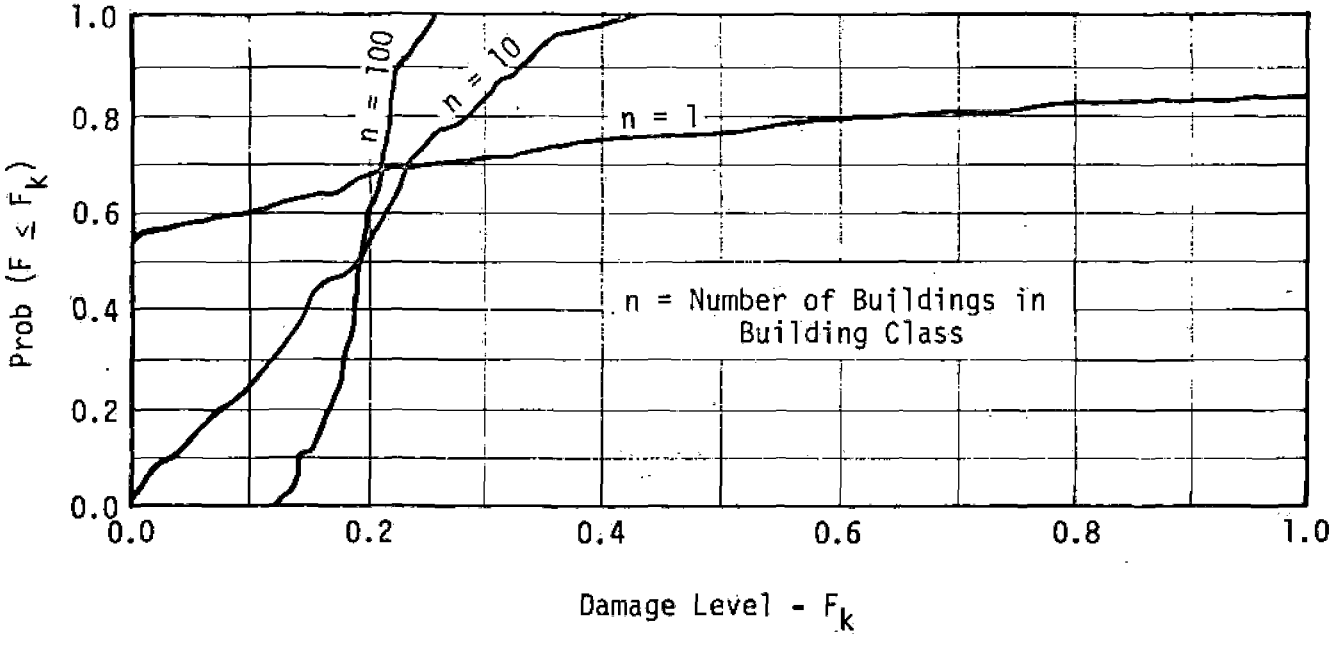

FIGURE 10 - EFFECT OF NUMBER OF BUILDINGS ON CUMULATIVE PROBABILITY DISTRIBUTION

The random variable Z_d is held constant for all buildings in the unit, but varied for each simulation. The random variable Y_d is varied for each building. Thus the term $(1 - \nu)Y_d$ represents the independent part of D and the term νZ_d represents the dependent part of D.

Figure 11 shows cumulative probability curves for the building class damage factor F_k, taking $\nu = 0.0$, 0.5, and 1.0, and using the same parameters that were used to derive the curves in Figure 10, with the number of buildings $n = 100$. The curve for $\nu = 0.0$ (independent D values for each building) corresponds to the curve in Figure 10 for 100 buildings.

Table 6 gives a summary of the statistics of the probability curves for $\widetilde{D/C} = 0.8$, $N = 3.0$, $C_v = 0.25$ and several values of n (the number of buildings in the building class) and ν (the coherence coefficient). For $\nu = 0$ (independent D values) the net effect of increasing n is to reduce the standard deviation. The standard deviation for this case is proportional to $1/\sqrt{n}$. Thus as the number of buildings becomes very large the standard deviation approaches 0 and the probability curve is defined by the median value of F_k. Increasing ν has just the opposite effect -- the standard deviation of F_k is increased. If we take $\nu = 1.0$ the cumulative probability curve for large n approaches the curve for the case where $n = 1$.

The difference between the median $\widetilde{F}_k$, and average $\overline{F}_k$, is a measure of the skewness of the probability density function. The probability density function is the derivative of the cumulative probability density function with respect to the independent variable, in this case F_k. For $\nu = 0$ and $n = 10$ or $n = 100$, the average and median are essentially the same which means that the probability density function is symmetric. From the central limit theorem[11], it can be shown that the probability density function for these cases approaches a normal distribution. For the case of $n = 1$ the probability distribution is essentially lognormal.

TABLE 6

EFFECT OF NUMBER OF BUILDINGS AND COHERENCE COEFFICIENT ON BUILDING CLASS DAMAGE FACTOR

Number of Buildings n	Coherence Coefficient ν	Average $\overline{F}_k$	Median $\tilde{F}_k$	Standard Deviation σ_{F_k}
1	*	0.15	0.00	0.29
10	0.0	0.19	0.19	0.11
10	0.5	0.11	0.06	0.14
10	1.0	0.16	0.00	0.28
100	0.0	0.19	0.19	0.03
100	0.5	0.11	0.05	0.13
100	1.0	0.19	0.01	0.33

* For $n = 1$ the damage statistics are independent of ν.

NOTES:

The values in the above table were obtained using the following parameters.

$$\tilde{D/C} = 0.80, \quad N = 3.0, \quad C_v = 0.25$$

Fifty simulations or samples were used to obtain the damage statistics for each case.

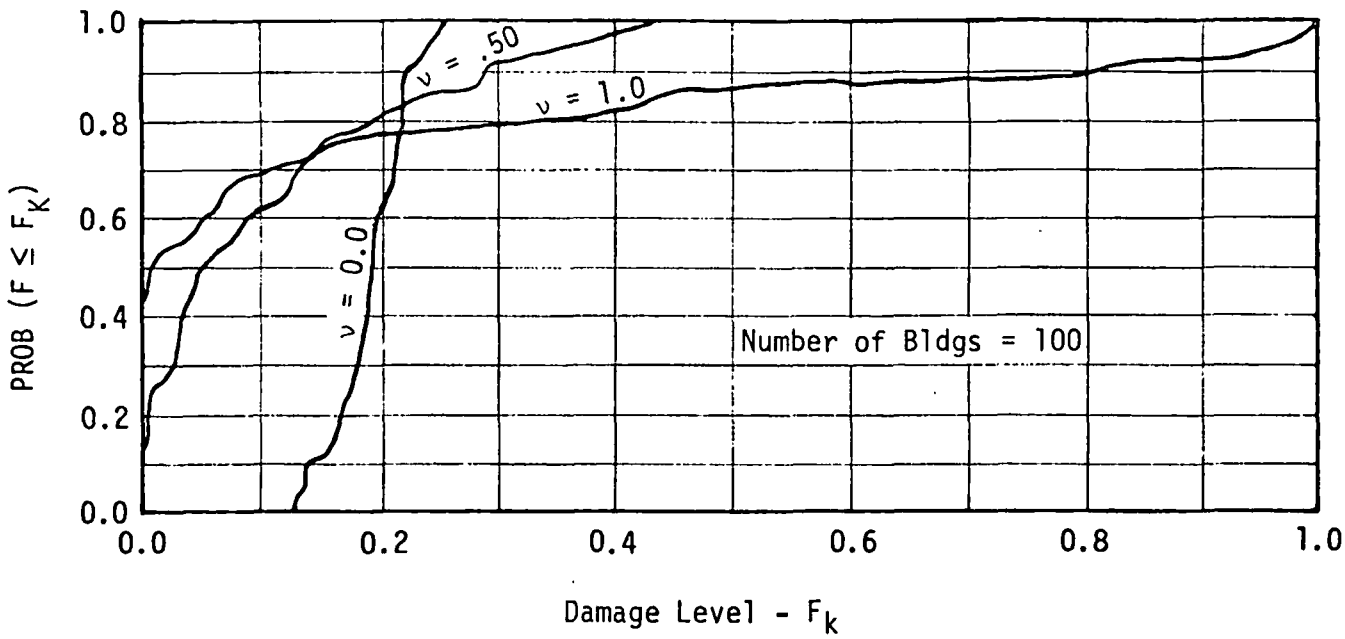

FIGURE 11 - EFFECT OF COHERENCE COEFFICIENT ON CUMULATIVE PROBABILITY DISTRIBUTION

Differences in average values of F_k for each case are due to the limited number of samples used to obtain the probability distributions. If a very large number of simulations were conducted the averages for all cases would be the same.

OPERATIONS IN SMM

The first step is to determine the total area A of interest and to break this down into appropriate units U. For each unit it is necessary to have a prediction of the spectral response S_v for 5% damping. In addition to the median value, a probability distribution and its parameter values are also needed for each unit. For example if lognormal distribution is used, for each unit and standard period band (usually in a plot of S_v versus T) there is needed S_v and N. The damping factor Ψ must also be determined from a consideration of the actual structures.

The next step is to determine whether certain units should be broken down into zones with soil factors S_z or building condition factors C_z other than unity.

The structures in each zone are categorized into classes K such as but not necessarily the same as in Table 2. Period ranges are also estimated for each class. Then for each class in each zone, the total dollar value E_{zk} is estimated and the mean capacity at yield in terms of velocity S_{v_y} is estimated together with factors α and λ. Table 3 is an example only, the values may vary considerably from those shown in other cases or locations.* It is also necessary to determine the probability distribution and its parameter values as, for example with Gaussian distribution, the mean and the coefficient of variation or the standard deviation.

---

* The February 9, 1971, earthquake in the San Fernando Valley and Los Angeles area caused high ground accelerations in some areas and considerable damage. However, away from the most intense shaking, and in some cases even in the intense areas, many structures had slight or no damage. This indicates the probabilistic nature of the problem and the fact that mean (rather than threshold) capacity values can be quite high, somewhat as indicated in Table 3.

The next step is to determine the model or models from Figure 7 that best represent the structures. Few buildings are as completely brittle as Type I although one must be constantly alert for them. Conversely usually only a few highly engineered modern structures with designed ductility and column confinement[7] can be safely considered to have the reserve qualities of Types III, VI, or VII. Type II has been used rather extensively thus far in the AEC structural response program.

With the data now assembled zone by zone, one is in a position to solve for any damage in each zone, and to get total damage by a summing process as in Table 5. It is noted that Equations 31 to 36 inclusive are in deterministic form in the sense that only specific D/C ratios are used. However the D,C sets could have been obtained probabilistically and thus represent such solutions. In general either the closed form probabilistic methods exemplified (for Model II) by Equations 42 to 46 would be used or, even more likely, the Monte Carlo technique with generated random numbers and large digital computers. Coherence related to independence must also be determined. See the following sections for more details.

If a nuclear event is being planned or if potential earthquake damage studies are being made, the energy level and location of energy release can be varied for reruns and parameter studies. This is a powerful planning or research device which also can be programmed in SMM as an automatic process.

Except for the simplest cases, it is obvious that damage predictions for entire areas can be obtained only by using the computation power of large high-speed digital computers. Several computer programs which are based upon Monte Carlo techniques outlined in the preceding sections have been written. As new information and data have become available the programs have been rewritten and modified. Several of the computer programs which are used in current damage prediction efforts in the AEC structural response program are discussed below.

BSM5 - General Purpose Damage Prediction

The BSM5 damage prediction program has been used for about 3 years to obtain damage predictions for several underground nuclear detonations including ADAGIO (later canceled), BOXCAR, BENHAM, GASBUGGY, RULISON, HANDLEY, and FAULTLESS.

For this program the units are usually assumed to be concentric rings around ground zero, as shown in Figure 12. For each unit a separate S_v curve is used for demand. Dollar values are assigned to each standard building class defined in Table 2 after detailed field surveys of the actual structures in the various units have been made.

Other data consists of the number of buildings, mean capacities, coefficient of variation, and range of periods in each building class.

When the number of buildings within a given unit and building class is very large -- for instance, one-story residential structures in Las Vegas -- the building class damage factor F_k has been computed using an arbitrary sample size of 250. The total damage for the

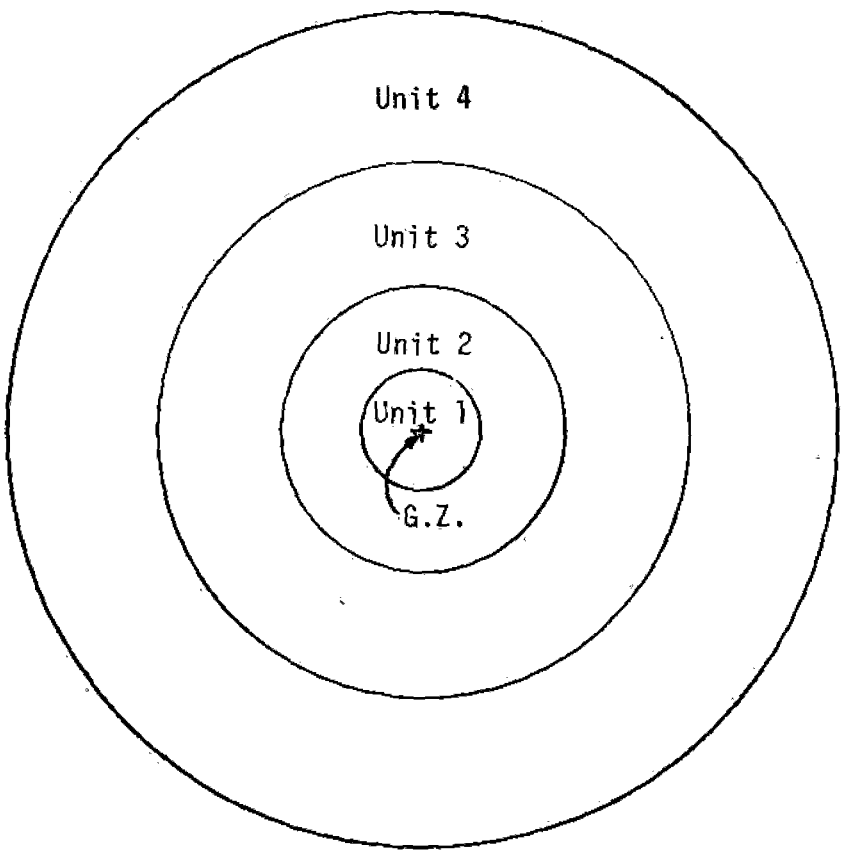

FIGURE 12 - DEFINITION OF UNITS FOR BSM5 PROGRAM

building class has then been computed by multiplying the total dollar value by the damage factor F_k computed from the sample size of 250.

Each S_v curve consists of discrete values for the median $\breve{S}_v$, and geometric standard deviation N, corresponding to an array of period values, which are also read in. $\breve{S}_v$ and N values at intermediate points are obtained using a second order polynomial interpolating subroutine.

The period of the structure is modeled as a random variable, as were demand and capacity. It is assumed that the distribution of period values for a given building class is uniform within a specified range.

To obtain the damage factor for an individual building, the computer program performs the following operations:

1) Determines period of the building

2) Interpolates to find D and N corresponding to the building period

3) Generates random variables for demand, based upon interpolated values for $\breve{D}$ and N; and capacity, based upon $\bar{C}$ and C_v

4) Computes the individual building damage factor, F

Damage factors are presently computed using Model Type II. The program calculates damage factors and dollar damage for each building class, unit, and simulation in a systematic manner. The D_A values are then sorted in ascending order and plotted as a cumulative probability function as shown in Figure 13. For most production runs, 50 simulations are used.

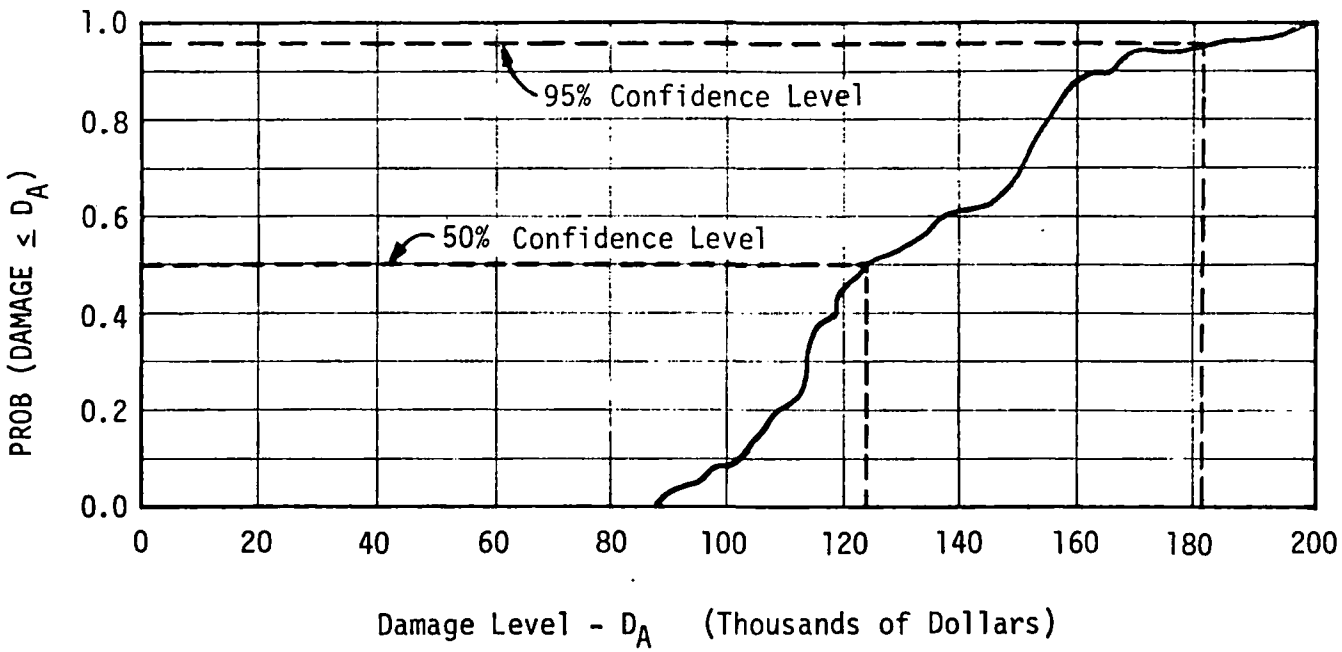

FIGURE 13 - CUMULATIVE PROBABILITY DISTRIBUTION FOR AREA DAMAGE

From the curve shown in Figure 13 statements can be made concerning probabilities of exceeding certain damage levels. For instance there is a 50% probability that the damage will exceed $124,000 and a 5% probability that the damage will exceed $181,000.

Note that the damage level in Figure 13 is in dollars. In order to go from the dimensionless damage factor F to dollar damage level, the building class damage factors are simply multipled by E_{zk} as indicated in Table 5. The area damage D_A is obtained by summing D_{zk} values over the entire area.

Figure 14 shows a macro flow chart for the BSM5 damage prediction program.

BSM99 - Inter-Oceanic Canal Study (IOCS) Damage Prediction Program

Damage prediction for the IOCS program involved a much more complex task than could readily be handled by the BSM5 damage prediction program. Within the range of interest almost a thousand separate towns, villages, or cities with populations greater than 500 were identified. In addition the proposed excavation plans for the routes of interest called for as many as 27 detonations, each in a separate location. The task of defining units and determining the number of buildings within each unit represented a formidable job in itself. In addition, small towns and villages close to ground zero were selected to be almost completely damaged by the ground motion levels presented in the original ground motion prediction studies.[15] Since the dwelling damage by a given detonation probably would not be repaired (until the program was completed), the total building population would change from one detonation to the next. It was therefore necessary to keep track of the extent of damage to each individual structure, to keep from accumulating damage beyond the original value of the structure.

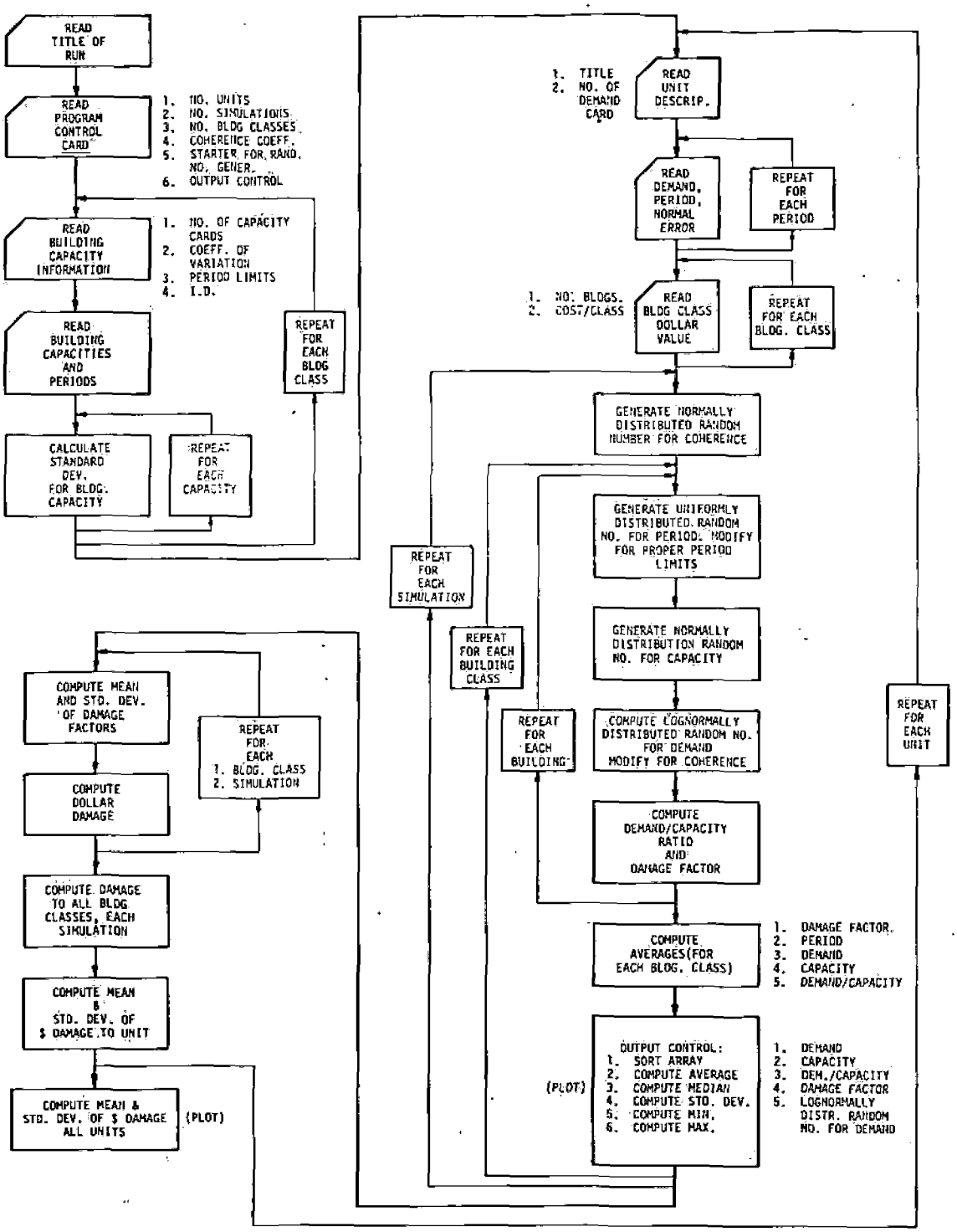

FIGURE 14 - FLOW CHART FOR BSM5 DAMAGE PREDICTION PROGRAM

Because of the vastly increased scope of this effort compared to previous damage predictions several significant changes and modifications were made to the computational procedures, although the basic ideas incorporated in the BSM5 program were retained.

In place of the concentric rings to represent units, each individual town or city was taken as a unit.

A file of each city and town in the Panama-Colombia area was generated. The file contained the following information:

1) An identification number

2) Name of the city

3) Latitude and longitude

4) Population

5) Country (Panama or Colombia)

This information was stored on magnetic tape which was used as input to the program. Because the type and quality of construction was considerably different than construction in this country, a separate set of building classes was used. The number and type of building classes were determined mainly from field surveys conducted in the area by JAB personnel. Because it was not feasible to conduct a village-by-village survey of structures, the population data was used to approximate the number of structures of each type. A subroutine in the program automatically calculated the number and dollar value of structures for each village, based upon information as to the population and country.

S_V predictions for each individual city and town were also generated automatically by another subroutine. The prediction equations were based upon regression parameters which were a function of structure period, yield, and distance from the detonation. Distances were

calculated using the latitude and longitude of each shot in conjunction with the latitude and longitude of each town. A later ERC-coded version of the S_v prediction subroutine also accounts for depth of burial effects. Because of the modular nature of the BSM99 program, this modification was very easy to incorporate. Figure 15 shows a flow chart for the BSM99 program.

BSM6 - Nevada Test Site-Central Nevada Testing Area (NTS-CNTA) Damage Prediction

The BSM6 program is very similar in structure to the BSM99 program. A magnetic tape containing information on buildings in Southern and Central Nevada is used to describe the type, location, and dollar value of structures. A printout of a sample editing form for one unit is shown in Figure 16. Note that the tape contains much information which is not relevant to the specific task of predicting structural and nonstructural damage. The additional information is used in other data processing activities such as damage complaint investigations. By keeping a complete up-to-date file on the NTS-CNTA building inventory on magnetic tape, we ensure that our damage predictions constantly reflect new information and modifications as they are reported by field personnel. Because of the careful attention given to the file structure of the building inventory tape, it is easy to extract specific information for specific tasks.

The BSM6 program uses the general S_v prediction equations given in Reference 10. At present ERC is working on station prediction equations for selected locations such as Beatty, Tonopah, and SE-6 (Las Vegas). As this information becomes available it can be easily incorporated into the BSM6 program. Figure 17 shows a flow chart of the BSM6 program.

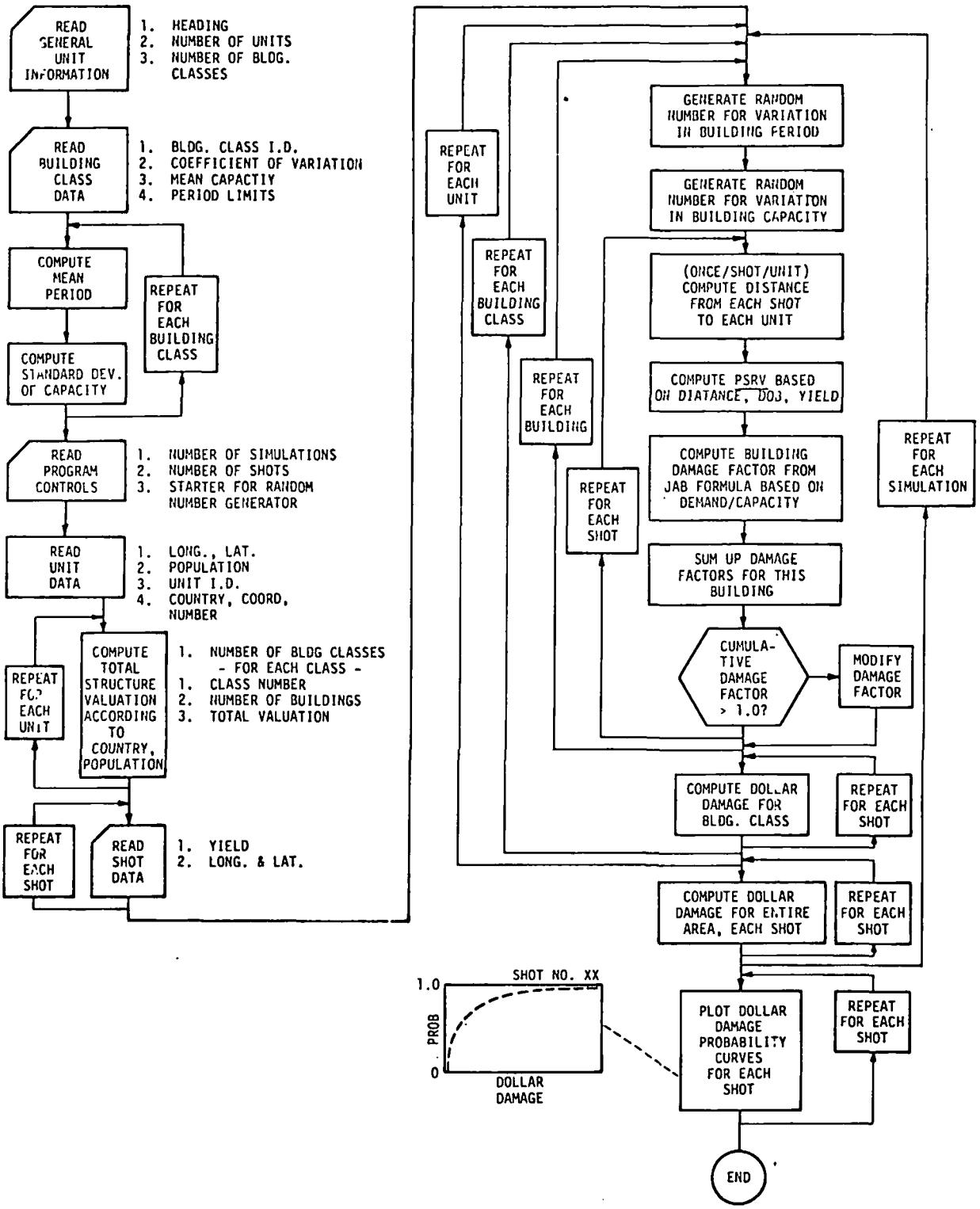

FIGURE 15 - FLOW CHART FOR IOCS MULTIPLE SHOT DAMAGE PREDICTION PROGRAM, BSM99

BUILDING INFORMATION

1	LOCATION NUMBER	CA001
2	LATITUDE	36 19
3	LONGITUDE	116 25
4	LOCATION NAME	DEATH VALLEY JUNCTION
5	DATE SEEN	10-31-68
6	OWNERS	A COMMUNITY IN CALIFORNIA
7	YEAR BUILT	
8	CONDITION NOW	GENERALLY FAIR
9	NUMBER OF STORIES	1 -- AMARGOSA HOTEL
10	TOTAL HEIGHT	ABOUT 15 FEET
11	LENGTH AND WIDTH (FEET)	50 × 150 AND 30 × 200
12	FRAME TYPE	WOOD
13	EXTERIOR WALL FINISH	STUCCO
14	INTERIOR WALL FINISH	PROBABLY GYPSUM WALLBOARD
15	GROUND FLOOR	CONCRETE SLAB
16	INTERMEDIATE FLOORS	NONE
17	ROOF	WOOD-TAR AND GRAVEL COVERED
18	CHIMNEYS (TYPE)	NONE
19	PERCENT OF WALL OPENINGS	N 10 E 50 W 25 S 10
20	BUILDING CLASSES	5 3 6
21	COST	$445,000 $50,000 $5,000
22	CONSTRUCTION COST OR ESTIMATED COST	$500,000
23	BRIEF DESCRIPTION OF HAZARDS (ITEMS WHICH ARE SUSCEPTIBLE TO DAMAGE)	IN ADDITION TO THE WOOD AND STUCCO AMARGOSA HOTEL, THERE ARE MANY OTHER STRUCTURES, E.G., A SERVICE STATION, CAFE, BARNS AND GARAGES, 2 WATER TANKS ON STEEL FRAME PLATFORMS 30 FEET HIGH, 1 LARGE TANK AT GROUND LEVEL, AND HOUSE TRAILERS. POPULATION OF DEATH VALLEY JUNCTION IS APPROXIMATELY 75. THE AMARGOSA HOTEL IS PRESENTLY BEING REBUILT. THERE IS ALSO A CALIFORNIA HIGHWAY MAINTENANCE STATION. TRAILERS ARE IN CLASS 6 AND ELEVATED TANKS ARE IN CLASS 9. PHOTOGRAPHS ARE AVAILABLE.

FIGURE 16 - EDITING FORM FOR STS-NTS BUILDING INVENTORY

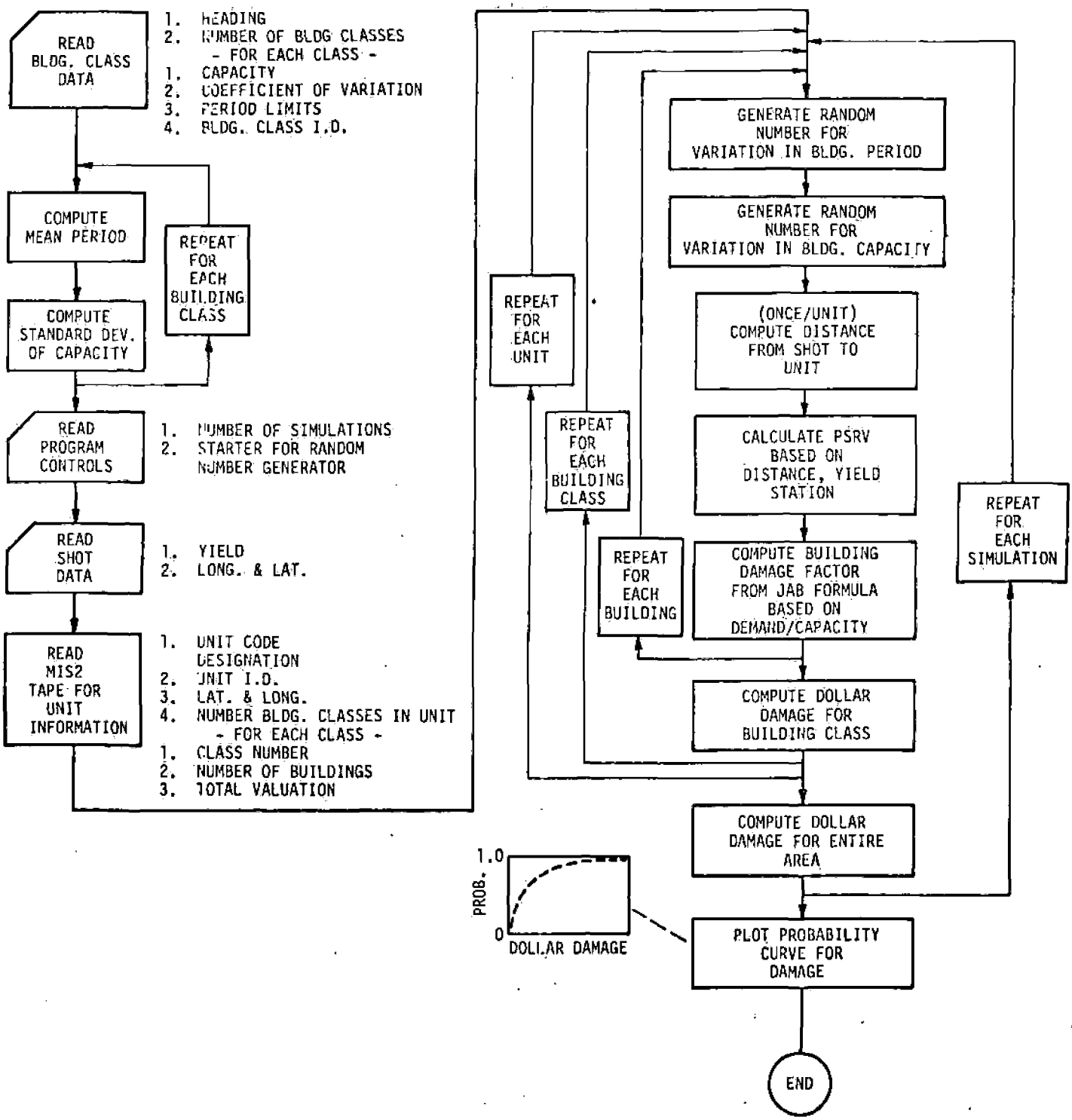

FIGURE 17 - FLOW CHART FOR STS-NTS DAMAGE PREDICTION PROGRAM, BSM6

SENSITIVITY STUDIES

A useful feature of the SMM programs is their capability for isolation of the effects of individual parameters. The closed form solution for joint probabilities given in Appendix A is also useful for judging the relative effects of various parameters.

From studies such as these it has been discovered that the damage predictions are extremely sensitive to the geometric standard deviation N. This indicates that refinements in the procedures for predicting deviations are needed. One step in this direction has been the development of S_v predictions for individual stations such as SE-6. Results of these studies indicate that the geometric standard deviations are usually substantially reduced which, of course, leads to predictions of less damage. By making S_v predictions for individual stations, the statistical perturbations associated with local soil conditions are considerably reduced. Thus it is reasonable to expect that the geometric standard deviation would be substantially less than the case where a more general statistical model was assumed.

The same is probably true for variances in buildings. However, since statistical deviation of values cannot in most cases be made, it is a simple task to select values which do not result in excessive sensitivity in the resultant dollar damage calculations.

PROPOSED EXTENSION OF SMM

The presentation has been devoted to the consideration of buildings as complete units. Experience has indicated that in addition to this basic approach, supplementary treatment may be desirable with the basic principles of SMM applied to especially vulnerable appendages or elements of buildings. For example, if chimney damage should be of much greater probability than main structure damage then the chimneys can be treated separately and thus improve the accuracy of the predictions. Only the cost evaluation and capacity of the chimneys would be used as input. The demand S_v can be modified to allow for its magnification from ground to roof level. Plaster cracking or glass breakage could be handled similarly. The basic building estimates would also be made but without the chimney, plaster, etc., cost repeated in the total exposure.

SUMMARY AND CONCLUSIONS

The Spectral Matrix Method (SMM) is a practical and powerful tool for predicting damage by an orderly synthesis of available theory, empirical data, and educated guesses where necessary. It is also valuable in parameter studies and research. Various implementations of SMM have been used over the past 3 years to arrive at damage predictions for Nevada Test Site and off-site events such as RULISON and GASBUGGY. The basic techniques used in SMM can be readily extended to other prediction efforts of interest such as earthquake damage or sonic boom damage.

We recognize that the answers are only as valid as the input data and the correctness of simplifying assumptions in the various mathematical models. As new information becomes available, it will be incorporated in the damage prediction efforts where applicable. In addition, we are developing improved structure modeling techniques in the long-range research program.

An evaluation of the numerical values used in SMM vis-a-vis the RULISON event is presently being performed. The results will be provided in a future report. We anticipate that some of the constants used currently to predict damage will be modified as a result of this study.

REFERENCES

1. Blume, John A., "Comments on Structural Response to Earthquake Motion as Related to Damage Risk," paper presented at U. S. Department of Commerce Meeting on Seismology and Engineering Seismology, Rockville, Maryland, January 30, 1967.

2. Blume, John A., "The Spectral Matrix Method of Damage Prediction: Description and Status," Report NVO-99-33 to the U. S. Atomic Energy Commission, Nevada Operations Office, March 1968.

3. Blume, John A., "An Engineering Intensity Scale for Earthquakes and Other Ground Motion," Bulletin of the Seismological Society of America, February 1970.

4. Biot, M. A., "A Mechanical Analyzer for the Prediction of Earthquake Stresses," Bulletin of the Seismological Society of America, April 1941.

5. Hudson, D. E., "Response Spectrum Techniques in Engineering Seismology," Proceedings, First World Conference on Earthquake Engineering, 1956.

6. Jenschke, V., Clough, R. W., and Penzien, J., "Analysis of Earth Motion Accelerograms," University of California, Berkeley, January 1964.

7. Blume, John A., Newmark, N. M., and Corning, Leo H., "Design of Multistory Reinforced Concrete Buildings for Earthquake Motions," Portland Cement Association, Chicago, Illinois, 1961.

8. Blume, John A., "The Motion and Damping of Buildings Relative to Seismic Response Spectra," Bulletin of the Seismological Society of America, February 1970.

9. Blume, John A., "Response of High-Rise Buildings to Ground Motion from Underground Nuclear Detonations," Bulletin of the Seismological Society of American, December 1969.

10. Lynch, R. D., "PSRV Prediction Equations for Pahute Mesa Events," Report NVO-1163-TM-8 to the U. S. Atomic Energy Commission, Nevada Operations Office, May 1969.

11. Blume, John A., "Earthquake Ground Motion and Engineering Procedures for Important Installations Near Active Faults," Proceedings, Third World Conference on Earthquake Engineering, New Zealand, 1965.

12. Parzen, E., "Modern Probability Theory and Its Applications," John Wiley & Sons, New York, 1960.

13. "Uniform Building Code," 1967 Edition, International Conference of Building Officials, Pasadena, California.

14. Blume, John A., "A Reserve Energy Technique for the Design and Rating of Structures in the Inelastic Range," Proceedings, Second World Conference on Earthquake Engineering, Japan, 1960.

15. Environmental Research Corporation, "Canal Predictions, Route 17A," attachment to letter ERC-14311 to the U. S. Atomic Energy Commission, Nevada Operations Office, September 1969.

APPENDIX A

JOINT PROBABILITY DISTRIBUTION OF A PRODUCT OF LOGNORMAL DISTRIBUTIONS

APPENDIX A

JOINT PROBABILITY DISTRIBUTION OF A PRODUCT OF LOGNORMAL DISTRIBUTIONS

A random variable X_i is said to have a lognormal distribution if its logarithm $\log_e X_i$ is normally distributed. If $\log_e X_i$ is normally distributed with mean m_i and standard deviation σ_i, a transformed normal variable with mean = 0 and standard deviation = 1 is defined by

$$Y_i = \frac{\log_e X_i - m_i}{\sigma_i} \tag{1A}$$

Equation 1A can be rewritten as

$$\log_e X_i = m_i + Y_i \sigma_i$$

$$X_i = e^{m_i + Y_i \sigma} = e^{m_i} e^{Y_i \sigma_i} \tag{2A}$$

Setting

$$\tilde{X}_i = e^{m_i} \tag{3A}$$

$$N_i = e^{\sigma_i} \tag{4A}$$

gives

$$X_i = \tilde{X}_i \cdot N_i^{Y_i} \tag{5A}$$

where

$\tilde{X}_i$ = median value of X_i

N_i = geometric standard deviation at $\tilde{X}_i$

It follows directly that a random variable Z of the form

$$Z = \frac{X_1 \cdot X_2 \cdot \text{---} X_k}{X_{k+1} \cdot X_{k+2} \cdot \text{---} X_n} \tag{6A}$$

is also lognormally distributed since

$$\log_e Z = \log_e X_1 + \log_e X_2 + \text{---} + \log_e X_k - \log_e X_{k+1} - \log_e X_{k+2} - \text{---} - \log_e X_n \tag{7A}$$

and the sum of n independent normally distributed random variables is known to be normally distributed with mean,

$$m_z = m_1 + m_2 + \text{---} + m_k - m_{k+1} - m_{k+2} - \text{---} - m_n \tag{8A}$$

and standard deviation,

$$\sigma_z = \left(\sigma_1^2 + \sigma_2^2 + \text{---} + \sigma_{k+1}^2 + \text{---} \sigma_n^2\right)^{1/2} \tag{9A}$$

We can express Z in the form

$$Z = \breve{Z} \cdot N_z^{Y_z} \tag{10A}$$

where

$$\breve{Z} = e^{m_z} = e^{m_1+m_2+\text{---}m_k-m_{k+1}-\text{---}-m_n} \tag{11A}$$

$$N_z = e^{\sigma_z} = e^{\left(\sigma_1^2+\sigma_2^2+\text{---}+\sigma_n^2\right)^{1/2}} \tag{12A}$$

and Y_z is again a standardized normal variable with mean = 0, standard deviation = 1.

Since $\log_e X_i = m_i$ and $\log_e N_i = \sigma_i$, Equations 11A and 12A can also be written as

$$\tilde{Z} = \log_e^{-1}\left(\log_e X_1 + \log_e X_2 + \cdots \log_e X_n\right) \tag{13A}$$

$$N_Z = \log_e^{-1}\left[\left\{\left(\log_e N_1\right)^2 + \left(\log_e N_2\right)^2 + \cdots \left(\log_e N_n\right)^2\right\}^{1/2}\right] \tag{14A}$$

Alternatively using Equation 5A,

$$Z = \frac{\tilde{Z}_1 \cdot \tilde{Z}_2 \cdot \cdots \tilde{Z}_k}{\tilde{Z}_{k+1} \cdot \tilde{Z}_{k+2} \cdot \cdots \tilde{Z}_n} \cdot \frac{N_1^{Y_1} \cdot N_2^{Y_2} \cdot \cdots N_k^{Y_k}}{N_{k+1}^{Y_{k+1}} \cdot N_{k+2}^{Y_{k+2}} \cdot \cdots N_n^{Y_n}} \tag{15A}$$

The preceding formulas will be used to derive joint probability distributions of interest in the damage prediction efforts

1) Joint Probability Distribution of D/C

Let

$$D = \tilde{D} \cdot N^{Y_d}$$

$$C = \tilde{C} \cdot M^{Y_c}$$

then,

$$\frac{D}{C} = \frac{\tilde{D}}{\tilde{C}} \cdot \frac{N^{Y_d}}{M^{Y_c}} = \frac{\tilde{D}}{\tilde{C}} \cdot \beta^Y \tag{16A}$$

where from Equation 14A,

$$\beta = \log_e^{-1}\left[\left\{\left(\log_e N\right)^2 + \left(\log_e M\right)^2\right\}^{1/2}\right] \tag{17A}$$

2) Joint Probability Distribution of $(D/C)^2$

$$\frac{D}{C} = \left(\frac{\tilde{D}}{\tilde{C}}\right)^2 \cdot \left(\frac{N^{Y_d}}{M^{Y_c}}\right)^2$$

$$= \left(\frac{\tilde{D}}{\tilde{C}}\right)^2 \left(N^2\right)^{Y_d} \left(M^2\right)^{-Y_c}$$

Let

$$\beta_F = \log_e^{-1}\left[\left\{\left(\log_e N^2\right)^2 + \left(\log_e M^2\right)^2\right\}^{1/2}\right]$$

$$= \log_e^{-1}\left[\left\{\left(2\log_e N\right)^2 + \left(2\log_e M\right)^2\right\}^{1/2}\right]$$

$$= \log_e^{-1}\left[2\left\{\left(\log_e N\right)^2 + \left(\log_e M\right)^2\right\}^{1/2}\right] \qquad (18A)$$

Then,

$$\left(\frac{D}{C}\right)^2 = \left(\frac{\tilde{D}}{\tilde{C}}\right)^2 \beta_F^Y \qquad (19A)$$

3) Probability Distribution of Damage Factor F

Let the damage factor

$$F = 0.10\left(\frac{D}{C}\right)^2 - 0.10 \qquad (20A)$$

Substituting Equation 18A in Equation 17A and taking logs of both sides yields

$$\log_e\left(F + 0.10\right) = \log_e\left(0.10\right) + 2\log_e\frac{\tilde{D}}{\tilde{C}}$$

$$+ Y\log_e\beta_F \qquad (21A)$$

The probability that the damage factor is less than some specified level, F_o ($0 \leq F_o \leq 1$), can then be found by evaluating the following expression:

$$P\left(F \leq F_o\right) = \frac{1}{\sqrt{2\pi}} \int_{-\infty}^{Y} e^{-k^2/2}\, dk \qquad (22A)$$

where Y is found from Equation 21A as

$$Y = \frac{\log_e\left(F_o + 0.10\right) - 2.30259 - 2\log_e\left(\frac{\breve{D}}{\breve{C}}\right)}{2\left[\left(\log_e N\right)^2 + \left(\log_e M\right)^2\right]^{1/2}} \qquad (23A)$$

If C is normally distributed, as was assumed in the text, it can be closely approximated by a lognormal distribution by taking the median $\breve{C}$ equal to the mean $\bar{C}$, and the geometric standard deviation $M = \log_e^{-1} C_V$. This approximation holds reasonably well for small values of C_V ($C_V < 0.30$).

The probability that the structure is not damaged is given by

$$P\left(F = 0\right) = \frac{1}{\sqrt{2\pi}} \int_{-\infty}^{Y} e^{-k^2/2}\, dk \qquad (24A)$$

in which

$$Y = \frac{\log_e\left(\frac{\breve{D}}{\breve{C}}\right)}{\left[\left(\log_e N\right)^2 + C_V^2\right]^{1/2}} \qquad (25A)$$

In the above expression for Y the lognormal approximation of the normally distributed quantity C was assumed.

The results derived in this section are applied to a sample calculation of damage probabilities pertaining to the Inter-Oceanic Canal

Study, for which nine building classes were used to describe structures in the Panama-Colombia area. Inelastic model Type II was used. Values for the median demand and geometric standard deviation N as a function of the natural period of the oscillator, yield and depth of burial of the cratering device, and distance from ground zero were taken from Environmental Research Corporation report NVO-1163-125, where the following values were assumed.

Distance to Ground Zero	=	180 km
Yield	=	11,000 kt
Depth of Burial	=	1615 ft

A coefficient of variation $C_V = 0.25$ was used for all building classes. Since the geometric standard deviation N ranged from approximately 2.5 to 3.0 in the period ranges of interest it is seen from Equation 25A that the variation in structural capacity can be neglected in comparison with the variation in demand. Thus we simplify Equation 25A to

$$Y = - \frac{\log_e \left(\frac{D}{C} \right)}{\log_e N} \qquad (26A)$$

A summary of damage calculations which shows the probability that the damage to a structure in a given building class is zero is shown in Table 1A.

Equation 22A gives an expression for the probability of damage to a single structure where it was assumed that both the structural capacity and ground motion demand were independent random variables. By evaluating Equation 22A for various values of F_o it is possible to construct a cumulative probability curve which will show at a glance the probability of exceeding a certain damage level. For instance, assume that $D/C = 0.80$, $C_V = 0.25$, and $N = 3.0$. Evaluating

Equation 22A for various values of F_o gives the cumulative probability curve shown in Figure 9 of the text.

TABLE 1A

DAMAGE PROBABILITIES USING
JOINT PROBABILITY DISTRIBUTIONS

Building Class	$\overline{CAP}$ (cm/sec)	$\overline{T}$ (sec)	N	$\log_e N$	$\widetilde{DEM}$ (cm/sec)	$\frac{\widetilde{DEM}}{\widetilde{CAP}}$	$\log_e \frac{\widetilde{DEM}}{\widetilde{CAP}}$	Y	P (F=0)
1	1.5	0.13	3.0	1.0981	0.140	0.093	-2.364	2.18	0.9857
2	2.0	0.13	3.0	1.0981	0.140	0.070	-2.525	2.32	0.9898
3	2.5	0.13	3.0	1.0981	0.140	0.056	-2.882	2.64	0.9959
4	3.0	0.13	3.0	1.0981	0.140	0.049	-3.060	2.80	0.9974
5	4.0	0.29	2.62	0.96317	0.390	0.098	-2.330	2.43	0.9925
6	5.0	0.29	2.62	0.96317	0.390	0.070	-2.430	2.52	0.9941
7	6.0	0.29	2.62	0.96317	0.390	0.065	-2.730	2.09	0.9841
8	7.5	0.55	2.54	0.93216	1.010	0.135	-2.02	2.16	0.9850
9	9.5	0.55	2.54	0.93216	1.010	0.106	-2.24	2.41	0.9920

DISTRIBUTION: JAB-99-81

Mr. R. A. Johnson, AEC/NVOO, Las Vegas, Nevada
Mr. R. R. Loux, AEC/NVOO, Las Vegas, Nevada (3 copies)
Mr. Marshall Page, AEC/NVOO, Las Vegas, Nevada
Mr. Robert Thalgott, AEC/NVOO, Las Vegas, Nevada
Mr. T. H. Blankenship, OPNE/NVOO, Las Vegas, Nevada (2 copies)
Dr. M. B. Biles, AEC/DOS, Hq., Washington, D.C.
Mr. J. S. Kelley, AEC/DPNE, Hq., Washington, D.C.
Maj. Gen. G. B. Giller, AEC/DMA, Hq., Washington, D.C. (2 copies)
Mr. R. Hamburger, AEC/DPNE, Hq., Washington, D.C.
Mr. E. Rechtin, ARPA, Washington, D.C.
Dr. L. S. Jacobsen, Santa Rosa, California
DTIE, Oak Ridge, Tennessee (2 copies)
Dr. W. E. Ogle, LASL, Los Alamos, New Mexico
Mr. R. W. Newman, AEC/NVOO, Las Vegas, Nevada
Dr. G. H. Higgins, LLL, Livermore, California
Dr. G. C. Werth, LLL, Livermore, California
Dr. Alfred Holzer, LLL, Livermore, California
Dr. J. W. Hadley, LLL, Livermore, California
Dr. W. J. Hannon, LLL, Livermore, California
Dr. J. E. Carothers, LLL, Livermore, California
Explosives Excavation Research Office, LLL, Livermore, California
Dr. D. M. Ellett, Org. 9150, Sandia Corp., Albuquerque, New Mexico
Dr. W. D. Weart, Org. 9111, Sandia Corp., Albuquerque, New Mexico
Dr. J. R. Banister, Org. 9150, Sandia Corp., Albuquerque, New Mexico (2 copies)
Dr. B. Grote, TCD-B, DASA, Sandia Base, Albuquerque, New Mexico (2 copies)
Mr. T. F. Thompson, 713 Crossway Rd., Burlingame, California
Dr. N. M. Newmark, University of Illinois, Urbana, Illinois
Dr. D. U. Deere, University of Illinois, Urbana, Illinois
Dr. C. Kisslinger, St. Louis University, St. Louis, Missouri

DISTRIBUTION: JAB-99-81 (continued)

Dr. J. T. Wilson, University of Michigan, Ann Arbor, Michigan
Resident Manager, H&N, Inc., Las Vegas, Nevada
Mr. K. W. King, NOAA/ESL, Las Vegas, Nevada (2 copies)
Mr. W. Mickey, NOAA/ESL, Rockville, Maryland
Dr. W. S. Twenhofel, USGS, Denver, Colorado
Dr. L. B. Werner, Teledyne Isotopes, Palo Alto, California
Mr. S. D. Wilson, Shannon & Wilson, Inc., Seattle, Washington
Dr. G. B. Maxey, AEC/NVOO, Las Vegas, Nevada
Mr. P. L. Russell, USBM, Denver, Colorado
Mr. L. G. von Lossberg, Sheppard T. Powell & Assoc., Baltimore, Maryland
Mr. Lyman Heller, WES, Vicksburg, Mississippi
Lt. Cmdr. R. O. Johnstone, ACDA/WEC, Washington, D.C.
Mr. Dean Power, El Paso Natural Gas, El Paso, Texas
Environmental Research Corporation, Las Vegas, Nevada (2 copies)
Mr. Paul Fillo, U.S. Bureau of Mines, Mineral Resources Office
1605 Evans Avenue, Reno,Nevada
Mr. Roger Ray, Assistant Manager for Operations, AEC/NVOO, Las Vegas, Nevada
Sandia Library, Sandia Corp., Albuquerque, New Mexico
Ken Medearis & Assoc., Suite 800 Savings Building, Fort Collins, Colorado 80521
Mr. Franklin D. Chin, Nuclear Energy Liability Insurance Association
85 John Street, New York, NY 10038
Mr. Jerry Lutekehans, CER Geonuclear Corp., P. O. Box 15090
Las Vegas, Nevada 89114

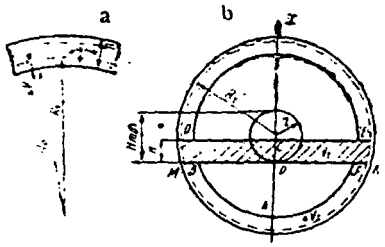

Fig.1 Variation of the volume of the drum of the mill as a function of variable factors; h is the thickness of the new lining; h' is the thickness of the lining at a given moment of operation of the mill; V_0 is the initial and thereby the smallest volume, corresponding to the unworn lining with $R_t = R_0$, $H = 0$, and $r = const$, $V_t + \Delta V_t$ is the current volume.

Fig.2 Range of variation in the volume of the mill (D_0, with new lining, $\Delta R = 0$; 3,4 - with worn lining, $\Delta R = \Delta R_{max}$) as a function of variat of the pulp H (1,3) and of the vari of the pulp and the size of the dis r (2,4).

Silicofluoride methods in the metallurgy of light metals

O S Ignat'ev (Moscow Institute of Steel and Alloys. Department of the Metallurgy of Light Metals).

In the technical progress of non-ferrous metallurgy and chemical technology fluoride methods are acquiring substantial importance. They are characterised by an independent and extremely effective trend associated with the use of H_2SiF_6 and its salts as fluorinating agents.

The silicofluoride compounds, obtained incidentally in the process of the treatment of natural phosphate raw material for fertilisers, are distinguished by lost cost and low corrosion activity. Thus, the cost of 1 ton of fluorine in H_2SiF_6, produced in Soviet superphosphate plants, amounts to about 20 roubles: in technical HF the cost amounts to 800 roubles, while in the principal fluorine-containing raw material (fluorite concentrate) it amounts to about 200 roubles.

Silicofluoride methods acquire special importance in the metallurgy of light metals. Thus, the use of H_2SiF_6 for the production of cryolite, aluminium fluoride and sodium fluoride makes it possible to obtain aluminium compounds, important for electrolysis, at almost half the cost of that entailed in the traditional method (with the use of HF).

Silicofluoride methods are promising for the production of cheap lithium fluoride compounds, required for the improvement of the electrolytic production of aluminium and other metals, from its natural raw material. The use of silicofluoride methods may secure a considerable reduction in the production costs of beryllium, caesium, rubidium and other light metals by metal-thermic reduction of their fluorides. An important technological characteristic of silicofluoride compounds is their chemical inertness towards silica. On the basis of this characteristic it is possible to create effective methods for the production of alumina, various fluorides and other compounds of light metals directly from natural aluminosilicates and their weathering products.

Silicofluoride methods is the name we give to those methods based on decomposition of minerals or compounds by fluorination, in which H_2SiF_6 and its salts are used as the fluorinating agent or for production of the fluorinating agent.

Currently known silicofluoride methods in the metallurgy of light metals can be divided into two groups: 1) solid-phase fluorinating methods, in which decomposition is realised by exchange fluorination reactions with heating (sintering) of the charge: 2) liquid-phase fluorination methods, realised through decomposition (dissolution) of the minerals and compounds in aqueous solutions of the fluorinating agent.

The solid-phase silicofluoride method for the treatment of natural aluminosilicates of beryllium was first used by Copoux, who proposed to sinter beryl at 750°C with sodium silicofluoride and then leach the obtained sodium fluoroberyllate[1]). The fluorination of the components of beryl took place according to the following scheme:

$$3BeO \cdot Al_2O_3 \cdot 6SiO_2 + 6Na_2SiF_6 \longrightarrow 9SiO_2 + 3Na_2BeF_4 + 2Na_3AlF_6 + 3SiF_4\uparrow$$

The reaction products differed in properties; Na_2BeF_4 is readily soluble in water, Na_3AlF_6 and SiO_2 are insoluble, and SiF_4 is released with the gas phase. On account of this, selective extraction of the beryllium is achieved during leaching of the sintering products. This process was improved by subsequent investigations[2]), and at the present time it is realised according to the following main reaction:

$$3BeO \cdot Al_2O_3 \cdot 6SiO_2 + 2Na_2SiF_6 + Na_2CO_3 = 3Na_2BeF_4 + 8SiO_2 + Al_2O_3 + CO_2$$

Investigations into the reaction of the natural lithium aluminosilicate α-spodumene with sodium silicofluoride at 740-750°C showed[3]) that its complete decomposition also takes place under these conditions. The process takes place by the reaction:

$$Li_2O \cdot Al_2O_3 \cdot 4SiO_2 + 3Na_2SiF_6 = 2LiF + 2Na_2SiF_6 + 6SiO_2 + SiF_4\uparrow$$

Solid-phase fluorination with sodium silicofluoride has been proposed for the treatment of pollucite[4]): The fluorination reaction takes place at 650°C according to the following scheme:

$$Cs_2O \cdot Al_2O_3 \cdot 4SiO_2 + 3Na_2SiF_6 = 2CsF + 2Na_3AlF_6 + 6SiO_2 + SiF_4\uparrow$$

The physicochemical characteristics of the decomposition of aluminosilicates by solid-phase fluorination with sodium silicofluoride have been studied in a fair amount of detail for the case of beryl[6]). A method for the production of a beryllium product by fluorination of beryl with sodium silicofluoride is used on an industrial scale at the Beryllium Corporation in the USA[6]).

Another variant of solid-phase silicofluoride methods is

ve method for the production of alumina from high-alumina aluminosilicates (kyanite, disthene, silmanite) by sintering with aluminium fluoride and isolation of the silica in the form of SiF_4 in the gas phase[7]). From the gas phase the fluorine is regenerated in the form of hydrofluosilicic acid, which is used for the production of recycled aluminium fluoride.

The chemical mechanism of this method is characterised by the following reactions:

$$3(Al_2O_3 \cdot SiO_2) + 4AlF_3 = 5Al_2O_3 + 3SiF_4\uparrow$$

$$3SiF_4 + 4H_2O = 2H_2SiF_6 + SiO_2 + H_2O$$

$$H_2SiF_6 + 2Al(OH)_3 = 2AlF_3 + SiO_2 + 4H_2O$$

A similar method by means of which it is possible to realise a cyclic silicofluoride-fluoride process is fluorination of beryl with ammonium fluoride or bifluoride, obtained from H_2SiF_6[8,9]). Fluorination is carried out at 200-250°C and is described by the equation:

$$3BeO \cdot Al_2O_3 \cdot 6SiO_2 + 60NH_4F = 3(NH_4)_2BeF_4 +$$
$$2(NH_4)_3 \cdot AlF_6 + 6(NH_4)_2 \cdot SiF_6 + 36NH_3 + 18H_2O$$

During leaching of the fluorination products ammonium silicofluoride and fluoroberyllate pass into the solutions, from which it is possible to isolate ammonium fluoroberyllate by crystallisation and to obtain ammonium fluoride for recycling[9 - p 59; 10]).

More varied are silicofluoride methods based on the liquid-phase fluorination of natural aluminosilicates, products from their secondary decomposition, and various compounds of light metals. Aqueous solutions of H_2SiF_6 and its salts are used as fluorinating agent. In the metallurgy of light metals H_2SiF_6 was evidently first used for lithium ores[11]). The probable mechanism of the reaction of spodumene with H_2SiF_6 can be represented by the following reaction:

$$Li_2O \cdot Al_2O_3 \cdot 4SiO_2 + 2H_2SiF_6 = Li_2SiF_6 +$$
$$+2AlF_3 + 5SiO_2 + 2H_2O$$

Lithium silicofluoride is readily soluble in water and passes into solution.

By our investigations it was established that liquid-phase fluorination with H_2SiF_6 can be used for the treatment of practically all natural aluminosilicates. The temperature of fluorination is here the determining factor.

The high-alumina silicate kyanite is distinguished by the greatest chemical stability. Its complete decomposition with aqueous solutions of H_2SiF_6 requires autoclave conditions, while a temperature of 30-40°C is sufficient to decompose nepheline.

The use of liquid-phase silicofluoride treatment opens up wide prospects for the complete rational utilisation of all the components of aluminosilicates and the possibility of obtaining from their silica and alumina parts the most favourable commercial forms of the product such as silica gel, amorphous silica, alumina, aluminium fluorides etc. Liquid-phase silicofluoride methods for the production of fluorides from various aluminium compouds have been most widely investigated at the present time.

Methods based on the direct reaction of H_2SiF_6 and aluminium hydroxide have found practical use for the production of aluminium fluoride and cryolite. The reaction takes place according to the following scheme:

$$\underset{\text{solution}}{H_2SiF_6} + 2\underset{\text{solid}}{Al(OH)_3} \longrightarrow \underset{\text{solution}}{2AlF_3} + \underset{\text{solid}}{SiO_2} + 4H_2O$$

The process is carried out at 50-100°C. The obtained aluminium hydrofluorides form stable supersaturated solutions, and this secures separation of the aluminium from the silica. Most of the aluminium fluoride is then isolated from the solutions by heating and seeding, and the mother solution is used for the production of cryolite by the reaction:

$$\underset{\text{solution}}{3NaF} + \underset{\text{solution}}{AlF_3} = \underset{\text{solid}}{Na_3AlF_6}$$

It is possible to use bauxite, clay and other aluminosilicates[12-14]) as source for aluminium in the production of aluminium fluorides by this method.

However, a series of problems in the direct utilisation of natural aluminosilicates for the production of fluorides by silicofluoride methods have still not been resolved in technological respects. Therefore, pure aluminium hydroxide obtained in the production of alumina from aluminium raw material is mainly used in practice.

Investigation of the kinetics and mechanism of this reaction showed[15]) that the process takes place in two stages. Aluminium silicofluoride is first formed according to the reaction:

$$3H_2SiF_6 + 2Al(OH)_3 = Al_2(SiF_6)_3 + 6H_2O$$

In the second slower stage it decomposes according to the following scheme:

$$Al_2(SiF_6)_3 + 6H_2O = 2AlF_3 + 3SiO_2 + 12HF$$

The hydrofluoric acid released in this reaction reacts with the excess of aluminium hydroxide:

$$4Al(OH)_3 + 12HF = 4AlF_3 + 12H_2O$$

Altogether the reaction is described by the equation:

$$H_2SiF_6 + 2Al(OH)_3 = 2AlF_3 + SiO_2 + 4H_2O$$

In the production of complex phosphate fertilisers (double superphosphate etc) the H_2SiF_6 obtained incidentally is contaminated with P_2O_5 impurity. In this case an ammoniacal silicofluoride-fluoride method is used to obtain aluminium fluoride of the required quality[16,17]).

Apart from liquid-phase fluorination with H_2SiF_6, methods have also been proposed for fluorination with aqueous solutions of its salts, and solutions of sodium or ammonium silicofluoride are mainly used for this purpose. Here the fluorination process requires a higher temperature and is carried out under autoclave conditions[18]).

It has been noted[17, 19]) that the requirement for fluoride compounds in the world aluminium and other branches of industry can only be fully satisfied through the use of H_2SiF_6, obtained as a by-product from the outgoing fluorine-containing gases from phosphate fertiliser plants. The data presented show that silicofluoride methods are extremely promising for the solution of a series of problems connected with the acceleration of technical progress in the metallurgy of light metals. The development of silicofluoride methods is held up by insufficient research into their physical and chemical principles and technological characteristics.

References

1) H C Coroux: R. Acad. Sci. Paris 1919, 168, 610.
2) US Patent Nos. 1929014, 1933; 2209131, 1940; 2145329, 1950.
3) N G Rudenko et alia: Nauchn. Tr. Irkutskogo NII, Redkikh Metallov 1961, (10), 357.
4) US Patent No. 2250851, 1940.
5) K R Hude et alia: Bull. Inst. Mining and Metallurgy 1961, (653), 9.
6) Materials of International Conference on the peaceful use of atomic energy: Vol. 8 Report p. 820 (USA), Metallurgizdat, Moscow 1958.
7) A I Lainer et alia: Authors' Certificate No. 285911, 10, XI, 1970, 34.
8) US Patent No. 1975482, 1934.
9) M A Mikhailov et alia: In: Chemical and physico-

Environmental considerations of solution mining

IN FOCUSING ON SPECIFIC ENVIRONMENTAL ASPECTS of in-situ mining and dump leaching, Jim V. Rouse, of the US Environmental Protection Agency (EPA), suggested that mining and hydrometallurgical mining solution systems should be designed to recycle chemical solutions in subsequent mining cycles, to be generally consistent with national water protection goals as stated in Public Law 92-500, the Federal Water Pollution Control Act (FWPCA) Amendments of 1972. He noted that in-situ mining and hydrometallurgical processing generally involve fewer problems of air and solid waste pollution than conventional mining and processing.

Rouse emphasized the following significant provisions of the FWPCA Amendments, noting that this act applies to water pollution and does not include problems of solid waste and air pollution:

Section 301 provides that the discharge of any pollutant by any person shall be unlawful, unless that person has a permit to discharge such pollutants. This restriction is applicable to all point sources throughout the nation. The term "point source" is defined as including "any discernible, defined, and discrete conveyance, including but not limited to, any pipe, ditch channel, tunnel conduit, well, discrete fissure, container, rolling stock, concentrated animal feeding operation, or vessel or other floating craft, from which pollutants are or may be discharged."

Section 402 provides for the establishment of the National Pollution Discharge Elimination System—a system of permitting and regulating contents of pollutant discharges. One provision of this section gives the States the opportunity to establish their own permit system and assume the operation of the Federal system. One of the requirements for State operation of a permit system is that the State must "control the disposal of pollutants into wells."

Section 307(a) provides that the EPA Administrator shall publish a list that includes "any toxic pollutant or combination of such pollutants for which an effluent standard (which may include a prohibition of discharge of such pollutants or combination of such pollutants) will be established." As of early 1974, the proposed list included the metals mercury and cadmium and the chemical compound cyanide and its associated compounds.

Section 311 regulates the discharge of oil and hazardous materials. This section of the law provides that persons who spill hazardous, non-removable substances can be fined up to $50,000 for each spill event. The section also requires prompt notification of the appropriate Federal agencies should such a spill occur, and provides for fines of $10,000 and imprisonment up to one year for the responsible party who failed to notify the appropriate agency.

As a final note of caution, Rouse warned that Section 504 provides for immediate court action if the EPA Administrator receives evidence that a pollution source or combination of sources is presenting an imminent and substantial danger to the health of persons or to the welfare of persons. Cases of ground water pollution endangering public water supplies could possibly fall under this provision, allowing the Administrator to bring immediate suit.

Monitoring ground water—a valuable safeguard

Rouse also suggested that all in-situ mining and dump leaching projects and nearby ground water streams should be properly monitored. He explained that a program of this nature would serve "not only as a protection for the environment, but as a protection for operators themselves. Such data could be extremely valuable for defense in the event of future law suits by property owners down-gradient from the mining operation." Observation holes should be designed and located to provide data on the direction of ground water and pollutant flow. A single ring of observation holes, concentric around the pond site, is not adequate. Rather, sufficient spatial data is required to permit calculation of direction and velocity of ground water movement beyond the injection site. □

Principles of hydraulic fracturing

THE CURRENT STATE-OF-THE-ART in hydraulic fracturing, an integral part of the in-situ mining process, was reviewed by Abbas Ali-Daneshy of Halliburton Services. He noted that actual applications of fluid injection can be a vital factor in the overall efficiency of any in-situ operation.

The data needed for optimizing hydraulic fracturing results include: fracture orientation and type; treatment fluid pressure and instantaneous shut-in pressure (the fluid pressure recorded immediately after the pumps are stopped with no fluid allowed to escape out of the well); the existence of barriers to fracture propagation; geology of the area; mechanical properties of the formation and its permeability, porosity, and chemical composition. Most of this information is obtained by carrying out one or more exploratory fracturing treatments in the area and at the depth of mineralization.

Information on the orientation of the induced hydraulic fractures is the basis for determining the fluid flow path, the location and spacing of the injection or withdrawal wells or tunnels, etc. The pressure recordings are used to compute the necessary horsepower for the main fracturing operations, the size, type and concentration of the propping agents, etc. Since not all formations fracture identically, the exploratory fracturing treatment should be designed to inspect possible barriers to fracture extension. Such information will prove useful in the design of hydraulic fractures for in-situ mining.

With proper planning and research, the author concluded, the use of hydraulic fracturing can make in-situ mining competitive with other mining methods. One reason is the great efficiency of hydraulic fractures, in terms of the input energy. This natural characteristic of hydraulic fractures is due to two phenomena. First, the mode of failure is tensile, which requires much less energy than compressive or shear failure. Second, the hydraulic fracture follows the propagation path which requires the least fluid pressure and, therefore, the least input energy.

Further elaborating on the fracturing process, Ali-Daneshy explained that the first stage is the actual initiation of the fracture. To achieve this, fluid is pumped into the well until the resulting pressure exceeds the resistance of the formation. At this point a hydraulic fracture initiates. Failure is indicated by a sudden drop in fluid pressure or an increase in the ability to pump fluid. The hydraulic fracture initiation is a result of tensile failure of the

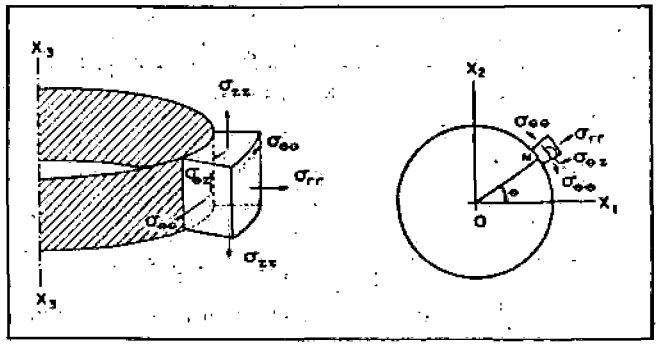

Fig. 1—Idealized stress components at the borehole wall.

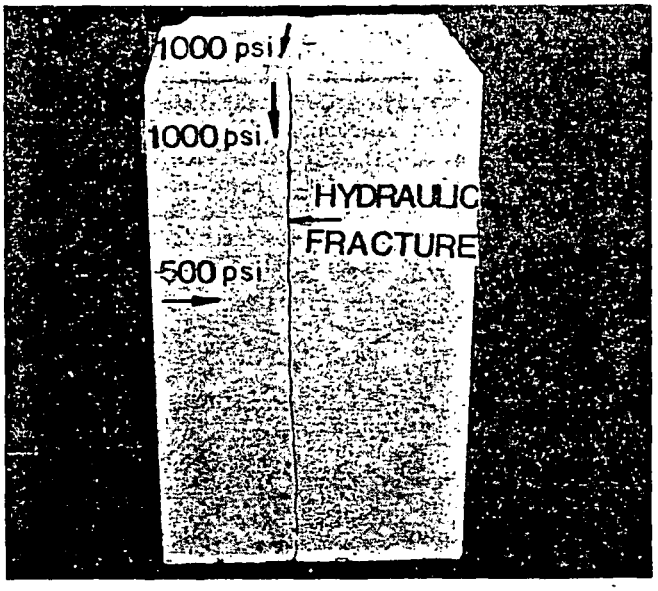

Fig. 2—Hydraulic fracture orientation with respect to principal stresses.

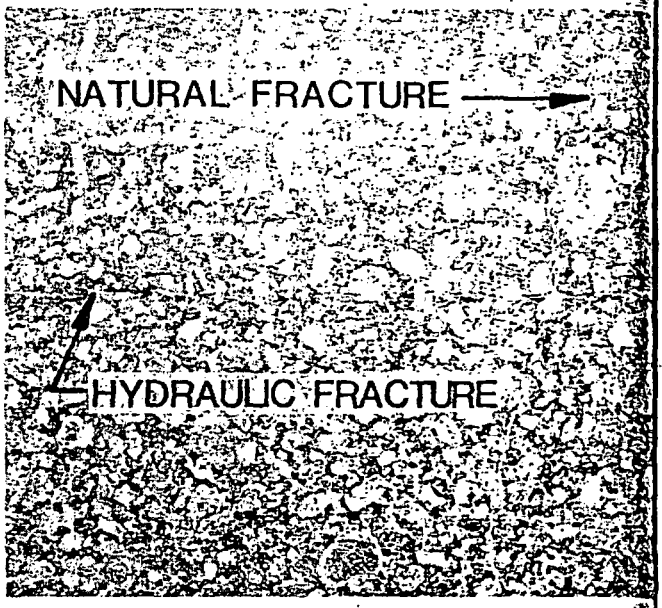

Fig. 3—Hydraulic fracture in a naturally fractured rock.

borehole wall. As one example, consider a cylindrical borehole in an assumed isotropic, homogeneous, poroelastic rock. The effective stresses around the borehole (Fig. 1) are of three kinds: in-situ principal stresses, fluid pressure inside the borehole (P_w) and fluid penetration into the porous rock. The magnitude of these stresses depends on whether the borehole is completed open-hole or cased.

To investigate fracture initiation in the open-hole condition, the maximum tensile stress induced at the borehole must first be calculated. Equating this with the tensile strength of the formation will yield the necessary criterion for fracture initiation. The maximum normal stress (σ_p) at point M is:

$$\sigma_p = \tfrac{1}{2}\left[\sigma_{\theta\theta} + \sigma_{zz} + \sqrt{(\sigma_{\theta\theta} - \sigma_{zz})^2 + 4\sigma_{\theta z}^2}\right]$$

which makes an angle γ_p with the borehole directrix:

$$\gamma_p = \tfrac{1}{2}\tan^{-1}\frac{2\sigma_{\theta z}}{\sigma_{\theta\theta} - \sigma_{zz}}$$

As the point M travels around the borehole, $\sigma_{\theta\theta}$, σ_{zz}, $\sigma_{\theta z}$ (the non-zero components of stress at the borehole which lie in a plane tangent to the borehole at M), and consequently σ_p and γ_p, change due to changes in the angle θ. The maximum tensile stress (σ_m) is therefore obtained by setting the derivative of σ_p with respect to θ equal to zero, and substituting the corresponding θ in the above equations. Equating σ_m with the tensile strength of the formation yields the criterion for fracture initiation. In practice this equation will yield the borehole fluid pressure (P_w = cavity pressure) necessary to start a hydraulic fracture.

The criterion for fracture initiation takes on a simple form whenever one principal stress direction is parallel to the borehole axis. Under this condition only vertical or horizontal fractures can initiate at the borehole. For vertical fractures,

$$P_c = P_o + \frac{\sigma_t - 3\sigma_{zz} + \sigma_{11}}{2 - \alpha\dfrac{1-2\nu}{1-\nu}}$$

and for horizontal fractures,

$$P_c = P_o + \frac{\sigma_t - \sigma_{zz}}{1 - \alpha\dfrac{1-2\nu}{1-\nu}}$$

where σ_t = tensile strength of the rock, P_o = reservoir fluid pressure, α = Biot's constant of the formation rock, and ν = Poisson's ratio of the formation rock.

In cased holes, hydraulic fracturing is achieved through perforations. Laboratory results to date have qualitatively indicated that cased-hole fracturing has a higher tendency to vertical initiation. Ali-Daneshy explains that this phenomenon can be attributed to two factors. First, the casing and cement cover up many of the weaknesses present in the rock which may have promoted horizontal fracture initiation. Second, fluid leak-off, which aids horizontal fracture initiation in open holes, is reduced in perforated holes.

The next state of the process is extension of the initiated fracture. Fluid injected after initiation will flow into the fracture and force its extension. The extent of fracture propagation depends on the volume of fluid pumped, plus formation and fluid properties. At a certain point during fracture extension, a propping agent is mixed with the treatment fluid and pumped into the fracture, to keep the fracture open and conductive to fluid flow after the treatment termination. □

Solution mining—a new challenge in blasting

THE RECENTLY INTENSIFIED EFFORT TO RECOVER METALS from low grade ore deposits by in-situ leaching has created new challenges for blasting specialists, reported D. D. Porter and H. G. Carlevato, of the Explosives Products Div. of E. I. du Pont de Nemours and Co., Inc. They noted, "Preparing blasts to condition orebodies for a leaching operation usually involves extraordinary conditions which require special studies and thorough engineering to augment judgments normally based mainly upon experience."

Although each deposit has its own set of problems, the authors presented a general outline that can be followed to engineer a blast for in-situ leaching. The checklist includes: shape of orebody, orebody characteristics, seismic consideration, missile consideration, type of explosive, powder factor, powder distribution, initiation system, delay system, loading logistics, economics of alternatives, and safety.

The shape of the orebody determines much of what can or cannot be done in fracturing an entire deposit in one blast. The blast design must be tailored to suit the orebody and its surroundings. The authors noted that the charge must be placed to result in equal displacement and uniform fragmentation in all parts of the orebody—which would strongly favor a downhole method. If the deposit is near the surface and is exposed on one or more sides as well as on the surface, the

choice of methods is much broader, and both downhole and tunnel blasting (coyote) can be considered. The depth of the deposit and the ratio between the depth and the lateral dimensions also affect the blast design. For a deposit with a high depth-to-width ratio, a large amount of overbreak at the surface would be likely, with poor explosive utility and generally undesirable overall results.

Orebody characteristics and the mechanics of rock behavior are also important factors in a blast design. Much of the end result depends on the rock's properties and its condition prior to the shot. On-site testing, with measurements that include pressure pulse, stress attenuation, and sonic velocities, will reveal the rock's characteristics. Such properties as brittleness and ability to absorb energy are also of interest.

The collected data make it possible to compute the stress wave shape produced by charges of various configurations. The wave shape is important in the blast design because of its effect on fragmentation and rock movement, and powder distribution and location of initiation points are guided accordingly. As one example, Fig. 2 illustrates the directional stress effect produced by a single coyote tunnel charge initiated at one end. Although the stress levels are not shown in absolute terms, it is possible to use the computed curve to arrange the charges in a position to give uniformly good fragmentation with the maximum stress levels applied where most needed.

Seismic considerations are vital in minimizing potential damage to neighboring structures, homes, and so forth. The authors considered this fact so important that "the entire feasibility of the project depends on it." Experience has shown that with the proper engineering, projects which initially appeared hopelessly restricted by vibration can be blasted with minimal damage to surrounding property. This is accomplished by obtaining basic field data from test blasts (frequency of ground motion, ground transmission constant, and wave amplitude). The predicted vibration levels are then compared with damage criteria for various structures, and the blast is designed to remain within an acceptable damage level.

Missile throw rock control can be engineered through empirical relationships developed both on a model scale and through large-scale experiments such as those conducted by the US Atomic Energy Commission. For blasting deposits close to the surface, the practice is to maximize the swell factor while minimizing the fly rock.

One reference found useful as a guide to ground movement in shot design is the curve developed by C. H. Noren of the University of Missouri at Rolla (see Fig. 3). This graph illustrates the relationship of burden velocity to the powder factor. For a 4 million-lb blast made by Ranchers Exploration and Development (see E/MJ, April 1972, p 98), a maximum rock velocity value of 58 fps was predicted, and subsequent measurements showed values ranging from 56 to 66 fps max. Although surface rock movement is related to the burden on the explosive, excessive fly rock can occur as a result of unexpected rock weaknesses or insufficient cover.

Factors governing the type of explosive chosen include the energy and water resistance of the explosive and its cost. While ANFO remains the cheapest blasting agent for large blasts, it has a relatively low density and relies entirely on packaging for water resistance. The authors reported that "only when attempts to apply ANFO fail for some insurmountable reason—such as a water problem or lack of energy—should a more costly explosive be considered."

It is vital to distinguish between the overall powder factor and specific localized powder factors. The former is used mostly for economic evaluation, etc., while the localized factor is used for shot design purposes, to account for variations in the orebody. Often a large shot is designed by putting together a number of smaller, individually designed shots, each with its own set of problems and limitations. For most blasting applications, powder factors range from less than 1 lb per yd to 4 or more lb per yd.

Powder distribution is an important consideration in obtaining optimum fragmentation and good permeability at the lowest possible cost. Two methods for placing the explosive are common: the conventional drillhole method and the placement of massive charges in adits and crosscuts, better known as the coyote method. In general, the drillhole shot is faster, easier to load, gives better explosive distribution, is easier to delay, and is therefore more flexible. It is also the most expensive method. The coyote blast, while less expensive, has a poorer explosive distribution, and is generally more difficult to delay.

An initiation system for very large blasts requires many built-in safety factors, including careful priming and initia-

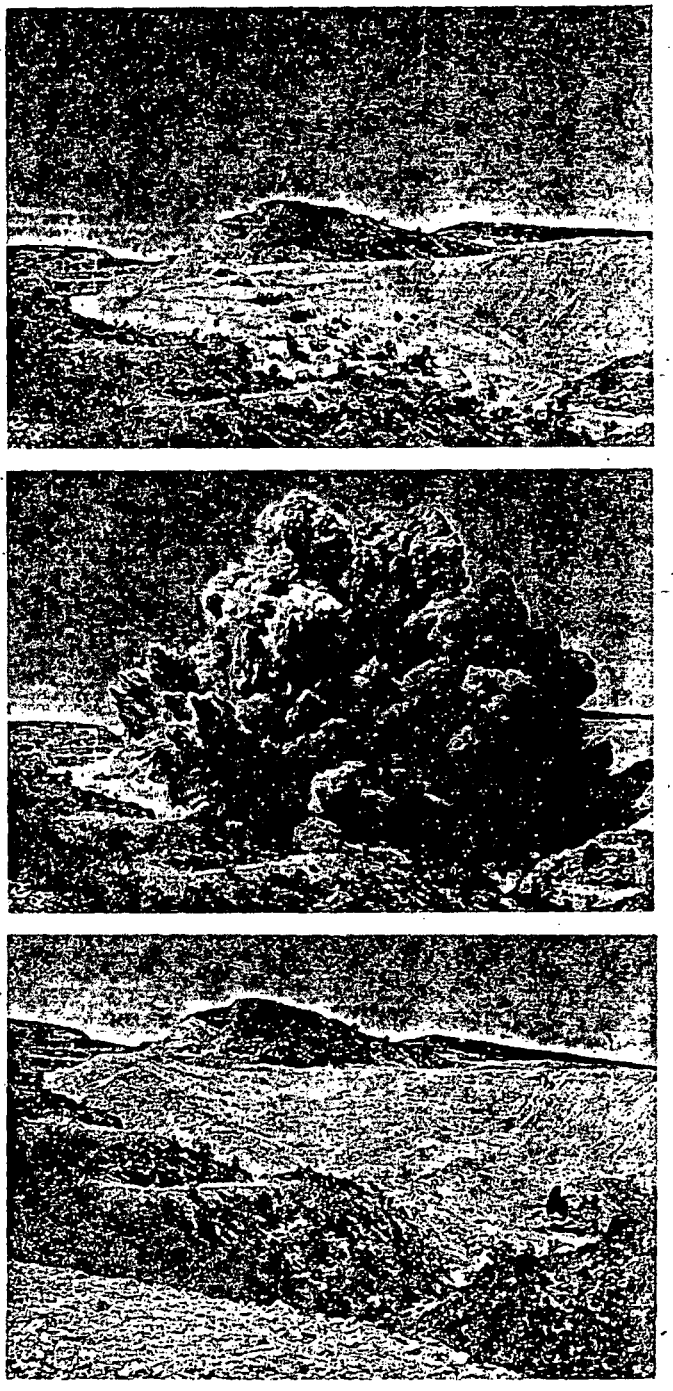

Fig. 1—Blast for McAlester Fuel Co. required 4.15 million lb of ANFO to fracture the orebody for in-situ leaching operations.

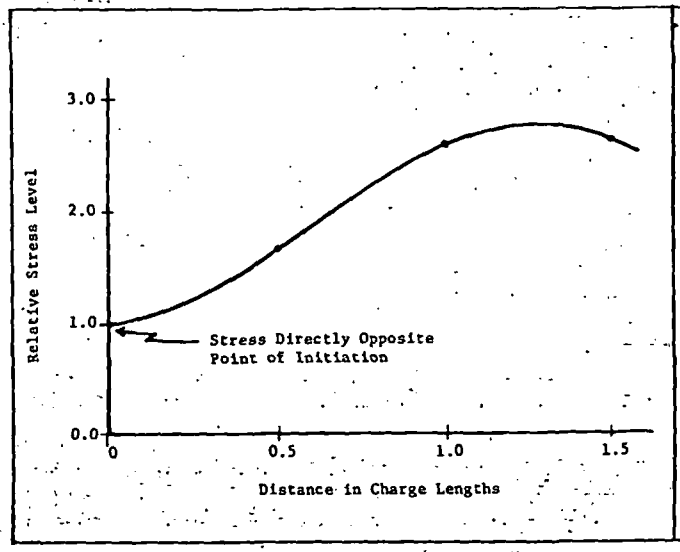

Fig. 2—Calculated relative stress level along line parallel to and one charge length away from charge (for given set of conditions).

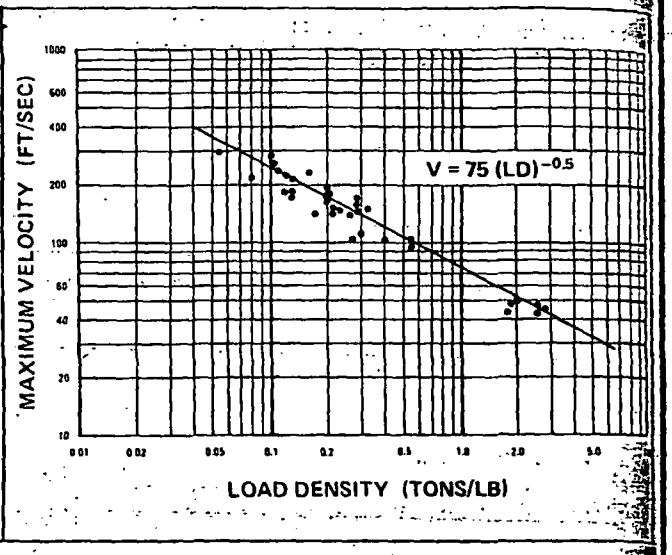

Fig. 3—Maximum burden velocity as a function of loading density.

tion techniques. Although cap and fuse can be used to initiate the blast, electric blasting caps are preferred, since they allow more exact synchronization with scientific instrumentation and a greater degree of personnel safety. Either delay caps or MS Primacord connectors can be used for desired delays. Again, safety during loading favors MS connectors.

Because of potential reliability loss, delayed charges are not commonly used for coyote blasting. However, when they are used, it is important to impart movement to upper levels before lower levels are shot. Long delays are usually not acceptable because they may damage the remaining lower charges. On the other hand, delays have to be long enough to permit sufficient movement to relieve the burden for the charge sequenced next.

While stating that it is important to produce blast results meeting project specifications at the lowest overall cost, the authors emphasized that merely applying the lowest cost explosives or the lowest cost mining method does not necessarily fulfill that objective. They added: "When considering the mining method, minimizing costs obviously is of major importance. However, the fragmentation and other factors such as depth and project timing discourage use of the lowest cost method. A higher cost method that will circumvent the limiting problems may be the only viable alternative."

Safety factors must be foremost in blast design. Safety precautions include the construction of sturdy bunkers to protect people and equipment within the range of the blast. The shot area must be thoroughly searched for livestock and bystanders prior to shot time. In this type of blasting, the authors have found that a countdown beginning up to 24 hr or more before shot time, with specific time checkpoints, is highly desirable. □

Fragmentation experiment for in-situ mining

THE USBM HAS BEEN ACTIVE in developing fragmentation technology for in-situ extraction systems, as reported by D. V. D'Andrea, R. A. Dick, R. C. Steckley, and W. C. Larson, of USBM. They explained that while the initial research is directed primarily at mining porphyry copper deposits, many of the results will be applicable to in-situ extraction of other mineral resources.

One recent USBM experiment was conducted at Duval Corp.'s Sierrita open pit mine in Pima County, Arizona, to determine blasting methods that would produce ideal fragmentation for maximum solution recoveries. In this fragmentation study, 10 blastholes, 9-in-dia. and 110 ft deep, were arranged to test blasthole spacings of 25, 20, and 15 ft (See Fig. 1). Blastholes had 60 ft of stemming and a 50-ft column of 10% aluminized slurry blasting agent. Three 120-ft-deep NX core drills mapped and detailed topographic features of the area. Holes were located to obtain samples in the middle of the 15-, 20-, and 25-ft blasthole spacing areas. In addition, 68 wooden stakes were used as station points so that elevation changes due to blasting could be determined within ±0.2 ft. The drill cores were analyzed to measure rock quality designation (RQD), size distribution, and standard physical properties.

The blast pattern was designed to test blasthole spacing based on equilateral triangles of 25, 20, and 15 ft. Blastholes were connected with 50-grain core load detonating cord, initiated by bottom-loaded 1-lb cast primers. The blast used a total of 17,440 lb of 10% slurry with a specific gravity of 1.20 and heat of detonation of 1.00 Kcal per gram. Each hole contained about 1,700 lb of slurry, and the maximum charge weight per delay interval was 5,300 lb. A portable three-component particle velocity-recording seismograph was used to measure ground vibrations at a distance of 800 ft from the blast. Powder factors, assuming infinite patterns, were 0.79, 1.24, and 2.20 lb per cu yd for the 25-, 20-, and 15-ft patterns, respectively.

Postshot studies included a topographic survey, detailed mapping of surface fractures, fragment-size distribution measurements of broken rock on the surface, and drilling of six NX diameter core holes into the broken zone. Diamond drilling into the broken zone did present problems, but six postshot holes were successfully drilled to 100-120 ft, and no holes were lost due to caving.

In reviewing the results, the maximum peak particle velocity recorded on the seismograph was 0.95 in. per sec at a distance of 800 ft. This value was lower than expected and indicated that the rock was weathered and fractured. Rubbleized surface material was well fragmented. Size distribution stud-

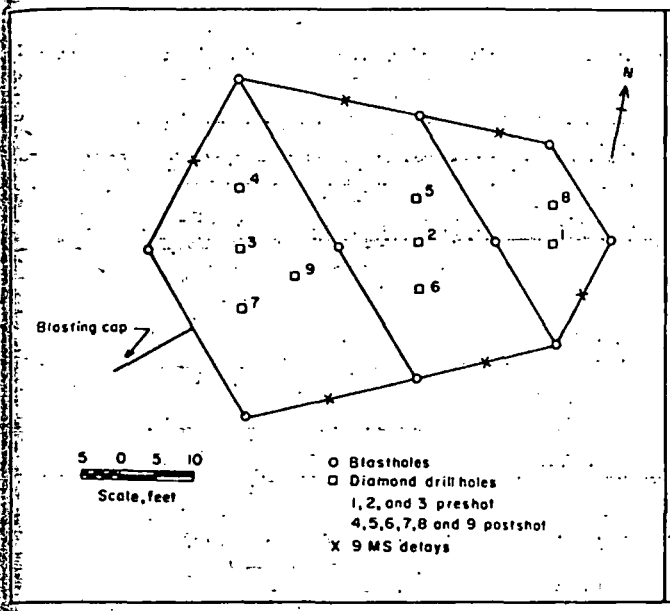

Fig. 1—Geometry of USBM test blast.

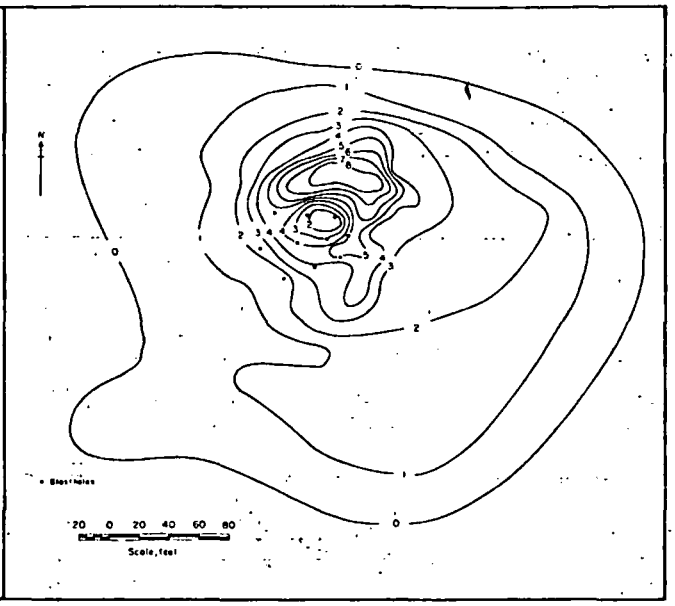

Fig. 2—Elevation changes produced by the test blast (contour intervals in feet).

ies of surface material showed that the greatest number of fragments were in the 2 to 3 in. range and the vast majority of pieces were less than 11 in. long. Blasting-induced fractures on the surface and outside of the rubble zone were found to have three preferred orientations—one controlled by the geologic structure, and the other two interpreted to be caused by blast-induced doming of the rock mass.

The greatest elevation changes were caused by rubble material being piled up about 40 ft to the northeast of the center of the blast. (See Fig. 2.) Three factors are believed to have contributed to this irregular muck pile distribution: a change in pattern from 25- to 15-ft blasthole spacing toward the northeast; initiation of the blast in the southwest, with the delay sequence proceeding to the northeast; and a falling-off of the surface in the northeast direction. The surface rise over the blast averaged about 5 ft, and the total volume increase produced by the blast was 5,100 cu yd. The swell factor was roughly estimated at 1.30.

Postshot diamond drill cores were sent to the lab for study. A comparison of the postshot cores with preshot cores showed that the blast had changed the RQD of the rock from "poor" to "very poor."

The largest piece of drill core averaged 14 in. for preshot holes, 11 in. for core from the 25-ft pattern, 8.5 in. for core from the 20-ft pattern, and 9 in. for core from the 15-ft pattern. The average size of core pieces 1 in. or greater was determined by dividing the total length of all pieces greater than 1 in. by the number of pieces greater than 1 in. This average size was about 3.2 in. for preshot core and between 2.2 and 2.8 in. for the postshot core.

For this test, the average fragment size was less than the 9-in.-dia fragments obtained at the Big Mike mine and within the 9-in. or less range at the Old Reliable mine.

Factors other than fragmentation affect copper recovery, and the authors believed that actual in-situ leaching tests would also have been desirable. However, they maintained that all three blasthole spacing patterns produced adequate breakage for in-situ leaching. □

In-situ leaching at the Big Mike mine

AT THE BIG MIKE COPPER MINE, in-situ mining was employed to maintain the active life after the economics of conventional open-pit techniques became unfavorable. Milton H. Ward, of Ranchers Exploration and Development Corp., explained the history of Big Mike's eventual development as an in-situ operation. Located 30 mi south of Winnemucca, Nev., the property was obtained by Ranchers Exploration in 1969 after extensive exploration by Cerro Corp. At that time the deposit was delineated, and reserves amounted to about 100,000 tons of 10.0% massive copper sulphide ore and 700,000 tons of 2.0% mixed oxide-sulphide ore. The orebody was a lenticular deposit, dipping at 50°. The massive sulphide mineralization was chalcocite and chalcopyrite, surrounded by a halo of lower grade mixed oxide-sulphide ore. The deposit measured 600 ft long and 300 ft wide and extended to a depth of 300 ft from the outcrop on the surface.

During the initial phase of operation, over 100,000 tons of high grade sulphides were mined and marketed. About 300,000 tons of low grade mixed ore was crushed to minus 2 in., stacked on an impermeable asphalt pad, and placed under leach. A precipitation plant, decanting area, and drying pad were constructed and are currently being used to produce cement copper.

After the high grade sulphide ore was removed, about 475,000 tons of mixed ore remained in the walls and bottom of the pit. Use of conventional methods to extract the remaining ore was considered, but a 6.5 to 1 stripping ratio was economically unacceptable. After extensive study, a decision was made to blast this ore into the pit and leach it in place.

Four requirements for successful in-situ production were reviewed: 1) dissolving the metal, 2) making the deposit permeable, 3) collecting the pregnant solutions, and 4) recovering the valuable product—copper. From a number of leach tests, it appeared that over 80% of the copper could be removed by adding high quantities of acid (13 lb acid per pound of copper). Further testing indicated that an acceptable recovery of about 70% could be obtained by using much lower quantities of acid and maintaining the leach solution at a pH of 2.0. The latter approach appeared most favorable, according to Ward.

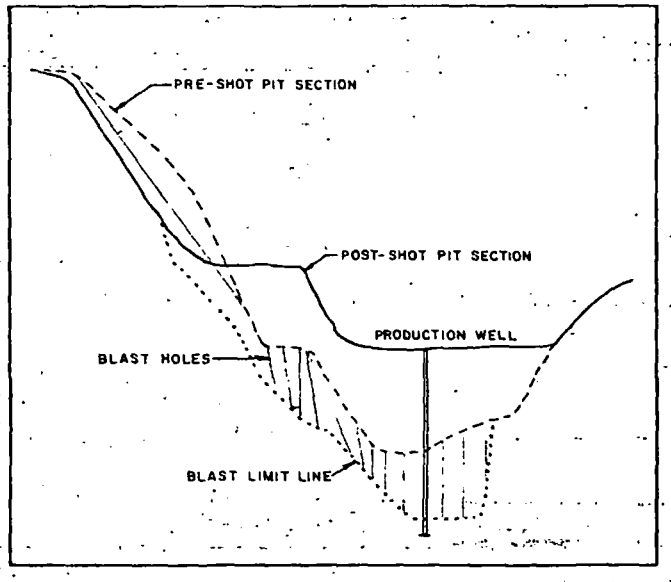

Fig. 1—Big Mike pit cross section before and after blast.

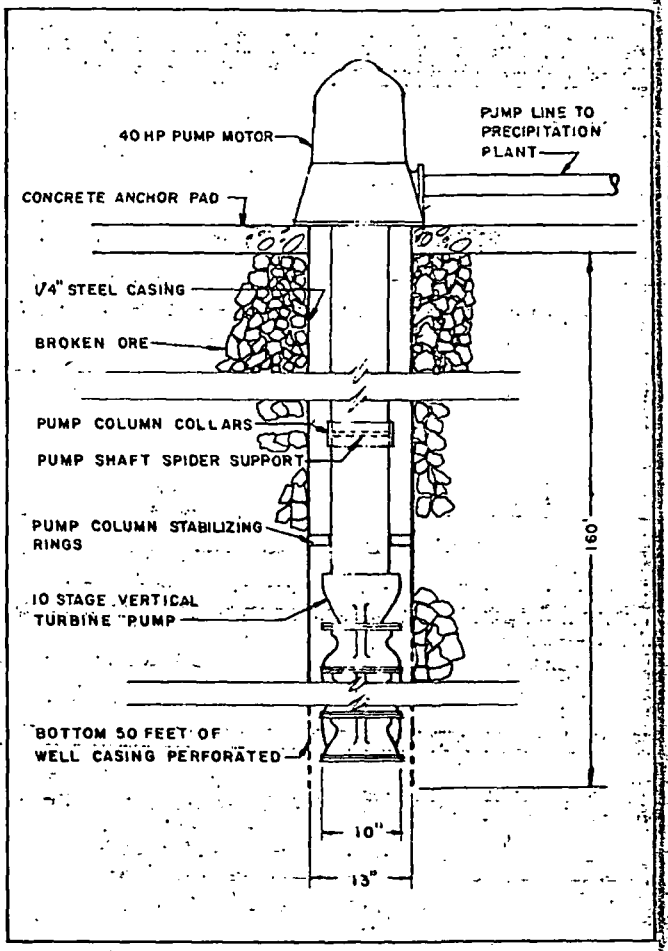

Fig. 2—How the recovery well pump column and casing was installed.

From the low grade ore that was earlier removed and leached, it was also apparent that an acceptable amount of copper could be dissolved. The question of what product to produce required no particular study because cement copper was already being produced and marketed.

The pit blast was designed with assistance from Du Pont Co. A conventional drill and blast scheme was chosen, primarily because of the steep wall configuration of the existing pit. A study of explosive factors and pit terrain indicated that the desired fracturing could be best obtained by utilizing large, closely spaced angled and vertical blastholes. Approximately 21,000 ft of 5¾-, 9-, and 9⅞-in.-dia blasthole drilling was required. Blastholes along the surrounding pit walls were loaded with ANFO and with occasional heavier-density water gels in areas of high rock burden. Closer to the water table, high density water-resistant explosive or water gel was used. All blastholes were connected with standard Primacord and initiated at the hole bottom by electric caps. Altogether, about 400,000 lb of explosives were used to fracture approximately 600,000 tons of material, giving a ratio of 1.5 lb of explosive per ton. (See Fig. 1.)

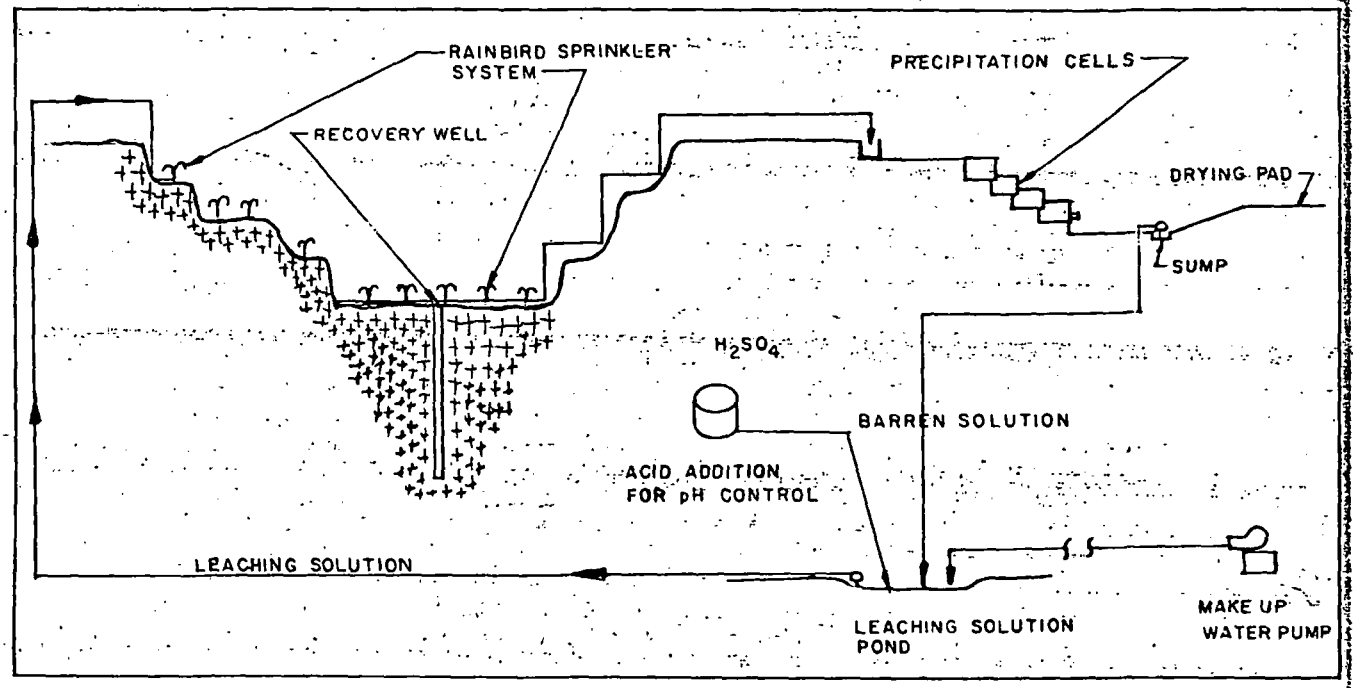

Fig. 3—Flowsheet of pit leach operation at Big Mike mine.

The solution collection system was located at the bottom of the Big Mike pit. Since a water table was present near the bottom of the Big Mike pit, and the tight pit walls would act as a barrier to the percolating solutions, this location was ideal for the ultimate solution collection device. Several monitoring wells were drilled near the pit along the most likely avenue of lateral water loss. Surveillance of these wells indicates that no loss or contamination is taking place so far.

The distribution of leaching solution is through sprinkler-heads attached to 2-in. PVC pipe branch lines, located on the four terraces created after the blast. Leach solution acid strength is maintained at a pH of 1.5 to 2.0. A single-stage stainless steel centrifugal pump picks up the solution from the storage pond and transports it at approximately 200 gpm to the pit distribution system (Fig. 3). The leach liquor is sprinkled onto the broken ore and percolates by gravity to the main collection well pump.

The actual solution recovery involves one production well in the pit bottom. A conventional churn drill well was drilled from the lower terrace to a depth of 180 ft (Fig. 2).

The sprinkling of the broken ore was started prior to completing the drilling of the recovery well, assuring a saturated orebody and immediate production once the recovery pump was operational. Pumping commenced at a rate of 250 gpm of 2.0 gm per liter of copper. It was anticipated that production for the first year would average 200 gpm at 2 gm per liter, and it appears that this goal will be attained.

The economic viability of the venture was greatly enhanced by the existing facilities and utilities, the physical layout, and the known types of rock at Big Mike. While copper recovery in the future is uncertain, a recovery of less than 10% was fortunately all that was required for the project to pay out. □

Microbe leaching of copper and molybdenum ores

Reprinted by permission of Canadian Journal of Microbiology.

THE TECHNIQUE OF BIOEXTRACTIVE METALLURGY has been known for some time and has been used in leaching copper from waste dumps and other areas formerly termed "economically unfavorable" under conventional methods. Corale L. Brierley, of the New Mexico Bureau of Mines and Mineral Resources, went on to explain that the organisms associated with copper leaching have been identified as "Thiobacillus thiooxidans" and "Thiobacillus ferrooxidans," whose functions in the leaching process are to oxidize sulphides to polythionates, and sulphate and ferrous iron to ferric iron. The combination of the oxidized metals and the increased level of acidity created by the biogenic activity results in a chemical lixiviant which produces an accelerated chemical alteration of the minerals.

The ability of these organisms to grow and perform their specific function is limited only by the availability of an energy source and nutrients and by environmental changes, particularly temperature, pH, and oxygen availability.

While the organisms mentioned and their relationship to bioextractive mining have been relatively well-studied, there have been no attempts to discover or study other microorganisms which may be more compatible with the high temperatures, low-oxygen environment, and heavy metal concentrations at leach dumps and in-situ mining operations.

An unidentified, high-temperature microbe, which oxidizes reduced inorganic sulphur and iron in an acid medium between 45° and 75°C at a pH of 2.0, has been the subject of further lab studies, according to Brierley. The morphology is unlike that of the thiobacilli, being pleomorphic rather than rod-shaped (Fig. 1). The organism ranges in size from 1 to 1½ µm. dia.

In tests of reactions with copper sulphide minerals, the microbe leached a chalcopyrite concentrate in a batch reactor using an acid medium (pH 2.5), with 0.02% yeast extract at 60°C. The copper is solubilized at a rate of 10-16 mg per liter per day from a chalcopyrite concentrate (27.6% copper—74-105 microns in particle size) over a 30-day period. The solubilization of copper in uninoculated flasks occurs at a rate of 1.0-1.8 mg per liter per day over the same period. Preliminary results indicate that about 50% of the copper in a low-grade ore (0.32% copper, -16 to +50 mesh, from the Chino mine of Kennecott Copper Corp.) is leached from the ore in 60 days at 60°C in an acid medium containing the organism. About half of this copper is solubilized by the acid medium.

The ability of the organism to tolerate soluble copper is essential to successful leaching of copper sulphide minerals. The tolerance of the organism to copper is ascertained by comparing the oxygen uptake of the organism when it is suspended in varying concentrations of soluble copper to the

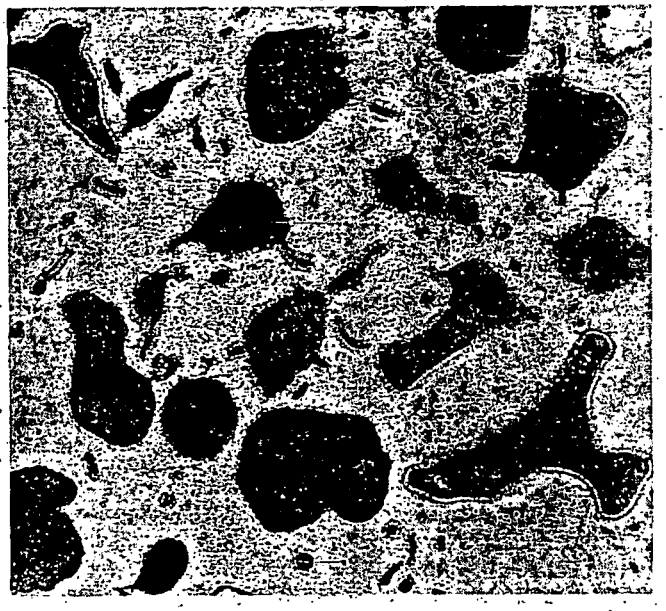

Fig. 1—Electron micrograph of a thin section of microorganism.

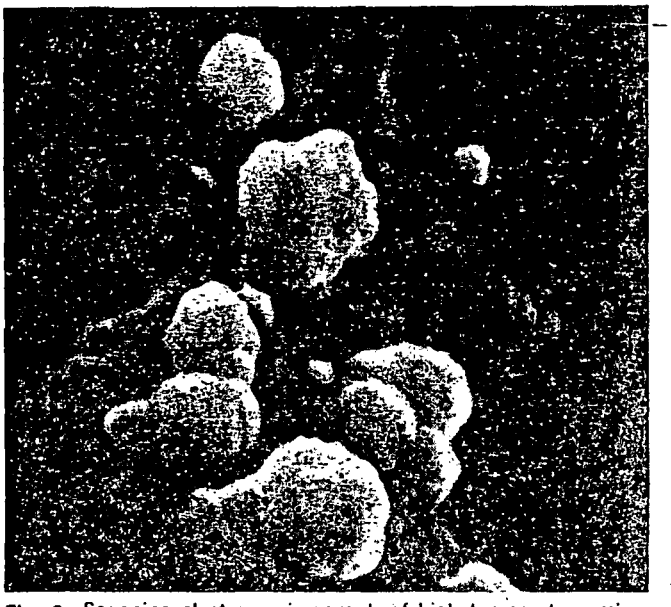

Fig. 2—Scanning electron micrograph of high temperature microorganism on molybdenite fines.

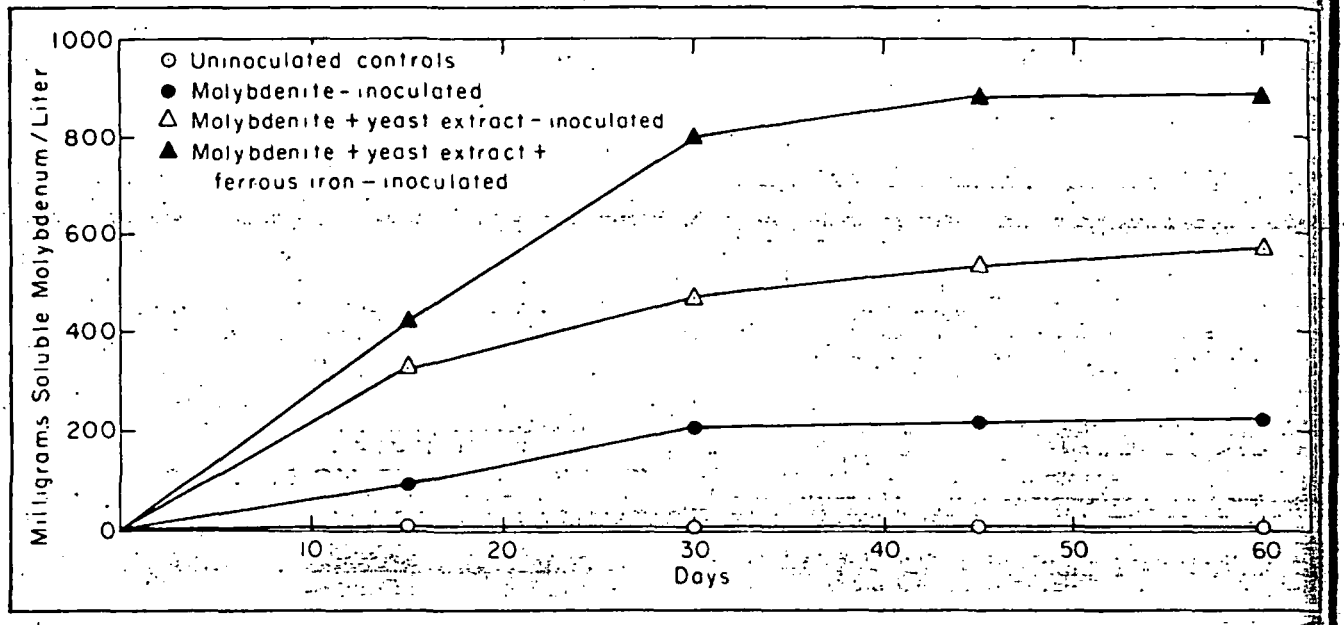

Fig. 3— Solubilization of molybdenum from molybdenite concentrate for 60 days.

oxygen uptake when no copper is present. Although the organism can tolerate more than 10.0 gpl copper, it is not able to grow when the concentration of copper exceeds 1.0 gpl. Growth tolerance is ascertained by suspending the organism in acid medium containing varying concentrations of soluble copper, 0.02% yeast extract as a growth enhancement factor, and elemental sulphur, an oxidizable energy source. The absence of microscopically observable microbes, protein production, and pH decline indicate the absence of growth.

A 98.5% molybdenite concentrate with a particle size of 12 to 62 microns is oxidized by the microbe at 60°C. Over a 30-day period, 3.3% of the molybdenum is solubilized from the molybdenite, according to Brierley, when it is suspended in an inoculated medium (pH = 2.5). It was also found that this yield can be increased to 8.3% in 30 days when 0.02% yeast extract is added. The addition of 0.02% yeast extract and 1% $FeSO_4 \cdot 7H_2O$ increases the yield to 13.3% in 30 days. In all cases, the leaching of molybdenite in uninoculated controls yields 0.1% molybdenum solubilized in 30 days (Fig. 2).

Structural and physiological studies had indicated that the high-temperature microbe is unrelated to the thiobacilli and is probably another type of microorganism that has neither been previously isolated nor considered for leaching purposes. Field studies indicated that temperatures within low-grade copper ore dumps may reach 80°C. These elevated temperatures probably inhibit the leaching activity of strains of sulphur- and iron-oxidizing bacteria whose optimum temperatures range from 25°C to 45°C. Brierly concluded that the economic implication of this new study, at least initially, is that it is technically feasible for the new microbe to biogenically extract copper at temperatures exceeding 45°C and that molybdenite can now be biogenically extracted. □

Effect of particle size on microbiological leaching

TO ASSESS THE LEACHABILITY of a particular waste ore, a representative sample is usually subjected to a series of column tests, to determine the maximum possible extraction, and to get some idea about the rate at which this extraction can be carried out. A. Bruynesteyn and D. W. Duncan, of the Mineral Microbiology Section of British Columbia Research, reported on one test performed in 6-ft-high by 6-in.-dia PVC columns, to determine the effect of particle size on the microbiological leaching of chalcopyrite bearing ore. They noted: "The information developed from such tests is of distinct value in assessing whether or not the material is leachable; the rate of extraction, and possibly the extent of extraction, are strongly influenced by the particle size of the material under test."

To further understand this relationship, tests were conducted on a 1,000-lb sample of minus 2 in. ore from the Britannia Beach operation of the Anaconda Co. in British Columbia. The ore consisted of a mixture of chalcopyrite, sphalerite, and pyrite, and was separated into six fractions. Each fraction was assayed for copper and zinc values (see

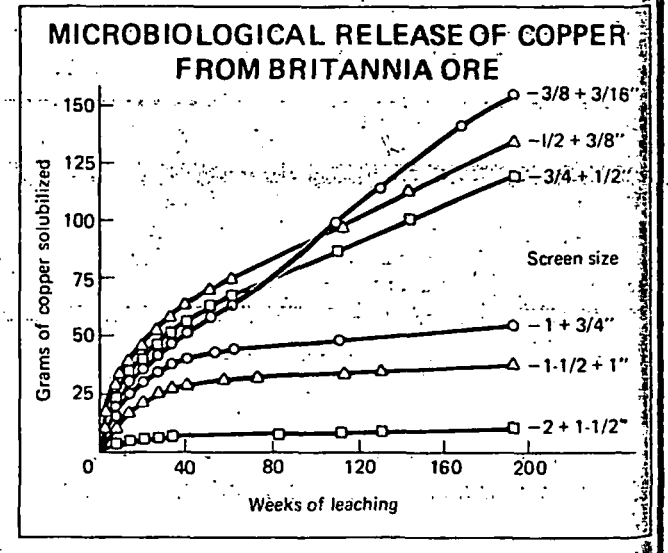

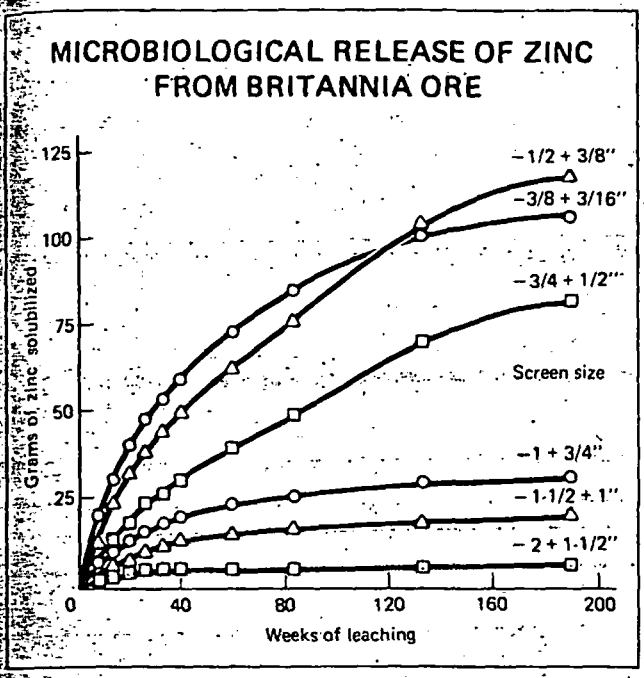

Table 1), after which 100-lb portions were leached in duplicate columns, utilizing a one-week leach, four-week rest cycle. Each column was inoculated with an active strain of thiobacillus ferrooxidans grown in shake flasks on finely ground chalcopyrite concentrate. All the columns were installed in a specially built room, where the temperature was maintained at 35°C. A total of 20 liters of leach solution, contained in a 50-liter plastic bucket placed underneath each column, was used to leach the charge in the column, with the aid of an air-lift water recycling system.

The data obtained, according to the authors, indicate that the relationship between extraction rate and particle size is a hyperbolic function. If the relationship was based solely on surface area, the results from the column studies would have given a straight line, since reducing the particle size of a fixed weight of mineralization results in an increase in the actual number of particles, proportional to the cube of the diameters, but also results in a reduction in surface area of the individual particle, proportional to the square of the diameter. The actual increase in surface area of a fixed weight of material is inversely proportional to the decrease in the diameter of the particles involved.

The authors concluded that the rate of microbiological leaching of a fixed weight of mineralization is not directly proportional to the surface area, but rather is influenced by the actual volume of the material which is exposed to the leaching environment. This exposed volume consists of the actual surface area plus the depth of penetration of both the leach liquors and the leaching bacteria.

The configuration of the zinc and copper rate curves obtained with this particular sample suggested that little improvement in leach rate can be effected by crushing, unless the ore is crushed to less than 2 in. At 2 in., the copper extraction rate was 0.15% per week, so that even with the ideal environment and physical conditions of the lab column test, it still would take 1,000 weeks or 19.2 years to get 15% extraction after the initial soluble copper has been removed. Most important, leach dumps of considerable height would have to be built in order to produce pregnant solutions, based on the results of the metal recovery rate curves.

These tests have shown that an evaluation of leaching rates for different particle sizes can yield valuable information about the actual performance of this material in a commercial leaching dump. The authors cautioned that if a column test is performed on only one particle size, the information obtained could result in erroneous scale-up to a dump-size-operation. However, if the information obtained from a test at various particle sizes indicates that leaching rates are substantial even at 2-in. particle sizes, then commercial dump performance could be reasonably predicted by extrapolating this rate curve. Finally, the particle size tests will yield information not only on the performance of the ore under test but also on leach liquor characteristics. □

Table 1 —Assays of head samples

Screen Size (in.)	% Cu	% Zn
−2 +1½ inch	0.53	1.48
−1½ +1 inch	1.00	0.46
−1 +3/4 inch	0.81	0.36
−3/4 +½ inch	0.95	0.42
−½ +3/8 inch	0.81	0.42
−3/8 +3/16 inch	0.82	0.33

Table 2—Theoretical and actual zinc to copper release ratios

Screen Size	Grams Metal Released per 100 Weeks		Actual Ratio Zn/Cu	Theoretical Ratio Zn/Cu
	Cu	Zn		
−3/8 +3/16 inch	65.1	51.8	0.80	0.40
−½ +3/8 inch	49.0	58.4	1.19	0.52
−¾ +½ inch	39.2	48.0	1.22	0.44
−1 +¾ inch	9.8	8.2	0.88	0.44
−1½ +1 inch	6.2	6.8	1.10	0.46
−2 +1½ inch	2.0	1.02	0.51	2.70

The editors of E/MJ express their appreciation to the Society of Mining Engineers of AIME and its Executive Secretary, Claude L. Crowley, for permission to summarize selected articles from the Dallas Solution Mining Symposium.

A special word of thanks is also due to: F. F. Aplan, chairman, Penn State University; W. A. McKinney, US Bureau of Mines; and A. D. Pernichele, Dames and Moore. It was their monumental task to compile and edit the large number of technical papers presented.

The entire text of the proceedings, bound in a single volume, is available at a price of $15.00 to non-AIME members, $10.00 to AIME members, and a special rate of $6.00 to student AIME members. Write to: Society of Mining Engineers, AIME, 540 Arapeen Drive, Salt Lake City, Utah 84108.

Solution mining opening new reserves

From hydraulic fracturing to microbe leaching, Dallas Solution Mining Symposium explored aspects of a technique that promises to cut mining costs and 'create' new ore reserves

THE GROWING US CONCERN ABOUT developing mineral resources is intensified by the rapid depletion of economically viable ore reserves and by an unprecedented increase in demand for mineral products. The US "horn of plenty"—shallow deposits of high grade ore—is quickly being depleted. Capital investment and operating costs continue to soar at unprecedented rates, while new developments in conventional surface and underground mining techniques are not sufficient to beat these rising costs. Against this background, F. F. Aplan, chairman of the Dallas Solution Mining Symposium, suggested: "Solution mining is one technique which offers the potential of providing substantial reductions, in both capit and operating costs."

While solution mining has been used for many years f heap leaching, salt extraction, and dump leaching, th stepped-up research on solution mining and its applicatio has expanded in scope to include a variety of metals an types of orebodies. Continued research in this area may d velop ore reserves from a resource bank that up to now h been termed "unrecoverable."

The following roundup summarizes various paper presented at the Symposium (Dallas, Tex., February 25-27).

What's behind the new interest in solution mining

"SOLUTION MINING, OR IN-SITU MINING, has received increasing attention in the past few years because the method offers many attractive possibilities for reducing the environmental impact of mining, as well as making feasible the extraction of deeper, low value mineral reserves," reported D. A. Shock and F. R. Conley, both of the Research and Development Department of Continental Oil Co. They suggested that "borehole mining" may be a more accurate description of the basic technique, which recovers a mineral value by drilling into the orebody, circulating an extractive fluid and removing the mineral value (possibly separating the mineral value from the fluid), and then recycling the fluid.

The authors classify borehole mining according to the following three types:

Complete solution mining—a significant method in the production of brines for the chemical industry and perhaps more important in the building of petroleum storage capacity.

Slurry mining—largely experimental as a means of producing phosphate rock, coal, and other minerals; has not yet progressed beyond the experimental stage.

Solution mining demands new blasting techniques.

Leach mining—dissolving mineral values in an extractio fluid, leaving the gangue minerals behind in the ground, an producing the solubilized mineral out of a borehole. Frasc sulphur is produced by an established process of this typ Much of the current leach mining research has been aimed recovering uranium, copper, lead, and zinc.

The borehole mining system offers advantages in thre areas: environmental, mineral utilization, and economic While a mining method that would leave the earth undi turbed is regarded as an impossible goal, the authors sugge that the method which least violates the earth should surel be considered, and borehole mining realizes this potential a great degree. However, the method is not without enviro mental drawbacks. Operating a reservoir extraction system s that solutions are contained within the orebody may be diffi cult, and contamination of ground water can be a problem Ground movement may also be troublesome, causing col lapse and shearing of the input tubing. However, eliminatio of the overburden removal stage is a solid plus for the solu tion mining method.

As for mineral utilization, borehole mining should be abl to reach deeper reserves and would be applicable to lowe mineral values. The authors cited as one example the reserv of a South Texas uranium field. Lowering the cutoff grad from 0.10% to 0.05% would more than double the magnitud of reserves. Extending the limits of economical mining depth would also boost reserves considerably, although the exact ex tension of reserves in that field is presently unmeasurable.

In terms of economic strategy, solution mining offers many advantages. Conventional mining techniques require a hig initial investment, with no cash flow for a significant period o time. The time-value of money thus requires a larger profi margin to enable a potential project to attract initial inves ment capital. With solution mining, the development of a orebody should be relatively inexpensive, and concentratio or separation of mineral values is not overly expensive. Thus if sufficient production can be maintained, the cash return starts in a much shorter time, for a better return on invest ment. Production rates are more flexible with a solution min ing system as they depend on the rate of development of a field. Field development can be scheduled by the cash gener ated by the profit from the operation. With the high cost o capital today, a less capital-intensive mining system is vital.

Environmental considerations of solution mining

IN FOCUSING ON SPECIFIC ENVIRONMENTAL ASPECTS of in-situ mining and dump leaching, Jim V. Rouse, of the US Environmental Protection Agency (EPA), suggested that mining and hydrometallurgical mining solution systems should be designed to recycle chemical solutions in subsequent mining cycles, to be generally consistent with national water protection goals as stated in Public Law 92-500, the Federal Water Pollution Control Act (FWPCA) Amendments of 1972. He noted that in-situ mining and hydrometallurgical processing generally involve fewer problems of air and solid waste pollution than conventional mining and processing.

Rouse emphasized the following significant provisions of the FWPCA Amendments, noting that this act applies to water pollution and does not include problems of solid waste and air pollution:

Section 301 provides that the discharge of any pollutant by any person shall be unlawful, unless that person has a permit to discharge such pollutants. This restriction is applicable to all point sources throughout the nation. The term "point source" is defined as including "any discernible, defined, and discrete conveyance, including but not limited to, any pipe, ditch channel, tunnel conduit, well, discrete fissure, container, rolling stock, concentrated animal feeding operation, or vessel or other floating craft, from which pollutants are or may be discharged."

Section 402 provides for the establishment of the National Pollution Discharge Elimination System—a system of permitting and regulating contents of pollutant discharges. One provision of this section gives the States the opportunity to establish their own permit system and assume the operation of the Federal system. One of the requirements for State operation of a permit system is that the State must "control the disposal of pollutants into wells."

Section 307(a) provides that the EPA Administrator shall publish a list that includes "any toxic pollutant or combination of such pollutants for which an effluent standard (which may include a prohibition of discharge of such pollutants or combination of such pollutants) will be established." As of early 1974, the proposed list included the metals mercury and cadmium and the chemical compound cyanide and its associated compounds.

Section 311 regulates the discharge of oil and hazardous materials. This section of the law provides that persons who spill hazardous, non-removable substances can be fined up to $50,000 for each spill event. The section also requires prompt notification of the appropriate Federal agencies should such a spill occur, and provides for fines of $10,000 and imprisonment up to one year for the responsible party who failed to notify the appropriate agency.

As a final note of caution, Rouse warned that Section 504 provides for immediate court action if the EPA Administrator receives evidence that a pollution source or combination of sources is presenting an imminent and substantial danger to the health of persons or to the welfare of persons. Cases of ground water pollution endangering public water supplies could possibly fall under this provision, allowing the Administrator to bring immediate suit.

Monitoring ground water—a valuable safeguard

Rouse also suggested that all in-situ mining and dump leaching projects and nearby ground water streams should be properly monitored. He explained that a program of this nature would serve "not only as a protection for the environment, but as a protection for operators themselves. Such data could be extremely valuable for defense in the event of future law suits by property owners down-gradient from the mining operation." Observation holes should be designed and located to provide data on the direction of ground water and pollutant flow. A single ring of observation holes, concentric around the pond site, is not adequate. Rather, sufficient spatial data is required to permit calculation of direction and velocity of ground water movement beyond the injection site. □

Principles of hydraulic fracturing

THE CURRENT STATE-OF-THE-ART in hydraulic fracturing, an integral part of the in-situ mining process, was reviewed by Abbas Ali-Daneshy of Halliburton Services. He noted that actual applications of fluid injection can be a vital factor in the overall efficiency of any in-situ operation.

The data needed for optimizing hydraulic fracturing results include: fracture orientation and type; treatment fluid pressure and instantaneous shut-in pressure (the fluid pressure recorded immediately after the pumps are stopped with no fluid allowed to escape out of the well); the existence of barriers to fracture propagation; geology of the area; mechanical properties of the formation and its permeability, porosity, and chemical composition. Most of this information is obtained by carrying out one or more exploratory fracturing treatments in the area and at the depth of mineralization.

Information on the orientation of the induced hydraulic fractures is the basis for determining the fluid flow path, the location and spacing of the injection or withdrawal wells or tunnels, etc. The pressure recordings are used to compute the necessary horsepower for the main fracturing operations, the size, type and concentration of the propping agents, etc. Since not all formations fracture identically, the exploratory fracturing treatment should be designed to inspect possible barriers to fracture extension. Such information will prove useful in the design of hydraulic fractures for in-situ mining.

With proper planning and research, the author concluded, the use of hydraulic fracturing can make in-situ mining competitive with other mining methods. One reason is the great efficiency of hydraulic fractures, in terms of the input energy. This natural characteristic of hydraulic fractures is due to two phenomena. First, the mode of failure is tensile, which requires much less energy than compressive or shear failure. Second, the hydraulic fracture follows the propagation path which requires the least fluid pressure and, therefore, the least input energy.

Further elaborating on the fracturing process, Ali-Daneshy explained that the first stage is the actual initiation of the fracture. To achieve this, fluid is pumped into the well until the resulting pressure exceeds the resistance of the formation. At this point a hydraulic fracture initiates. Failure is indicated by a sudden drop in fluid pressure or an increase in the ability to pump fluid. The hydraulic fracture initiation is a result of tensile failure of the

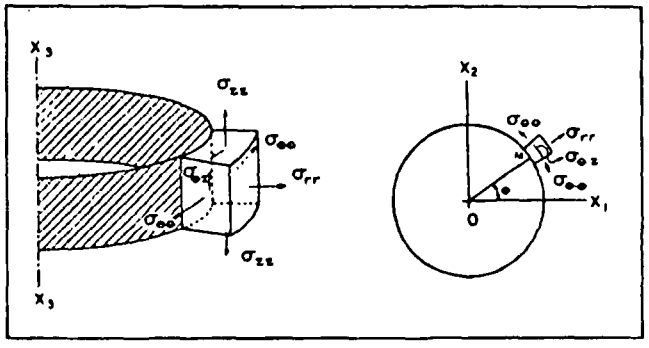

Fig. 1—Idealized stress components at the borehole wall.

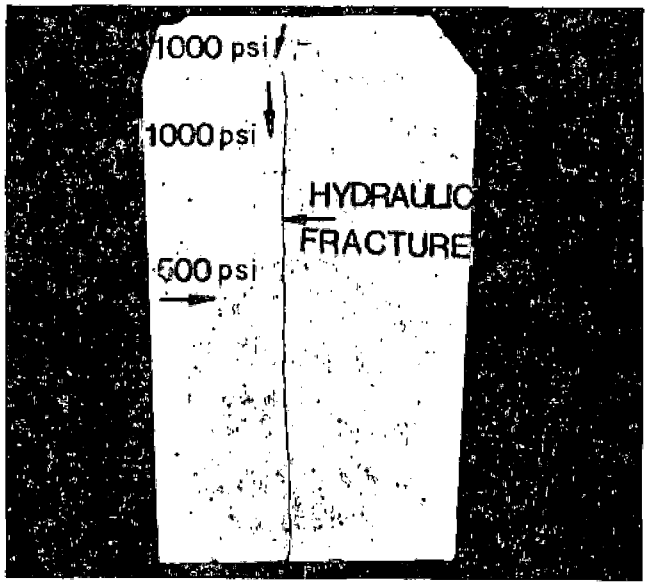

Fig. 2—Hydraulic fracture orientation with respect to principal stresses.

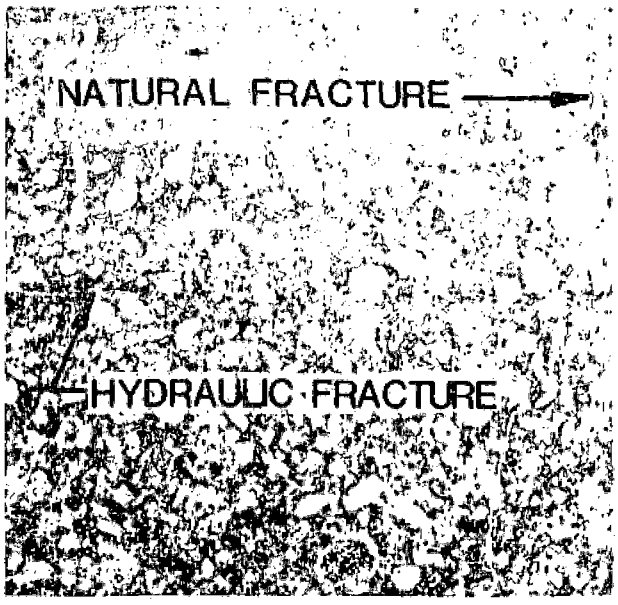

Fig. 3—Hydraulic fracture in a naturally fractured rock.

borehole wall. As one example, consider a cylindrical borehole in an assumed isotropic, homogeneous, poroelastic rock. The effective stresses around the borehole (Fig. 1) are of three kinds: in-situ principal stresses, fluid pressure inside the borehole (P_w) and fluid penetration into the porous rock. The magnitude of these stresses depends on whether the borehole is completed open-hole or cased.

To investigate fracture initiation in the open-hole condition, the maximum tensile stress induced at the borehole must first be calculated. Equating this with the tensile strength of the formation will yield the necessary criterion for fracture initiation. The maximum normal stress (σ_p) at point M is:

$$\sigma_p = \tfrac{1}{2}\left[\sigma_{\theta\theta} + \sigma_{zz} + \sqrt{(\sigma_{\theta\theta} - \sigma_{zz})^2 + 4\sigma_{\theta z}^2}\right]$$

which makes an angle γ_p with the borehole directrix:

$$\gamma_p = \tfrac{1}{2}\tan^{-1}\frac{2\sigma_{\theta z}}{\sigma_{\theta\theta} - \sigma_{zz}}$$

As the point M travels around the borehole, $\sigma_{\theta\theta}$, σ_{zz}, $\sigma_{\theta z}$ (the non-zero components of stress at the borehole which lie in a plane tangent to the borehole at M), and consequently σ_p and γ_p, change due to changes in the angle θ. The maximum tensile stress (σ_m) is therefore obtained by setting the derivative of σ_p with respect to θ equal to zero, and substituting the corresponding θ in the above equations. Equating σ_m with the tensile strength of the formation yields the criterion for fracture initiation. In practice this equation will yield the borehole fluid pressure (P_w = cavity pressure) necessary to start a hydraulic fracture.

The criterion for fracture initiation takes on a simple form whenever one principal stress direction is parallel to the borehole axis. Under this condition only vertical or horizontal fractures can initiate at the borehole. For vertical fractures,

$$P_w = P_0 + \frac{\sigma_t - 3\sigma_{yy} + \sigma_{xx}}{2 - \alpha\,\dfrac{1-2\nu}{1-\nu}}$$

and for horizontal fractures,

$$P_w = P_0 + \frac{\sigma_t - \sigma_{zz}}{1 - \alpha\,\dfrac{1-2\nu}{1-\nu}}$$

where σ_t = tensile strength of the rock, P_0 = reservoir fluid pressure, α = Biot's constant of the formation rock, and ν = Poisson's ratio of the formation rock.

In cased holes, hydraulic fracturing is achieved through perforations. Laboratory results to date have qualitatively indicated that cased-hole fracturing has a higher tendency to vertical initiation. Ali-Daneshy explains that this phenomenon can be attributed to two factors. First, the casing and cement cover up many of the weaknesses present in the rock which may have promoted horizontal fracture initiation. Second, fluid leak-off, which aids horizontal fracture initiation in open holes, is reduced in perforated holes.

The next state of the process is extension of the initiated fracture. Fluid injected after initiation will flow into the fracture and force its extension. The extent of fracture propagation depends on the volume of fluid pumped, plus formation and fluid properties. At a certain point during fracture extension, a propping agent is mixed with the treatment fluid and pumped into the fracture, to keep the fracture open and conductive to fluid flow after the treatment termination. □

Solution mining—a new challenge in blasting

THE RECENTLY INTENSIFIED EFFORT TO RECOVER METALS from low grade ore deposits by in-situ leaching has created new challenges for blasting specialists, reported D. D. Porter and H. G. Carlevato, of the Explosives Products Div. of E. I. du Pont de Nemours and Co., Inc. They noted, "Preparing blasts to condition orebodies for a leaching operation usually involves extraordinary conditions which require special studies and thorough engineering to augment judgments normally based mainly upon experience."

Although each deposit has its own set of problems, the authors presented a general outline that can be followed to engineer a blast for in-situ leaching. The checklist includes: shape of orebody, orebody characteristics, seismic considerations, missile consideration, type of explosive, powder factor, powder distribution, initiation system, delay system, loading logistics, economics of alternatives, and safety.

The shape of the orebody determines much of what can and cannot be done in fracturing an entire deposit in one blast. The blast design must be tailored to suit the orebody and its surroundings. The authors noted that the charge must be placed to result in equal displacement and uniform fragmentation in all parts of the orebody—which would strongly favor a downhole method. If the deposit is near the surface and is exposed on one or more sides as well as on the surface, the

choice of methods is much broader, and both downhole and tunnel blasting (coyote) can be considered. The depth of the deposit and the ratio between the depth and the lateral dimensions also affect the blast design. For a deposit with a high depth-to-width ratio, a large amount of overbreak at the surface would be likely, with poor explosive utility and generally undesirable overall results.

Orebody characteristics and the mechanics of rock behavior are also important factors in a blast design. Much of the end result depends on the rock's properties and its condition prior to the shot. On-site testing, with measurements that include pressure pulse, stress attenuation, and sonic velocities, will reveal the rock's characteristics. Such properties as brittleness and ability to absorb energy are also of interest.

The collected data make it possible to compute the stress wave shape produced by charges of various configurations. The wave shape is important in the blast design because of its effect on fragmentation and rock movement, and powder distribution and location of initiation points are guided accordingly. As one example, Fig. 2 illustrates the directional stress effect produced by a single coyote tunnel charge initiated at one end. Although the stress levels are not shown in absolute terms, it is possible to use the computed curve to arrange the charges in a position to give uniformly good fragmentation with the maximum stress levels applied where most needed.

Seismic considerations are vital in minimizing potential damage to neighboring structures, homes, and so forth. The authors considered this fact so important that "the entire feasibility of the project depends on it." Experience has shown that with the proper engineering, projects which initially appeared hopelessly restricted by vibration can be blasted with minimal damage to surrounding property. This is accomplished by obtaining basic field data from test blasts (frequency of ground motion, ground transmission constant, and wave amplitude). The predicted vibration levels are then compared with damage criteria for various structures, and the blast is designed to remain within an acceptable damage level.

Missile throw rock control can be engineered through empirical relationships developed both on a model scale and through large-scale experiments such as those conducted by the US Atomic Energy Commission. For blasting deposits close to the surface, the practice is to maximize the swell factor while minimizing the fly rock.

One reference found useful as a guide to ground movement in shot design is the curve developed by C. H. Noren of the University of Missouri at Rolla (see Fig. 3). This graph illustrates the relationship of burden velocity to the powder factor. For a 4 million-lb blast made by Ranchers Exploration and Development (see E/MJ, April 1972, p 98), a maximum rock velocity value of 58 fps was predicted, and subsequent measurements showed values ranging from 56 to 66 fps max. Although surface rock movement is related to the burden on the explosive, excessive fly rock can occur as a result of unexpected rock weaknesses or insufficient cover.

Factors governing the type of explosive chosen include the energy and water resistance of the explosive and its cost. While ANFO remains the cheapest blasting agent for large blasts, it has a relatively low density and relies entirely on packaging for water resistance. The authors reported that "only when attempts to apply ANFO fail for some insurmountable reason—such as a water problem or lack of energy—should a more costly explosive be considered."

It is vital to distinguish between the overall powder factor and specific localized powder factors. The former is used mostly for economic evaluation, etc., while the localized factor is used for shot design purposes, to account for variations in the orebody. Often a large shot is designed by putting together a number of smaller, individually designed shots, each with its own set of problems and limitations. For most blasting applications, powder factors range from less than 1 lb per yd to 4 or more lb per yd.

Powder distribution is an important consideration in obtaining optimum fragmentation and good permeability at the lowest possible cost. Two methods for placing the explosive are common: the conventional drillhole method and the placement of massive charges in adits and crosscuts, better known as the coyote method. In general, the drillhole shot is faster, easier to load, gives better explosive distribution, is easier to delay, and is therefore more flexible. It is also the most expensive method. The coyote blast, while less expensive, has a poorer explosive distribution, and is generally more difficult to delay.

An initiation system for very large blasts requires many built-in safety factors, including careful priming and initia-

Fig. 1—Blast for McAlester Fuel Co. required 4.15 million lb of ANFO to fracture the orebody for in-situ leaching operations.

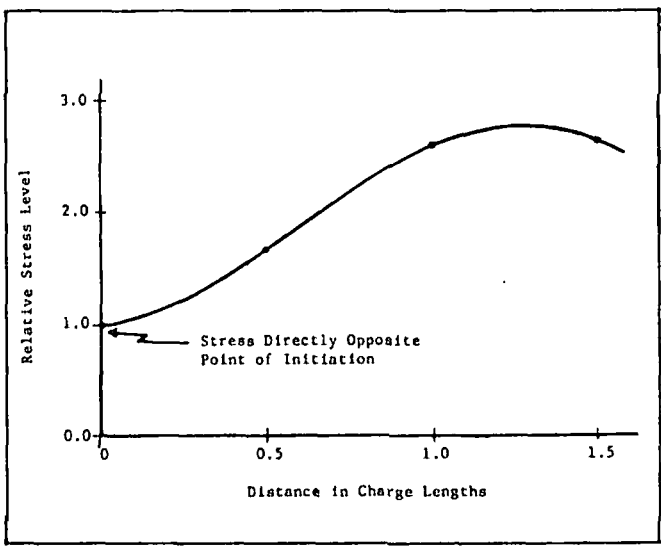

Fig. 2—Calculated relative stress level along line parallel to and one charge length away from charge (for given set of conditions).

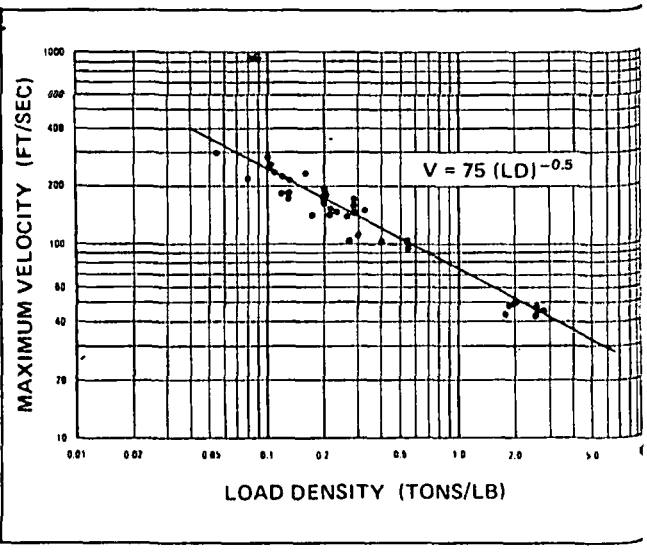

Fig. 3—Maximum burden velocity as a function of loading density.

tion techniques. Although cap and fuse can be used to initiate the blast, electric blasting caps are preferred, since they allow more exact synchronization with scientific instrumentation and a greater degree of personnel safety. Either delay caps or MS Primacord connectors can be used for desired delays. Again, safety during loading favors MS connectors.

Because of potential reliability loss, delayed charges are not commonly used for coyote blasting. However, when they are used, it is important to impart movement to upper levels before lower levels are shot. Long delays are usually not acceptable because they may damage the remaining lower charges. On the other hand, delays have to be long enough to permit sufficient movement to relieve the burden for the charge sequenced next.

While stating that it is important to produce blast results meeting project specifications at the lowest overall cost, the authors emphasized that merely applying the lowest cost explosives or the lowest cost mining method does not necessarily fulfill that objective. They added: "When considering the mining method, minimizing costs obviously is of major importance. However, the fragmentation and other factors such as depth and project timing discourage use of the lowest cost method. A higher cost method that will circumvent the limiting problems may be the only viable alternative."

Safety factors must be foremost in blast design. Safety precautions include the construction of sturdy bunkers to protect people and equipment within the range of the blast. The shot area must be thoroughly searched for livestock and bystanders prior to shot time. In this type of blasting, the authors have found that a countdown beginning up to 24 hr or more before shot time, with specific time checkpoints, is highly desirable. □

Fragmentation experiment for in-situ mining

THE USBM HAS BEEN ACTIVE in developing fragmentation technology for in-situ extraction systems, as reported by D. V. D'Andrea, R. A. Dick, R. C. Steckley, and W. C. Larson, of USBM. They explained that while the initial research is directed primarily at mining porphyry copper deposits, many of the results will be applicable to in-situ extraction of other mineral resources.

One recent USBM experiment was conducted at Duval Corp.'s Sierrita open pit mine in Pima County, Arizona, to determine blasting methods that would produce ideal fragmentation for maximum solution recoveries. In this fragmentation study, 10 blastholes, 9-in-dia. and 110 ft deep, were arranged to test blasthole spacings of 25, 20, and 15 ft (See Fig. 1). Blastholes had 60 ft of stemming and a 50-ft column of 10% aluminized slurry blasting agent. Three 120-ft-deep NX core drills mapped and detailed topographic features of the area. Holes were located to obtain samples in the middle of the 15-, 20-, and 25-ft blasthole spacing areas. In addition, 68 wooden stakes were used as station points so that elevation changes due to blasting could be determined within ±0.2 ft. The drill cores were analyzed to measure rock quality designation (RQD), size distribution, and standard physical properties.

The blast pattern was designed to test blasthole spacing based on equilateral triangles of 25, 20, and 15 ft. Blastholes were connected with 50-grain core load detonating cord, initiated by bottom-loaded 1-lb cast primers. The blast used a total of 17,440 lb of 10% slurry with a specific gravity of 1.20 and heat of detonation of 1.00 Kcal per gram. Each hole contained about 1,700 lb of slurry, and the maximum charge weight per delay interval was 5,300 lb. A portable three-component particle velocity-recording seismograph was used to measure ground vibrations at a distance of 800 ft from the blast. Powder factors, assuming infinite patterns, were 0.79, 1.24, and 2.20 lb per cu yd for the 25-, 20-, and 15-ft patterns, respectively.

Postshot studies included a topographic survey, detailed mapping of surface fractures, fragment-size distribution measurements of broken rock on the surface, and drilling of six NX diameter core holes into the broken zone. Diamond drilling into the broken zone did present problems, but six postshot holes were successfully drilled to 100-120 ft, and no holes were lost due to caving.

In reviewing the results, the maximum peak particle velocity recorded on the seismograph was 0.95 in. per sec at a distance of 800 ft. This value was lower than expected and indicated that the rock was weathered and fractured. Rubbleized surface material was well fragmented. Size distribution stud-

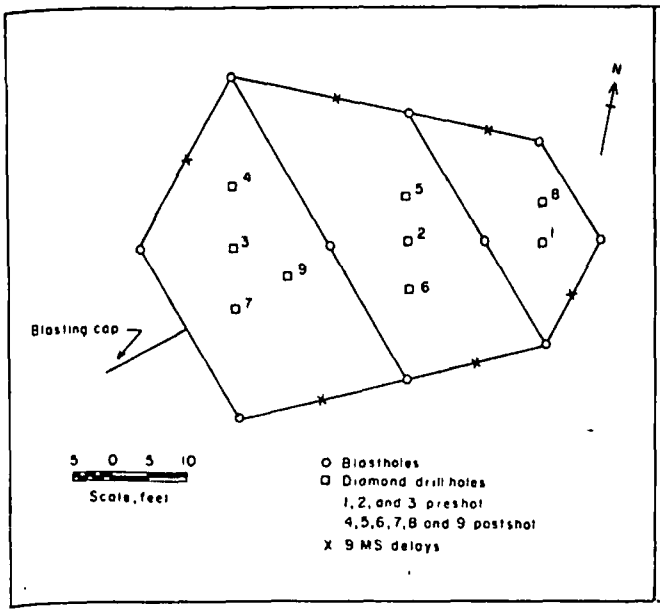

Fig. 1—Geometry of USBM test blast.

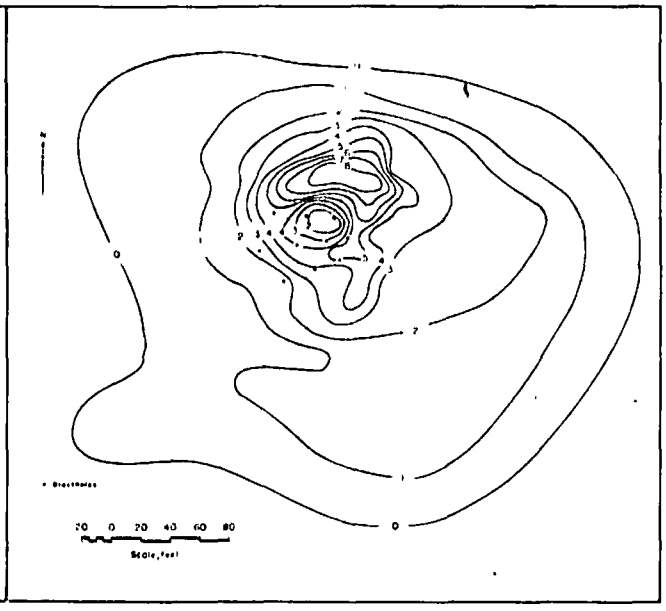

Fig. 2—Elevation changes produced by the test blast (contour intervals in feet).

ies of surface material showed that the greatest number of fragments were in the 2 to 3 in. range and the vast majority of pieces were less than 11 in. long. Blasting-induced fractures on the surface and outside of the rubble zone were found to have three preferred orientations—one controlled by the geologic structure, and the other two interpreted to be caused by blast-induced doming of the rock mass.

The greatest elevation changes were caused by rubble material being piled up about 40 ft to the northeast of the center of the blast. (See Fig. 2.) Three factors are believed to have contributed to this irregular muck pile distribution: a change in pattern from 25- to 15-ft blasthole spacing toward the northeast; initiation of the blast in the southwest, with the delay sequence proceeding to the northeast; and a falling-off of the surface in the northeast direction. The surface rise over the blast averaged about 5 ft, and the total volume increase produced by the blast was 5,100 cu yd. The swell factor was roughly estimated at 1.30.

Postshot diamond drill cores were sent to the lab for study. A comparison of the postshot cores with preshot cores showed that the blast had changed the RQD of the rock from "poor" to "very poor."

The largest piece of drill core averaged 14 in. for preshot holes, 11 in. for core from the 25-ft pattern, 8.5 in. for core from the 20-ft pattern, and 9 in. for core from the 15-ft pattern. The average size of core pieces 1 in. or greater was determined by dividing the total length of all pieces greater than 1 in. by the number of pieces greater than 1 in. This average size was about 3.2 in. for preshot core and between 2.2 and 2.8 in. for the postshot core.

For this test, the average fragment size was less than the 9-in.-dia fragments obtained at the Big Mike mine and within the 9-in. or less range at the Old Reliable mine.

Factors other than fragmentation affect copper recovery, and the authors believed that actual in-situ leaching tests would also have been desirable. However, they maintained that all three blasthole spacing patterns produced adequate breakage for in-situ leaching. □

In-situ leaching at the Big Mike mine

AT THE BIG MIKE COPPER MINE, in-situ mining was employed to maintain the active life after the economics of conventional open-pit techniques became unfavorable. Milton H. Ward, of Ranchers Exploration and Development Corp., explained the history of Big Mike's eventual development as an in-situ operation. Located 30 mi south of Winnemucca, Nev., the property was obtained by Ranchers Exploration in 1969 after extensive exploration by Cerro Corp. At that time the deposit was delineated, and reserves amounted to about 100,000 tons of 10.0% massive copper sulphide ore and 700,000 tons of 2.0% mixed oxide-sulphide ore. The orebody was a lenticular deposit, dipping at 50°. The massive sulphide mineralization was chalcocite and chalcopyrite, surrounded by a halo of lower grade mixed oxide-sulphide ore. The deposit measured 600 ft long and 300 ft wide and extended to a depth of 300 ft from the outcrop on the surface.

During the initial phase of operation, over 100,000 tons of high grade sulphides were mined and marketed. About 300,000 tons of low grade mixed ore was crushed to minus 2 in., stacked on an impermeable asphalt pad, and placed under leach. A precipitation plant, decanting area, and drying pad were constructed and are currently being used to produce cement copper.

After the high grade sulphide ore was removed, about 475,000 tons of mixed ore remained in the walls and bottom of the pit. Use of conventional methods to extract the remaining ore was considered, but a 6.5 to 1 stripping ratio was economically unacceptable. After extensive study, a decision was made to blast this ore into the pit and leach it in place.

Four requirements for successful in-situ production were reviewed: 1) dissolving the metal, 2) making the deposit permeable, 3) collecting the pregnant solutions, and 4) recovering the valuable product—copper. From a number of leach tests, it appeared that over 80% of the copper could be removed by adding high quantities of acid (13 lb acid per pound of copper). Further testing indicated that an acceptable recovery of about 70% could be obtained by using much lower quantities of acid and maintaining the leach solution at a pH of 2.0. The latter approach appeared most favorable, according to Ward.

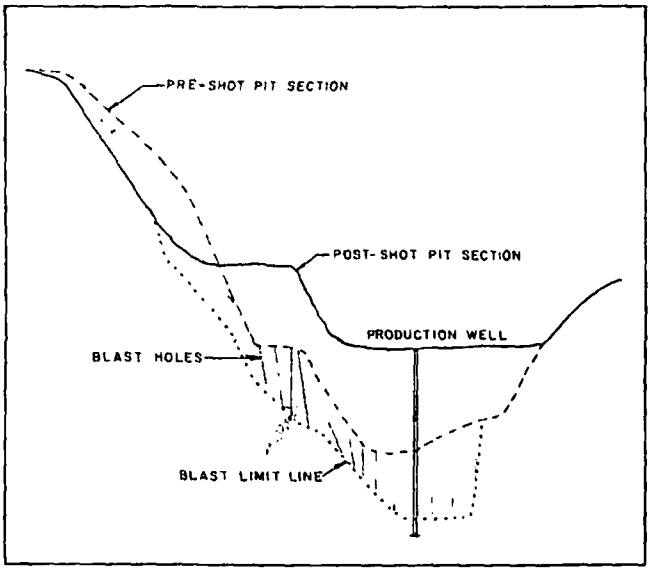

Fig. 1—Big Mike pit cross section before and after blast.

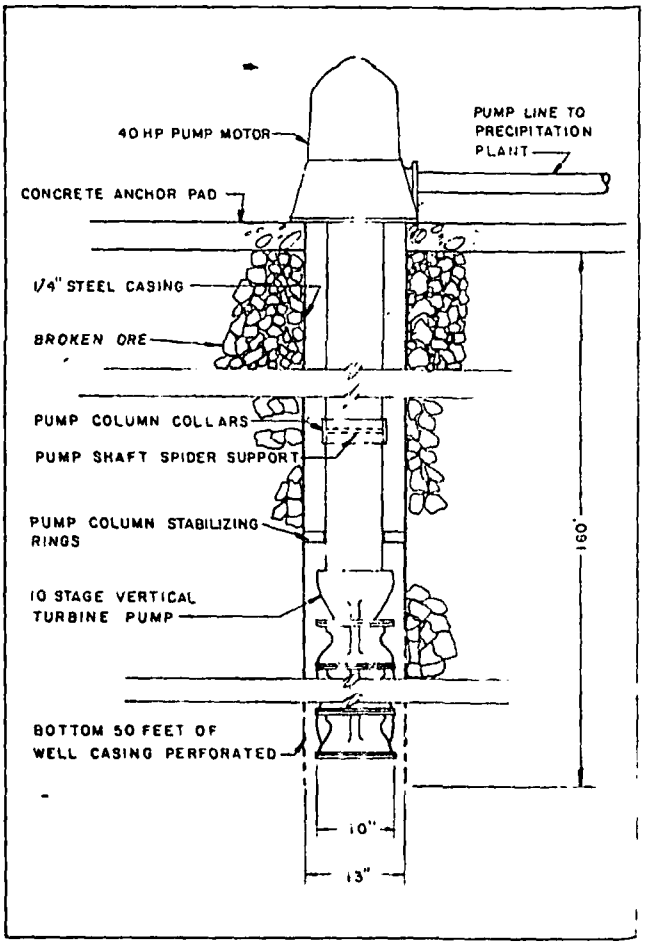

Fig. 2—How the recovery well pump column and casing was installed.

From the low grade ore that was earlier removed and leached, it was also apparent that an acceptable amount of copper could be dissolved. The question of what product to produce required no particular study because cement copper was already being produced and marketed.

The pit blast was designed with assistance from Du Pont Co. A conventional drill and blast scheme was chosen, primarily because of the steep wall configuration of the existing pit. A study of explosive factors and pit terrain indicated that the desired fracturing could be best obtained by utilizing large, closely spaced angled and vertical blastholes. Approximately 21,000 ft of 5¾-, 9-, and 9⅞-in.-dia blasthole drilling was required. Blastholes along the surrounding pit walls were loaded with ANFO and with occasional heavier-density water gels in areas of high rock burden. Closer to the water table, high density water-resistant explosive or water gel was used. All blastholes were connected with standard Primacord and initiated at the hole bottom by electric caps. Altogether, about 400,000 lb of explosives were used to fracture approximately 600,000 tons of material, giving a ratio of 1.5 lb of explosive per ton. (See Fig. 1.)

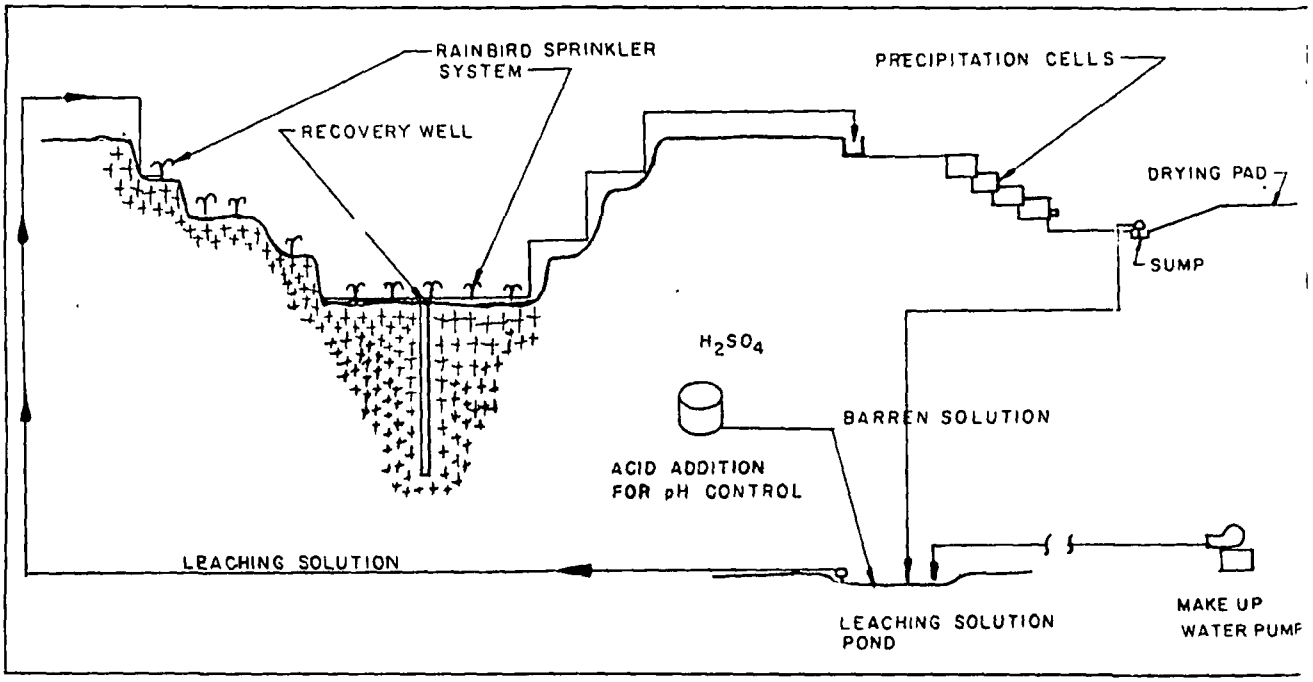

Fig. 3—Flowsheet of pit leach operation at Big Mike mine.

The solution collection system was located at the bottom of the Big Mike pit. Since a water table was present near the bottom of the Big Mike pit, and the tight pit walls would act as a barrier to the percolating solutions, this location was ideal for the ultimate solution collection device. Several monitoring wells were drilled near the pit along the most likely avenue of lateral water loss. Surveillance of these wells indicates that no loss or contamination is taking place so far.

The distribution of leaching solution is through sprinkler-heads attached to 2-in. PVC pipe branch lines, located on the four terraces created after the blast. Leach solution acid strength is maintained at a pH of 1.5 to 2.0. A single-stage stainless steel centrifugal pump picks up the solution from the storage pond and transports it at approximately 200 gpm to the pit distribution system (Fig. 3). The leach liquor is sprinkled onto the broken ore and percolates by gravity to the main collection well pump.

The actual solution recovery involves one production well in the pit bottom. A conventional churn drill well was drilled from the lower terrace to a depth of 180 ft (Fig. 2).

The sprinkling of the broken ore was started prior to completing the drilling of the recovery well, assuring a saturated orebody and immediate production once the recovery pump was operational. Pumping commenced at a rate of 250 gpm of 2.0 gm per liter of copper. It was anticipated that production for the first year would average 200 gpm at 2 gm per liter, and it appears that this goal will be attained.

The economic viability of the venture was greatly enhanced by the existing facilities and utilities, the physical layout, and the known types of rock at Big Mike. While copper recovery in the future is uncertain, a recovery of less than 10% was fortunately all that was required for the project to pay out. □

Microbe leaching of copper and molybdenum ores

Reprinted by permission of Canadian Journal of Microbiology.

THE TECHNIQUE OF BIOEXTRACTIVE METALLURGY has been known for some time and has been used in leaching copper from waste dumps and other areas formerly termed "economically unfavorable" under conventional methods. Corale L. Brierley, of the New Mexico Bureau of Mines and Mineral Resources, went on to explain that the organisms associated with copper leaching have been identified as "Thiobacillus thiooxidans" and "Thiobacillus ferrooxidans," whose functions in the leaching process are to oxidize sulphides to polythionates, and sulphate and ferrous iron to ferric iron. The combination of the oxidized metals and the increased level of acidity created by the biogenic activity results in a chemical lixiviant which produces an accelerated chemical alteration of the minerals.

The ability of these organisms to grow and perform their specific function is limited only by the availability of an energy source and nutrients and by environmental changes, particularly temperature, pH, and oxygen availability.

While the organisms mentioned and their relationship to bioextractive mining have been relatively well-studied, there have been no attempts to discover or study other microorganisms which may be more compatible with the high temperatures, low-oxygen environment, and heavy metal concentrations at leach dumps and in-situ mining operations.

An unidentified, high-temperature microbe, which oxidizes reduced inorganic sulphur and iron in an acid medium between 45° and 75°C at a pH of 2.0, has been the subject of further lab studies, according to Brierley. The morphology is unlike that of the thiobacilli, being pleomorphic rather than rod-shaped (Fig. 1). The organism ranges in size from 1 to 1½ μm.-dia.

In tests of reactions with copper sulphide minerals, the microbe leached a chalcopyrite concentrate in a batch reactor using an acid medium (pH 2.5), with 0.02% yeast extract at 60°C. The copper is solubilized at a rate of 10-16 mg per liter per day from a chalcopyrite concentrate (27.6% copper—74-105 microns in particle size) over a 30-day period. The solubilization of copper in uninoculated flasks occurs at a rate of 1.0-1.8 mg per liter per day over the same period. Preliminary results indicate that about 50% of the copper in a low-grade ore (0.32% copper, -16 to +50 mesh, from the Chino mine of Kennecott Copper Corp.) is leached from the ore in 60 days at 60°C in an acid medium containing the organism. About half of this copper is solubilized by the acid medium.

The ability of the organism to tolerate soluble copper is essential to successful leaching of copper sulphide minerals. The tolerance of the organism to copper is ascertained by comparing the oxygen uptake of the organism when it is suspended in varying concentrations of soluble copper to the

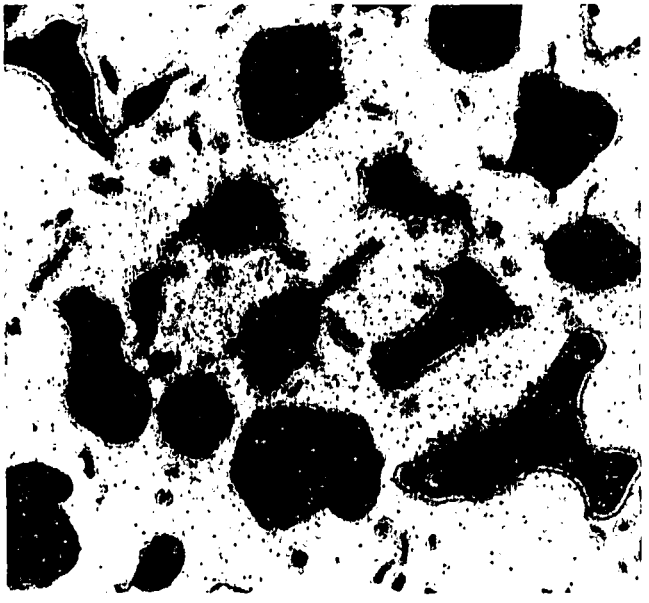

Fig. 1—Electron micrograph of a thin section of microorganism.

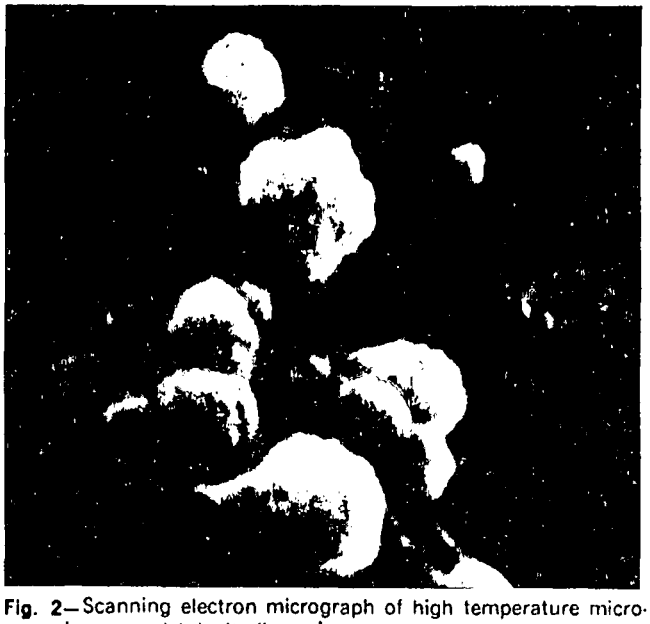

Fig. 2—Scanning electron micrograph of high temperature microorganism on molybdenite fines.

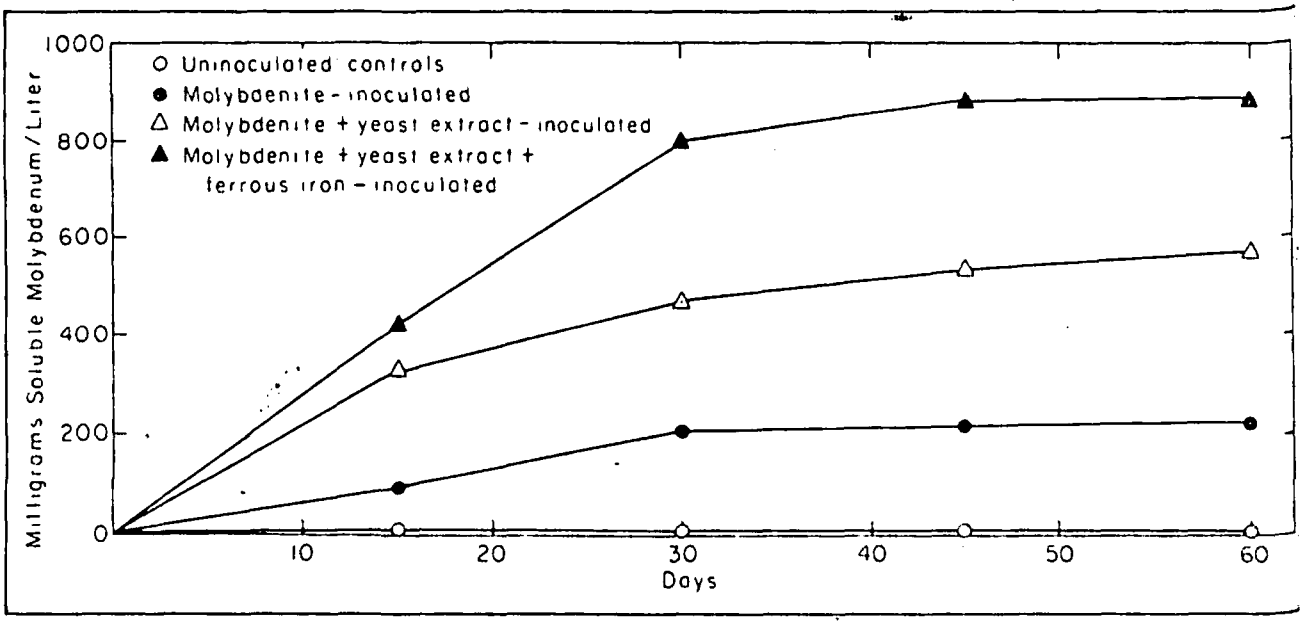

Fig. 3— Solubilization of molybdenum from molybdenite concentrate for 60 days.

oxygen uptake when no copper is present. Although the organism can tolerate more than 10.0 gpl copper, it is not able to grow when the concentration of copper exceeds 1.0 gpl. Growth tolerance is ascertained by suspending the organism in acid medium containing varying concentrations of soluble copper, 0.02% yeast extract as a growth enhancement factor, and elemental sulphur, an oxidizable energy source. The absence of microscopically observable microbes, protein production, and pH decline indicate the absence of growth.

A 98.5% molybdenite concentrate with a particle size of 12 to 62 microns is oxidized by the microbe at 60°C. Over a 30-day period, 3.3% of the molybdenum is solubilized from the molybdenite, according to Brierley, when it is suspended in an inoculated medium (pH = 2.5). It was also found that this yield can be increased to 8.3% in 30 days when 0.02% yeast extract is added. The addition of 0.02% yeast extract and 1% $FeSO_4 \cdot 7H_2O$ increases the yield to 13.3% in 30 days. In all cases, the leaching of molybdenite in uninoculated controls yields 0.1% molybdenum solubilized in 30 days (Fig. 2).

Structural and physiological studies had indicated that the high-temperature microbe is unrelated to the thiobacilli and is probably another type of microorganism that has neither been previously isolated nor considered for leaching purposes. Field studies indicated that temperatures within low-grade copper ore dumps may reach 80°C. These elevated temperatures probably inhibit the leaching activity of strains of sulphur- and iron-oxidizing bacteria whose optimum temperatures range from 25°C to 45°C. Brierly concluded that the economic implication of this new study, at least initially, is that it is technically feasible for the new microbe to biogenically extract copper at temperatures exceeding 45°C and that molybdenite can now be biogenically extracted. □

Effect of particle size on microbiological leaching

TO ASSESS THE LEACHABILITY of a particular waste ore, a representative sample is usually subjected to a series of column tests, to determine the maximum possible extraction, and to get some idea about the rate at which this extraction can be carried out. A. Bruynesteyn and D. W. Duncan, of the Mineral Microbiology Section of British Columbia Research, reported on one test performed in 6-ft-high by 6-in.-dia PVC columns, to determine the effect of particle size on the microbiological leaching of chalcopyrite bearing ore. They noted: "The information developed from such tests is of distinct value in assessing whether or not the material is leachable; the rate of extraction, and possibly the extent of extraction, are strongly influenced by the particle size of the material under test."

To further understand this relationship, tests were conducted on a 1,000-lb sample of minus 2 in. ore from the Britannia Beach operation of the Anaconda Co. in British Columbia. The ore consisted of a mixture of chalcopyrite, sphalerite, and pyrite, and was separated into six fractions. Each fraction was assayed for copper and zinc values (see

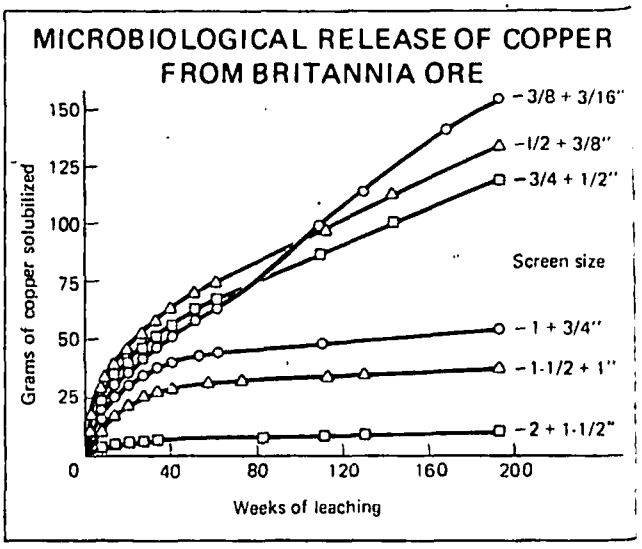

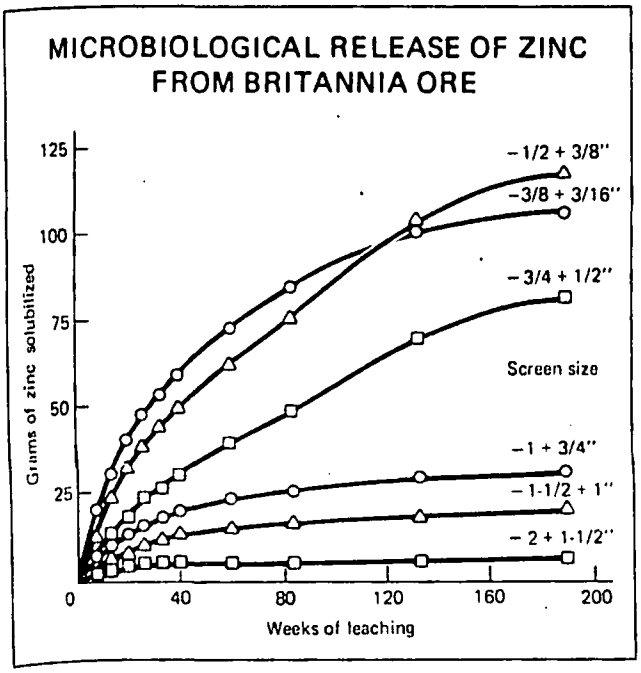

Table 1), after which 100-lb portions were leached in duplicate columns, utilizing a one-week leach, four-week rest cycle. Each column was inoculated with an active strain of thiobacillus ferrooxidans grown in shake flasks on finely ground chalcopyrite concentrate. All the columns were installed in a specially built room, where the temperature was maintained at 35°C. A total of 20 liters of leach solution, contained in a 50-liter plastic bucket placed underneath each column, was used to leach the charge in the column, with the aid of an air-lift water recycling system.

The data obtained, according to the authors, indicate that the relationship between extraction rate and particle size is a hyperbolic function. If the relationship was based solely on surface area, the results from the column studies would have given a straight line, since reducing the particle size of a fixed weight of mineralization results in an increase in the actual number of particles, proportional to the cube of the diameters, but also results in a reduction in surface area of the individual particle, proportional to the square of the diameter. The actual increase in surface area of a fixed weight of material is inversely proportional to the decrease in the diameter of the particles involved.

The authors concluded that the rate of microbiological leaching of a fixed weight of mineralization is not directly proportional to the surface area, but rather is influenced by the actual volume of the material which is exposed to the leaching environment. This exposed volume consists of the actual surface area plus the depth of penetration of both the leach liquors and the leaching bacteria.

The configuration of the zinc and copper rate curves obtained with this particular sample suggested that little improvement in leach rate can be effected by crushing, unless the ore is crushed to less than 2 in. At 2 in., the copper extraction rate was 0.15% per week, so that even with the ideal environment and physical conditions of the lab column test, it still would take 1,000 weeks or 19.2 years to get 15% extraction after the initial soluble copper has been removed. Most important, leach dumps of considerable height would have to be built in order to produce pregnant solutions, based on the results of the metal recovery rate curves.

These tests have shown that an evaluation of leaching rates for different particle sizes can yield valuable information about the actual performance of this material in a commercial leaching dump. The authors cautioned that if a column test is performed on only one particle size, the information obtained could result in erroneous scale-up to a dump-size operation. However, if the information obtained from a test at various particle sizes indicates that leaching rates are substantial even at 2-in. particle sizes, then commercial dump performance could be reasonably predicted by extrapolating this rate curve. Finally, the particle size tests will yield information not only on the performance of the ore under test but also on leach liquor characteristics. □

Table 1 —Assays of head samples

Screen Size (in.)	% Cu	% Zn
-2 +1½ inch	0.53	1.48
-1½ +1 inch	1.00	0.46
-1 +3/4 inch	0.81	0.36
-3/4 +½ inch	0.95	0.42
-½ +3/8 inch	0.81	0.42
-3/8 +3/16 inch	0.82	0.33

Table 2—Theoretical and actual zinc to copper release ratios

Screen Size	Grams Metal Released per 100 Weeks		Actual Ratio Zn/Cu	Theoretical Ratio Zn/Cu
	Cu	Zn		
-3/8 +3/16 inch	65.1	51.8	0.80	0.40
-½ +3/8 inch	49.0	58.4	1.19	0.52
-3/4 +½ inch	39.2	48.0	1.22	0.44
-1 +3/4 inch	9.3	8.2	0.88	0.44
-1½ +1. inch	6.2	6.8	1.10	0.46
-2 +1½ inch	2.0	1.02	0.51	2.70

The editors of E/MJ express their appreciation to the Society of Mining Engineers of AIME and its Executive Secretary, Claude L. Crowley, for permission to summarize selected articles from the Dallas Solution Mining Symposium.

A special word of thanks is also due to: F. F. Aplan, chairman, Penn State University; W. A. McKinney, US Bureau of Mines; and A. D. Pernichele, Dames and Moore. It was their monumental task to compile and edit the large number of technical papers presented.

The entire text of the proceedings, bound in a single volume, is available at a price of $15.00 to non-AIME members, $10.00 to AIME members, and a special rate of $6.00 to student AIME members. Write to: Society of Mining Engineers, AIME, 540 Arapeen Drive, Salt Lake City, Utah 84108.

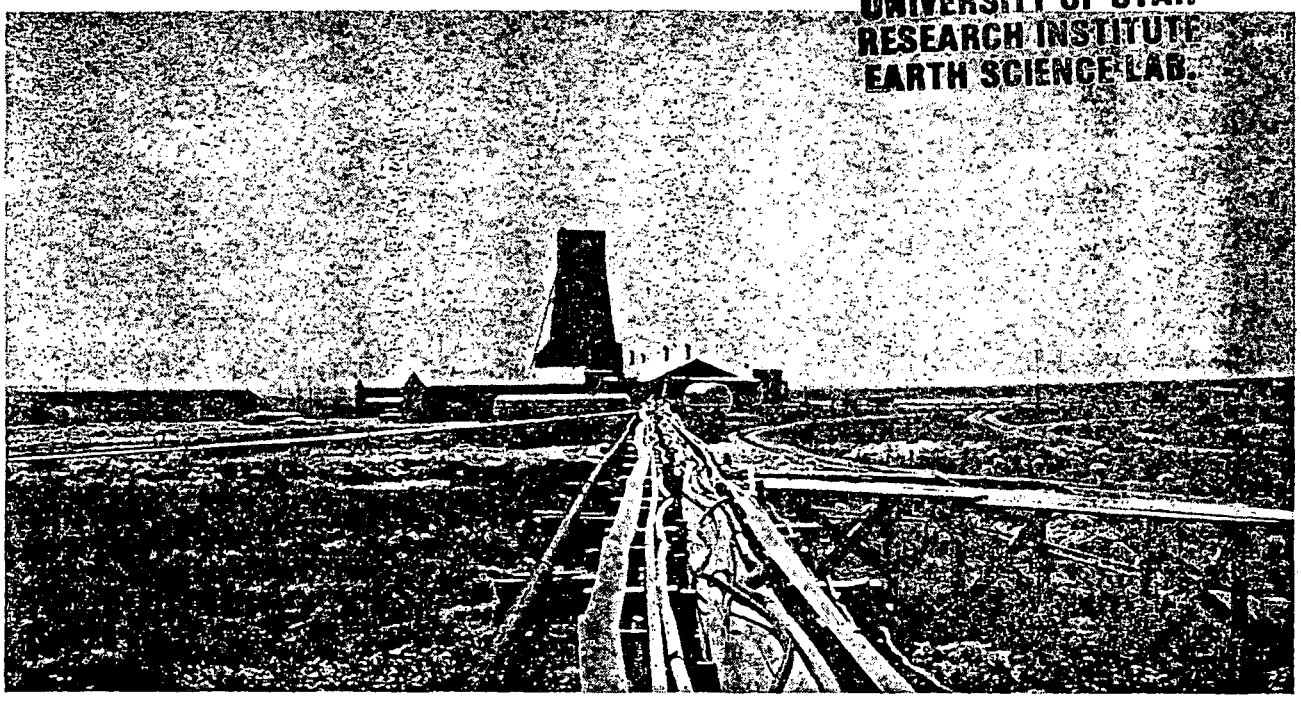

Solution Mining of Uranium

By J. S. ANDERSON
Vice President and
Manager of Uranium Operations
and
M. I. RITCHIE
Mine Manager
Lucky Mc and Shirley Basin Mines
Utah Construction & Mining Co.

Still in the development stage, the solution mining process has been demonstrated to be a workable production method for uranium when applied under proper conditions

IN early 1960, Utah Construction & Mining Co. started producing uranium ore from an underground mine in Shirley Basin, Wyo. This was the first production of uranium from the district, which had been discovered three years earlier. Nothing was known about ground conditions prior to shaft sinking, but difficulties in the sinking operation gave some indication of what could be expected in mining.

After mining had been carried on for some months, and when the ground had been well drained, conditions improved. However, the square-set method which had to be used was costly, so a study aimed at finding another production method that would be reliable, safe, and economical was initiated. The method selected for investigation was solution mining, or in-place leaching.

At Shirley Basin, uranium occurs some distance below the natural water table. A study of problems which might be encountered in solution mining led to the belief that control and recovery of leaching solutions would be difficult. It was guessed that if natural ground water could be made to act as a containment shell for leaching solutions, dewatering of the area to be treated would be unnecessary.

Feasibility determined by specific considerations

As a first step in the investigation of solution mining, reservoir engineers had been consulted. This had been

helpful, but it was realized that the expected chemical environment and reactions made the problems much different than those encountered in petroleum recovery operations. A decision was made to proceed with a test pattern using logical assumptions, with the objective of identifying problems and working out solutions. Work was started in early 1961 and has continued to the present time. The first two years are considered a research period, but since 1963 the process has been the only production method used by the company at Shirley Basin.

Certain requirements exist for solution mining of uranium:

(1) Uranium ore should occur in a generally horizontal bed underlain by a relatively impermeable stratum.[1]
(2) Uranium ore must occur below the static water table.
(3) Direction and velocity of regional water flow must be known.
(4) Mineralogy of the ore should be determined so that its amenability to the proposed process may be known. Material recovered by core drilling is normally sufficient to make this determination.
(5) One requirement, though an obvious one, should be emphasized. Mineral content of the area must be more than sufficient to repay the anticipated cost of the operation. Leaching is not an inexpensive process, and, in this case, solution mining should not be considered as a scavenging operation.

Groundwater flow major factor in pattern design

Undoubtedly the most critical consideration in solution mining as practiced at Shirley Basin is the pattern geometry. Size, shape, and orientation of patterns have undergone numerous changes. During the experimental phase, patterns were square or triangular, with the production well in the center. The area was bounded by inflow wells that were located irrespective of regional groundwater flow direction. Hydraulic interrelationship between wells was ascertained by measuring drawdown in the inflow wells during pumping tests. A balanced inflow vs production rate was achieved by maintaining flowrates to hold water levels in surrounding observation wells below original static levels.

This procedure left quantitative interflow between wells and overall performance to be determined by nitrate recovery and calculated uranium recovery. During the early period of operation, nitric acid was used as a leaching agent. Nitrate recovery could be determined. Calculated uranium recovery was the actual recovered uranium as a percentage of that calculated to be contained in the area bounded by the inflow wells.

Analyses of uranium and nitrate recoveries for patterns mined during this phase indicated that solution losses were occurring and that there was substantial dilution in the effluent produced. It was also apparent that uranium recovery did not correlate with nitrate recovery. This might be the result of uranium leaching beyond the area bounded by the geometric shape of the drilled well pattern.

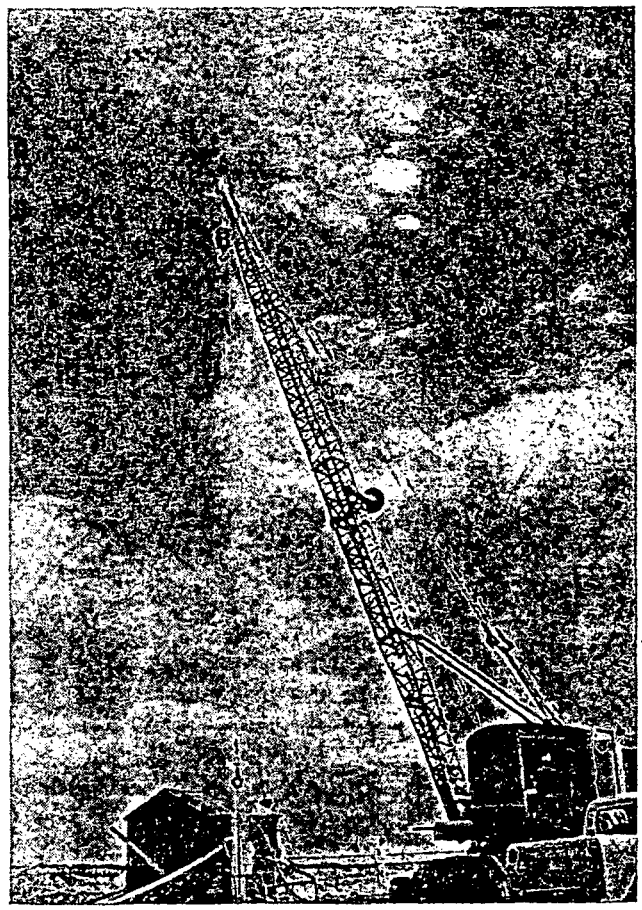

After placement of screens and casing, wells are developed by high-pressure jet

In an attempt to correct these problems, a complete restudy was initiated. As a result, pattern design was changed, which gave improvement in solution recovery and better correlation between nitrate and uranium recovery. The current design is based on the fact that interflow between wells in an aquifer having regional flow can be controlled by varying inflow-effluent rates, by distance between wells, and by aligning wells at specific angles to the direction of groundwater flow.

The present pattern consists of three inflow wells upstream from a production well, with the center inflow well directly upstream on the regional groundwater flow direction. The remaining two inflow wells are located on radii diverging at an angle of 75° from one another, equally spaced from the center inflow well. Distance from inflow wells to production well is about 25 ft.

Since uranium recovery would be confined to the interflow area, that is, the area through which solution will flow from the inflow wells to the production well, the following procedure was established to determine this area:

1. Determine hydraulic gradient within the pattern by measuring static water elevations in developed wells.
2. Conduct drawdown tests, using the inflow wells as observation wells, to provide data to calculate co-

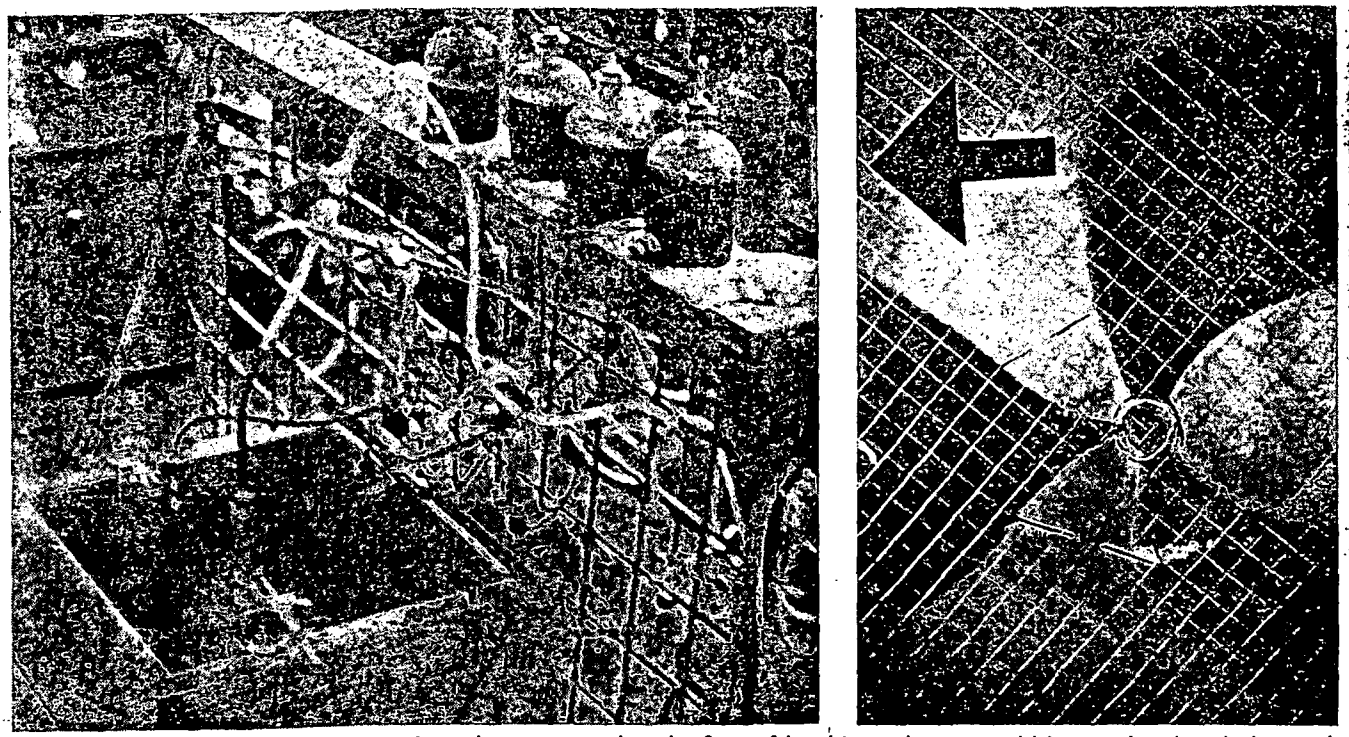

Laboratory equipment was set up in such a manner that the flow of leaching solutions could be simulated and observed. One test pattern has the production well in the center and three inflow wells surrounding it. Groundwater flow is in the direction of the arrow

efficient of transmissibility, in gallons per day per foot, for the aquifer within the pattern.

3. Draw flow nets for production well and inflow wells wells at operating rates in gallons per day using transmissibility and hydraulic gradient as calculated above.
4. Complete the interflow net as graphical resultants of inflow nets and production well net.
5. Calculate uranium contained within the interflow area using U_3O_8 values obtained through interpretation of gamma logs of well pilot holes.

The calculated size and shape of the interflow area as well as uranium recovery from that area can be verified by drilling.

Wells developed by high-pressure jet

Well drilling and development are important for satisfactory operation of a solution mining pattern. Except for the finished diameter, the procedure for drilling and completion of inflow and production wells is the same. Wells are first pilot drilled and probed, after which they are reamed to take the required casing. Inflow well casing is three-in. diam stainless steel, and production well casing is eight in. diam, with stainless steel on the bottom 40 ft. Stainless steel screens are placed through the ore zone in all wells, and cement baskets are placed on the casing just above the ore. Clay layers swell and seal the hole above the baskets. After the screens and casing have been placed, the wells are developed by means of a high-pressure jet. This operation is continued until the wells are capable of a satisfactory rate of inflow by water test.

Standard production pump is an eight-stage, Advance submersible pump, constructed of #316 stainless steel and equipped with a 20-hp Franklin motor in a stainless steel case. Electric power to the pump is via submersible cable fastened to the pump column. An ammeter is put on each leg of the three-phase power supply.

Overall recovery depends on pattern design and operation

Pattern operation starts with the introduction of leaching solution to the three inflow wells. Sulfuric acid is now used instead of the nitric acid previously employed. Simultaneously with the start of inflow, pumping is started in the production well, at a rate which barely exceeds total input to the inflow wells. Patterns start with an acid inflow of 1 to 1.5 grams per liter until titratable acid is measured in the effluent, at which time concentration of sulfuric acid may be increased in increments to a maximum of five grams per liter. The cautious introduction of sulfuric acid at the start is made to be sure that the theoretical solubility of calcium sulfate in water is not exceeded. Lime in the formation is considered neutralized when acid appears in the effluent. Any deposition of gypsum in the sandy formation can thereafter be considered minimal. After an acid condition has been established in the pattern network, uranium leaching is enhanced by the addition of small quantities of sodium chlorate. Measurements are made of the electromotive force in the effluent so a negative 450 can be maintained. A flocculant is infrequently used to promote solution flow in less permeable formations, and the amounts used are 5 to 10 parts per million.

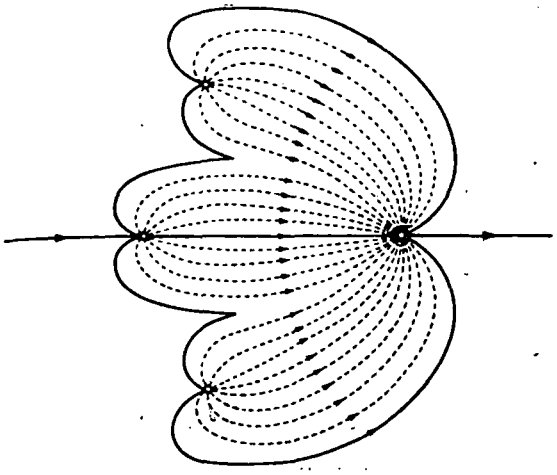

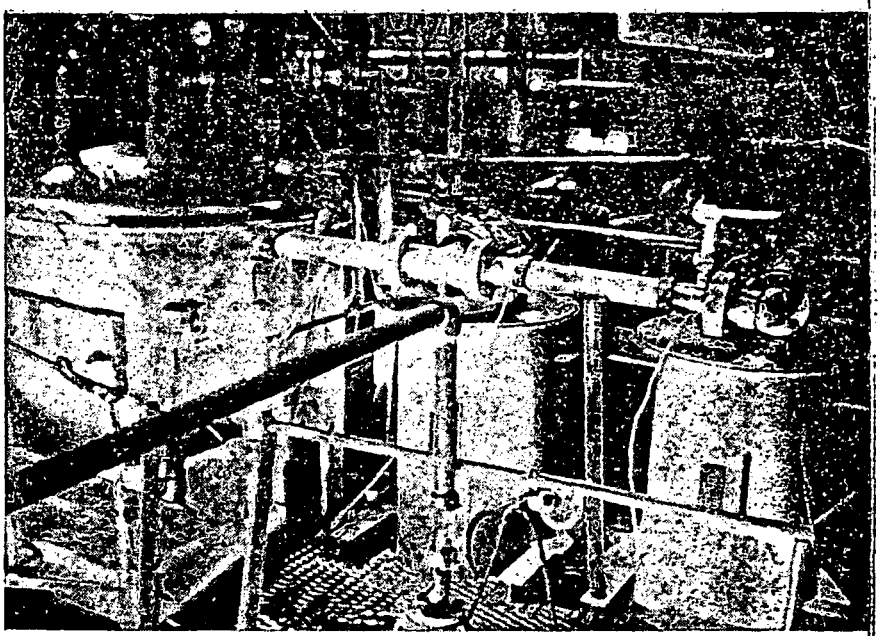

(Left) The well pattern currently used for production consists of three inflow wells located upstream in the regional groundwater flow from a production well. The center well is directly upstream and the other two wells are on radii diverging at an angle of 75° from one another. Inflow wells are 25 ft from the production well. The recovery plant (right) has two circuits incorporating a continuous ion-exchange column, two elution, or stripping, columns and a fixed resin-bed column

There is much variation in the behavior of individual patterns, but normal expectancy is that uranium values appear in the effluent in less than-48 hours. The uranium concentration might continue to build up for a week or more, but, with sulfuric acid as the leaching agent, maximum pregnant solution value seldom exceeds 0.35 grams per liter, and typically will remain between 0.20 and 0.30 grams per liter. Thus, it can be calculated that a pattern area containing 5000 lb of U_3O_8 and pumped at 75 gpm will require more than a month's operation, allowing for a drop-off in grade toward the end of the period. Normally, three to five patterns are in operation simultaneously.

After a pattern has been finished, the pump is removed from the production well, after which screens and casings are salvaged. Special equipment and techniques have been developed for this, and a high recovery of screens and casing is experienced.

Uranium recovery from a leached area is difficult to calculate; however, indications are that overall recovery equals or exceeds that accompanied in underground mining in the same area. In general, it is calculated that recovery approaches 100 percent within the interflow nets. Overall recovery depends on the skill with which patterns are designed and operated. The principle cause of unrecovered uranium is a multiple-horizon area, where upper horizons are not underlain by impervious layers.

Two ion-exchange columns utilized in processing

Uranium-bearing solution produced from all production wells is pumped through individual lines to the uranium recovery plant. The recovery plant is divided into two circuits, a continuous ion-exchange column with two attendant elution, or stripping, columns and a fixed resin-bed column.

The unique, continuous ion-exchange column is five ft in diameter, has a seven-ft straight side and a conical base along with a domed, bolt-on top. Segmented screens, top and bottom, retain the minus 20 plus 40-mesh anionic ion-exchange resin during solution flow. The resin inventory in this column is 135 cu ft, and is divided into nine imaginary 15-cu ft slugs.

Uranium-bearing liquor, having a grade between 0.10 and 0.30 grams per liter U_3O_8, is pumped upflow through a resin bed. Since the column is packed with resin, a minimum of turbulence occurs in the bed. The normal flowrate is between 7.5 and 10 gpm per square foot of bed area—ideal for good uranium ion exchange.

Calculations based on volume and uranium grade determine when the bottom imaginary 15-cu ft slug of resin is saturated. At this time upflow of pregnant solution is temporarily discontinued while a slug of stripped resin is hydraulically moved from one elution column into the top of the adsorption column, forcing the saturated 15 cu ft out of the bottom into the other elution column. The entire bed shifts down, setting conditions for resumption of the loading cycle.

The loaded slug which has been moved to the elution column is stripped with a mixture of nitric acid, sodium nitrate, and sulfuric acid in a shorter space of time than it takes to saturate the next slug in the bottom of the adsorption column. Thus the cycle operates on an almost continuous basis. Under ideal conditions as much as 270 cu ft of resin can be treated in a 24-hour period. The barren solution emanating from the top of the column is discarded as waste into completely captive tailings ponds. Some acid is discarded with this solution; however, it could not be recycled underground due to its dissolved calcium content.

(*Continued on p. 26*)

Anderson

Ritchie

J. S. Anderson is vice president and manager of uranium operations for Utah Construction & Mining Co. and has been with the company since 1957. Earlier, he was associated with Chile Exploration Co., the Bunker Hill Co., Bradley Mining Co., and Manganese, Inc. in various mining posts.

M. I. Ritchie joined Utah Construction in 1957 as mill superintendent and is now mine manager of the Lucky Mc and Shirley Basin mines in Wyoming. Prior to this, he served five years as a uranium hydrometallurgist with New Consolidated Goldfields Ltd. and New Union Goldfields in South Africa and one year with Rio Algom Mines Ltd. in Canada.

The purified, concentrated strip solution, assaying between 10 and 15 grams per liter U_3O_8, is batch precipitated with dolomitic lime or magnesium slurry to pH 7.5. The resultant uranium slurry is concentrated by decantation prior to being shipped, still in slurry form, to the Lucky Mc mill. The decant, containing neutral nitrate salt, is recirculated to eluate makeup with nitric acid.

The second ion-exchange column is four ft in diameter and has a straight-side dimension of 10 ft. It is partially filled with 100 cu ft of resin, and is used as a fixed-bed system, scavenging uranium from solutions containing less than 0.10 gram per liter U_3O_8. It is stripped batchwise after loading without movement of the resin bed.

Safety and low cost among advantages

The cost of producing uranium by solution mining is a function of a number of complex, interrelated factors. Local drilling and labor costs, together with the success of equipment salvage operations after the patterns have been depleted, determine field costs. Permeability and other ground conditions vary the leaching cycle, and thereby make for cost variations in leaching operations. Plant costs are relatively stable, assuming that patterns can be so scheduled that poundage recovered per day is relatively uniform. Overhead and other fixed costs must be charged against pounds produced, and therefore depend on production rate. At Shirley Basin,

Simplified Solution Mining FLOWSHEET

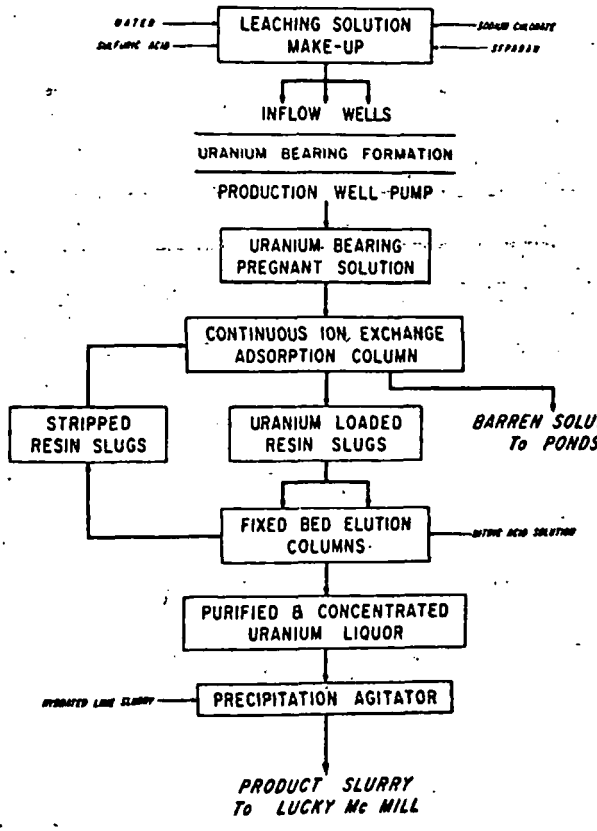

under existing conditions, it is believed that minimum production cost approaches open pit costs in a similar area, taking into account the difference in milling costs of ore and slurry. Unfortunately, under adverse conditions these costs may increase by a factor or two or even more. Costs, however, have been found to be well below those which were previously experienced in the underground operation.

The outstanding advantages of solution mining process are safety and relatively low cost. Since all operations are carried on from the surface, many of the normal mining hazards are eliminated. Additional advantages are modest capital investment, both for field and plant operations. It is to be noted that a precipitation plant can be substituted for an ion-exchange circuit during development in order to reduce initial expenditure.

The principal disadvantages of solution mining are the dependence on permeability and other uncontrollable ground conditions and the difficulty in getting acceptable recovery in multiple ore horizons. Additional research and experience should result in improvements in these areas.

[1] King, John W. and S. Ralph Austin. "Some Characteristics of Roll-Type Uranium Deposits at Gas Hills, Wyoming," Mining Engineering, May 1966.

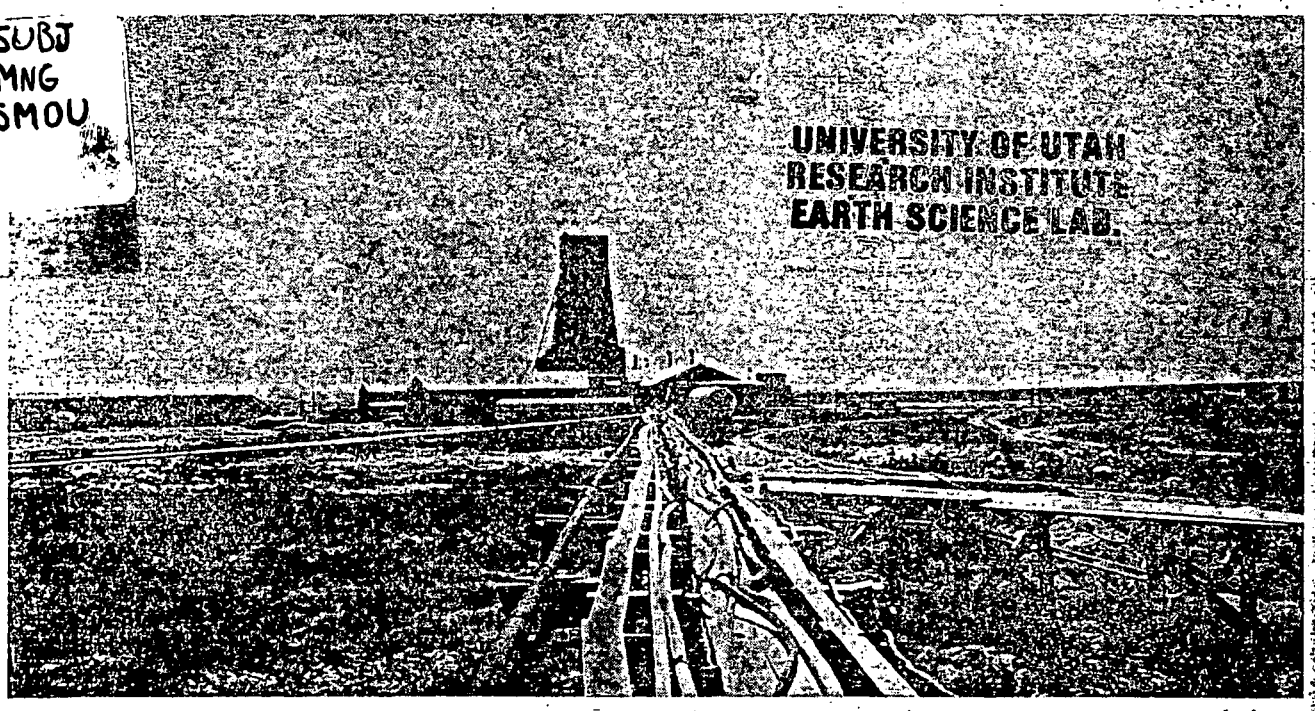

Solution Mining of Uranium

By J. S. ANDERSON
Vice President and
Manager of Uranium Operations
and
M. I. RITCHIE
Mine Manager
Lucky Mc and Shirley Basin Mines
Utah Construction & Mining Co.

Still in the development stage, the solution mining process has been demonstrated to be a workable production method for uranium when applied under proper conditions

IN early 1960, Utah Construction & Mining Co. started producing uranium ore from an underground mine in Shirley Basin, Wyo. This was the first production of uranium from the district, which had been discovered three years earlier. Nothing was known about ground conditions prior to shaft sinking, but difficulties in the sinking operation gave some indication of what could be expected in mining.

After mining had been carried on for some months, and when the ground had been well drained, conditions improved. However, the square-set method which had to be used was costly, so a study aimed at finding another production method that would be reliable, safe, and economical was initiated. The method selected for investigation was solution mining, or in-place leaching.

At Shirley Basin, uranium occurs some distance below the natural water table. A study of problems which might be encountered in solution mining led to the belief that control and recovery of leaching solutions would be difficult. It was guessed that if natural ground water could be made to act as a containment shell for leaching solutions, dewatering of the area to be treated would be unnecessary.

Feasibility determined by specific considerations

As a first step in the investigation of solution mining, reservoir engineers had been consulted. This had been

helpful, but it was realized that the expected chemical environment and reactions made the problems much different than those encountered in petroleum recovery operations. A decision was made to proceed with a test pattern using logical assumptions, with the objective of identifying problems and working out solutions. Work was started in early 1961 and has continued to the present time. The first two years are considered a research period, but since 1963 the process has been the only production method used by the company at Shirley Basin.

Certain requirements exist for solution mining of uranium:

(1) Uranium ore should occur in a generally horizontal bed underlain by a relatively impermeable stratum.

(2) Uranium ore must occur below the static water table.

(3) Direction and velocity of regional water flow must be known.

(4) Mineralogy of the ore should be determined so that its amenability to the proposed process may be known. Material recovered by core drilling is normally sufficient to make this determination.

(5) One requirement, though an obvious one, should be emphasized. Mineral content of the area must be more than sufficient to repay the anticipated cost of the operation. Leaching is not an inexpensive process, and, in this case, solution mining should not be considered as a scavenging operation.

Groundwater flow major factor in pattern design

Undoubtedly the most critical consideration in solution mining as practiced at Shirley Basin is the pattern geometry. Size, shape, and orientation of patterns have undergone numerous changes. During the experimental phase, patterns were square or triangular, with the production well in the center. The area was bounded by inflow wells that were located irrespective of regional groundwater flow direction. Hydraulic interrelationship between wells was ascertained by measuring drawdown in the inflow wells during pumping tests. A balanced inflow vs production rate was achieved by maintaining flowrates to hold water levels in surrounding observation wells below original static levels.

This procedure left quantitative interflow between wells and overall performance to be determined by nitrate recovery and calculated uranium recovery. During the early period of operation, nitric acid was used as a leaching agent. Nitrate recovery could be determined. Calculated uranium recovery was the actual recovered uranium as a percentage of that calculated to be contained in the area bounded by the inflow wells.

Analyses of uranium and nitrate recoveries for patterns mined during this phase indicated that solution losses were occurring and that there was substantial dilution in the effluent produced. It was also apparent that uranium recovery did not correlate with nitrate recovery. This might be the result of uranium leaching beyond the area bounded by the geometric shape of the drilled well pattern.

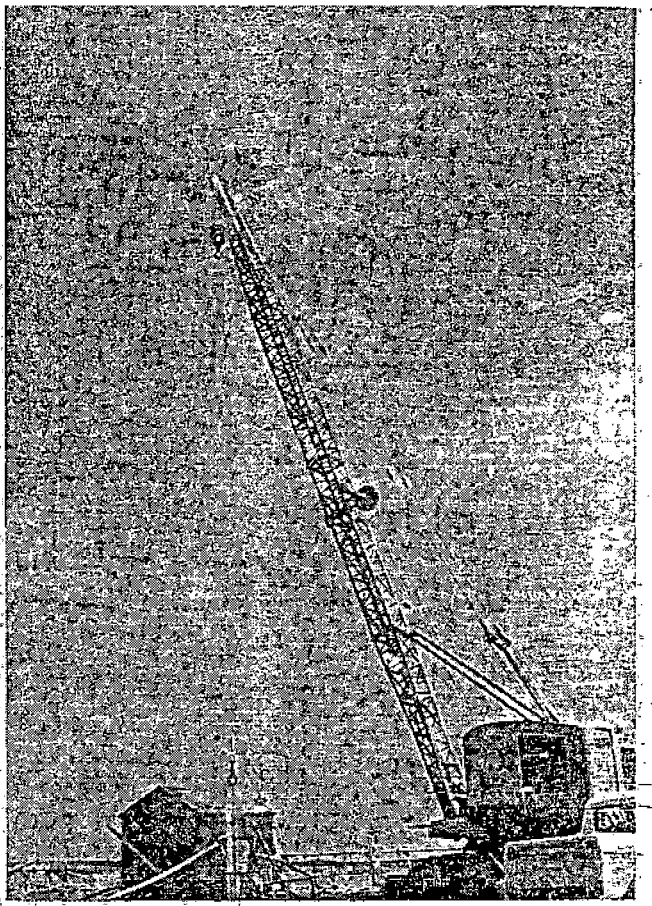

After placement of screens and casing, wells are developed by high-pressure jet

In an attempt to correct these problems, a complete restudy was initiated. As a result, pattern design was changed, which gave improvement in solution recovery and better correlation between nitrate and uranium recovery. The current design is based on the fact that interflow between wells in an aquifer having regional flow can be controlled by varying inflow-effluent rates, by distance between wells, and by aligning wells at specific angles to the direction of groundwater flow.

The present pattern consists of three inflow wells upstream from a production well, with the center inflow well directly upstream on the regional groundwater flow direction. The remaining two inflow wells are located on radii diverging at an angle of 75° from one another, equally spaced from the center inflow well. Distance from inflow wells to production well is about 25 ft.

Since uranium recovery would be confined to the interflow area, that is, the area through which solution will flow from the inflow wells to the production well, the following procedure was established to determine this area:

1. Determine hydraulic gradient within the pattern by measuring static water elevations in developed wells.
2. Conduct drawdown tests, using the inflow wells as observation wells, to provide data to calculate co-

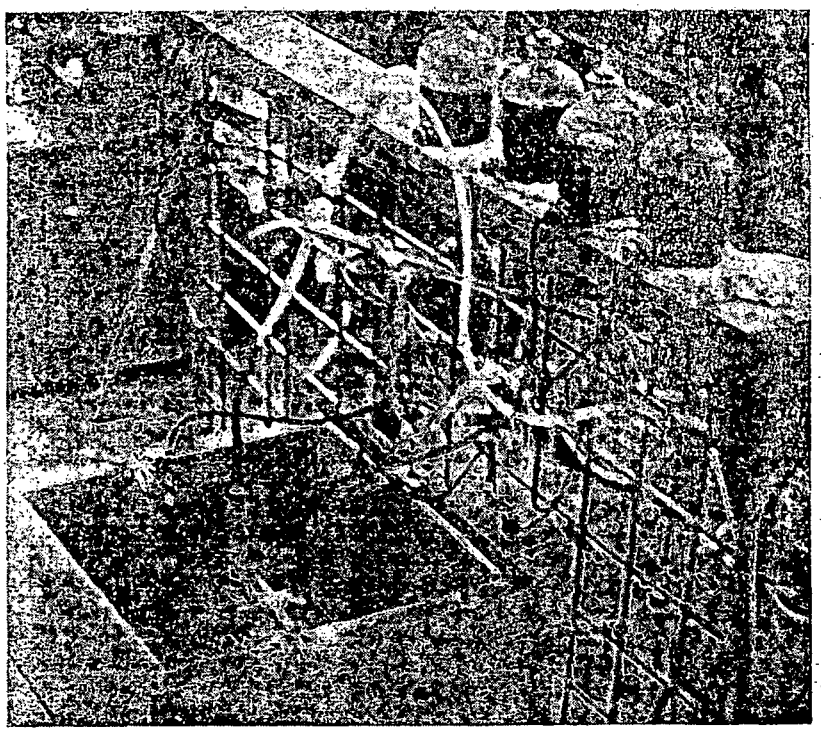

Laboratory equipment was set up in such a manner that the flow of leaching solutions could be simulated and observed. One test pattern has the production well in the center and three inflow wells surrounding it. Groundwater flow is in the direction of the arrow

efficient of transmissibility, in gallons per day per foot, for the aquifer within the pattern.

3. Draw flow nets for production well and inflow wells wells at operating rates in gallons per day using transmissibility and hydraulic gradient as calculated above.
4. Complete the interflow net as graphical resultants of inflow nets and production well net.
5. Calculate uranium contained within the interflow area using U_3O_8 values obtained through interpretation of gamma logs of well pilot holes.

The calculated size and shape of the interflow area as well as uranium recovery from that area can be verified by drilling.

Wells developed by high-pressure jet

Well drilling and development are important for satisfactory operation of a solution mining pattern. Except for the finished diameter, the procedure for drilling and completion of inflow and production wells is the same. Wells are first pilot drilled and probed, after which they are reamed to take the required casing. Inflow well casing is three-in. diam stainless steel, and production well casing is eight in. diam, with stainless steel on the bottom 40 ft. Stainless steel screens are placed through the ore zone in all wells, and cement baskets are placed on the casing just above the ore. Clay layers swell and seal the hole above the baskets. After the screens and casing have been placed, the wells are developed by means of a high-pressure jet. This operation is continued until the wells are capable of a satisfactory rate of inflow by water test.

Standard production pump is an eight-stage, Advance submersible pump, constructed of #316 stainless steel and equipped with a 20-hp Franklin motor in a stainless steel case. Electric power to the pump is via submersible cable fastened to the pump column. An ammeter is put on each leg of the three-phase power supply.

Overall recovery depends on pattern design and operation

Pattern operation starts with the introduction of leaching solution to the three inflow wells. Sulfuric acid is now used instead of the nitric acid previously employed. Simultaneously with the start of inflow, pumping is started in the production well, at a rate which barely exceeds total input to the inflow wells. Patterns start with an acid inflow of 1 to 1.5 grams per liter until titratable acid is measured in the effluent, at which time concentration of sulfuric acid may be increased in increments to a maximum of five grams per liter. The cautious introduction of sulfuric acid at the start is made to be sure that the theoretical solubility of calcium sulfate in water is not exceeded. Lime in the formation is considered neutralized when acid appears in the effluent. Any deposition of gypsum in the sandy formation can thereafter be considered minimal. After an acid condition has been established in the pattern network, uranium leaching is enhanced by the addition of small quantities of sodium chlorate. Measurements are made of the electromotive force in the effluent so a negative 450 can be maintained. A flocculant is infrequently used to promote solution flow in less permeable formations, and the amounts used are 5 to 10 parts per million.

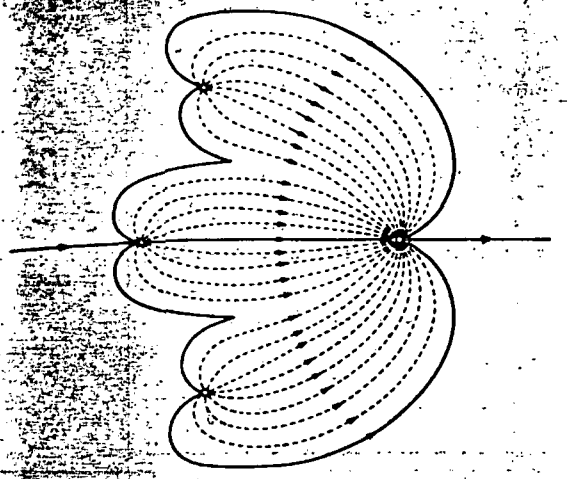

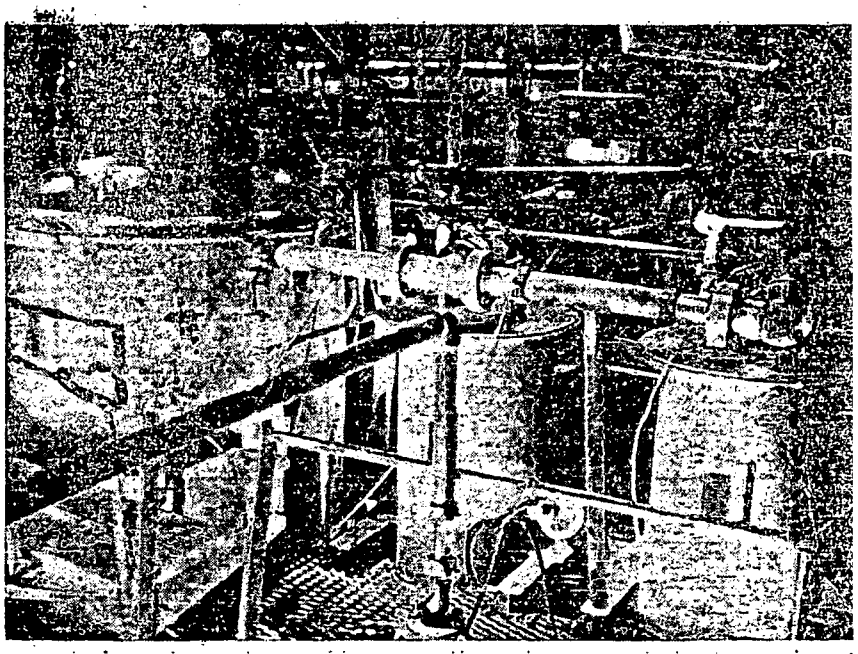

(Left) The well pattern currently used for production consists of three inflow wells located upstream in the regional groundwater flow from a production well. The center well is directly upstream and the other two wells are on radii diverging at an angle of 75° from one another. Inflow wells are 25 ft from the production well. The recovery plant (right) has two circuits incorporating a continuous ion-exchange column, two elution, or stripping, columns and a fixed resin-bed column

There is much variation in the behavior of individual patterns, but normal expectancy is that uranium values appear in the effluent in less than 48 hours. The uranium concentration might continue to build up for a week or more, but, with sulfuric acid as the leaching agent, maximum pregnant solution value seldom exceeds 0.35 grams per liter, and typically will remain between 0.20 and 0.30 grams per liter. Thus, it can be calculated that a pattern area containing 5000 lb of U_3O_8 and pumped at 75 gpm will require more than a month's operation, allowing for a drop-off in grade toward the end of the period. Normally, three to five patterns are in operation simultaneously.

After a pattern has been finished, the pump is removed from the production well, after which screens and casings are salvaged. Special equipment and techniques have been developed for this, and a high recovery of screens and casing is experienced.

Uranium recovery from a leached area is difficult to calculate; however, indications are that overall recovery equals or exceeds that accompanied in underground mining in the same area. In general, it is calculated that recovery approaches 100 percent within the interflow nets. Overall recovery depends on the skill with which patterns are designed and operated. The principle cause of unrecovered uranium is a multiple-horizon area, where upper horizons are not underlain by impervious layers.

Two ion-exchange columns utilized in processing

Uranium-bearing solution produced from all production wells is pumped through individual lines to the uranium recovery plant. The recovery plant is divided into two circuits, a continuous ion-exchange column with two attendant elution, or stripping, columns and a fixed resin-bed column.

The unique, continuous ion-exchange column is five ft in diameter, has a seven-ft straight side and a conical base along with a domed, bolt-on top. Segmented screens, top and bottom, retain the minus 20 plus 40-mesh anionic ion-exchange resin during solution flow. The resin inventory in this column is 135 cu ft, and is divided into nine imaginary 15-cu ft slugs.

Uranium-bearing liquor, having a grade between 0.10 and 0.30 grams per liter U_3O_8, is pumped upflow through a resin-bed. Since the column is packed with resin, a minimum of turbulence occurs in the bed. The normal flowrate is between 7.5 and 10 gpm per square foot of bed area—ideal for good uranium ion exchange.

Calculations based on volume and uranium grade determine when the bottom imaginary 15-cu ft slug of resin is saturated. At this time upflow of pregnant solution is temporarily discontinued while a slug of stripped resin is hydraulically moved from one elution column into the top of the adsorption column, forcing the saturated 15 cu ft out of the bottom into the other elution column. The entire bed shifts down, setting conditions for resumption of the loading cycle.

The loaded slug which has been moved to the elution column is stripped with a mixture of nitric acid, sodium nitrate, and sulfuric acid in a shorter space of time than it takes to saturate the next slug in the bottom of the adsorption column. Thus the cycle operates on an almost continuous basis. Under ideal conditions as much as 270 cu ft of resin can be treated in a 24-hour period. The barren solution emanating from the top of the column is discarded as waste into completely captive tailings ponds. Some acid is discarded with this solution; however, it could not be recycled underground due to its dissolved calcium content.

(Continued on p. 20)

Anderson

Ritchie

J. S. Anderson is vice president and manager of uranium operations for Utah Construction & Mining Co. and has been with the company since 1957. Earlier, he was associated with Chile Exploration Co., the Bunker Hill Co., Bradley Mining Co., and Manganese, Inc. in various mining posts.

M. I. Ritchie joined Utah Construction in 1957 as mill superintendent and is now mine manager of the Lucky Mc and Shirley Basin mines in Wyoming. Prior to this, he served five years as a uranium hydrometallurgist with New Consolidated Goldfields Ltd. and New Union Goldfields in South Africa and one year with Rio Algom Mines Ltd. in Canada.

Simplified Solution Mining FLOWSHEET

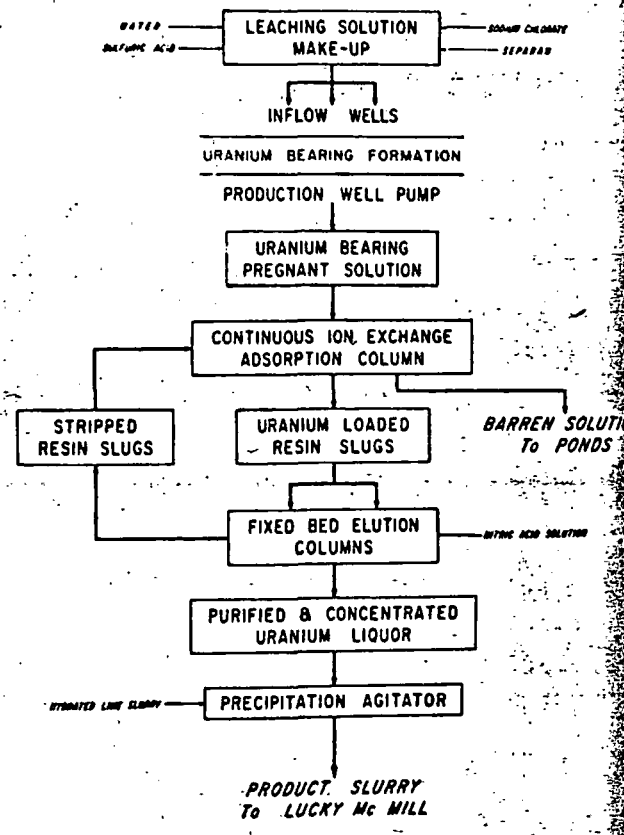

The purified, concentrated strip solution, assaying between 10 and 15 grams per liter U_3O_8, is batch precipitated with dolomitic lime or magnesium slurry to pH 7.5. The resultant uranium slurry is concentrated by decantation prior to being shipped, still in slurry form, to the Lucky Mc mill. The decant, containing neutral nitrate salt, is recirculated to eluate makeup with nitric acid.

The second ion-exchange column is four ft in diameter and has a straight-side dimension of 10 ft. It is partially filled with 100 cu ft of resin, and is used as a fixed-bed system, scavenging uranium from solutions containing less than 0.10 gram per liter U_3O_8. It is stripped batchwise after loading without movement of the resin bed.

Safety and low cost among advantages

The cost of producing uranium by solution mining is a function of a number of complex, interrelated factors. Local drilling and labor costs, together with the success of equipment salvage operations after the patterns have been depleted, determine field costs. Permeability and other ground conditions vary the leaching cycle, and thereby make for cost variations in leaching operations. Plant costs are relatively stable, assuming that patterns can be so scheduled that poundage recovered per day is relatively uniform. Overhead and other fixed costs must be charged against pounds produced, and therefore depend on production rate. At Shirley Basin, under existing conditions, it is believed that minimum production cost approaches open pit costs in a similar area, taking into account the difference in milling cost of ore and slurry. Unfortunately, under adverse conditions these costs may increase by a factor or two or even more. Costs, however, have been found to be well below those which were previously experienced in the underground operation.

The outstanding advantages of solution mining process are safety and relatively low cost. Since all operations are carried on from the surface, many of the normal mining hazards are eliminated. Additional advantages are modest capital investment, both for field and plant operations. It is to be noted that a precipitation plant can be substituted for an ion-exchange circuit during development in order to reduce initial expenditure.

The principal disadvantages of solution mining are the dependence on permeability and other uncontrollable ground conditions and the difficulty in getting acceptable recovery in multiple ore horizons. Additional research and experience should result in improvements in these areas.

[1] King, John W. and S. Ralph Austin. "Some Characteristics of Roll-Type Uranium Deposits at Gas Hills, Wyoming," Mining Engineering, May 1966.

ment of the University of Newcastle-Upon-Tyne introduced a device for measuring differential displacement of points in boreholes. This instrument utilizes hydraulic anchors, ball-and socket joints and potentiometric transducers and can be used in boreholes of 2½-in. diam. Boyles Industries, Ltd. (Central Africa) introduced an expanding hard neoprene anchor for borehole wire extensometers. Slot cutting for anchors is eliminated and the unit cost is less than for mechanical anchors. However, the number of wires that can be installed in a hole is reduced.

Keeping the Roof Up

Several new types of rock bolts were introduced in 1968, such as Bayliss, Jones and Bayliss, Ltd.'s reusable ripping lip bolt; the reusable Worley Roof Bolt which has the revolutionary feature in that it grips the walls for the entire length of the hole in which it is rather than gripping a small area at the anchor only; Ohio Brass Co.'s tandem expansion bolts and Universal Anchorage Co., Ltd.'s anchorage cone system for use in both soils and rock. LKAB at Kiruna, Sweden, has now standardized on the use of a wedge-type reinforcing bar, mortar or resin grouted in the hole for immediate roof support.

The use of powered support systems pioneered and used to such a great extent today by the coal mining industry should not be ignored by the metal mining industry. A good deal of the technology and "know-how" of ground support and control developed in this area will no doubt be utilized in the highly mechanized mining systems still to be developed for vein mines, etc. An excellent summary of the history, present usage and possible future developments in powered supports was supplied by W. S. Adcock at the Annual General Meeting of the Canadian Institute of Mining and Metallurgy at Ottawa in March 1967.

The mechanics of draw control in caving has been a bugbear to the mining engineer throughout the history of controlled caving methods. The use of models by such groups as the Royal Institute of Stockholm, Creighton Mine, and Craigmont Mine has led to some reconciliation between theoretical calculations of behavior and actual working practice.

The year 1968 has been one of continued development in underground mining technology and with the many new ideas for undergeound mining methods and equipment currently being worked upon; the year 1969 promises to be one of considerable interest. ME

Solution Mining

GEORGE POTTER
U.S. Bureau of Mines
Salt Lake City, Utah

More than 15% of the U. S. domestic production of new copper is now derived from solution mining methods applied to dumps, heaps and in-place areas. Theoretical and practical aspects of copper dump leaching were described in a paper presented at the SME Fall Meeting in Minneapolis.[1] The use of radiation logging for studying dump leaching processes at Chino was noted.[2] Kennecott's Ray Mines Division, Arizona, was preparing a new $35 million silicate copper leaching plant to start treating 10,000 tpd of ore early in 1969.[3] Inspiration's new Ox Hide Division in Arizona will soon start leaching 6000 tons of low-grade copper oxide ore per day.[3] Rancher's Exploration and Development Corp.'s new Blue Bird mine operation in Miami, Ariz., was the first commercial solvent extraction plant operating on copper leach liquors. It is designed to produce 30,000 lbs of copper per day via stripping and electrowinning.[4] Copper leaching practices in the Western United States were summarized in a Bureau of Mines report.[5] How copper leach solution is injected into tightly packed dumps at Butte was reviewed.[6]

Still pending action at year's end was the Kennecott "Project Sloop", a proposal to fracture a low-grade oxidized copper zone near Safford, Ariz., with nuclear explosives in preparation for *in situ* leaching with sulfuric acid solution.[7] A USBM report discussed nuclear blasting and *in situ* leaching of copper.[8]

Abroad, heap leaching at Rum Jungle was described,[9] and copper waste dump leaching was discussed,[10] both in papers of the Australasian Institute of Mining and Metallurgy. A Canadian article reported the kinetics of synthetic digenite and chalcocite dissolution in aqueous acidic ferric sulfate solutions.[11] A Japanese journal contained an article on the leaching of copper sulfide minerals by iron-oxidizing bacteria.[12] The winning of useful elements from minerals by leaching underground was reviewed.[13]

In-place solution mining as practiced at the Shirley Basin, Wyo., uranium properties of the Utah Construction and Mining Co. includes controlled injection and recovery of leaching solutions. Uranium is extracted from the solutions in a two-circuit recovery plant.[14] The recovery of byproduct uranium from copper dump leach liquors with new ion exchange techniques was covered in a *Mining Engineering* technical article. The study included the operation of a 20 gpm pilot unit on 12 ppm uranium solutions.[15] An article in *Engineering and Mining Journal* discussed the cost of leaching U_3O_8 in stopes and pumping solution to the surface.[16] ME

taining information without restraint at lower levels.

Even though periodic literature on the application of OR methodology in other industries is becoming rather voluminous, it still remains difficult to compile any extensive bibliography relating to its application in mining. Major sources of information were articles published in the mining trade journals and the publications of professional societies of mining engineers and geologists. The annual AIME and SME Fall meetings had a combined

ming and dynamic modeling are starting to gain importance with the appearance of third-generation computing equipment. With the trend toward larger mine plants and increased mechanization and automation, expanded use of OR and computers will be seen in the pursuit of reduced maintenance costs. Probabilistic approaches to investment planning are being considered and will probably be used quite extensively in the future. Digital plotting is rapidly coming to the forefront as an important application in mining. It appears to be the first graphic output technique to raise interest in the

Static Mechanical Properties and Shock Loading Response of Granite

R. N. SCHOCK AND H. C. HEARD

University of California, Lawrence Livermore Laboratory, Livermore, California 94550

In granitic rocks the quasi-static uniaxial strain loading paths are often observed to diverge from their failure envelopes (uniaxial stress). Similar behavior is observed in Westerly granite and Climax stock granodiorite when they are tested in uniaxial strain to 10 kbar and in uniaxial stress to 22 kbar at strain rates $\dot{\epsilon}$ of 10^{-4} s^{-1}. Failure in the latter tests occurs only by brittle fracture. Plane shock loading occurs under conditions of uniaxial strain, and upon loading to slightly above the Hugoniot elastic limit, yielding is consistent only with brittle fracture. The shock data cannot be reconciled with the low $\dot{\epsilon}$ results if loading occurs along the uniaxial strain path at low $\dot{\epsilon}$. A plausible explanation may be made, however, if the low $\dot{\epsilon}$ uniaxial strain path and the failure envelope are adjusted to strain rates consistent with those of shock deformation. Thus in response to a shock wave, granite loads to peak stresses near 30 kbar; beyond this a slight relaxation occurs. As peak stress is further increased, relaxation is followed by a sudden loss of rigidity in the 50- to 60-kbar range, which is interpreted as intersection with the failure envelope.

Laboratory tests over a range of low strain rates are used extensively to model rock deformation at much higher strain rates, and strain rate effects are accounted for by extrapolation. This approach is used because of the difficulty in obtaining data during the short times available in the process of shock loading. In loading a solid at very high strain rates ($\dot{\epsilon} > 10^4$ s^{-1}) the stress wave propagates as a shock wave. If the wave is planar, inertial and symmetry requirements predict that loading will occur under conditions of uniaxial strain, where the only principal nonzero component of strain is normal to the wave front. For an elastic solid the loading path may be determined if the elastic constants are known. Rocks, however, demonstrate pronounced inelastic effects over a broad range of stresses [*Walsh*, 1965*a*, *b*, *c*; *Walsh and Brace*, 1972]. Thus increasing attention has been paid to loading in uniaxial strain at quasi-static strain rates in an attempt to simulate rock response to dynamic loading [*Swanson and Brown*, 1971; *Brace and Jones*, 1971; *Brace and Riley*, 1972]. Such a path is shown in Figure 1 for a granodiorite studied in our laboratory.

It is apparent from these data that the uniaxial strain loading path diverges from the failure surface, an observation also made by *Swanson and Brown* [1971] on two holocrystalline igneous rocks, Westerly granite, and Cedar City tonalite. In a perfectly elastic solid loaded to a shock state slightly above a yield point a single shock wave is unstable, and two waves are propagated: one at the elastic wave velocity and the other at the appropriate shock velocity [*Rice et al.*, 1958]. The amplitude of the first wave σ_1 is called the Hugoniot elastic limit (HEL). *Petersen* [1969] has studied the Climax stock granodiorite in shock deformation by several techniques of measurement and has observed a distinct two-wave structure, indicating a discontinuous process. Although there is some scatter in these data, probably representing sample variability, most of the HEL points lie between 42 and 48 kbar, the mean value being 45 kbar. This discontinuous process can be interpreted as loading under nearly elastic conditions followed by yield resulting from (1) brittle fracture, (2) plastic flow, or (3) a polymorphic phase transformation.

Two minerals, quartz and plagioclase feldspar, constitute over 90% by volume of this rock [*Borg*, 1970]. Data on quartz [*Wackerle*, 1962] and feldspar [*Ahrens et al.*, 1969] indicate transformations to new crystallographic structures only at pressures above 100 kbar, apparently ruling out possibility 3 as being responsible for the observed HEL in this rock. In Figure 1 the stress state representing the average of Petersen's HEL points cannot be shown as a specific point because only the maximum principal stress σ_1 can be derived from the shock wave data. A range of stress states in minimum principal stress σ_3 versus shear stress $(\sigma_1 - \sigma_3)/2$ space having $\sigma_1 =$ 45 kbar is shown in the upper right corner of Figure 1. The $-\frac{1}{2}$ slope of this line results from the derivative of $(\sigma_1 - \sigma_3)/2\sigma_3$ when σ_1 is constant.

Extrapolation of the quasi-static uniaxial strain loading path to the range of HEL values measured by Petersen results in a stress state with a mean stress of about 30–35 kbar. At these pressures the two principal minerals are still brittle when they are deformed at static rates [*Christie et al.*, 1964; *Seifert*, 1969]. For dense aggregates composed predominantly of quartz and feldspar an increase in the rate of deformation suppresses flow and enhances brittle fracture [*Heard*, 1962; *Heard and Carter*, 1968]. Plastic flow only becomes important in these minerals at temperatures above approximately 600°C at 10-kbar pressure [*Heard and Carter*, 1968, *Borg and Heard*, 1971]. The remaining 10% by volume of the Climax granodiorite, consisting principally of the more ductile biotite and chlorite, is not likely to account for the pronounced double-shock structure reported by Petersen. *Etheridge et al.* [1973] have shown that biotite plastically deforms at pressures of 3 kbar ($\dot{\epsilon} \doteq 10^{-4}$ s^{-1}). Therefore an HEL at 45 kbar is not likely to be caused by the onset of plastic flow in these minerals, even at very much higher shock loading rates. Thus possibility 2 also seems to be ruled out. One must conclude that in this rock the observed HEL is associated with a brittle fracture process.

It is clear from Figure 1 that the uniaxial strain loading path and the failure surface cannot intersect at a value consistent with Petersen's HEL measurement. It should be noted that in a study of the loading path dependence of failure in two granitic rocks, *Swanson and Brown* [1971] demonstrated

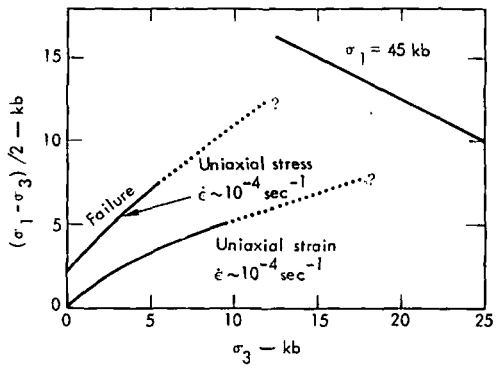

Fig. 1. Uniaxial stress failure envelope and loading path in uniaxial strain for Climax stock granodiorite, Nye county, Nevada. Failure curve is based on data from *Giardini et al.* [1968] and *Heard* [1970]. Constant σ_1 line (45 kbar) represents mean value of HEL determination [*Petersen*, 1969]; σ_1 and σ_3 are the maximum and minimum principal stresses, respectively.

that a loading path that is neither uniaxial stress nor uniaxial strain does not affect the maximum failure stress attained in uniaxial stress loading when the intermediate and minimum principal stresses (σ_2, σ_3) are equal. Therefore the maximum failure stress with respect to the uniaxial strain loading path is represented by the upper surface shown in Figure 1. *Handin et al.* [1967] and *Logan and Handin* [1970] have shown, however, that the failure envelope is raised with increasing rate of deformation and is dependent on the value of σ_2 compared with σ_1 and σ_3. No data exist on the effect of strain rate for uniaxial strain loading in terms of principal stresses. Nevertheless, in plane shock loading of an isotropic material the intermediate and minimum principal stresses are required to be equal.

In this paper we present the results of a series of experiments to determine the failure surface to 20 kbar for two granitic rocks. These data are compared with recent uniaxial strain results [*Schock et al.*, 1973], with determinations of the onset of dilatant behavior (uniaxial stress), and with HEL measurements.

Experimental Techniques

The uniaxial stress and uniaxial strain data were obtained in a piston-cylinder pressure vessel, where the piston is used to load a cylindrical sample [*Schock et al.*, 1973], and in a second vessel where fluid is used to supply the load [*Schock and Duba*, 1972]. In both cases, fluid is used for the confining pressure. The samples used range between 1 and 2.5 cm in diameter and 3 and 6 cm in length. Fluid pressures are measured to 7 kbar with a Bourdon tube gage; above this pressure a manganin coil is used. Accuracy is estimated at 1%. The load applied to the sample by the solid loading piston is measured by an internal load cell calibrated for the effect of confining pressure. Strains are measured with constantan foil strain gages bonded around the sample midsection so as to measure both circumferential strain and axial strain. The samples are jacketed with either 0.03 mm of epoxy or 0.16 mm of copper to prevent penetration of the pressure fluid into the pore space. Both jacket materials give identical results. Strain readings accurate to 1% are corrected for the pressure effect on the gage resistance, the effect of curvature on the gage output, and the effect of pressure on the gage factor [*Schock and Duba*, 1973]. When the failure surface is shown, it represents the maximum shear stress attained on initial loading at constant confining pressure. In all data here the radial stresses σ_2, σ_3 are equal, and strain is taken as negative in compression.

Results

In Figure 2 we show the failure surface determined for Westerly granite (ρ_0 = 2.63 g cm^{-3}) to 20-kbar confining pressure at $\dot{\epsilon}$ near 10^{-4} s^{-1}. At all pressures up to 20.1 kbar the granite failed in a brittle manner. This was determined from inspection of the σ-ϵ curve, the audible release of stored elastic strain energy, and examination of the sample after removal from the apparatus. Single and occasionally multiple shear fracture planes with abundant slickensides were evident in the ruptured material. In all cases, loading along the stress-strain curve was nearly linear up to the rupture stress. The locus of rupture stresses determined from uniaxial stress tests defines the failure envelope for this granite. The data in Figure 2 are in excellent agreement with the results of *Byerlee* [1967] to 11 kbar. However, beyond 11 kbar we find no indication of any appreciable increase in ductility as evidenced either by plastic flow or by homogeneously distributed microfracturing, as suggested by Byerlee.

The $\dot{\epsilon}$ dependence of failure in granitic rocks has been demonstrated by many investigators, most notably *Green and Perkins* [1968], *Kumar* [1968], *Logan and Handin* [1970], and *Green et al.* [1972]. Further, *Scholz* [1968*b*] and *Martin* [1972] have demonstrated that the fracture process in brittle silicate materials is time dependent. The high $\dot{\epsilon}$ data of Logan and Handin ($\dot{\epsilon}$ = 10^{-2} and 1 s^{-1}) have been plotted in Figure 2. The increase in $\dot{\epsilon}$ raises the failure surface, as was observed for other granitic rocks [*Kumar*, 1968]. However, the increase in strength for an order of magnitude increase in $\dot{\epsilon}$ is approximatley 0.10. This value is about twice the values compiled by *Brace and Jones* [1971] for many rock types, including granite. Nevertheless, the high $\dot{\epsilon}$ data in Figure 2 indicate the magnitude of the $\dot{\epsilon}$ dependence of the failure surface.

From limited observations of the effect of strain rate on ductility in granite at 500°C and 5 kbar [*Heard*, 1962] and with the results of *Logan and Handin* [1970] it may be inferred that ductile behavior cannot be expected at $\dot{\epsilon} > 1$ s^{-1} at the highest confining pressure used here but only at much lower rates. Similar data on many other rock types also support this contention [*Serdengecti and Boozer*, 1961; *Handin et al.*, 1967; *Heard and Carter*, 1968]. Thus it can be expected that at the $\dot{\epsilon}$ characteristic of shock loading ($\sim 10^4$–10^6 s^{-1}) the level of the failure envelope will be raised at least 50 to 60%.

The quasi-static uniaxial strain loading path to 10-kbar confining pressure is also shown in Figure 2. The uniaxial

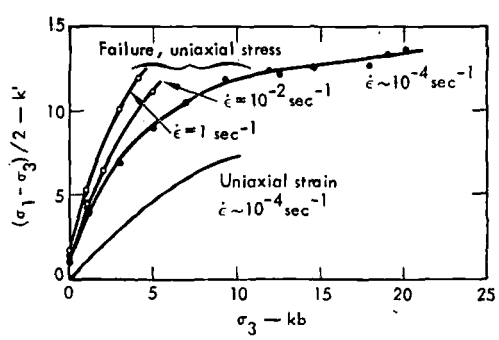

Fig. 2. Relations between failure envelopes and the uniaxial strain loading path for Westerly granite. Failure data in uniaxial stress at $\dot{\epsilon}$ = 1 s^{-1} and 10^{-2} s^{-1} are from *Logan and Handin* [1970].

strain path is determined by increasing the confining pressure as the sample is axially loaded at a rate sufficient to maintain a constant radial strain. *Brace et al.* [1966] have demonstrated that granitic rocks such as Westerly granite exhibit dilatancy before failure in uniaxial stress loading; this dilatancy has been correlated with the onset of fracturing on a microscopic scale [*Scholz*, 1968*a*].

In Figure 3 we have plotted some points at which dilatancy occurs in Climax stock granodiorite as measured in a uniaxial stress test [*Schock et al.*, 1973]. These data represent the point at which the loading in mean pressure-volume space begins to depart from the hydrostat. Similar work on Westerly granite has demonstrated that the onset of dilatant behavior is $\dot{\epsilon}$ dependent [*Brace et al.*, 1966]. At constant $\dot{\epsilon}$ the onset of dilatancy has been shown to be independent of loading path [*Schock et al.*, 1973] in much the same manner as it was for the failure surface [*Swanson and Brown*, 1971]. We also show the uniaxial strain loading path from Figure 1. *Brace et al.* [1966] also observed that dilatant behavior was associated with large increases in circumferential strain, whereas axial strain remained relatively unaffected. They suggest that axial cracks play a major role in dilatancy and hence are ultimately associated with failure. The significance of these observations and those on the path independence of the onset of dilatancy is that if a stress state is reached on uniaxial strain loading, where dilatant behavior may begin and circumferential strain tends to increase, then the confining pressure is automatically increased, and continued loading will be controlled by the lower limit of the dilatant region. Indeed *Brace and Riley* [1972] observed that in Westerly granite, stress states corresponding to the onset of dilatant behavior lie at higher shear stresses than the quasi-static uniaxial strain loading path at low confining pressures but are nearly coincident at high confining pressures. The same observation may be made from examination of the data on Climax stock granodiorite (Figure 3).

If the lower limit of the region of dilatant behavior does indeed serve as an upper limit to uniaxial strain loading, as is shown above, then a test of this hypothesis would be to load the rock in uniaxial strain from some higher confining pressure and to observe the loading path. Increasing pressure generally raises the effective Poisson ratio ν, and since the slope in Figure 3 is proportional to ν through $(\sigma_1 - \sigma_3)/\sigma_3 = (1 - 2\nu)/\nu$, one would therefore expect a slightly lower slope at higher pressures. If deformation remains elastic, the two loading paths would diverge. In Figure 3 we show a uniaxial strain loading path for a sample of Climax stock granodiorite loaded from 1-kbar confining pressure. As is evident, this

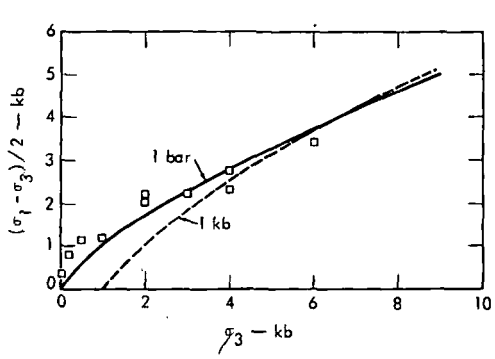

Fig. 3. Uniaxial strain loading paths from 1-bar (Figure 1) and 1-kbar confining pressure for Climax stock granodiorite. The open squares represent onset of dilatant behavior as determined in uniaxial strain [*Schock et al.*, 1973].

loading path joins that loaded from 1 bar. These curves converge with increasing pressure as if both were controlled by the same inelastic process. We suggest that this process is the onset of dilatancy.

Considering the most likely path followed during shock wave loading it is probable that in the first few kilobars of axial stress, uniaxial strain loading predominates. Some nonlinearity caused by the closing of cracks may occur, as suggested by *Walsh and Brace* [1972] from observations at low $\dot{\epsilon}$. The intersection of this path with the dilatant region can be expected at somewhat higher stresses in shock loading because of the influence of $\dot{\epsilon}$ on the onset of dilatancy [*Brace et al.*, 1966]. If the loading were to continue under uniaxial strain, this would limit the loading path to the onset of the dilatant behavior region at these high $\dot{\epsilon}$. But if the loading were not constrained to be in uniaxial strain, barring an inelastic process or change in effective elastic constants, loading would continue along a path with the same initial slope.

Returning to Westerly granite, we show in Figure 4 a hypothetical loading path with an initial slope based on an effective Poisson ratio of 0.26. This is taken from *Walsh* [1965*c*] as the intrinsic value for Westerly granite, i.e., the value for the rock without the influence of its inherent cracks. The cracks have been shown to be mostly closed by stresses of less than 0.5 kbar [*Simmons and Brace*, 1965; *Walsh*, 1965*a*, *b*; *Schock and Duba*, 1972], and we ignore their influence here only for illustrative purposes. We show the loading path as linear to 27-kbar axial stress. At 27 kbar the shock wave experiments of *Rosenberg* [1971] indicate a very slight break in the slope of the shock loading front. Examinations of the failure envelopes in Figure 2 together with the foregoing arguments on the expected trend of failure strengths with $\dot{\epsilon}$ (Figure 4) indicate that it is most unlikely that this break represents complete failure. If the shear modulus decreases discontinuously at the stress where dilatancy begins, a discontinuity will result. From the previous description of dilatant behavior a large increase in circumferential strain ϵ_r relative to axial strain ϵ_l will increase shear strain $\epsilon_{sh} = \epsilon_l - \epsilon_r$, and the shear modulus $\mu = (\sigma_1 - \sigma_3)/2(\epsilon_l - \epsilon_r)$ will be reduced. Therefore it is more likely that the break observed at 27 kbar by Rosenberg is the onset of microfracturing, which in the quasi-static experiments, results in dilatant behavior. Dilatancy is a gradual and continuous process beginning at stress levels approximately one half the failure value [*Brace et al.*, 1966; *Schock et al.*, 1973]. As a result, a large stress relaxation such as that observed by Petersen in the Climax stock granodiorite would not be expected when microfracturing begins.

The peak stresses attained by *Rosenberg* [1971] are only slightly above 60 kbar, in contrast to a level of 180 kbar attained in some of the experiments of *Petersen* [1969]. Interpretation of *Rosenberg*'s [1971] data as indicating brittle failure at stresses above 60 kbar seems consistent with the results presented in Figure 4. On loading to stresses above the level at which microfracturing begins this process will continue until complete cohesion in the sample is lost. At this point, if behavior at low $\dot{\epsilon}$ in uniaxial stress loading is representative, the stress increase can be expected to change discontinuously. When the attained peak stresses in shock loading are just above those corresponding to failure, a precursor will precede the shock wave. In Figure 4 we have shown the expected shear stresses at failure for two strain rates: 10^{-1} and 10^{5} s^{-1}. These are based on the 10^{-4} s^{-1} $\dot{\epsilon}$ results increasing by 0.05 per order of magnitude change in $\dot{\epsilon}$, consistent with the general value reported by *Brace and Jones*

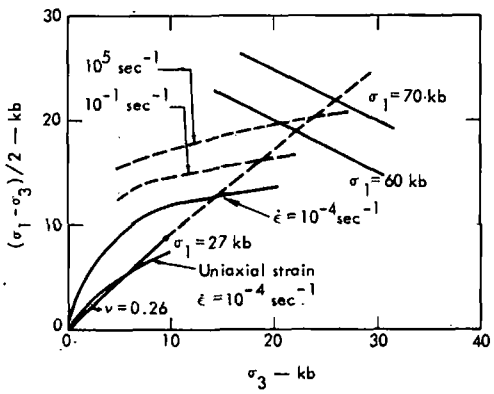

Fig. 4. Hypothesized shock loading path in Westerly granite showing inferred onset of microfracturing at 27 kbar. Inferred failure envelopes are also shown for several $\dot{\epsilon}$ along with failure data from Figure 2.

[1971]. The loading path above 27 kbar is shown in Figure 4 with a slightly lower slope than the initial loading. It is meant only to indicate schematically a slight relaxation as a result of microfracturing. In reality the slope of the loading path may decrease as the intensity of microfracturing increases on approaching the failure surface.

A similar diagram is shown in Figure 5 for Climax stock granodiorite (ρ_0 = 2.67 g cm^{-3}). As before, we have assumed a 5% increase in shear stress at failure per order of magnitude increase in $\dot{\epsilon}$. We have used an initial loading slope corresponding to an effective Poisson ratio of 0.28. This value is calculated from acoustic velocity data obtained in this laboratory between 5- and 10-kbar hydrostatic pressure. *Walsh* [1965*c*] believes that for Westerly granite the value of ν obtained in this manner is essentially the intrinsic value for the rock. Close examination of the shock wave profile in Climax stock granodiorite [*Petersen*, 1969] reveals a slight break in slope, similar to that observed by Rosenberg in Westerly granite at a stress level of about 30–35 kbar. This range is plotted in Figure 5 on the loading slope. Further extrapolation, with a slight decrease in slope as in Figure 4, is shown by a dashed line that intersects the extrapolated failure envelope at an axial stress somewhat above 60 kbar. Thus if the large discontinuity observed by Petersen is to represent failure, the initial loading slope must be steeper, or there must be a smaller, perhaps nonlinear, effect of $\dot{\epsilon}$ on the failure envelope for the granodiorite, or both.

In reality, we know little about either of these possibilities. We have chosen the supposed intrinsic values of ν to represent the initial loading slope for both rocks. However, in shock loading the effective ν will determine the loading slope with reference to the failure envelope, but we have no assurance that the value chosen is correct. It should be emphasized that the loading is very sensitive to the value of ν chosen. For example, in Figure 4, if ν were lowered slightly from 0.28 to 0.23, our inferred high $\dot{\epsilon}$ failure curve would be in good agreement with Petersen's HEL measurements. Poisson's ratios have been shown to vary between 0.17 and 0.28 on the same rock in a variety of stress configurations, depending on the relative interaction of cracks and pores [*Walsh and Brace*, 1972]. In addition, the effect of $\dot{\epsilon}$ on ν is unknown. Although the compilations of *Brace and Jones* [1971] on the effect of $\dot{\epsilon}$ on failure seem to indicate about a 5% effect per 10-fold increase in $\dot{\epsilon}$, values as low as 3% are noted in some silicate rocks. We have very little indication of the stress level or the degree of relaxation at which microfracturing takes place. Thus we are unable to use the present results to calculate quantitatively the magnitude of the $\dot{\epsilon}$ effect on strength.

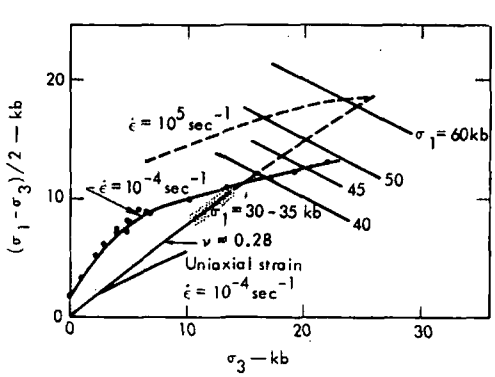

Fig. 5. Hypothesized shock loading path in Climax stock granodiorite showing onset of microfracturing at 30–35 kbar. Hypothesized failure envelope is also shown for $\dot{\epsilon}$ = 10^6 s^{-1}.

Instead, the collective quasi-static and shock data may be interpreted as indicating loading under shock conditions into the region of microfracturing with some associated relaxation in stress rate and if the stress pulse is large enough, continued loading to failure by brittle fracture. Simplified numerical models that treat loading as elastic to the failure surface have in the past calculated nuclear shots in granodiorite [*Cherry and Peterson*, 1970; *Cameron and Scorgie*, 1970] and in granite [*Michaud and Maury*, 1970] with moderate success, using the effective moduli at atmospheric pressure. If the actual shock loading slope (Figures 4 and 5) were very much lower (higher ν) than that based on the intrinsic elastic constants, one would not expect the radius of rock fractured on compression, as predicted by this method, to be in agreement with measured postshot values. Instead, one would expect to observe less brittle fracturing, whereas one generally observes more. It would appear then that when inelastic effects that are well known from quasi-static investigations are ignored, the calculations are more accurate than if they had been taken into account. This finding may be additional evidence that inelastic processes are $\dot{\epsilon}$ dependent.

Many more data are needed if the conclusions drawn from the limited data presented here are to be proved. The most critical needs seem to be to understand (1) the effect of $\dot{\epsilon}$ on uniaxial strain loading while all principal stresses are monitored and (2) the $\dot{\epsilon}$ dependence of both failure and dilatant behavior at mean pressures to 30 kbar. Neither is a simple task.

CONCLUSIONS

Based on the properties of these rocks and the nature of the uniaxial strain experiment, the quasi-static uniaxial strain path is in all likelihood not representative of the shock loading path. When $\dot{\epsilon}$ effects are neglected, the presence of a region of dilatant behavior and the concomitant increase in radial strain seem to preclude loading into this region because uniaxial strain loading conditions do not allow radial strain. Available data on rock fracturing indicate that brittle failure in granitic rocks is everywhere preceded by microfracturing and dilatant behavior. *Brace et al.* [1966] postulated the disappearance of this dilatancy region with increasing mean stress. Under these circumstances, uniaxial strain loading might be expected to intersect the failure surface. However, for granitic rocks there are no data that indicate at what

pressure this may take place. *Schock et al.* [1973] have shown for a different rock type (graywacke) that dilatancy diminishes only as the failure mechanism changes from brittle fracture to macroscopic ductile flow. There is no evidence for this transition in the granitic rocks we investigated to at least 22 kbar, as well as in an additional granitic rock tested in torsion to 50 kbar [*Schock et al.*, 1972]. Neither is there evidence for plastic deformation in either of the two principal minerals in these rocks, quartz and feldspar, at these mean pressures and shock loading rates. Thus as was noted earlier, the observed HEL places an upper limit on the value of the mean stress associated with this yielding.

Acknowledgments. Work was performed under the auspices of the U.S. Atomic Energy Commission. Hedley Louis and Howard Washington have provided outstanding laboratory assistance.

REFERENCES

Ahrens, T. J., D. L. Anderson, and A. E. Ringwood, Equations of state and crystal structures of high-pressure phases of shocked silicates and oxides, *Rev. Geophys. Space Phys., 7*, 667, 1969.

Borg, I. Y., Survey of the Piledriver event and preliminary interpretation of three postshot cores in and near the cavity, *Rep. UCRL-50865*, Lawrence Livermore Lab., Calif., 1970.

Borg, I. Y., and H. C. Heard, Experimental deformation of plagioclases, in *Rock Deformation*, edited by P. Paulitsch, pp. 375–403, Springer, New York, 1971.

Brace, W. F., and A. H. Jones, Comparison of uniaxial deformation in shock and static loading of three rocks, *J. Geophys. Res., 76*, 4913, 1971.

Brace, W. F., and D. K. Riley, Static uniaxial deformation of 15 rocks to 30 kb, *Int. J. Rock Mech. Mining Sci., 9*, 271, 1972.

Brace, W. F., B. W. Paulding, Jr., and C. Scholz, Dilatancy in the fracture of crystalline rocks, *J. Geophys. Res., 71*, 3939, 1966.

Byerlee, J. D., Frictional characteristics of granite under high confining pressure, *J. Geophys. Res., 72*, 3639, 1967.

Cameron, I. G., and G. C. Scorgie, Theoretical model of the early phases of an underground explosion, Proceedings of Symposium on Engineering with Nuclear Explosives, *Conf-700101*, vol. 1, pp. 221–229, Amer. Nucl. Soc., Hinsdale, Ill., 1970.

Cherry, J. T., and F. L. Peterson, Numerical simulation of stress wave propagation from underground nuclear explosions, Proceedings of Symposium on Engineering with Nuclear Explosives, *Conf-700101*, vol. 1, pp. 142–173, Amer. Nucl. Soc., Hinsdale, Ill., 1970.

Christie, J. M., H. C. Heard, and P. N. LaMori, Experimental deformation of quartz single crystals at 27 to 30 kilobars confining pressure and 24°C, *Amer. J. Sci., 262*, 26, 1964.

Etheridge, M. A., B. E. Hobbs, and M. S. Paterson, Experimental deformation of single crystals of biotite, *Contrib. Mineral. Petrol., 38*, 21, 1973.

Giardini, A. A., J. F. Lakner, D. R. Stephens, and H. D. Stromberg, Triaxial compression data on nuclear explosion shocked, mechanically shocked, and normal granodiorite from the Nevada test site, *J. Geophys. Res., 73*, 1305, 1968.

Green, S. J., and R. D. Perkins, Uniaxial compression tests at varying strain rates on three geologic materials, in *Proceedings of 10th Symposium on Rock Mechanics*, edited by K. E. Gray, pp. 35–54, American Institute of Mining, Metallurgical and Petroleum Engineers, Austin, Tex., 1968.

Green, S. J., J. D. Leasia, R. D. Perkins, and A. H. Jones, Triaxial stress behavior of Solenhofen limestone and Westerly granite at high strain rates, *J. Geophys. Res., 77*, 3711, 1972.

Handin, J., H. C. Heard, and J. M. Magouirk, Effects of the intermediate principal stress on the failure of limestone, dolomite, and glass at different temperatures and strain rates, *J. Geophys. Res., 72*, 611, 1967.

Heard, H. C., The effect of large changes in strain rate in the experimental deformation of rocks, Ph.D. dissertation, 202 pp., Univ. of Calif., Los Angeles, 1962.

Heard, H. C., The influence of environment on the inelastic behavior of rocks, Proceedings of Symposium on Engineering with Nuclear Explosives, *Conf-700101*, vol. 1, pp. 127–141, Amer. Nucl. Soc., Hinsdale, Ill., 1970.

Heard, H. C., and N. L. Carter, Experimentally induced "natural" intragranular flow in quartz and quartzite, *Amer. J. Sci., 266*, 1–42, 1968.

Kumar, A., The effect of stress rate and temperature on the strength of basalt and granite, *Geophysics, 33*, 501–510, 1968.

Logan, J. M., and J. Handin, Triaxial compression testing at intermediate strain rates, in *Proceedings of 12th Symposium on Rock Mechanics*, edited by G. B. Clark, pp. 167–194, American Institute of Mining, Metallurgical and Petroleum Engineers, Rolla, Mo., 1970.

Martin, R. J., III, Time-dependent crack growth in quartz and its application to the creep of rocks, *J. Geophys. Res., 77*, 1406–1419, 1972.

Michaud, L., and J. Maury, Effets mécaniques en zone proche d'une explosion nucléaire souterraine dans le granite, *Transl. UCRL-10615-5*, Lawrence Livermore Lab., Calif., 1972.

Petersen, C. F., Shock wave studies of selected rocks, Ph.D. dissertation, 92 pp., Stanford Univ., Stanford, Calif., 1969.

Rice, M. H., R. G. McQueen, and J. M. Walsh, Compression of solids by strong shock waves, *Solid State Phys., 6*, 1–63, 1958.

Rosenberg, J. T., Dynamic shear strength of shock-loaded granite and polycrystalline quartz, Final report, *Rep. DASA-2718*, Stanford Res. Inst., Menlo Park, Calif., 1971.

Schock, R. N., and A. Duba, Quasi-static deformation of solids with pressure, *J. Appl. Phys., 43*, 2204–2210, 1972.

Schock, R. N., and A. G. Duba, Pressure effects on the response of foil strain gages, *Exp. Mech., 13*, 43–44, 1973.

Schock, R. N., A. E. Abey, H. C. Heard, and H. Louis, Mechanical properties of granite from the Taourirt Tan Afella Massif, Algeria, *Rep. UCRL-51296*, Lawrence Livermore Lab., Calif., 1972.

Schock, R. N., H. C. Heard, and D. R. Stephens, Comparison of the behavior of a granodiorite and two graywackes on loading to 20 kbar, *J. Geophys. Res., 78*, 5922–5941, 1973.

Scholz, C., Microfracturing and the inelastic deformation of rock in compression, *J. Geophys. Res., 73*, 1417–1432, 1968*a*.

Scholz, C., Mechanism of creep in brittle rock, *J. Geophys. Res., 73*, 3295–3302, 1968*b*.

Seifert, K. E., Strength of Adirondack anorthosite at elevated temperatures and pressure, *Geol. Soc. Amer. Bull., 80*, 2053–2060, 1969.

Serdengecti, S., and G. D. Boozer, The effects of strain rate and temperature on the behavior of rocks subjected to triaxial compression, in *Fourth Symposium on Rock Mechanics*, pp. 83–97, Pennsylvania State University, University Park, 1961.

Simmons, G., and W. F. Brace, Comparison of static and dynamic measurements of compressibility of rocks, *J. Geophys. Res., 70*, 5649–5656, 1965.

Swanson, S. R., and W. S. Brown, An observation of loading path independence of fracture in rock, *Int. J. Rock Mech. Mining Sci., 8*, 277–281, 1971.

Wackerle, J., Shock-wave compression of quartz, *J. Appl. Phys., 33*, 922, 1962.

Walsh, J. B., The effect of cracks on the compressibility of rock, *J. Geophys. Res., 70*, 381–389, 1965*a*.

Walsh, J. B., The effect of cracks on the uniaxial elastic compression of rocks, *J. Geophys. Res., 70*, 399–411, 1965*b*.

Walsh, J. B., The effect of cracks in rocks on Poisson's ratio, *J. Geophys. Res., 70*, 5249–5257, 1965*c*.

Walsh, J. B., and W. F. Brace, Elasticity of rock in uniaxial strain, *Int. J. Rock Mech. Mining Sci., 9*, 7–15, 1972.

(Received June 18, 1973.)

Solution Mining

W. C. Larson, USBM, reported uranium in situ leaching operations have increased significantly since 1975. There were 27 active projects in 1980, including 16 commercial scale or under construction operations and 11 pilot scale operations. US design capacity for in situ leach mining has grown from 227 kt in 1975 to an estimated 2.6 Mt in 1980, while estimated production has gone from 68 kt in 1975 to 1.8 Mt in 1980.

South Texas and Wyoming uranium districts have been prominent in early field experiments as well as commercial application of this recovery technique, although uranium in situ leach tests are now being conducted in Colorado and New Mexico.

The growing number of commercial-scale operations is evidence that in situ mining offers a third option to pit and underground mining of uranium from sandstone. Most recent information showed an estimated 9% of US uranium production was from in situ mining.

In situ leaching has the potential to open up resources currently uneconomic to mine by conventional methods and to do it with less disturbance to the local environment. However, in situ uranium mining is not without its environmental problems. Primary emphasis is on control of leach solutions during mining and demonstration of ground water quality restoration.

The basic in situ leaching principle involves recovery of metal values by transporting fluids through rock and is best suited for deep-lying, lower grade, and water-saturated minerals, with high flow conductivity and mineral contact with water. Significant progress has been made over the past decade in developing in situ leaching technology for uranium and copper recovery. The July 1980 *MCJ* reviewed in situ leaching technology and economics and discussed three key engineering tasks: selection of metal concentrations, oxygen injection for uranium and sulfide operations, and well pattern design considerations.

Research

One in situ leaching technique being researched is drilling and completing multiple branched boreholes. These multiple-branch wells contain two or more boreholes drilled from a single vertical hole and can cut drilling costs by reducing total footage drilled. As reported to the American Society of Mechanical Engineers by Larson; D. W. Dareing, Mauer Engineering Inc.; E. T. Wood, Completion Technology; and D. H. Davidson, TRW Energy Systems Group; branch drilling can reduce well costs when applied to ore bodies deeper than 457 m. The practical limit for number of branches drilled and completed from one vertical wellbore is three. The first step in developing branch well completion equipment is to limit initial branch wells to include only two hole bottoms. Experience gained by developing templates and guides for dual branch wells could be extended to three hole bottoms. Further study is needed, the authors concluded.

Field tests are planned for a USBM lab research project showing the advantages of ore body conditioning with a chloride solution before in situ uranium leaching with a carbonate solution. Results show reduced ore body permeability loss upon injection of the carbonate solution. In addition, the difficulty of complying with current regulations concerning restoration of groundwater quality after leaching with ammonium carbonate may be avoided if potassium carbonate can be substituted economically for ammonium carbonate. In addition, flushing the ore body with potassium chloride before leaching satisfies cation exchange sites with potassium from relatively cheap potassium chloride, thereby reducing the consumption of the more expensive potassium carbonate (D. R. Tweeton, USBM, and T. R. Guilinger, W. M. Breland, and R. Schechter, University of Texas, 1980 SPE Fall Conference).

Another USBM research project concerned the first restoration of pilot scale acidic leaching of a uranium ore body at the Nine Mile lake site near Casper, WY. Using acid as a leachant sidesteps many of the environmental problems associated with ammonium carbonate-bicarbonate leachants, the most notable being the reluctant release of ammonium ions from clays under restoration fluid flushing. The successful restoration of this site adds to the viability of sulfuric acid as an alternative leachant for uranium contained in low-calcium carbonate ores (W. H. Engelmann, P. E. Phillips, D. R. Tweeton, K. W. Loest, and M. T. Nigbor, USBM, 1980 SPE Fall Conference).

USBM also tested various geophysical resistivity measuring techniques to identify a rapid, reliable method for detecting underground migration of lixiviant outside of planned limits. R. F. Kehrman, Westinghouse Electric Corp.; A. J. Farstad, a private consultant; and D. R. Tweeton, USBM, reported at the 1980 SME Fall Meeting that surface and downhole galvanic resistivity and controlled source audio-magneto-telluric (AMT) methods were tested at an in situ uranium mine in northern Wyoming during startup of a new mining area. The lixiviant monitoring program demonstrated that resistivity measurement techniques can be used during production to track leach solution migration. Downhole galvanic and AMT were the most promising techniques.

1980 Developments

Mobil Oil Co.'s El Mesquite plant, 80 km east of Laredo, TX, is one of the most recently opened in situ leaching operations in the south Texas uranium district. The plant is designed to operate at 12 kL/min and produce 295 t/a of yellowcake. Commercial production of U_3O_8 involves in situ leaching, extraction, concentration of uranium ions from the leach solution, and precipitation (*E/MJ*, Jan. 1981).

Cyanide leaching of micron-size gold from ores at the old Silver Cross mine in central Arizona was started and will be expanded by Amca Industries Ltd. Three leaching pads are used and at full capacity the pads will treat 36-kt heaps. About 454 t/d of ore is bulldozed from the side of Silver Cross Mountain and crushed to 51 mm for leaching. Ore assays average 9 g of gold and 47 g of silver per ton. Diamond drilling indicates more than 136 kt of reserves with the same values, a company official said (*E/MJ*, Oct. 1980).

G. E. McClelland, USBM, (1980 AMC Mining Convention) investigated particle agglomeration to increase leach solution percolation rates, in heap leaching clayey or finely crushed low grade gold-silver ores. Ore sample tests indicated percolation rate of the cyanide leach solution could be enhanced by mixing the ore with controlled amounts of binders—like lime or portland cement and water—agglomerating the resultant admixture, and aging the agglomerated feed prior to percolation leaching. In addition, gold and silver extraction rates increased without sacrificing recovery.

The Fourth Annual Uranium Seminar, sponsored by the South Texas Mineral Section AIME and held in September in Corpus Christi, TX, concentrated on aspects of in situ uranium mining. D. E. Stover, Everest Minerals Corp., outlined methods for controlling grade during in situ uranium leaching to produce desired concentrations of dissolved uranium. Grade control "is the most exciting engineering task associated with in situ leaching of uranium," he said. Other seminar topics included solution mining, alternate mill, and leasing and regulatory concepts (*E/MJ*, Dec. 1980).

Nerco Inc. and Teton Exploration Co. continued participation in a uranium solution mining joint venture test plant in Wyoming. The pilot plant project is designed to evaluate underground uranium solution leach mining, to produce yellowcake. Though results were successful, no decision has yet been made to start commercial production.

Synthetic Fuels

In 1980, President Carter signed into law the $20-billion Synthetic Fuels Act. The act established a federally chartered, quasi-independent financial enterprise called the US Synthetic Fuels Corp., with a goal of attaining domestic production of 80 dam³ (500 000 bbls/d) of synthetic fuels by 1987.

The act also provided that until the corporation is fully operational, the President, under the Defense Production Act, has authority to stimulate synfuel development to meet national defense needs through a system of purchase agreements, loans, and loan guarantees. But recent political events in Washington have made the future of the Synthetic Fuels Corp. uncertain.

With significant US oil shale development underway, prospects for expanding the industry in Utah, Colorado, and Wyoming appeared strengthened in late November when the Senate Committee on Energy and Natural Resources and the House approved an oil shale leasing bill. The legislation would allow holders of existing oil shale leases to acquire additional leases on federal land to be used for spent shale disposal or for shale processing plants. However, Colorado Senator Gary Hart blocked the pending legislation, voicing concern over a provision allowing a five-year time limit extension during which lease holders could apply for offset waste disposal allowance. Hart wanted offsite disposal allowance only for operators with oil shale leases that were effective in 1980 or earlier (*E/MJ*, Jan. 1981).

In January 1981, the Department of Energy picked three proposed synthetic fuel plants for possible Federal aid awards of $3 billion. The three projects were picked from among 25 proposals submitted to former President Carter's administration late last year. The chosen projects were Tosco Corp.'s Colony oil shale project and Union Oil of California's Parachute Creek oil shale project, both near Rifle, CO, and a Tennessee synfuels project to convert coal to gasoline. The Colony project will reportedly cost $3.34 billion; Union's, about $3 billion. Each will produce about 8 dam³/d (50 000 bbl/d) of synthetic oil. Tosco has a 40% interest in Colony. Colony's 60% owner, Exxon Corp., did not seek government help (*ME*, Feb. 1981).

In another shale-related development in 1980, the US Supreme Court ruled pre-1920 oil shale discovery claims are valid and may be taken to patent if annual assessment work has been done. The Interior Department estimated as much as 0.02 Mm² (5 million acres) of land may be involved in the pre-1920 claims, though the US 10th Circuit Court of Appeals—whose earlier ruling in the case was upheld by the Supreme Court—suggested only 40 000 claims might be involved. A Bureau of Land Management official said that "probably very few claims have been maintained with $100 annual assessment work." In any event, claimants will have to prove to BLM's satisfaction the annual assessment work was done. The Interior Department argued before the high court that with pre-1920 shale discovery claims there was no valid discovery of valuable mineral deposits because there was no commercial recovery system in existence at the time. The court disagreed with that line of reasoning (*E/MJ*, July 1980).

Developments to Watch

In January 1981, *ME* presented a special issue on the oil shale industry. A historical perspective, a summary of the status of current US oil shale projects, oil shale mining techniques and recovery methods, environmental issues, and the role of the federal government were discussed. But oil shale remained a subject of disagreement throughout the year, some arguing the need to get on with it, others not so sure.

Institutional problems were cited as the major remaining impediments to oil shale development by A. E. Lewis of the University of California's Lawrence Livermore Laboratory. Water and environmental problems such as air quality are often given as problems to commercial oil shale production. "But the real problem is that we lack the national commitment that is required and the institutional framework necessary to overcome the obstacles preventing use of this resource," said Lewis, addressing the 13th Annual Oil Shale Conference at the Colorado School of Mines. He said the Mahogany zone of Colorado's Piceance Basin contains some 114.5 km³ (720 billion bbl) of oil, suitable for open-pit mining and containing an average of 83.4 L/t of shale oil. Lewis said above-ground retorts should be used because they are more efficient. He also noted the US oil shale resource is more than adequate to replace imported oil. "We have technology that is good enough to start with and can soon be improved. The economic cost appears to be well below the cost of imported oil."

At least one person, W. T. Slick, Exxon Corp., agreed with Lewis about the necessity for open pit mining of shale. At a July congressional hearing in Denver, CO, he said "massive surface mining" would be needed. Massive indeed, at least under the Exxon scenario: 95.4 dam³ (600 000 bbl/d) from shale by 1990; 240 dam³ (1.5 million bbl/d) by 1995, 477 dam³ (3 million bbl/d) by 2000, and further incremental increases to 1.3 hm³ (8 million bbl/d). To achieve the synfuel production level postulated by Exxon, the federal government's oil shale leasing policy would need to be expanded, said Slick. He noted that Exxon studies indicate sufficient water in the Colorado River Basin to sustain a production level of 240 dam³ (1.5 million bbl/d), but at a higher level—after 1995—an interbasin water transfer would be needed. The best source would probably be Lake Oahe in the Missouri River Basin in central South Dakota, Slick said. He acknowledged there would "have to be some modification of the Clean Air act if we go to 1.3 hm³ (8 million bbl/d) (in the Piceance Basin)." Colorado officials were not enthused by Exxon's shale projections. Monte Pascoe, Colorado Department of Natural Resources, said the state would strongly resist such large-scale development of oil shale. (*E/MJ*, Aug. 1980).

Not all oil shale companies agreed with Lewis and Exxon that shale oil was indeed an idea whose time had come. R. Loper, Chevron Shale Oil Co. president, cited technological risks in developing oil shale. Though there are thousands of oil shale patents in the US, "the fact is, there is no process proven which produces shale oil from rock in anything like commercial quantities. The difficulties of handling many thousands of tons of shale through processing steps requiring heating of the entire mass to 482°C, capturing the vapors, and cooling and disposing of the spent shale are enormous," he told a hearing in 1980 before the Colorado Energy Coordinating Advisory Committee.

Air Quality

Meanwhile, air quality might cause some real problems for the incipient oil shale industry. There is already an intra-industry dispute about it. Occidental Oil Shale Co. applied to the Colorado Air Pollution Control Com-

with the formation of a new phase, which is the analogue of natural mohawkite [γ phase according to Hiller and Probstain [3]] with the composition wt.%: 33.2 Fe; 34.7 Cu; 32.0 S. At 600°C, as a result of the excess of sulphur above the stoichiometric [illegible]t for mohawkite, it decomposes into a α and β-chalcopyrite. The stoichiometry of mohawkite is obtained at 800°C, [illegible]e mineral grains cooled from 800°C are therefore [illegible]eneous. Locally, at points with the most intensive [illegible]al of sulphur, free copper is formed near the pores. [illegible]oss in weight here amounts to 5-5.5%). Above 800°C [illegible]ferential removal of sulphur along the intergranular [illegible]ries of mohawkite lead to enrichment of these sections with copper to form bornite. The mohawkite, being depleted in copper and sulphur, changes its structure and is converted into a phase analogous with natural heikokite (36.4 wt.% Fe, 30.0 wt.% Cu, 32.6 wt.% S). In the mass of this mineral the amount of bornite with the following composition (wt.%) increases with increase in the heating temperature to 870-930°C: 16.3 Fe; 56.4 Cu; 27.3 S. This leads to the separation of a certain amount of pyrrhotite from the heikokite mass. At 1 000°C the stable minerals are heikokite, bornite, troilite and metallic copper. The metallization process is considerably intensified. As at low temperatures, only the copper is metallized.

Thus, the process of the removal of sulphur from the samples takes place extremely slowly on heating in argon. Only at high temperatures (>700°C) are the bonds in the structure of the sulphides weakened so much that the sulphur atoms [illegible] are removed and pass into the gas phase in the form of elemental sulphur. The phase transformations here are therefore hindered, and the structural and magnetic transformations are characteristic.

References

1) H Haraldsen: Anorg. Allgem. Chem. 1937, 231.
2) N V Belov: Mineralogicheskii Sbornik L'vovskogo Gos. Un-ta 1974, 28, (3).
3) I E Hiller and K Probstain: Z. Kirst. 1956, 108, (1&2).

UDC 661.183.12:546.161

Sorption of the ions of elements in group 2 of the periodic system from solutions of ammonium fluoride with granulated iron hydroxide

V S Pakholkov and V F Markov (Urals Polytechnical Institute - Department of the Metallurgy of Rare Metals)

Summary

The sorption of Be^{2+}, Cu^{2+}, Zn^{2+}, Cd^{2+}, Mn^{2+}, Co^{2+} and Ni^{2+} from solutions of their fluorides containing ammonium fluoride under dynamic conditions by iron hydroxide which had been granulated by freezing was investigated. It was shown that the cations are arranged in the following order of decreasing sorbability: $Cu^{2+} > Zn^{2+} > Cd^{2+} > Co^{2+} \geq Ni^{2+} > Mn^{2+}$. This is consistent with the order of decrease in the pK values for the instability of the hydroxy complexes $Me(OH)^{+}$.

The sorption of beryllium is determined by the concentration of the complex anions and by the concurrent sorption of fluoride ions. The sorbability decreases with increase in the ammonium fluoride content of the solution and becomes practically zero at a concentration of 0.5 mole/l. The possibility of using the differences in the behaviour of the elements during sorption and desorption to purify solutions of BeF_2 and $(NH_4)_2BeF_4$ from impurities and to separate the pairs of elements by means of granulated iron hydroxide was established and confirmed.

UDC 669.2

Relationships governing the dissolution of the metals of the anode slime during electrolytic refining

A D Pogorelyi and L I Reznichenko (North-Caucasian Mining-Metallurgical Institute - Department of General Metallurgy)

During the electrolytic refining of a metal with a large amount of electropositive impurities a porous layer of anode slime, consisting mainly of undissolved metals, remains on the surface of the dissolving anode. In the course of time, as the crust of the anode slime becomes thicker, difficulties arise in the production of a cathode deposit of the required standard on account of the progressive contamination of the cathode metal by the electropositive impurities which accumulate in the slime. The contamination is due not to mechanical dispersion of the slime in the electrolyte and transfer of its particles to the cathode but by electrochemical dissolution of the metals of the anode slime during the electrolysis process.

Experience in the electrolysis of alloys of lead with bismuth or antimony [1]) shows that there is a clearly defined correlation between the thickness of the crust and the purity of the cathodic lead in respect of the impurity which accumulates in the slime.

There is an even closer correlation between the purity of the cathode metal and the potential difference in the layer of the anode slime. This potential drop, which depends on the density of the electrolysis current, the time of electrolysis, and other secondary factors, can be considered to be the main reason for the progressive contamination of the cathode deposit.

During the anodic dissolution of a two-phase alloys both metals pass into solution in ratios corresponding to their positions in the potential series and to identical potential differences in the metal-solution system. The concentrations (or activities) of the ions can be calculated by means of the Nernst equation:

$$\lg\left[Me_2^{n_2+}\right] = \left\{\epsilon_1^{\circ} - \epsilon_2^{\circ} + \frac{RT}{n_1 F} \lg\left[Me_1^{n_1+}\right]\right\}\frac{n_2 F}{RT} \qquad (1)$$

where:
$\left[Me_2^{n_2+}\right]$ and n_2 = the concentrations of the ions and the valence of the electropositive impurity, and
$\left[Me_1^{n_1+}\right]$ and n_1 = the characteristics of the metal being refined.

As electrolysis proceeds the electropositive phase is retarded with dissolution, and its inclusions project above the surface of the dissolving main phase, forming a porous layer of slime, which becomes thicker with time (fig. 1). The spaces between the slime crystals are filled with elec-

Caking was observed in the region of temperatures corresponding to intense contraction. Thus, at 1050°C during roasting of the Bakyrchik calcine a small amount of soft lumps was formed, which were easily broken. Harder lumps were formed in a considerable amount (70-80% of the total volume) at 1100°C. During the roasting of the Zodskii calcine the calcine remained unchanged in granulometric composition right up to 1150°C. By comparison of the results from these observations with the temperatures corresponding to the beginning of shrinkage of the specimens it can be concluded that the liquid phase appears at temperatures above the temperature corresponding to the beginning of contraction.

The temperatures corresponding to intense contaction and softening are close. Consequently, intense contraction is due not only to removal of the sublimed components of the calcine but also to the appearance of a liquid phase. The highest temperature corresponding to intense contraction was given by the Zodskii calcine, which had a low content of alkali metals (table 3). Alkali metals probably take part in the formation of the liquid phases. In fact, during the roasting of the Zodskii calcine with additions of Na_2CO_3 and K_2CO_3 at the rate of 5% the formation of lumps was observed at 1050°C and caking was observed at 1100°C. The beginning of caking was observed · 25-30 min. Further evidence for the involvement of i metals in the appearance of the liquid phases was pro- l by some decrease in the temperature corresponding : beginning of intense contraction in the case of the ing of the calcine in the presence of NaCl and $CaCl_2$ at the rate of 5% for the Bakyrshik and 10% for the tasskii, Itakinskii, and Zodskii calcines (table 2).

ture corresponding to intense contraction of the pyramids and by the presence of alkali metals.

In spite of the smaller content of alkali metals compared with the Bakyrchik calcine, the Kokpatasskii calcine had the lowest temperature for the beginning of intense contraction, However, it was characterised by a relatively high high content of calcium oxide, on account of which (as established by crystal-optical investigation) eutectics with the following composition are formed %: 63 $Na_2O \cdot Fe_2O_3$ and 37 $2CaO \cdot SiO_2$. They melt at 1110 ± 10°C, close to the temperature corresponding to intense contraction of the Kokpatasskii calcine. The eutectic also contained Na_2O in its composition.

Thus, to eliminate or reduce caking it is necessary as far as possible to reduce the amount of added NaCl. The appearance of liquid phases became stronger with the presence of carbon in the charge. This led to reduction of Fe^{3+} to Fe^{2+} and the formation of various types of silicates. The formation of the silicate form of iron in the presence of carbon was established by chemical phases analysis. In individual samples the iron silicate content amounted to 10%. Iron-calcium and iron-aluminocalcium silicates melting at 1030-1050°C could probably form. To avoid the formation of iron silicates it is necessary to realise the chloride sublimation process from the calcine with the minimum possible content of FeO and in the absence of reducing agents in the charge.

Thus, the main reason for the appearance of liquid phases

Table 3: Chemical composition of the calcines (%)

Calcine	Fe	SiO_2	Al_2O_3	CaO	MgO	Na_2O	K_2O	S_{euc}	S_{SO_4}	As	Cu	Zn	Pb	C	Au g/t
Bakyrchik	19.8	45.1	13.8	1.8	1.0	1.75	2.6	0.9	0.9	0.65	0.32	0.4	0.03	1.0	105
Zodskii	34.5	23.7		1.76	12.6	0.01		2.33	2.3	0.9	0.3	1.1	0.08	-	60.5
Kokpatasskii	34.5	20.8	7.55	3.2		0.61	2.0	0.7	0.65	0.35	0.06	0.2	0.009	0.8	42
Itakinskii	16.3	61.0	4.9	2.3	1.5	0.5	0.16	1.27	1.2	0.9	0.02	0.009	0.02	0.8	49.2

The presence of alkali metals in the composition of the calcines and charges led to the formation of fusible compounds of the ferrite and silicate type. During the crystal-optical investigation the presence of a glassy phase with a variable refractive index of 1.520-1.540 was observed in individual samples. The colour of the glass was olive-green. Inclusions of a ferrite phase and a nontransparent black mass were detected (sometimes in considerable amounts). According to crystal-optical analysis the appearance of the liquid phases for the Bakyrshik and Itakinskii calcines is due to the formation of a eutectic with the composition %: 36 $Na_2O \cdot Fe_2O_3$ and 64 Fe_2O_3 melting at 1135°C. The formation of the eutectic with this composition was confirmed by the tempera-

and caking in the chloride sublimation of gold-containing products is the presence of alkali-metal and alkaline-earth metal compounds and ferrous oxide in the charge. Consequently, to eliminate or reduce caking it is necessary to undertake a preliminary oxidising roasting process calculated for almost complete oxidation of iron to the trivalent state and for the removal of carbon present in the calcine and also to realise the chloride sublimation process with the minimum possible addition of the chlorinating reagents NaCl and $CaCl_2$.

The undesirable effect of caking is reduced in the treatment of charges prepared in the treatment of charges prepared in the form of granules.

UDC 661.877:66.061.5+541.9

Separation of molybdenum and iron by extraction with tri-*n*-butyl phosphate

A M Zelikman, V S Kagerman'yan, T Segarchanu, G M Vol'dman and F Oprya (Moscow Institute of Steel and Alloys. Department of Rare and Radio-active metals and powder metallurgy)

In the treatment of molybdenite concentrates and of intermediate products with the use of nitric acid decomposition and also in schemes for the regeneration of molybdenum from various production wates (e.g. spent catalysts in petrochemical production, waste materials from the electronics and electrotechnical industry etc) acidic solutions containing a considerable amount of iron impurity (5-20g/l) in addition to molybdenum are obtained. At the present time there is no satisfactory method for the purification of the solutions from iron or for the selective extraction of molybdenum from such solutions.

The present article gives results on the separation of molybdenum and iron by extraction with tri-*n*-butyl phosphate (TBP), obtained jointly by Soviet and Rumanian investigators.

The extraction was realised in 100ml separating funnels with equal volumes of aqueous and organic phases and 20ml of each phase. Tributyl phosphate of chemically pure grade, iron nitrate and sulphate of analytical grade, and hydrogen peroxide, nitric acid and sulphuric acid of chemical purity were used in the work.

The initial solutions were prepared by dissolving the salts in distilled water. The acid was then added to the required

pH value, and in the case of extraction from a peroxide medium hydrogen peroxide was added to the molybdenum-containing solution at the rate of two moles for 1g-atom of molybdenum, after which the solutions of molybdenum and iron were mixed. The molybdenum content in the initial aqueous solution amounted to about 10 and the iron content to about 2-3g/l.

After extraction the molybdenum and iron were determined by a photocolorimetric method, and the concentration of molybdenum and iron in the extract was then obtained from the difference between the initial content of the metals and the content in the refined product. In a number of cases a control determination of iron in the extract after re-extraction with 10% sodium hydroxide solution was undertaken.

Separation of molybdenum and iron by extraction from sulphate solution. Molybdenum is extracted satisfactorily from weakly acidic solutions containing several grams of molybdenum per litre[1-3]. With variation in the pH value from 6 to 0.5 the distribution coefficient D_{Mo} increases from 0.2 to 10. Best results on extraction are observed in the pH range of 1.5-2, where D_{Mo} reaches values from 2-3 to 10 (according to data from various authors).

It was determined experimentally (fig. 1, curve 1) that the curve for the extraction of molybdenum has a maximum at pH = 1.5, at which $D_{Mo} \approx 10$. With decrease in the pH value from 1.5 to ~0.5 (~5N H_2SO_4) D_{Mo} decreases regularly to 0.06. Tests on sulphate solutions containing molybdenum and iron together in order to determine their stability region show that they do not decompose to form ferrio-molybdates only at pH ≤ 0.65. Therefore, the extraction separation of molybdenum and iron was investigated in the region of acidity in H_2SO_4 from pH = 0.65 to pH = ~0.5 (~5N H_2SO_4). With increase in the acidity of the solution the extractability decreases continuously from D_{Mo} = 2.8 at pH = 0.65 to 0.06 at pH = ~0.5 (fig. 2).

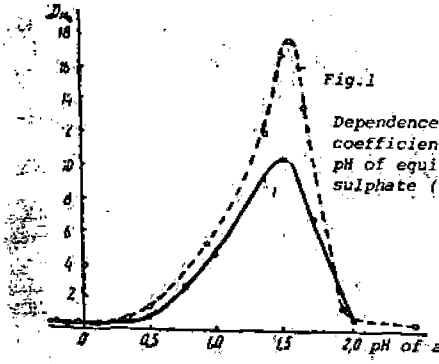

Fig.1

Dependence of the distribution coefficient of molybdenum on the pH of equilibrium solutions of sulphate (1) and nitrate (2).

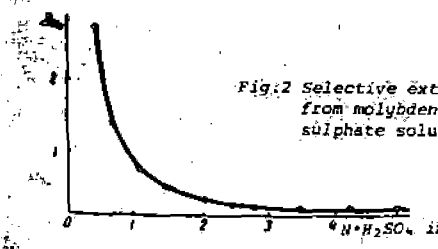

Fig.2 Selective extraction of molybdenum from molybdenum-iron-containing sulphate solution.

Iron is hardly extracted at all by TBP under these conditions ($D_{Fe} \approx 0.001$). Consequently, the selective extraction of molybdenum for separation from iron must be carried out at pH = 0.6-0.7.

For molybdenum concentrations of 0.2-10g/l at pH = 0.65 the extraction isotherm is linear (fig. 3), and under these conditions D_{Mo} retains a constant value. Iron does not have an effect on the extraction of molybdenum even with small concentrations of the latter in the solution, and the molybdenum and iron are clearly not chemically combined under the investigated conditions. The nature of the isotherm makes it possible to conclude that it is possible to separate molybdenum completely from iron with the use of several steps of continuous counterflow extraction. According to graphical calculation, five to six theoretical steps of the continuous counterflow process are required to obtain a refined product containing less than 0.1g/l of molybdenum.

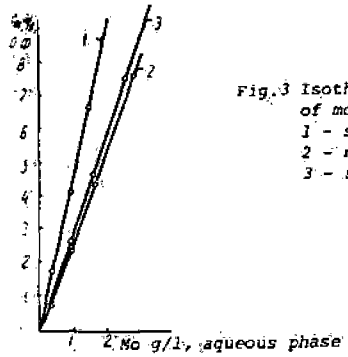

Fig.3 Isotherm for extraction of molybdenum by TBP:
1 - sulphate peroxide;
2 - nitrate peroxide;
3 - sulphate solution.

We also studied the extraction of molybdenum from nitrate solutions (fig. 1, curve 2). The results show that molybdenum and iron can be successfully separated at pH = 1-1.6, and here D_{Mo} is fairly high and iron is hardly extracted at all by TBP. However, the tests revealed that solutions simultaneously containing 10g/l of molybdenum and 3g/l of iron are unstable with the above-mentioned acidity. When present together the metals only remain in solution at pH < 0.1, where D_{Mo} amounts to 0.1-0.15. It is therefore impossible to separate the metals by extraction from a nitrate medium.

Separation of molybdenum and iron by extraction from peroxide solutions. According to available published data, in weakly acidic solutions in the presence of hydrogen peroxide molybdenum forms complex anions MoO_8^{4-} and $HMo_2O_8^{-}$ [6-8]) or a binuclear diperoxy anion $Mo_2O_{11}^{2-}$ and the respective acids[15-18]). More recent investigations, in which both solid peroxy molybdates[12]) and the state of molybdenum in a weakly acidic peroxide solution and organic derivatives of peroxy molybdates[6]) were studied, showed that the binuclear form $Mo_2O_{11}(H_2O)_2^{2-}$ predominates.

Iron does not form peroxy compounds in solution. As we established, the addition of hydrogen peroxide at the rate of 2 moles for 1g-atom of molybdenum in mixed solutions of molybdenum and iron eliminates the separation of ferrio-molybdate in a nitric acid medium even at pH = 0.4-0.5, whereas in solutions containing hydrogen peroxide precipitates separate at pH = 0.2. In sulphuric acid solutions hydrogen peroxide stabilises the metals in the solution even at pH = 1.

Fig. 4 shows the results from extraction of molybdenum from mixed molybdenum-iron-containing solutions in the presence of hydrogen peroxide. The curve for the dependence of D_{Mo} on pH for the nitric acid solution (fig. 4, curve 2) has a wide maximum, after which the distribution coefficient decreases to D_{Mo} = 0.05. Over the whole range of acidity the iron is hardly extracted at all. The iron content of the organic phase does not exceed 10^{-3}-10^{-4} g/l. Thus, the optimum conditions for selective extraction of molybdenum and its separation from iron from nitric acid solutions are created with an equilibrium pH value of 0.4-0.5 in the refined product.

In the case of a sulphuric acid medium (fig. 4, curve 1) D_{Mo} increases continuously with increase in the activity of hydrogen ions in the solution and at pH 0.42 it amounts to 4.25 (ε_{Mo} = 80%). It is clear that for effective separation of the metals by extraction from sulphuric acid media it is expedient to realise the process with a sulphuric acid content of 3-4N in the solution.

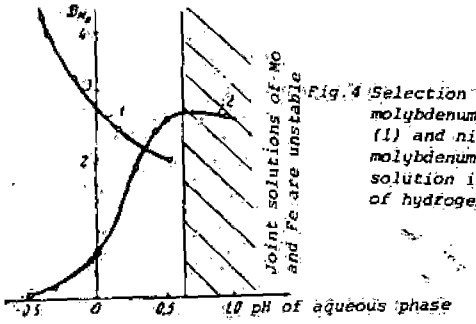

Fig. 4 Selection extraction of molybdenum from sulphate (1) and nitrate (2) molybdenum-iron-containing solution in the presence of hydrogen peroxide.

Since technological solutions can contain a mixture of sulphuric and nitric acids (e.g. after nitric acid decomposition of concentrates or solutions in the electrotechnical industry), the effect of additions of 0.1-0.5N of nitric acid to sulphuric acid peroxide solutions on the extraction of molybdenum and iron was investigated. The sulphuric acid concentration in the solution amounted to 2.816N, and the molybdenum content was 10g/l, and the iron content was 3g/l. Increase in the amount of nitric acid in the sulphuric acid solution from 0.1-0.15 to 0.5N (fig. 5) reduces D_{Mo} from 2.94 (ε_{Mo} = 77.4%) to 2.19 (ε_{Mo} = 67.6%). In the absence of nitric acid during extraction from 2.816N sulphuric acid D_{Mo} = 3.6 (ε_{Mo} = 78.5%).

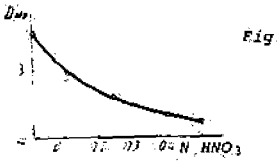

Fig. 5 Selective extraction of molybdenum from nitric acid molybdenum-iron-containing solutions in the presence of hydrogen peroxide.

Consequently, satisfactory separation of molybdenum from iron in mixtures of the two acids is possible with a nitric acid content not higher than 0.25N and a nitric acid content of less than 0.1N does not essentially reduce the effectiveness of the extraction separation of the metals.

Isotherms for the extraction of molybdenum in the presence of iron from a peroxide solution of nitric acid with pH = +0.5 (fig. 3) and a peroxide solution of sulphuric acid (0.3N) were constructed. The concentration of molybdenum in the initial aqueous phase amounted to 0.2-10g/l. The relationships plotted for the conditions of selective extraction of molybdenum retain linear character.

In the case of the mixture of acids the character of the isotherms and the graphical calculations reveal the possibility of highly selective extraction of molybdenum by TBP if 5-6 theoretical steps of extraction in a continuous counterflow process are used. The molybdenum content in the refined product resulting from this process did not exceed 0.1g/l with a molybdenum extraction of 99%.

Re-extraction of molybdenum by solutions of ammonia. The re-extraction of molybdenum from the organic phase can be suitably and conveniently carried out with solutions of ammonia to produce ammonium paramolybdate as the final product.

Re-extraction was carried out with 10% NH_4OH solutions with the addition of 5% NH_4NO_3 or $(NH_4)_2SO_4$ for better separation of the phases (aqueous:organic = 1:5). The investigations showed that the re-extraction of molybdenum can be brought to complete extraction into the re-extract. By graphical calculation, realised for the above-mentioned conditions, with a molybdenum content of 10-11g/l in the organic phase it was established that practically all the molybdenum (99.8%) passes into the re-extract in a continuous counterflow regime after 4-5 theoretical re-extraction steps.

Conclusions

1. The extraction of molybdenum and iron from sulphuric and nitric acid solutions by TBP was investigated. It was established that molybdenum is extracted from weakly acidic solutions of both acids with high distribution coefficients. Molybdenum is hardly extracted at all from concentrated solutions of nitric and sulphuric acids.
2. The conditions were determined for the effective separation of molybdenum and iron from weak solutions of sulphuric acid. The optimum pH value for selective extraction of molybdenum by TBP amounts to 0.65-0.75.
3. The relationships for the extraction separation of molybdenum from iron in solutions of sulphuric and nitric acid in the presence of hydrogen peroxide were investigated. It was shown to be possible to separate molybdenum and iron effectively by extraction from nitric acid solutions at pH = 0.5 and from sulphuric acid solutions with concentrations of 3-4N and also from mixtures of these acids.
4. It was shown that molybdenum is fully re-extracted from the organic phase by a solution of 10% NH_4OH +5% NH_4NO_3.

References

1) A N Zelikman: Izv VUZ Tsvetnaya Metallurgiya 1968, (3), 85.
2) K H Arend et alia: Z. Anorg. und Allgem. Chem. 1964, 18, 333.
3) N Iordnov et alia: Dokl. Akad. Nauk. Bolg. 19, (10), 913.
4) Yu B Gerlit: Second Geneva Conference - Reports of Societ scientists: Vol. 4, Atomizdat 1959, p. 181.
5) K F Iahr et alia: Ber. 1938, 71, 894, 903, 1123, Ber. Freund. Techn. Hochschule, Berlin 1939, 91, K F Iahr: Angew. Chemie 1940, 53, 20.
6) L I Csanyi: Acta Chim. Acad. Scient. Hung. 1958, 14, 69.
7) W J Fergusson: Chem. Soc. 1962, 2136.
8) R G Beiles et alia: Zh. Neorgan. Khim. 1965, (10), 1618.
9) A N Zelikman et alia: Zh. Neorgan. Khim. 1972, (1), 178.
10) G Tridot: Ann. Chimie. 1955, (10), 255.
11) E Richardson: Less common metals: 1960, (2), 360.
12) P Souchay et alia: Bull. Soc. Chim. France 1955, 1519.
13) K F Iahr et alia: Z. Anorgan. Chem. 1953, (272), 45.
14) W P Griffit: J. Chem. Soc. 1963, 5345.
15) W P Griffit: J. Chem. Soc. 1964, 5248.
16) R Stromberg: Acta Chem. Scand. 1968, (4), 22.
17) R Stromberg et alia: Acta Chem. Scand. 1969, (1), 23.
18) A I Lizogor et alia: Ukr. Khim. Zh. 1965, (9), 31, 895.
19) E Wendling: Bull. Soc. Chim. France 1965, (2).
20) A Kiss: Magyar rem. folyoirat 1963, 69, (12), 524.

UDC 669.881

Effect of intermediate products on the kinetics of the chlorination of vanadium oxides in molten salts

S A Kutsenko, S A Amirova and N N Chizhov (Perm Polytechnical Institute. Department of the Technology of Inorganic Materials).

Summary

The rule of the molten medium in the liquid-phase chlorination is so varied that there is no common opinion about the mechanism of the chlorination of oxide raw material. The predominating factors are the solubility of chlorine, the solubility of the oxides, the catalysing effect of chlorides with variable valence, carbon-chlorine radicals formed during chlorination of the carbon, and a series of other factors such as viscosity and surface tension.

The results are given from investigations into the effect of additions of potassium tetrachloro-oxovanadate (IV) on the yield of $VOCl_3$ during the chlorination of vanadium pent-

Economic Geology
Vol. 74, 1979, pp. 232–259

Sechura Phosphate Deposits, Their Stratigraphy, Origin, and Composition

T. M. CHENEY, G. H. MCCLELLAN, AND E. S. MONTGOMERY

Abstract

The phosphate deposits in the western Sechura Desert, Peru, occur as pelletal phosphate in marine sediments of Miocene age. Most of the pellets are concentrated in beds 1 to 1.5 meters thick that contain about 20 percent P_2O_5. Interbedded with the phosphorites are diatomite beds 3 to 20 meters thick, that contain 1 to 7 percent P_2O_5. Combinations of these beds form three major phosphatic zones which, in ascending order, are about 38 meters thick with 5.2 percent P_2O_5, 6 meters thick with 9.0 percent P_2O_5, and 2.5 meters thick with 5.2 percent P_2O_5. Within these zones are combinations of beds that are relatively thick and of higher grade, such as the upper part of the lower zone which is about 10 meters thick and contains about 12 percent P_2O_5. The composition, general character, thickness, and P_2O_5 content of the individual phosphorite and diatomite beds are highly uniform over large areas. Sandstone and tuffs form a minor but characteristic part of this sequence.

Ore from the individual beds and zones is easily upgraded by washing and desliming because of the marked differences between the diatomite particles and the phosphate pellets in size, shape, and density.

Low-amplitude folds and possibly minor faults that developed during deposition play an important role in the distribution of beds within the phosphatic sequence which range from 135 to 215 meters thick.

The Sechura deposits are different from other major marine deposits in that they consist chiefly of phosphate and diatomite and the pellets are composed of a fluorine-deficient carbonate hydroxyl apatite of a type not known in other marine deposits. The apatite, however, is somewhat similar in composition to that in Holocene diatomaceous ooze on the sea floor off the coasts of Chile and Peru.

Introduction

THE Sechura phosphate deposits occur in marine sediments of middle Miocene age (MacDonald, 1956) and are made up of pelletal phosphate interbedded primarily with diatomite but also with some sand and tuff beds. They are located in the western half of the Sechura Desert along the northern coast of Peru, 800 kilometers north of Lima (Fig. 1). The Sechura Desert is an area of about 22,000 square kilometers and is, for the most part, a featureless plain sloping gently from the foothills of the Andes to the Pacific Ocean, abruptly interrupted on the west by features of the Illescas Peninsula (Fig. 2).

The Illescas Mountains are the westernmost and most prominent feature of the peninsula. They trend slightly west of north and rise to a height of 480 meters (Fig. 2). Other prominent features are the Virrila Estuary, the Tablazo, and the Sechura Depression. The Virrila Estuary is a shallow body of sea water and brackish water extending inland from Sechura Bay. The Tablazo is a large tableland; its north, east, and south sides drop off in cliffs, 15 to 75 meters in height. The Tablazo is separated from the Illescas Mountains by a low area no more than 60 meters in elevation and is divided into a northern and southern part by the Sechura Depression whose sides are marked by steep cliffs 30 to 45 meters high. The foot of these cliffs is about on sea level. The floor of the depression is flat and about 22.5 meters below sea level.

The phosphate deposits have been extensively explored by a program of field mapping, drilling, and trenching, and the results are summarized in geologic maps, correlation charts, and analytical and reserve data. This report presents results of the first year of this work, which was directed by T. M. Cheney, who was assisted by E. S. Montgomery, and of studies of phosphate mineralogy by G. H. McClellan and J. R. Lehr. Mr. Hugo B. Ramirez, civil engineer, surveyed the triangulation network and determined the elevations and coordinates of all the control points, drill holes, and trenches shown in Figure 3 and in the other diagrams and maps.

In the period September 1960 to August 1961, 168 holes were drilled to obtain a total of 5,125 meters of core, virtually all of which was recovered. Each lithologic unit of more than 0.3 meter usually was sampled separately; thinner units were sampled with thicker units, but they were described separately.

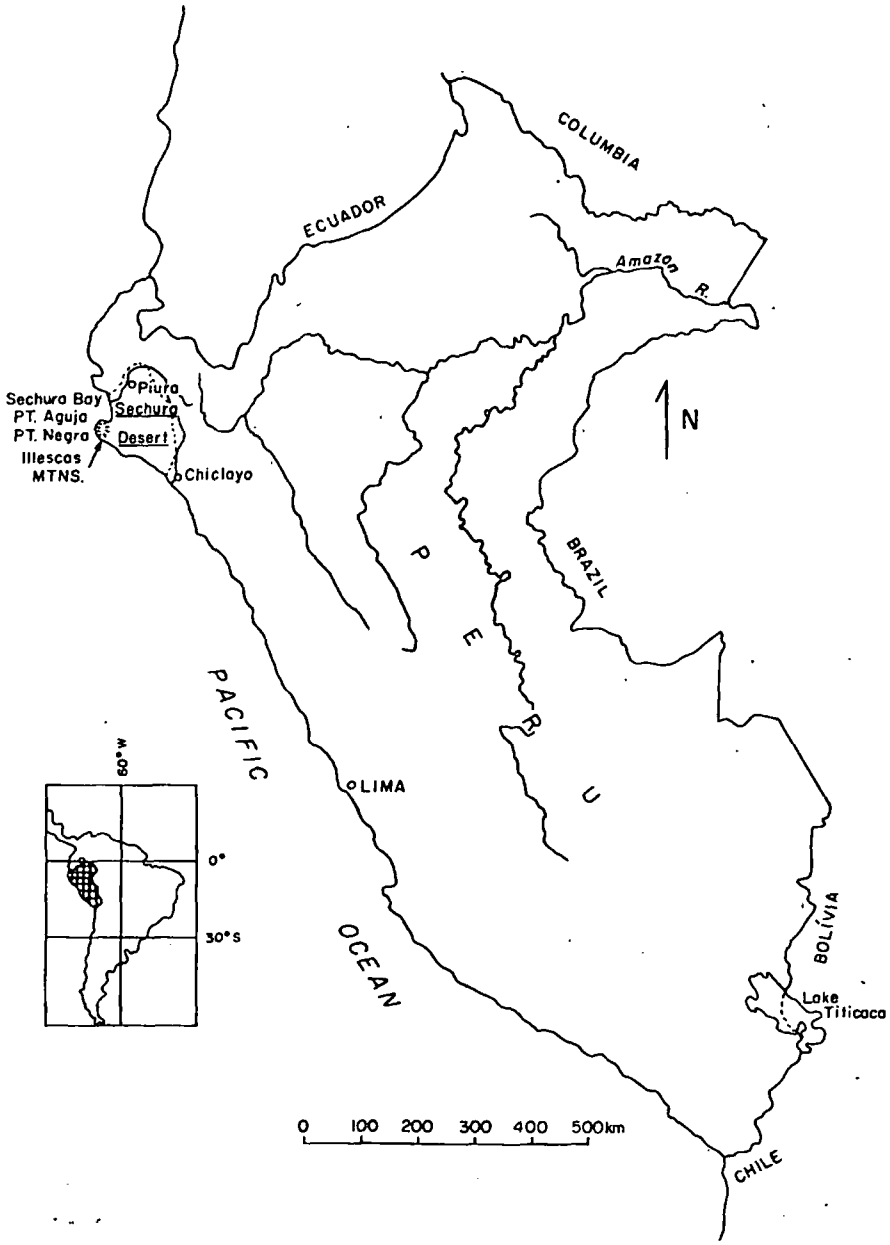

FIG. 1. Location of Sechura Desert phosphate area in Peru.

Most sample intervals were no more than 1.5 meters.

In addition to drill holes, 30 hand trenches and 20 bulldozer trenches were dug to obtain small samples for phosphorus determination and larger samples for metallurgical study. Some 3,200 samples were analyzed for phosphorus and a number of samples were analyzed for sodium, sulfur, calcium, magnesium, potassium, aluminum, iron, chlorine, fluorine, carbon dioxide, organic matter, and loss on ignition.

Geologic Setting

The western Sechura Desert is underlain by a thick series of marine sediments that range in age from Eocene through Pliocene and were deposited in a shallow north-trending basin between the Andes and the Illescas Mountains. They are overlain by alluvium and windblown sand of Recent age.

The general distribution and thickness of the Miocene strata that contain the phosphatic beds are shown in Figure 4. The deposits described in this report are in the upper 135 to 215 meters of the Miocene strata (Fig. 5). They are overlain unconformably by Pliocene strata and underlain by older Miocene strata.

Little deformation has occurred since the deposition of these strata. The beds dip so gently east-

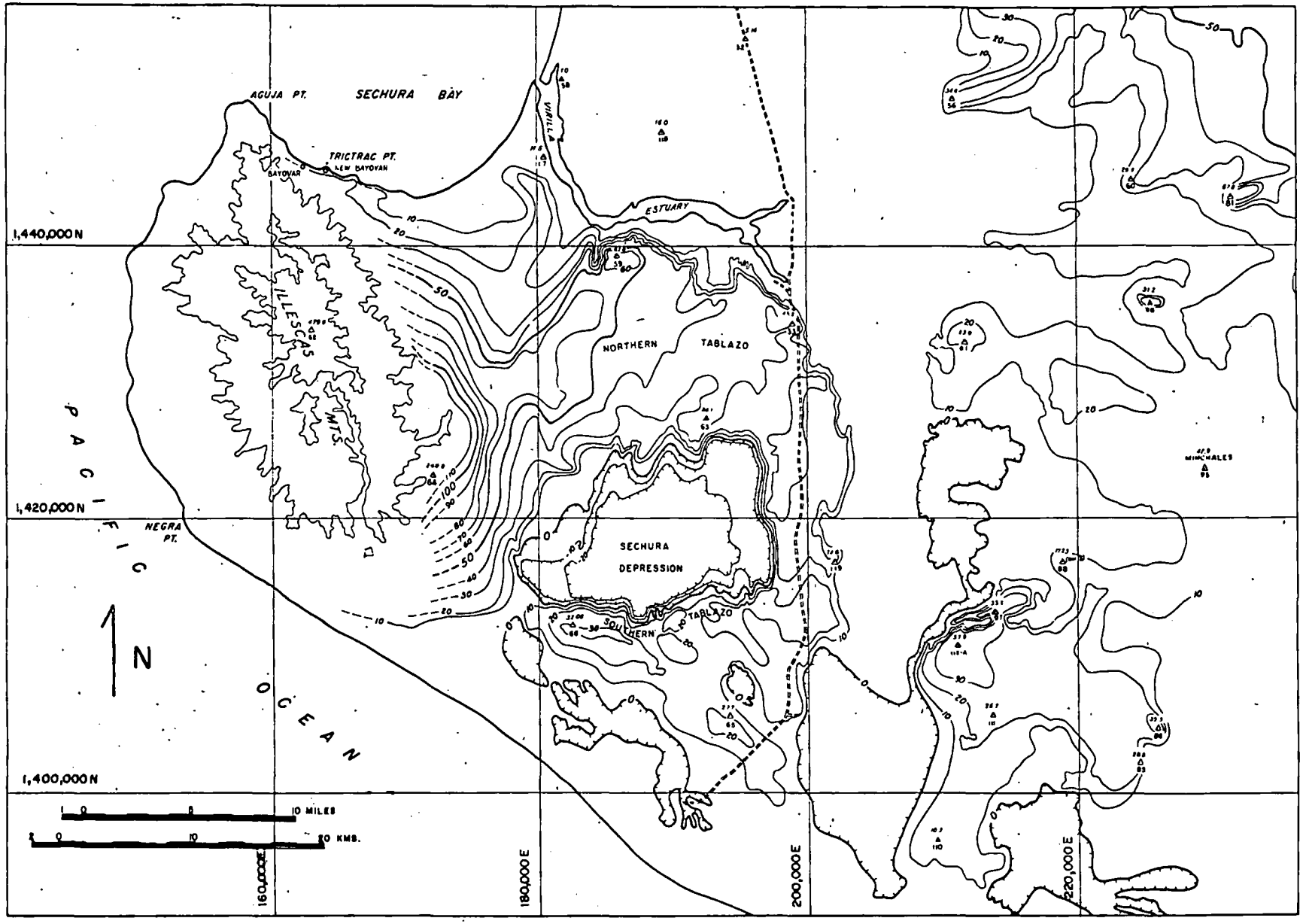

FIG. 2. General topographic relationships of the Sechura Desert, Peru; the form line interval is 10 meters.

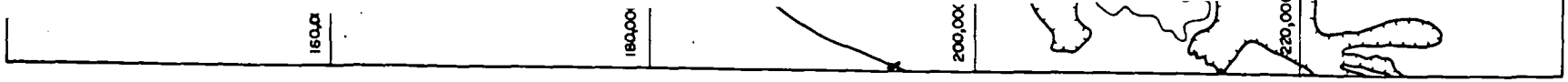

FIG. 2. General topographic relationships of the Sechura Desert, Peru; the form line interval is 10 meters.

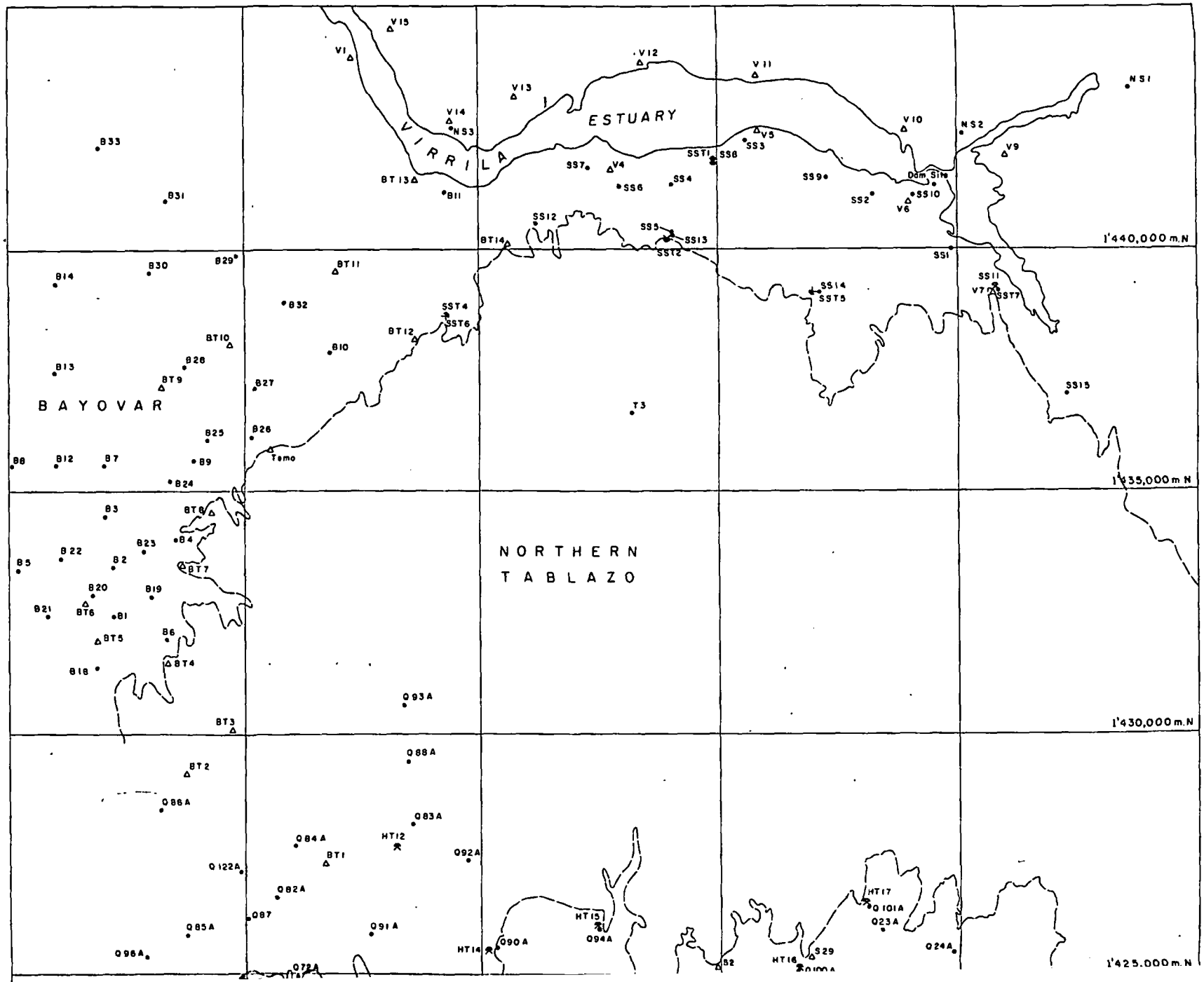

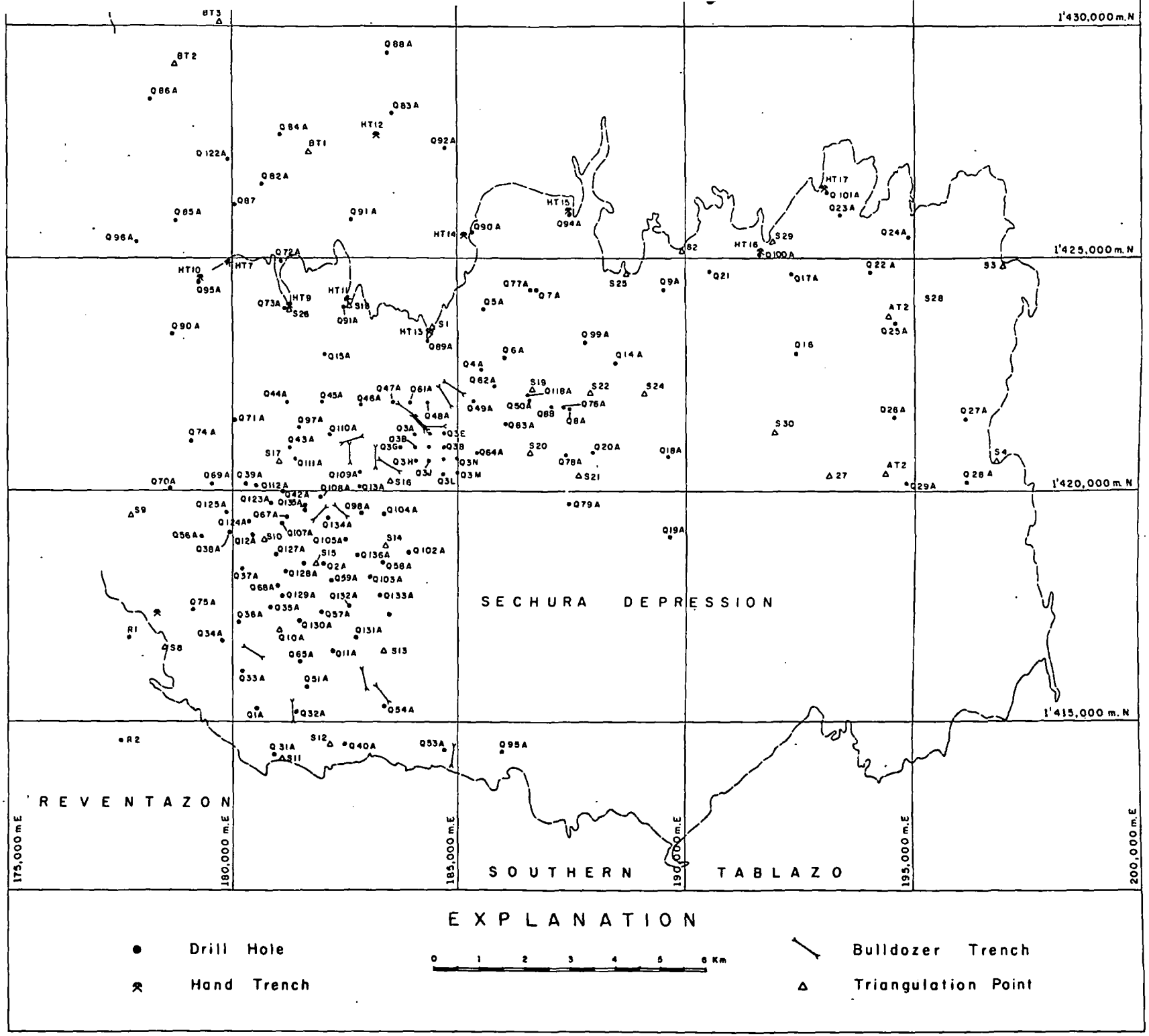

FIG. 3. Location of drill holes, trenches, and control points in western Sechura Desert phosphate area, Peru (1961).

ward that they appear to be horizontal. A few faults are present in the area of the phosphate deposits, but only three have displacements great enough to show on the geologic map (Fig. 6). and only one has a displacement as large as 30 meters. Two unconformities, one within the Miocene strata and one beneath the Pliocene, affect the present distribution of ore zones because parts of the strata had been removed prior to deposition of younger strata. In some places this condition facilitates recovery of phosphate, but in others it does not.

All the strata are very soft. They can be cut or carved easily with a knife, but they are competent enough to hold their shape. Many drill holes remained intact for at least 6 months.

Stratigraphy

Miocene phosphate-bearing strata

There are phosphate-bearing marine strata about 200 meters thick in the western Sechura Desert. These strata consist of a series of interbedded friable light brown to black phosphorite, soft white to black diatomite, and mixtures of the two; a few small beds of sandstone and gray tuff occur in small parts of the series. For general mapping purposes (Fig. 6) these strata were divided into four members, which are from top to bottom:

Barren Diatomite
Upper Diatomite and Phosphorite
Clam Bore Sandstone
Lower Diatomite and Phosphorite

Within these strata, three major phosphate zones have been identified: (1) the Diana phosphate zone in the Lower Diatomite and Phosphorite member, and the (2) Zero and (3) Minerva phosphate zones in the Upper Diatomite and Phosphorite member. The composite stratigraphic column (Fig. 5) shows the relationship between the mapped units and the phosphate zones. The figure includes data on the average thickness and grade of the main stratigraphic units.

Key beds and correlation

Individual beds of the Sechura phosphate deposits are laterally continuous over large areas and markedly regular in P_2O_5 content, thickness, and general character. Entire groups of beds exhibit these characteristics. This scientifically and economically important continuity and regularity is not unique to the Sechura deposits but is characteristic of many marine phosphorite deposits in other areas of the world. Because of this continuity, correlation of major stratigraphic units and individual beds was simple and accurate once the composite stratigraphic

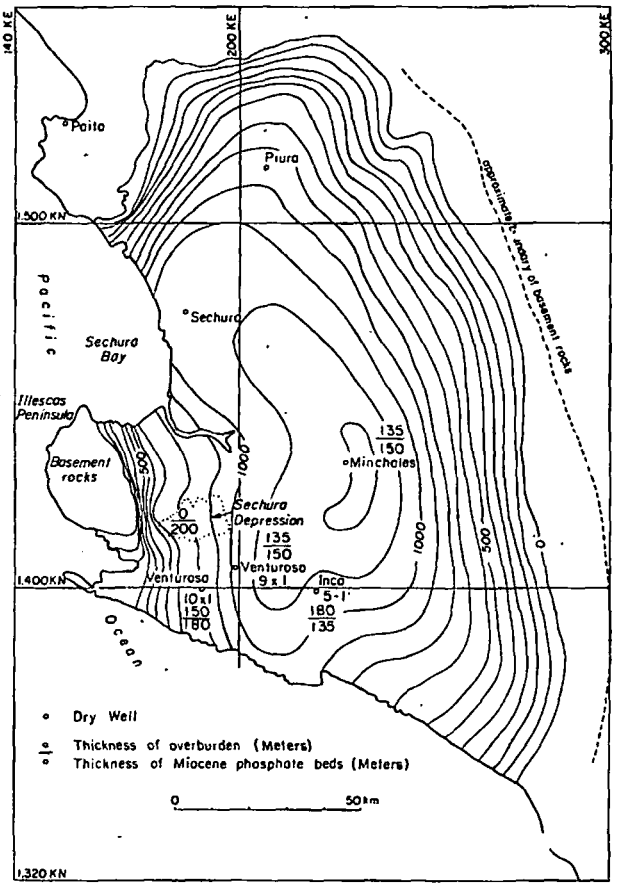

FIG. 4. Isopach map of Miocene beds, modified after McDonald (1956), showing the thickness of the phosphatic sequence.

sequence had been established. The sequence in this area was pieced together by correlating beds from one drill hole to another and by tracing beds and zones in outcrops over large areas. In several areas a drill hole was placed a few feet from the edge of the cliff so that the core and core logs could be compared with the strata exposed in the cliff and other drill hole logs.

The key beds used in the correlations are the phosphorite, sandstone, and tuff beds. The phosphorite beds differ from one another in phosphate content; in size, shape, and sorting of the grains; and in type and amount of impurities. The unique Clam Bore Sandstone is a key bed. The tuff beds are easily recognizable by their distinctive color and composition. Many of the key beds can be identified singly in the core and outcrops, but where this is not possible a sequence of three or more of the beds is sufficient to establish their stratigraphic position.

The correlations shown on Figures 7 through 11, in which each phosphate bed is designated by number, do not illustrate all the characteristics used in the correlation, but the bar graphs of P_2O_5 content

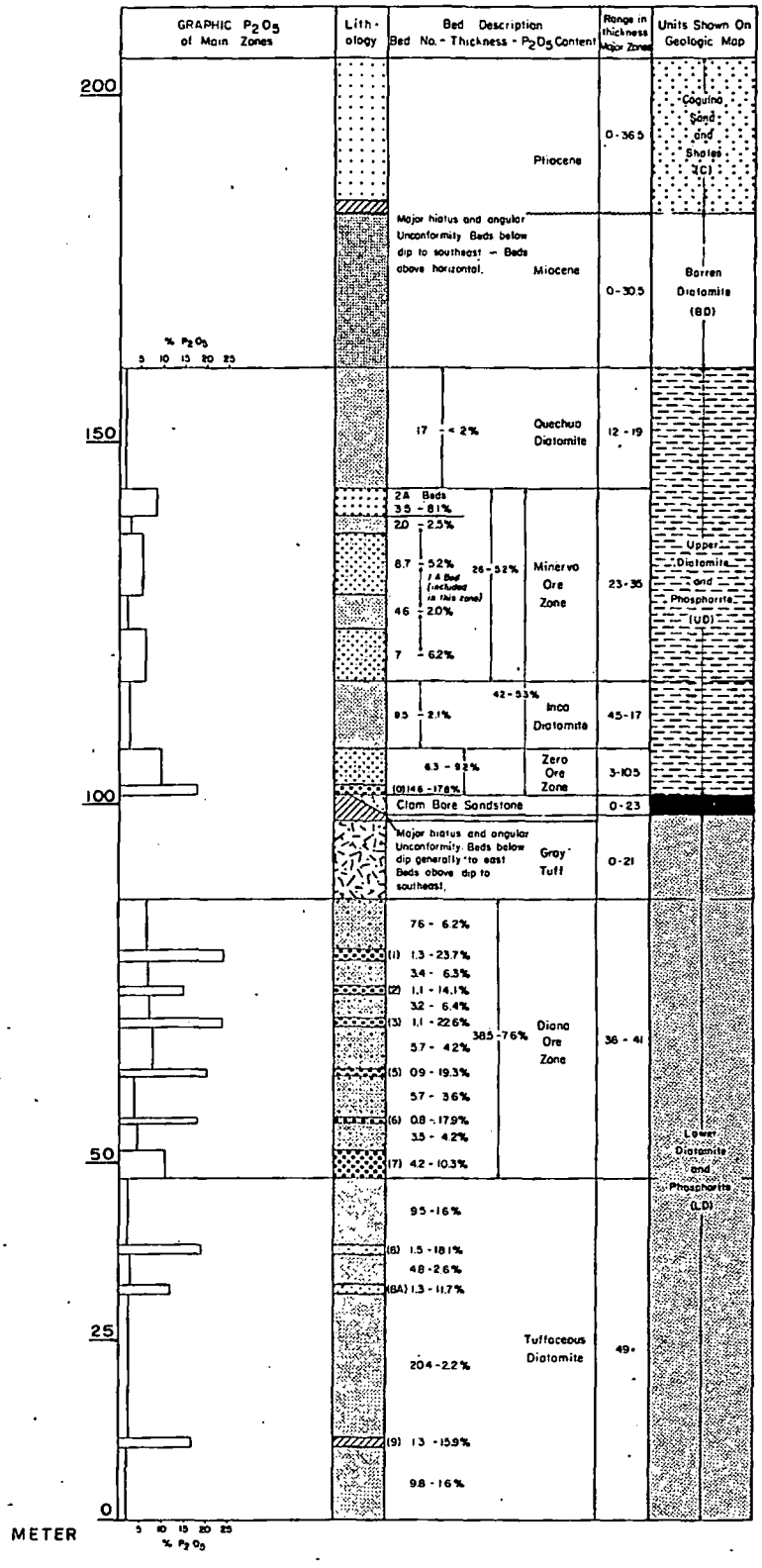

FIG. 5. Composite stratigraphic section, western Sechura Desert, Peru. All thickness and P_2O_5 values are an average for each unit (September 1961).

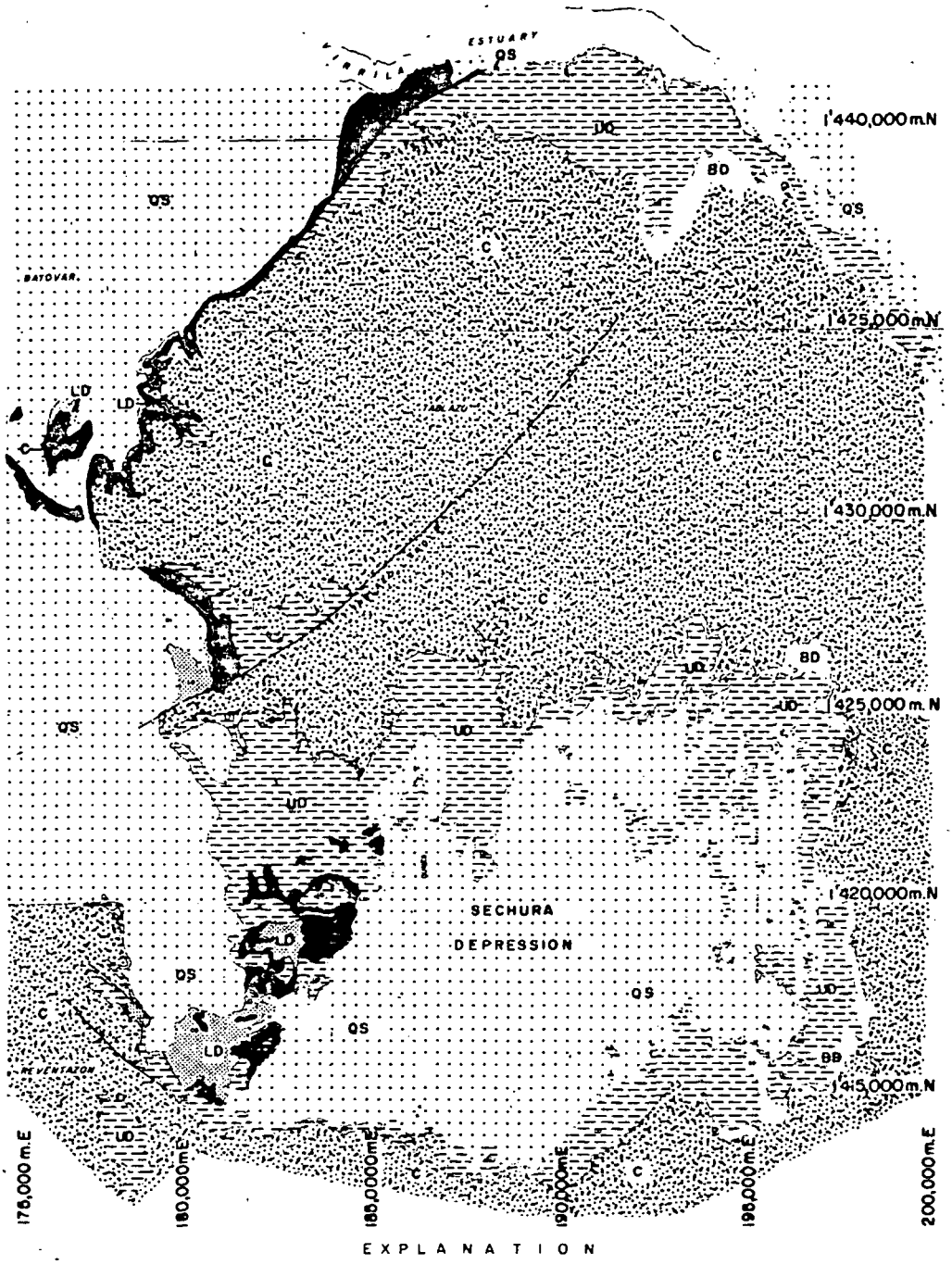

FIG. 6. Geologic map, western Sechura Desert, Peru (1961).

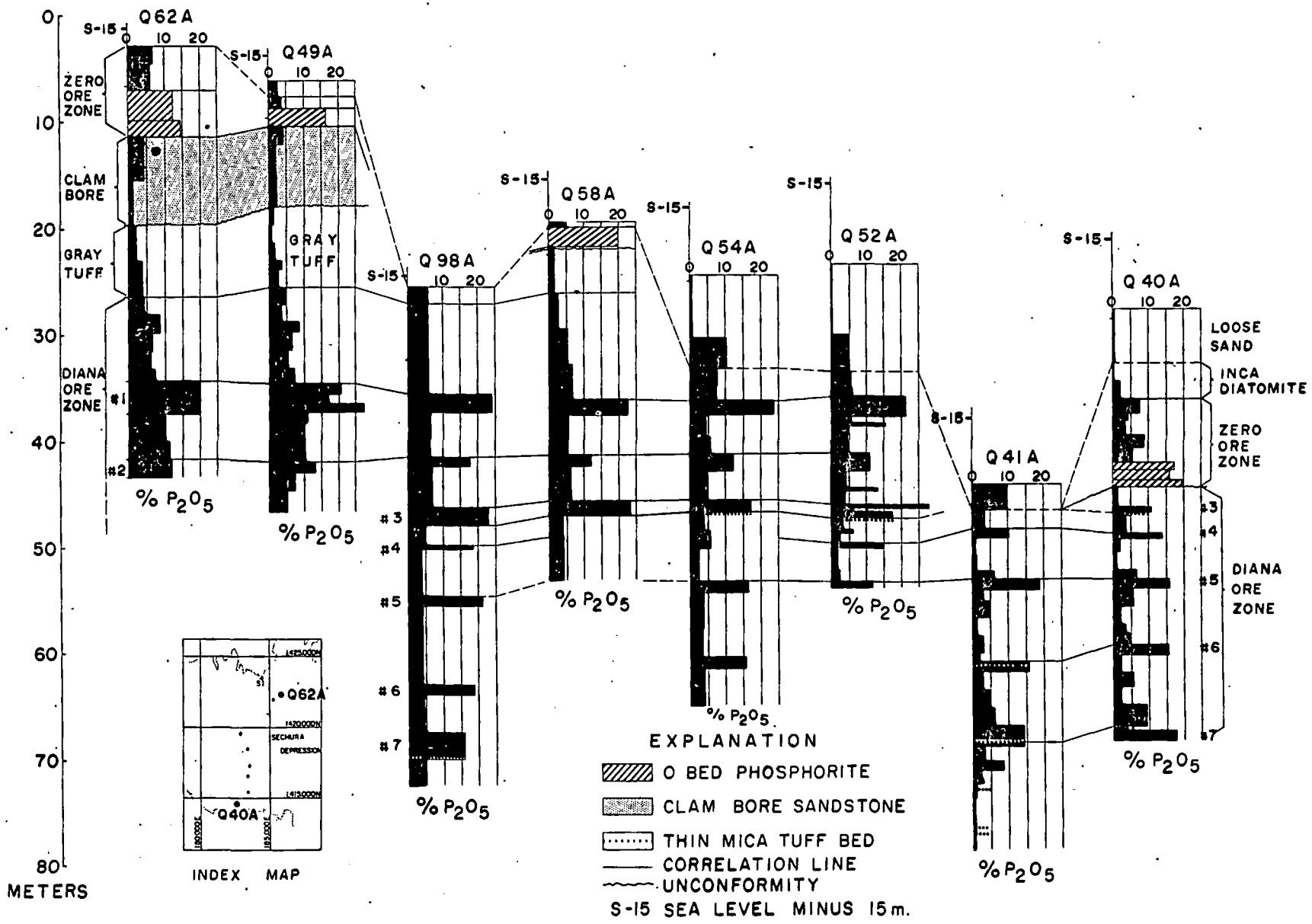

FIG. 7. Northeast-southwest correlation chart from drill holes Q-62A to Q-40A.

FIG. 7. Northeast-southwest correlation chart from drill holes Q-62A to Q-40A.

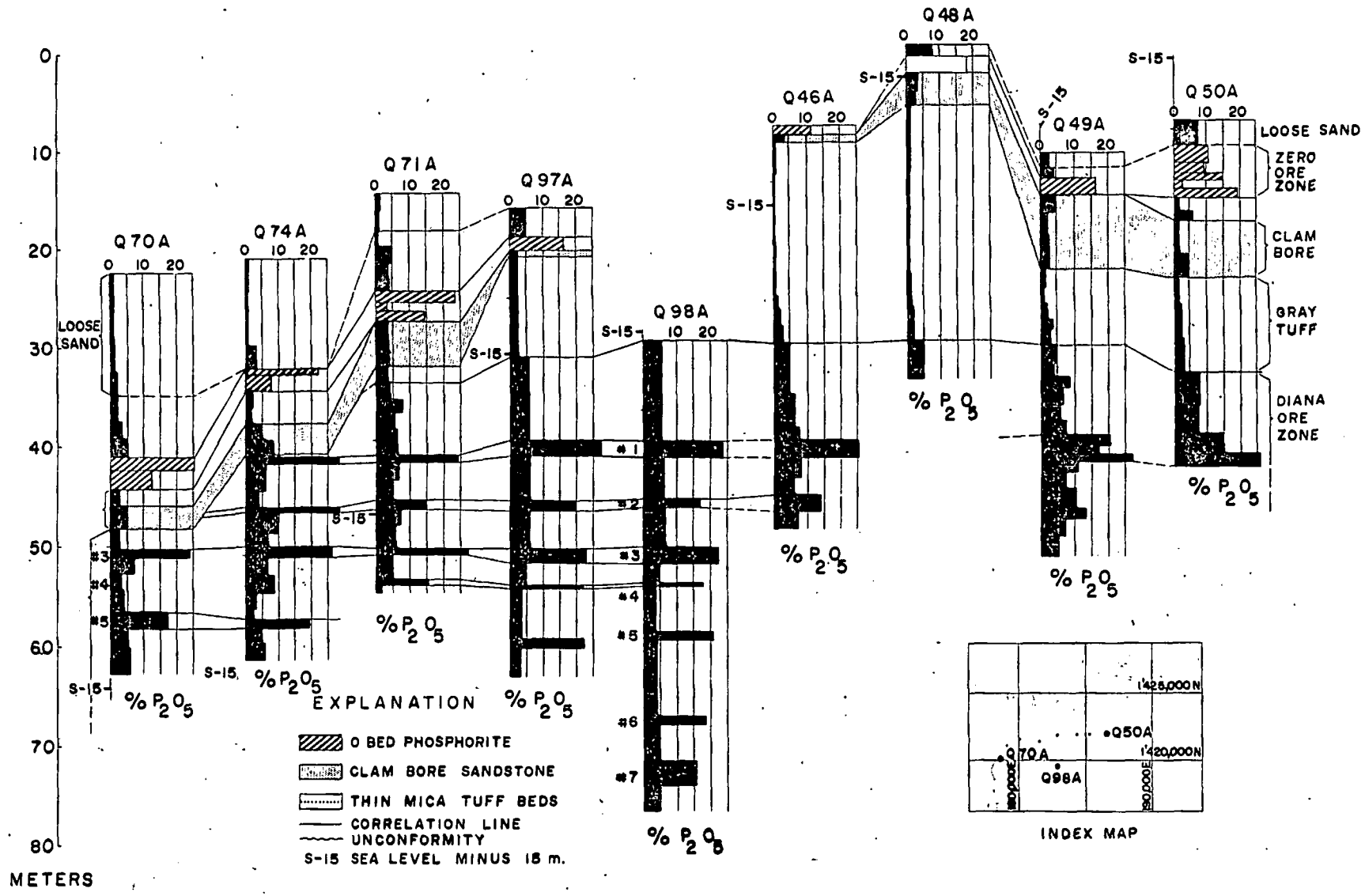

FIG. 8. East-west correlation chart from drill holes Q-70A to Q-50A.

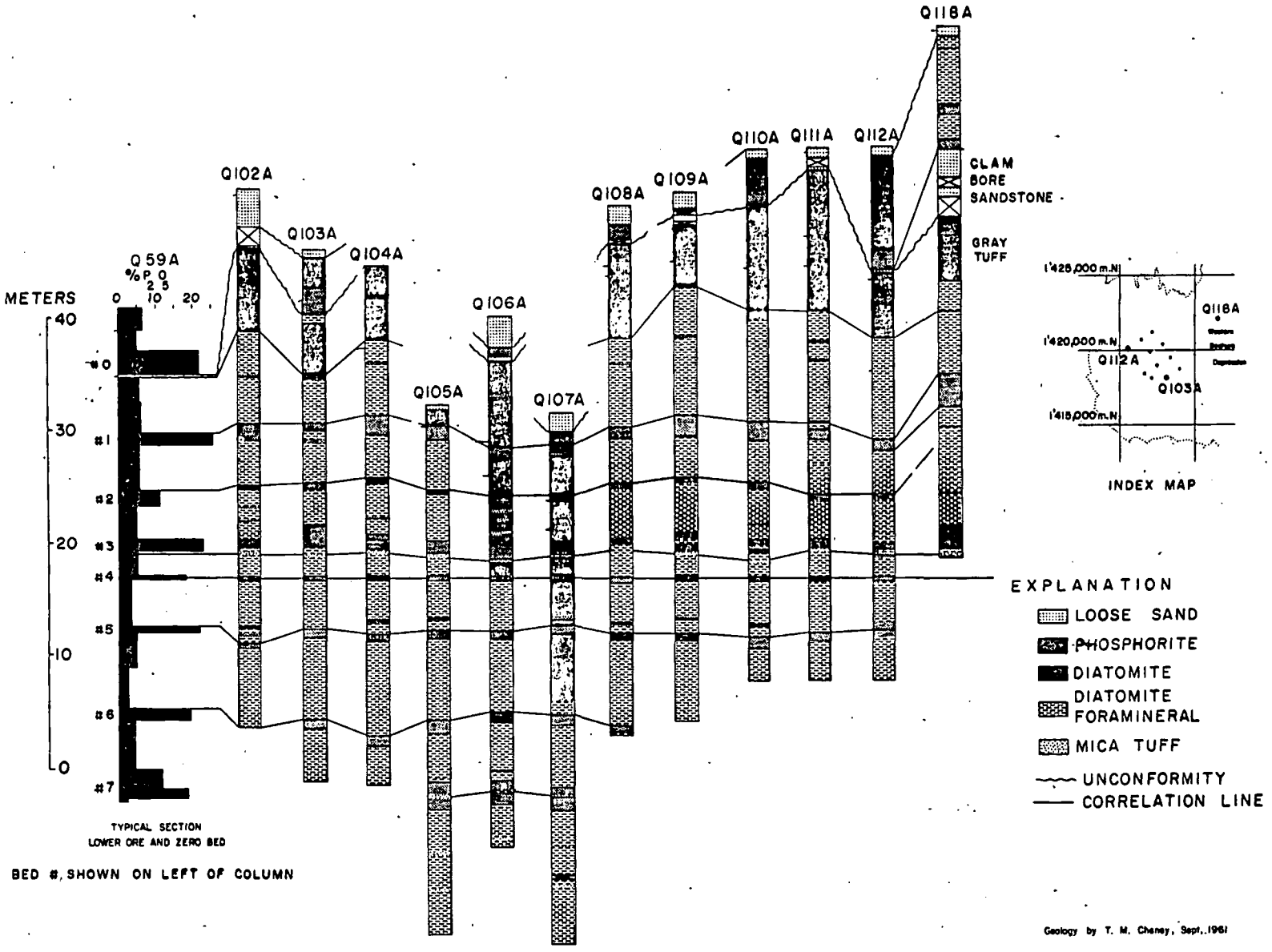

FIG. 9. Correlation diagram from drill holes Q-102A to Q-112A and Q-118A, showing Q-59A as a typical section. Datum is no. 4 bed where penetrated.

Geology by T. M. Cheney, Sept, 1961

FIG. 9. Correlation diagram from drill holes Q-102A to Q-112A and Q-118A, showing Q-59A as a typical section. Datum is no. 4 bed where penetrated.

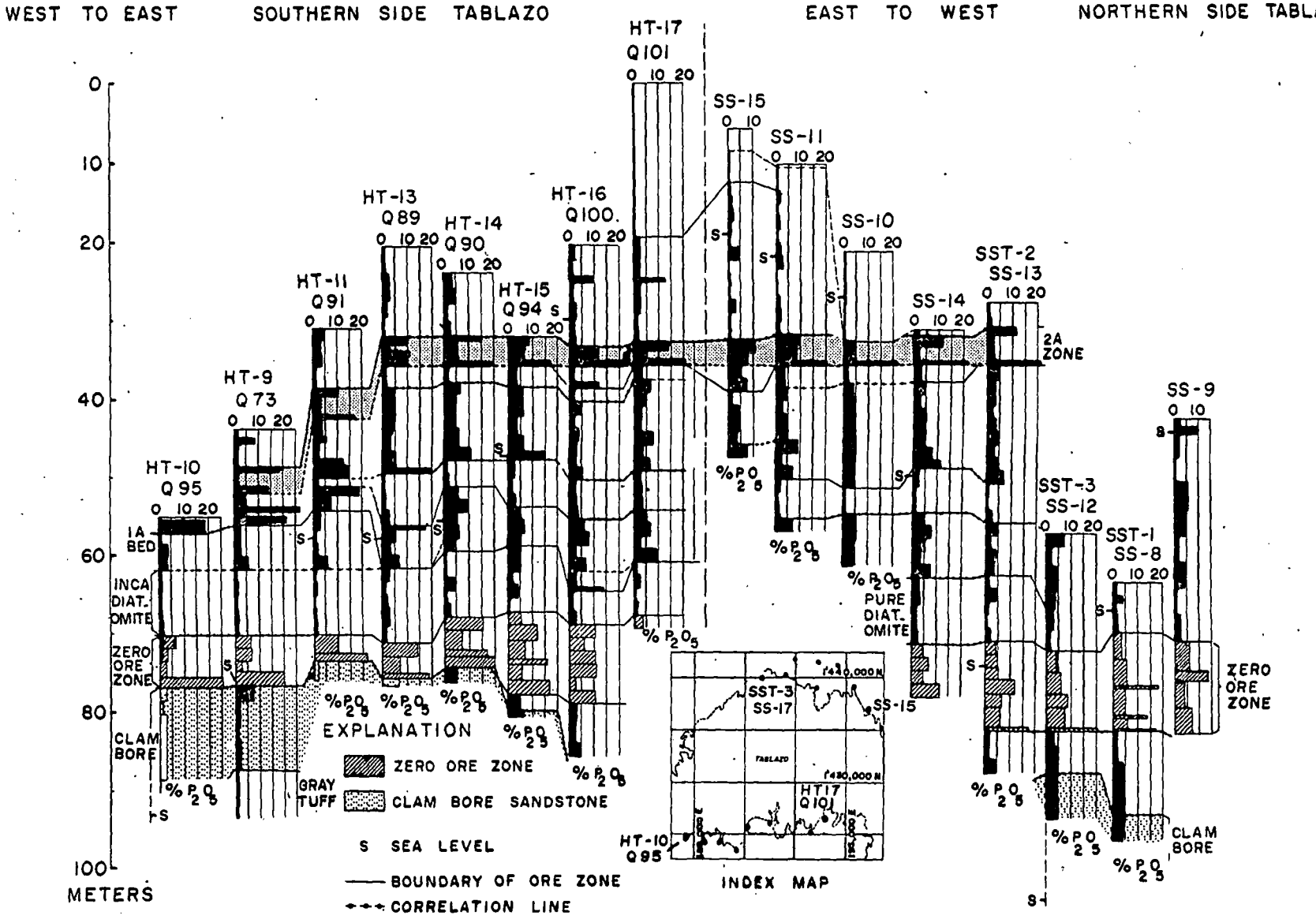

FIG. 10. Correlation diagram of composite sections from drill holes and hand trenches on north (estuary) side and south (depression) side of the Tablazo.

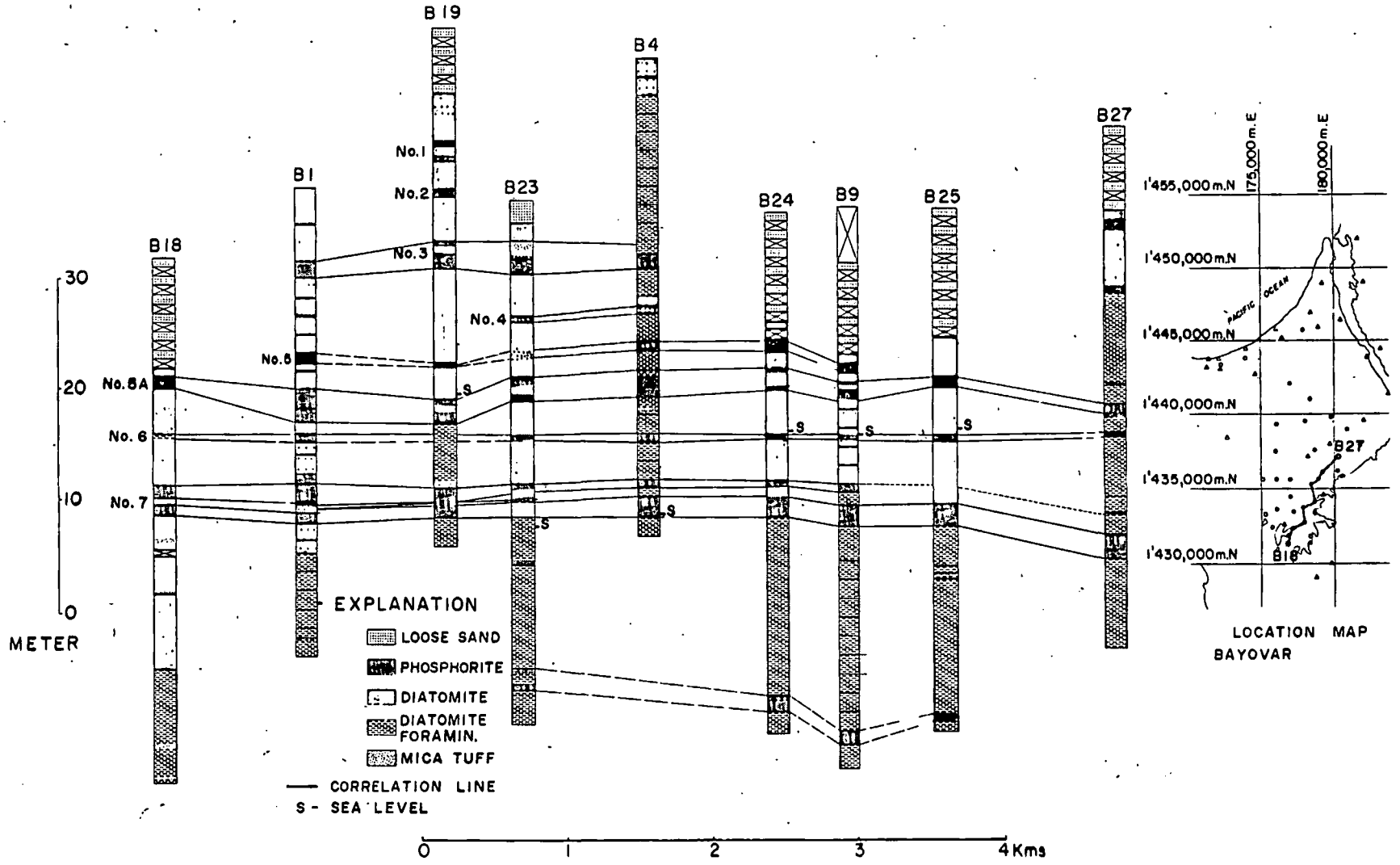

FIG. 11. Correlation diagram, Bayovar, from drill hole B-18 northeast to B-27.

of the beds, combined with such key units as the Clam Bore Sandstone and thin tuff beds (Figs. 7, 8, and 10), illustrate well the continuity of the beds. The regularity of the stratigraphic sequence is shown also by use of only lithologic characteristics for the correlation as in Figure 9. The strata encountered in every drill hole and trench were placed in their proper stratigraphic positions through correlations like those illustrated. The composite stratigraphic section of these strata (Fig. 5) is based on these correlations.

Lower Diatomite and Phosphorite member

The Lower Diatomite and Phosphorite member crops out in the southwestern part of the Sechura Depression, in an area north of the Tablazo fault and in the cliffs in the southern part of the Bayovar area (Fig. 6). This member has been drilled extensively in the western Sechura Depression and Bayovar areas, and a few holes have penetrated it in the western part of the Tablazo. The member consists of three units, which are from top to bottom:

Gray Tuff
Diana Ore Zone
Tuffaceous Diatomite

Tuffaceous Diatomite: The Tuffaceous Diatomite is the lowermost unit drilled in the western Sechura Desert. The maximum thickness measured in drill holes was about 48 meters, but its entire thickness was not drilled. The unit consists mostly of foraminiferal diatomite containing less than 2 percent P_2O_5 and characteristically contains many thin beds of mica tuff. Three phosphorite beds have been recognized—8, 8A, and 9 (Fig. 5).

Diana Ore Zone: The Diana Ore Zone is the richest and thickest of the three major ore zones in the western Sechura Desert. It underlies much of the area and crops out in the western part of the Sechura Depression and in the Bayovar area. It is 35 to 40 meters thick and contains 7 to 8 percent P_2O_5. Most of the phosphate is concentrated in seven beds, which have been designated from top to bottom as Nos. 1 to 7 (Fig. 5). The phosphorite beds generally are separated by diatomite that contains as much as 6.5 percent P_2O_5, mostly as pelletal phosphate.

Diana Ore Zone—western Sechura Depression: The Diana Ore Zone underlies all but the extreme southwestern part of the western Sechura Depression and crops out in much of the area. Sections of the Diana and typical correlations within the zone drill holes are shown in Figures 7, 8, and 9. In this area, the Diana can be divided into two parts. The contact between them is at the base of No. 3 bed (Fig. 5), which is marked by a persistent gray mica tuff about 0.3 meter thick in the top of the underlying diatomite.

The lower part of the Diana averages about 21 meters thick and 6.4 percent P_2O_5. It crops out in much of the southwestern Sechura Depression and undoubtedly underlies all the northwestern part, but it was too deep to penetrate with the available drill. Phosphorite beds Nos. 4 to 7 are in this part of the Diana. The No. 4 bed is generally less than 0.3 meter thick; Nos. 5 and 6 generally are a little less than 1 meter thick, and all these beds contain about 18 percent P_2O_5. The diatomite between the phosphate beds 3 to 6 meters thick contains 3.0 to 6.0 percent P_2O_5. The No. 7 bed is about 4.3 meters thick and contains up to 10 percent P_2O_5. It consists of interbedded phosphorite and diatomite, and it includes a gray micaeous tuff bed, about 0.1 to 0.3 meter thick, which is a distinctive marker. The phosphate pellets are more poorly sorted than in other beds in the interval. The base of the Diana generally is at the base of the No. 7 bed, but in some areas the 1.5 to 1.8 meters of diatomite beneath it contains significant phosphate.

Results of preliminary tests indicate that ore from the lower part of the Diana can be upgraded by washing and cycloning to about 27 percent P_2O_5 with recovery of more than 65 percent of the P_2O_5.

The upper part of the Diana base of No. 3 bed to top of phosphatic diatomite above No. 1 bed (Fig. 5) is higher in grade than the lower part. The upper part averages 17.7 meters thick and 9.0 percent P_2O_5 and is richer and thicker in the northeasternmost part of the area drilled. The phosphorite beds are extremely well sorted and fine grained (Fig. 12) and contain few impurities other than diatomite. The thickest and richest unit in the area is from the top of No. 1 bed to the base of No. 3 bed—about 10.0 meters thick with 11.6 percent P_2O_5. Results of preliminary tests indicate that the ore from this unit can be upgraded by washing and cycloning to more than 30 percent P_2O_5 with recovery of about 75 percent of the P_2O_5.

The contact between the Diana and the overlying Gray Tuff unit is gradational over about 3 meters; phosphatic diatomite beds become tuffaceous 6 to 7.5 meters above the No. 1 bed, and grade into the overlying Gray Tuff, which contains practically no phosphate.

Diana Ore Zone—Bayovar area: In the Bayovar area (Fig. 3), the Diana Ore Zone consists of three main units: an upper ore, a middle barren unit, and a lower ore. The upper ore is stratigraphically equivalent to the upper part of the Diana Ore Zone in the Sechura Depression. It is composed of phosphorite beds Nos. 1, 2, and 3 (Fig. 11) with intervening phosphatic diatomite beds. The barren unit cor-

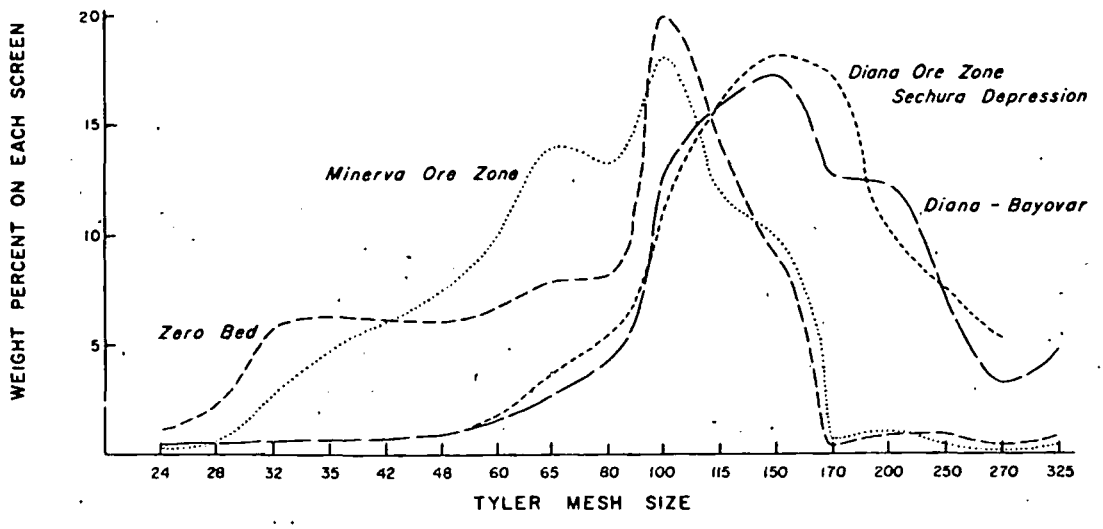

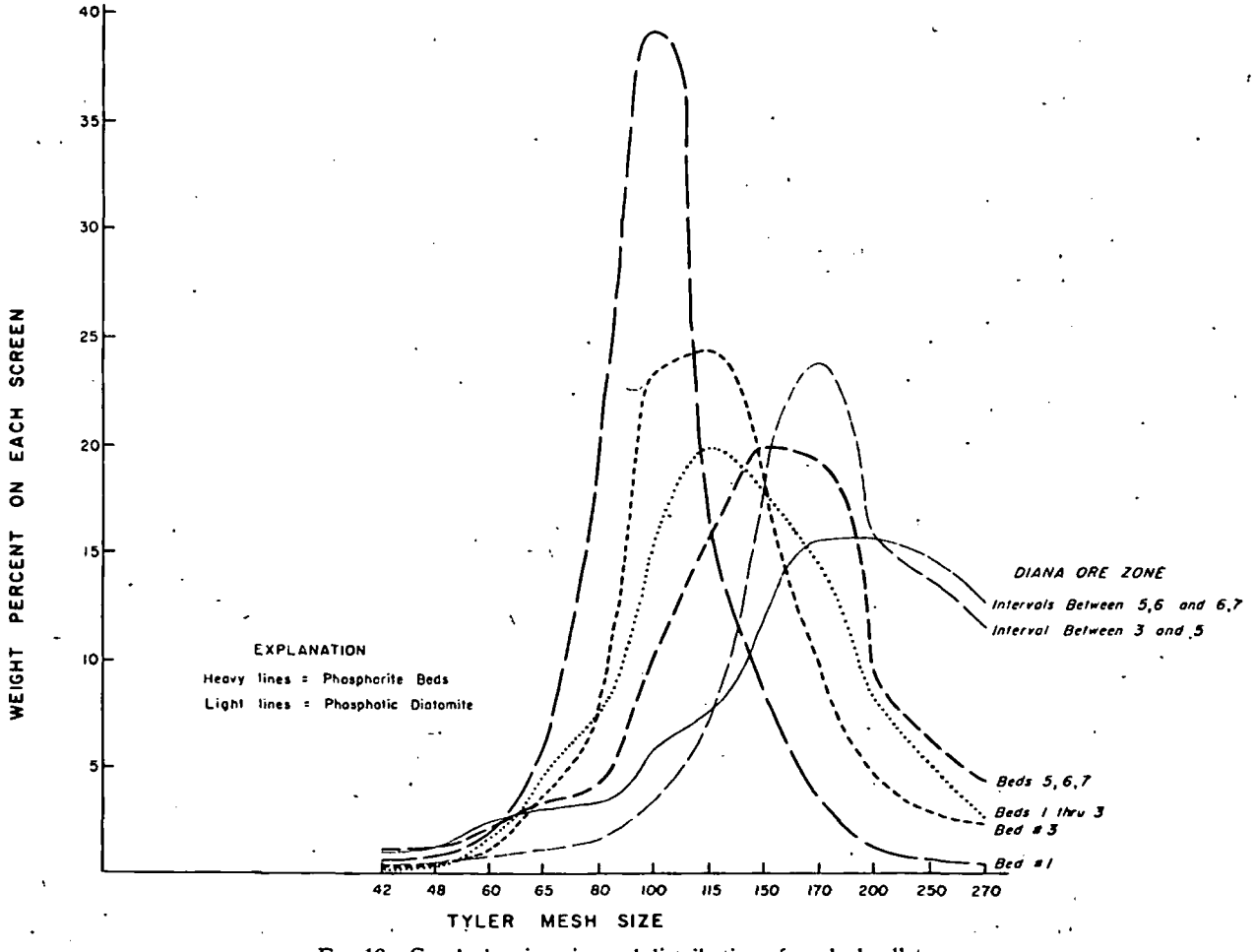

FIG. 12. Graph showing size and distribution of washed pellets.

responds to the interval between the base of the No. 3 bed and beds slightly below the No. 5 bed in the area of the depression. It is considered barren because phosphorite beds Nos. 4 and 5 are very thin or absent, and the intervening diatomite contains fewer phosphate pellets. The lower ore unit of the Diana zone generally is equivalent to the Sechura Depression from the interval slightly below the No. 5 bed to the base of the No. 7 bed.

The Diana Ore Zone is present in all drill holes

except B-21 and B-8, where it had been eroded prior to deposition of the Clam Bore Sandstone. In the Bayovar area the lower ore unit constitutes the bulk of the ore, because phosphorite beds Nos. 1, 2, and 3 are thin or absent, having been eroded from much of the area, either before deposition of the Clam Bore Sandstone or more recently.

The lower ore unit of the Diana Ore Zone in the Bayovar area averages 10 meters thick and 7.3 percent P_2O_5. It is marked at the top by the bed designated No. 5A, which lies below the No. 5 bed. The base of the unit is at the base of the No. 7 bed. The No. 6 bed is present in nearly every drill hole but generally is less than 0.3 meter thick and it apparently is represented by a mica tuff bed in part of the area. The No. 7 bed characteristically contains a gray mica tuff bed like that in the Sechura Depression. This mica tuff bed is not present in all drill holes but where absent usually is represented by a thin diatomite bed.

The middle unit of the Diana zone is mostly diatomite; it ranges from 5 to 12 meters thick and contains less than 3 percent P_2O_5. The No. 4 bed is present only in drill holes B-4 and B-23. The No. 5 bed is distributed irregularly and is thin; its position usually is marked by a slight concentration of phosphate pellets. On the other hand, in drill hole B-6 it is well developed, and the column here is similar to that in the western Sechura Depression.

The upper ore unit of the Diana zone has been eroded from all but the extreme south-central part of the area. Its maximum thickness, in the vicinity of drill hole B-19, is about 15 meters. Its average thickness, however, is about 6 meters, and it contains 7 to 15 percent P_2O_5.

Gray Tuff: Overlying the Diana Ore Zone in the western Sechura Depression and in a small part of the Bayovar area is a soft gray diatomaceous tuff. It crops out in the western depression in the vicinity of drill holes Q-98A, Q-2A, and Q-105A and in the Bayovar area, in the vicinity of drill hole B-4 (Fig. 3). The contact with the underlying Diana is gradational.

The original thickness of the Gray Tuff is not known because it was eroded prior to deposition of the Clam Bore Sandstone. Its present thickness is shown in Figure 13. It attains a maximum thickness of about 21 meters, in the northwestern part of the western depression; it thins westward, southward, and eastward. It is absent in the entire southwestern part of the depression and in the western part of the Bayovar area.

Clam Bore Sandstone member

The Clam Bore Sandstone unconformably overlies the Lower Diatomite and Phosphorite member. It is predominantly quartz sand but on the north side of the Tablazo the uppermost part is a limestone coquina. It crops out in (Fig. 6) much of the western Sechura Depression, along the western edge of the Tablazo, north of the Tablazo fault, in the cliffs west and south of the Bayovar area, and in the cliffs along the north side of the Tablazo from the Bayovar area in the estuary. Where the member is too thin to map, it is included in the base of the Upper Diatomite and the Phosphorite member. The Clam Bore was penetrated in drill hole SS-12 in the Estuary area and in most of the drill holes in the northwestern part of the depression. Its thickness is shown on the isopach map (Fig. 14). It generally is less than 0.3 meter in the southwestern part of the depression, but it thickens gradually northward to its maximum measured thickness of 23 meters in the Bayovar area near drill hole B-1. Where the sandstone is less than 1.5 meter thick it usually fills small channels and swales 0.3 to 0.6 meter deep in the underlying beds.

The Clam Bore Sandstone is one of the most easily recognized units in the stratigraphic section. It is characteristically composed of fine- to medium-grained quartz sand, which contains molds of pelecypods, gastropods, and pelecypod and worm borings. It contains small amounts of phosphate pellets and nodules and a few pebbles of quartz and metamorphic rocks. In general, it is finer grained where less than 0.3 to 0.6 meter thick and coarser grained where thicker. Where thickest on the northern and western edges of the Tablazo, it characteristically contains a lower, predominantly sandstone unit and an upper unit of coquina.

Upper Diatomite and Phosphorite member

The Upper Diatomite and Phosphorite member crops out in the cliffs around the Sechura Depression and in the cliffs between the Tablazo and the Virrila Estuary. Its distribution in the depression and in the cliffs along the Tablazo is shown on the geologic map (Fig. 6). It also underlies the Tablazo area. The member consists of four units, which are from top to bottom (Fig. 5):

Quechua Diatomite
Minerva Ore Zone
Inca Diatomite
Zero Ore Zone

Zero Ore Zone: The Zero Ore Zone underlies much of the western Sechura Depression and the Tablazo. It crops out in the western depression, on the western edge of the Tablazo, and in the cliffs along the northern edge of the Tablazo between the Virrila Estuary and the Bayovar area. It is known to underlie the Reventazon area (Fig. 3).

The Zero Ore Zone is composed mostly of the Zero phosphorite bed and overlying diatomite that

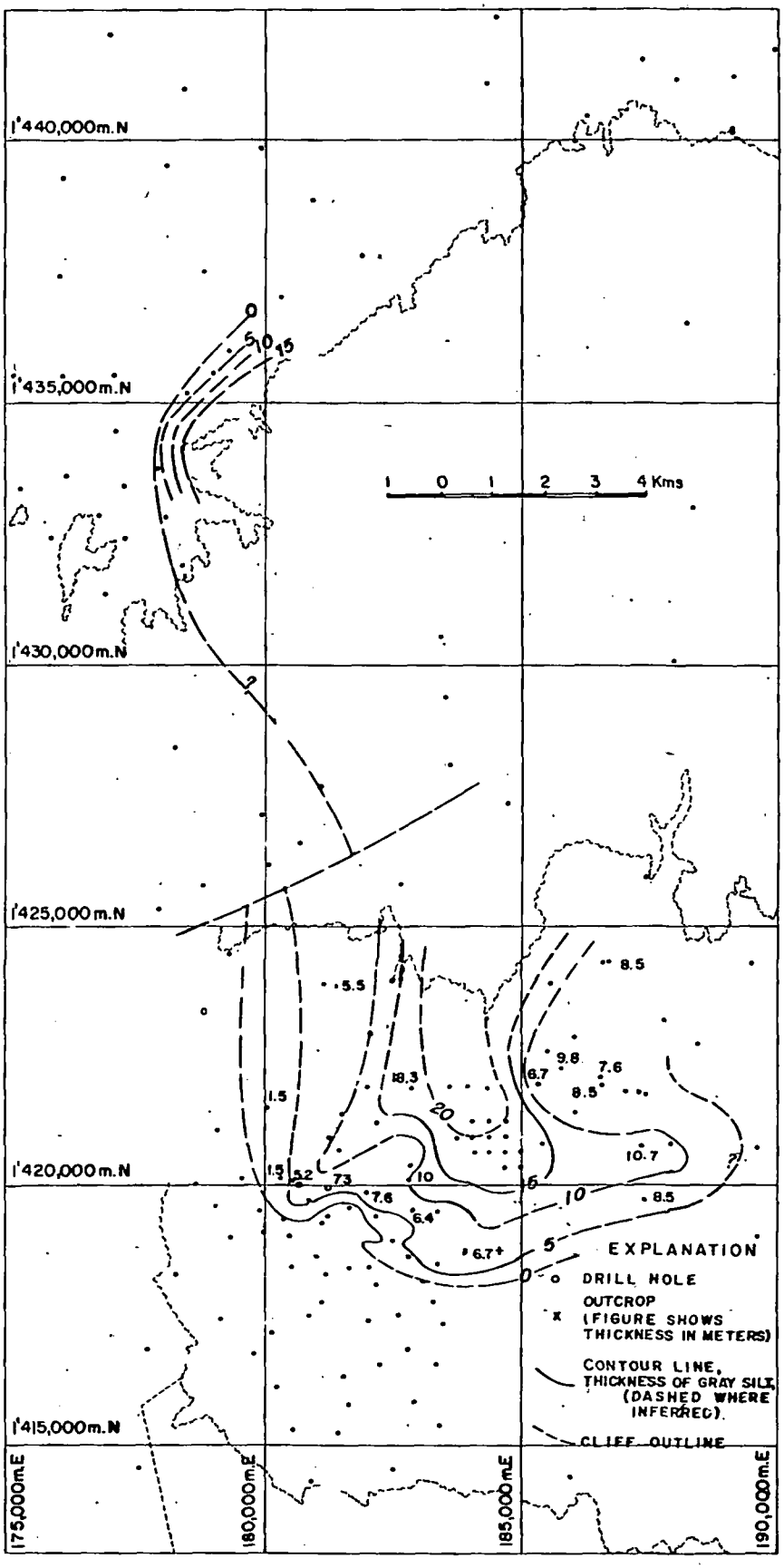

FIG. 13. Isopach map of Gray Tuff.

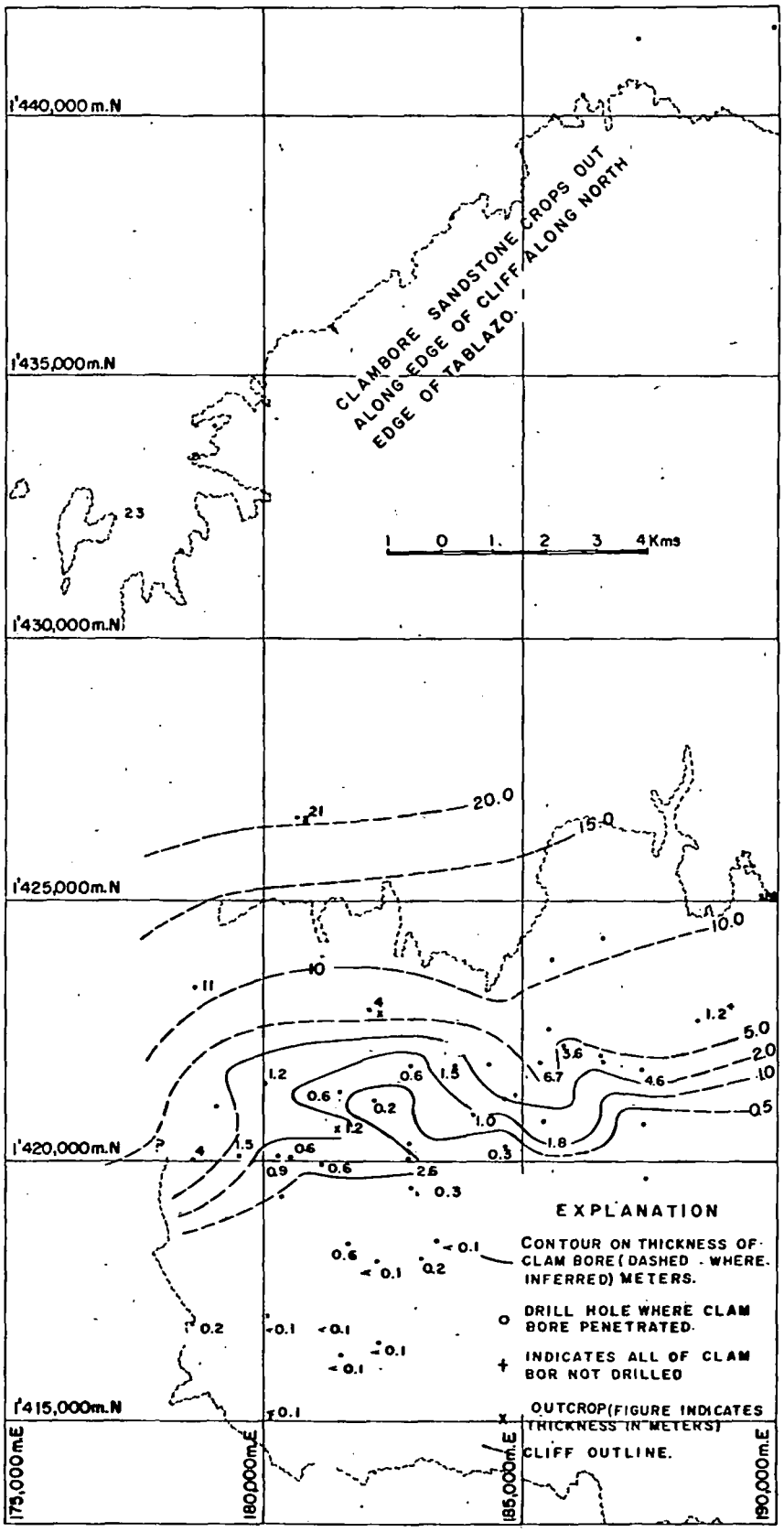

FIG. 14. Isopach map of Clam Bore Sandstone.

contains pelletal phosphate. It averages 6.3 meters thick and 9 percent P_2O_5.

The Zero bed is one of the more poorly sorted, slightly coarser grained phosphorite beds in the stratigraphic section (Fig. 12) and contains more sand grains than the other phosphate beds. Results of preliminary tests suggest that it can be upgraded by washing and cycloning to 24 to 25 percent P_2O_5. The overlying phosphatic diatomite contains phosphate pellets that are finer grained than those in the Zero bed.

The contact of the Zero Ore Zone with the underlying Clam Bore Sandstone generally is gradational, but at a few of the westernmost and northernmost drill holes in the Sechura Depression and in the Estuary area, a thin diatomite unit is present between the Clam Bore and the Zero bed. In some places this unit contains more than 4 percent P_2O_5.

Lateral changes in the Zero Ore Zone can be noted in Figures 7 to 9. In the western and southwestern parts of the Sechura Depression, the zone is composed of two distinct units, the Zero bed and overlying phosphatic diatomite Q-40A (Fig. 7) and HT-10 to Q-95A (Fig. 10). Eastward the zone thickens and the phosphate is more evenly distributed in the column. Comparison of sections along the north side of the Tablazo with those along the south side also shows a slight northeastward decrease in P_2O_5 values.

Inca Diatomite: The Inca Diatomite is 3 to 17 meters thick and contains about 1.0 percent P_2O_5 although some beds contain as much as 2.8 percent P_2O_5. It is composed almost entirely of diatoms and apparently contains no quartz silt or other impurities except the phosphate, which is mostly fish scales. The Inca crops out in the northwestern part of the Sechura Depression in the area from a line between drill holes Q-46A and Q-50A northward to the cliffs along the Tablazo. It is present also in the cliffs on the western edge of the Tablazo, on the northern edge of the Tablazo from triangulation point Temo to the Virrila Estuary (Figs. 3 and 4), and on the western and southwestern edges of the Sechura Depression. The Inca is thickest and purest in the western part of the area (HT-9 to Q-73A, Fig. 10). It thins northeastward, probably by an increase in phosphate content in both the lower and upper parts.

Minerva Ore Zone: The Minerva Ore Zone underlies the Tablazo north and south of the Sechura Depression. It is exposed in the cliffs all around the depression and in the cliffs between the Tablazo and the Estuary. It also has been penetrated by drill holes in the Reventazon area (Fig. 3).

The Minerva Ore Zone characteristically contains an abundance of bones, fish scales, and fish teeth, and certain beds contain many very large bones that were identified tentatively as whale bones. Some of the phosphorite beds are composed partially of phosphate nodules.

The average thickness and grade of units within the Minerva are shown in Figure 5. In the southwestern part of the Tablazo area, south of the Tablazo fault, the Minerva contains two phosphorite units. The overall composition and character of the Minerva Ore Zone is remarkably constant over a very large area, but it is relatively more variable than any of the other ore units. The phosphorite beds thin, and the diatomite beds thicken, from west to east. In the western parts of the Tablazo this zone is thin and high grade, as at HT-9 to Q-73A, where it is 6.7 meters thick and contains 10.3 percent P_2O_5. Eastward it thickens markedly: east of HT-13 to Q-89A it is more than 26 meters thick and contains 5 to 6 percent P_2O_5. Whereas the total amount of phosphate has doubled between these two sections, the thickness has quadrupled. Most of the increase in thickness reflects an increase in the content of diatomite.

The phosphorite pellets in the Minerva Ore Zone are more poorly sorted than those in the Diana but show about the same sorting as those in the Zero Ore Zone (Fig. 12). The Minerva zone contains less sand and silt-sized impurities than the Zero Ore Zone and slightly more than the Diana zone. Results of preliminary metallurgical tests on samples from HT-7 through HT-15 in the southwestern Tablazo area indicated that ore from the Minerva zone can be upgraded by washing and cycloning to at least 26 percent P_2O_5 with recovery of at least 60 percent of the P_2O_5.

Quechua Diatomite: The Quechua Diatomite ranges in thickness from 0 to 14 meters. It is thickest in the northeastern part of the Sechura Depression, but its thickness is somewhat irregular, perhaps because it interfingers with and grades into the overlying Barren Diatomite member. The Quechua is composed mostly of diatoms and is relatively pure, but it contains one or two thin phosphorite beds. In the depression, one thin phosphorite bed which is rather high grade (HT-16 to HT-17, Fig. 10) contains many bones and teeth and large amounts of quartz. It probably correlates with a similar bone-bearing bed that cropped out in the extreme southeastern corner of the Sechura Depression.

Barren Diatomite Member: The Barren Diatomite member is the uppermost Miocene unit in the western Sechura Desert. It ranges from absence to an estimated 40 meters thick, having been eroded prior to the deposition of the overlying Pliocene sediments; it thickens toward the east (Fig. 6). The member is present in the cliffs around the eastern part of the depression and along the eastern part of the

estuary. In outcrop it usually is stained a yellowish to reddish orange. Although the composition of this unit is not well known, mica flakes are a characteristic component, and the stain in the outcrops suggests the presence of other minor impurities.

Pliocene coquina, sand, and shale

Pliocene strata consisting of an interbedded series of coquina, sand, and shale unconformably overlie the phosphate-bearing strata in part of the western Sechura Desert. Their distribution is shown on the geologic map in Figure 6. These strata are best exposed in the cliffs around the Sechura Depression and on the edges of the Tablazo.

Recent loose sand, alluvium, and windblown sand

Recent loose sand, alluvium, and windblown sand are present over much of the area. Where they are estimated to be more than 1.0 meter thick they are shown in Figure 6. Most of these sediments are windblown sand in the form of dunes or thin sheets of loose sand. Most of the unit QS on the geologic map is windblown sand.

Structure

The structure of Miocene and younger strata in the Sechura Desert is very simple. Slight tilting, minor folding, and minor faulting constitute the extent of deformation. These strata were deformed in at least three different periods: one during the Miocene, one prior to deposition of Pliocene sediments, and one after the Pliocene.

After deposition of the Lower Diatomite and Phosphorite member, the beds were tilted to the northeast and their general strike is now about N10°W. They dip northeast 11 to 14 meters per kilometer (Fig. 15). They also were slightly compressed and gently folded. Axes of almost all the folds plunge gently northeastward. The amplitude of these folds is very small and practically unrecognizable in the field.

After and perhaps during this deformation, the Lower Diatomite and Phosphorite member and Gray Tuff were partly eroded from the western part of the area. The Clam Bore Sandstone was then deposited on these truncated beds as shown on the geologic map of beds as they probably appeared prior to deposition of the Clam Bore Sandstone (Fig. 15).

The unconformity beneath the Clam Bore Sandstone had a marked effect on the present distribution of the Diana Ore Zone. In general, the Clam Bore was deposited on the essentially plane surface eroded on gently northeast dipping beds, so that it rests on progressively older beds toward the southwest.

The unconformity beneath the Clam Bore not only is demonstrated by correlation of drill hole data but also is evident in surface outcrops. In most of the northwestern part of the depression, the Clam Bore rests on Gray Tuff, as observed in outcrops near drill holes Q-105A and Q-108A and as evident from drill holes (Figs. 3 and 9). Southwestward, in the vicinity of drill hole Q-2A, the Clam Bore rests on the upper part of the Diana Ore Zone. In the vicinity of drill hole Q-36A, it rests on phosphatic (pelletal) diatomite that overlies the No. 7 bed. Still farther southwestward, it rests on the Lower Diatomite and Phosphorite member. On the western edge of the Tablazo in the vicinity of drill holes Q-82A and Q-87A, most of the Diana Ore Zone has been removed by erosion prior to deposition of the Clam Bore; in the vicinity of drill holes Q-85A and Q-96A, the Diana Ore Zone is absent. In much of the Bayovar area the Diana Ore Zone is absent, as at drill holes B-18 and B-21, because of pre-Clam Bore erosion. Hence, in the extreme western and southwestern parts of the Sechura Desert the unconformity marks the limit of the area of economic interest.

After deposition of the Clam Bore Sandstone, the strata evidently were not deformed again significantly until after deposition of the Upper Diatomite and Phosphorite member. They were then slightly tilted to the southeast (Fig. 16). They strike about N15°E and dip 6 to 8 meters per kilometer to the southeast. They were also compressed slightly so that several minor asymmetrical eastward-trending folds were formed that plunge slightly to the east.

It is possible that during the first two periods of deformation there was minor faulting because some of the folds shown in Figures 15 and 16 could have resulted partly from faulting. One in particular that may be a fault is shown as a sharp flexure on Figure 15 near grid line 1,420,000 N.

During or after the eastward tilting of the Miocene beds they were uplifted and eroded, so that Pliocene beds were deposited on the truncated surface. The Pliocene beds are horizontal insofar as can be determined.

The latest deformation known to have affected any of the strata is definitely post-Pliocene and may be Recent. Evidence of this deformation are the faults shown in Figure 6 that cut the Pliocene beds. Other evidence for post-Pliocene deformation is the presence of at least one major fault along the east side of the Illescas Mountains, where older alluvial fan material has been dropped against metamorphic rocks.

Petrography

Diatomite

The diatomite is marine in origin and consists of indistinct pellets that are aggregates of diatom parti-

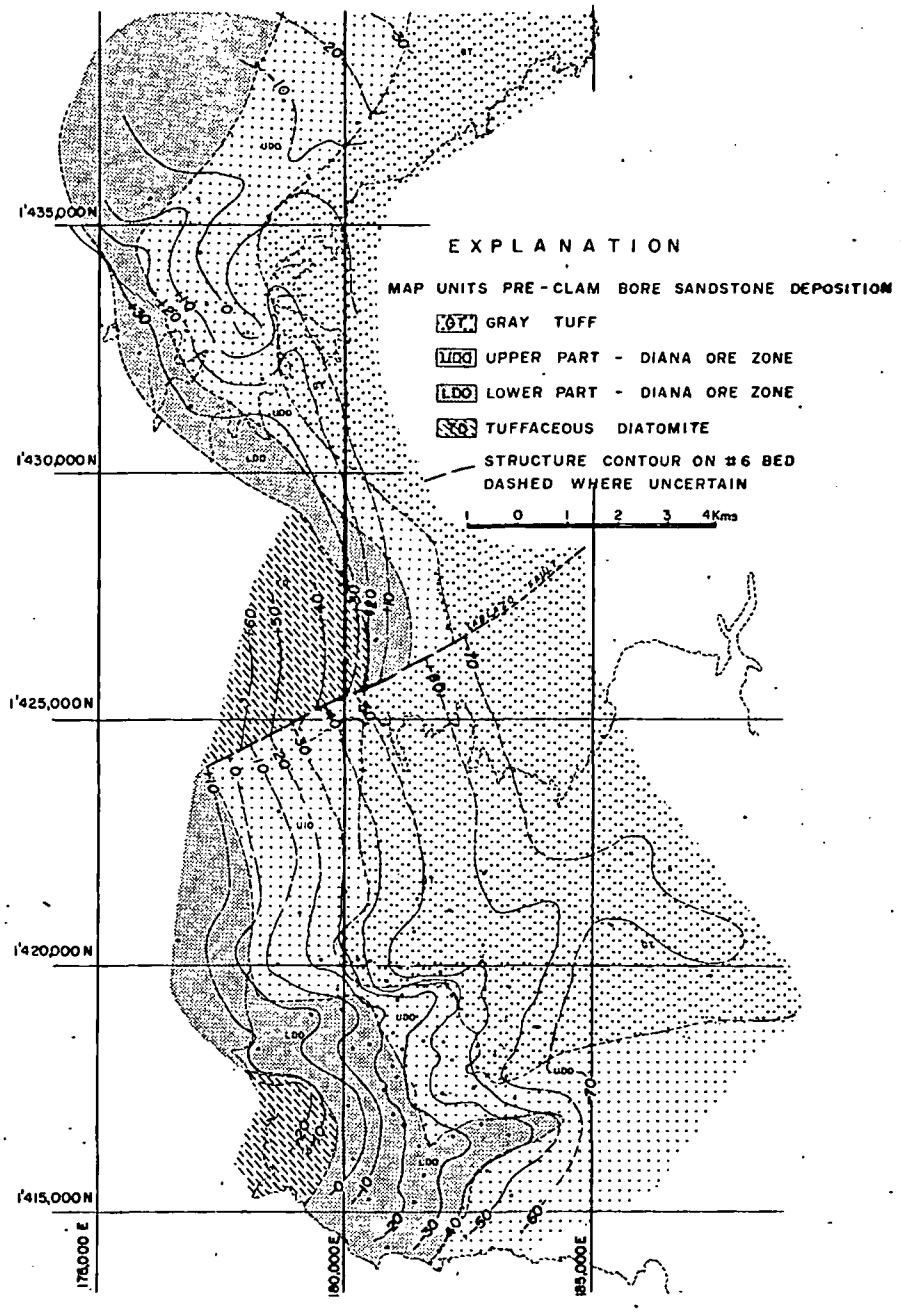

FIG. 15. Structure contours on No. 6B, C, D and geologic map prior to deposition of Clam Bore Sandstone.

cles. These particles are of many shapes and appear to be rather poorly sorted; they range in size from about 0.074 mm (200 mesh) to 3 or 4 microns. The diatom particles are composed of opaline silica, probably $SiO_2 \cdot nH_2O$. The chief impurities in the diatomite are phosphatic fish scales, siliceous sponge spicules and skeletons, and calcareous foram shells. As much as 5 percent of spicules has been observed in a diatomite, the P_2O_5 content of diatomites usually is less than 2 percent, and the foram shells probably supply less than 1 percent $CaCO_3$. The foram shells are very fragile and disintegrate on the slightest washing.

The diatomite is soft and its pellets disintegrate at the slightest touch. The diatomite beds are generally massive, but some contain extremely thin (most less than 2 mm thick) stringers of phosphate parallel to bedding, particularly a few feet below

the main phosphorite beds. Cross-bedding can be seen within some of these stringers.

The color of the diatomite ranges from pure white through brown to dark olive green. The variation in color reflects differences in the interstitial material, because washed diatom particles are white and subtranslucent to transparent. The color apparently reflects the state of oxidation of the organic material, and the same bed may be white, black, or brown, depending on its location with respect to the water table or to its water content. We have tended to class the darker beds as foraminiferal diatomites and the white beds as diatomite, mainly because we can see the forams in the darker beds, but they are difficult to see in the lighter colored beds without a microscope.

Because the diatomite beds are composed of microscopic irregular particles and because they are not

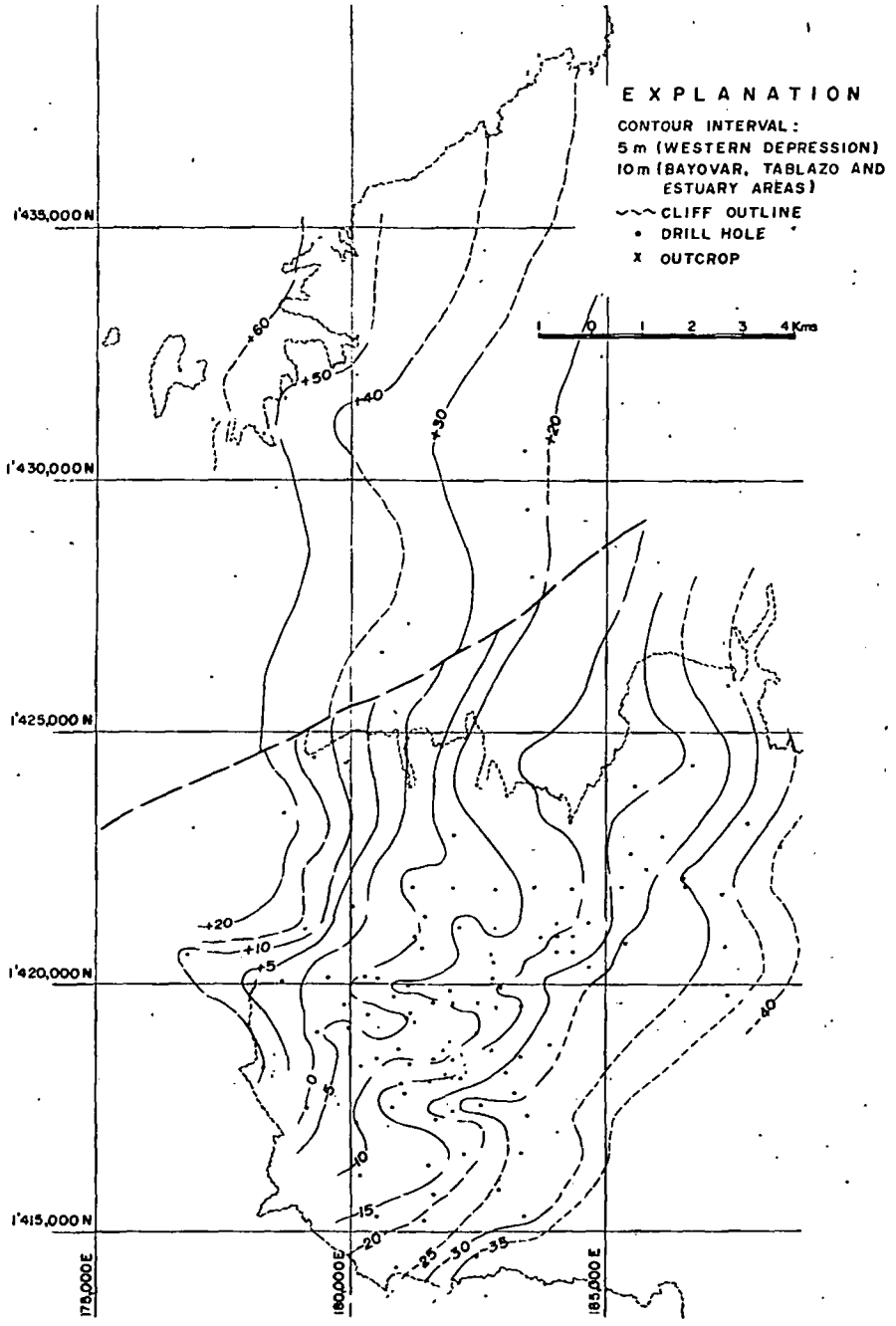

FIG. 16. Structure contours on Clam Bore Sandstone.

highly compacted, the porosity is extremely high, about 90 percent. Because of its high porosity the apparent specific gravity of the pure diatomite is low, about 0.5. Its permeability, however, is low.

Sandstone and tuff

The major sandstone and tuff beds are the Clam Bore Sandstone and the Gray Tuff. Minor beds of Gray Tuff are present in the Diana Ore Zone and the Tuffaceous Diatomite.

The sandstone is of marine origin and consists mostly of fine to medium quartz grains, but it contains also scattered phosphate pellets, grains of feldspar and black metamorphic rocks, a few pebbles of quartz and metamorphic rock, and marine fossils. These extraneous materials are distributed homogeneously throughout the sandstone and there is little evidence of stratification. The sandstone generally is friable, but in local areas it is hard, especially where it is dry. The color ranges from light brown to a characteristic yellowish orange.

The tuff is also of marine origin and is soft and friable and disintegrates readily in water. It consists mostly of fine to coarse silt and very fine sand-size grains of volcanic glass, feldspar, quartz, and diatoms. The modal grain size is probably slightly less than 0.62 mm. The minor constituents in this tuff are mica, amphiboles, sponge spicules, forams, foram tests, and heavy minerals.

The tuff is generally massive bedded and gray to light grayish green. The tuff beds in the Diana Ore Zone and the Tuffaceous Diatomite are a distinctive light gray in color whether above or below the water table. The Gray Tuff is generally light to medium grayish green where dry and dark grayish green where wet.

Phosphate

The phosphate is marine in origin and consists mostly of pellets of phosphorite, a fluorhydroxycarbonate apatite. Impurities in the phosphorites are, in decreasing order of abundance, fragments of diatoms; volcanic glass; soluble sodium, potassium, and magnesium salts; quartz; feldspar; sponge spicules; gypsum; mica; and organic matter.

Although the individual pellets are hard, the phosphorites are friable and all the subsurface phosphorites disintegrate in water. The phosphorites in some small areas are cemented, but this is a rare surface or very near surface phenomenon. Gypsum, a secondary mineral, occurs mainly as fracture fillings near the surface and comprises less than 2 percent of the beds penetrated by drill holes.

The phosphorite beds are generally massive and show no apparent evidence of planar stratification. Cross-bedding is common in the lower part of the phosphate beds but is very indistinct. The upper contact of the phosphorite bed with diatomite is always planar and very sharp, but the lower contact with diatomite beds is nearly always irregular and gradational. The upper part of the diatomite beds contains many irregular pockets and stringers of phosphate, and the lower part of the phosphorite beds contains irregular masses and disseminated diatomite.

The phosphorite beds have a high degree of sorting (Fig. 12) and so should be highly porous, but much of the pore space is filled with diatomite and fine silt-sized particles.

The apatite pellets are mostly structureless. They usually contain less than 1 to 2 percent of impurities —fragments of diatoms, sponge spicules, volcanic glass, very fine quartz grains, organic matter, and mica. The apatite pellets in the Zero bed contain more impurities than those in the other main phosphorite beds. A few of the pellets from the Zero bed have large cores of quartz or feldspar.

Most apatite pellets are subelliptical to ovoid in shape, but rod-shaped and irregularly knobby pellets are not uncommon. The finer pellets are more regular in shape, the larger pellets more irregular. The larger pellets usually have a pitted surface and the smaller pellets a smooth, shiny surface. Many of the larger pellets and nodules probably are agglomerates of fine pellets.

The pellets range in color from white to dark brownish black, and pellets from different parts of the same bed may be of different colors. For example, pellets from the No. 1 bed are white at one end of an outcrop, reddish brown about 100 meters away, and nearly black at 500 meters, where the bed is below the surface. Hence, color is of no value in correlation or recognition of different beds. In general, however, most of the phosphorite beds are usually light brown or darker, and the difference in color probably reflects the state of oxidation of the organic matter present.

The specific gravity of the individual phosphate pellets ranges from 2.8 to 2.93; the average is about 2.9. The specific gravity of a relatively pure bed, such as the No. 1 phosphorite bed, which contains 28 percent P_2O_5, is about 1.65. The specific gravity of washed ore that contains 31 percent P_2O_5 is about 1.7.

In the Sechura deposits the apatite is present mostly as discrete pellets. Other forms present in minor amounts are nodules (elliptical and irregular masses larger than 2 mm); oolites (similar to pellets but with internal concentric structure); fish teeth, scales, and bones; and casts and internal molds of foraminifera. The pellets range in size from less than 0.43 mm to 2 mm, but 95 percent are between

0.06 mm (270 mesh) and 0.6 mm (35 mesh) (Fig. 12), and the modal grain size is between 0.175 mm (80 mesh) and 0.12 mm (150 mesh). More than 75 percent of the apatite pellets are larger than 200 mesh, but there are significant differences in the size of the pellets in different beds of the deposit. The pellets in the phosphorite beds are usually slightly coarser and better sorted than those in the phosphatic diatomite beds. The pellets in the phosphorite beds from the Zero and Minerva Ore Zones, which are above the Clam Bore Sandstone, are coarser and more poorly sorted than those in the beds below the Clam Bore Sandstone. The pellets in the upper part of the Diana Ore Zone are coarser and better sorted than those in the lower part of the Diana.

Mineralogy and Chemical Composition of Phosphates

The phosphates of the Sechura deposits are apatites, complex calcium phosphates that are the major commercial source of phosphates and are known collectively as phosphate rock. They have only one property in common—the structural arrangement of the ions—and their compositions differ considerably from that of fluorapatite, $Ca_{10}(PO_4)_6F_2$, which has long been considered the phosphatic component of phosphate rock. Differences in chemical composition, however, are reflected in differences in behavior of commercial phosphate concentrates in their conversion to fertilizer materials. The differences in the several types of apatites reflect the history of their formation in igneous, metamorphic, and sedimentary environments.

The chemical compositions of sedimentary apatites range widely; significant amounts of magnesium and sodium may be substituted for calcium, and as much as 25 percent of the phosphorus may be replaced by a joint substitution of carbonate and fluorine, and these apatites are known as francolites, a distinct minerals class (McClellan and Lehr, 1969). Important sedimentary phosphorite deposits are found in North Africa (Senegal, Togo, Morocco, Algeria, Tunisia), and Near East (Jordan, Israel, Egypt), Asia (India, China, Russia, Vietnam), Australia, North America (United States, Mexico), and South America (Colombia, Peru, Brazil).

Characterization methods

Since apatites are the most important commercial source of phosphate, the characterization methods described here are discussed only with respect to apatites. The methods have been applied to apatites from most of the phosphate deposits in the world, and some representative results have been selected to provide a basis for explaining the properties of the Sechura apatite. The examinations included chemical analysis, X-ray powder diffraction, optical microscopy, and infrared analysis, and a rapid, preliminary characterization suitable for broad classification of phosphorites can be made by these techniques (McClellan and Gremillion, 1976).

TABLE 1. Substitutions in the Apatite Structure

Constituent ion	Substituting ion
Fluorapatite $Ca_{10}(PO_4)_6F_2$	
Ca^{+2}	Na^{+1}, Sr^{+2}, Mn^{+2}, K^{+1}, U^{+4} Mg^{+2}, $RE^{+2,+3}$ (lanthonons and yttrium)
P^{+5}	C^{+4}, S^{+6}, Si^{+4}, As^{+5}, V^{+5} Cr^{+6}, Al^{+3}
F^{-1}	OH^{-1}, Cl^{-1}
O^{-2}	F^{-1}, OH^{-1}
Francolite $Ca_{10-a-b}Na_aMg_b(PO_4)_{6-x}(CO_3)_xF_{0.4x}(F, OH)_2$	

Chemical characterization

Most of the more than 25 minor elements that have been reported to occur in fluorapatites (Table 1) are present in insignificant amounts, and the apatites described in the literature are usually igneous or metamorphic. It has been shown (Lehr et al., 1967; McClellan and Lehr, 1969), however, that the apatites in sedimentary phosphate rocks are adequately described by their CaO, Na_2O, MgO, P_2O_5, F, and CO_2 contents. Their compositions are represented adequately by the series with end-member empirical formulas of:

fluorapatite, $Ca_{10}(Po_4)_6F_2$, and
francolite, $Ca_{10-a-b}Na_aMg_b(PO_4)_{6-x}(CO_3)_xF_{0.4x}F_2$.

The electrostatic imbalance resulting from the substitution of CO_3^{-2} for PO_4^{-3} is only partially corrected by addition of F^{-1}, and a coupled monovalent cation substitution for calcium is required to maintain electrostatic neutrality. In sedimentary apatites the cation that most often replaces calcium is sodium, Na^{+1}. The compositions of the theoretical end members are shown in Table 2.

TABLE 2. Theoretical Composition of Fluorapatite and Francolite

Constituent (%)	Fluorapatite (x = 0)	Francolites $x/(6 - x) \simeq 0.30$[1]
CaO	55.6	55.1
P_2O_5	42.2	34.0
CO_2	0	6.3
F	3.77	5.04
Na_2O	0	1.4
MgO	0	0.7

[1] Maximum degree of substitution predicted for francolite-type apatites.

TABLE 3. Some Typical Phosphate Rock Compositions

Source	Composition (%)					
	CaO	MgO	Na_2O	P_2O_5	CO_2	F
Western U. S.	55.6	0.13	0.26	40.1	1.59	4.09
Tennessee	55.5	0.24	0.47	38.7	2.71	4.31
Sechura, Peru	51.8	0.29	1.20	32.2	5.68	3.30
Florida	55.5	0.36	0.72	37.1	3.95	4.56
Morocco	55.4	0.43	0.85	36.3	4.53	4.68
North Carolina	55.3	0.52	1.04	35.3	5.36	4.85
Tunisia	55.2	0.60	1.20	34.7	5.70	4.93

The compositions of these substituted apatites can be estimated with a degree of certainty suitable for routine analytical evaluation of phosphate concentrates using the method described by McClelland and Gremillion (1976) and the following empirical equations.

$$a_{obs} = 9.369 - 0.185(x/(6 - x)) \quad (1)$$

in which

a_{obs} = crystallographic a-axis dimension as determined by X-ray diffraction (a observed)

x = subscript for CO_3 in the formula for francolite

$x/(6 - x)$ = mole ratio $CO_3:PO_4$ in the francolite

or

$$i = 1.633 - 0.1264(x/(6 - x)) \quad (2)$$

in which

i = average index of refraction of the phosphorite

From the value of $x/(6 - x)$ determined from either equation (1) or equation (2),

$$a = 1.327(x/(6 - x)) \quad (3)$$

$$b = 0.515(x/(6 - x)) \quad (4)$$

TABLE 4. Mineral Compositions of Selected Phosphate Rocks[1]

Source	Weight (%)	
	Apatite[2]	Gangue minerals
Western U. S.	79.8	20.2
Tennessee	82.7	17.3
Sechura, Peru	86.4	13.6
Florida	86.3	13.7
Morocco	88.2	11.8
North Carolina	90.7	9.3
Tunisia	92.2	7.8

[1] Calculated assuming all samples contain 32 percent P_2O_5.
[2] Weight percent apatite = actual P_2O_5/theoretical P_2O_5 (100% apatite).

in which a and b are the subscripts for Na and Mg, respectively, and appear in the subscript for Ca in the formula of the francolite.

Compositions of typical commercial phosphate rock concentrates among those from which these relationships were derived are listed in Table 3. These compositions are arranged in approximate order of carbonate substitution, but they do not cover the entire range of possible compositions indicated in Table 2.

Effect of apatite composition on rock composition

The composition of the apatite in a phosphorite determined by this procedure is a useful index to the properties of the phosphate ore. This is illustrated by comparing the theoretical apatite compositions of a representative series of phosphate rocks in Table 4.

This comparison, which is based solely on the calculated apatite composition and the P_2O_5 content of the phosphate rock, shows that the amount of gangue is not related directly to the P_2O_5 content of the rock. Further use can be made of the weight distribution data if the contents of other important constituents of the rock are included. With this additional information, the distribution of key impurities between the apatite and gangue-mineral fractions can be determined.

This treatment of the data is illustrated in Table 5 with a Sechura phosphate rock. The theoretical apatite composition was calculated from equations (1), (3), and (4), and an overall value of $a = 9.339$ angstroms. The calculation of the calcium and carbonate contents of the apatite permits calculation of the distribution of these constituents between the apatite and the gypsum and calcite in the ore.

It is apparent that knowledge of the composition of the apatite provides a means for comparing im-

TABLE 5. Modal Analysis of Chemical Constituents in a Sechura Phosphate Rock Sample

	Apatite (Theor.)	Phosphate rock	Apatite fraction[1] (87%)	Gangue fraction[2] (13%)
CaO	55.27	51.8	47.9	3.9
P_2O_5	37.18	32.2	32.2	—
F	4.53	3.3	3.9	—[3]
CO_2	3.84	5.7	3.3	2.4
Na_2O	0.70	1.2	0.60	0.6
MgO	0.35	0.29	0.30	—
Al_2O_3		0.21		0.21
Fe_2O_3		0.07		0.07
SiO_2		4.10		4.10
Sulfate-S		1.31		1.31

[1] Estimated amounts, derived from the P_2O_5 ratio (32.2/37.2).
[2] Includes all nonphosphate diluents such as calcite (5%), gypsum (2%), quartz and silica (4%), and traces of iron-aluminum oxides and halite.
[3] See discussion of fluorine content in text.

TABLE 6. Chemical Composition of Selected Phosphate Rocks

Deposit source	Constituent (%)									
	CaO	P_2O_5	F	CO_2	R_2O_3	Na_2O	MgO	SiO_2	CaO/P_2O_5	F/P_2O_5
Central Florida	48.9	33.4	3.9	3.0	2.12	0.53	0.29	4.5	1.464	0.117
North Carolina	48.5	30.2	3.7	5.5	1.14	0.83	0.54	2.1	1.606	0.122
Morocco	51.6	32.1	4.1	5.3	0.55	0.79	0.43	1.4	1.607	0.128
Gafsa, Tunisia	48.3	28.8	3.4	6.3	1.22	1.30	0.59	1.8	1.677	0.118
Taiba, Senegal	51.2	37.4	4.0	1.7	2.06	0.20	0.06	2.9	1.369	0.107
Togo	52.3	36.6	4.0	1.8	1.78	0.27	0.11	1.8	1.429	0.109
Kola, Russia	52.0	38.2	3.1	0.2	3.14	0.50	0.06	2.0	1.361	0.081
Sechura, Peru	46.5	30.2	2.9	4.4	1.65	1.85	0.50	3.2	1.539	0.096
Sechura, Peru	46.8	32.1	2.9	4.5	2.19	2.10	0.55	1.9	1.458	0.090
Sechura, Peru	51.8	32.2	3.3	5.7	0.28	1.20	0.29	4.1	1.609	0.102
Sechura, Peru	46.7	31.8	3.1	4.6	1.29	2.23	0.58	2.0	1.468	0.097
Fluorapatite[1]	55.6	42.2	3.8	—	—	—	—	—	1.317	0.089

[1] Theoretical for $Ca_{10}(PO_4)_6F_2$.

portant economic differences among phosphate ores. The presence of free carbonates, chlorides, and other gangue minerals is an important guide to the mineral processing engineer, who has to upgrade the ore, and to the mineral consumer, who will convert it to the final product. In addition, the composition of the apatites may be useful in studying the origins of phosphorites and interpreting their geologic history.

Comparison of phosphate rocks

The compositions of a number of phosphate rocks are listed in Table 6; only the significant constituents are included. The Sechura samples taken during exploration are primarily from the upper phosphatic horizons.

The data show that all sedimentary phosphate rocks have higher CaO/P_2O_5 ratios than that in pure fluorapatite. This is because, as shown by the model in Table 2, the CaO in francolite-type apatites remains nearly constant while the P_2O_5 varies with substitution of carbonate and fluorine which raises the CaO/P_2O_5 ratio from 1.317 in fluorapatite to 1.620 in a highly substituted francolite. Similarly, the F/P_2O_5 ratio rises from 0.089 in fluorapatite to 0.148 in a highly substituted francolite.

The CaO/P_2O_5 ratios in Table 6 are difficult to interpret because of the isomorphous substitutions in francolite-type apatites and the frequent presence of calcite and dolomite as accessory minerals. The F/P_2O_5 ratio is more reliable as an indication of the composition of the apatite because the amounts of fluorine-bearing accessory minerals are insignificant in many sedimentary phosphate rocks. On the basis of the F/P_2O_5 ratio, the apatite in Sechura phosphate rock should have properties somewhat between those of the Taiba, Senegal, sedimentary apatites and the igneous Kola apatites.

Sechura sedimentary apatite

Good statistical correlations have been established between the crystal chemical compositions of francolite-type apatites and their unit-cell parameters and index of refraction (Figs. 17 and 18). Through use of the methods described by McClellan and Lehr (1969) and routine petrographic methods, these properties of the apatites in several sedimentary phosphate rocks were determined and are compared in Table 7.

The unit-cell data indicate that the Sechura apatites have compositions similar to those of the moderately high carbonate-substituted apatites characteristic of the Florida and Morocco deposits. The refractive index data indicate, however, that the Sechura apatites have the highest levels of carbonate substitution, such as that in North Carolina and Tunisia rocks. Apatites with these properties should have F/P_2O_5 ratios between 0.118 and 0.128 instead

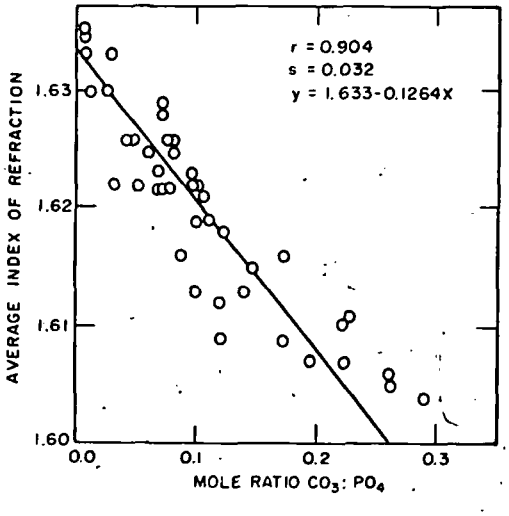

FIG. 17. Relation between refractive index and francolite composition.

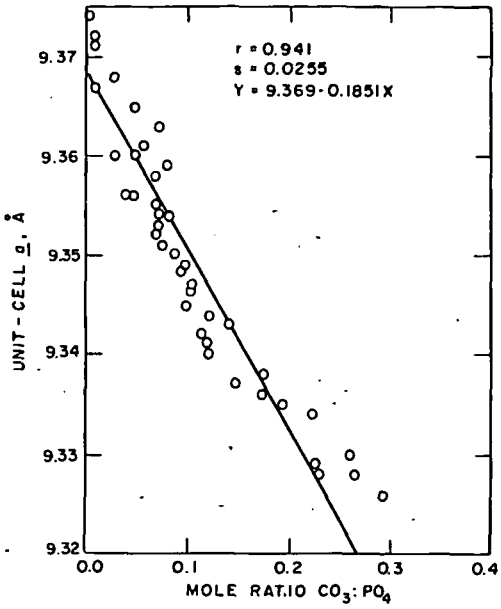

FIG. 18. Relation between unit-cell *a* parameter and francolite composition.

of the observed 0.090 to 0.102. This would indicate that the Sechura apatite is a fluorhydroxycarbonate apatite with an approximate empirical formula of

$$Ca_{9.68}Na_{0.23}Mg_{0.09}(PO_4)_{5.12}(CO_3)_{0.88}F_{1.79}(OH)_{0.56}.$$

In a typical francolite-type apatite, all the hydroxyls would be replaced by fluorine. Infrared absorption spectra of Sechura apatites, however, confirm the presence of hydroxyls by the weak O-H absorption bands at 2.8 and 15 microns on hand-picked phosphate pellets. Chemical measurements of reactivity based on solubility in dilute acids support the crystallographic data in showing that Sechura apatites are highly carbonate substituted.

The low fluorine content and high carbonate substitution found in the Sechura apatite may indicate a unique process of deposition of the phosphate. Burnett (1977) has shown recently that authigenic apatites with low F/P_2O_5 ratios are associated with Holocene diatomaceous oozes along the sea floor off the coasts of Chile and Peru. The silica in these deposits acts as a nucleation site for precipitation of phosphate. It is probable that the fluorine associated with the phosphate forms complexes with available silica, calcium, aluminum, and iron, and the solubility of these complexes is very pH dependent so that the fluorine might precipitate under conditions in which the phosphate is still soluble. This would lower the fluorine content of the pore water below that required for the stoichiometry of the apatites and so make the apatites deficient in fluorine.

The Sechura apatites thus may have resulted from a unique series of events in which authigenic phosphate, which has undergone little if any postdepositional alteration, is preserved in the presence of its diatomaceous source bed. Examinations by one author (G.H.M.) of hundreds of other sedimentary apatites from many locations around the world have revealed no other phosphate with the unique characteristics of the Sechura apatite. Other siliceous phosphorites from Colombia, Upper Volta, Australia, Pakistan, and the United States are the expected francolite-type apatites. The unusual properties of the Peruvian phosphorite should encourage others interested in the origin of phosphorites to use detailed mineralogical studies to interpret the geochemical evolution of these minerals.

TABLE 7. Crystallographic Data on Some Selected Apatites

Source	Unit-cell *a*, angstrom	Mean refractive index, η
Central Florida	9.336	1.613
North Florida	9.334	1.607
Morocco	9.341	1.618
Gafsa, Tunisia	9.326	1.602
Taiba, Senegal	9.352	1.621
Togo	9.351	1.619
Kola	9.365	1.630
North Carolina	9.322	1.602
Sechura[1]	9.336	1.601
Sechura[1]	9.340	1.604

[1] These ratios represent the maximum and minimum values measured on eight different samples of Sechura rock.

Summary and Conclusions

The Sechura sedimentary phosphate deposits are of Miocene age and are the world's largest known reserves in which the two principal components are phosphate and diatomite.

The low fluorine content and high carbonate contents of the Sechura apatite are unique and unmatched by any of hundreds of samples of sedimentary apatites from many worldwide locations that range in age from Proterozoic through the Tertiary. The Sechura apatite is most similar to the low-fluorine apatite associated with the Holocene diatomaceous ooze on the sea floor off the coasts of Chile and Peru as recently described by Burnett (1977).

More data are needed than presented here to explain all the details of the origin of the apatite, but the following conclusions have been reached.

1. The phosphate pellets in the phosphorite beds were subjected to the movement of currents after their formation; this removed smaller grained material from the area of deposition. The action of

currents is demonstrated by (a) the differences in sorting of the phosphorite pellets in the individual beds; a higher degree of sorting is accompanied by a higher P_2O_5 content, i.e., more pellets and less fine-grained interpellet dilutants, (b) tangential contacts of pellets, (c) erosional basal contacts of phosphorites with diatomites, and (d) local cross-bedding.

2. The diatomites and phosphatic diatomites were formed in areas subjected to much less current movement as evidenced by smaller grain size, poorer sorting of contained pellets, and planar basal contacts of diatomite with phosphorite.

3. Tectonism was taking place to a significant degree in the area as evidenced by the folding and erosion before deposition of the Clam Bore Sandstone and the presence of tuffs which indicate vulcanism in nearby areas.

Acknowledgments

Many people contributed directly to the success of the initial exploration. Chief among these were the late George L. Nicol, Edward S. Montgomery, Dr. Alberto Benevides, Dr. Charles F. Park, Jorge Vera Tudela, Joe Huseby, Kathleen Montgomery, and Hugo Ramirez B. Many others gave advice and suggestions that contributed indirectly to the results presented herein, such as Richard P. Sheldon, V. E. McKelvey, and David S. Robertson.

We are particularly indebted to Dr. Donald Everhart for his insistence and persistence in convincing us that the data and results presented herein would be of value 15 years after completion of the senior author's work in Sechura.

T. M. C.
Rio Doce Geologia e Mineração (Docegeo)
Grupo CVRD
Rio de Janeiro, Brazil
G. H. McC.
International Fertilizer Development Center
P. O. Box 2040
Muscle Shoals, Alabama 35660
E. S. M.
Duval Corporation
4715 East Fort Lowell
Tucson, Arizona 85712
October 6, 1978

REFERENCES

Altschuler, F. S., Jaffee, E. B., and Cuttitta, Frank, 1956, The aluminum phosphate zone of the Bone Valley Formation, Florida, and its uranium deposits: U. S. Geol. Survey Prof. Paper 300, p. 495–504.

Burnett, W. C., 1977, Geochemistry and origin of phosphorite deposits from off Peru and Chile: Geol. Soc. America Bull., v. 88, p. 813–823.

Lehr, J. R., McClellan, G. H., Smith J. P., and Frazier, A. W., 1967, Characterization of apatites in commercial phosphate rocks: Colloque International sur Les Phosphates Mineraux Solids, Toulouse, May 16–20, 1967.

MacDonald, G. H., 1956, Miocene of the Sechura Desert, Piura: Sociedad Geologica del Peru, Primeira Congresso Nacional de Geologia, Tome 30, p. 225–242.

McClellan, G. H., and Gremillion, L. R., 1976, Evaluation of Phosphatic Raw Materials: The role of phosphorus in Agriculture, joint TVA-ASA-CSSA-SSSA symposium, June 1–3, 1976, Muscle Shoals, Alabama.

McClellan, G. H., and Lehr, J. R., 1969, Crystal chemical investigation of natural apatites: Am. Mineralogist, v. 54, p. 1374–1391.

Moore, P. B., 1973, Pegmatite phosphate: Descriptive mineralogy and crystal chemistry: Mineralog. Record, v. 4, p. 103–130.

Trueman, N. A., 1965, The phosphate, volcanic and carbonate rocks of Christmas Island (Indian Ocean): Geol. Soc. Australia Jour., v. 12, p. 261–283.

SORPTION PROCESSES IN RARE ALKALINE ELEMENT TECHNOLOGY

SUBJ
MNG
SPIR

UDC 669.885.3

L. I. Vodolazov, S. S. Pokrovskii,
E. K. Spirin, L. I. Gromok, and G. S. Rodionova

Small amounts of rubidium and cesium pass into the liquid phase in processing carnallites, lepidolite, and non-ferrous ores containing hydromicas and chlorites. Even when the content of these elements in the production solutions is very low, the scales on which raw materials are processed at a number of non-ferrous metallurgy enterprises make it possible to regard these solutions as a potential source of rubidium and cesium salts as by-products, using sorption for extraction. Inorganic sorbents which are selective in relation to cesium are used for extraction, particularly zirconium and titanium phosphates [1], ferrocyanides of iron, nickel, and other heavy metals [2], and sorbents based upon manganese dioxide [3].

Ion exchangers with high mechanical strength used in pulp processes for extraction of gold, molybdenum, copper, etc. [4] were impregnated, and their efficiency compared[1] with that of natural manganese dioxide, a mineral sorbent with one of the highest capacities [5].

Sorption of cesium by natural manganese dioxide. In the extraction of cesium, the capacity of pyrolusite proved to be the same (200 mg/kg of sorbent) with various sizes (Table 1). This ensures that cesium is concentrated 60-70 times when it is extracted. Practically complete saturation of pyrolusite with cesium is achieved in 120 hr.

When the effective capacity of pyrolusite (at pH 8) and artificial manganese dioxide is the same, mechanical strength gives the latter some advantages.

Cesium extraction by natural pyrolusite with a sorption time of 1 hr in sulfuric acid (I) and nitric acid (II) solutions is as follows (in %):

C_{acid}, g/l	I	II	C_{acid}, g/l	I	II
5	100	100	100	19.1	7.6
10	96	93	150	6.6	0
25	80.1	74.8	200	0	0

Extraction of cesium E_{Cs} is fairly high (93-100%) with excess acidity in the sulfuric and nitric solutions (5-10 g/liter). Extraction falls to 27-80% with an increase in acidity to 25-50 g/liter, and 15-20% acid solutions can be used as eluents for desorption of cesium.

The efficiency of cesium absorption increases in an alkaline medium when the pH is brought up with potassium or sodium alkalis, but the capacity figures decline when ammonia is used.

Chemical and thermal activation were used to increase the capacity of natural manganese dioxide [6]. The complete dynamic exchange capacity (CDEC) of third-grade natural pyrolusite is 418 mg/kg of sorbent at an initial cesium concentration of 8 mg/liter. The CDEC of the pyrolusite increased slightly (to 420-474 mg/kg) after treatment with 20-80% H_2SO_4 in the cold; dry heat treatment at 80-160°C for 3 hr increased the CDEC to 548-585 mg/kg, while wet treatment with steam at 110-120°C for 1 hr raised the CDEC to 702 mg/kg. The CDEC of pyrolusite falls to 364 kg/kg of sorbent after treatment with 25% ammonia.

Thus it was confirmed that natural pyrolusite could be used to extract cesium from lean solutions with a concentration of 3-8 g/liter, and it was demonstrated that cesium could be concentrated 25-30 and 85 times at the sorption stage by using natural pyrolusite and pyrolusite activated with moist steam respectively.

Sorption of cesium by sorbents of ferrocyanide ion-exchanger type.

Ferrocyanide ion exchangers vary in their capacity to extract cesium from standard solutions (Table 2). These

Table 1
Effect of Pyrolusite Size Upon Kinetics of Cesium Sorption from Standard Solutions (C_{init} = 3 mg/liter)

Size, mm	Capacity of pyrolusite for cesium (mg/kg) in τ, hr						
	0.25	1.00	6.00	60.0	120	200	400
−0.074	110	130	170	184	191	200	200
−0.56+0.074	70	93	120	156	184	196	200
−0.92+0.56	60	71	100	134	181	200	200

Table 2
Effectiveness of Ion Exchanger Ferrocyaniding by Kazakov's Method [7]

Texsit	Ion exchanger base	Coordinating ion	Unit swelling, G, l/g	Bulk density, g/cm³	E, mg-eq/kg at C_p, mg/liter: 5	200
1	AV-17	Cu^{2+}	3.3	0.66	16.3	451
2	AAM-3	Fe^{3+}	2.17	0.57	29.4	470
3	VPR	Ni^{2+}	2.8	0.69	22.6	510
4	Amberlite, IRA-900	Cu^{2+}	4.4	0.67	17.1	136
5	Amberlite IRA-45	Cu^{2+}	2.6	0.67	9.0	126
6	KM-2p (t)	Cu^{2+}	3.3	0.72	64.5	743
7	KM-2p (g)	Cu^{2+}	3.6	0.78	140	1054

[1] S. G. Vecherkin took an active part in the work.

ion exchangers can be arranged in the following series according to efficiency in cesium absorption (CDEC) from a solution with an initial cesium concentration C_p = 5 mg/liter: KM-2p (g) > KM-2p (t) > AM-3 > VPK > IRA-900 > AV-17 > IRA-45. The positions in the CDEC series alter somewhat when the cesium equilibrium concentration increases to 200 mg/liter: KM-2p (g) > KM-2p (t) > VPK > AM-3 > AV-17 > IRA-900 > IRA-45. "Tseziit-7" sorbent based upon high-strength porous previously hydrolyzed KM-2p (g) cation exchanger has the maximum capacity for cesium in all cases: 140 and 1054 mg-eq/kg of sorbent. This capacity provides the solution for applied problems in cesium ion-exchange technology in the processing and refining of solutions.

The isothermal line parameters for cesium sorption on "Tseziit-7" Sorbent (Fig. 1) ensure that a small number of theoretical plates is necessary for complete extraction of cesium from solution.

It is apparent from the kinetic curves (Fig. 2) that equilibrium is established fairly quickly in the ion-exchange absorption process, i.e., in the course of 10-20 min, whereas several dozen hours are required in the case of pyrolusite.

Capacity gradually increases with a rise in the solution pH from 1.0, reaching a peak at pH 10-11 then falling sharply (Fig. 3). The high capacity over a wide range of pH values makes it possible to use "Tseziit-7" for by-product extraction both from solutions or pulps after acid decomposition of ore material and from natural waters and carnallites at pH 6-8.

Rubidium is sorbed with cesium in approximately the same amounts, although it has slight kinetic advantages (see Fig. 2).

Two solutions were used as examples to test efficiency in cesium extraction on "Tseziit-7" sorbent.

Example 1. Sulfuric acid solutions containing (in g/liter) 0.141 K, 0.48 Na, 0.005 Cs, 0.62 Ca, 0.726 Al, 0.475 Mo, 2.031 Fe_{total}, 0.813 Mn, 0.211 Mg, 26.6 SO_4^{2-}, and 11.3 H_2SO_4. The sulfuric acid solutions were passed through a column containing the sorbent at a speed of 2.18 m/hr (ratio of sorbent layer depth to column diameter 7 : 1). Solutions for disposal containing 0.5 mg/liter Cs were produced at the column outlet (90% extraction). The capacity of the saturated sorbent was 14.4 mg/g, giving alkali metal concentration of more than 2,000 times.

Example 2 [8]. Sorption of cesium and rubidium from carnallite solutions containing (in g/liter) 1.5 Cs, 274 Rb, 191 K, 18 Na, and 12.9 Mg was carried out under similar conditions. The solutions for disposal at the column outlet contained 0.4 mg/liter Cs (76% extraction). The capacity of the sorbent for cesium was 0.9 mg/g, which gives cesium concentration of ~ 600 times in the presence of a large excess of rubidium [8].

The possibility of extracting cesium from pulp. The development of the rare metals industry in recent years has involved the necessity for processing ores from new genetic types of rare metal deposit with exceptionally fine grain and complex mineral composition [9]. This calls for the use of new filtrationless sorption and solvent-extraction methods of extracting the useful constituents [4].

Acid leaching processes are used, among others, to expose cesium material [10]. Hydrohalic acids are most frequently used in these circumstances: hydrofluoric, hydrochloric, or hydrobromic, sulfuric acid being used only occasionally. The efficiency of the sulfuric acid leaching method is underestimated because of the existing methods of chemical refining; this alters significantly when sorption methods are used. Autoclave methods increase leaching efficiency [11], which in turn emphasizes the necessity for developing intensive processes for extracting cesium from pulps which are difficult to filter produced after leaching of clay material.

We attempted to extract cesium directly from pulps, using "Tseziit-7" as the sorbent. The physicochemical properties of the ion exchanger are as follows:

Ion exchanger	"Tseziit-7"
Structure	Porous
Granule size, mm	+0.8-1.5
Bulk density, g/ml	0.78
Unit swelling, ml/g	3.60
Salt form	K^+
Mechanical strength*, %	93.50

*In swollen state when grinding in a ball mill for 1 hr. in accordance with OST Standard 95.291-75.

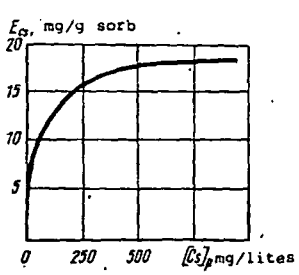

Fig. 1. Isothermal line for cesium sorption from lean salt solutions on "Tseziit-7" ion exchanger.

The efficiency of "Tseziit-7" sorbent in extracting cesium from pulps was tested in sulfuric acid pulp with excess acidity of 46.3 g/liter and a pulp liquid phase containing 4.8 mg/liter Cs, 12 mg/liter Rb, remainder (in g/liter) 0.87 K, 9.44 Na, 0.41 Fe^{3+}, 0.3 Al, 0.814 Ca and 0.270 Mg, 0.140 Mn^{2+} and 0.09 Si, and 50.1 SO_4^{2-} (combined).

The sorption process may slow down, due to an increase in pulp viscosity when its density increases. The capacity of the sorbent when 5 liters of pulp of various densities and 1 g of sorbent are mixed for 2 hr is as follows, mg/hr:

Y, g/l	s:l of pulp*	E_{Cs}, mg/g	Y, g/l	s:l of pulp*	E_{Cs}, mg/g
1.750	1:0.5	1.2	1.270	1:2	13.0
1.600	1:0.7	4.4	1.120	1:5	13.6
1.450	1:1	7.3	1.060	1:10	14.0
1.395	1:1.5	12.7	Pure clarified soln.	-	14.2

*Cs concentration same in pulp of various densities (4.8 mg/l).

It was apparent that the cesium capacity of the saturated sorbent was practically the same over the 1 : 1.5 to 1 : 10 range of solid-to-liquid ratios (12.7-14.0 mg/g of sorbent). When the pulp density increases to solid-to-liquid ratios of 1.1, 0.7, and 0.5 the capacity of the sorbent decreases to 7.3, 4.4, and 1.2 mg/g respectively. This indicates the necessity for regulating the pulp solid-to-liquid ratio within the 1 : 1.5 to 1 : 2 range before it is fed to the sorption process; this coincides with practice in the use of pulp processes in other branches of the national economy [4].

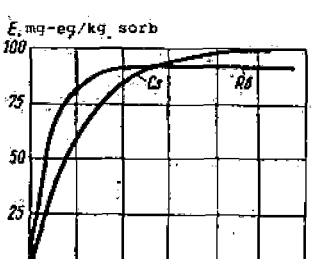

Fig. 2. Kinetics of "Tseziit-7" ion exchanger saturation with cesium and rubidium ions.

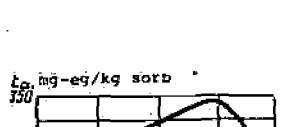

Fig. 3. Effect of solution pH upon capacity of "Tseziit-7" for cesium.

The efficiency of cesium extraction from pulps using "Tseziit-7" sorbent has been tested. It proved to be very high, because it was possible to extract ~ 90% Cs into the sorbent in a counterflow routine with only one Pachuca with a sorbent loading of 10% of pulp volume in the sorption cycle and a pulp time in the Pachuca of 1 hr. The initial pulp contained 4.8 mg/liter Cs, while the treated pulp at the apparatus outlet contained < 0.5 mg/liter Cs; E_{Cs} = 12.7 mg/g of sorbent, E_{Rb} = 9.36 mg/g of sorbent, and only 0.5 mg of sodium per g of sorbent. Thus a cesium concentration rate of over 2,000 times was achieved in the process of cesium sorption from sulfuric acid pulps, while the rubidium concentration rate was only 600 times. The coefficient of cesium purification in terms of sodium is 24.

Separate desorption of cesium and rubidium from the saturated sorbent is easy to achieve by generally known methods, using eluents of ammonium nitrate type [12], ammonium chloride, which has successfully withstood pilot-plant tests [13], or nitric acid [14].

REFERENCES

1. C. Amphlett, Inorganic Ion Exchangers, Moscow, Mir, 1966, 118 pages, illustrated.
2. I. V. Tananaev, G. B. Seifer, Yu. Ya. Kharitonov, et al., The Chemistry of Ferrocyanides, Moscow, Nauka, 1971, 237 pages, illustrated.
3. V. V. Vol'khin and G. V. Leont'eva, Neorganicheskie Materialy, 1969, No. 5, 122-127.
4. B. N. Laskorin, Tsvetnye Metally, 1975, No. 8, 10-13.
5. A. I. Mun, A. S. Sabaev, R. S. Darer, et al., Izv. Akad. Nauk Kazakh SSR, Seriya Khimicheskaya, 1974, No. 5, 16-20.
6. E. Aripov, Activation and Modification of Natural Mineral Sorbents, Tashkent, Branch of Academy of Sciences, 1970, 136 pages, illustrated.
7. E. V. Kazakov and I. F. Karpova, Vestnik Leningrad. Gos. Univ., 1967, No. 4, Issue 1, 136-137.
8. E. K. Spirin, L. I. Gromok, G. S. Rodionova, et al., Summaries of All-Union Conference on Solvent Extraction and Sorption of Rare Alkaline Elements, Novosibirsk, Siberian Section, Academy of Sciences of the USSR, 1976, pp. 32-33.
9. V. A. Solodov and N. F. Chelishchev, in: Research in the Field of Rare and Trace Elements, Moscow, 1975, pp. 8-19.
10. V. E. Plyushchev and B. D. Stepin, Chemistry and Technology of Lithium, Rubidium, and Cesium Compounds, Moscow, Khimiya, 1970, 334 pages, illustrated.
11. L. V. Zverev, N. V. Petrova, N. S. Mikhailova, et al., in: Hydrometallurgy - 74, Moscow, Nauka, 1974, pp. 60-61.
12. J. Inorg. Nucl. Chem., 1964, 26, 1761-1765.
13. B. I. Yakovenko, E. I. El'tsov, and V. V. Vol'khin, Tsvetnaya Metallurgiya, 1975, No. 4, 34-46.
14. E. V. Kazakov and N. A. Ovchinnikova, Ion-Exchange Materials in the National Economy, Moscow, Khimiya, 1975 (NIITEKhIM), pp. 69-70.

SUBJ
MNG
SPMD

SYNOPSIS OF PRECIOUS METAL DEPOSITS
through 1977
by Bruce Kilpatrick

GOLD

Alaska-Juneau SE Alaska
Quartz veins in slate and greenstone w arsenopyrite, sphal., gal.
Bulk mined 1880-1944.
Production: 2,874,361 oz Au + approx. $2x10^6$ oz Ag.
References: USGS Prof. Paper 610; USGS Bull. 287.

Carlin deposit Nevada, USA
Epithermal (disseminated)--Leached carbonate strata of Roberts Mtn. Formation in window of Roberts Mtn. thrust fault continuous dissemination. Au Assoc. with Hg, As, Sb in silic & pyritized zone. Oxide + carbonac. ore.
Production: present avg. grade ∿ 0.15 oz Au/ton, 2000 tpd open pit mine.
References: Hansen & Kerr, 1968, in Ore Deposits of US 1933-1967, p. 908-940; Min. Cong. Jour. (1965), v. 52, no. 11, p. 26-39; Nev. Bur. Mines Rept. 13, pt. A, p. 73-83.

Concepcion del Oro Mexico
Pyronutasematic
References: USGS Prof. Paper 424D, p. 316-320; USGS Circ. 534; Econ. Geol. v. 64, p. 526-537.

Cortez deposit Nevada, USA
Epithermal (disseminated)--Au in silty, carbonac. limestone of Roberts Mtn. Formation (in window of Roberts Mtn. thrust fault). Calcite replaced by silica central ore zone.
References: USGS Prof. Paper 424D, p. 316-320; USGS Circ. 534; Econ. Geol., v. 64, p. 526-537.

Cripple Creek district Colorado, USA
Epithermal Tert. volcanics in steep-walled caldera cutting Pε granite & gneiss. Alkalic dikes cut volcanics. Mineralization qtz.-fluorite-pyrite veins; Au/ Ag telluride in qtz-carbonate veins, w/py, shal., gal., tetrahed; qtz-w/py, Hgs, calcite in fract.
Production: 1891-1959--19,100,867 oz Au.
References: USGS Prof. Paper 610, p. 117-118; Colo. Sci. Soc. Proc., v. 13 no. 6, p. 217-435; USGS Bull. 955B, p. 19-60; Mineral Res. of Colo., 1947, p. 387.

Getchell mine Nevada, USA
Epithermal (disseminated)
References: Econ. Geol. v. 46, p. 267-309; USGS Bull. 1198A,

Goldfield district Nevada, USA
Epithermal--Tert. volcanics (dacite, andesite, rhyolite) cut by silicfied shear zones w/complex sulfides (bi) + dissem. native Au. Alunite common gangue.
Production: 1903-1959, 4,194,800 oz Au + minor Ag.
References: USGS Prof. Paper 610, p. 177-178; USGS Prof. Paper 66, 1909; Nevada Univ. Bull., v. 42, no. 5 Geol. & Mining Serv. 48; Econ. Geol., v. 68, p. 747-764.

Grass Valley district California, USA
(incl. Nevada City)
Qtz. veins in granodior-greenstone (serpent. + diabase), assoc. w/py, gal.,

sphal., arsenopy, cp.
Production: approx. 10,408,000 oz Au from lodes + 2,200,000 from placers
References: USGS Prof. Paper 610, p. 70-71; USGS Prof. Paper 194 (1940).

Homestake mine South Dakota, USA
Qtz. veins in Pε greenstone; qtz. lodes localized in folds, assoc. w/ minor pyrrhotite, py., arsenopy. in cummingtonite schist.
Production: total 6,554,249 oz Ag + 27,961,276 oz Au 1878-1965; mined underground. tons ore 1941-1965: 32,979,000; oz Au 11,478,088--avg. grade 0.34 oz/ton. oz Ag 1941-1965=2,352,824; avg. Ag grade=0.07 oz/ton. Early product 0.7 oz Au/ton; 0.32 oz/ton by 1880.
References: Slaughter, in Ridge ed., 1968, Ore Deposits in U.S. 1933-1967, AIME, N.Y. p. 1438-1459; USGS Prof. Paper 610, p. ; GSA Bull., v. 61, p. 221-251 (1950).

Kalgoorlie district Western Australia
Qtz. veins in Pε greenstone
Production: (1895-1971) 92×10^6 m. tons; 1,107,721, kg Au, avg. 12 g/ton or, 33.56×10^6 oz @ 0.36 oz/ton.
References: Aust. Inst. Min. Met., Monograph 5

Kirkland Lake district Ontario, Canada
Qtz. veins in Pε greenstone-Au + AuTe in fissure qtz. veins, shear zones, stkwks in syenite & mineralized meta rhyolite. (Alkakic igneous rx) major deposits in fault zones, assoc. w/qtz., carbonates, minor sulfides. Irreg. stkwrk zones common. Very deep (+8000 ft). One genesis prob. related to alkalic volcanism + subvolcanic instrus; assoc. iron formation.
Production: 93.6×10^6 ton, ore, 34×10^6 oz Au, 4.9×10^6 Ag-avg. 0.36 cr Au/ton, 0.05 oz. Ag/ton. (as of 1962, re Goodwin, 1965)
References: GSC Geol. Rept. 1, v.1, 1970, Geology and Economic Minerals of Canada (5th ed.); Canada Dept. Mines and Resources, Econ. Geol., Ser. no. 15, 1946, Canadian Lode Gold Areas.; Econ. Geol., v. 60, no. 5, p. 955-971; Ont. Dept. Mines Ann. Rept. v. 57, pt. 5, p. 54-188; Ont. Dept. 644-653; 24th Int. Geol. Congress Guidebook A39, p. 27-95; Geol. Soc. Can. Prodc. v. 21, p. 33-42.
Resources: (1966) at: Kerr. Addison mine 4.6×10^6 tons @ 0.44 oz Au/top Macassa Mine--4.6×10^6 tons at 0.43 oz Au/ton. Upper Canada Mine-4.1×10^6 tons @ 0.30 oz. Au/ton.

Kolar Goldfield Mysone, India
Qtz. veins in Pε greenstone.
References: Emmons, 1937, Gold Deposits of the World; Econ. Geol. v. 55, p. 1429-1459; Econ. Geol., v. 42, p. 93-136; Econ. Geol. v. 34, p. 622-653.

Morro Velho Minais Gerais, Brazil
Qtz. veins in Pε greenstone--metased + metavolcanics. Qtz. w/pyrrhotite, arsenopy + py selectively replacing granlite bed. Minor WO_4 mineral assoc. Au avg. 0.25-0.3002/ton, evenly distributed along lode.
Production: 1834--present.
References: Park and MacDiarmid, 1964, Ore Deposits, p. 272-278; Matheson, 1956, Can. Min. Met. Bull., v. 77, p. 1-7.

Mother Lode district California, USA
Qtz. veins in greenstones. Mineralized belt 1-4 mi. wide x 120 mi. long along west flank Sierra Nevada. Slates, phyllite, amphib. + greenstone cut by serpent.; gabbro, granodior. Tabular qtz. veins w/minor assoc. sulfides free Au. (arsenopy, + py.) w./qtz, ankerite, albite. Total

product. approx. 12,779,700 oz from several hundred mines.
References: USGS Prof. Paper 610, p. 55-57; USBM Bull. 413 (1938); USBM Bull. 424, 1940; Calif. Jour. Mines & Geol. v. 51, no. 1, p. 369-591 (1956) USGS Prof. Paper 157 (1929).

Porcupine district — Ontario, Canada
Qtz. veins in Pε greenstone--qtz-carbonate veins in metavolcanics + metasediments, assoc. w/minor sulfides (py + pyrrh.) near vol.-sed., contact and meta proph. intrusives (subvolcanic) Stkwrks + dissem.
Production: 187.2×10^6 tons ore, 49×10^6 Ag-avg. grade 0.26 oz Au/ton, 0.05 oz Ag/ton. (as of 1962, re Goodwin, 1965). Dome Mines Ltd. presently mining to 5000 ft., 2000 tpd @ 0.22 oz Au/ton. Costs reported at $20/ton, or $90/oz.
Reserves: 1.9×10^6 tons.
References: G.S.C. Geol. Rept. 1, v. 1, 1970, Geology and Economic Minerals of Canada (5th ed.), Canada Dept. Mines & Resources Econ. Geol. Ser. no. 15, 1946, Canadian Lode Gold Areas; Struct. Geol. Can. Ore Deposits: CIMM, p. 442-456; Econ. Geol., v. 60, no. 5, p. 955-971; 24th Int. Geol. Cong. Guidebook A-39, p. 57-73.

Republic district — Washington, USA (GOLD-SILVER)
Epithermal-Tertiary volcanics and volcanic clastics (dom. andesite + rhyodanite cut by veins of chalcedonic qtz + silic zones q/py, stephanite, namannite, native Ag + electrum as fine dissem.
Production: 2,500,000 tons ore, gross value $50 million, est. 836,393 oz Au 1896-1959; avg. grade ∿ 0.33 oz/ton.
References: USGS Prof. Paper 610; Full in Ore Deposits of US 1933-1967, AME, p. 1481-1494.

Treadwell Group — SE Alaska
Disseminations + minor qtz. veins w/arsenopy, in greenstones; Bulk mined (caved) 1880-1922.
Production: 1880-1905, approx. 1,328,000 oz Au from 18×10^6 tons ore.
References: USGS Prof. Paper 610, (1968), USGS Bull. 755A. (1924), USGS Bull. 662B (1918).

Witwatersrand district — South Africa
Fossil Placer-Au in Pε cgl.
References: Pelleteir, 1964, Mineral Resources of South-Central Africa; Boveluvs, 1961, Commonwealth Mining Met. Cong. 7th, So. Africa, trans. V. 2, p. 489-506 EMJ; Econ. Geol. v. 71, p. 157-176.

SILVER

Bathurst District
Byproduct Ag in massive sulfides.
References: Can. Ins. Min. Met., v. 63, p. 24-29, 66-73; Geol. Survey Canada Bull. 160.

Broken Hill Australia
Byproduct Ag in massive sulfides.
References: Geol. Soc. American Bull., v. 61, p. 1369-1437; 5th Empire Min. & Met. Cong. Geol. Australian Ore Deposits, v. 1, p. 578-600, 658-673; Proc. Aust. Inst. Min. Met. no. 198, p. 309-367; Proc. Aust. Inst. Min. Met. no. 67, p. 187-219.

Buchans deposit Newfoundland, Canada
Byproduct Ag in massive sulfides. Paleoz. volcanics and clastic sediments w/ large lenses of mass. Sulfides in volc. breccia & tuff. Mineralization galena, sphalertite, chalcopy., tetrahed., py. Avg. grade ore 15.5% zn, 7.8% Pb, 1.4% cu., 3.5 oz/ton Ag, 0.05 oz/ton Au. Ag native, argentite, tetrahed., gal. (GSC Bull. 160)
Production: 16×10^6 tons ore @ 14.9% zn, 7.7% Pb, 1.36% cu, 3.7 oz Ag, 0.045 oz Au (1928-1975)--total 59.2×10^6 oz Ag.
References: Can. Inst. Min. Met. Trans. v LXV, p. 288-296; Geol. Survey Canada Bull. 160, p. 161; Econ. Geol. v. 70, p. 130-144.

Butte district Montana, USA
Byproduct Ag in Cu-Pb-Zn; replacements & veins. Composite vein system in Laramide qtz. monz. batholith. Vein mineralization displays crudely concentric zones of manganese & zinc around a central zone of copper. Dissem. Cu-Mo mineralization toward center & at depth. Cu mineral is cp.-born.-enarg., covell-digenite. Secondary Cu enrichment near surface important. Veins mined to 5000 ft. deep.
Production: (1880-1964): 326.8×10^6 tons ore, 16.19×10^9 lb. Cu, 4.792×10^9 lb Zn, 3.703×10^9 lb Mn, 836.7×10^6 lb Pb, 644.8×10^6 oz Ag, 2.506×10^6 oz Au. Avg. grades: 1.97 oz Ag/ton.
References: Meyer, Charles and others, 1968, Ore Deposits at Butte, Montana, in Ridge, J.D. (ed.) Ore Deposits in the United States 1933-1967.

Casapalca district Peru
Ag-base metal veins
References: Econ. Geol. v. 60, p. 407-476; Econ. Geol. v. 27, p. 501-524, Econ. Geol., v. 72, p. 943-1016.

Cerro de Pasco deposit Peru
Byproduct Ag in Pb-Zn (+ Cu) replacement mainly l.s.; folded Triassic ls. intruded by Tert. volcanic vent (pyroclast. bx cut by plugs & dikes of qtz. monz. porph. Massive replacement of l.s. by funnel shaped qtz. pyrite body cut by fissure veins. Also funnel-shaped Pb-Zn mass superimposed on pyrite. Enarg.-tetrahed. veins cut Pb-Zn mineralization. Also pipes of mass pyrrhotite in central part of ore zone.
Production: (1906-1976) 65.9×10^6 tons, 215.1×10^6 oz Ag; avg. grade 3.26 oz Ag/ton. Est. total 100×10^6 tons pyrite, 4×10^6 tons Zn, 2×10^6 tons Pb, + 1×10^6 tons Cu, 2.4×10^8 oz Ag. (10^4 tons.)
References: Econ. Geol. v. 72, no. 6, p. 893-924, Econ. Geol. v. 60, p. 407-476; Econ. Geol. v. 56, p. 402-422.

Cobalt district Ontario, Canada
Co-Ag veins; Pε metavolcanics and metasediments overlain by diabase sill. Fault controlled veins in greenstones & overlying clastic metasediments. Veins contain native Ag and Co-Ni arsenides (cobaltite, smaltite, skutterudite, etc.) in calcite gangue.

Production: (1904-1964) $400x10^6$ oz Ag, $25x10^6$ lb Co, $3x10^6$ lb Ni, $1.5x10^6$ lb Cu.
References: Geol. Survey Canada Bull. 160, p. 164-169; Thomson in Struct. Geol. Canada Ore Deposits, v. 2, p. 377-388; Econ. Geol., v. 20, p. 1-24.

Coeur D'Alene district — Idaho, USA
Mesothermal. Ag-base metal veins. Argillites and qtzites of Pε Belt Group cut by fault-controlled vein system. Mineralization weak near surface, but improves with depth, espec. in qtzite horizon. Ore shoots very persistent with depth (2000-4000 ft). Gal.-sphal. most common sulfides, followed by tetrahed., cp., py., arsenopy, in siderite gaugue. District zoning, Zn-Pb-Cu, west to east. Ag highest in tetrahed, but also in gal. + sphal. Avg. grade Ag mined 20-30 oz/ton. Individ. ore zones $0.5\text{-}2.0x10^6$ tons.
Production: (1884-1965) $705.3x10^6$ oz Ag, $112x10^3$ tons Cu, $6.90x10^6$ tons Pb, $2.45x10^6$ tons Zn.
References: Hobbs, S.W., in Ore Deposits US 1933-1967, p. 1418-1434; USGS Prof. Paper 445.

Candalaria — Nevada, USA
Bulk low grade, Ag deposits: Tuffac. shales of Jura-Triassic Candelaria Fm. cut by veins & contain dissem. w/jaros. Epithermal. FeOx after sulfides. Considerable oxide Ag ore produced 1870-1890. (Presently controlled by Occidental Minerals, sublease from Congdon & Coney?) Primary mineralization py., gal., cp., arsenopy. Oxides limonite MnOx, $PbSo_4$, $ZnCo_3$.
Production: Est. low grade ore $10\text{-}30x10^6$ tons @ 3 oz. Ag-prob (1870-1890) production $20x10^6$ oz Ag? Potential $90x10^6$ oz Ag?
References: Watson, 1976; USGS Bull. 610, USGS Bull. 735A, p. 1-22.

Delamar Silver Mine — Idaho, USA
Bulk low-grade Ag deposit, Epithermal; Tert. rhyolite volcanics cut by silic. veins with Ag selenides (naumannite) + minor sulfides. Deposit being operated by Earth Resources.
Production: Est. $10\text{-}20x10^6$ tons reserves (10 provm) @ 4.5 oz Ag ton. Annual Ag product. $2.5x10^6$ oz. total by approx. $30x10^6$ oz. Substant. Au produced in early years.
References: Watson, 1976; Geol. Bull. 138.

East Tintic district — Utah, USA
Byproduct Ag in Pb-Zn replacements (mainly l.s.) Blind ore bodies in Paleoz. sed. (mainly ls + dolom.) concealed beneath hydrothermal altered volcanics. Massive replacements in ls contain Ag, Pb, Zn, Mn. fissure veins in qtzites contain Au, Ag, Cu. Main ore minerals argentite, gal. & sphal. w/minor argent. tennant, proustite, rtemi? barite, rhodochros, calcite, qtz., jasper, gangue. Native Au + tetrahed., enargite in veins. Extensive secondary minerals in oxide zone, with included supergene Ag ore locally.
Production: (1909-1966) $3.617x10^6$ tons ore, $5.37x4x10^5$ oz Au, $62.81x10^6$ oz Ag, $27.65x10^6$ lb Cu, $743.0x10^6$ lb Pb, $28.44x10^6$ lb Zn. Avg. grade: 17.4 oz Ag/ton locally ore much higher grade Ag; 20-30 oz Common in gal. Veins avg.
References: Shepard, W.M., 1968, Ore Deposits US 1933-1967, p. 941-963.

Flathead (Hog Heaven) — Montana, USA
Bulk low-grade Ag deposit, Epithermal; Tert. alkalic volcanics overlying Pε Belt sediments. Silic veins & bx zones in volcanics + dissem. in volcaniclastic sediments. Primary mineralization py., gal., mutildite, enarg., Mine area owned by Annaconda, controlled by Congdon & Carey = CoCa Mines.
Production: (1928-64)--Approx. $7x10^6$ oz Ag, $23x10^6$ lb Pb, form. $230x10^3$ tons ore. Aug Ag grade $\sim$ 30 oz/ton. Pot. low grade mineralization 3-4 oz/ton, tonnage $10\text{-}20x10^6$ tons?

References: Watson, 1976, Mont. Bur Mines Geol. Bull. 79, p. 137-142.

Fresnillo mine Zacatecas, Mexico
Ag. base metal veins.

Gilman Colorado, USA
Byproduct Ag in Cu-Pb-Zn replacements & veins; Paleoz. sediments intruded by Tert. qtz latite sill. Ore is mass. sulfide replacement in carbonate strata (dolomitized Miss. l.s.)--pipe-like mantos & funnel-shaped chimneys. Ore minerals near mabite + galena in pyrite-siderite & gaugue in mantos. Chimneys have py, cp, tetrahed, freiberg., galena + sphal.
Production: (1880-1964) 10×10^6 tons ore, 348,000 oz Au, 6.41×10^6 oz Ag, 206.2×10^6 lb Cu, 255.6×10^6 lb Pb, 1.294×10^9 lb Zn. Avg. grades: 6.4 ox Ag/ton
References: Radebaugh, 1968, in Ore Deposits in the U.S. 1933-1967, p. 641-663.

Guanajuato district Mexico
Epithermal-veins + lodes; Mesozoic sediments cut by granite intrus. overlain by Tert., cgl. & volcanics, all cut by qtz-calc.-adularia veins along NW faults. Also stockworks along veins struct. 20 to 90 m. wide. Main Ag minerals acanthite, aguilarite, naumannite. Also native Au + electrum. Sulfide ore avg. 13.6 oz Ag/ton, 0.076 oz Au/ton. Ore shoots fade out at depth, but veins persist. Deep ore discovered in "lower" ore zone. (Up. & lwr zone in veins separated by barre zone.)
Production: $> 1 \times 10^9$ oz Ag + 4×10^6 oz Au (1550-1970)
References: Econ. Geol., v. 70, p. 1175-1189; Econ. Geol., v. 69, p. 1078-1085. Econ. Geol., v. 23, p. 1-44; Cons. Rec. Nat. No. Rev. Pub. 17E.

Hardshell deposit Arizona, USA
Bulk low-grade Ag deposit, epithermal; Mesozoic volcanics + volcaniclastics overlying Paleoz. carbonates. Mauto-like replacement by silica, py, trgal. + MnOx. Ag in secondary minerals (halides, MnOx, etc.) Refractory ore.
Production: Est. 10×10^6 tons @ 4.5 oz Ag (poss. larger)
References: Watson, 1976.

Hornsilver deposit (San Francisco district) Utah, USA
Epithermal veins + lodes
References: U.S. Geol. Survey Prof Paper 80, USGS Prof Paper 111, Utah Min. & Geol. Survey Bull. 73.

Iron King mine Arizona, USA
Byproduct Ag in massive sulfides; massive sulfides in Pε metavolcanics at contact between rhyolitic tuff and andesitic tuffs & sediments. Series of conformable en-echelon lenses of mass. py., qtz., sphal., & gal., cp-rich zone in hanging wall.
Production: (1906-64) 5.007×10^6 tons ore, 616.5×10^3 oz Au, 18.49×10^6 oz Ag, 250.7×10^6 lb. Pb, 735.1×10^6 lb Zn, 19.10×10^6 lb Cu. Ave grades: 3.69 oz/ton Ag, 0.123 oz/ton Au.
References: Gilmour and Still, in Ore Deposits US 1933-1967, p. 1239-1255.

Jerome (United Verde, UVX) Arizona, USA
Byproduct Ag in massive sulfides
References: USGS Prof. Paper 308.

Kidd Creek (Timmins) Ontario, Canada
Byproduct Ag from massive sulfides; Massive sulfide deposit in Atabiti greenstone belt-complexly folded Pε metavolcanics & metasediments. Deposit is concordant lens in steeply dipping rhyolitic volcaniclastics overlain by barren mafic volcanics. Ore dominantly prite, lesser sphalerite, minor cp., tr. galena. Ag occurs native & in acanthite, tetrahed., tennant., stromeyerite, stephanite,

pyrargerite, pearceite. Sn minor component of ore. Ore averages 4.3 oz Ag/ton. Production: (1964-1975) $25x10^6$ tons ore avg. 9.75% zn, 1.52% cu, 0.40% Pb, 4.3 oz Ag ($107x5x10^6$ oz total) Ore reserves + $100x10^6$ tons; i.e. > $500x10^6$ oz Ag production approx. 10,000 tpd., ∿ $15x10^6$ oz Ag 1 year.
References: Econ. Geol. v. 70, no. 1, p. 80-89.

Kuroko deposits — Japan
Byproduct Ag in massive sulfides; Kuroko deposits massive sulfide lenses in Tert. volcanics-zoned ore. Cp-rich yellow (oko) pyritic ore, banded black (kuroko) ore mainly gal.-spha., w/abund. tetrahed + tennatite bearing Ag. Ag grades in Kuroko ore between 200 & 1000 gm/ton (6 to 30 oz.)
Production:
References: Tatsunie, Volcanism & Ore Genesis.

Leadville district — Colorado, USA
Byproduct Ag in Pb-Zn replacements; Deposits occur as manto & pipe-like replacements, also veins, pods, and stockworles. Manto, occur in dolom. beneath porphyry sills or quartzite, beds, often have vein "roots" or branches. (mainly l.s.) Extensive dikinutucm alteration halos. Primary ore mainly mix of py., spal., gal., in jaspery-ankerite gaugue (also abund. $MnCo_3$) Ag contained as argentite. Grade avg. 12-15% comb. Pb-zn, w/2-4 oz Ag/ton. Veins contain more Au + Ag than mantos-Ag in argent, tetrahed, pyarg. Secondary mineralization important-oxidat. 500 ft deep; supergene enrichment of Ag + Cu also Au. Most Ag produced from supergene ore.
Production: $2.986x10^6$ oz Au, $240x10^6$ Ag, 33,109 tons Cu, $1.088x10^6$ tons Pb, $7.854x10^5$ tons Zn.
References: in Ore Deposits US 1933-1967, p. 681-704.

Magma mine — Arizona, USA
Byproduct Ag in CuPbZn, replacement & veins; Mesothermal vein cutting Pε metamorphics + Pε & Paleoz. sediments. Also replacement in Devon. l.s., Minerals cp born., enarg., tennantite, chalcocite, sphal. Orig. was much supergene Ag enrichment upper part of mine in oxide zone. Mined underground to 4900 ft. Most current production from l.s. replacement ore.
Production: 1911-1964--13,696,000 tons ore; $1.42x10^9$ lb. Cu, $25.12x10^6$ oz Ag--avg. grade 5.69% Cu, 1.93 oz Ag/ton.
References: Hammer and Peterson, 1968 in Ore Deposits in US, 1933-1967, p. 1282-1309.

Mount Isa — Australia
Byproduct Ag in massive sulfides.
Production: (1930-1975)--$41.6x10^6$ m. tons @ 3.0% Cu; $32.6x10^6$ m. tons @ 7.4% Pb, 5.8% Zn, 178g/ton Ag. total--$5.8x10^9$g tg (175x10^6 oz); 5.4 oz/ton
Reserves: $140x10^6$ m. tons @ 3.0% Cu; $56x10^6$ m. tons @ 6.9% Pb, 6.3% Zn, 149g/ton Ag (4.5 oz/ton). Total $8.34x10^9$ g. Ag, or $14.14x10^9$g orig.--$42.7x10^6$ oz.
References: Int. Geol. Congr., 18th, pt. 7, p. 195-205; 5th Emp. Min. Met. Congr., Geol. Australian Ore Deposits; p. 578-600; Mongraph 5, Aust. Inst. Min. Met.

Pachua district — Hidalgo, Mexico
Epithermal-Tertiary volcanics (andesite, dacite, rhyolite) cut by fault-controlled veins. Ore in qtz., w/py, sphal., galena., cp, argent, polybasite, stephanite, acanthite (both hyp. & supergene). Gangue calcite, dolom., rhodochros, barite. Oreshoots stop below surface (60-800 ft). Dissem. in wall rx. Ore peters out with depth (1000-2000 ft.) Abund. supergene Ag enrichment.
Production: 1526 to present--est. 40,000 tons Ag. Ag/Au=200/1 or, est. $960x10^6$ oz Ag total.
References: Park and MacDiarmid, Ore Deposits, p. 323-327 ; Econ. Geol., v. 43, p. 53-65; AIME Trans. v. 66, p. 27-41; Wisser, 1942, in Ore Deposits as related to structural features.

Park City district Utah, USA
Byproduct Ag in Pb-Zn replacements (mainly l.s.) Lodge and bedded replacements in folded and faulted Permo-Triassic sediments cut by diorite intrusives. Replacements mainly in l.s. & qtzite of Park City fm. Mineralization galena, tetrahed, sphal., py in qtz-calcite gangue, locally oxidized. Supergene Ag enrichment, locally important.
Production: (1875-1964) $14x64x10^6$ tons ore, $9.721x10^5$ oz Au, $237.6x10^6$ oz Ag, $2.541x10^9$ lb Pb, $1.316x10^9$ lb Zn, $1.099x10^8$ lb Cu. Avg. grade-16.2 oz A/ton, but much ore 20 oz Ag or better. Park City ventures reserves $3x10^6$ tons proven @ 6-9% Pb, 4-5 oz Ag, 7-12% Zn, .01 Au, 0.2 Cu.
References: Barnes and Simos, 1968, in Ore Deposits of US 1933-1967, p. 1102-1126.

Pioche district Nevada, USA
Byproduct Ag in PbZn replacement (mainly l.s.) Cambrian qtzite with fissure veins + bedded replacements in l.s. Mineralization spahl. + argentite galena, assoc. w/py. & abund manganite., siderite. Strong oxidation, with extensive Mn,feOx, Supergene enrich. or Ag. MnOx shipped, ore divided into oxide & sulfide.
Production: approx. $6x10^6$ tons ore (1924-53), $25x10^6$ oz Ag. grade mined w/ore type, but overall avg. 4.4 oz/ton.
References: Geunill, in Ore Deposits US 1933-1967, p. 1129-1146; USGS Prof. Paper 171.

Potosi deposits Bolivia
Epithermal-veins + lodes; Funnel-shaped mass of Tert. quartz porph intruding tuffs cut by multiple veins & stockwoks, sheeted zones w/qtz., qtz., arsenopy., stannite, py., cassiterite + complex Ag-bearing sulfides + sulfosalts (tetrahed., proustite, etc.) at higher levels of deposit. Primary Ag-Sn ore avg. 10-15 oz/ton Ag, 1-5% Sn. Deep oxidation (+1000 ft), with extensive supergene enrichment of Ag (limon., cerargyrite, native Ag, argent., proustite) Enriched ores Avg. 100 oz Ag/ton.
Production: (1544-1960)-- + $2x10^9$ oz Ag.
References: GSC Bull. 160, Econ. Geol., v. 55, p. 217-254, 574, 606--Econ. Geol., v. 66, p. 215-255; Econ. Geol. v. 23, p. 253-262.

Real de los Angeles Zacatecas, Mexico
Bulk low grade Ag deposit (epithermal); Calcar. Cretaceous sandstones + siltstones cut by veins & stockworks, + dissem. Mineralization Ag-gal., sphal., py., arsenopy + minor cp. + tetrahed.
Production: Est. $50x10^6$ tons @ 2.5 oz. Ag/tons, 1% Pb, 1% Zn.
References: Watson, 1976.

Rochester district Nevada, USA
Bulk low-grade Ag deposit (epithermal), Mesozoic, metarhyol + trachyitic volc. cut by qtz veins & stockwoks + dissem. Mineralization Ag-gal., sphal., py., arsenopy, + minor cp. + tetrahed.
Production: Est. $50x10^6$ tons @ 2.5 oz Ag/ton, 1% Pb, 1% Zn.
References: Watson, 1976.

Rochester district Nevada, USA
Bulk low-grade Ag deposit (epithermal), Mesozoic, metarhyol + trachyitic volc. cut by qtz veins & stockwoks with Ag, mainly in limon. oxides. Orgi. production from supergene-enriched zones. Property controlled by Asarco.
Production: (1912-1929) Tonnage-low grade not known; avg. grade 2-4 oz Ag/ton?
References: Watson, 1976; USGS Bull. 762.

Sam Goosly deposit British Columbia, Canada
Bulk low grade; Ag deposit (epithermal); Jurass. andes. tuffs + breccias with dissem. + stockwok veinlets cut by syenitic stock. Mineralization py, cp,

pyrrh., sphal. Deposit controlled by Congdon and Carey; under development.
Production: Est. $40x10^6$ tons (+) @ 7.8 oz Ag, 0.33 Cu, 0.02 Au--potential $120x10^6$ oz Ag.
References: Watson, 1976.

Santa Eulalia district — Chihuahua, Mexico
Byproduct silver in Pb-Zn replacements (mainly l.s.); Cretac. limestones, shales, argillites, cut by porph. dikes & sills, Mass. bedded replacements in l.s. also x-cutting pipes. Primary ore gal.-sphal.-py., pyrrh., minor cp., tetrahed.; avg. 10% Pb, 10% Zn, 10 oz Ag/ton. Abundant oxide ore, supergene enriched Ag-avg 15.25 oz Ag/ton. Also silicified zones with 20 oz Ag/ton.
Production:
References: Geol. Survey Can. Bull. 160, p. 153-154; Horcasitas and Snow, in 20th Inst. Geol. Congress Guidebook Excursion A-2 & A-5, p. 51-61.

Silverton district — Colorado, USA
Epithermal-veins & lodes; Radial and concentric veins assoc. w/caldera structures in Tert. volcanics also bx pipes & lodes. Mineralogy of veins complex-py., gal., sphal., cp., tennant., tetrahed., proustite most common. Extensive phyllic & argillic alteration in volcanics.
Production: $33.867x10^6$ tons (1875-1964) ore; $7.634x10^6$ oz Au; $160x4x10^6$ oz Ag; 109,280 tons Cu; 700,689 tons Pb; 341,332 tons Zn. Avg. grade: A.74 oz Ag/ton (Mary mines)
References: Steven, T.A., in Ore Deposits US 1933-1967, p. 715-732; Burbank in Vandermilt (ed.) Mineral Resources of Colo., p. 396-446.

Sullivan mine — British Columbia, Canada
Byproduct Ag in massive sulfides; Large stratiform massive sulfide lens in Pε argillite, siltstone & quartzite. Zoned ore body-central core mass: pyrrho, minor gal. + sphal. Beyond are banded gal., sphal., + pyrrh. in separate horizons. Pyrite dominant on margins of ore body. Dimensions 5000 ft. diam. x 200-300 ft. thick.
Production: Orig. reserves est. $200x10^6$. Product. to 1975--$130x10^6$ tons @ 7% Zn, 7% Pb, 3 oz. Ag/ton. Est. silver content deposit approx. $500x10^6$ oz? Product. to $75=260x10^6$ Ag.
References: Fellows, 1976, Notes on Sullivan mine trip; Int. Geol. Cong. 24th, Field Excursion Guidebook A24-C24, Major Lead-Zinc deposits of western Canada.

Taxco district — Mexico
Mesothermal? Ag-base metal veins.

Tintic district — Utah, USA
Byproduct Ag in Pb-Zn replacements (mainly l.s.); Folded and faulted Paleozoic l.s. + dolom. with large replacement bodies & lesser veins. Ore zones blind or concealed. Mammoth ore zone, a columnar mass. Ore main Tintic dist. dominantly galena & sphalerite containing 5-50 oz. Ag/ton. Ag content highest in galena; Ag occurs as argentite. Also local tetrahed/tennant, enargite w/nel. high Au (0.5 oz +) and 10-20 oz Ag. Extensive oxidation of sulfide ores, secondary Ag minerals (cerargyrite, argentojaros.), native Ag, argentite, pearceite)
Production: (1869-1965) $13.44x10^6$ tons ore, $2.150x10^6$ oz Au, $197.4x10^6$ oz Ag, $2.208x10^8$ lb Cu, $1.287x10^9$ lb Pb, $138.0x10^6$ lb Zu-avg grade 14.7 oz Ag/ton.
References: Morris, in Ore Deposits in the US 1933-1967, p. 1043-1073; USGS Prof. Paper 107.

Tombstone district — Arizona, USA
Byproduct Ag in Pb-Zn replacements (mainly l.s.); Cretac. clastic + calcar. sediments cut by laramide granodior & qtz. monz. porph. Veins & bedded replacements in sediments-gal., sphal., + minor cp. Strong oxidat. + supergene enrich. of Ag

in near surface deposits (Ag in halides, plumbojaros + MnOx). local high-grade Au in veins.
Production: (1880-1970) Est. $22x5x10^3$ tons Pb, $30x10^6$ oz Ag, $240x10^3$ oz Au + some Cu, Zn, MnOx. Most production 1880-1886 from bonanza ores.
References: Ariz. Bur. Mines Bull. 143; Ariz. Bur. Mines Bull. 187; Newell, 1975.

Tonopah district Nevada, USA
Epithermal-Tert. volcanics cut by veins in fault zones; veins + lodes; ore is electrum, argentite, polybasite, pyrargerite-mainly primary sulfides. Mainly Ag producer; definite Au/Ag zonation.
Production: 1901-1959-1,880,000 oz Au.
References: USGS Prof Paper 610; Nevada Univ. Bull. v. 29, no. 5 (1935); Econ. Geol., v. 68; p. 747-764.

Virginia City (Comstock lode) Nevada, USA
Epithermal-folded & faulted Triassic sediments cut by Jurassic veins + lodes qtz. monz., overlain by Tert. volcanics (rhyolite + andesite), in turn cut by Miocene diorite. Veins occupy faults cutting Tert. rocks. Lode occupies complex shear zone 13,000 ft. long & several hundred ft. wide. Ore is argentite, stephanite, antive Au, minor sphal., gal., py., cp. Strong wallrock alter. Total Au production 1859-1959-8,560,000 oz Au (production Ag producer.)
References: USGS Prof. Paper 610; Nev. Univ. Bull. v. 44, no. 1, 1950; USGS Bull. 735-C; USGS Bull 1042-C; Nev. Univ. Bull. V. 30, no. 9 Econ. Geol. v. 68, p. 747-764.

Waterloo deposit California, USA
Bulk low grade, Ag deposit, (Epithermal); Tert. sediments + volcanics, partly intrus. cut by silic veins. Mineralization in veins and dissem. in volcaniclastic sediments. Primary mineral pyrite with barite; abund. jaros & Mn oxides; Ag in secondary minerals. Deposit held by Asarco.
Production: Est. $25x10^6$ tons @ 2-3 oz Ag/ton (potential $75x10^6$ oz Ag)
References: Watson, 1976.

SORPTION OF PRECIOUS METALS ON POLYFUNCTIONAL SULFUR-CONTAINING RESINS

UDC 66.074.7

N. I. Antipov, N. A. Dragavtseva, V. I. Skobeleva, and N. I. Matveeva

It is well known that platinum metals and gold absorb from chloride solutions on strongly-acid ion exchangers, etc.

The literature has no data on precious-metals extraction from solutions by sorbents with functional sulfur-containing groupings; however, there are data on extraction with compounds with analagous groupings in the composition.

Since the mechanism of metals interaction with extractives and sorbents can be similar, sulfur-containing resins can also be used for sorption.

This paper reports on a study of the sorption capacity of polyfunctional sulfur-containing resins PSO and VPSO-3.

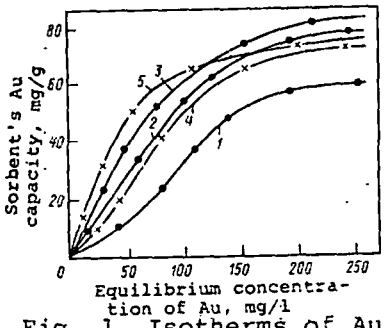

Fig. 1. Isotherms of Au sorption on PSO resin 1 - 0.1-N HCl; 2 - 0.5-N HCl; 3 - 1.0-N HCl; 4 - 0.1-N HCl, 0.75-N NaCl; 5 - 0.1-N HCl; 1.0-N NaCl

The sorbent under the index PSO was synthesized on a divinylbenzene base and it contains ionogenic groupings S.=0, $-SO_2H$, $-SO_3H$, and >S.

In the research, a sorbent was used in the H-form, the sulfur content being 12%, and 3.2 mg-eq-/g of 0.1-N NaOH batches of SOE.

Resins under the index VPSO-3 was synthesized on a base of vinylpyridine and contains ionogenic groupings >N, $-SO_2H$; >SO; $-SO_3H$, and >S. The sulfur content is 4.3% , with 1.9 mg-eq/g of 0.1-N batches of SOE.

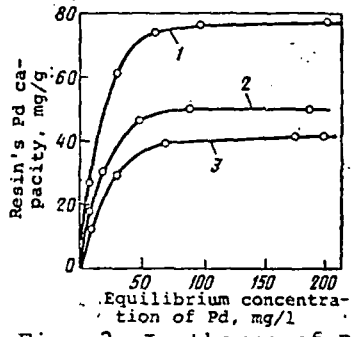

Fig. 2. Isotherms of Pd sorption on PSO resin: 1 - pH = 2; 2 - pH = 2; 1.0-N NaCl; 3 - pH = 2 2.0-N NaCl.

Sorption tests were conducted under static conditions while mixing in hydrochloric acid solutions. The sorption capacity was gauged from the changes in the precious metals content in a solution. Colorimetric methods were used for analysis.

Studies on the kinetics of gold sorption by PSO resin showed that equilibrium is established in 3 hours.

Sorbent capacity increases as solution acidity rises (Fig. 1, curves 1, 2, and 3). Since an increase in acidity suppresses dissociation of HAuCl one can conclude that sorption results chiefly from the formation of the hydrogen bond.

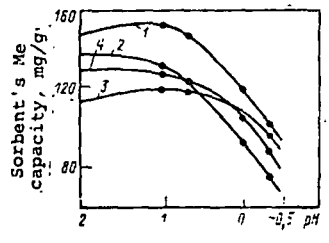

Fig. 3. Effect of solution acidity on Pt and Pd sorption using resins AN-251 and VPSO-3 (τ = 6 hr); C_{st} = 100 mg/l; sorbent:solution = 1:2000): 1 - Pt on AN-251; 2 -Pt on VPSO-3; 3 - Pd on AN-251; 4 - Pd on VPSO - 3.

Introduction of sodium chloride to the solution increases the stability of the complex anion and improves the sorption process: the capacity increases and the path of the isotherm becomes steeper (see Fig. 1, curves 4 and 5).

The kinetic parameters of PSO resin are worse with respect to palladium than with respect to gold. The bulk of the metal is removed in 8 hours; in order to establish equilibrium between the sorbent and the solution, it would take about 20 hours.

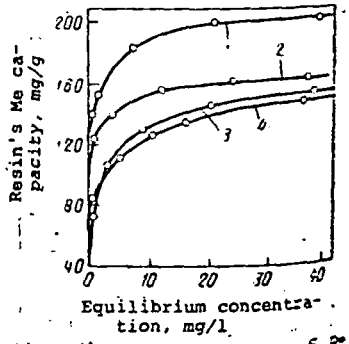

Fig. 4. Isotherms of Pt and Pd sorption on resins AN-251 and VPSO-3 (pH - 1): 1 - Pt on AN-251; 2 - Pt on VPSO-3; 3 - Pd on AN-251; 4 - Pd on VPSO

However, the isotherms of Pd sorption (Fig. 2) show a rather steep path, indicating the applicability of the the resin for the extraction of palladium from diluted solutions.

An increase in solution acidity leads to a drop in the sorbent capacity. Thus, for 0.01, 0.1, and 1-N HCl, the resin's palladium capacities are 77, 71, and 62 mg/g.

Introducing sodium chloride lowers the capacity of the sorbent (Fig. 2, curves 2 and 3), evidently as a result of the competing influence of the chlorine-ions.

Platinum and iridium on PSO resin do not sorb in hydrochloric acid solutions.

Parallel studies were made into sorption on resin VPSO-2, with tests made on a vinyl-pyridine base (anionite AN-251). As tests have shown, equilibrium between sorbents AN-251 or VPSO-3 and the solution is established after 16 hours.

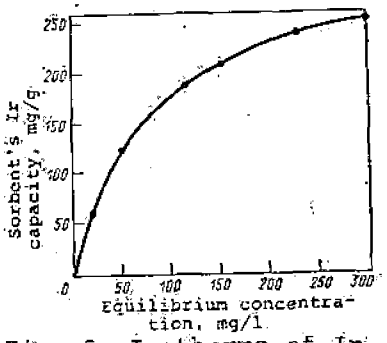

Fig. 5. Isotherms of Ir sorption on resin VPSO-3 (1.0-N HCl).

Data obtained in solutions with different acidity (Fig. 3) showed that polyfunctional groupings on platinum sorption have a negative effect within the entire range of examined acidity values (from pH = 2 to 2-N HCl), evidently as a result of the steric factor.

The presence of polyfunctional groupings has a positive effect on palladium sorption. Depending on concentration, the sorption isotherms (Fig. 4) have a steep path and resins AN-251 and VPSO-3 are useful to extract platinum and palladium from weak solutions. When the equilibrium concentration of metals is lower than 1 mg/l, the platinum capacity of anionite AN-251 is 140 mg/g, and of sorbent VPSO-3, 108 mg/g; the palladium capacity of the resin is 60 and 80 mg/g.

Keeping in mind the tendency of iridium compounds toward hydrolysis, tests were conducted only on 1-N HCl. The tests showed that iridium sorption in resins AN-251 and VPSO-3 occur practically identically; therefore, data are given for only one sorbent (Fig. 5). Ion-exchange equilibrium is established after 6 hours; the isotherm has a smooth path.

CONCLUSIONS

Resin PSO can be used to extract gold and palladium from chloride solutions. An increase in the concentration of hydrochloric acid and sodium chloride will have a positive effect on gold sorption and a negative effect on palladium sorption.

Platinum and palladium will not be sorbed on PSO resin.

Resin VPSO-3, as compared with its base (AN-251) exhibits better sorption properties with respect to palladium and worse with respect to platinum.

Iridium sorption occurs practically identically on resins AN-251 and VPSO-3

Congo Deposit Is Potential New Source for Columbium

An important deposit of pyrochlore containing two types of carbonatite ore is being developed by a new firm called Somikubi (Societe Miniere de Nyamukuki), formed by Comite National du Kivu and Compagnie Miniere des Grands Lacs Africain.

The deposit is northwest of Rutshuru in the Kivu of the Belgian Congo. It is composed partly of unaltered carbonatite and partly of ferruginous ore, both connected with a syenite core. The hard unaltered core is mainly of the sovite type and contains 0.55 percent Cb_2O_5; the adjacent, but unconsolidated, ferruginous deposit contains at least 30,000,000 tons assaying 1.34 percent Cb_2O_5.

The characteristics of the deposit are favorable to economic development. The pyrochlore is not too fine grained and is not coated with iron oxides. It is easily accessible. Concentration processes are now being studied.

Carbonatite is the term given to carbonate rocks which are associated with alkaline igneous intrusions. There is no unanimity of opinion regarding its origin—that is, whether it is of intrusive origin or not.

In the past 10 years, a large number of these carbonatites have been discovered in central Africa, extending along or near the great Rift Valley from Nyasaland north into Tanganyika. All of them contain columbium minerals; in fact, a number have been considered as a commercial source of columbium. Probably the best known and most extensively developed is the Panda Hill deposit at Mbeya, Tanganyika, where the Mbeya Exploration Company has developed about 300,000,000 tons carrypyrochlore $[(CaNa)_2(Cb,Ta)_2O_6F]$. A pilot plant has been built to treat 200 tons per day.

At least three columbium-bearing carbonatites are known in Nyasaland. These include one on Chilwa Island, one at Tundula Hill, and the recently mapped Ilomba Hill in the northern section close to the boundaries of Tanganyika and Northern Rhodesia.

Probably the nearest thing to the African carbonatite in the United States is a similar deposit near Powderhorn, in Gunnison County, Colorado, owned by the Du Pont Company, which is estimated to contain 100,000 tons of columbium oxide. Du Pont has conducted aerial surveys and has diamond drilled the deposit as a columbium reserve because the firm has done extensive research into production and use of the metal and its alloys.

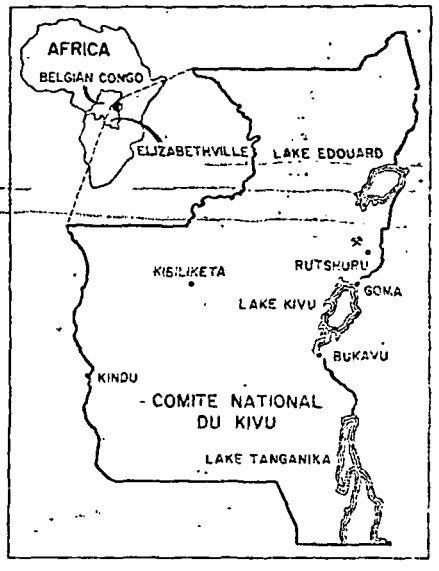

Segregation Process To Be Used at New Copper Project

Transarizona Resources, Inc., has started stripping operations on a copper deposit 28 miles south of Casa Grande, Arizona. By next spring the company expects to have the first commercial plant in North America in operation using the widely discussed segregation process. The segregation process is reported to produce a fine flake copper which is then recovered by conventional copper flotation methods.

The property consists of three patented claims in the Lake Shore group, a section of ground adjoining the Papago Indian Reservation, and 20 additional claims known as the Drake group. The blocked out ore reserve is said to grade 2 percent copper and 15 percent recoverable iron.

Transarizona has purchased the flotation mill of the Three C Ranch mine at Oracle, Arizona and will move the equipment to the property under development. Plans call for an initial production rate of 500 tons per day with an increase to 1,000 tons per day just as soon as the recovery process has been proven.

The segregation process consists of heating oxidized or mixed oxide-sulphide copper ore to 500 to 800° C. in the presence of a halide salt and a solid reducing agent, such as coal or coke. The mechanism and reactions of the segregation process are not clearly defined. It is believed that on application of heat to the charge of ore, salt, and coke, the salt decomposes and reacts with hydrous clay minerals with the formation of hydrochloric acid. The acid attacks the copper minerals to form volatile unstable cupric and stable cuprous chlorides. The unstable cupric chlorides probably decompose with the formation of cuprous chloride and free chlorine. The atmosphere in the furnace is weakly reduced under ideal conditions and the copper chlorides are reduced to metallic copper on the surface of the carbon particles by any one of a number of reactions.

The segregated copper tends to agglomerate during the furnacing with formation of flakes finer than 65 mesh. Careful manipulation of furnacing conditions are required to obtain ideal reduction of copper in a segregated condition in the charge. The furnace calcines are then cooled and subjected to flotation.

George Freeman of Casa Grande is operating manager of Transarizona in which a controlling interest is held by Transcontinental Resources Ltd. Consulting geologist for the project is Manning W. Cox of the firm Wisser and Cox in San Francisco.

United States Patent [19]

Girard et al.

[11] 3,841,705

[45] Oct. 15, 1974

[54] STIMULATION OF PRODUCTION WELL FOR IN SITU METAL MINING

[75] Inventors: Lucien Girard, Boxboro; Robert A. Hard, Lexington, both of Mass.

[73] Assignee: Kennecott Copper Corporation, New York, N.Y.

[22] Filed: Sept. 27, 1973

[21] Appl. No.: 401,484

[52] U.S. Cl. 299/4, 166/247, 166/271

[51] Int. Cl. E21b 43/28

[58] Field of Search 299/4; 166/247, 271, 299

[56] References Cited

UNITED STATES PATENTS

3,278,233	10/1966	Hurd et al.	299/4
3,490,534	1/1970	Grady	166/271
3,542,131	11/1970	Walton et al.	166/299 X

Primary Examiner—Ernest R. Purser

Attorney, Agent, or Firm—Lowell H. McCarter; John L. Sniado

[57] ABSTRACT

Metal values are economically leached in situ by rubblizing a portion of an ore body, injecting a lixiviant for the metal values through one or more injection wells in the ore body located adjacent to but outside the rubblized portion of the ore body, and collecting the lixiviant containing the dissolved metal values from one or more production wells located in a rubblized zone of the ore body.

10 Claims, 2 Drawing Figures

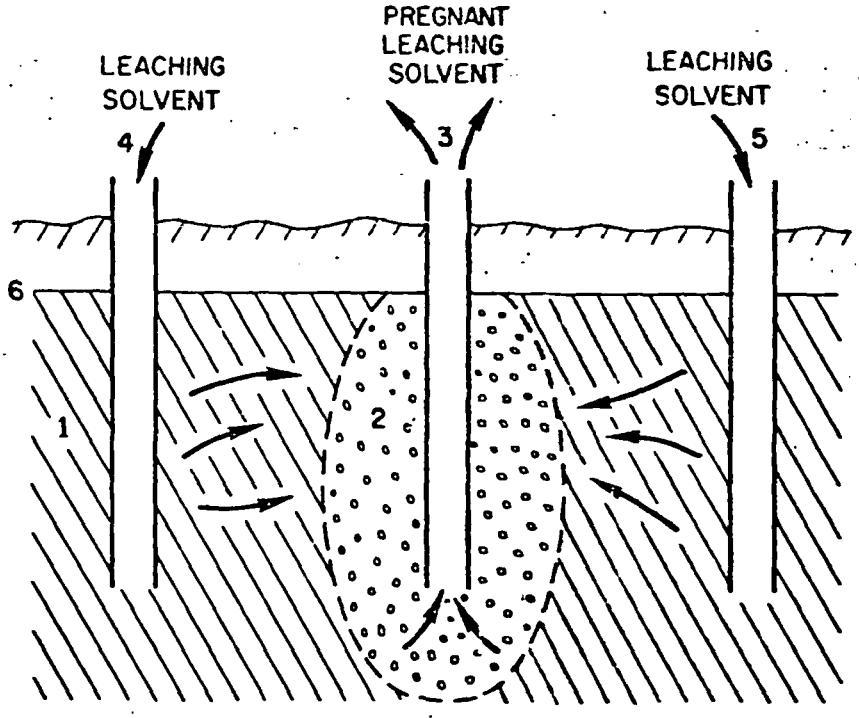

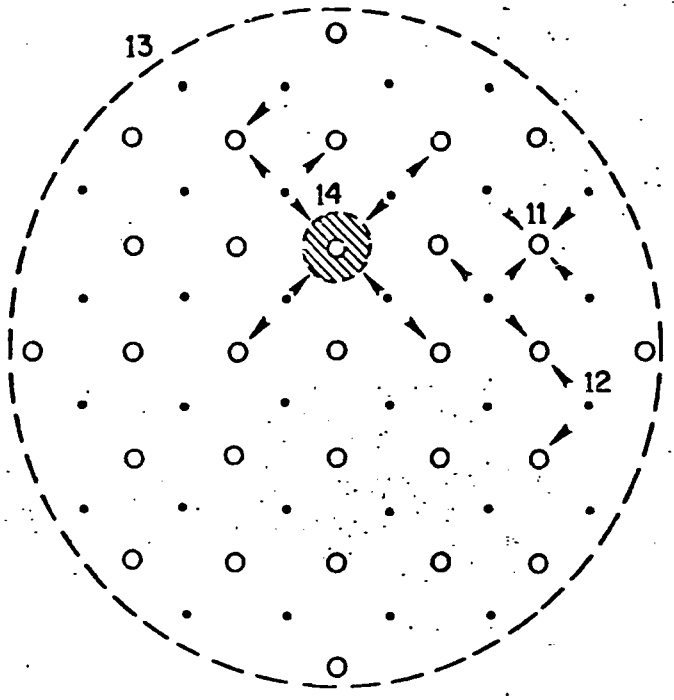

FIGURE 1

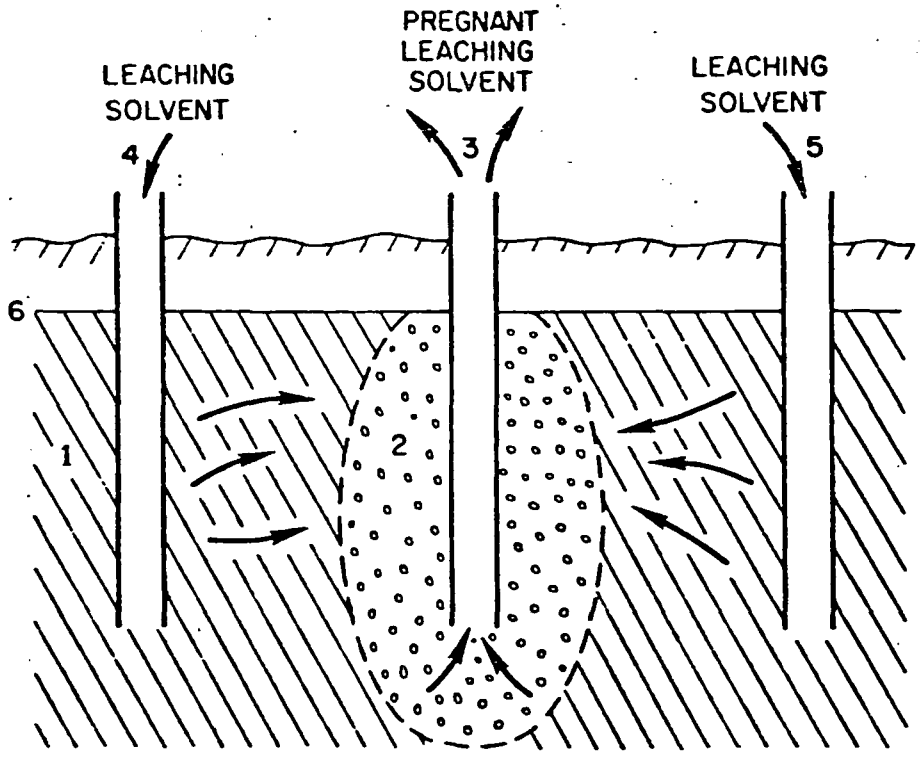

FIGURE 2

UNITED STATES PATENT OFFICE
CERTIFICATE OF CORRECTION

Patent No. 3,841,705 Dated October 15, 1974

Inventor(s) Lucien Girard et al.

It is certified that error appears in the above-identified patent and that said Letters Patent are hereby corrected as shown below:

Column 2, line 53, "a of lower" should read -- a zone of higher --; line 54, "high" should read -- low --. Column 4, line 57, "shows" should read -- show --; line 58, "igenous" should read -- igneous --.

Signed and sealed this 18th day of February 1975.

(SEAL)
Attest:

RUTH C. MASON
Attesting Officer

C. MARSHALL DANN
Commissioner of Patents
and Trademarks

FORM PO-1050 (10-69)

USCOMM-DC 60376-P69
U.S. GOVERNMENT PRINTING OFFICE: 969-930

STIMULATION OF PRODUCTION WELL FOR IN SITU METAL MINING

FIELD OF INVENTION

In situ mining of valuable minerals has been explored as a means of economically recovering the metal values from low grade ores or otherwise inaccessible ore bodies. Recent work in the area has, in general, dealt with pumping of a leaching liquid or lixiviant into an ore formation, allowing sufficient residence time and removing the pregnant liquid from the formation. Many problems have surfaced with respect to the movement of fluids in the subsurface ore bodies and some investigation has been accomplished. U.S. Pat. Nos. 3,278,233 and 3,574,599 are cited as showing the present state of in situ leaching art.

Other recent investigatory work has been done in the area of nuclear explosive applications in forming lixiviation cavities in subsurface formations. Very recent art in this area, however, teaches the use of the explosive to create a closed system or series of closed systems in the ore body in which to introduce the lixiviant. Adelmann, Canadian Pat. No. 855,525 and Lewis, U.S. Pat. No. 3,640,579, demonstrate this use of the nuclear blast. This use of a closed system may well lead to efficient leaching within the rubblized zone but as Lewis indicates, the blast area is confined and, therefore, so is the leaching liquid. The quantity of ore which can be thus contacted and leached is thereby limited to the rubblized region. The present invention proposes to increase the volume of ore which can be contacted and leached effectively, without increasing the rubblized region.

SUMMARY

The invention is a process of in situ mining comprising the steps of rubblizing a portion of an ore body by detonating one or more strategically placed explosive devices to form a rubblized zone or chimney, injecting a leach solution into one or more injection wells, the injection well or wells being located in the ore body adjacent to but outside of the rubblized chimney, such that the leach solution will pass through the non-rubblized ore body removing the metal values therefrom and into the rubblized chimney, and recovering a pregnant leach solution from one or more production wells located within the rubblized zone or chimney.

In an alternate method an ore body is solution mined in-situ by first injecting a lixiviant into the ore formation under pressure through an array of injection wells. The pregnant solution is then recovered from the formation through one or more production wells that has been stimulated with a nuclear or chemical explosion subsequent to the injection of the leaching solution. The explosive charge causes rubblization in the area of the production well, but not in the immediate area of the injection wells, such that the rubblization reduces the resistance to lixiviant flow into the production well to the extent that the pregnant solution can be withdrawn from the production well nearly as fast as leaching liquid can be injected into the ore formation.

BRIEF DESCRIPTION OF DRAWINGS

FIG. 1 shows one possible array for well placement, commonly known as the 5-spot pattern.

FIG. 2 shows the rubblization around the centrally located production well and the flow of leaching solvent from the distant injection wells into the rubblized zone.

DESCRIPTION OF INVENTION

In situ solution mining of a metal value requires injection of a leaching solution into the ore body, contact with the mineral containing the metal values to be extracted, and recovery of the pregnant solution from the ore formation. The problem to be overcome in the process is the restricted flow rates of leaching solution between the injection and the production wells, especially in igneous rock systems, due to the relatively low permeability of the igneous rocks. This restriction to fluid flow means that the leaching solution can be injected into the formation faster than it can be withdrawn.

The above situation is termed a production limited system because overall recovery of pregnant solution, and therefore recovery of leached metallic element, is dependent on how fast solution can be withdrawn from the production well. The present invention is an attempt to reach an injection limited system such that recovery of pregnant solution is limited by the amount of solution which can be injected into the formation. This situation would typically result in much greater productivity than the production limited system.

Referring now to FIG. 1, the ore body 13 is located and an array of injection wells 12 and production wells 11 are bored. The particular pattern shown in FIG. 1 is commonly known as a 5-spot pattern which allows the nearest neighbor of any injection well to be a production well and vice versa. It is within the scope of the invention described herein that any other desired pattern of wells may be used.

In a preferred embodiment all the production wells 11 will be rubblized with a chemical or nuclear explosive device to provide a rubblized zone 14 around each production well. The area of rubblization 14 indicates the relative extent of the blast area with respect to the placement of the injection wells. It will be noticed here, and in greater detail in FIG. 2, that there remains relatively undisturbed regions between the rubblized area and the injection well. The arrows around the rubblized area 14 indicate the direction of fluid flow from nearby injection wells. The injection wells may be between about 50 feet up to about 700 feet from the boundaries of the rubblized chimney area 14. The distance between production and injection wells will depend on permeability profile of the rock mass surrounding the chimney.

The rubblized area surrounding the production wells 11 creates a of lower permeability thus resulting in the flow of fluid from the high permeability igneous rock surrounding the injection wells 12 toward the production wells 11 rather than a fluid flow into other areas of the ore body where the fluid may be lost.

From FIG. 2 it can be seen that the rubblized zone 2, caused by the nuclear or chemical explosion, does not extend to the injection wells 4 and 5. However the nuclear chimney from the blast may extend upward from the ore formation 1 to a point above the water table 6. In this respect the invention relates to the recovery of metal values found in mineral formations located beneath the water table and, hence, the rubblized zone of the production well will be below the water table. This fact, in turn, means that the hydrostatic pressures be-

neath the water table contribute integrally to the flow properties of leaching solution into the production well.

If desired it is possible to have more than one explosive detonation. For example, rubblized chimneys of desired geometric configurations can be formed by strategically placing and detonating the explosives in proper sequence. See U.S. Pat. No. 3,470,953. Explosive reaction mixtures may be formed in concentric regions in the ore body around the wellbore by alternately injecting a propping agent and then an explosive reaction mixture. Upon detonation of the concentric regions of explosive reaction mixtures, the resulting fractures propagate both outwardly into the ore body and inwardly toward the wellbore so as to enhance the subsequent recovery of metal values from both the fractured areas and the areas between the injection well or wells and the centrally located production well. For further details, see U.S. Pat. No. 3,593,793.

The present invention of an in situ leaching process has particular application to copper ore deposits, for example chalcopyrite, chalcocite, covellite and bornite. However the process is not limited to recovering copper but can be used in recovering many other metallic elements from their ores. Of interest would be nickel, zinc, molybdenum, silver, gold and other valuable metals.

With respect to recovery of copper from primary sulfide deposits, the leaching solvent injected into the formation would typically be water, sulfuric acid, and ferrous sulfate, in various proportions, together with an oxidizing agent. The oxidizing agent is preferably an oxygen-bearing gas such as air, oxygen and any and all mixtures thereof. The oxygen-bearing gas may be introduced into the ore body prior to, during, or subsequent to the leaching solution. On contact with the leaching solution the copper is leached from the ore as a sulfate, and is later recovered from the solution by electrolysis, or in a precipitation process using de-tinned iron to replace the copper in solution.

More particularly, for instance, when a soluble substance such as copper is to be recovered from an ore, which contains either metallic copper or copper oxide in igneous rock, the present invention provides for very efficient in situ leaching by an appropriate acid or alkaline liquid extractant, such as aqueous sulfuric acid of moderate strength, e.g., acid containing 0.5 to 30 percent, and preferably 2 to 10 percent, H_2SO_4 by weight. Such sulfuric acid is pumped into the injection well in the copper ore in quantity sufficient to provide therein about 20 to 80 pounds H_2SO_4 per ton of ore to be treated when such ore contains between about 0.5 and 2 percent copper by weight. The pressures developed in pumping the leach solution into the ore body may vary over a wide range. Preferably the injection pressure will be below the formation fracture pressure. Recovery of copper from the formation by such leaching should be between about 40 and 85 percent or more, e.g. 70 percent somewhat depending on proportion and strength of acid used, permeability of the formation, concentration of copper therein, etc.

When the metal is in the ore as a sulfide, arsenide, telluride or a sulfo-salt, it can be recovered from such a sulfide-type ore either by converting it by in situ oxidation to the oxide by blowing air underground and then extracting the oxide as described above.

If nuclear stimulation of the production well is selected as the rubblizing agent, the nuclear explosives useable may range in yield from as little as 10 kiloton up to 2,000 kilotons, it being noted that the cost of such explosives is relatively independent of the energy yield. Consequently, the largest size device that can be employed at the given depth appropriate for a particular job is generally the most economical one.

The following examples illustrate the invention with reference to copper containing ore bodies. It is to be understood that this is done solely by way of example and is intended neither to delineate the scope of the invention nor limit the ambit of the appended claims, since the invention is applicable to the in situ recovery of other lixiviant soluble metal values from ore bodies.

EXAMPLE I

An embodiment of the invention as applied to the recovery of copper from a formation which contains copper oxide will next be described. The Copper ore deposit to be treated is a stratum 1,000 feet thick and has 2,000 feet of overburden above it. This stratum contains copper in a concentration of about 1 percent in igneous gangue.

At the beginning of the operation a 50 kiloton thermo-nuclear explosive is placed in the formation through a well at a depth of 3,200 feet. When the well is sealed and the device detonated, a chimney approximately 650 feet high is created above the shot point. It is estimated that the chimney will have a diameter of about 265 feet and contain about 2 million tons of rubble. If it is found that additional copper ore need be caved down, this may be produced by placing or detonating a further nuclear device in the formation.

Aqueous sulfuric acid having an H_2SO_4 content of about 5 weight per cent is then pumped into the injection wells located some distance outside the rubblized chimney. Sufficient volume of acid of proper strength should be introduced into the injection wells to allow for the ultimate consumption of about 40 pounds H_2SO_4 per ton of broken rock treated in the process. After the acid is introduced in the injection wells it will percolate through the ore body and take some copper oxide into solution, which will accumulate as a body of liquid in the lower part of the chimney.

After a period of time the accumulation of pregnant leach solution in the chimney cavity can be pumped out through the production well located in the chimney. The copper is then recovered from the pregnant leach solution by known methods.

EXAMPLE II

An ore body 100 acres in area and averaging 100 feet in thickness lies at an average depth of 3,000 feet below the surface of the earth. Samples of the ore shows that it is composed primarily of granitic igenous rock and that it contains chalcopyrite as the principle copper mineral. The ore samples also show that it contains approximately 1.4 weight percent chalcopyrite and that the total copper content of the ore averages 0.5 percent. The volume of ore in the deposit is, therefore, 10^4 acre-feet, or 4.356×10^8 cubic feet. The specific gravity of the granitic ore is 2.6. Therefore the total weight of the ore in the deposit is 3.54×10^7 tons, and the copper content of the ore body is 3.54×10^8 pounds.

Wells are drilled into the body in an array such that the well density is one per acre. Position of production wells is determined. Liquid slurry or nuclear explosives are strategically placed and detonated such that the injection well positions remain outside of the rubblized chimney area. By measurements on core samples and by injection and production tests on individual wells, it is determined that the void volume within the randomly oriented fracture system is equivalent to 2 percent of the bulk ore volume, that the fracture spacing averages 6 inches, and that the permeability of the ore body to liquid averages about 25 millidarcys.

Petrographic examination of core samples taken from the ore body shows that about 2 percent of the rock surface area exposed by the fractures is covered by the chalcopyrite mineral and that the rock matrix bounded by the fracture system is substantially cubical in configuration.

Thus the surface-to-volume ratio of the ore blocks bounded by the fractures is approximately equal to that for cubically shaped blocks, and the surface area to volume ratio for the ore blocks is equal to 6/L, where L is the length of the side of a cube. In this case L = 0.5 feet, and the surface area to volume ratio is equal to 12 square feet/cubic foot.

The total surface area of ore exposed by the fracture network is equal to $12 \times 4.356 \times 10^8$, or 5.227×10^9 square feet. The surface area of the chalcopyrite mineral exposed by the fracture system is equal to 2 percent of the total surface area, or 1.045×10^8 square feet.

Laboratory tests with the ore samples showed that ferric sulfate solutions will dissolve copper from the chalcopyrite of the ore body at a rate equal to 0.002 pound of copper per square foot of chalcopyrite surface area per day. The initial maximum rate of copper production attainable from the ore body by in situ leaching with ferric sulfate would be $0.002 \times 1.045 \times 10^8 = 209{,}000$ pounds of copper per day. The laboratory tests also showed that by allowing a 0.4 molar solution of ferric sulfate to react completely with the chalcopyrite, and other minerals in the ore, a pregnant leach solution containing 3.0 pounds of copper per barrel (42 gallons) could be obtained. Therefore in order to supply 0.4 molar ferric sulfate solution to the ore body at the optimum rate, i.e., at the rate sufficient to produce the maximum amount of copper and at the same time allow total reaction of the ferric iron, the 0.4 molar ferric sulfate solution must be injected initially at a rate of 69,700 barrels/day. The required average residence time for the solution within the ore body is fixed by the injection rate and the void volume of the ore body:

Average Residence Time = void volume/injection rate

$= (0.02)\ (4.34 \times 10^8)$ cubic feet/(69,700 bbl./day) (5.515 cu.ft./bbl.) = 22.2 days

The injection and withdrawal rates of the wells are thus regulated to permit the ferric sulfate solution to remain in the ore body for approximately 22 days.

This average residence time, or the average time required for the fluid to traverse the ore body between injection and production wells, must be increased as the chalcopyrite mineral is depleted and the surface area of chalcopyrite exposed to the leaching solution diminishes. Over the useful life of the in situ leaching operation, the optimum average residence time for the 0.4 molar ferric sulfate solution will be continuously increasing and may be substantially greater than the 22.2 days calculated as the optimum average residence time at the start of the operation.

In most cases, the injection and production rates should be approximately equal in order to minimize migration of fluids into or away from the ore body being subjected to the solution mining process. In this example if half of the wells are used as injection wells, and the other half of the wells are used as production wells, the average injection and production rates will be initially:

69,700 barrels/day/50 wells = 1,394 barrels/(day)(well)

The injection and production rates at individual wells may be varied as necessary to maintain an approximate overall balance between total injection and total production, and to maintain the residence time required for essentially complete reaction of the ferric iron in the leaching solution with the ore minerals.

As noted above, it will be necessary to adjust the residence time of the leaching solution within the ore body to maintain the optimum residence time as the ore minerals are depleted. The need for such adjustment will be indicated by the appearance of ferric iron in increasing concentrations in the fluids produced from the production wells. When ferric iron is observed in the fluid produced from a production well, the rate of fluid withdrawal from that well should be adjusted until ferric iron is no longer found in the fluid produced from the well. The injection rates at nearby injection wells should then be correspondingly reduced to maintain an overall balance between injection and production. This operation should be repeated as necessary to maintain the optimum residence time for the leaching fluid.

We claim:

1. An improved process for recovering metal values by in-situ leaching an ore body located below the water table which comprises:
   a. forming a rubblized zone in an ore body whereby the rubblized zone contains fractured metal bearing ore particles;
   b. injecting a leach solution through one or more injection wells located in the ore body adjacent to but outside the rubblized zone, the leach solution solubilizing metal values in the ore body and in the rubblized zone; and
   c. recovering a metal containing leach solution through one or more production wells located in the rubblized zone.

2. The process of claim 1 wherein the rubblized zone is produced by detonating one or more strategically placed explosives in the ore body, said explosive selected from nuclear and chemical explosives.

3. The process of claim 1 wherein the one or more injection wells are located between at least about 50 feet and up to about 700 feet from the one or more production wells.

4. The process of claim 1 wherein the ore body contains a copper bearing ore.

5. The process of claim 4 wherein the leach solution is injected through the one or more injection wells at a pressure less than the formation fracture pressure.

6. The process of claim 5 wherein the leach solution contains a dispersion of an oxygen bearing gas.

7. The method of leaching a metal bearing ore in place which comprises:

a. injecting a leach solution at a pressure below the formation fracturing pressure through at least one injection well located in a non-rubblized zone of a metal bearing ore body located below the water table;

b. allowing the leach solution to remain in the ore body to solubilize metallic ions present in the ore body, and

c. recovering metallic ion containing leach solution from at least one production well located in a rubblized zone in the ore body.

8. The process of claim 7 wherein the ore body contains copper bearing ore.

9. The process of claim 8 wherein the leach solution is aqueous sulfuric acid containing an oxygen bearing gas.

10. The process of claim 9 wherein at least one injection well is located between about 50 feet and about 700 feet from at least one production well.

* * * * *

Solution Mining

Ronald J. Roman

Chief Research Metallurgist
New Mexico Bureau of Mines and
Mineral Resources

Research in solution mining has moved from laboratory studies to field tests and in some cases to commercial operations which themselves are being watched by many companies as though these operations were pilot plants. Several companies are actively evaluating solution mining as an alternative to conventional mining and processing. The success of the Old Reliable mine in Arizona has led to solution mining being applied at the Big Mike mine in Nevada and the Zonia mine in Arizona. Kennecott Copper Corporation and the AEC's Lawrence Livermore Laboratory are cooperating in a joint program to evaluate the feasibility of in-place solution mining of primary copper sulfide ore which has been rubblized by nuclear explosives.[1,2] The joint study will address the overall economic, environmental and technical feasibility with respect to both the underground operations and the surface plant facilities. This project does not represent a revival of the old Sloap project considered in 1967 but incorporates newer concepts that were evolved at the Lawrence Livermore Laboratory.

Bartlett[3] has demonstrated that ore in the rubble chimney from a nuclear blast could leach at a rate considerably faster than originally anticipated. This is due to two factors. First, the reactions are exothermic and the rock being a poor conductor of heat, the temperature in the chimney could rise accelerating the leaching rate. Second, a deep deposit could be leached under a hydrostatic head in excess of 2000 ft. of water. This high pressure can allow high oxygen concentrations in the leach solution which will accelerate the rate of leaching. This study did not include any heat effects from the acid reaction with the feldspars which is also an exothermic reaction.

The Anaconda Company at Butte, Montana is continuing to experiment with dump configurations. The size and shape of the finger dumps are being varied in an attempt to determine an optimum configuration.[4] Copper extraction from a dump appears to be in part determined by how effectively air penetrates the dump. As the dumps are made smaller the percentage of the dump volume which air reaches increases and therefore copper production should increase. Operating cost increases with small dumps, however, therefore an economic optimum dump size probably exists. Recognizing the importance of air penetration into a dump, Air Products and Chemicals, a major builder of on-site oxygen plants is looking into the feasibility of oxygen injection into dumps.[5]

Solution distribution is also being studied by Anaconda. Injection of solution into the dump through holes drilled a right angle to the slope of the dump. Improved copper production was noted for 30 days but diminished after this. It appears now that sufficient information is available to show the importance of heap geometry and construction on heap productivity. A fruitful area for further research will be in developing better techniques for laying down heaps so that good solution distribution is insured.

During the past year the academic community has been actively investigating the various phases of solution mining. Emphasis has been on developing models which could be used to predict results of heap and in-situ leaching and allow scale-up of laboratory tests. The models developed at Stanford[6] and the New Mexico Bureau of Mines[7] both recognize diffusion of reactance through the leached outer layer of the rock as being a primary rate controlling step in the overall leaching process. The two models differ only slightly in that one model assumes an instantaneous chemical reaction between the reactance and the copper mineral once the reactance have diffused to the reaction site, and the other model assumes a slower chemical reaction rate. Both models appear to predict accurate results for different ores. The mathematical complexity of the Stanford model is such that simplification may be necessary before it can be applied to heap leaching. It appears to be applicable to leaching when the leach solution composition is the same in all parts of the leach zone (such as a rubble chimney in which the solution is constantly being mixed by air injection). The New Mexico Bureau of Mines model, on the other hand, appears to have more use in analyzing heap leaching of oxide ore or an ore in which the chemical reactions are fast compared to the diffusion process.

Also at the New Mexico Bureau of Mines, a division of New Mexico Institute of Mining and Technology, a newly discovered microbe is being studied[8] which will oxidize reduced sulfur, iron and molybdenum compounds between 45-70°C. *Thiobacillus* microbes are not effective at this high of a temperature. It is known that the internal temperature of dumps is high and it is thought that this new microbe could be introduced into dump to enhance leaching in the hotter zones of the dump and in addition extract molybdenum.

Scanning electron photomicrograph of newly discovered microbe. Microbes are 1-2 microns in size and are attached to a MoS_2 surface.

Several projects are underway in the college division of New Mexico Institute of Mining and Technology. One group is presently following a

controlled-solution-composition approach to leaching of porphyry-copper type ores.[5] The object of this study is to minimize interaction between the leach solution on gangue silicates. It is hoped that the prevention of the formation of clays would allow better solution distribution in dumps.

Large columns are being erected at New Mexico Tech which will be used to test various heap leaching operating philosophies as well as in a general study of solution mining. The columns are 40 feet in height, 10 feet in diameter and will hold approximately 200 tons. These columns will be under the direction of the John D. Sullivan Center for Insitu Mining Research, an organization set up to promote interdisciplinary studies on solution mining.

Leaching Jointly Studied

At the University of Utah the kinetics of chalcopyrite leaching is being studied jointly with the U.S. Bureau of Mines research group in Salt Lake City. The result of this work suggests that basic iron sulfates, dissolved by introducing acid provide an oxidizing agent in the absence of oxygen.[6] They also noted that the oxygen uptake increased with a lowering of the pH, and suggest that precipitation of basic ion salts with pore channels is the reason leaching follows parabolic kinetics.

The U.S. Bureau of Mines in Reno has reported on the effect of chloride and nitrate addition to the leach solution for leaching chalcopyrite.[10] The results indicate both enhance the leaching rate.

Solution mining is well on its way to becoming a serious alternative to conventional mining and milling. The low capital costs required and low operating costs demonstrated by dump leaching operations are the incentives which have caused a great deal of effort to be expended in developing solution mining techniques. Together with the success of the new solution mining operations during the past year the climate is right to see some major advances in the next few years.

References

[1] Braun, R. L., Private Communication, 1973.

[2] ———, "AEC and KCC will jointly study potential of nuclear blasting to mine copper," E & MJ, Vol. 174, No. 4, April 1973, pp. 26.

[3] Bartlett, R. W., "A Combined Pore Diffusion and Chalcopyrite Dissolution Kinetics Model for Insitu Leaching of a Fragmented Copper Porphyry," International Symposium on Hydrometallurgy, 1973, pp. 331-374.

[4] Fisher, T. J., Private Communication.

[5] Harbison, E. J., Private Communication.

[6] Olsen, C. L., "A Diffusion Leaching Model and an Example of its Application to Heap Leaching," M.Sc. Thesis, NMIMT, 1973. 63 pp.

[7] Brierley, C. L., Private Communication.

[8] Bean, R. E., Private Communication.

[9] Auck, Y. T. and Wadsworth, M. E., "Physical and Chemical Factors in Copper Dump Leaching," International Symposium on Hydrometallurgy, 1973, pp. 645-700.

[10] Carnahan, T. G. and Heinen, H. J., "Simulated Insitu Leaching of Copper from a Porphyry Ore," TPR 69, May 1973, USBM, 11 pp.

Rock Mechanics

L. J. West

Associate
Dames & Moore

In reviewing the progress made in the field of rock mechanics during 1973, it is readily apparent that the greatest advance has been an enhanced appreciation of the usefulness of rock mechanics techniques and measurements by the mining industry, rather than any specific advances in hardware or in technology. This trend toward greater use of rock mechanics tools has probably been due largely to an increased demand by industry for more rational design procedures in order to reduce costs and control safety hazards. Unfortunately for today's mine operators, the greatest rock mechanics efforts in the past have gone into theoretical and laboratory studies rather than into practical applications. This has created a gap between practice and theory as well as a major communication problem between the researcher and the practitioner. As a result, many of the good rock mechanics developments have been largely ignored for long periods of time by operators who considered them to be impractical, untried, or the exclusive province of a small group of scientists who converse in symbols, formulas, and finite elements.

The development of rock mechanics from an art of ground control into a branch of engineering has been very slow indeed in spite of the obvious financial benefits from good engineering. This has been due primarily to the fact that even yet many of the rock mechanics practitioners are very theoretical in their approach toward solving real ground control problems. It is interesting to note that during this past year, which is well over a decade since rock mechanics was considered by many to be an established discipline, that most of the published literature is of little real value to an actual mining operation. However, there are some notable exceptions, such as a recent series of articles by Parker[1] on practical rock mechanics for miners. These articles are a major step forward in establishing better communications between theoreticians and practitioners. Another significant publication, "Rock Slope Engineering" by Professor E. Hoek, has just been completed. It is the result of several years of practical rock slope stability research at the Imperial College of Science and Technology in London. Another 1973 rock mechanics paper worth noting, which is by Piteare,[2] deals with rock joint properties in relationship to ground control problems.

In spite of the fact that the majority of literature this year is still very theoretical, there is a definite trend toward applied research. There also seems to be a greater amount of industry participation in rock mechanics research and with rock mechanics meetings and committees. This is needed for proper direction of major research work and other rock mechanics efforts. For example, there are early indications that industry will play a major role in the September, 1974 International Society of Rock Mechanics Conference to be held in Denver, Colorado.

There is an overwhelming feeling among rock mechanics practitioners and mine operators, through a recent private survey in regard to rock mechanics developments, that a major amount of applied ground control research is certainly needed. It was the opinion of the majority of those surveyed that further theoretical or laboratory research work would be largely a waste of effort until a few years of intensive applied research has been completed. They emphasized the need for accumulating data from case histories of ground control problems, the need for developing simpler and better ways of evaluating in-situ ground conditions, and the very great need to establish a high level of confidence in existing rock mechanics techniques through many applications. The plea this year seems to be for all research efforts to be in an applied direction.

Research Activities

A large amount of excellent research is currently under way. Fortunately, most of it has the promise of yielding information that will be applicable to many types of mining problems. The best example of such a research effort is a major five-year program of research into open pit slope design by the Canadian Department of Mines and Resources. This work has been under way for two years, although no results are yet available.

A three-year cooperative research study in the Coeur d'Alene Mining District by the University of Utah and the Bureau of Mines (USBM) appears to have resulted in a significant advance in the technology necessary for predicting the performance of fill and its influence on underground mining. Of particular interest from a rock mechanics point of view is the fact that the finite element method of analysis was used successfully in this study for predicting stope wall closure and fill pressure.[3] The USBM has also made significant progress in their own or sponsored research work in regard to roof support with pillars,[4,5] shotcrete,[6] rockbolts,[7] and stress control.[8] The USBM has also sponsored a major research effort designed to develop a ground support prediction model.[9] This study, which is to be completed in early 1974, is based on

VOL. 78, NO. 26 JOURNAL OF GEOPHYSICAL RESEARCH SEPTEMBER 10, 1973

Stress-Strain Behavior of a Granodiorite and Two Graywackes on Compression to 20 Kilobars

R. N. SCHOCK, H. C. HEARD, AND D. R. STEPHENS

University of California, Lawrence Livermore Laboratory, Livermore, California 94550

The complete stress-strain equation of state for a granodiorite and two graywacke sandstones has been determined on loading to 20 kb axial stress at room temperature. Data under conditions of hydrostatic, uniaxial stress at various confining pressures and uniaxial strain loading are synthesized to define the behavior of these rocks. For the granodiorite it is observed that the onset of dilatancy as well as intersection of the failure envelope is independent of loading path. No dilatant behavior is observed on uniaxial strain loading to 12 kb axial stress. Both sandstones are observed to load below the hydrostat (increased compressibility) in either uniaxial stress or uniaxial strain loading. This enhanced compaction at relatively low pressures is believed to result from the influence of the additional shear stresses, which facilitate intergranular movements in these porous rocks. Dilatant behavior greatly diminishes at higher mean stresses where the rock undergoes a transition in failure mechanism from throughgoing narrow tensile and shear fractures (predominantly intergranular) to pervasive small-scale fracturing (predominantly intragranular). Dilatancy again becomes important at the highest stresses, where most of the initial porosity has been removed. The data on both rocks are used to delimit areas of characteristic behavior that are uniquely defined in stress space, independent of loading path.

The characterization of the mechanical response of an isotropic elastic solid at a given mean stress requires the measurement of principal stresses and strains along a loading path with variable shear stress. The mean stress dependence of this response must then be studied in a succession of measurements. For rocks, which are in general inelastic and often nonisotropic, the redundancies inherent to isotropic elasticity diminish, and there is no unique measurement that yields the relation between the stress tensor and strain tensor for the material. Several paths of loading over a range of shear stresses must be investigated to determine the tensor at a given stress state. In this paper we present the results of extensive stress and strain measurements along several loading paths on two rock types, a holocrystalline acidic igneous rock (granodiorite) and a clastic fine-grained sedimentary rock (graywacke). Our purpose is to determine as accurately as possible the complete stress-strain equation of state for these very different materials upon compression so as to attempt to delineate those physical properties that are fundamental to the observed behavior.

The granodiorite studied was from the Climax stock, Area 15, Nevada Test Site, Nye County, Nevada, and is referred to in various publications under the names Hardhat and Piledriver (nuclear experiments detonated in this stock). For a description of the shot sites see, for example, *Houser and Poole* [1959], *Butkovich* [1965], *Short* [1966], and *Borg* [1972]. Geophysical survey data are given by *Allingham and Zietz* [1962]. The material density is 2.67 g cm^{-3}, and the crack porosity from grain density determinations is 0.7%.

Two sandstones were studied. One was from the 3358-meter depth of a well drilled in the Green River basin near Pinedale, Wyoming, the proposed site of the Wagon Wheel nuclear gas stimulation experiment. The second sample was from the 1309-meter depth of the Gasbuggy emplacement well in the San Juan basin near Farmington, New Mexico. The Wyoming sample (Lance formation) is fine grained and moderately sorted; it contains altered feldspar (<7% by volume) and possesses a high detrital quartz (>65%) content [*Borg*, 1971]. These rocks are considered to be lithic sandstones (subgraywacke-protoquartzite) by *Pettijohn* [1957] or low-rank graywackes by *Krynine* [1948] and appear to be representative

of the major type of sandstone present in the geologic section [*Pettijohn*, 1957]. The rock has a measured density of 2.45 g cm^{-3} with 8.5% porosity and 1 wt % water released on heating to 110°C. The sample from New Mexico (Pictured Cliffs formation) is, like the sample from Wyoming, classified as a fine-grained subgraywacke. It is slightly more porous (~10%) and contains relatively unaltered feldspar (~12% by volume) [*Borg*, 1971].

In all tests discussed below, the principal stresses and strains are referred to a Cartesian coordinate system. In all cases the stresses normal to the cylindrical sample axis are equal ($\sigma_2 = \sigma_3$), and the associated strains are likewise assumed to be equal (planar isotropy). In all tests reported here the sandstones were tested with the plane of the bedding normal to the cylinder axis. Separate studies [*Schock et al.*, 1970] indicate an anisotropy of about 20% in static linear compressibility for the Lance sandstone. The anisotropy in shear properties is considerably less (~7%); both decrease with increasing pressure. The strain rates ($\dot{\epsilon}$) associated with all but three individual tests are near 10^{-4} sec^{-1}; all tests were performed at room temperature. Three separate tests were made at a strain rate of about 8 sec^{-1}. Three types of loading path, in which a variety of stress states may be achieved in compression, are described. Stress is taken as positive and strain as negative in compression. Our tests are limited to experiments in which all applied stresses are compressive. In the simplest case, the specimen is loaded hydrostatically, that is, the three principal stresses are always equal. In a second type of experiment, the intermediate and minimum principal stresses are equal (confining pressure) and remain constant while the axial stress (σ_1) is increased. This is a condition of uniaxial stress (although the material is under various fixed confining pressures). In the third type of experiment, the axial stress is increased with the condition that the radial strain ϵ_r remain constant. This test, aside from being a well-defined loading path, is significant in representing the conditions thought to exist during the passage of a plane shock wave [*Duvall and Fowles*, 1963], where inertial and symmetry requirements allow strain only in the direction of propagation of the wave. However, the strain rates during shock loading are in the region of 10^4–10^6 sec^{-1}, and the associated temperatures are 10°–200°C higher, depending primarily on initial porosity and peak stress. Although strictly comparable only to a planar solution, these conditions approximate the effects of a spherical shock front for radii of several tens of meters or greater.

The nonlinearity of stress-strain data on rocks makes it necessary to calculate moduli (coefficients relating stress to strain) using stress and strain increments representative of a general state of stress. These effective moduli no longer have the conventional assumption of elasticity associated with them, but they are, nevertheless, useful in relating stress to strain at specified stress states.

SYMBOLS AND DEFINITIONS

$\sigma_1, \sigma_2, \sigma_3$ maximum, intermediate, and minimum principal stresses, respectively. $\sigma_2 = \sigma_3 = P$, confining pressure.

$\epsilon_1, \epsilon_2, \epsilon_3$ maximum, intermediate, and minimum principal strains, respectively. $\epsilon_1 = \epsilon_l$, longitudinal strain. $\epsilon_2 = \epsilon_3 = \epsilon_r$, radial strain. $V = \epsilon_l + 2\epsilon_r = \epsilon_v$, volumetric strain.

K isothermal bulk modulus, $-VdP/dV$.

μ shear modulus, $(\sigma_1 - \sigma_3)/2(\epsilon_l - \epsilon_r)$.

ν Poisson's ratio, $-\epsilon_r/\epsilon_l$.

V_p compressional wave velocity.

τ maximum shear stress, $(\sigma_1 - \sigma_3)/2$.

P_m mean pressure, $(\sigma_1 + 2\sigma_3)/3$.

EXPERIMENTAL TECHNIQUES

Quasi-hydrostatic pressure-volume data to 40 kb are obtained in a piston cylinder device where the advance of the piston is monitored with increasing load [*Stephens*, 1964; *Stephens and Lilley*, 1970]. The pressure medium is a weak metal (lead or tin), and the maximum deviation from hydrostatic loading imparted to the sample is limited by the shear strength of the metal (typically 20–70 bars) at the appropriate confining pressure. Specimen volume is about 3 cm^3. For more detailed work at lower pressures (to 20 kb), metal-jacketed cylindrical samples (1.9-cm diameter × 3 cm) are compressed by using a fluid pressure medium. The jacketing material is either 0.15-mm annealed copper or 0.25-mm lead. The samples are me-

chanically sealed at their ends between steel pistons. The jackets are seasoned with 200 bars hydrostatic pressure, and electrical resistance strain gages are bonded to the metal jackets. Samples with similar dimensions are used to obtain uniaxial stress and uniaxial strain loading data. The latter samples can be loaded to a maximum stress (σ_1) of 40 kb with the piston of a piston cylinder die in which fluid-confining pressure (to 10 kb) can be independently controlled by means of a separate intensifier. Axial load is measured with a load cell placed in mechanical series with the sample inside the pressure vessel. For work at axial stress levels below 5 kb, a unique loading system [*Schock and Duba,* 1972] is used in which a 2.5-cm-diameter by 6.1-cm-long cylinder is axially loaded by means of a fluid. In this system, confining pressures may range up to 4 kb, and O-ring seals adjacent to the sample isolate the two working pressure fluids. This effectively removes problems associated with loading by a solid piston (e.g., piston misalignment and an elastic compliance mismatch, either of which gives rise to nonuniform stress fields). Instead of a metal jacket, the sample is encased with a thin (0.03 mm) layer of semiflexible epoxy to which the strain gages are bonded. The loading stresses are directly controlled, and the resulting strains are monitored by a small computer. Pressures are measured with a noninductively wound manganin coil calibrated against both known transitions and a Bourdon tube gage accurate to 0.1%, with a resulting accuracy of 1% in pressure. Strains are measured with 1-cm electrical resistance strain gages accurate to better than 1% at strains ranging to 0.05. These strain gages are larger than individual grains and measure strain on the surface of the sample. We assume that these strains are homogeneously distributed throughout, as is indicated by work on elastic solids and crystals [*Schock and Duba,* 1972]. Corrections are made for the effect of pressure on the strain gages [*Brace,* 1964; *Schock and Duba,* 1973].

EXPERIMENTAL OBSERVATIONS

Granodiorite. The failure envelope for dry granodiorite is illustrated in Figure 1 as determined in uniaxial stress loading at various

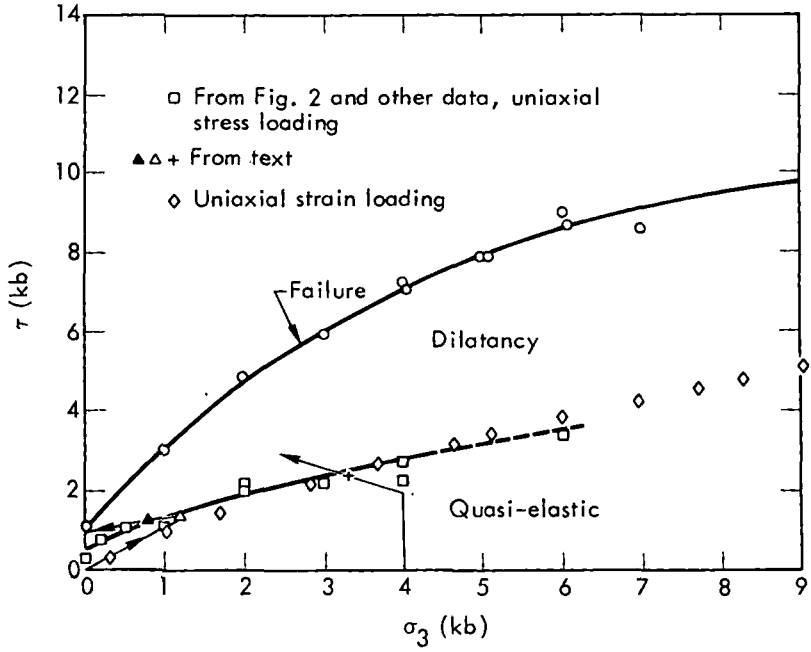

Fig. 1. Failure envelope for dry Climax stock granodiorite. Also shown are the boundary marking onset of dilatant behavior in uniaxial stress loading and the path followed during uniaxial strain loading. Two less common loading and unloading paths are also plotted with their onset of dilatancy (see text).

levels of confining pressure. This envelope represents the locus of points of maximum shear stress at failure on initial loading at the pressures noted. In all cases the granodiorite failed in a brittle manner; that is, the permanent axial strain before macroscopic fracture was less than 1%, and both tensile and shear fractures were observed [*Griggs and Handin*, 1960]. At low pressures, both are common, but as the confining pressures are increased, shear fractures become predominant.

The measured volume strains observed during uniaxial stress loading for several confining pressures are plotted against mean pressure in Figure 2. For comparison, the hydrostat is also shown for rock from the same block (Piledriver site). The characteristic volume increase (dilatancy) preceding failure [*Brace et al.*, 1966] is apparent. The shear stress at which the volume strain on uniaxial stress loading departs from the hydrostat is plotted in Figure 1 for these and additional data. In general, the locus of these points indicating onset of dilatancy defines a second curve below that of the failure envelope. This is the locus of points at which the effective bulk modulus exceeds that observed during hydrostatic loading. The region between the two curves then represents a dilatant region as defined in uniaxial stress loading. The onset of this dilatancy, as defined, is identical to that used by *Bieniawski* [1967] to indicate the onset of fracture initation, which gives rise to dilatant behavior and ultimately to failure.

Volume strain as referenced to the hydrostat is probably the most sensitive precursor (in terms of strain) to gross failure during uniaxial stress loading. In each case, the experiments were terminated at the first abrupt decrease in axial stress. At this point the strain gages were rendered inoperable and the jacket was generally ruptured, allowing fluid to enter the rock. Thus the total amount of dilatant behavior reported here is likely dependent on the experiment (i.e., partially controlled by the jacket strength, thickness, and ductility) and is considered to be a minimum value. *Swanson and Brown* [1971] have shown that the failure envelope for brittle rocks is independent of stress path (σ_1/σ_3) on initial compressive loading and is uniquely defined in shear stress-mean stress (stress deviator-invariant) space.

In our work, experiments along various loading paths on the Hardhat granodiorite show that this is also true for the curve establishing

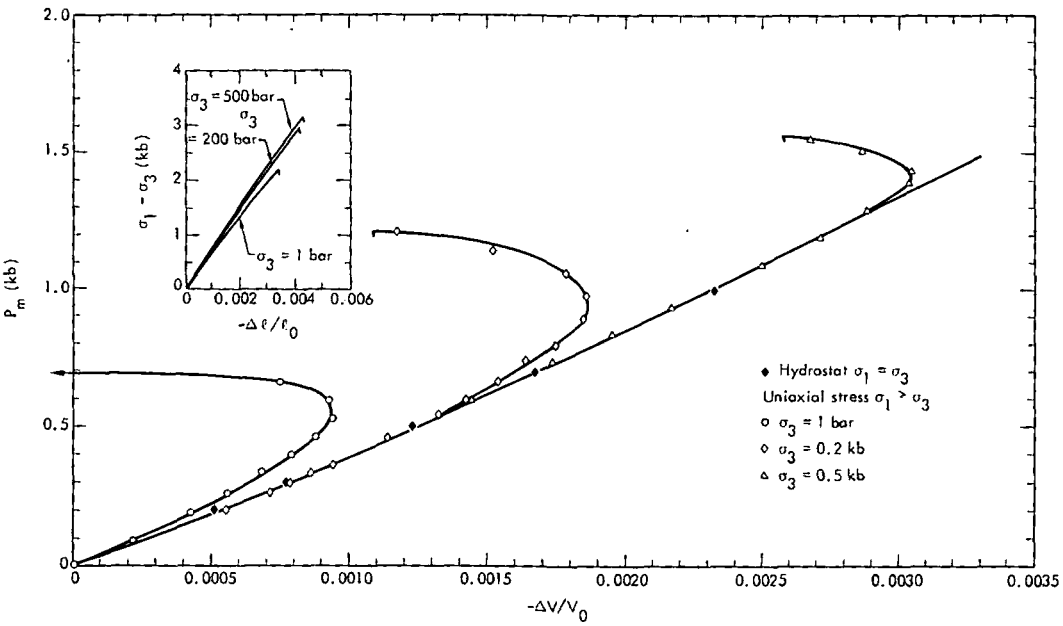

Fig. 2. Volume strain as a function of mean pressure for Climax stock granodiorite during uniaxial stress loading at several confining pressures. The hydrostat is shown for comparison. Inset shows axial stress-strain relationships observed for each.

the onset of dilatancy. An example is shown in Figure 3 and in Figure 1. A sample was first loaded to 4 kb σ_1, with $d\sigma_1/d\sigma_3 = 3.3$ (open triangle in Figure 1), without showing any evidence of dilatancy and was then unloaded with $d\sigma_1/d\sigma_3 = 1.75$. The upper limit of loading is very close to the dilatancy region as defined in Figure 1, and the unloading path chosen intersects this region in a very oblique fashion. As is apparent in Figure 3, after the hydrostat was loaded up the sample dilated on unloading. The shear stress associated with the onset of this dilatancy is 1.1 kb and that point (a solid triangle) is shown in Figure 1 for comparison. Similar data on a slightly different loading path and at a higher mean pressure are also shown (plus sign).

The stress states obtained on uniaxial strain loading from 1 bar are also shown (open diamond) in Figure 1. It is immediately apparent that loading under these conditions results in a path that is slightly curved, apparently away from the failure surface, an observation made by *Swanson and Brown* [1971] on two other brittle igneous rocks (Westerly granite and Cedar City tonolite). However, the loading path in Figure 1 apparently leads to intersection, or near intersection, with the dilatancy region. From the available data in Figure 1 it is impossible to determine whether the loading path in uniaxial strain is affected by this intersection. This is because of combined experimental scatter and the similarities in the slopes of the lower boundary of the dilatancy region and the uniaxial strain loading path. The observed relationship between volume strain and mean pressure for uniaxial strain loading is shown in Figure 4 and is compared with the hydrostat. There is no indication of dilatant behavior within the experimental error. The absence of dilatancy on uniaxial strain loading is not surprising. *Brace et al.* [1966] correlated dilatant behavior with large nonlinear circumferential strains during uniaxial stress loading in Westerly granite and thereby attributed this behavior to the formation of axial tensile cracks. In the uniaxial strain experiment a change in circumferential strain is precluded, and thus, once the dilatant region is intersected during uniaxial strain loading, the rock must load along the lower limit of this region.

In shock wave measurements the data are usually reported in terms that are reducible through the shock equations to σ_1 and ϵ_v and thus may be compared with the uniaxial strain data in Figure 4. Although there are no available shock data on material from the same block as the samples used in obtaining results in Figures 1–4 (Piledriver), data are available on samples from another locality in the stock [*Petersen*, 1969]. Our uniaxial-strain loading data for a sample from the same locality (Hardhat) are shown in Figure 4. All our data are observed to load directly toward the vicinity of the Hugoniot elastic limit (HEL) points

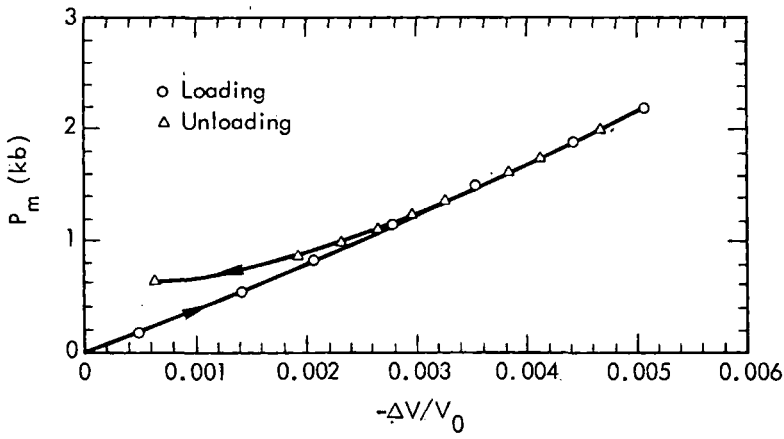

Fig. 3. Relationship between volume strain and mean pressure for Climax stock granodiorite loaded with $\sigma_1/\sigma_3 = 3.3$ without dilatant behavior and then unloaded along a path toward higher σ_1/σ_3. Dilatant behavior is observed on unloading.

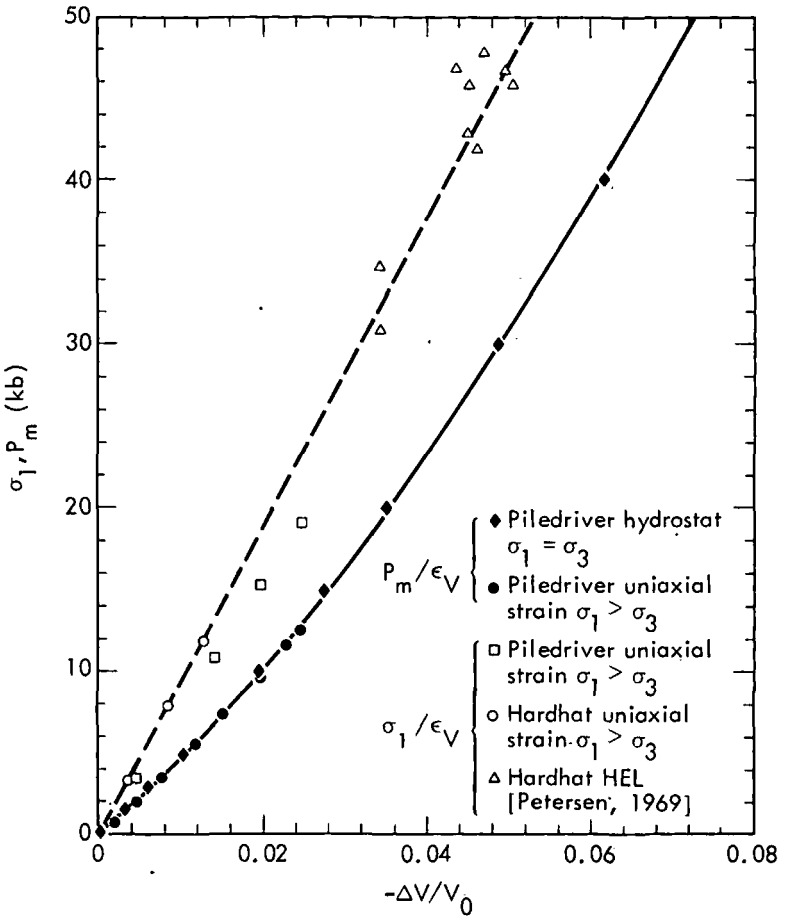

Fig. 4. Volume strain for Climax stock granodiorite as a function of mean pressure and axial stress during uniaxial strain loading. The hydrostat and HEL from *Petersen* [1969] are shown for comparison.

and show no curvature up to the maximum axial stress (12 kb). Similar results from the Piledriver locality are also shown in Figure 4; the Piledriver samples are somewhat more compressible than the Hardhat samples. This difference is consistent with the difference in the hydrostatic loading paths determined for the samples from the two localities. The conventional interpretation of an HEL is an intersection of the shock loading path (uniaxial strain) either with the failure surface or with a phase boundary [*Duvall and Fowles*, 1963]. Neglecting a phase transition, we can reconcile the observed diversion of the uniaxial strain loading path from the failure surface with the interpretation of the HEL as resulting from either (1) a strain rate effect whereby, in shock loading, dilatancy is diminished at high strain rate, as is suggested by the data of *Brace et al.* [1966], or (2) a diminishing of the dilatancy region with increasing confining pressure such that the lower limit of this region intersects the extension of the failure envelope at very high mean pressures (Figure 1), or from both. It is clear from the data in Figures 1 and 4 that the HEL observed for Hardhat does not correspond to intersection of the dilatancy region as defined in Figure 1 by the uniaxial strain loading path. The dilatancy region is intersected at an axial stress σ_1 of about 8–9 kb (3.5 kb σ_3). In Figure 4 the agreement between shock and static data shows there is little, if any, strain rate dependence in the axial stress-strain relationship, at least to the stress levels mea-

sured. This has also been observed by *Brace and Jones* [1971] for Westerly granite. However, this agreement does not prove or disprove a strain rate dependence of dilatancy, since in a uniaxial strain experiment the radial stress (σ_3) must increase to prevent dilatancy. The stress σ_3 is not plotted in Figure 4 because it is not derivable from the shock wave data.

Sandstone. The failure envelope for the Lance sandstone is shown in Figure 5 as determined in uniaxial stress loading at a strain rate of about 10^{-4} sec^{-1}. At relatively low mean stresses, the rock fails in a brittle manner. This is defined by the shape of the σ_1/ϵ_1 curve and the obvious tensile and shear fracture planes truncating the sample. At mean stress levels above about 6 kb (confining pressure ~3 kb) the rock is observed to deform in a macroscopically ductile manner [*Heard*, 1960]; i.e., axial strains greater than 5% are attained with more or less well distributed deformation. Cohesion is retained in the bulk sample. On the microscopic scale, the predominant deformation mechanism is cataclasis of the brittle silicates (quartz, chert, and siliceous cement) in both regions. However, in the brittle region, the deformation is localized, and only a few grains near the throughgoing fracture surfaces are involved. In the ductile regime, cataclasis of the silicate grains with consequent rotation of fragments is pervasive [*Borg*, 1971]. At confining pressures greater than about 3 kb, instead of fracture there is continued compression of the sample in the axial direction and expansion in the radial direction; the axial stress-strain curve becomes distinctly nonlinear, shows strong work hardening, and becomes irreversible on unloading. In Figure 5 the brittle fracture envelope is extended into the ductile range along the curve representing 5% permanent axial strain.

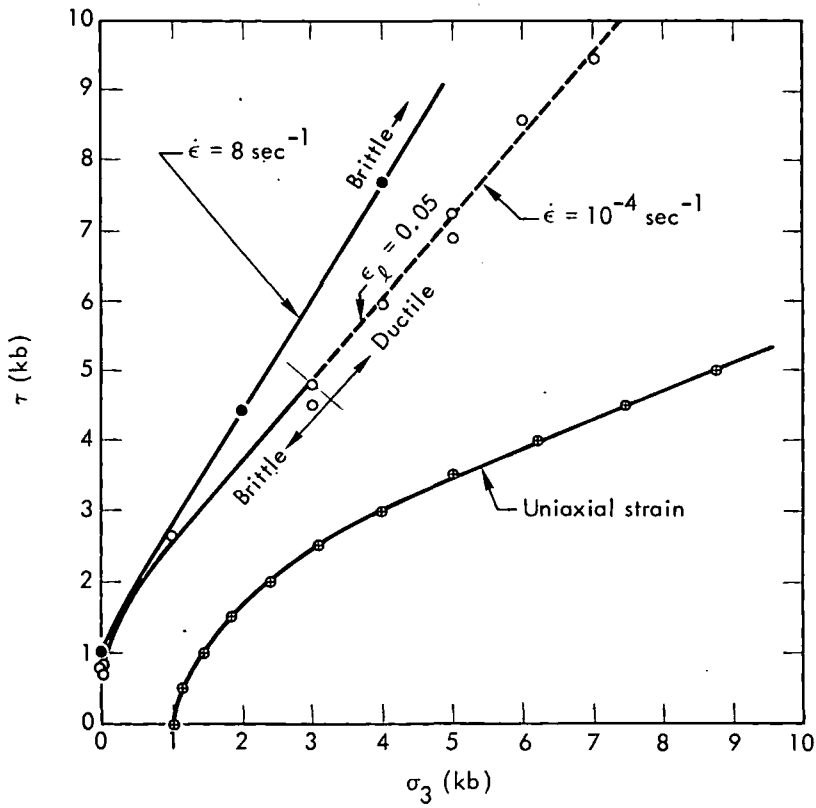

Fig. 5. Failure envelope for Lance sandstone based on uniaxial stress tests (dry) at strain rates of approximately 10^{-4} and 8 sec^{-1}. Loading behavior in uniaxial strain for the Lance sandstone (from 1 kb pressure) is also shown. The high strain rate data are from *Handin* [1972].

Also shown in Figure 5 is the failure surface based on similar uniaxial stress-strain data taken at a strain rate higher by a factor of about 8×10^4. Comparison of these curves shows that at the higher rate the shear stress at failure is larger by about 25% at confining pressures of 2–4 kb. This increase in strength with rate (average about 5% per decade) is identical to that observed for sandstone and a number of other silicate and carbonate rocks deformed at room temperature [e.g., *Handin et al.*, 1967; *Logan and Handin*, 1970; *Brace and Jones*, 1971]. As defined above, the relative ductility of this sandstone is much less at the higher rate as compared with the normal rate of testing. The brittle-ductile transition at 8 sec^{-1} is estimated to occur at a pressure in excess of about 5 kb, compared with the 3-kb value noted at the 10^{-4} sec^{-1} deformation rate (Figure 5).

The hydrostat for this sandstone is shown in Figure 6 with the volume strain data observed on uniaxial stress loading at several confining pressures. At low mean stresses the sandstone is observed to dilate in a manner similar to the granodiorite (Figure 2). At higher pressures this material compresses beyond the strains that are characteristic of comparable pressure on the hydrostat. On uniaxial stress loading in this region, compaction occurs, followed by dilation. Thus the bulk modulus becomes first smaller and then greater than the bulk modulus given by the hydrostat (Figures 6 and 7). Similar behavior was observed by *Morgenstern and Phukan* [1969] for a sandstone with 13% porosity when tested in uni-

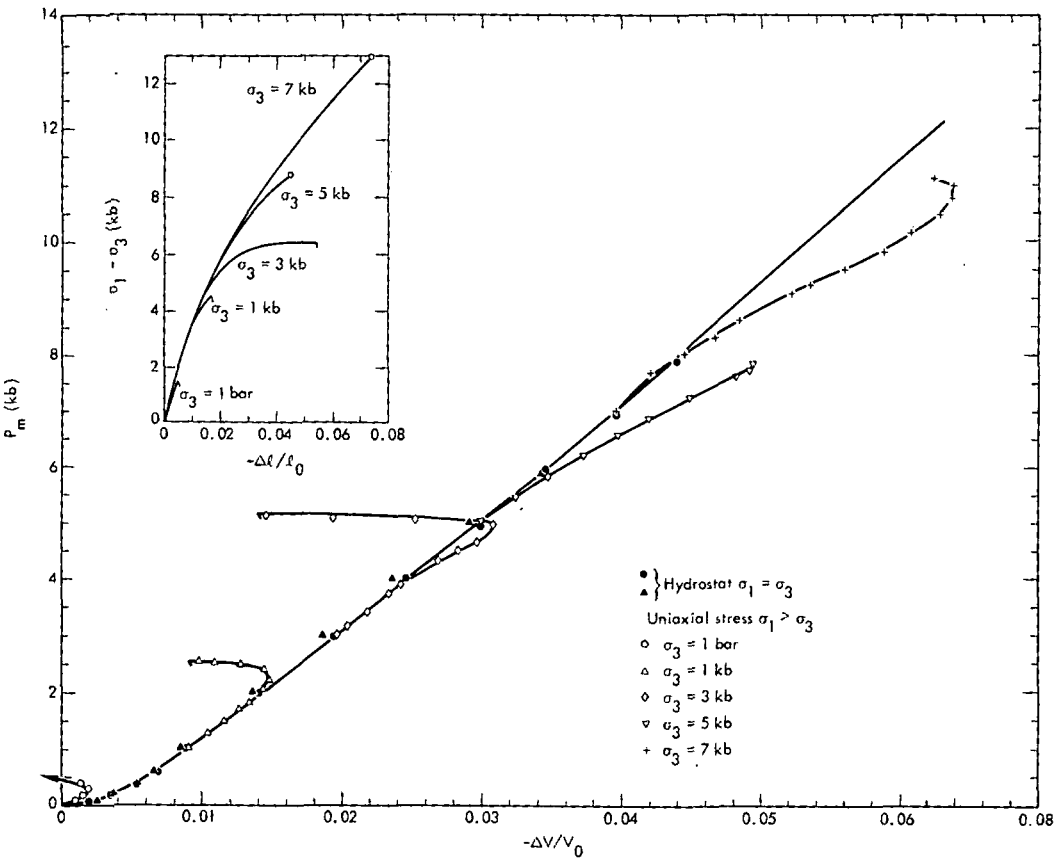

Fig. 6. Volume strain for Lance sandstone plotted as a function of mean pressure during uniaxial stress loading at several confining pressures and compared with the hydrostat. Inset shows axial stress-strain relationships observed for each loading.

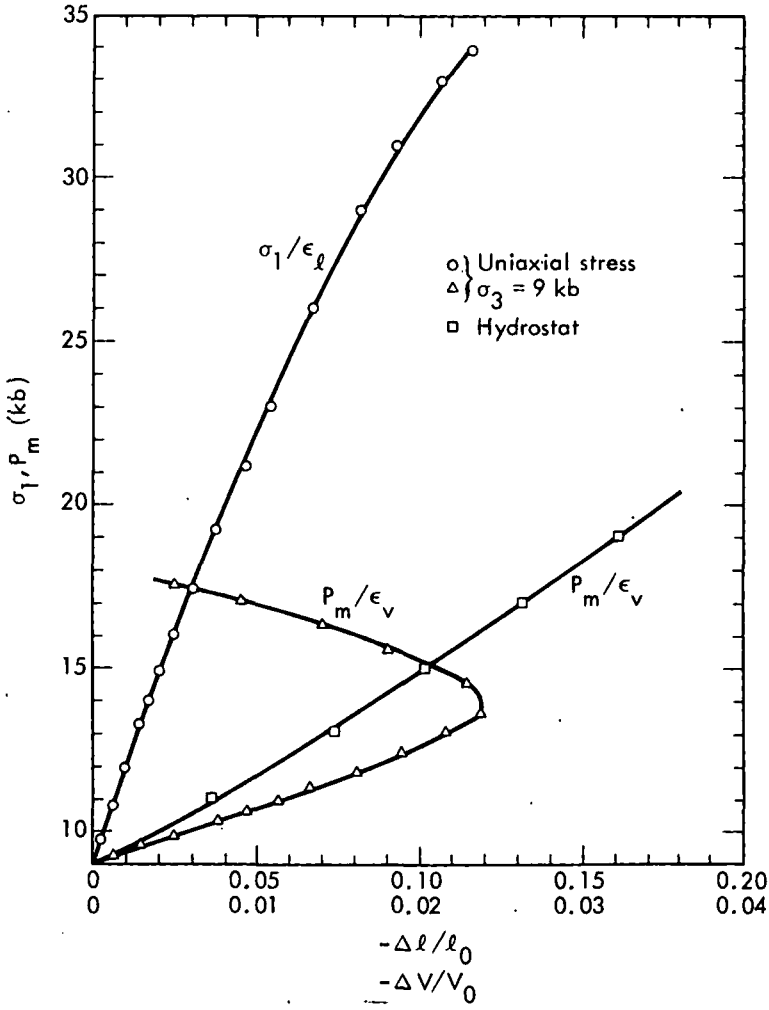

Fig. 7. Observed volume strain for Lance sandstone during uniaxial stress loading at 9 kb confining pressure. Axial stress-strain curve and hydrostat plotted for comparison.

axial stress after hydrostatic loading. In the brittle behavior region (Figure 5) the shear stress corresponding to onset of dilatancy is observed to become a progressively larger fraction of the fracture stress as the confining pressure is increased. Additionally, it is very difficult to reach a state of dilatant behavior in the ductile region (at mean pressures in excess of 6 kb). Instead, at confining pressure of 5–7 kb the axial stress is difficult to maintain, and only a small amount of apparent dilatant behavior is observed (Figure 6). Some of this apparent dilatancy at these confining pressures may be attributed to barreling of the sample resulting from friction with the steel end pieces. Tests that were not terminated by brittle failure were ended either by decoupling of the strain gage or by the inability to increase end load while axial strain was continued. Each test was begun at strain rates of approximately 10^{-4} sec^{-1}, but as the response became noticeably nonlinear, the strain rate diminished. The apparent inconsistency between the uniaxial stress results in Figures 5 and 6 is a direct result of the different strain rate histories.

At higher confining pressures (~9 kb) the axial stress, and hence mean pressure, could

be increased without difficulty. Significant dilatant behavior was observed, but only as a slowly increasing function of shear stress (Figure 7). There was some tendency for stress relaxation during incremental loading, but the end load and the axial strain could always be increased to the point where the strain gages were rendered inoperable. In this region, the axial stress-strain curve shows strong work hardening.

In Figure 8 the stress-strain path of the Lance sandstone is shown for loading in uniaxial strain from 1 kb hydrostatic pressure (approximate overburden pressure). A distinct break in the axial stress-strain data is seen at about 5 kb axial stress and corresponds to a mean stress of slightly less than 3 kb. Beyond this mean stress the material loads below the hydrostat. Collectively, the data in Figures 6 through 8 indicate that the observed compaction must result from the presence of a macroscopic shear stress component in the mean pressure not present under hydrostatic loading. When shear stress is present, the material compacts at a lower value of mean stress than when shear stress is absent, a behavior not observed in the granodiorite. However, like the granodiorite the path followed by this sandstone during uniaxial strain loading also deviates from the failure surface but in a much more pronounced fashion and beginning at lower pressures (Figure 5).

Virtually identical behavior to that demonstrated in Figure 8 is shown for a similar material in Figure 9. The Pictured Cliffs sandstone has been loaded from a hydrostatic pressure of 300 bars. This pressure represents its approximate overburden pressure at depth. Comparison with Figure 8 shows this sandstone to be slightly more compactable on loading than the Lance sandstone. The break in slope in the axial stress-strain loading data shown in both these figures is identical to what is observed at the HEL in shock wave experiments. However, it is apparent from the data in Figure 5 that this break does not represent intersection of the failure envelope, although if observed in low-stress shock wave data it might be interpreted as such. On the basis of shock data, *Petersen* [1969] suggests that failure may be initiated at axial stress levels below 2 kb for the Pictured Cliffs sandstone. The failure envelope data, illustrated inset in Figure 9, do not show a failure surface at this low level on the indicated loading path; the phenomenon is more likely to be enhanced compaction. It is, of course, apparent that this sandstone (as well as the Lance sandstone) cannot continue to load indefinitely below the hydrostat and that, as the porosity is progressively removed, its bulk modulus must increase and the pressure-volume path must rejoin the hydrostat at some higher mean pressure. The pronounced departure from the failure surface of both sandstones

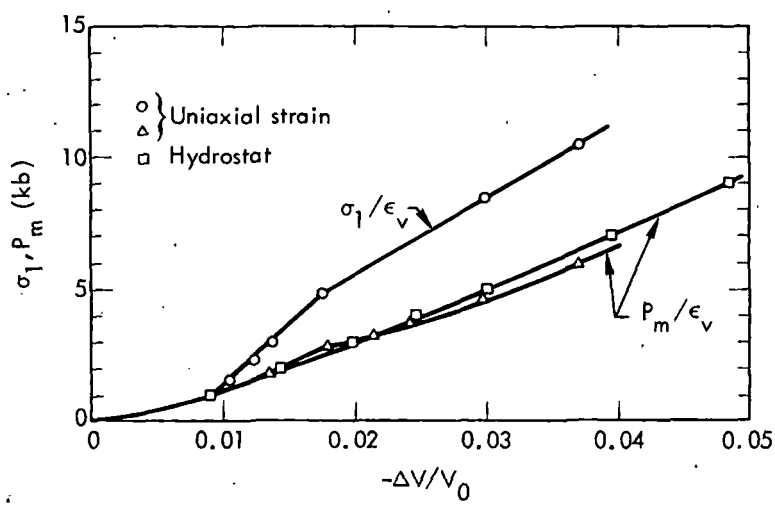

Fig. 8. Measured volume strain versus σ_1 and mean pressure for Lance sandstone during uniaxial strain loading. Hydrostat shown for comparison.

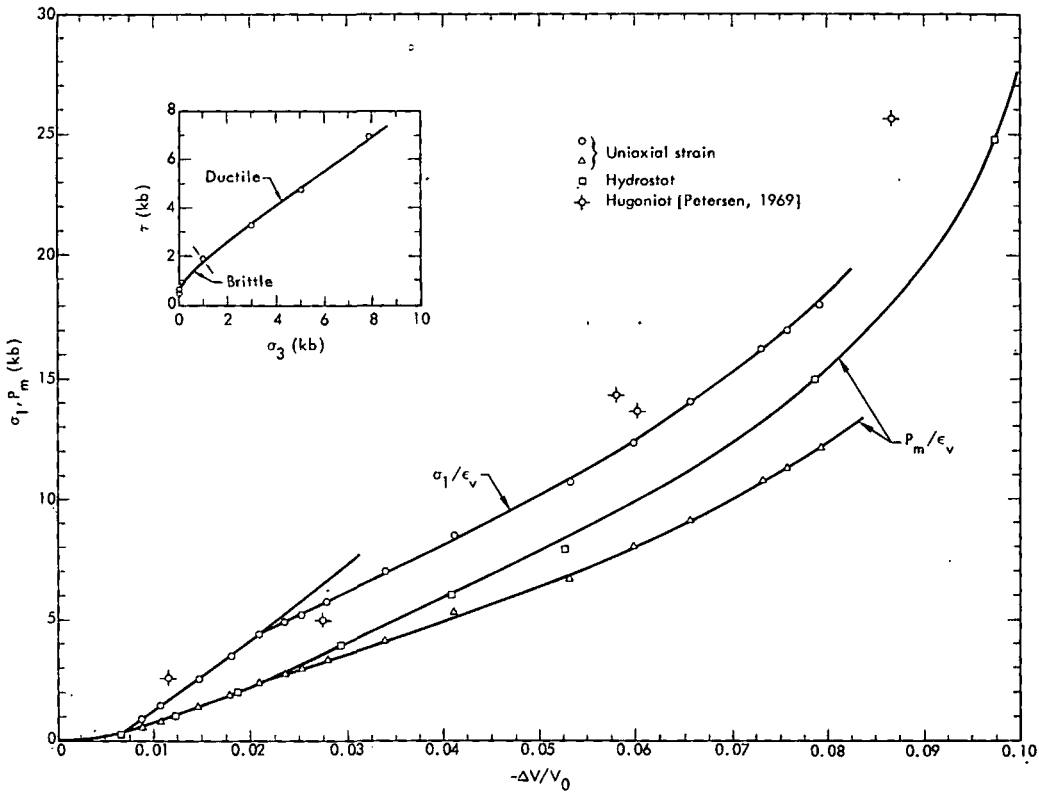

Fig. 9. Measured volume strain versus σ_1 and mean pressure for Pictured Cliffs sandstone during uniaxial strain loading. The hydrostat and Hugoniot data [*Petersen*, 1969] are plotted for comparison.

in uniaxial strain loading is related to the shear properties during compaction and therefore to the compaction itself. Thus the loading curve might be expected to eventually stiffen.

Several points determined along the Hugoniot [*Petersen*, 1969] are also shown in Figure 9. These points are determined on loading from atmospheric pressure and, to be strictly comparable to the static data, must be offset to the right by a ΔV initially corresponding to 300 bars. This amount of offset will decrease with increasing axial stress. It is probable that by 5 kb mean pressure, after significant compaction has taken place, the difference in initial pressure will be insignificant for the observed strain. The shock wave data are in general agreement with the laboratory static results, considering the uncertainties and reproducibility involved. Under shock conditions in the enhanced compaction region there is a slight tendency toward a steeper loading (Figure 9), which may indicate some strain rate dependence associated with enhanced compaction. This dependence may be related to the demonstrated effect of strain rate on strength for the Lance sandstone (Figure 5).

It appears that the initial quasi-linear portion of the axial stress-strain loading path in uniaxial strain represents nearly elastic loading in this graywacke. This is supported to some degree by comparing the calculated compressional velocity with that measured in the laboratory. Under conditions of uniaxial strain and under the assumption of elasticity, the slope σ_1/ϵ_1 is $V_P^2\rho_0$. The V_P derived from the initial loading slope in Figure 9 is 3.36 km sec^{-1}, as compared with a measured velocity of 3.5 km sec^{-1} at 300 bars. For the initial slope of the loading curve for the Lance sandstone in Figure 8, the calculated velocity is 4.25 km sec^{-1}. The measured velocity at 1 kb is 4.9 km sec^{-1}. The difference in both instances is probably real, indicating

that although the initial loading slopes under conditions of uniaxial strain tend toward linearity, the rock shows a small amount of inelasticity. This is probably a result of the influence of cracks, voids, and other imperfections present in the rock. At stress levels beyond the break in slope in Figures 8 and 9, pronounced inelastic behavior is observed as a result of the enhanced compaction.

As with the granodiorite, these observations can be used to delimit areas in shear stress-mean pressure space that represent the generalized volume strain behavior to be expected at a given stress-strain state along a loading path. This is done schematically in Figure 10 for the sandstones discussed above. The area of observed dilatancy is defined from the sandstone uniaxial stress loading data in the same manner as from the granodiorite, except that where the sample is loaded below the hydrostat (enhanced compaction), dilatant behavior is taken as beginning when the slope (on a $P_m - \epsilon_v$ plot) is greater than the slope at the corresponding mean pressure on the hydrostat. This is somewhat arbitrary and is only considered to represent the approximate stress level where dilatancy begins. In this sandstone, enhanced compaction apparently competes with dilatant behavior over a range of stress, and therefore the indicated boundaries are only to be considered approximate. The region of enhanced compaction is determined from both uniaxial stress and uniaxial strain data; it is defined from the stress conditions on loading, where the volumetric strains are larger (compaction) than for equivalent mean pressures on the hydrostat. As so defined, onset of this phenomenon seems to be independent of the loading path. Within the accuracy of the stress measurements there is no discernible difference in stress state between enhanced compaction observed by loading in uniaxial stress at various confining pressures and loading in uniaxial strain. At mean pressure beyond 2.5–3.0 kb, a slight softening (decreasing bulk modulus) in the hydrostatic pressure-volume curve is observed (Figure 6). In Fig-

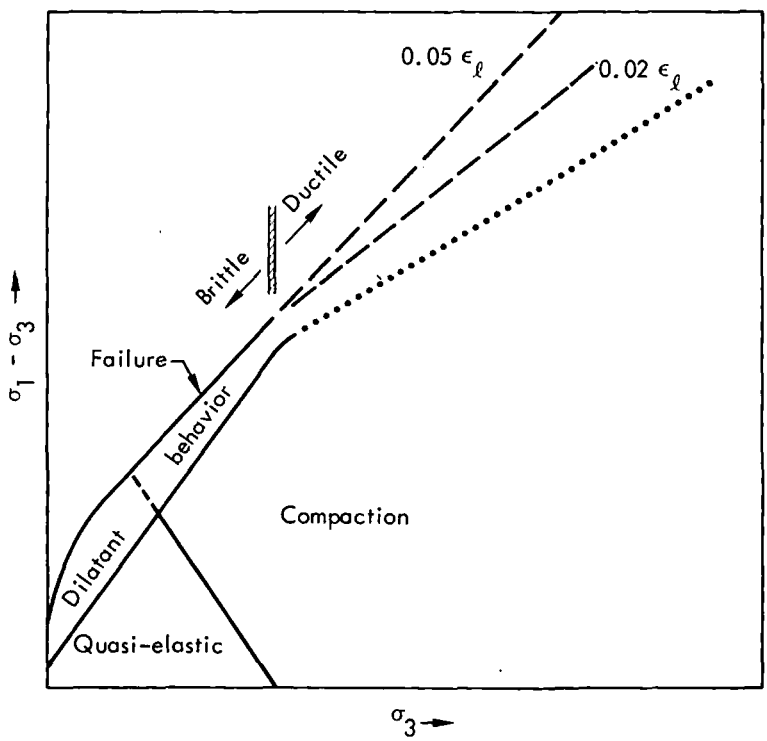

Fig. 10. Schematic representation of boundaries in stress difference-confining pressure space for the Lance and Pictured Cliffs sandstones. Axial strains shown for ductile failure are permanent values.

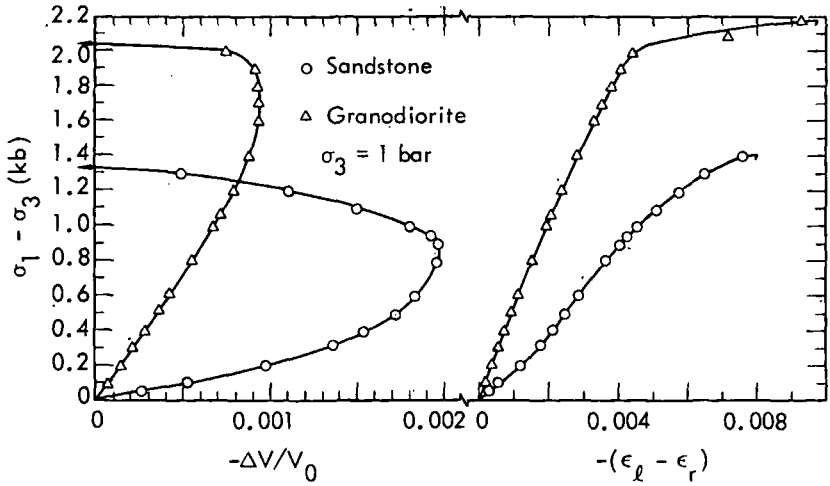

Fig. 11. Loading behavior in uniaxial stress at 1 bar confining pressure for the granodiorite and the Lance sandstone.

ure 10, constant mean pressure lines have a slope of $-\frac{1}{3}$; it is observed that the boundary denoting the onset of enhanced compaction has this slope, intersecting the abscissa at the point of softening of the hydrostat. Although the onset of enhanced compaction appears to depend only on the mean stress state, the amount of compaction observed with stress change obviously depends on the shear stress level (Figure 6). Not shown in Figure 10 is the elimination of the enhanced compaction regime when the material approaches theoretical density.

The importance of dilatancy apparently decreases as mean stress is increased up to the pressure characteristic of the brittle-ductile transition (Figure 6). This is shown in Figure 10 as a near-intersection of the line denoting onset of dilatant behavior with the failure surface at about 3 kb. This is consistent with the hypotheses of *Scholz* [1968] and *McClintock and Walsh* [1963] that dilatancy is associated with macroscopic brittle fracture. At confining pressures of about 3 kb, dilatancy seems minimal but again becomes large as confining pressure increases (see Figure 7). In this intermediate pressure range the decrease in dilatancy before fracture (at large strains) is believed to be partially a result of the competing influence of pore compaction. At 9 kb (and higher) this pore collapse has already taken place before the nonhydrostatic loading is begun, and the radial displacements again dominate, as was described for low pressure. Dilatancy can now take place because of the fracture of the brittle quartz grains throughout the entire rock. At very high pressures ($\gg$30 kb), where the porosity approaches zero and the quartz and other brittle phases become plastic (intragranular flow) [*Christie et al.*, 1964], dilatancy can be expected to be much less important.

Comparison of granodiorite and graywacke behavior. In Figure 11, the uniaxial stress loading behavior of the Lance sandstone at 1 bar confining pressure is compared with that of the granodiorite. Although the strengths are comparable and both show dilatant behavior prior to failure, the sandstone not only has a lower shear modulus but is also more compressible. However, the sandstone shows a much higher resistance in shear strain relative to bulk compression. This is demonstrated by the ratio of slopes at the right of Figure 11, where each slope is twice the effective shear modulus μ, compared with the ratio on the left, where each slope is proportional to the effective bulk modulus K. Thus, although both moduli are smaller for the sandstone, the ratio of the effective shear modulus to the effective bulk modulus is much larger for the sandstone than for the granodiorite. Poisson's ratio furnishes a measure of the relationship of μ to K:

$$\nu = \frac{-\epsilon_r}{\epsilon_l} = \frac{3 - 2\mu/K}{6 + 2\mu/K}$$

In Figure 12 the effective Poisson's ratio is shown for the data in Figure 11. The initial ν for the sandstone is, in this case, low enough that the shear modulus is greater than the bulk modulus. This is characteristic of many sandstones with appreciable quartz content [*Birch*, 1966].

In quartzitic sandstones, the detrital quartz grains are generally described as having rounded edges but not as being highly spherical. Packing of such particles allows for the familiar interlocking texture [*Pettijohn*, 1957] where grain edges fit into the surface depressions on neighboring grains in an irregular manner. This presumably imparts a resistance to lateral (or shear) movement while at the same time only slightly affecting the relative movement of grains toward each other. The intergranular matrix and cement are composed primarily of microscopic clay mineral particles and calcite, which strongly affect compressibility in this sandstone. However, once the initial resistance to shear is overcome, intergranular movement takes place and contributes to a rapidly decreasing ratio of shear modulus to bulk modulus. In contrast, the granodiorite shows much less relative resistance to shear deformation. Narrow cracks and intercrystalline contacts common to crystalline rock are much more linear and pervasive, which results in much lower porosity and more relative freedom of shear movement. As was mentioned in discussing the granodiorite data, dilatant behavior in the sandstone is correlated with large nonelastic circumferential strains. When these large strains occur, the effective Poisson's ratio exceeds 0.5, a limiting value for an elastic solid.

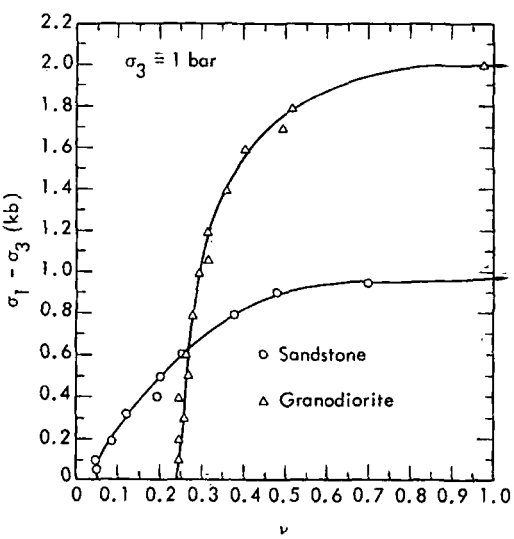

Fig. 12. Effective Poisson's ratio in uniaxial stress loading to failure at 1 bar confining pressure for the granodiorite and the Lance sandstone.

In Figure 13 we compare the behavior of the two rocks in response to initial loading in uniaxial strain. The respective failure surfaces are also shown for reference. The steep initial slope shown by the sandstone reflects the low initial value of the effective Poisson's ratio; as the shear stress is increased this slope is rapidly decreased. In contrast, the slope of the granodiorite loading curve is initially less steep but more nearly linear to higher levels of shear stress. Both results are in agreement with the observations in uniaxial stress loading noted above.

In summary, the stress-strain behavior in a variety of stress states has yielded data on two dissimilar rock types that show many similarities in terms of their overall behavior. Both rocks exhibit characteristic dilatant behavior prior to brittle failure. In the sandstone, however, increasing mean pressure is seen to progressively decrease the amount of dilatancy until, as the failure mechanism changes from brittle fracture to macroscopic ductile flow, dilatant behavior ceases. Hence dilatancy is directly associated with large-scale intergranular brittle fracture. A second episode of dilatant behavior is observed in the sandstone at very high mean pressures. In this pressure region, when the data are plotted in $\sigma_1 - \epsilon_v$ space, very gradual dilation occurs. The observed large positive volume strains are believed to result from pervasive intragranular fracture in contrast to the localized macroscopic fracture observed at low mean pressures. This, in turn, results in strong work hardening at the high pressure. Thus the homogeneous distribution of fragments on such a fine scale yields large overall distortional strains.

The laboratory uniaxial strain data for both rocks indicate loading below and apparently away from the failure envelope. If the observed HEL really represents intersection of the uniaxial strain loading path with the failure surface, either a strain rate dependent loading process or a diminishing of dilatancy with in-

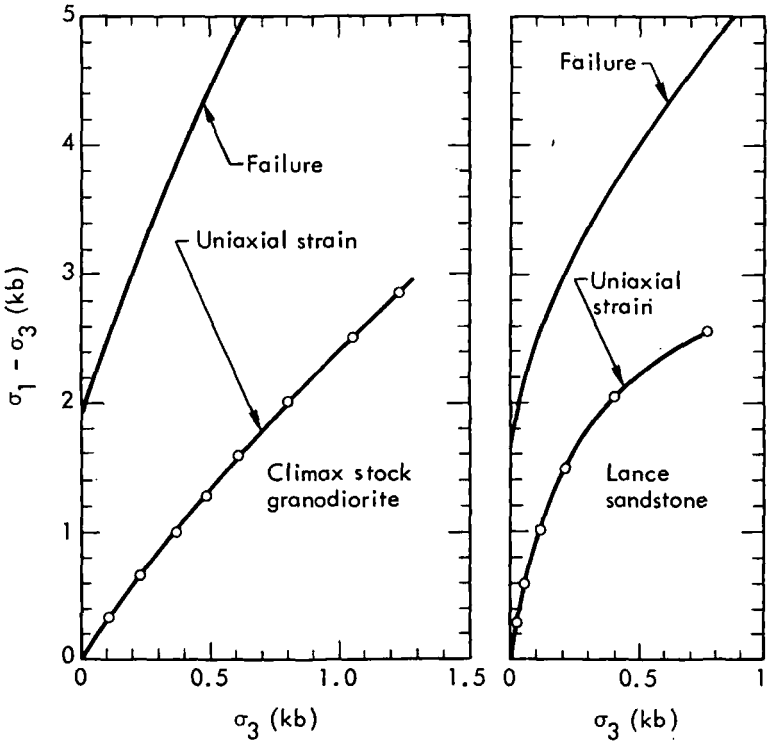

Fig. 13. Initial loading behavior in uniaxial strain. The respective failure surfaces for the granodiorite and sandstone are shown from Figures 1 and 5 for comparison.

creasing pressure, or both, must be responsible. The enhanced compaction shown by the sandstone is not observed in the granodiorite. This compaction is believed to result from the combination of relatively weak cement and matrix with the associated porosity. Such particle-pore interaction would then allow a small shear stress to move grains with respect to each other, thus resulting in more efficient packing and a permanent decrease in volume.

Discussion and Conclusions

The enhanced compaction observed in Figures 6 through 8 is apparently related to the nature and packing of the internal constituents of the sandstone and would be expected to be characteristic of quartzitic sandstones with small amounts of siliceous cement and several percent porosity. Very porous rocks often exhibit collapse of the pores beginning at stresses as low as 0.1 kb [*Stephens et al.*, 1970; *Stephens and Lilley*, 1970]. If they are examined carefully, the hydrostatic data in Figure 6 show a slight softening beginning in the vicinity of 3 kb (Table 1); in addition, the rock exhibits irreversible compaction on unloading. The resulting pore collapse is thought to occur by one or both of two processes: by flow or fracture of the cement between the grains and, at higher stress levels, by motion and fracturing of individual grains with consequent displacement and rotation of the resulting fragments into

TABLE 1. Lance Sandstone Compressibility as a Function of Pressure

P, bar	β, Mb^{-1}
45	21.7
145	14.6
300	9.3
505	6.7
805	5.4
1505	5.1
2495	4.8
3490	5.7
4470	5.1
5435	5.2
6455	4.9
7455	4.5

the existing pores. Although the breakdown of the cement seems to be, within experimental error, a function only of the total macroscopic stress state (mean pressure), the compaction subsequently observed is strongly a function of macroscopic shear stress. The initial breakdown of the cement is by failure on a microscopic level resulting from localized stress concentrations. This breakdown is, in turn, caused by the interaction of pores, grains, and the external macroscopic stress. Once the breakdown takes place, the grains or the resulting fragments or both may move relative to one another to fill the available pore space. The process envisioned involves both intracrystalline flow as well as cataclasis of the component grains, with the latter dominating. There is ample microscopic evidence for this interpretation [e.g., *Borg et al.*, 1960; *Friedman*, 1963].

As mean pressure is increased, the degree of dilatancy observed in the sandstone is sharply curtailed. It was observed from the data in Figure 6 that at mean stress levels about 6 kb it was very difficult to obtain dilatant behavior and that the samples no longer failed in a brittle manner, that is, by localized throughgoing tensile and shear fractures. Thus dilatant behavior is much attenuated or has disappeared when the rock no longer fails in a macroscopically brittle manner. Ductile behavior is, in turn, correlated with very well distributed cataclastic flow and intergranular movements. At still higher mean stress levels (Figure 7) strong dilatancy is again observed but is associated here with an axial stress-strain curve exhibiting strong work hardening. At these stress levels it is suggested that the mean pressures are high enough so that most of the pores have already been removed and the intergranular friction from these high normal stresses leads to strong work hardening. The resulting high-stress differences are then sufficient to form additional intergranular fractures and to open existing fractures, thus leading to dilation. This interpretation is reinforced by the microscopic observations of *Borg* [1971], where quartz and chert grains become increasingly fractured as the sandstone is deformed at progressively higher pressures in the ductile regime.

Several conclusions are suggested by comparing the stress states and corresponding areas of behavior of the granodiorite and the graywacke. In the sandstone the pronounced pinching out of the area of observed dilatant behavior near the brittle-ductile transition (Figure 10) suggests the possibility that similar behavior may also occur in this region in the granodiorite at mean stresses well beyond the limit shown in Figure 1, where most crystalline species within the rocks begin to deform plastically. In the sandstone the amount of dilatancy is seen to be a function of mean stress, whereas with the granodiorite data alone this could only be suggested. The granodiorite is inherently more brittle and is lacking appreciable weak constituents as well as the porosity of the sandstone. The predominant mineral species such as quartz and feldspar deform by intragranular flow only at mean stresses considerably in excess of 50 kb at 25°C [*Christie et al.*, 1964; *Seifert*, 1969].

Both the cataclasis and the intragranular flow associated with the brittle and ductile regimes of the failure envelope have been demonstrated to be rate (and temperature) dependent in quartz [*Heard and Carter*, 1968; *Martin*, 1972] and can be expected to behave similarly for other mineral species. The differential stress necessary to initiate each process is also found to be markedly dependent on the rate of deformation. Therefore, at the strain rate characteristic of shock loading, both the brittle-ductile transition pressure and the entire failure envelope can be expected to be displaced toward higher levels of shear stress and mean pressure than are observed at the usual laboratory testing rates (Figure 5).

The gross similarity in the general behavior of both the sandstone and the granodiorite in shear stress-mean stress space suggests that the applicability of this approach may not be limited to these rock types. This is supported by the data of *Green et al.* [1971] on a shale that exhibits characteristics similar to the Lance sandstone. The shale is somewhat different, however, in that the enhanced compaction takes place at lower mean pressures than for the sandstone studied here. Thus, a plot of observed behavior regions for this rock would be similar to the plot in Figure 10, except that all stress values would be lowered slightly. Similar behavior has also been reported recently in Solnhofen limestone [*Green et al.*, 1972].

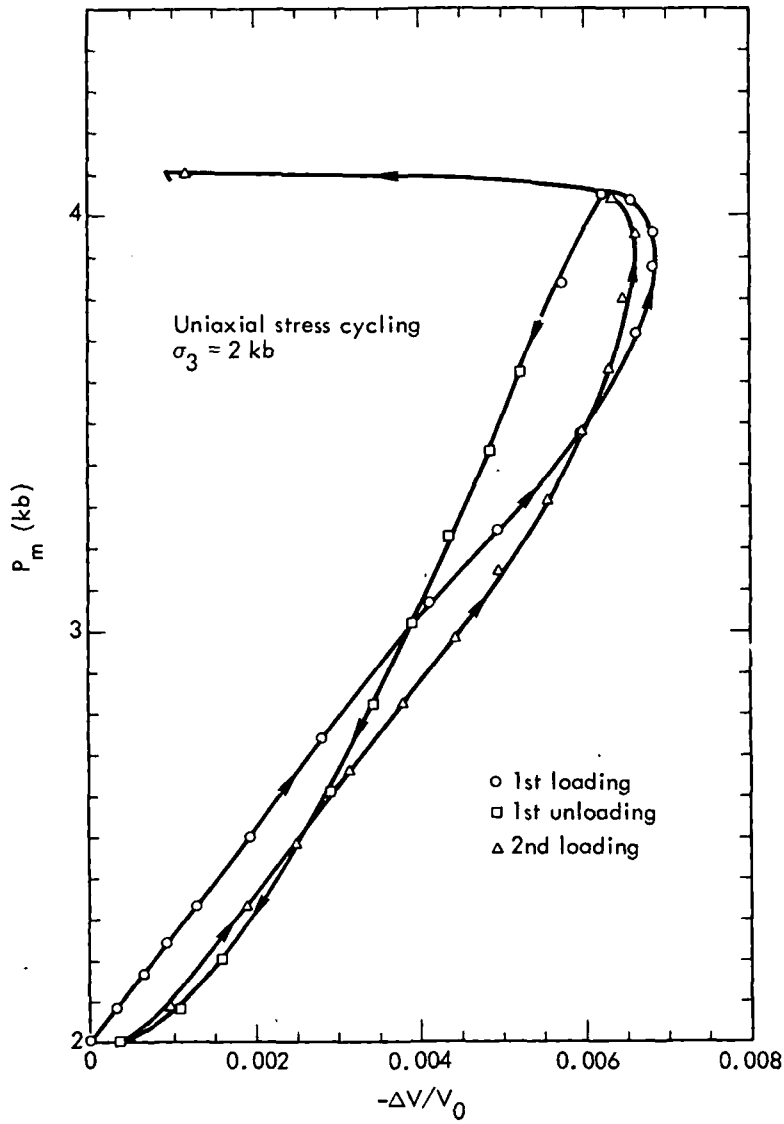

Fig. 14. Observed volume strain as a function of mean pressure for a Climax stock granodiorite sample at 2 kb confining pressure first loaded into the dilatancy region (without failure) and then unloaded before being reloaded to failure.

Edmond and Paterson [1972] have reported volume strain data obtained by a dilatometric technique at constant confining pressure on several materials including a limestone, a marble, and a porous sandstone. Their data demonstrate the competing processes of compaction and dilatancy for materials that are primarily ductile. We believe that these results and the interpretation offered by Edmond and Paterson are compatible with the present interpretation.

In presenting the foregoing data we have suggested that the levels of shear stress and mean stress are fundamental indicators of the behavior of a rock, at least in macroscopic compression with equal intermediate and minimum principal stresses. The ability to predict, within experimental error, a phenomenon indic-

ative of a type of behavior (e.g., failure, dilatancy, compaction) by using these parameters, independent of loading paths, certainly supports this suggestion. As a result, any relationship that is chosen to represent this behavior in a theoretical model should be simplified, as, for example, in a numerical simulation [*Cherry and Petersen*, 1970; *Cherry et al.*, 1970]. The ability to uniquely determine the presence or absence of a type of behavior on loading enables the simplified handling of loading response in any model to be used in such a calculation. Instead of one complex equation to model the complete response of a rock over a specified loading path, several simple equations can be used, each suitable only for a well-defined region in stress space. The type of behavior to be modeled at the stress state given would then be determined by a numerical test, which is incorporated into the calculation. Since the stress-strain relationships within a given region are now less complex, each equation necessarily involves fewer terms than an equation used to model complete behavior from initial loading to failure. In essence, the apparent uniqueness of stress state on loading can be used to simplify a model that seeks to obtain a reasonably accurate description of the response of a given medium to the imposed stress.

It should be reemphasized that the general behavior patterns observed and the conclusions drawn therefrom pertain only to the compressive loading of these materials, and perhaps of similar materials, when $\sigma_2 = \sigma_3$. Unloading phenomena for the rocks discussed here are distinctly different; irreversible phenomena are common. For example, a rock that has dilated but has not failed will not unload along the same stress-strain curve as was attained on loading. At low mean stresses a large portion of the bulk volume increase due to dilatant behavior remains on the release of shear stress [*Brace et al.*, 1966]. In contrast, at higher mean pressures, some of the increase in bulk volume may disappear on the release of shear stress (Figure 14).

The implication from the data on granodiorite and sandstone, when strain rate effects are neglected, is that little dilatancy may take place on shock loading. On subsequent unloading, especially from below the failure surface, this situation may be entirely different. On unloading, the particle velocity, having increased instantaneously at the shock front, will generally decay unless a rarefaction wave is present, in which case the particle velocity will increase gradually [*Petersen et al.*, 1970; *Fowles and Williams*, 1970]. Thus unloading is likely to be above the uniaxial strain loading path because the axial stress is maintained by the particle motion normal to the shock front (σ_1), whereas the stress parallel to the shock front (σ_3) may relax. The dilatant region as defined in Figures 1 and 11 might therefore be entered on unloading, and the amount of dilatancy retained on complete unloading is a function of the rate of decay of radial stress. Preliminary indications are that unloading phenomena are similar to loading phenomena: i.e., dependent on shear stress and mean stress. However, further work is necessary to determine the nature of these relationships.

Acknowledgments. We gratefully acknowledge the assistance of the following: H. Louis, H. Washington, and E. Lilley were instrumental in obtaining the data reported. Discussions with J. Cherry have added to understanding of the phenomenology involved in the deformation of granodiorite on the basis of the Hardhat and Piledriver experience and of numerical calculations. A. Duba was instrumental in obtaining a portion of the data and in discussing the results therefrom. L. Rogers and the El Paso Natural Gas Company generously supplied the sandstone cores. I. Borg supplied samples of Piledriver granodiorite and performed post-test petrographic examination of many samples. We thank J. Logan and J. Magouirk of Texas A&M University for their help in obtaining the high strain rate data reported in Figure 5.

This work was performed under the auspices of the U.S. Atomic Energy Commission.

REFERENCES

Allingham, J. W., and S. Zeitz, Geophysical data on the Climax stock, NTS, Nye Co., Nevada, *Geophysics*, *28*, 599, 1962.

Bieniawski, Z. T., Mechanism of brittle fracture of rock, *Int. J. Rock Mech. Mining Sci.*, *4*, 395–430, 1967.

Birch, F., Compressibility: Elastic constants, in *Handbook of Physical Constants, Mem. 97*, rev. ed., edited by S. P. Clark, Jr., pp. 97–173, Geological Society of America, Boulder, Colo., 1966.

Borg, I. Y., M. Friedman, J. Handin, and D. V. Higgs, Experimental deformation of St. Peter sand: A study of cataclastic flow, in *Rock Deformation, Mem. 79*, edited by D. T. Griggs

and J. Handin, pp. 133–191, Geological Society of America, Boulder, Colo., 1960.

Borg, I. Y., Microscopic examination of undeformed and laboratory deformed Wagon Wheel rocks, *Rep. UCRL-51014*, 17 pp., Lawrence Livermore Lab., Livermore, Calif., 1971.

Borg, I. Y., Some shock effects in granodiorite to 270 kbar at the Piledriver site, in *Flow and Fracture of Rocks, Geophys. Monogr. Ser.*, vol. 16, edited by H. C. Heard, I. Y. Borg, H. L. Carter, and C. B. Raleigh, pp. 293–311, AGU, Washington, D.C., 1972.

Brace, W. F., Effect of pressure on electrical distance strain gages, *Exp. Mech., 4*, 212, 1964.

Brace, W. F., and A. H. Jones, Comparison of uniaxial deformation in shock and static loading of three rocks, *J. Geophys. Res., 76*, 4913–4921, 1971.

Brace, W. F., B. W. Paulding, Jr., and C. Scholz, Dilatancy in the fracture of crystalline rocks, *J. Geophys. Res., 71*, 3939–3953, 1966.

Butkovich, T. R., Calculation of the shock wave from an underground nuclear explosion in granite, *J. Geophys. Res., 70*, 885–892, 1965.

Cherry, J. T., and F. L. Petersen, Numerical simulation of stress wave propagation from underground nuclear explosions, *Proceedings of Symposium on Engineering with Nuclear Explosives*, vol. 1, pp. 142–220, American Nuclear Society, Hinsdale, Ill., 1970.

Cherry, J. T., S. Sack, G. Maenchen, and V. Kransky, Two-dimensional stress-induced adiabatic flow, *Rep. UCRL-50987*, 62 pp., Lawrence Livermore Lab., Livermore, Calif., 1970.

Christie, J. M., H. C. Heard, and P. N. LaMori, Experimental deformation of quartz single crystals at 27 to 30 kilobars confining pressure and 24°C, *Amer. J. Sci., 262*, 26–55, 1964.

Duvall, G. E., and G. R. Fowles, Shock waves, in *High Pressure Physics and Chemistry*, vol. 2, edited by R. S. Bradley, pp. 209–291, Academic, New York, 1963.

Edmond, J. M., and M. S. Paterson, Volume changes during the deformation of rocks at high pressures, *Int. J. Rock Mech. Mining Sci., 9*, 161–182, 1972.

Fowles, G. R., and R. F. Williams, Plane stress wave propagation in solids, *J. Appl. Phys. 41*, 360–363, 1970.

Friedman, M., Petrofabric analysis of experimentally deformed calcite-cemented sandstones, *J. Geol., 71*, 12–37, 1963.

Green, S. J., R. M. Griffin, and H. R. Pratt, Material properties of a shale for shock calculation, *Rep. TR 71-12*, 34 pp., Terra Tek, Inc., Salt Lake City, Utah, 1971.

Green, S. J., J. D. Leasia, R. D. Perkins, and A. H. Jones, Triaxial stress behavior of Solenhofen limestone and Westerly granite at high strain rate, *J. Geophys. Res., 77*, 3711–3724, 1972.

Griggs, D., and J. Handin, Observations on fracture and a hypothesis of earthquakes, in *Rock Deformation, Mem. 79*, edited by D. T. Griggs and J. Handin, pp. 347–364, Geological Society of America, Boulder, Colo., 1960.

Handin, J., Studies in rock fracture, final report, U.S. Army Corps of Eng. contract DACA 73-68-C-0004, 34 pp., Texas A&M Univ., College Station, 1972.

Handin, J., H. C. Heard, and J. N. Magouirk, Effects of the intermediate principal stress on the failure of limestone, dolomite, and glass at different temperatures and strain rates, *J. Geophys. Res., 72*, 611–640, 1967.

Heard, H. C., Transition from brittle fracture to ductile flow in Solenhofen limestone as a function of temperature, in *Rock Deformation, Mem. 79*, edited by D. T. Griggs and J. Handin, pp. 193–226, Geological Society of America, Boulder, Colo., 1960.

Heard, H. C., and N. L. Carter, Experimentally induced 'natural' intragranular flow in quartz and quartzite, *Amer. J. Sci., 266*, 1–42, 1968.

Houser, F. N., and F. G. Poole, Granite exploration hole, area 15, Nevada Test Site, Nye County, Nevada, *U.S. Geol. Surv. Rep. TEM-836A*, 1959.

Krynine, P. D., The megascopic study and field classification of sedimentary rocks, *J. Geol., 56*, 130–165, 1948.

Logan, J. M., and J. Handin, Triaxial compression testing at intermediate strain rates, in *Proceedings of the 13th Symposium on Rock Mechanics*, edited by G. B. Clark, pp. 167–194, American Institute of Mining, Metallurgical, and Petroleum Engineers, Rolla, Mo., 1970.

Martin, R. J., III, Time-dependent crack growth in quartz and its application to the creep in rocks, *J. Geophys. Res., 77*, 1406–1419, 1972.

McClintock, F. A., and J. B. Walsh, Friction on Griffith cracks in rocks under pressure, *Proceedings of 4th U.S. Congress on Applied Mechanics*, edited by R. M. Rosenberg, pp. 1015–1021, American Society of Mechanical Engineers, New York, 1963.

Morgenstern, N. R., and A. L. Tamuly Phukan, Non-linear stress-strain relations for a homogeneous sandstone, *Int. J. Rock Mech. Mining Sci., 6*, 127–142, 1969.

Petersen, C. F., Shock wave studies of selected rocks, Ph.D. thesis, 92 pp., Stanford Univ., Stanford, Calif., 1969.

Petersen, C. F., W. J. Muri, and M. Cowperthwaite, Hugoniot and release-adiabat measurements for selected geologic materials, *J. Geophys. Res., 75*, 2063–2072, 1970.

Pettijohn, F. J., *Sedimentary Rocks*, 2nd ed., 526 pp., Harper and Row, New York, 1957.

Schock, R. N., and A. G. Duba, Quasi-static deformation of solids with pressure, *J. Appl. Phys., 43*, 2204–2210, 1972.

Schock, R. N., and A. G. Duba, Pressure effects on the response of foil strain gages, *Exp. Mech., 13*, 43–44, 1973.

Schock, R. N., H. C. Heard, and D. R. Stephens, High-pressure mechanical properties of rocks from Wagon Wheel No. 1, Pinedale, Wyo., *Rep. UCRL-50963*, 18 pp., Lawrence Livermore Lab., Livermore, Calif., 1970.

Scholz, C. H., Microfracturing and the inelastic deformation of rock in compression, *J. Geophys. Res., 73*, 1417–1432, 1968.

Seifert, K. E., Strength of Adirondack anorthosite at elevated temperatures and pressures, *Geol. Soc. Amer. Bull., 80*, 2053–2060, 1969.

Short, N. M., Effects of shock pressures from a nuclear explosion on mechnical and optical properties of granodiorite, *J. Geophys. Res., 71*, 1195–1215, 1966.

Stephens, D. R., The hydrostatic compression of eight rocks, *J. Geophys. Res., 69*, 2967–2978, 1964.

Stephens, D. R., and E. M. Lilley, Loading-unloading pressure-volume curves for rocks, *Proceedings of Symposium on Engineering with Nuclear Explosives*, vol. 1, pp. 89–109, American Nuclear Society, Hinsdale, Ill., 1970.

Shephens, D. R., E. M. Lilley, and H. Louis, Pressure-volume equation of state of consolidated and fractured rocks to 40 kbar, *Int. J. Rock Mech. Mining Sci., 7*, 257–296, 1970.

Swanson, S. R., and W. S. Brown, An observation of loading path independence of fracture in rock, *Int. J. Rock Mech. Mining Sci., 8*, 277–281, 1971.

(Received January 5, 1973;
revised June 8, 1973.)

VOL. 13, NO. 3 REVIEWS OF GEOPHYSICS AND SPACE PHYSICS JULY 1975

The State of Stress in the Earth's Crust

Bezalel C. Haimson

Department of Metallurgical and Mineral Engineering, University of Wisconsin, Madison, Wisconsin 53706

This article is limited to a short state of the art report on available methods of stress determination in situ and a summary of findings to date.

Stress Relief Methods

Stress determination at depth requires the drilling of a hole to the level of interest. Most of the methods employ sophisticated instrumentation down the hole and require overcoring for relieving the stresses. Because of the necessity to overcore, hole length is limited to 30–40 m. Hence these methods are useful only in stress measurements near the surface of the earth or at depth if previous access has been obtained through underground chambers, tunnels, or mine openings. A variety of measuring methods have been developed which determine either changes in hole diameter or strain on the bottom of the hole resulting from the complete relief of the stress due to overcoring.

One of the earliest methods of measuring stresses at depth and away from the rock face was devised by *Hast* [1958] for the purpose of determining rock pressures in mines. It consists of inserting and prestressing a magnetostrictive nickel alloy spool against the wall of a hole drilled into the rock and overcoring and measuring the change in stress by recording the drop in potential of the solenoid wound around the spool. The stress is measured in three different directions, all perpendicular to the hole axis. Three such readings yield the secondary principal stresses acting in the plane normal to the hole. To determine the complete stress ellipsoid, three measurements in each of three nonplanar holes are necessary. The most common type of transducer used to determine in situ stresses has been the electrical resistance strain gage. The 'borehole deformation cell' incorporates four strain gages bonded to each of its three beryllium copper cantilevers so as to form a complete wheatstone bridge. Changes in the size of the borehole after overcoring cause deflections in the cantilevers which yield diametral deformations in three different directions. Knowledge of the elastic parameters of the rock is necessary in calculating the secondary principal stresses acting in a plane perpendicular to the hole axis [*Merrill*, 1967; *Hooker et al.*, 1974]. Another common method of secondary principal stress determination is the 'doorstopper' technique, which incorporates a strain rosette bonded directly to the surface of the rock at the flat end of the drilled hole. With this method, stress relief is achieved by merely lengthening the hole by using a diamond drill coring crown with an outside diameter equal to the diameter of the hole. Stresses are calculated by using an empirical formula which incorporates the elastic parameters of the rock [*Leeman*, 1971]. A large number of variations of these two-dimensional overcoring methods have been attempted but have not received wide acceptance. An exhaustive bibliography on stress-measuring techniques prior to 1969 has been published by *Leeman* [1969]. For the field geologist, quick overcoring techniques for measuring biaxial stresses right on the surface of the rock have been developed [*Brown*, 1973; *Swolfs et al.*, 1974; *Engelder and Sbar*, 1975].

New developments in overcoring techniques have been associated with triaxial cells for the direct determination of the complete stress ellipsoid from measurements in one hole [*Leeman*, 1971; *Rocha and Silverio*, 1969; *Rocha et al.*, 1974]. These instruments involve the use of three or more strain rosettes bonded to the wall of the borehole at known directions and inclinations, thus yielding sufficient data for the calculation of the six independent components of stress acting at the point of measurement. The triaxial techniques, although they are still in the developing stage, have already been used in actual measurements with some degree of success [*Rocha and Silverio*, 1969; *Gay*, 1975].

Ingenious nonovercoring stress relief techniques, which could be used at considerably greater depths, have recently been suggested by *Hoskins and Oshier* [1973], *de la Cruz and Goodman* [1969], and *de la Cruz* [1975]. These methods, however, have either been abandoned or are still in the development stage.

Hydrofracturing

The only method available today for measurements of stress at great depths is hydrofracturing. Unlike the methods mentioned above, it is not a strain relief method and does not require the lowering of sophisticated instrumentation into the hole and overcoring. Rather, it is based on the elastic solution of the bursting pressure in a brittle elastic hollow cylinder and on the crack direction and crack internal pressure in a large solid under stress. The method consists of hydraulically pressurizing a sealed off segment of a borehole until fracture occurs. Additional pumping of fluid extends the fracture. The pressures required to initiate the fracture and keep it open can be related directly to the two principal stresses acting normal to the hole axis. The latter is assumed to be parallel to the third principal stress. The orientation of the artificial crack is, on the basis of both theory and numerous laboratory results, perpendicular to the direction of the least principal stress. Thus both the magnitudes and the directions of the principal stresses can be estimated directly without the intermediate steps of first determining deformations and/or strains which require accurate knowledge of the elastic parameters in order to calculate the stresses. The stress-pressure relationships in hydrofracturing were first suggested by *Hubbert and Willis* [1957] and later confirmed and complemented by *Scheidegger* [1962], *Kehle* [1964], *Fairhurst* [1964], and others. *Haimson and Fairhurst* [1967, 1970] extended the stress-pressure relationship to include the common situation in which the hydrofracturing fluid penetrates the surrounding rock, this situation creating an additional stress field due to pore pressure gradient. They also reported an extensive testing program which verified the theoretical assumptions of hydrofracturing. More recent basic work on the applicability of the method in short holes around underground openings [*von Schonfeldt and Fairhurst*, 1972] as very deep holes, say, 10,000 m [*Haimson and Edl*, 1972], and in

homogeneous, anisotropic, and even prefractured rock [*Haimson*, 1975, 1974*b*] has yielded encouraging results regarding the potential of hydrofracturing as a reliable stress-measuring technique.

Crustal Stress

The great majority of stress measurements conducted so far have been related to engineering projects. Very few were carried out for the sole purpose of determining regional states of stress in the earth's crust [*Engelder and Sbar*, 1975; *Bredehoeft et al.*, 1975]. Regardless of the method employed the results appear to be consistent within a region with respect to both stress magnitude and direction. *Hast* [1967, 1969, 1973] finds surprising uniformity in stress magnitudes measured at some thirty locations in Fennoscandia. The horizontal stress field appears to be several times greater than the weight of the overlying strata. At surface the mean horizontal principal stress is about 100 bars, and it increases linearly with depth, reaching 150 bars at 100 m and 600 bars at 1000 m. The latter is the lowest depth tested by Hast. He also establishes a range of 0.3–0.75 as the ratio between the minor and the major principal stresses in Fennoscandia. The difference between the two principal stresses does not vary with depth. Interestingly, *Hast* [1973] also finds that the horizontal stresses in other parts of the world, namely Ireland, British Columbia, Zambia, Mont Blanc, and Iceland, exhibit the same behavior as those in the Fennoscandian bedrock. In particular, *Hast* [1973] measured the stresses in five locations in Iceland and found again that both the major and the minor principal stresses were horizontal, the maximum principal stress being oriented approximately perpendicular to the coastline. Similar directional trends were found in Norway.

It should be noted that Hast's instrument has not been used by other workers. Also, no attempt has been made to verify his measurements by different methods. However, a more complete compilation of horizontal stresses obtained with various strain relief techniques [*Herget*, 1973, 1974] in five continents appears to confirm Hast's results in that a large majority of measured mean horizontal stresses are considerably larger than the weight of the overlying rock. On the other hand, the measured vertical stresses are close to the weight of the overburden. Herget compiled data from a large number of strain relief measurements and found that the average variation with depth is 19 bars plus 0.27 bar/m for the vertical stress and 83 bars plus 0.4 bar/m for the mean horizontal stress. *Gay* [1975] assembled all the available results on in situ stress measurements in southern Africa, including Zambia, Rhodesia, and South Africa. The methods used were *Hast's* [1958] stress meter and *Leeman's* [1971] doorstopper and triaxial cell. He finds that the vertical stresses increase linearly with depth at a rate corresponding to the increase in overburden. The average horizontal stresses, however, often exceed the vertical stresses at shallow depths (less than 1 km) but become smaller at greater depths (1–2.5 km), such that the ratio of horizontal stress to vertical stress settles at approximately 0.6. The variations in this ratio with depth appear to correlate well with *Voight's* [1966] model of superficial denudation effect under conditions of full bilateral restraint. *Von Schonfeldt et al.* [1973], using data from hydraulic fracturing treatments of some 3000 oil and gas wells, determined regional stress fields in the upper crust of the United States, with particular reference to Oklahoma and west Texas. They found that the maximum horizontal stress varies with depth at a rate of between 0.16 and 0.29 bar/m for the continental United States but only between 0.20 and 0.25 bar/m for Oklahoma and between 0.23 and 0.27 bar/m for west Texas. The least principal stress varies between 0.11 and 0.34 bar/m for the continental United States, and a similar range was determined for Oklahoma and Texas.

A considerable amount of work has been undertaken by the U.S. Bureau of Mines, using its own borehole deformation gage, both in near-surface measurements [*Hooker and Johnson*, 1969] and in deep mines [*Ageton*, 1967; *Hooker et al.*, 1972]. Stresses were measured along the Appalachian piedmont, in New England, Missouri, Oklahoma, Texas, the Colorado Rockies, and the Idaho panhandle. One common result, at least in the near-surface measurements, has been the high compressive values for both the least and the largest horizontal stresses. As a typical example, at Stone Mountain, Georgia, the horizontal principal stress magnitudes were 82 bars and 170 bars at a depth of merely 10 m, where the weight of the overburden is only about 3 bars.

Probably one of the first large-scale geophysical investigations which employed in situ stress measurements was the experiment at Rangely, Colorado. Stresses were measured on and near the surface by means of a number of strain relief methods [*de la Cruz and Raleigh*, 1972]. In addition, hydrofracturing was used for a stress measurement in a newly drilled oil well at a depth of nearly 1900 m [*Haimson*, 1972, 1973]. The well location and depth were chosen for their closeness to the zone where many earthquakes originated and their proximity to the major fault in the area. Surprising correlation was found between the surface measurements and the hydrofracturing as far as principal stress directions are concerned (N70°E for the largest horizontal stress). Hydrofracturing also provided stress magnitudes: 310 bars for the least horizontal principal stress, 590 bars for the largest horizontal stress, and 435 bars for the vertical stress. These results indicated strike slip faulting and right lateral slip. This was in accord with fault plane solutions in the area [*Raleigh et al.*, 1972]. The stress magnitudes and directions were used to predict a critical pore pressure of 240 bars for fault slip to occur. This value was within 10% of earthquake-related pore pressures monitored at the site.

Additional hydrofracturing measurements have since been conducted. At the Nevada test site [*Haimson et al.*, 1974], principal stresses of 35 bars and 90 bars in the horizontal plane (acting at N55°W and N35°E, respectively) and 70 bars in the vertical direction were determined at a depth of 380 m. Very similar results were obtained by using the borehole deformation gage from the available underground tunnel [*Hooker et al.*, 1971]. Recently, *Bredehoeft et al.* [1975] determined the state of stress on a regional scale in the Piceance basin of northwest Colorado. They tested seven oil shale test holes ranging in depth from 60 to 460 m. The horizontal principal stresses were found to be nearly equal, increasing linearly with depth. The average direction of the largest horizontal principal stress was N70°W. Hydrofracturing has been increasingly accepted not just by researchers at universities and government agencies but also by private industry in mining and underground construction. More deep stress measurements have been conducted recently (results not yet available), and more are planned for the coming year, so that the wealth of information on the state of stress in the earth's crust is slowly but continually building up.

A comprehensive study of the horizontal stresses in eastern

clinoenstatite transformation as competing rate processes in enstatite, J. Geophys. Res., 76, 4011-4022, 1971.

...R.B., Environment of deformation, Monkton quartzite, Shelborne Bay, Western Vermont, Geol. Soc. Amer. Bull, 85, 233-246, 1974.

..., R.L., and M.F. Ashby, On the rheology of the upper mantle, Rev. Geophys. Space Phys., 11, 391-426, 1973.

..., L. and H. Spetzler, Hot creep observed by holographic interferometry, EOS, 54, 452, 1973.

...lis, J., Quartz: Preferred orientation in rocks produced by Dauphine twinning, Science, 168, 1342-1344, 1970.

...lis, J. and T. Tullis, Preferred orientation of quartz produced by mechanical Dauphine twinning: Thermodynamics and axial experiments, Amer. Geophys. Un. Mono., 16, 67-82, 1972.

...lis, J., J.M. Christie and D.T. Griggs, Microstructures and preferred orientations of experimentally deformed quartzites, Geol. Soc. Amer. Bull., 84, 297-314, 1973.

...ette, this issue, 1975.

Twiss, R.J., Structure and significance of planar deformation features in synthetic quartz, Geology, 2, 329-332, 1974.

Vaughn, P.J. and R.B. Coe, Some observations and experimental data on creep of magnesium orthogermanate, EOS, 56, 1194, 1974.

Weertman, J., Dislocation climb theory of steady-state creep, Trans. ASME, 61, 681-694, 1968.

Weertman, J., The creep strength of the earth's mantle, Rev. Geophys. Space Phys., 8, 145-168, 1970.

White, S., Deformation lamellae in naturally deformed quartz, Nature Phys. Sci., 245, 26-28, 1973.

Wickham, J.S., Structural history of a portion of the Blue Ridge, northern Virginia, Geol. Soc. Amer. Bull., 83, 723-760, 1972.

Wilson, C.J.L., The prograde microfabric in a deformed quartzite sequence, Mount Isa, Australia, Tectonophysics, 19, 39-81, 1973.

Zimmerman, J. and N.L. Carter, Internal structure of the Vourinos complex, EOS, 54, 461-462, 1973.

The State of Stress in the Earth's Crust

Bezalel C. Haimson

...l, J. F., Evaluation of stress instrumentation for project Payette, U.S. Geol. Survey, Rep. M474-61, 58 pp., 1970.

...ton, R. W., Stress ellipsoid determination in a rock burst prone area at a 4,000-foot depth, Galena mine, Wallace, Idaho, BuMines RI 6997, 1967.

...ton, R. W., Deep mine stress determinations using flatjack and borehole deformation methods, BuMines RI 6887, 1967.

...ith, W. G., Development of a stress relief method with a three directional borehole deformation gauge, Report U.S. Bur. Reclam. Denver, Colo. Roc-Ode-70-10, 1970.

...olmstein, H. U., and G. H. Eisbacher, In-situ stress determinations and tectonic fabric at Elliot Lake, Ontario, Proc. Sixth Canadian Rock Mechanics Symp., 91-101, 1971.

...olmstein, H. U., and K. Barron, In-situ stresses, Proc. Seventh Canadian Rock Mechanics Symp., 3-14, 1972.

...chore, F., and C. Fairhurst, Results of an in situ comparison of different techniques for rock stress determination, Proc. Int'l. Symp. on the Determination of Stresses in Rock Masses, Lisbon, 334-358, 1969.

...croft, J. D., R. G. Wolff, W. S. Keys and E. Shutter, Hydraulic fracturing to determine the regional state of tectonic stress, Piceance Basin, Colorado, 1975 (in press).

..., A., In situ strain measurement by photoelastic bar gages, Tectonophysics, 19, 383-397, 1973.

..., A., Photoelastic measurement of recoverable strain at four sites, Tectonophysics, 21, 135-164, 1974.

..., B. W. and R. M. Potter, Results from hydraulic fracturing experiments in deep crystalline rock, EOS Trans. AGU, 55, 425, 1974.

...y, A. A., A study of inclined hydraulic fractures, Soc. Pet. Engr. J., 13, 61-68, 1973.

...la Cruz, R. V. and R. E. Goodman, The borehole deepening method of stress measurement, Proc. Int'l. Symp. on the Determination of Stresses in Rock Masses, Lisbon, 230-244, 1969.

de la Cruz, R. V. and C. B. Raleigh, Absolute stress measurements at the Rangely anticline, Northwestern Colorado, Int. J. Rock Mech. Min. Sci., 9, 625-634, 1972.

de la Cruz, R. V., Jack-fracturing technique of stress measurement, 1975 (in press).

Engelder, J. T. and M. L. Sbar, Strain relief measurements in the Potsdam sandstone north of Plattsburgh, New York, Northeastern Sectional Meeting of the Geological Society of America, 1975.

Fairhurst, C., Measurement of in situ rock stresses with particular reference to hydraulic fracturing, Rock Mechanics and Engineering Geology, 11, 129-147, 1964.

Friedman, M. and D. W. Stearns, Relations between stresses inferred from calcite twin lamellae and microfractures, Teton Anticline, Montana, Geol. Soc. Am. Bull, 82, 3191-3162, 1971.

Friedman, M. Residual elastic strain in rocks, Tectonophysics, 15, 297-330, 1972.

Friedman, M., and H. C. Heard, Principal stress ratios in Cretaceous limestones from Texas gulf coast, The American Assoc. of Petroleum Geologists Bulletin, 58, 71-78, 1974.

Gay, N. C., Virgin rock stresses at Doorfontein gold mine, Carletonville, South Africa, J. of Geology, 80, 61-80, 1972.

Gay, N. C., In situ stress measurements in southern Africa, Tectonophysics (Int'l. Symp. on Recent Crustal Movements, Zurich), 1975 (in press).

Haagen, T., Rock stress measurement with rigid stress gauges, Theory and practice, Proceedings, IVA, Stockholm (Rock Mech. Conf.), 71-86, 1971.

Haimson, B., Hydraulic fracturing in porous and nonporous rock and its potential for determining in-situ stresses at great depth, Technical Report 4-68, Missouri River Division Corp of Engineers, 235 pp., 1968.

Haimson, B. C., Stress measurements in the Weber sandstone at Rangely, Colorado, (Abstract) Trans. Am. Geoph. Union, 53, 524, 1972.

Haimson, B. C., Earthquake related stresses at Rangely, Colorado in New Horizons in Rock Mechanics, Proc. Fourteenth Symp. on Rock

Mechanics, H. R. Hardy and R. Stefanko, eds., ASCE, N.Y., 689-708, 1973.

Haimson, B. C., Stress measurements in anisotropic and prefractured rocks, Proceedings 15th Symp. on Rock Mechanics, Custer State Park, S. Dakota, September 17-19, 1975 (in press).

Haimson, B. C., A simple method for estimated in-situ stresses at great depths, in Field Testing and Instrumentation of Rock, ASTM Special Technical Publ. 554, 156-182, 1974a.

Haimson, B. C., Determination of in-situ stresses around underground excavations by means of hydraulic fracturing, Final Technical Report to the U.S. Bureau of Mines (H0220080), 113 pp., 1974b.

Haimson, B. C., and J. W. Edl, Hydraulic fracturing of deep wells, 47th Annual Meeting of SPE of AIME, paper #SPE 4061, 1972.

Haimson, B. and C. Fairhurst, Initiation and extension of hydraulic fractures in rock, Soc. Petr. Engr. J., 71, 310-318, 1967.

Haimson, B. and C. Fairhurst, In-situ stress determination at great depth by means of hydraulic fracturing, in Rock Mechanics--Theory and Practice, W. H. Somerton, ed., Proc. Eleventh Symp. on Rock Mechanics, AIME, N.Y., 559-584, 1970.

Haimson, B. C., J. LaComb, S. J. Green, A. H. Jones, Deep stress measurements in turf at the Nevada Test Site, in Advances in Rock Mechanics, Proc. Third Congress of the Int'l. Soc. for Rock Mechanics, Vol. II, Part A, 557-562, 1974.

Hast, N., The measurement of rock pressure in mines, Sveriges Geologiska Undersökning, Stockholm, Ser. C, 52, 1-183, 1958.

Hast, N., The state of stresses in the upper part of the earth's crust, Engineering Geology, 2, 5-17, 1967.

Hast, N., The state of stress in the upper part of the earth's crust, Tectonophysics, 8, 169-211, 1969.

Hast, N., Stability of stress distributions in the earth's crust during geologic times and the formation of iron ore lenses at Malmberget, Phys. Earth Planet. Interiors, 6, 221-228, 1972.

Hast, N., Global measurements of absolute stress, Phil. Trans. R. Soc. London, 274, 409-419, 1973.

Hawkes, I., Theory of the photoelastic biaxial strain gauge, Int. J. Rock Mech. Min. Sci., 5, 57-63, 1968.

Hawkes, I., Photoelastic strain gages and in situ rock stress measurements, Proc. Int'l. Symp. on the Determination of Stresses in Rock Masses, Lisbon, 359-375, 1969.

Hawkes, I., and V. E. Hooker, The vibrating wire stressmeter, in Advances in Rock Mechanics, Proc. Third Congress of the Int'l. Soc. for Rock Mechanics, Vol. II, part A, 439-444, 1974.

Healy, J. H., J. C. Roller, Q. A. Goton, Jr., R. Lamson, In Situ stress measurements in fractured rock, EOS Trans. AGU, 55, 465, 1974.

Herget, G., The stress field in the Urquhart Shales at Mount Isa (Queensland, Australia) based on structural investigation, Felsmechanik U. Ingenieurgeol., 6, 190-200, 1968.

Herget, G., Variation of rock stresses with depth at a Canadian iron mine, Int. J. Rock Mech. Min. Sci., 10, 37-51, 1973.

Herget, G., Ground stress determinations in Canada, Rock Mechanics, 6, 53-64, 1974.

Hiltscher, R., and K. Ingevald, Long term observation of rock stresses using cemented strain gauges, Proceedings, IVA, Stockholm (Rock Mech. Conf.), 87-94, 1971.

Hiltscher, R., Comparison of different methods for rock stress measurements, Proceedings, IVA, Stockholm (Rock Mech. Conf.), 103-110, 1971.

Hooker, V. E., J. R. Aggson, and D. L. Bickel, Report on in situ determination of stresses, Rainier Mesa, Nevada Test Site, BuMines Report, 7 pp., 1971.

Hooker, V. E., J. R. Aggson, and D. L. Bickel, Improvements in the three-component borehole deformation gage and overcoring techniques, BuMines RI 7894, 29 pp., 1974.

Hooker, V. E., D. L. Bickel, and J. R. Aggson, In situ determination of stresses in mountainous topography, BuMines RI 7654, 19 pp., 1972.

Hooker, V. E. and D. L. Bickel, Overcoring equipment and techniques used in rock stress determination, BuMines IC 8618, 32 p., 1974.

Hooker, V. E. and C. F. Johnson, Near-surface horizontal stresses including the effects of rock anisotropy, BuMines RI 7224, 29 pp., 1969.

Hoskins, E. R., Primary stress measurements at Mt. Isa, in Basic and Applied Rock Mechanics, Proc. Tenth Symp. on Rock Mechanics, K. E. Gray, ed., SME of AIME, N.Y., 475-501, 1972.

Hoskins, E. R. and E. H. Oshier, Development of a deep hole stress measurement device, in New Horizons in Rock Mechanics, Proc. Fourteenth Symp. on Rock Mechanics, H. R. Hardy and R. Stefanko, eds., ASCE, N.Y., 299-310, 1973.

Hubbert, M. K. and D. G. Willis, Mechanics of hydraulic fracturing, AIME Trans., 210, 153-168, 1957.

Kehle, R. O., Determination of tectonic stresses through analysis of hydraulic well fracturing, J. Geoph. Res., 69, 259-273, 1964.

Le Francois, P., In-situ measurement of rock stresses for the Idikki hydro-electric project, Proc. Sixth Canadian Rock Mechanics Symp., Mines Branch, Ottawa, 65-90, 1971.

Leeman, E. R., The borehole deformation type of rock stress measuring instrument, Int'l. J. Rock Mech. Min. Sci., 4, 23-44, 1967.

Leeman, E., The determination of the complete state of stress in rock in a single borehole--laboratory and underground measurements, Int. J. Rock Mech. Min. Sci., 5, 31-56, 1968.

Leeman, E. R., The measurement of stress in rock: a review of recent developments (and a bibliography), Proc. Int'l. Symp. on the Determination of Stresses in Rock Masses, Lisbon, 200-229, 1969.

Leeman, E. R., The CSIR 'doorstopper" and triaxial rock stress measuring instruments, Rock Mechanics, 3, 25-50, 1971.

Leeman, E. R. and M. G. Demkhaus, Determination of stress in rock with linear or non-linear elastic characteristics, Rock Mech., 1, 198-206, 1969.

Martinetti, S. and R. Ribacchi, Result of state-of-stress measurements in different types of rock masses, in Advances in Rock Mechanics, Proc. Third Congress of the Int'l. Soc. for Rock Mechanics, Vol. II, part A, 458-463, 1974.

Merrill, R. H., Three-component borehole deformation gage for determining the stress in rock, BuMines RI 7015, 38 pp., 1967.

Molodtsova, L. S., and E. A. Melnikov, On the transition from stresses at the end of a borehole to the stresses in the solid rock, Soviet Min. Sci. #1, Jan-Feb, 32-35, 1970.

Norman, C. E., Geometric relationships between geologic structure and

stresses near Atlanta, Ga., BuMines RI 7365, 24 pp., 1970.

Determination of stress in rock--a state-of-the-art report, Special Technical Publication No. 429, 56 pp., 1967.

... and T. Bain, A means of determining the complete state of stress in a single borehole, Int. J. Rock Mech. Min. Sci., 7, 503-515, 1970.

... C. B., J. H. Healy and J. D. Bredehoeft, Faulting and crustal ... at Rangely, Colorado, in Flow and Fracture of Rocks, ... Mon. 16, AGU, 275-284, 1972.

... C. B., Crustal stress and global tectonics, in Advances in Rock ..., Proc. Third Congress of the Int'l. Soc. for Rock Mechanics, ... I, part A, 593-597, 1974.

... and A. Silverio, A new method for the complete determination of ... state of stress in rock masses, Geotechnique, 19, 116-132, 1969.

... C., A. Silverio, J. O. Pedro, J. S. Delgado, A new development of ... stress tensor gage, in Advances in Rock Mechanics, Proc. ... Congress of the Int'l. Soc. for Rock Mechanics, Vol. II, ... A, 464-467, 1974.

... E. C. and C. Fairhurst, The deep stress probe--a tool for stress ...determination, in New Horizons in Rock Mechanics, Proc. Fourteenth ... on Rock Mechanics, H. R. Hardy and R. Stefanko, eds., ASCE, ... 1., 1973.

... E. C., The importance of the permeability factor in in situ ... determination, EOS Trans. AGU, 55, 425, 1974.

... L., G. G. Lambert, In-situ strain orientations, a comparison of ... techniques, BuMines RI 7575, 17 pp., 1971.

... E. and J. R. Hoskins, Residual stresses in rock, in New Horizons ... Mechanics, Proc. Fourteenth Symp. on Rock Mechanics, H. R. ... and R. Stefanko, eds., ASCE, N.Y., 1-24, 1973.

... L. and L. R. Sykes, Contemporary compressive stress and seismicity ... North America: an example of intra-plate tectonics, ... Society of America Bulletin, 84, 1861-1882, 1973.

... E., Stresses in the earth's crust as determined from ... fracturing data, Geologie und Bauwesen, 27, 45-53, 1962.

... E., Determination of rock stress in evaporites, Austral. Min., ... 1973.

Smith, R. B. and M. L. Sbar, Contemporary tectonics and seismicity of the western United States with emphasis on the intermountain seismic belt, Geological Soc. of America Bulletin, 85, 1205-1218, 1974.

Stephenson, B. R., Stresses and joint directions correlated at Cobar Mines Pty. Ltd., Proc. Australian Rock Mechanics Symp., 109-117, 1969.

Swolfs, H. S., J. Handin, H. R. Pratt, Field measurements of residual strain in granitic rock masses, in Advances in Rock Mechanics, Proc. Third Congress of the Int'l. Soc. for Rock Mechanics, Vol. II, part A, 563-568, 1974.

Sykes, L. R. and M. L. Sbar, Intraplate earthquakes, lithospheric stresses and the driving mechanism of plate tectonics, Nature, 245, 298-302, 1973.

Van Heerden, W. L., The influence of various factors on the triaxial strain cell results, CSIR Report ME 1178, 1973.

Voight, B., 1966, Beziehung zwischen grossen horizontalen spannungen in Gebirge und der Tektonik und der Abtragung, Proc. First Congress of the Int'l. Soc. for Rock Mechanics, 2, 51-56, 1966.

Voight, B., Determination of the virgin state of stress in the vicinity of a borehole from measurements of a partial anelastic strain tensor in drill cores, Felsmechanik U. Ingenieurgeol., 6, 201-215, 1968.

Voight, B., Prediction of in situ stress patterns in the earth's crust, Proc. Int'l. Symp. on the Determination of Stresses in Rock Masses, Lisbon, 111-131, 1969.

Voight, B., Stress history and rock stress, in Advances in Rock Mechanics, Proc. Third Congress of the Int'l. Soc. for Rock Mechanics, Vol. II, part A, 580-582, 1974.

Voight, B., A mechanism for "locking-in" orogenic stress, American J. of Science, 274, 662-665, 1974.

von Schonfeldt, M. and C. Fairhurst, Field experiments on hydraulic fracturing, Soc. Petr. Engr. J., 12, 69-77, 1972.

von Schonfeldt, H. A., R. O. Kehle, and K. E. Gray, Mapping of stress field in the upper earth's crust of the U.S., Final Technical Report to USGS (14-08-0001-12278), 40 pp., 1973.

Williams, F. T. and A. Owens, Measurement of in-situ stress in rock, Tunnels and Tunnelling, 5, 138-142, 1973.

Fracture in Rock

Melvin Friedman

... E., E. Winster, and D. Cole, The effect of oriented cracks ... velocities, J. Geophys. Res., 79, 4011-4015, 1974.

... E., and P. C. Perkins, Application of the stress corrosion ... of crack propagation to geophysical problems (abstract), ... 56, 1193, 1974.

... E., and I. W. Farmer, Fatigue behavior of rock, Int. J. Rock ... Min. Sci., 10, 1-9, 1973.

... E., The effect of strain rate and temperature on the yield ... of hydrolytically weakened synthetic quartz, J. Geophys. Res., ... 6022, 1974.

... E., and C. Simmons, Progress in microcrack decoration (abstract), ... 55, 342, 1971.

... E., and G. H. Bowers, A photoelastic study of the effects of ... geometry on fault movements, Proc. 3rd Cong. Int. Soc. Rock ... IIA, 185-190, 1974.

Barenblatt, G. I., The mathematical theory of equilibrium cracks in brittle fracture, in Advances in Applied Mechanics, Academic Press, 7, 55-129, 1962.

Barnard, P. R., Researches into the complete stress-strain curve for concrete, Mag. Concrete Research, 16, 49, 1964.

Baurat, H. D., H. C. Mont, and Leopold Müller, Rock mass behavior-determination and application in engineering practice, Proc. Third Cong. Int. Soc. Rock Mech., IA, 205-215, 1974.

Barnais, Jean, Properties of rock and rock masses, Proc. Third Cong. Int. Soc. Rock Mech., IA, 9-38, 1974.

Bieniawski, Z. T., Mechanisms of brittle fracture of rock, Part I: Theory of the fracture process, Int. J. Rock Mech. Min. Sci., 4, 395-406, 1967a.

Bieniawski, Z. T., Mechanisms of brittle fracture of rock, Part II: Experimental studies, Int. J. Rock Mech. Min. Sci., 4, 407-423, 1967b.

ture in tension and under long term loading, Int. J. Rock Mech. Min. Sci., 4, 425-430, 1967c.

Bieniawski, Z. T., Determination of rock properties, South Afr. Council F. Sci. and Ind. Res. Rep., No. Mep. 518, 1967d.

Bieniawski, Z. T., Failure of fractured rock, Int. J. Rock Mech. Min. Sci., 6, 323-341, 1969.

Bilby, B. A., and J. D. Eshelby, Dislocations and the theory of fracture, in Fracture, An Advanced Treatise, H. Liebowitz ed., Academic Press, N.Y., 1, 99-182, 1968.

Blacic, J. D., Effect of water on the experimental deformation of olivine, in Flow and Fracture of Rocks, AGU Monograph, 16, 109-116, 1972.

Blacic, J. D., Hydrolytic weakening of quartz and olivine, Ph.D. Thesis, Univ. California at Los Angeles, 205 p., 1971.

Boland, J. N., and B. E. Hobbs, Microfracturing processes in experimentally deformed peridotite, Int. J. Rock Mech. Min. Sci., 10, 623-626, 1973.

Bombolakis, E. G., Photoelastic study of initial stages of brittle fracture in compression, Tectonophysics, 6, 461-473, 1968.

Bombolakis, E. G., Study of the brittle fracture process under uniaxial compression, Tectonophysics, 18, 231-248, 1973.

Borg, I. Y., Some shock effects in granodiorite to 270 kilobars at the Piledriver Site, in Flow and Fracture of Rocks, AGU Monograph, 16, 293-311, 1972.

Borg, I. Y., Extent of pervasive fracturing around underground nuclear explosions, Int. J. Rock Mech. Min. Sci., 10, 11-18, 1973.

Borg, I., and J. Handin, Experimental deformation of crystalline rocks, Tectonophysics, 3, 249-368, 1966.

Brace, W. F., Brittle fracture of rocks, in State of Stress in the Earth's Crust, W. R. Judd ed., Am. Elsevier Pub. Co., N.Y., 110-174, 1964.

Brace, W. F., Micromechanics in rock systems, in Structure, Solid Mechanics and Eng. Design, M. Te'eni ed., Wiley Interaci., John Wiley and Sons, London, 187-204, 1971

Brace, W. F., Dilatancy-related electrical resistivity changes in rocks (abstract), Eos Trans. AGU, 56, 1195, 1974.

Brace, W. F., and E. G. Bombolakis, A note on brittle crack growth in compression, J. Geophys. Res., 68, 3709-3713, 1963.

Brace, W. F., A. S. Orange, and T. M. Madden, The effect of pressure on the electrical resistivity of water-saturated crystalline rocks, J. Geophys. Res., 70, 5669-5678, 1965.

Brace, W. F., B. W. Psulding, Jr., and C. Scholz, Dilatancy in the fracture of crystalline rocks, J. Geophys. Res., 71, 3939-3954, 1966.

Brace, W. F. and A. S. Orange, Electrical resistivity changes in saturated rocks during fracture and frictional sliding, J. Geophys. Res., 73, 1433-1445, 1968a.

Brace, W. F., and A. S. Orange, Further studies of the effects of pressure on electrical resistivity of rocks, J. Geophys. Res., 73, 5407-5420, 1968b.

Brace, W. F., and J. B. Walsh, Some direct measurements of the surface energy of quartz and orthoclase, Amer. Min., 47, 1111-1122, 1962.

Brady, B. T., A mechanical equation of state for brittle rock, Part I, Int. J. Rock Mech. Min. Sci., 7, 385-421, 1970.

Brady, B. T., A mechanical equation of state for brittle rock, Part II, Int. J. Rock Mech. Min. Sci., 10, 291-309, 1973.

Bridwell, R. J., Dilatancy and faulting (abstract), Eos Trans. AGU, 55, 432, 1974a.

Bridwell, R. J., Dilation and the slip-patch hypothesis (abstract), Eos Trans. AGU, 56, 1196, 1974b.

Brown, J. W., An investigation of microseismic activity in rock under tension, M.S. Thesis, Penn. State Univ., 84p, 1965.

Buf, Y. B., R. E. Thill and K. E. Hjelmstad, An ultrasonic method for determining the elastic symmetry of materials, U.S. Bureau of Mines R.I. 7333, 23p., 1969a.

[illegible] an ultrasonic method for determining the attenuation symmetry of materials, U.S. Bureau of Mines, R.I. 7335, 8p., 1969b.

Byerlee, J. D., Acoustic emission in rock during fluid injection, Proc. Third Cong. Int. Soc. Rock Mech., IIA, 633-637, 1974.

Cain, P. J., S. S. Peng, and E. R. Podniaks, Rock fragmentation by high frequency fatigue, Proc. Third Cong. Int. Soc. Rock Mech., IIA, 367-372, 1974.

Christie, J. M., D. T. Griggs, and N. L. Carter, Experimental evidence of basal slip in quartz, Jour. Geol., 72, 734-756, 1964.

Christie, J. M., and A. J. Ardell, Substructures of deformation lamellae in quartz, Geology, 2, 405-408, 1974.

Chinnery, M. A., The deformation of the ground around surface faults, Bull. Seismol. Soc. Amer., 51, 355-372, 1961.

Chinnery, M. A., The stress changes the accompany strike-slip faulting, Bull. Seismol. Soc. Amer., 53, 921-932, 1963.

Chinnery, M. A., Earthquake displacement fields, in Earthquake Displacement Fields and the Rotation of the Earth, L. Mansinha, D. E. Smylie, and A. E. Beck, eds., D. Reidel, Dordrecht, Netherlands, 17-37, 1970.

Chinnery, M. A., and J. A. Petrak, The dislocation fault model with variable discontinuity, Tectonophysics, 5, 513-529, 1968.

Chugh, Y. P., H. R. Hardy, Jr., and R. Stefanko, Investigation of the frequency spectra of microseismic activity in rock under tension, in Basic and Applied Rock Mech., K. E. Gray, ed., Proc. Tenth Symp. Rock Mech., Austin, Tx., May 1968, AIME, 73-113, 1972.

Cloos, E., "Feather" joints as indicators of the direction of movement on faults, thrusts, joints, and magmatic contacts, Natl. Acad. Sci. Proc., 18, 145-154, 1932.

Colback, P. S. B., and B. L. Wiid, The influence of moisture content on the compressive strength of rock, 3rd Canadian Symp. on Rock Mech., Toronto, Canada, 65-83, 1965.

Conrad, R. E. II, Microscopic feather fractures in the faulting process, M.S. Thesis, Dept. of Geology, Texas A&M University, August, 1974.

Cook, N. G. W., The failure of rock, Int. J. Rock Mech. Min. Sci., 2, 389-403, 1965.

Cornet, F. H., Pore fluid and the mechanical behavior of rock, in Stability of Rock Slopes, Proc. 13th Symp. Rock Mech., ASCE, New York, 875-844, 1972.

Crouch, S. L., Experimental determination of volumetric strains in failed rock, Int. J. Rock Mech. Min. Sci., 7, 589-603, 1970.

Cruden, D. M., The static fatigue of brittle rock under uniaxial compression, Int. J. Rock Mech. Min. Sci., 11, 67-73, 1974.

Dav, C. P., F. T. Howell, and F. A. Woodhead, The effect of applied stress upon the permeability of some Permian and Triassic sandstones of Northern England, Proc. Third Cong. Int. Soc. Rock Mech., IIA, 337-343, 1974.

Dieterich, J. H., Computer modeling of earthquake stimulation by fluid injection (abstract), Eos Trans. AGU, 52, p. 343, 1971.

Douglas, C., and D. J., McDougall, Strain energy build-up in fatigue cycling, in New Horizons in Rock Mech., Proc. 14th Symp. Rock Mech., Penn. St. Univ., June 1972, ASCE, New York, 121-126, 1973.

Dunn, D. E., L. T. LaFountain, and R. E. Jackson, Porosity dependence and mechanism of brittle fracture in sandstones, J. Geophys. Res., 78, 2403-2417, 1973.

Dyke, L. D., Experimental deformation of multilithologic specimens simulating sedimentary facies changes (abstract), Geol. Soc. Amer. Abstr. with Programs, 7, South-Central Section Meeting, March 1975.

Engelder, J. C., Cataclasis and the generation of fault gouge, Geol. Soc. Amer. Bull., 85, 1515-1522, 1974.

Everall, M. D., C. Berget, R. Sage, and D. F. Coates, Mechanical properties of rocks and rock masses, Proc. Third Cong. Int. Soc. Rock Mech., 1A, 101-108, 1974.

Thill, An ultrasonic method for
try of materials, U.S. Bureau of

ock during fluid injection, Proc.
IIA, 633-637, 1974.

ieks, Rock fragmentation by high
R. Int. Soc. Rock Mech., IIA,

. Carter, Experimental evidence
.. 72, 734-756, 1964.

ructures of deformation lamellae
4.

ground around surface faults,
372, 1961.

accompany strike-slip faulting,
932, 1963.

fields, in Earthquake Displace-
Earth, L. Mansinha, D. E. Smylie,
drecht, Netherlands, 17-37, 1970.

slocation fault model with vari-
3, 513-529, 1968.

sfanko, Investigation of the
tivity in rock under tension,
I. Gray, ed., Proc. Tenth Symp.
IME, 73-113, 1972.

of the direction of movement
tic contacts, Natl. Acad. Sci.

luence of moisture content on
Canadian Symp. on Rock Mech.,

tures in the faulting process,
A&M University, August, 1974.
I. Rock Mech. Min. Sci., 2, 389-

l behavior of rock, in Stability
Mech., ASCE, New York, 825-844.

f volumetric strains in failed
589-603, 1970.

rock under uniaxial compres-
, 67-73, 1974.

, The effect of applied stress
nd Triassic sandstones of
. Soc. Rock Mech., IIA, 537-542.

quake stimulation by fluid
2, p. 343, 1971.

ergy build-up in fatigue
Proc. 14th Symp. Rock Mech.,
ork, 121-126, 1973.

son, Porosity dependence
dstones, J. Geophys. Res.,

ilithologic specimens simu-
act), Geol. Soc. Amer. Abstr.
Meeting, March 1975.

of fault gouge, Geol. Soc.

Coates, Mechanical properties
R. Int. Soc. Rock Mech., 10

...area earthquakes and the Rocky Mountain arsenal well,
...gist., 1, 23-36, 1966.

..., and O. Fornai, Microfissuration, deformation, and compressi-
... of rocks under triaxial stress, Proc. Third Cong. Int. Soc.
...chanics, IIA, 138-143, 1974.

..., O., and F. Mosavenzadeh, Crack initiation and propagation in
...ll, Dept. of Civil Eng. Res. Rept., R 68-29, 126p., 1968.

...mal, Kinematics of transform and transcurrent faults, Tectono-
...s, 21, 93-134, 1974.

..., Structural analysis of fractures in cores from the Saticoy
...ntura County, California, Bull. Am. Assoc. Petroleum Geologists,
...1899, 1969.

..., Survey analysis of residual elastic strain in quartzose rocks,
...ed and Applied Rock Mech., K. E. Gray, ed., Proc. 10th Symp.
...ech., Austin, Tx., May 1968, AIME, 573-595, 1972a.

..., Geological aspects of residual elastic strain in rocks,
...Geology, 15, 297-330, 1972b.

..., Mechanical properties of rock affecting earthquake predic-
...tion and control, Semi-Annual Progress Rept., Grant No. 14-08-0001-
...G-0.0.8., Center for Tectonophysics, Texas A&M University, 23p.,

..., and J. M. Logan, The influence of residual elastic strain
...on orientation of experimental fractures in three quartzose
...rocks, J. Geophys. Res., 75, 387-405, 1970a.

..., and J. M. Logan, Microscopic feather fractures, Geol. Soc.
...Amer. Bull., 81, 3417-3420, 1970b.

..., B. B. Perkins, and S. J. Green, Observations of brittle-
...ductile rock features at the maximum stress of Westerly Granite and
...Solenhofen Limestone, Int. J. Rock Mech. Min. Sci., 7, 297-306, 1970.

..., J. M. Logan, J. Handin, D. W. Stearns, Experimental "drape-
...folding" of rocks under confining pressure (abstract), Geol. Soc.
...Amer., Abstr. with Programs, 4, 512-513, 1972a.

..., J. Handin, C. Alani, Fracture-surface energy of rocks,
...Int. J. Rock Mech. Min. Sci., 9, 757-766, 1972b.

..., J. M. Logan, and K. D. Min, Petrofabric analysis of experi-
...mentally folded and upthrusted (abstract), Eos Trans. AGU, 54, 458,

..., and Logan, J. M., Liders bands in experimentally deformed
...sandstones and limestones, Geol. Soc. Amer. Bull., 84, 1465-1476, 1973.

..., and T. R. Orr, Investigations of the relations among residual
...stress, fracture, and ultrasonic attenuation and velocity in
...rock, Int. J. Rock Mech. Min. Sci., 11, 221-234, 1974.

..., and D. W. Stearns, Relations between stresses from calcite
...twin lamellae and microfractures, Teton Anticline, Montana, Geol.
...Soc. America Bull., 82, 3151-3161, 1971.

..., Jr., Griffian theory applied to the tensile fracture of
...crystal grains (abstract), Eos Trans. AGU, 56, 1195, 1974.

..., Jr., M. Friedman, J. Handin, G. M. Sowers, Experimental
...deformation to microfracture in sandstone, Tectonophysics, 21,

..., Jr., and R. E. York, Tensile strength of sand grains
...(abstract), Eos Trans. AGU, 55, 421, 1974.

...diffusion model of earthquake prediction: A criti-
...cism (abstract), Eos Trans. AGU, 56, 1196, 1974.

...growth around openings in thick-walled cylinders of
...subjected to hydrostatic compression, Int. J. Rock Mech. Min.
...Sci., 8, 333-433, 1971.

...measurement of surface energies of crystals, J.
...Appl. Phys., 31, 2208-2218, 1960.

..., and D. B. Stacey, Ultrasonic pulse velocity as a rock
...property, Tectonophysics, 21, 39-45, 1974.

Goodman, Richard, Mechanical properties of joints, Proc. Third Cong. Int. Soc. Rock Mech., IA, 127-140, 1974.

Gramberg, J., Internal stresses in rock as a result of granular structure and axial cataclasis, Proc. Third Cong. Int. Soc. Rock Mech., IIA, 549-556, 1974.

Green, H. W. II, and S. V. Radcliffe, Deformation processes in the Upper Mantle, in Flow and Fracture of Rocks, AGU Monograph, 16, 139-156, 1972.

Griffith, A. A., The phenomena of rupture and flow in solids, Phil. Trans. Roy. Soc. London, A221, 163-198, 1921.

Griffith, A. A., Theory of rupture, Proc. First International Cong. Appl. Mech., Delft, 55-63, 1924.

Griggs, D. T., A model of hydrolytic weakening in quartz, J. Geophys. Res., 79, 1653-1661, 1974.

Griggs, David, and John Handin, Observations on fracture and a hypothesis of earthquakes, Geol. Soc. Amer. Mem., 79, 347-364, 1960.

Griggs, D. T., and J. D. Blacic, Quartz: anomalous weakness of synthetic crystals, Science, 147, 292-295, 1965.

Griggs, D. T., Hydrolytic weakening of quartz and other silicates, Geophys. J. Roy. Astron. Soc., 14, 19-31, 1967.

Habib, P., Fracture of rock masses, Ann. Inst. Tech. Batim. Et. Trav. Publ. Supplement, N306, 7p., 1973.

Hadley, Kate, Laboratory investigation of dilatancy and motion on fault surfaces at low confining pressure, Proc. Conf. Tect. Prob. of San Andreas Fault System, School of Earth Sci., Stanford Univ., Geol. Sci., 13, 427-435, 1973.

Hadley, Kate, and W. F. Brace, Azimuthal variation of dilatancy (abstract), Eos Trans. AGU, 55, 431, 1974.

Haimson, B. C., Mechanical behavior of rock under cyclic loading, Proc. Third Cong. Int. Soc. Rock Mech., IIA, 373-378, 1974.

Haimson, B. C., and C. M. Kim, Mechanical behavior of rock under cyclic failure, in Stability of Rock Slopes, Proc. 13th Symp. Rock Mech., ASCE, New York, 845-863, 1972.

Haimson, B. C., C. M. Kim, and T. M. Tharp, Tensile and compressive cyclic stresses in rock, in New Horizons in Rock Mech., 14th Symp. on Rock Mech., Penn. St. Univ., June 1972, ASCE, New York, 1973

Haimson, B. C., The state of stress in the earth's crust, Rev. Geophys. Space Phys., 13, this issue, 1975.

Hallbauer, D. K., H. Wagner, and N. G. W. Cook, Some observations concerning the microscopic and mechanical behavior of quartzite specimens in stiff, triaxial compression tests, Int. J. Rock Mech. Min. Sci., 10, 713-726, 1973.

Handin, John, On the Coulomb-Mohr failure criterion, J. Geophys. Res., 74, 5343-5348, 1969.

Handin, John, Mechanical properties of rocks affecting earthquake generation, Semi-Annual Progress Rept., 2, U.S.G.S. Contract No. 14-08-0001-12723, 19-28, 1973.

Handin, John, H. C. Heard, and J. N. Magouirk, The effect of the intermediate principal stress on the failure of limestone, dolomite, and glass at different temperatures and strain rates, J. Geophys. Res., 72, 611-640, 1967.

Handin, J., M. Friedman, J. M. Logan, L. F. Pattison, and H. S. Swolfs, Experimental folding of rocks under confining pressure - Buckling of single-layer rock beams, in Flow and Fracture of Rocks, AGU Monograph 16, 1-28, 1972.

Handin, J., and C. B. Raleigh, 1972, Manmade earthquakes and earthquake control, Proc. Symp. Percolation through Fissured Rock, Int. Soc. Rock Mech., Stuttgart, T2-D, 1-10, 1972.

Hanson, M. E., A. R. Sanford, and R. J. Shaffer, A source function for a dynamic bilateral brittle shear fracture, J. Geophys. Res., 76, 3375-3383, 1971.

Hardy, H. R. Jr., and Y. P. Clugh, Failure of geological materials under

low-cycle fatigue, Sixth Canadian Symp. on Rock Mechanics, Montreal, May, 1970.

Hardy, H. R. Jr., R. Y. Kim, R. Stefanko, and Y. J. Wang, Creep and microseismic activity in geological materials, in Rock Mech. Theory and Practice, W. H. Somerton, ed., Proc. Eleventh Symp. Rock Mech. Berkeley Calif., June 1969, AIME, 377-413, 1970.

Hardy, H. P., J. A. Hudson, and C. Fairhurst, The failure of rock beams, Part I - Theoretical studies, Int. J. Rock Mech. Min. Sci., 10, 53-67, 1973.

Healy, J. H., W. W. Rubey, D. T. Griggs, and C. B. Raleigh, The Denver earthquakes, Science, 161, 1301-1310, 1968.

Healy, J. H., Recent highlights and future trends in research on earthquake prediction and control, Rev. Geophys. Space Phys., 13, this issue, 1975.

Heard, H. C., Steady-state flow in polycrystalline halite at pressure of 2 kilobars, in Flow and Fracture of Rocks, AGU Monograph, 16, 191-210, 1972.

Heinze, W. D., and C. Goetze, Numerical simulation of stress concentrations in rocks, Int. J. Rock Mech. Min. Sci., 11, p. 131-135, 1974.

Hoagland, R. G., G. T. Hahn, and A. R. Rosenfield, Influence of microstructure on fracture propagation in rock, Rock Mech., 5, 77-106, 1973.

Hobbs, B. E., A. C. McLaren, and M. S. Paterson, Plasticity of single crystals of synthetic quartz, in Flow and Fracture of Rocks, AGU Monograph, 16, 29-54, 1972.

Hoek, E., Rock fracture under static stress conditions, C.S.I.R. Report, MEG 383, Pretoria, 1965.

Hoshino, K., and H. Koide, Process of deformation of the sedimentary rocks, Proc. 2nd Congress of the Int. Soc. Rock Mech., Beograd, 1, Paper 2-13, 1970.

Hudson, J. A., H. P. Hardy, and C. Fairhurst, The failure of rock beams, Part II - Experimental studies, Int. J. Rock Mech. Min. Sci., 10, 69-82, 1973.

Irwin, G. R., Fracture mechanics, in Structural Mechanics, Goodier and Hoff eds., Pergamon Press, London, 557-592, 1960.

Jackson, R. E., L. J. LaFountain, and Mike Swain, Sliding surface features, Hertzian fractures, and stick-slip (abstract), Eos Trans. AGU, 55, 428, 1974.

Jackson, R. E., and D. E. Dunn, Experimental sliding friction and cataclasis of foliated rocks, Int. J. Rock Mech. Min. Sci., 11, 235-249, 1974.

Jackson, R. E., N. H. MacMillan, and A. R. C. Westwood, Chemical enhancement of rock drilling, Proc. Third Cong. Int. Soc. Rock Mech., IIB, 1487-1493, 1974.

Jaeger, J. C., Brittle fracture of rocks, in Failure and Breakage of Rock, C. Fairhurst, ed., Eighth Symp. Rock Mech., U. of Minn., AIME, 3-57, 1967.

John, K. W., Properties of rock masses in research and engineering practice, Proc. Third Cong. Int. Soc. Rock Mech., IA, 173-176, 1974.

Jones, F. O., A laboratory study of the effect of confining pressure on fracture flow and storage capacity in carbonate rocks, Soc. Pet. Engs., Paper No. 4569, 48th Annual Fall Mtg., Las Vegas, Nev., Oct., 1973.

Koons, M. L. and C. C. Ulmer, Brittle fracture in oceanic basalts (abstract), Eos Trans. AGU, 53, 511-512, 1972.

Kranz, R. L., and C. H. Scholz, Cyclic recovery of dilatancy (abstract), Eos Trans. AGU, 55, 431, 1974.

Krech, W. W., The energy balance theory and rock fracture energy measurements for uniaxial tension, Proc. Third Cong. Int. Soc. Rock Mech., IIA, 167-173, 1974.

Lajtai, E. Z., A theoretical and experimental evaluation of the Griffith theory of brittle fracture, Tectonophysics, 11, 129-156, 1971.

Lajtai, E. Z., and V. N. Lajtai, The evolution of brittle fracture in rocks, J. Geol. Soc. Lond., 130, 1-18, 1974.

Lewis, W. E., Research Program summaries, Twin Cities Mining Research Center, Bureau of Mines U.S. Dept. of the Interior, April 13, 1966.

Liebowitz, H., Fracture: An advanced Treatise, Academic Press, New York, 1-7, 1968-1972.

Lindholm, U. S., L. M. Yeakley, and A. Nagy, The dynamic strength and fracture properties of Dresser Basalt, Int. J. Rock Mech. Min. Sci., 11, 181-192, 1974.

Logan, J. M., Friction in rocks, Revs. of Geophys. and Space Sci., 13, this issue, 1975.

Martin, R. J., III, Time-dependent crack growth in quartz and its application to the creep of rocks, J. Geophys. Res., 77, 1406-1419, 1972.

McCarter, M. K., and J. E. Willson, Strength versus energy dissipation in sandstone, in New Horizons in Rock Mech., Proc. 14th Symp. on Rock Mech., Penn. St. Univ., June 1972, ASCE, New York, 225-245, 1973.

McClintock, F. A., and J. B. Walsh, Friction on Griffith cracks in rocks under pressure, Proc. Fourth U.S. Congress on Applied Mech., Am. Soc. Mech. Eng., N.Y., 1015-1021, 1963.

McLaren, A. C., J. A. Retchford, D. T. Griggs, and J. M. Christie, Transmission electron microscope study of Brazil twins and dislocations experimentally produced in natural quartz, Phys. Status Solidi, 19, 631-644, 1967.

McLaren, A. C., R. G. Turner, J. M. Boland, and B. E. Hobbs, Dislocation structure of lamellae in synthetic quartz, Contr. Mineralogy and Petrology, 29, 104-115, 1970.

McLaren, A. C., and B. E. Hobbs, Transmission electron microscope investigation of some naturally deformed quartz, in Flow and Fracture of Rocks, AGU Monograph, 16, 55-66, 1972.

McWilliams, J. R., The role of microstructure in the physical properties of rock, Testing Techniques for Rock Mech., STP 402, 175-189, Amer. Soc. Test. and Materials, Philadelphia, 1966.

Min, K. D., Analytical and petrofabric studies of experimental faulted drape-folds in layered rock specimens, Ph.D. Dissertation, Dept. of Geophysics, Texas A&M University, 90 p., Dec. 1974.

Moavenzadeh, F., R. B. Williamson, and A. E. Z. Wissa, Rock fracture research, M.I.T. Dept. of Civil Eng. Res. Rept., R66-56, 85p., 1966.

Mogi, K., Study of elastic shocks caused by the fracture of heterogeneous materials and its relation to the earthquake phenomena, Bull. Earthquake Res. Inst. Tokyo Univ., 40, 125-144, 1962.

Mogi, K., Effect of the triaxial stress system on the failure of dolomite and limestone, Tectonophysics, 11, 111-127, 1971.

Mogi, Kiyoo, Earthquakes as fractures in the Earth, Proc. Third Cong. Int. Soc. Rock Mech., I, 559-568, 1974.

Mogi, K., On the pressure dependence of strength of rocks and the Coulomb fracture criterion, Tectonophysics, 21, 273-285, 1974.

Montoto, M., Fatigue in rocks: failure and internal fissuration of Barre Granite under loads cyclically applied, Proc. Third Cong. Int. Soc. Rock Mech., IIA, 379-389, 1974.

Mordecai, M., and L. B. Morris, An investigation into the changes of permeability occurring in a sandstone when failed under triaxial stress conditions, in Dynamic Rock Mechanics, C. B. Clark, ed., 12th Symp. Rock Mech., Am. Inst. Min. Met. Pet. Engs., 221-240, 1971.

Muehlberger, W. R., Conjugate joints sets of small dihedral angle, Jour. Geol., 69, 211-219, 1961.

Nascimento, U., C. B. Falcao, A. Pinelo, and M. Marques, Influence of intermediate stress upon internal friction in block masses, Proc. Third Cong. Int. Soc. Rock Mech., IIA, 288-293, 1974.

Nelson, R. A., Fluid Flow Through Fractured Porous Reservoirs - An Experimental and Field Approach, Ph.D. Dissertation, Dept. of Geology, Texas A&M University, May 1975.

...ed, J., F. A. Witherspoon, and T. L. Brekke, A method for coupled stress and flow analysis of fractured rock masses, U. of Calif., Berkeley, Dept. of Civil Eng., Inst. of Trans. and Traffic Eng., Pub. No. 71-6, 128p., 1971.

...rvis, B. K., The mesoscopic fabric of rock masses about some Canadian coal mines, Proc. First Intern. Cong. Rock Mech., 1, 191-198, 1966.

...rvis, B. K., Structural analysis of the Queensway folds, Ottawa, Canada, Can. J. Earth Sci., 4, 299-321, 1967.

...rvis, B. K. Comparative study of the Castle River and other folds in the Eastern Cordillera of Canada, Bull. Geol. Sur. Canada, 205, 98 p., 1971.

..., A., and G. Simmons, Stress induced velocity anisotropy in rocks, An experimental study, J. Geophys. Res., 74, 6667-6674, 1969.

..., Amos, Dilatancy, pore fluids and premonitory variations of V_s/V_p travel times, Bull. Seismol. Soc. Amer., 62, 1217-1222, 1972.

...ert, Leonard, Brittle fracture of rocks, in Fracture, H. Liebowitz ed., Academic Press, 7, 94-155, 1972.

...shi, Yuzo, and R. E. Goodman, Results of Laboratory tests on water pressure and flow in joints, Proc. Third Cong. Int. Soc. Rock Mech., IIA, 660-666, 1974.

...son, W. A., Microfracturing and faulting in a limestone, Tectonophysics, 24, 277-285, 1974a.

...son, W. A., Microcrack nucleation mechanisms in marble (abstract), Eos Trans. ACU, 55, 421, 1974b.

...n, E., Classical and dislocation theories of brittle fracture, in Fracture, Wiley and Sons, N.Y., 147-160, 1959.

...ison, L. J., Petrofabric analysis of experimentally folded multi-lithologic, layered rocks, MS Thesis, Dept. of Geology, Texas A&M University, 71 p., 1972.

...erson, E. L., *and H. C. F. Wilsdorf, Experimental observations of* dislocations, in Fracture, An Advanced Treatise, H. Liebowitz, ed., Academic Press, N.Y., 1, 184-242, 1968.

...ding, B. M., Jr., Crack growth during brittle fracture in compression, Ph.D. Thesis, Dept. of Geology, M.I.T., 1965.

...n, S. S., Time-dependent aspects of rock behavior as measured by a servo-controlled hydraulic testing machine, Int. J. Rock Mech. Min. Sci., 10, 235-246, 1973.

...n, S. S., and A. M. Johnson, Drack growth and faulting in cylindrical specimens of Chelmsford Granite, Int. J. Rock Mech. Min. Sci., 9, 37-86, 1972.

...n, S. S., E. M. Podnicks, and P. J. Cain, Study of rock behavior in cyclic loading, Soc. Pet. Engs. of AIME Paper No. SPE 4249, 181-186, 1973.

...ao, P. C., and Anderson, O. L., Crack propagation as a mechanism of magma transport through the lithosphere (abstract), Eos Trans.AGU, 54, 1193, 1974.

...s, T. K., and L. E. Bartlett, Surface energies of rocks measured during cleavage, Soc. Petrol. Engrs. J., 3, 307-313, 1963.

...s, T. K., and W. W. Krech, Effect of cleavage rate and stress level on apparent surface energies of rocks, Soc. Petrol. Engrs. J., 6, 308-314, 1966.

...r, Fred, Gerald Dollinger, and John Christie, Transmission electron microscopy of experimentally deformed olivine crystals, in Flow and Fracture of Rocks, AGU Monograph, 16, 117-138, 1972.

...R. M., and B. R. Dennis, Seismic and fluid pressure response from a series of hydraulic fractures in granite (abstract), Eos Trans. ACU, 55, 430, 1974.

...N. J., Mechanics of jointing in rocks, Geol. Mag., 96, 149-167, 1959.

...N. J., Fault and joint development in brittle and semi-brittle rock, Pergamon, London, 176p., 1966.

...N. J., A dynamic mechanism for the development of second order faults, in Kink Bands and Brittle Deformation, A. J. Baer and D. K. Norris, eds., Geol. Sur. Canada Paper 68-52, 49-78, 1968.

Price, N. J., Laws of rock behavior in the Earth's Crust, in Rock Mechanics - Theory and Practice, W. H. Somerton, ed., Proc. Eleventh Symp. on Rock Mechanics, Soc. Min. Engs. of AIME, New York, 3-23, 1970.

Price, N. J., The development of stress systems and fracture patterns in undeformed sediments, Proc. Third Cong. Intern. Soc. Rock Mech., IA 487-496, 1974.

Price, N. J., and P. L. Hancock, Development of fracture cleavage and kindred structures, 24th Int. Geol. Cong., Section 3, 584-592, 1972.

Ragan, D. M., and N. J. Price, Second order faults (abstract), Eos Trans. ACU, 56, 1193, 1974.

Raleigh, C. B., J. H. Healy, and J. D. Bredehoeft, Faulting and Crustal Stress at Rangely, Colorado, in Flow and Fracture of Rocks, ACU Monograph, 16, 275-254, 1972.

Rao, M. V. M. S., and Y. V. Ramana, Dilatant behavior of ultramafic rocks during fracture, Int. J. Rock Mech. Min. Sci., 11, 193-203, 1974.

Roegiers, J. C., and D. W. Brown, Geothermal energy: a new application of rock mechanics, Proc. Third Cong. Int. Soc. Rock Mech., IIA, 674-680, 1974.

Rummel, F., Changes in the P-wave velocity with increasing inelastic deformation in rock specimens under compression, Proc. Third Cong. Int. Soc. Rock Mech., IIA, 517-523, 1974.

Rummel, F., and C. Fairhurst, Determination of the post-failure behavior of brittle rock using a servo-controlled testing machine, Rock Mech., 2, 189-204, 1970.

Sanford, A. R., Analytical and experimental study of simple geological structures, Geol. Soc. Amer. Bull., 70, 19-53, 1959.

Sangha, C. M., C. J. Talbot, and R. K. Dhir, Microfracturing of a sandstone in uniaxial compression, Int. J. Rock Mech. Min. Sci., 11, 107-113, 1974.

Santhanam, A. T., and Y. P. Gupta, Cleavage surface energy of calcite, Int. J. Rock Mech. Min. Sci., 5, 253-259, 1968.

Savanick, G. A., and D. I. Johnson, Adhesion at crystalline interfaces in rock, U.S. Dept. of the Interior, Bureau of Mines R.I. 7709, 16p., 1972.

Savanick, G. A., and D. I. Johnson, Measurements of the strength of grain boundaries in rock, Int. J. Rock Mech. Min. Sci., 11, 173-180, 1974.

Savich, A. I., V. I. Koptev, and A. M. Zamakhaiev, In situ ultrasonic investigation of failure of limestone, Proc. Third Cong. Int. Soc. Rock Mech., IIA, 418-423, 1974.

Schapery, R. A., A theory of crack initiation and growth in viscoelastic media, Parts I-IV, Int. J. Fracture, 11, in press, 1975.

Schatz, J. F., M. M. Carroll, and D. H. Chung, A model for the inelastic volume deformation of dry porous rocks (abstract), Eos Trans. ACU, 56, 1195, 1974.

Scholz, C. H., The frequency-magnitude relation of microfracturing in rock and its relation to earthquakes, Bull. Seism. Soc. Amer., 58, 399-415, 1968a.

Scholz, C. H., Microfracturing and the inelastic deformation of rock in compression, J. Geophys. Res., 73, 1417-1432, 1968b.

Scholz, C. H., Experimental study of the fracturing process in brittle rock, J. Geophys. Res., 73, 1447-1453, 1968c.

Scholz, C. H., Mechanism of creep in brittle rock, J. Geophys. Res., 73, 3295-3302, 1968d.

Scholz, C. H., Microfractures, aftershocks, and seismicity, Bull. Seism. Soc. Amer., 58, 1117-1130, 1968e.

Scholz, C. H., L. R. Sykes, and Y. P. Aggarwal, Earthquake prediction: A physical basis: Science, 181, 803-810, 1973.

Shockey, D. A., and M. Austin, P. S. De Carli, J. Kalthoff, Lynn Seaman, and D. R. Curran, Quantitative prediction of dynamic fracture and

fragmentation of hard rocks (abstract), Eos Trans. AGU, 56, 1197, 1974a.

Shockey, D. A., D. R. Curran, Lynn Seaman, J. T. Rosenberg, C. F. Petersen, Fragmentation of rock under dynamic loads, Int. J. Rock Mech. Min. Sci., 11, 303-317, 1974b.

Simmons, G., D. Richter, T. Todd, and H. Wang, Microcracks: their potential for obtaining P-T history of rocks, Geol. Soc. Amer. Abstr. with Programs, 5, 810, 1973.

Simmons, Gene, and Dorothy Richter, Microcracks in rocks, in The Physics and Chemistry of Rocks and Minerals, Proc. NATO Petrophysics Mtg., April 1974, in press, 1975.

Simmons, Gene, Terry Todd, and W. Scott Baldridge, Toward a quantitative relationship between elastic properties and cracks in low porosity rocks, Amer. J. Sci., in press, 1975.

Singh, B., Continuum characterization of jointed rock masses, Part I The constitutive equations, Int. J. Rock Mech. Min. Sci., 10, 311-336, 1973a.

Singh, B., Continuum characteristics of jointed rock masses, Part II Significance of low shear modulus, Int. J. Rock Mech. Min. Sci., 10, 337-350, 1973b.

Sprunt, E. S., and W. F. Brace, Direct observation of microcavities in crystalline rocks, Int. J. Rock Mech. Min. Sci., 11, 139-150, 1974a.

Sprunt, E. S., and W. F. Brace, Some permanent structural changes in rocks due to pressure and temperature, Proc. Third Cong. Int. Soc. Rock Mech., IIA, 524-529, 1974b.

Sriruang, S., and B. Hamil, The relation of mineralogy and microstructure to morphology and trajectory of rock fracture, in New Horizons in Rock Mech., Penn. St. Univ., June 1972, ASCE, New York, 1973.

Stearns, D. W., Macrofracture patterns on Teton Anticline, northwest Montana, Am. Geophys. Union Trans., 45, 107-108, 1964.

Stearns, D. W., Certain aspects of fracture in naturally deformed rocks, in Rock Mechanics Seminar, R. E. Riecker, ed., Terrestrial Sci. Lab., Air Force Cambridge Res. Labs., Hanscom Field, Bedford, Mass., Clearinghouse for Fed. Sci. and Tech., AD 669375, 1, 97-118, 1968.

Stearns, D. W., Fracture as a mechanism of flow in naturally deformed layered rock, in Kink Bands and Brittle Deformation, A. J. Baer and D. K. Norris, eds., Geol. Sur. Canada Paper 68-52, 79-95, 1969.

Stearns, D. W., Structural interpretation of the fractures associated with the Bonita fault, New Mexico Geol. Soc. Field Conf. Guidebook, 23, 161-164, 1972.

Stearns, D. W., and M. Friedman, Reservoirs in fractured rock, Am. Assoc. Petroleum Geologists Mem., 16, 82-106, 1972.

Stekatee, J. A., Some geophysical applications of the elasticity theory of dislocations, Can. J. Phys., 36, 1168-1197, 1958.

Stokes, R. J., Microscopic aspects of fracture in ceramics, in Fracture, An Advanced Treatise, H. Liebowitz, ed., Academic Press, N.Y., 7, 157-241, 1972.

Stuart, W. D., Constitutive equations of dilatant rocks and applications to precursory phenomena (abstract), Eos Trans. AGU, 55, 432, 1974.

Stuart, W. D., and J. A. Dieterich, Continuum theory of rock dilatancy, Proc. Third Cong. Int. Soc. Rock Mech., IIA, 530-534, 1974.

Summers, D. A., John Corwine, and Li-king Chen, A comparison of methods available for the determination of surface energy, in Dynamic Rock Mechanics, C. B. Clark, ed., Proc. 12th Symp. Rock Mechanics, Rolla, Mo., 1970, AIME, New York, 241-261, 1971.

Swolfs, H. S., Chemical effects of pore fluids on rock properties, Amer. Assoc. Petroleum Geologists Mem., 18, 224-234, 1972.

Swolfs, H. S., H. R. Pratt, A. D. Black, W. F. Brace, A. S. Orange, and K. A. Cronseth, In situ properties of a jointed granite (abstract), Eos Trans. AGU, 55, 432, 1974.

Tapponnier, P., and W. F. Brace, A closer look at dilatant microcracks (abstract), Eos Trans. AGU, 56, 1195, 1974.

Tchalenko, J. S. and Ambraseys, N. N., Structural analysis of the Dasht-e Bayaz (Iran) earthquake fractures, Geol. Soc. Amer. Bull., 81, 41-60, 1970.

Thill, R. E., Acoustic methods for monitoring failure in rock, in New Horizons in Rock Mech., Proc. 14th Symp. on Rock Mech., Penn. St. Univ., June 1972, ASCE, New York, 649-687, 1973.

Thomsen, Leon and F. T. Wu, Microfracturing of Westerly Granite under creep conditions (abstract), Eos Trans. AGU, 55, 431, 1974.

Turcotte, D. L., and D. A. Spence, An analysis of strain accumulation on a strike slip fault, J. Geophys. Res., 79, 4407-4412, 1974.

Turner, P. W., and P. R. Barnard, Stiff constant strain-rate testing machine, Engineer, 214, 146-148, 1962.

Turner, W. T., and D. T. Secor, Jr., Effective confining pressure and fluid discharge along fractures (abstract), Eos Trans. AGU, 55, 431, 1974.

Voight, Barry, Thermoelastic stress and fracture history of sedimentary, metamorphic, and igneous rocks (abstract), Geol. Soc. Amer. Abstr. with Programs, 5, 852, 1973.

Voight, Barry, and B. H. P. St. Pierre, Stress history and rock stress, Proc. Third Cong. Int. Soc. Rock Mech., IIA, 580-582, 1974.

Voight, Barry, and H. D. Dahl, Numerical continuum approaches to analysis of nonlinear rock deformation, Can. J. Earth Sci., 7, 814-830, 1970.

Vutukuri, V. S., The effect of liquids on the tensile strength of limestone, Int. J. Rock Mech. Min. Sci., 11, 27-29, 1974.

Wawersik, W. R., Detailed analysis of rock failure in laboratory compression tests, Ph.D. Thesis, Dept. Mining Eng., U. of Minnesota, 1968.

Wawersik, W. R., and C. A. Fairhurst, A study of brittle rock fracture in laboratory compression tests, Int. J. Rock Mech. Min. Sci., 7, 561-575, 1970.

Wawersik, W. R., and W. F. Brace, Post-failure behavior of granite and diabase, Rock Mechanics, 3, 61-85, 1971.

Wawersik, W. R., Stress-strain and fracture behavior of Westerly Granite (abstract), Eos Trans. AGU, 52, 346, 1971.

Weertman, J., Continuum distribution of dislocations on faults with finite friction, Bull. Seismol. Soc. Amer., 54, 1035-1038, 1964.

Weertman, J., Relationship between displacements on a free surface and stress on a fault, Bull. Seismol. Soc. Amer., 55, 945-953, 1965.

Weertman, J., Water-flow paths around a dislocation on an earthquake fault, J. Geophys. Res., 79, 3291-3293, 1974.

Westbrook, J. H., and P. J. Jorgensen, Effects of water desorption on indention microhardness anisotropy in minerals, Am. Mineralogist, 53, 1899-1909, 1968.

Westwood, A. R. C., D. L. Goldheim, and R. C. Lye, Rebinder effect in MgO, Philos. Mag., 16, 505-519, 1967.

Westwood, A. R. C., D. L. Goldheim, and R. C. Lye, Further observations on Rebinder effect in MgO, Philos. Mag., 17, 951-959, 1968.

Witherspoon, P. A., J. E. Gale, R. L. Taylor, and M. Ayatollahi, Fluid injection and withdrawal in a fault zone with deformable fractures (abstract), Eos Trans. AGU, 55, 353, 1974a.

Witherspoon, P. A., J. E. Gale, R. L. Taylor, and M. S. Ayatollahi, Effect of permeability anisotropy and tectonic stress orientation on fluid injection in a fault zone (abstract), Eos Trans. AGU, 56, 1191, 1974b.

Whitcomb, J. H., J. D. Garmany, and D. L. Anderson, Earthquake prediction: Variation of seismic velocities before the San Francisco Earthquake, Science, 180, 632-635, 1973.

White, S., The dislocation structures responsible for the optical effects in some naturally deformed quartzes, Jour. Mat. Sci., 8, 490-499, 1973a.

White, S., Deformation lamellae in naturally deformed quartz, Nature, Phys. Sci., 245, 26-28, 1973b.

Wiederhorn, S. M., Influence of water vapor on crack propagation in soda-lime glass, Am. Ceramic Soc. J., 50, 407-414, 1967.

Willard, R. J., and J. R. McWilliams, Microstructural techniques in the

Some Shock Effects in Granodiorite to 270 Kilobars at the Piledriver Site

I. Y. Borg

Lawrence Livermore Laboratory, University of California
Livermore, California 94550

Postshot exploration around the 61 ± 10 kT Piledriver underground nuclear explosion in granodiorite indicates that the cavity radius r_c is 40.1 meters. The shape of the vertical chimney, which extends 277 meters above the shot level, was influenced by pre-existing joints and fractures and is asymmetric. The limit of detectable shock-induced microfracturing is 2.7 ± 0.2 r_c, at which point rocks have been subjected to peak radial pressures of 6–8 kb. Extensive fracturing occurs at distances to the shot point of $<1.3 \pm 0.2\ r_c$, corresponding to pressures exceeding the granodiorite Hugoniot elastic limit of 45 kb. The onset of slip and twinning in mineral constituents is correlated with measured shock pressures at estimated strain rates of $\leq 10^4$–10^5 sec^{-1}, ambient temperatures of 30°C, and calculated Hugoniot temperatures for granodiorite of <300°C. For quartz, planar lamellas are detectable in some grains subjected to pressures of 75–78 kb and in all grains subjected to a pressure of 205 kb. Mechanical $(\bar{1}01)$ twinning in hornblende and sphene (110) is evident in rock that has experienced pressures of 24–40 and 14–18 kb, respectively. Some kinking in biotite is associated with shock pressures as low as 15–16 kb; above 75 kb all biotite contains kink bands. At ≤270 kb no shock-induced twinning or planar lamellar structure was noted in either the orthoclase or the albite-oligoclase component of the granodiorite, although there was a noticeable loss of birefringence in both. Glass occurs within the chimney rubble and in distant fractures within the surrounding granodiorite where it was injected by expanding gases. No diaplectic glass was noted in rock forming the cavity walls (270 kb). Dissociation of the hydrous phases, biotite and hornblende, in wall rock surrounding the cavity is attributed to the permeation of hot gases along fractures.

The Piledriver event, a nuclear explosion in granodiorite at the Nevada Test Site, provided an opportunity to study shock effects, since it occurred adjacent to a highly instrumented tunnel drift system and was accompanied by an extensive re-entry and postshot drilling program. Close-in stress gages, instruments measuring particle velocities and accelerations, and in situ cameras recording displacements operated satisfactorily at the time of the shock propagation and provided an unusually complete set of data, which was used to check preshot predictions. Under these circumstances, the specific behavior of the rock surrounding the explosion (vaporization, melting, plasticity, and fracture) can be associated with particular pressures with a minimum of uncertainty.

Postshot exploration resulted in the recovery of three 3-inch cores, one of which penetrated the lower portions of the cavity produced by the explosion. This paper summarizes the mode of failure of the granodiorite and the mineral constituents within these cores as functions of radial distance and peak radial pressure.

Rubble and glass recovered within the cavity chimney are largely ignored in this account. The position of such material at the time of the explosion, and hence the magnitude of the pressure pulse that they saw, cannot be known precisely. The maximum radial stress experienced by any recovered core outside the cavity is 270 kb.

PILEDRIVER EXPERIMENT

The Piledriver site, which is located within the Climax stock of area 15 of the Nevada Test Site, is about 0.4 km from the 5-kT Hardhat experiment, which was conducted in 1962. In both instances a well-instrumented underground tunnel drift complex existed at shot time (Figures 1 and 2). The area of the stock exposed at the surface is 3.4 km^2; however, the

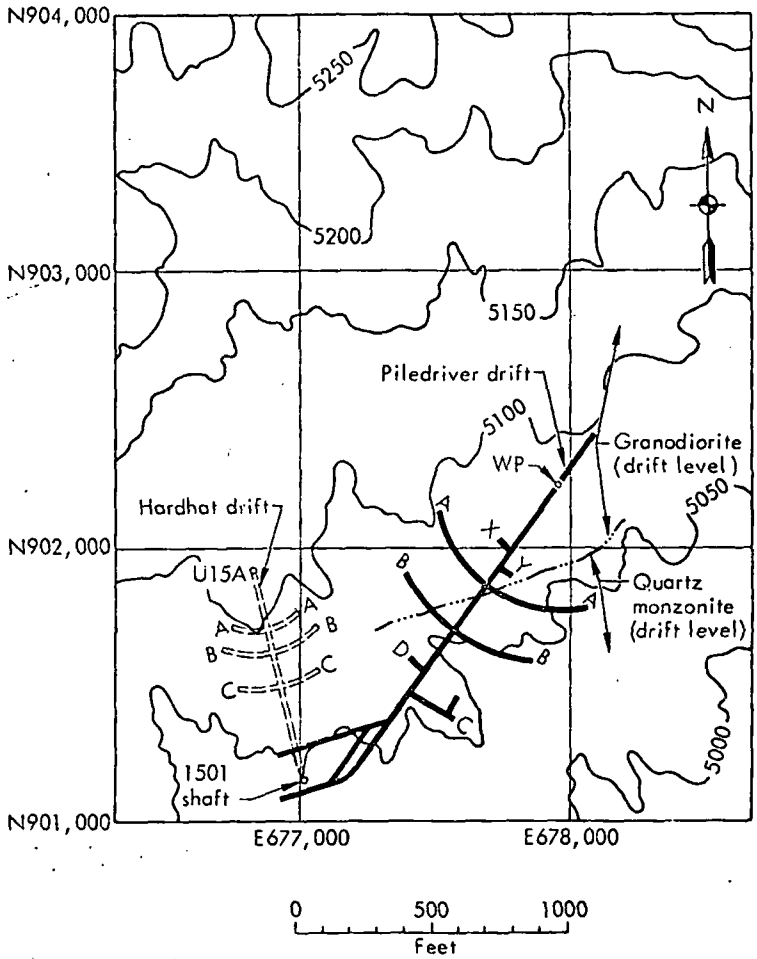

Fig. 1. Piledriver and Hardhat sites in Area 15, NTS. Contours show the surface elevation in feet above sea level. WP marks the shot point. (C. J. DiStephano, D. R. Williams, and H. A. Jack, personal communication, 1969.)

rock mass broadens to a diameter of 9.7 km at a depth of 396 meters [*Allingham and Zietz*, 1962]. The stock consists of a granodiorite and a younger porphyritic quartz monzonite. Although most of the instrumentation surrounding both Hardhat and Piledriver was placed in the quartz monzonite part of the intrusive, the shot points were located well within the granodiorite (Figure 1). Similarly, the three postshot Piledriver holes were cored within the granodiorite. The device was emplaced below the water table encountered at 1372 meters mean sea level (msl); however, perched water was encountered at variable depths (24–112 meters) during preshot drilling and tunneling operations. These findings suggest that it is localized by major fracture and shear zones [*Houser and Poole*, 1961]. Additional data concerning the event are summarized in the appendix with previously published results and postshot observations.

In situ stress measurements and displacements. In addition to instrumentation in the drifts and associated slant holes, five close-in radial boreholes were fitted with stress gages (Figure 2, holes A–F) by contracting agencies. Data from reliable gages are plotted in Figure 3 as a function of distance from the shot point. Also included are peak radial stresses calculated from peak particle velocities. The curve is an arbitrary straight-line fit of the data, which theoretically can deviate from linearity [*Cherry and Rapp*, 1968].

The expansion and heave of the cavity follow-

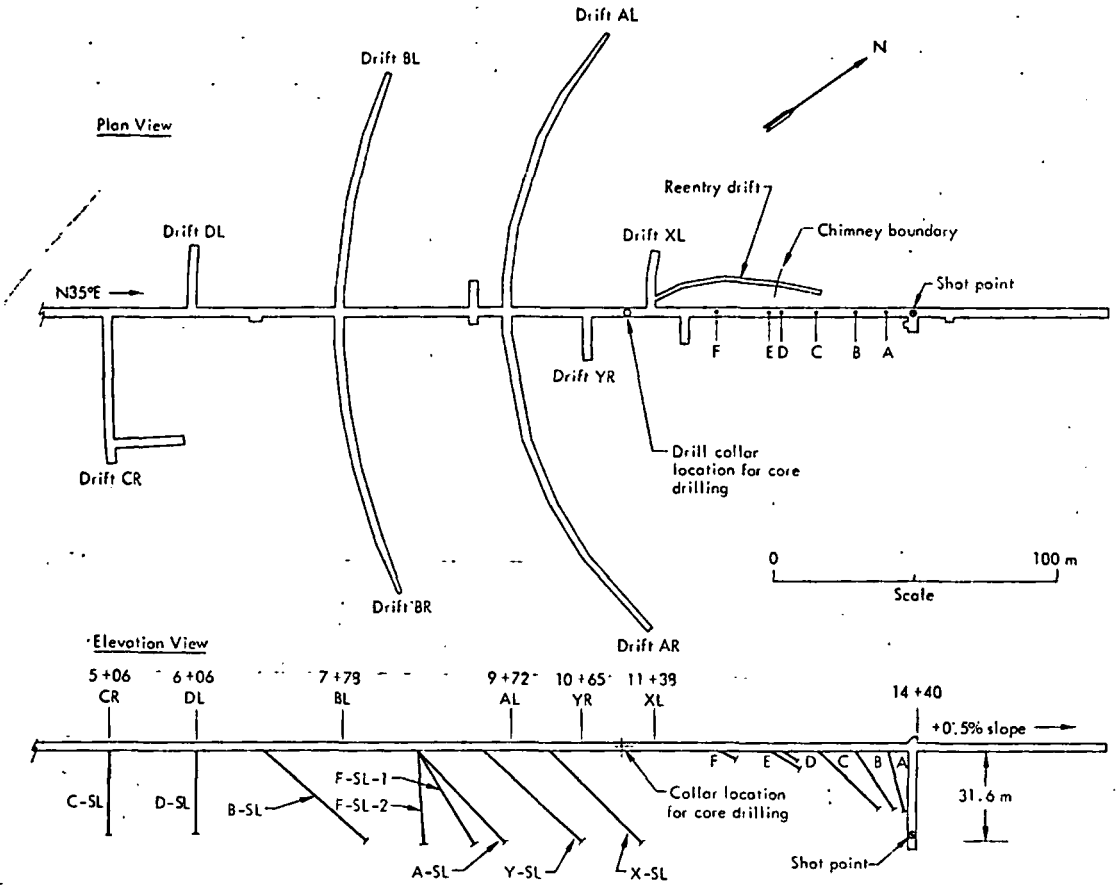

Fig. 2. Piledriver tunnel and drift complex showing locations of instrumented boreholes at shot time. Stations indicated on elevation (e.g., 5 + 06) are referenced to the 15.01 shaft (0 + 00), which is off the diagram. (Modified from drawing by K. Willits of Fenix and Scisson, Inc., Project Engineer, 1968, Piledriver project station 15.01, drawing MER-192 14d-1501, Nevada Operations Office, U.S. Atomic Energy Commission.)

ing the passage of the main shock wave result in displacements of the surrounding rock that diminish in magnitude with distance from the shot point. In order to correlate data such as peak pressures measured within 100 msec of the time of detonation (Figure 3) with observed shock effects in postshot cores and drifts, real displacements must be estimated. Comparing preshot and postshot positions of markers in access tunnels and drifts is somewhat unsatisfactory, because movements along pre-existing joints and faults were facilitated by the tunnel and the drifts. Another measure of displacements is the residual radial displacement calculated by the integration of particle velocity or the double integration of acceleration curves. Such calculated displacements are strongly affected by base line errors in the initial data and characteristically show great scatter. Data of these types are plotted as a function of preshot distance in Figure 4 with displacements calculated from the SOC code [*Cherry and Peterson*, 1970]. Agreement between measured and calculated values is reasonably good when they can be compared, and thus it is indicated that the SOC calculation can be used fairly accurately over the whole range. In the linear portions of the curve, underground displacements are proportional to the inverse of the square of the radial distance. A similar relationship was established from permanent particle displacements at depth in two earlier granite events at the Nevada Test Site (Hardhat and Shoal), despite greater scatter in the data (J. L. Merritt, personal communication, 1969).

Strain rate of shock loading in field experi-

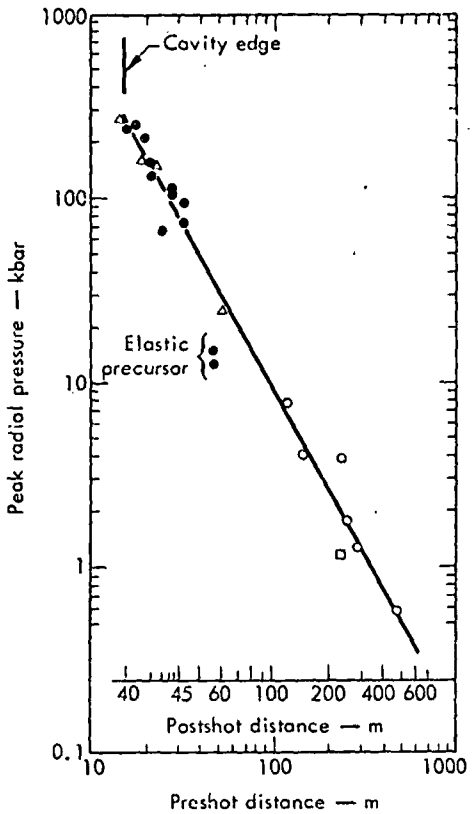

Fig. 3. Measured peak radial stress versus preshot and postshot distance from the Piledriver shot point. Triangles, data from manganin gages (C. T. Vincent and J. Rempel, personal communication, 1968); solid circles, data from electrolytic gages (P. Liebermann, personal communication, 1967); open circles, data calculated from particle velocity and from acceleration data [*Perrett*, 1968]; squares, datum from the quartz piezoelectric gage [*Perrett*, 1968].

ments. In pressure regimes of >100 kb the strain rate associated with shock loading in the field (nuclear) experiment is assumed to be slightly less than that for the flying-plate type of laboratory shock experiment (10^6–10^9 sec^{-1}). From free-field measurements of strain ϵ or particle velocities u_p and pressures σ_1 and from records of rise times it is possible to calculate strain rates $\dot{\epsilon}$ below about 14-kb pressure, a limit set by satisfactory operation of the gages. From stress and strain gages, strain rates of 10^{-1} sec^{-1} can be calculated for peak pressures of 1–1.5 kb. With the relation

$$\epsilon = \rho_0 u_p^2/\sigma_1$$

derived from shock equations, strain rates of 7 to 7 × 10^2 sec^{-1} can be calculated in the interval 7–14 kb. The measured rise time to maximum velocity or strain normally includes the time for cables and instruments to transmit and record the signal. The lag time, estimated for velocity gages to be of the order of 3 × 10^{-3} sec (C. J. Sisemore, personal communication, 1971), has been subtracted from the measured rise times for the calculations. Nonetheless, uncertainties in the exact lag time correction limit the accuracy of the calculated strain rates. They are probably accurate to within a factor of 10. The important observation is that the strain rate falls off with distance from the shock source to low values, in relation to the values associated with shock loading in the >100-kb regime.

Vaporization and melting in the cavity. Also plotted in Figure 4 is a calculated point (inverted triangle) based on the difference between the measured cavity radius and the calculated radius of combined vaporized and melted rock. Although cavity development is a continuous process, it is convenient to describe it as being discontinuous, involving shock vaporization, shock melting, and melting resulting from solid-vapor interactions. The solid-vapor interactions involve thermal conduction and exothermic condensation of ionized and vaporized elements on solid-rock interfaces exposed by slumping of the shock-melted zones to lower portions of the cavity. *Butkovich* [1967, 1968] has estimated the amount of granitic rock in grams per kiloton involved in the three types of transformations:

Shock vaporized	70 × 10^6
Shock melted	350 × 10^6
Melted by solid-vapor interactions	250 to 300 × 10^6

From these estimates the volume of rock affected can be calculated, and the radii of concentric zones can be determined. The difference between the measured cavity radii (40.1 meters) and the calculated outermost zone of melted rock (15.6 ± 1.0 meters) represents the distance that the rock at the present cavity wall has been displaced by gas expansion (24.5 meters).

Temperature associated with the shock wave. The presence of glass along fractures and the dissociation of the hydrous mineral phases (e.g., biotite and hornblende) indicate that the gran-

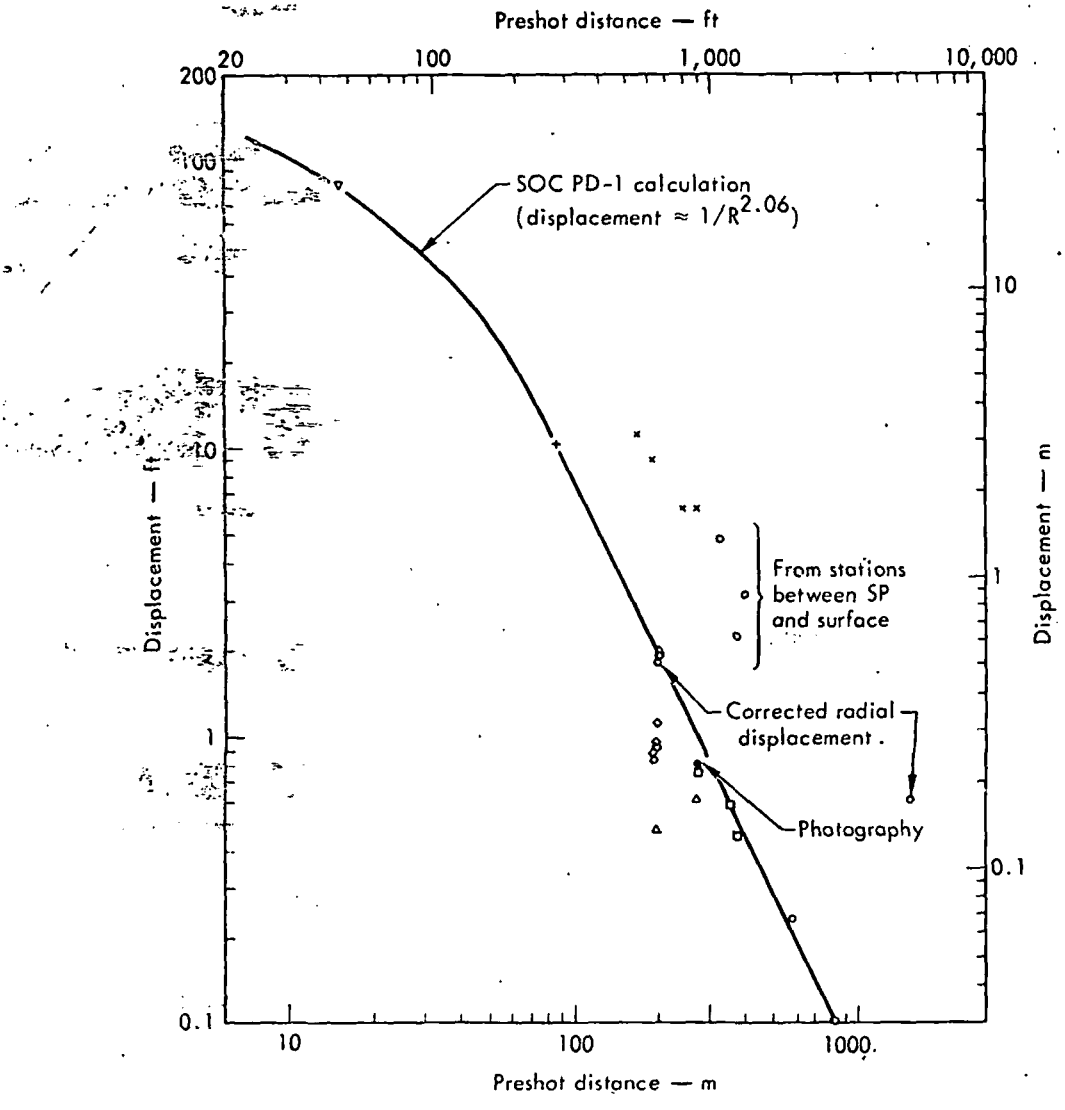

Fig. 4. Measured and calculated displacements as functions of preshot distance from the shot point. Open circles, residual radial displacements [*Perrett*, 1968; *Hoffman and Sauer*, 1969]; crosses, postshot survey in the access tunnel; triangles, average permanent displacement of a test section (C. J. DiStephano and L. J. Asbaugh, personal communication, 1969); squares, horizontal movement of bench marks (C. J. DiStephano, D. R. Williams, and H. A. Jack, personal communication, 1969); diamonds, average packing displacement (H. H. Holmes, H. M. Hanson, and A. O. Bracket, personal communication, 1969); pluses, displacement in the tunnel (D. Rabb, personal communication, 1970); inverted triangles, difference between final cavity radius and the radius of melted and vaporized rock; solid circle, photographic techniques [*Smith*, 1969].

odiorite has been heated to temperatures of >700°C. In order to determine whether the heat was derived from the passage of the shock wave, temperatures were calculated along the Hugoniot at a series of volumes with the method of *Walsh and Christian* [1955]. The equation describing the conservation of energy in a shock wave,

$$dE = \frac{v_0 - v}{2}\,dp - \frac{p + p_0}{2}\,dv$$

where v_0, p_0 and v, p are initial states and final

states, respectively, when combined with the first law of thermodynamics, yields the expression

$$TdS = \frac{p - p_0}{2}\,dv + \frac{v_0 - v}{2}\,dp \qquad (1)$$

Using the identity $dS = C_v(dT/T) + (\partial p/\partial T)_v dv$, in which C_v is the specific heat at constant volume, and equating $(\partial p/\partial T)_v$ by the chain rule to α/β, where α is the thermal expansion and β the isothermal compressibility, we obtain the expression

$$TdS = C_v\,dT + (\alpha/\beta)T\,dv \qquad (2)$$

Entropies of the phase transformations of quartz and feldspar that produce anomalous compressions above 140–150 kb have been neglected. That portion of the total energy of the system is difficult to estimate, because the transformations are incomplete below 300–400 kb and mixed phases exist up to those pressures [*Ahrens and Rosenberg*, 1968; *Ahrens, et al.*, 1969*a*]. Omission of transformation energies leads to calculated Hugoniot temperatures that are higher than they would be if the energies were taken into account. Inasmuch as the maximum Hugoniot temperature in the interval 0–270 kb is of particular interest here, the simplification is defensible.

When (1) and (2) are combined with the definition of the Grüneisen constant,

$$\gamma_0 = V(\partial p/\partial E)_v = \alpha V/C_v\beta$$

where V is the specific volume at standard temperature and pressure, the temperature difference between the ambient and the shocked condition of the material is

$$dT = \frac{p - p_0}{2C_v}\,dv + \frac{v_0 - v}{2C_v}\,dp - \frac{\gamma_0 T}{v_0}\,dv \qquad (3)$$

Hence,

$$T_i = \frac{T_{i-1}[1 - (\gamma_0 v/2V)] + \{[(\langle p\rangle - p_0)\,\Delta v + (v_0 - \langle v\rangle)\,\Delta p]/2C_{v_{i-1}}\}}{1 + (\gamma\,\Delta V/2V)}$$

where $\langle p\rangle$ and $\langle v\rangle$ are mean values of points i and $i - 1$ on the Hugoniot. In the calculations, (γ/V) for the low and high (>370 kb) phases was taken to be a constant. From $\gamma = 0.62$ and $\rho = 3.96$ g/cm³ for granite [*Ahrens et al.*, 1969*b*], $\gamma/V = 1.73$ g/cm³ for the high-pressure phase, and, from a calculated $\gamma = 0.645$ and $\rho = 2.68$ g/cm³, $\gamma/V = 2.46$ g/cm³ for the low-pressure phase under ambient conditions. The value of C_v was approximated by the equations given by *Birch et al.* [1942] for C_p as a function of temperature. The equation-of-state data were compiled from shock experiments on the Climax granodiorite [*Van Thiel*, 1966]. Data for $P - V$ below 40 kb were taken from isothermal compressibilities [*Stephens et al.*, 1970].

The results of the calculations are plotted in Figure 5 with comparable calculations for single-crystal quartz [*Wackerle*, 1962], oligoclase [*Ahrens et al.*, 1969*a*], and Coconino sandstone, 24% porosity [*Ahrens and Gregson*, 1964]. As might be expected, below 400 kb the granodiorite data closely parallel the quartz and oligoclase data. Above 400 kb, conversion to high-pressure phases of quartz and oligoclase is almost complete, and all the temperature calculations are subject to uncertainties arising from assumed values of ρ_0 (high), γ, C_v, and the entropies of the transformations, if they were taken into account. Thus the differences apparent between the single-crystal and granodiorite curves do not merit close examination. It is sufficient to note that at 270 kb the shock temperature is <300°C and not high enough to account for the high-temperature effects noted in granodiorite adjacent to the cavity wall. However, the shape of the release adiabat curves for both quartz and plagioclase [*Ahrens and Rosenberg*, 1968] indicates that a certain amount of stored energy is released as heat during unloading. Nevertheless, as was demonstrated for oligoclase [*Ahrens et al.*, 1969*a*], it is unlikely that the temperature of the granodiorite during release from 270 kb rises as high as 700°–900°C; thus the decomposition temperature of biotite and the observed thermal breakdown of the hydrous phases are more reasonably attributed to the permeation of hot gases into shock-induced fractures.

Measurements and predictions of cavity size. Before the postshot exploration of the chimney cavity, various estimates of the expected cavity size were made. In Table 1, nine calculations are

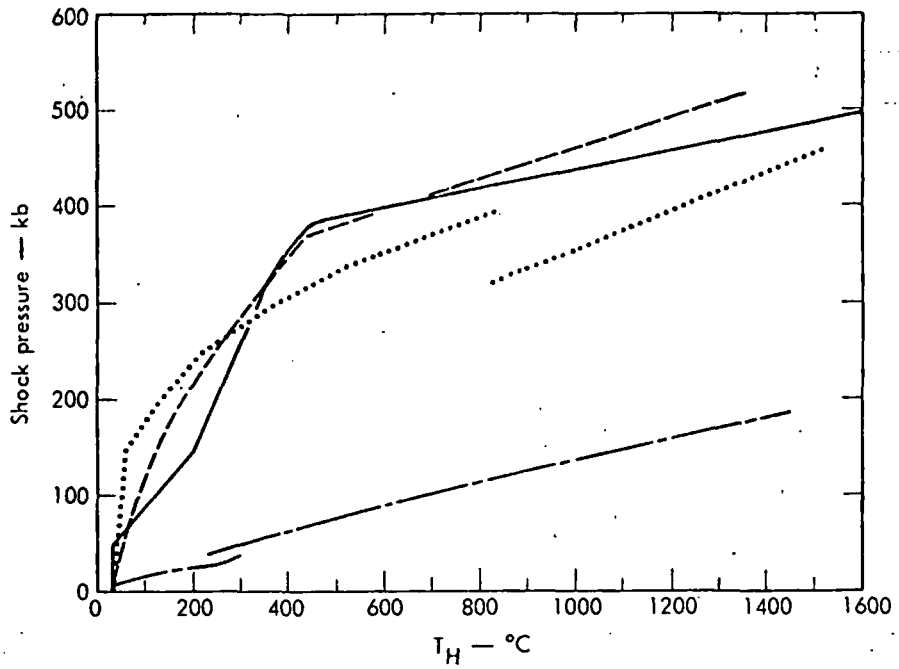

Fig. 5. Hugoniot temperature as a function of shock pressure in granite, quartz, and sandstone. The oligoclase data above 400 kb are based on $\gamma = 1.00$, $\Delta E_{I\to A} = 0.97$, and $\rho = 3.69$ g/cm³ for the high-pressure phase. Dashed line, granodiorite; solid line, quartz [*Wackerle*, 1962]; dotted line, oligoclase [*Ahrens et al.*, 1969*a*]; long dashed line, Coconino sandstone [*Ahrens and Gregson*, 1964].

compared. All the calculations are within 18% of the measured radius, and most are within 5%. Thus, if appropriate physical parameters describing the granodiorite are given, the cavity radius can be predicted accurately.

POSTSHOT CORES

Location of cores and chimney definition. The locations of four postshot drill holes are indicated in Figure 6. The drilling demonstrated that the southwest wall of the chimney is canted about 13° from the vertical [*Sterrett*, 1969] and controlled by one or two of the four well-developed joint fracture systems in the stock. The attitude of other parts of the chimney wall is not known. However, the one explored section through the adjacent Hardhat chimney demonstrated that its north-northwest and south-southeast walls are nearly vertical. Since the major joint fracture systems in the stock are pervasive, the north-northwest and south-southeast walls of the Piledriver chimney may also be vertical. By similar reasoning, the unexplored southwest wall of the Hardhat chimney may depart from the vertical.

Description of cores. Figure 7 contains photographs of recovered 3-inch-diameter core from U 15.01 PS-3. Caliper and γ logs in the hole indicate that the granodiorite cavity debris contact occurs at a slant hole distance (SHD) of 71.0 meters (233 feet) [*Sterrett*, 1969]. Recovered core from that depth (Figure 7*c*) contains a very sharp interface between the highly deformed granodiorite and the black vesicular melted counterpart. Figure 7*a* shows a core recovered at 70.7 meters (232 feet) SHD, which is coherent although highly fractured, plastically deformed, and partially decomposed (hydrous phases). Figure 7*b* was recovered from a slant hole distance of 68.9 meters (226 feet). Glass seams filling reopened joints are conspicuous in these samples and others in the SHD of 50.0–71.0 meters (164–233 feet) of PS-3. Injected siliceous glasses can occur along gross fractures and pre-existing shear zones as far as 42.7 meters horizontally from the cavity chimney edge; however, glassy pseudomorphs of minerals constituting the granodiorite, or devitrified counterparts, do not occur within core collected up to the cavity wall.

TABLE 1. Predictions and Measurements of Piledriver Cavity Radius

Predicted Radius		
meters	feet	Prediction Method
32.7	108	SOC calculation assuming constant overburden and no free surface [*Cherry and Rapp*, 1968]
36.4	119	$r_c = 21.0\ W^{0.306}E^{0.514}/\rho^{0.244}\mu^{0.576}h^{0.161}$ [*Closmann*, 1969]
40.1	131.5	$r_c = CW^{1/3}/(\rho h)^{\alpha}$, where $C = 103$ (granodiorite) and $\alpha = 0.32$ (2% H_2O) [*Higgins and Butkovich*, 1967]
40.1	131.5	Measured value, accepted as most probable cavity radius on basis of γ and caliper logs of core hole PS-3, which intersected cavity below level of shot point [*Sterrett*, 1969]
40.1+	131.7	Assuming adiabatic expansion of cavity gas to twice overburden pressure [*Chapin*, 1969, Figure 2, granite]
40.9	134	$r_c = C\ W^{1/3}/(\rho h)^{1/4}$, where $C = 61.6$ (granite) [*Boardman*, 1967]
41.2	135	$r_c = 16.3\ W^{0.29}E^{0.62}/h^{0.11}\rho^{0.24}\mu^{0.67}$ (H. C. Heard and F. J. Ackerman, personal communication, 1967)
41.6	136	$r_c = 52\ \alpha^{1/3}W^{1/3}/(\rho gh + C_s)^{1/3\gamma}$, where $C_s = 30$ bars (granite), $\gamma = 1.05$ (granite with 2.5% H_2O), [*Michaud*, 1968]
44.5	146	Calculated from void volume of the chimney determined from chimney pressurization tests [*Boardman*, 1967]
45.1	148	$r_c = (3R^2\Delta\sigma)^{1/3}$ from average corrected residual particle displacements at two slant holes (204- and 470-meters radial distance) [*Perrett*, 1968]
45.7	>150	SOC calculation assuming variable overburden and rarefaction at a free surface [*Cherry and Rapp*, 1968]

r_c = cavity radius.
W = yield (kT).
E = Young's modulus (Mb).
ρ = density of rock (g/cm³).
μ = shear modulus (Mb).
h = depth of burst (meters).
α [*Higgins and Butkovich*, 1967] = $1/3\gamma$.
γ = coefficient of adiabatic expansion.
α [*Michaud*, 1968] = 1.0 (coefficient related to size of the shot chamber).
C_s = coefficient related to the 'contraints of the structure.'
R = radial range (meters).
Δs = residual displacement (meters).

Orientation of core fractures. It is customary to assume that at least three types of fracture systems symmetric about the point source develop around an underground explosion: a set inclined at an acute angle to the peak radial stresses (i.e., shear fractures), a radial set, and a set tangential to concentric spheres about the source. To test the assumption, the attitude of several thousand macroscopic fractures was measured in three postshot cores. Because only the bearing of the core axis is known, such fractures cannot be oriented uniquely in space. However, at any particular position along the core length it is possible to test whether the attitude of the fracture with respect to the core axis is consistent with a radial, a tangential, a shear, or a random orientation. Results of this study [*Borg*, 1970a] are that the fractures are demonstrably nonrandomly oriented. Their positions are consistent with failure along pre-existing regional joints, fractures, and shear zones. With the exception of a short interval of core near a pre-existing tunnel wall where rarefaction of the shock front was probable, the orientation of the fractures is not consistent with radial or tangential positions in any core interval. With the core information available the test for shear failure is not sufficiently precise to determine whether the fractures are also consistent with this possibility.

Fracturing radius. Microfracturing in the Piledriver cores was assessed as a function of distance from the shot point. Approximately 75 thin sections were examined; the results are shown in Figure 8. In general, core PS-3 is slightly more fractured than PS-1 at comparable postshot distances. This finding is in keeping with a lower over-all core recovery record (89 versus 61%) [*Sterrett*, 1969], which reflects different drilling techniques.

Samples were assigned to one of five categories on the basis of the over-all amount of fracturing present: intensely fractured (crushed), highly fractured, moderately fractured, slightly frac-

tured, and unfractured samples. Assignment to one of the five categories was not difficult; however, the usefulness of such a qualitative assessment of fracturing is limited to comparisons made by a single observer. On this account, fracturing in the Hardhat cores was also as-

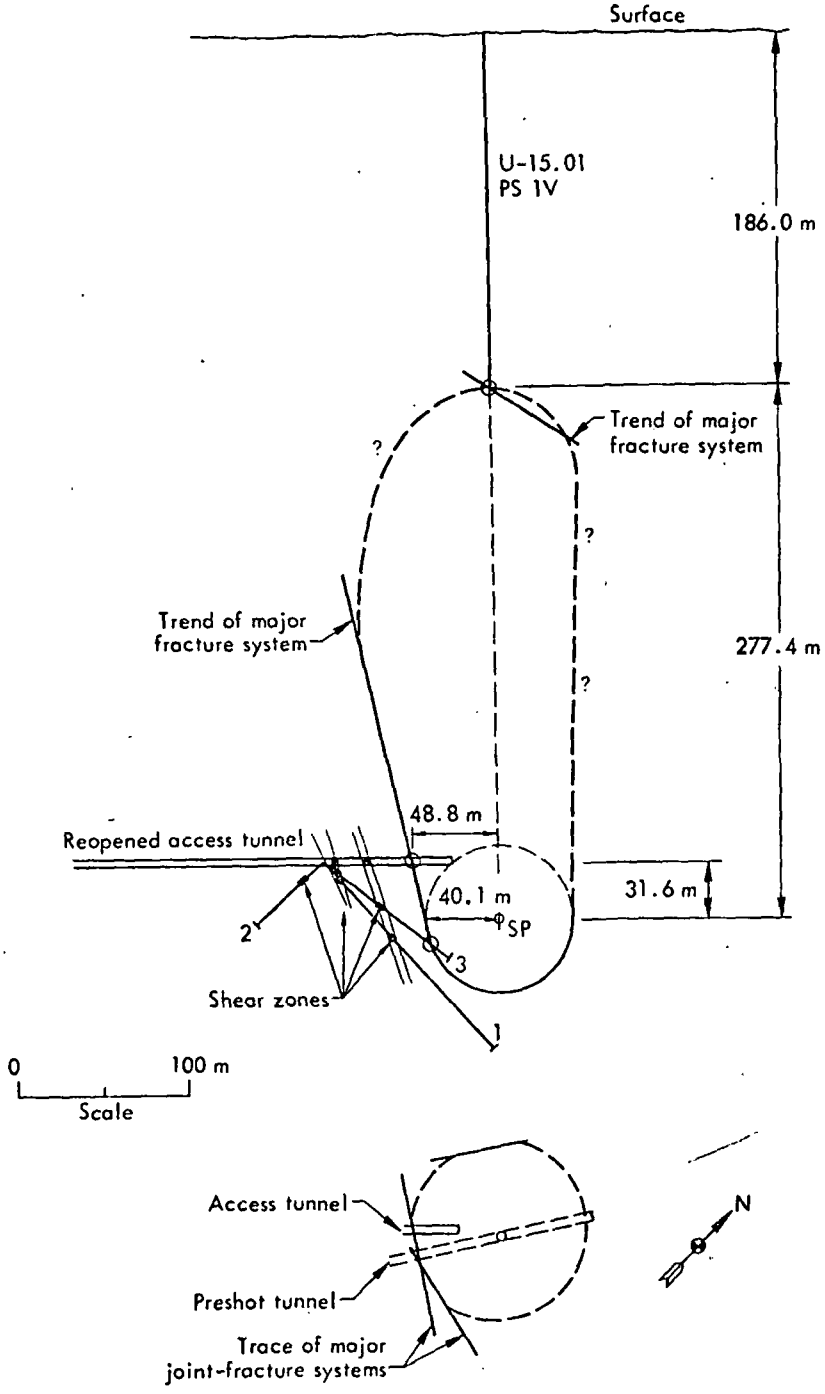

Fig. 6. Vertical cross section (top) and horizontal cross section at the tunnel level (bottom) of the chimney shape resulting from the Piledriver event. Open circles, points established by postshot exploration; solid circles, injected radioactive glass in the tunnel.

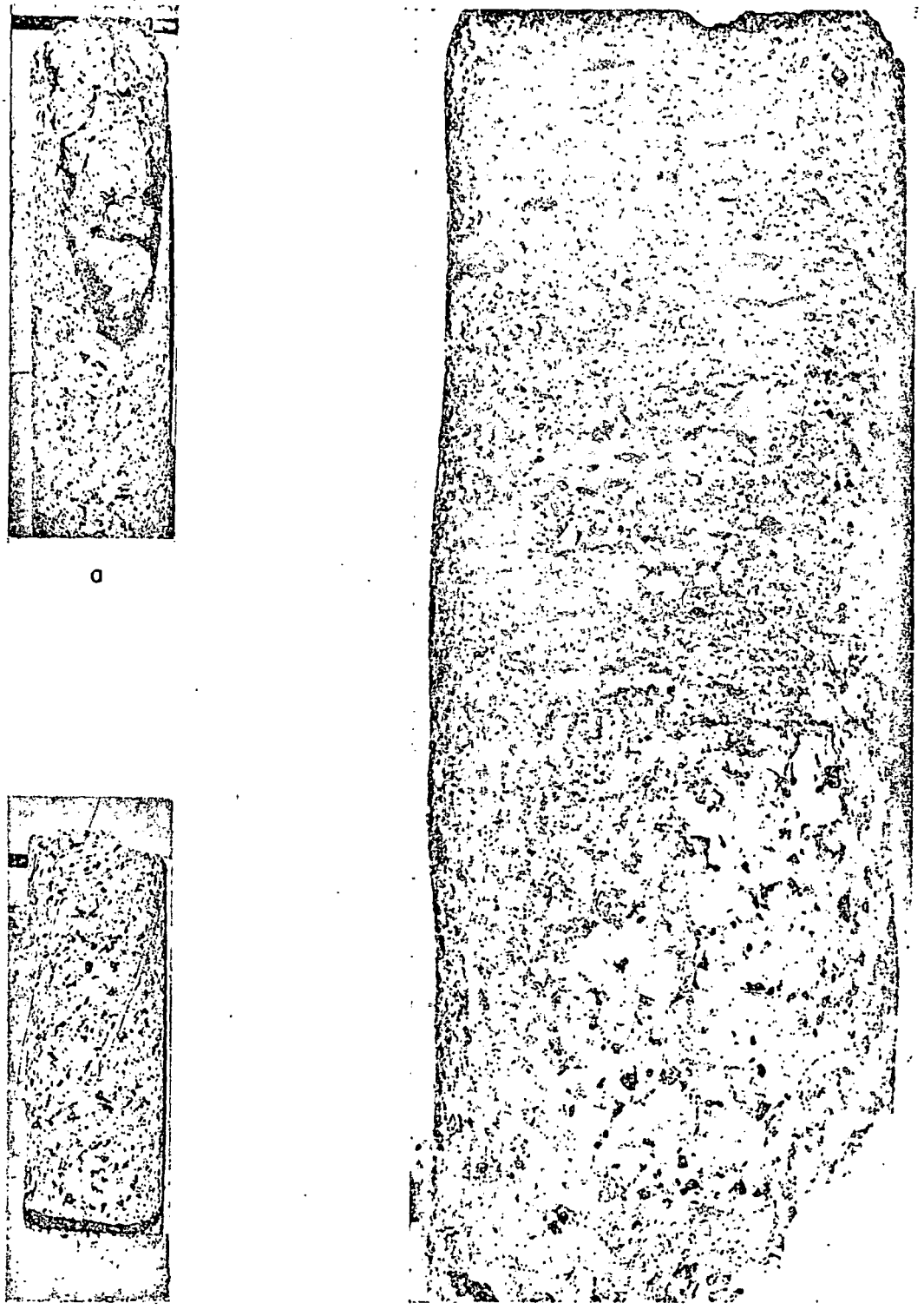

Fig. 7. Sections from hole PS-3 showing glass seams filling fractures (top and bottom left) and contact between granodiorite and cavity debris (right).

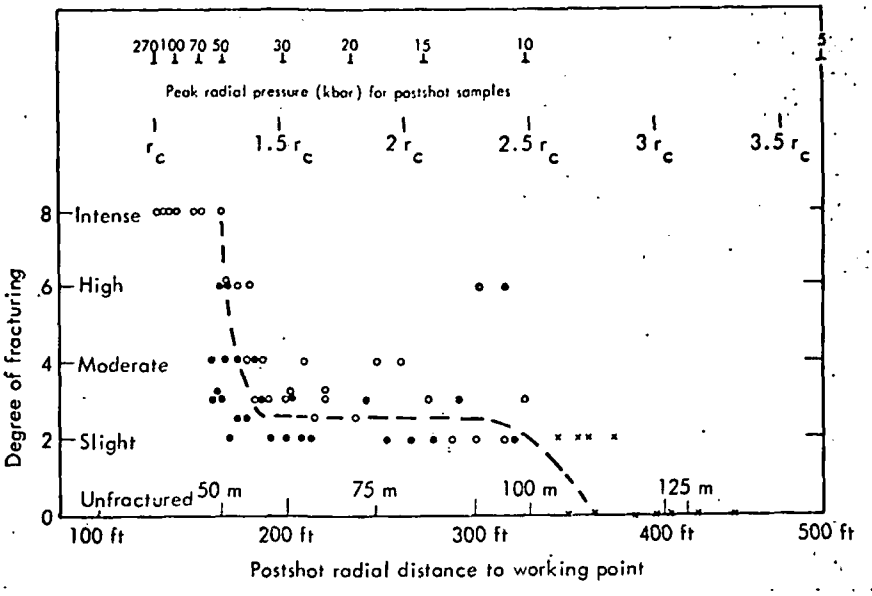

Fig. 8. Degree of microfracturing in the Piledriver postshot cores as a function of postshot radial distance and peak radial pressure. Solid circles, postshot hole 1; crosses, postshot hole 2; open circles, postshot hole 3.

sessed, and the new data are included in Table 2, which summarizes the fracture radii r_f. It was not possible to duplicate the semiquantitative fracturing indices computed by *Short* [1966] for the Hardhat material, but the results of both studies are consistent. When reduced to multiples of the cavity radii (r_f/r_c, Table 2) and associated with peak radial stresses, the limits given in Table 2 for the two events are seen to be closely related. Comparable limits of crushed and fractured zones (boundary between 600- and 60-millidarcy fracture zones) in French Hoggar granite underground tests are 1.4 and 2.8 r_c, respectively [*Delort and Supiot*, 1970].

The limits of extensive and detectable shock-induced microfracturing occur between peak radial stresses of 42–45 and 6–8 kb, respectively. The first stress, 42–45 kb, corresponds to the

TABLE 2. Microfracturing in Piledriver and Hardhat Postshot Cores

	Piledriver			Hardhat		
		r_f/r_c	Peak radial stress, kb		r_f/r_c	Peak radial stress, kb
Limit of intensely and highly fractured rock	51.8 ± 3.0 meters (170 ± 10 feet)	1.3 ± 0.1	45	24.4 ± 3.0 meters (80 ± 10 feet)	1.3 ± 0.2	42
Limit of detectable microfracturing	109.8 ± 6.1 meters (360 ± 20 feet)	2.7 ± 0.2	8	54.9 ± 7.6 meters (180 ± 25 feet)	2.9 ± 0.4	6
Cavity radius, r_c	40.1 meters (131.5 feet)			19.2 meters (63 feet)		
Chimney height, h_c	277.4 meters (910 feet)			85.7 meters (281 feet)		

measured Hugoniot elastic limit [*Cherry and Peterson*, 1970]. The second, 6–8 kb, corresponds to the normal pressure associated with the expected onset of appreciable fracturing under shock loading [*Cherry*, 1970]. It is assumed that shock loading at low pressures approximates a one-dimensional rather than two-dimensional strain model, such as that used to describe conventional triaxial laboratory deformations of rock.

PLASTICITY

In connection with research at sites of meteor impact, several attempts have been made to correlate plastic phenomena in particular rock-forming minerals to specific critical shock pressures [*Chao*, 1968; *Engelhardt and Stöffler*, 1968; *Stöffler*, 1971]. By necessity, such estimates have been based on shock data from laboratory tests and to a lesser extent on results from static deformations. The perfection and small size of the sample in shock tests and the comparatively slow strain rate in triaxial tests mitigate against an exact analogy with behavior in either meteoric impact or nuclear detonation in a large structurally inhomogeneous body of rock. On this account, plastic phenomena, meaning in this context intracrystalline slip and twinning, observed in recovered core, are described in some detail and correlated with measured peak radial shock pressures. These data are subject to errors of two kinds: those related to the pressure measurements themselves and those related to the accuracy of locating the sample within the drill hole. The pressures are taken from the curve of Figure 3 and believed to be accurate to 10%; the probable error in the locations of the samples is <1 meter. A detailed description of the phenomena in individual mineral species follows.

Quartz. Microscopic structures associated with the plasticity of quartz in high-pressure regimes have been extensively studied both in the laboratory and in the field. The literature is too extensive to review in toto, and the papers of *Carter* [1968] and *Engelhardt and Bertsch* [1969] are recommended to the reader for résumés.

Following *Hörz* [1968], the distinction drawn by *Carter* [1968] between deformation lamellas and planar features has not been attempted here. Apart from being technically impossible for all lamellas that can be measured on a universal stage, the significance of the optical phenomena associated with deformation lamellas and planar features is still a matter of conjecture. Furthermore, it has yet to be demonstrated either in the shock laboratory or in the field that recognition of one or the other type permits any profound inferences to be drawn concerning the conditions attending the shock metamorphism of a particular rock. In this context three groups of microstructures have been recognized: (1) widely spaced planar discontinuities parallel to rational planes (cleavage), (2) singular irregular irrational surfaces (fractures), and (3) closely spaced planar or nearly planar structures (lamellas).

Insofar as planar features and/or deformation lamellas mark the onset of plasticity in quartz, the following estimates of critical pressures at ambient temperatures have been made: threshold for 'planar fracture sets' in nuclear shocked rock, 50–75 kb [*Short*, 1966]; 'deformation lamellas' in meteoritic impact sites, 30–100 kb [*Chao*, 1968] (the lower limit is described as 'appearance of a trace amount' [*Chao*, 1968, Figure 1 and p. 222]); and 'planar features' in shock-loading experiments, 100–120 kb [*Hörz*, 1968] and 105–140 kb [*Müller and Défourneaux*, 1968]. The lower limit of the pressure seen by the bulk rock indicated by the present data is 75–78 kb. At this point they are rare, short, and barely detectable with conventional microscopy techniques. At 155 kb, 89% of the quartz contains one or more sets of lamellas; at pressures of >205 kb all grains contain lamellas. At 155, 234, and 263 kb there are 1.6, 2.8, and 3.0 sets per grain, respectively. The maximum number of sets observed in any one grain corresponding to the above three pressures is 5, 7, and 7. On the basis of measurements of approximately 100 lamellas in each sample, the amount of lamellas that form angles of 65°–72° to [0001] is 41%, 53%, and 59%, in order of increasing pressure.

Most of the lamellas in this range appear to be $\{10\bar{1}3\}$, as has been noted by all observers. When a planar $\{10\bar{1}1\}$ rhombohedral parting is also developed, the lamellas can be shown to occur within or close to the $\langle 01.0 \rangle$ zones. However, as a rule, fractures are conchoidal, and true cleavages are rare; as a consequence, indexing is tenuous. Any error in measurement of either the

c axis or the lame
assignment. The fr
its optically biaxia
the lowered birefi
shocked samples m
in any one grain v
positive recognitio
always possible. I
identified as the n
and 11% at 155, 2
The frequencies are
histograms describ
tory-shocked quar
Bertsch's [1969] a
frequencies at the
Clearwater Lake
few instances, {10
identified. Howeve
evidence from me
lamella sets that th
occurring at 56°–6
parallel to $\{10\bar{1}2\}$
surprising since i
200 kb the form be
[*Carter*, 1968]; in ad
conspicuous in ex
shocked quartz, e.

Fig. 9. Phot

c axis or the lamellas greatly affects the zonal assignment. The fractured nature of the quartz, its optically biaxial and strained character, and the lowered birefringence in the more highly shocked samples make meaningful measurements in any one grain very difficult. On this account, positive recognition of other lamellas was not always possible. Form $\{10\bar{1}1\}$ was positively identified as the next most common one (3, 10, and 11% at 155, 234, and 263 kb, respectively). The frequencies are in keeping with *Hörz*'s [1968] histograms describing planar features in laboratory-shocked quartz as well as *Engelhardt and Bertsch*'s [1969] and *Carter*'s [1968] absolute frequencies at the Ries meteorite crater and the Clearwater Lake structure, respectively. In a few instances, $\{10\bar{1}2\}$ lamellas were positively identified. However, there was no compelling evidence from measurement of angles between lamella sets that the 4–9% of lamellas recorded as occurring at 56°–60° to the *c* axis were, in fact, parallel to $\{10\bar{1}2\}$. This finding is somewhat surprising since in shock experiments above 200 kb the form becomes increasingly prominent [*Carter*, 1968]; in addition, the form is recorded as conspicuous in extreme examples of naturally shocked quartz, e.g., type D of *Robertson et al.* [1968] and *Engelhardt and Bertsch* [1969]. Basal and sub-basal (within 10° of $\{0001\}$) lamellas are sparse; they comprise 1, 4, and 6% of the total observed in the 155-, 234-, and 263-kb samples. Assignment of indices to the remainder of the lamellas (~30% in each of the three samples) was attended by ambiguity. In the 155-kb sample there was a lack of adequate crystallographic control; on the other hand, in the 234- and 263-kb samples, intense fracturing and subsequent rotation of fragments allowed only the approximate position of the lamellas within the structure to be described. In all three cases, 90–93% of the observed lamellas are at angles of >45° to the *c* axis (namely, pole to lamellas [0001] <54°). The only noteworthy aspect of any of the unidentified group was a 12% concentration at 45° ± 2° to [0001] in the 263-kb sample. Most of these sets are cozonal with *c* $\{0001\}$ and *m* $\{10\bar{1}0\}$ and, therefore, are of the form $\{10\bar{1}l\}$.

Well-formed rhombohedral and prismatic cleavages are better developed in nuclear shocked rock than in tectonically deformed quartz but are rare as compared with those formed in laboratory shock experiments (Figure 9) [*Hörz*, 1968; *Müller and Défourneaux*, 1968].

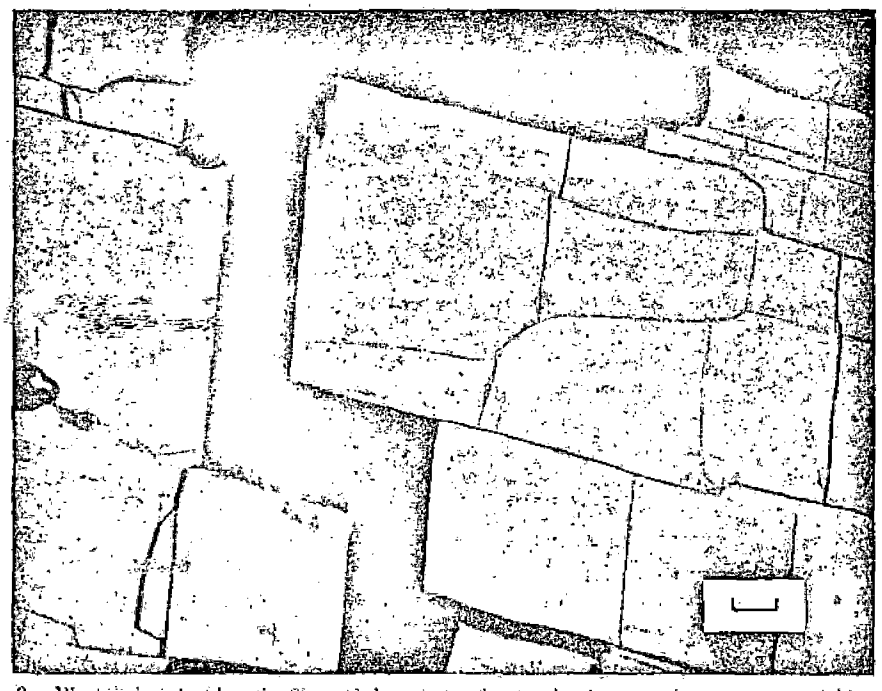

Fig. 9. Photomicrograph of recovered quartz from shock experiment at ~10-kb peak pressure. The scale shown is 1 mm.

From all indications, under shock conditions they are release or tensile phenomena and are best developed on release from low to moderate pressures, i.e., below the Hugoniot elastic limit. Cleavage development has been described from the West Hawk Lake crater, Quebec [*Robertson et al.*, 1968, Figure 4], the Meteor crater, Arizona [*Bunch*, 1968, Figure 2], the Flynn Creek structure, Tennessee [*Short and Bunch*, 1968, Figure 4], and the Ries crater, Germany [*Engelhardt and Bertsch*, 1969].

A weak preferred orientation of lamellas exists in each of the three samples. However, it appears to be related to the pre-existing preferred crystallographic orientation of the grains themselves rather than to a preferential development of certain lamellas in a homogeneous stress field. Occurrence of lamellas at grain boundaries and near fractures suggests that local stress concentrations have been important. A strong preferred orientation is unlikely in view of the rarefaction of the shock wave(s) at discontinuities, which gives rise to a heterogeneous stress history for any rock unit.

Hornblende. The main evidence of plasticity in hornblende is development of polysynthetic twins parallel to $(\bar{1}01)$ or (001), depending on the choice of cell axes. The twin-glide system, as established by *Rooney et al.* [1970], *Buck and Paulitsch* [1969], and *Buck* [1970], is $K_1 = (\bar{1}01)$, $N_1 = [101]$, $K_2 = (100)$, and $N_2 = [001]$ for the $C2/m$ setting, and $K_1 = (001)$, $N_1 = [100]$, $K_2 = (100)$, and $N_2 = [001]$ for the $I2/m$ setting. The twinning is analogous to a twin-glide system recognized for the monoclinic pyroxenes, $C2/c$ [*Griggs et al*, 1960; *Raleigh and Talbot*, 1967]; $K_1 = (001)$, $N_1 = [100]$, $K_2 = (100)$, and $N_2 = [001]$, in keeping with the custom of using the body-centered cell ($I2/m$) in amphiboles to illustrate morphological and structural similarities between the two groups of chain silicates.

Onset of twinning in the group of shocked rocks is potentially difficult to recognize, since, at low stresses, lamellas are sparse and thin and in many respects resemble $(\bar{1}01)$ exsolution lamellas [e.g., *Jaffe et al.*, 1968; *Ross et al.*, 1968]. The rarity of any lamellas in the unshocked hornblende and the absence of (100) exsolution lamellas in shocked hornblende that commonly accompany $(\bar{1}01)$ exsolution lamellas argue for a deformational origin for all lamellas observed. Occasional simple (100) twins represent the only unusual feature of the undeformed hornblende. Twin lamellas were first detected in hornblende that had seen a 24- to 40-kb peak radial stress, and the maximum shear stress, $(\sigma_1 - \sigma_3)/2$, on any plane is 4 kb. This stress is considerably lower than the estimated 200-kb pressure associated with development of planar features in amphiboles [*Chao*, 1968; *Engelhardt and Stöffler*, 1968] and higher than the 10-kb axial pressure, $(\sigma_1 - \sigma_3)/2 = 1.3$, associated with the onset of twinning at 20°C and a strain rate of 10^{-4} sec^{-1} [*Buck*, 1970]. At higher stress levels, optics and cleavages within the lamellas can be readily measured. 'Rotation' of the {110} cleavage within the lamellas is definitive for twinning since exsolution intergrowths result in a near coincidence of cleavages (Figure 10).

Decomposition of hornblende can be noticed in rock that has been shocked to 140–150 kb. It is probably a thermal effect, reflecting not so much the shock temperature as the proximity to steam and other gases emanating along fractures from the expanding cavity.

Sphene. Polysynthetic twinning in shocked sphene has previously been described from the access drifts at the Piledriver site [*Borg*, 1970*b*]. The geometry of mechanical twinning in sphene is described by the following elements: $K_1 \simeq \{221\}$, $N_1 = \langle 110 \rangle$, $K_2 = \{\bar{1}31\}$, and $N_2 =$ irrational line. The thinnest twin lamellas are recognized by a 'play' of second- and third-order interference colors when viewed obliquely to the composition plane. However, the paucity of sphene crystals in the granodiorite, $<1\%$, poses a sampling problem in ascertaining the point at which stresses are high enough to produce twinning in a few properly oriented grains. A previous estimate based on rock collected in the drift walls was 5–8 kb and a stress difference of $\sim$1 kb. In view of the free surfaces that existed at the time of shock propagation, i.e., the drift walls, and of the results of laboratory deformations of the mineral [*Borg and Heard*, 1972], these values are considered to be too low. Core data indicate that 14–18 kb (from stress gages) and 8–9 kb (from SOC calculations) are more likely values for the peak stress and the stress differential, respectively, under field shock conditions. The 'weakly developed' planar features associated with very high shock pressures (>300 kb) by *Chao* [1968, p. 239] possibly owe their origin to yet another slip mechanism.

Fig. 10. Shock twinning on {$\bar{1}$01} in hornblende (PS-3 core, 67 meters (220 feet) SHD). The scale shown is 0.1 mm.

At 270 kb, sphene is highly twinned and fractured and appears metallic in reflected light, although decomposition to ilmenite recorded by *El Goresy* [1968] was not detected.

Biotite. Kinking in biotite concomitant with bend gliding on (001) has been the subject of numerous investigations both in the laboratory and in the field. *Hörz and Ahrens* [1969] and *Hörz* [1969] in laboratory shock experiments set the lower limit for their formation at >37.5 and ~10 kb for propagation normal and parallel to (001), respectively. *Cummings* [1965, 1968] has investigated biotites from nuclear shocked granodiorite from the Hardhat event and indicates that some kinking occurs as low as 10-kb peak radial stress. It appears, however, that, in using calculated peak pressures as a function of preshot distance from the nuclear explosion, Cummings neglected to consider the 1- to 4-meter displacements seen by the core samples studied. Thus the specimens examined from Hardhat cores have seen pressures higher by 3–7 kb than those suggested by their postshot radial distances from the shot point. Displacements and ΔP given are based on postshot radial distances of 24–43 meters for core samples studied by *Cummings* [1968, Figure 6]. *Short* [1966] estimated the lower limit for kinking at the Hardhat site at 25–30 kb. The data presented here suggest that incipient kinking is first recognizable in rock that has seen a 15- to 16-kb peak radial stress. Above 75 kb all biotite grains contain kinks. Figure 11 shows the progressive development of kinking as a function of peak radial stress. In all cases the *c* axis of the grain is nearly normal to the photograph. The examples represent the most highly kinked biotites at that orientation in the sample. At 205 kb the biotites are largely decomposed, magnetic, and opaque. Magnetite, forsterite, and fluor-phlogopite (?) are detectable in Debyé-Scherrer X-ray photographs of single grains. Comparable phases are not recognizable in biotite shocked to 313 kb in the laboratory (sample by courtesy of T. Ahrens), nor are they recognized below an estimated 300 kb at sites of meteor impacts [*Chao*, 1968; *Engelhardt and Stöffler*, 1968]. Decomposition observed in the Piledriver biotite is a thermal effect connected primarily with the heat of the explosion rather than a transient temperature associated with the passage of the shock wave.

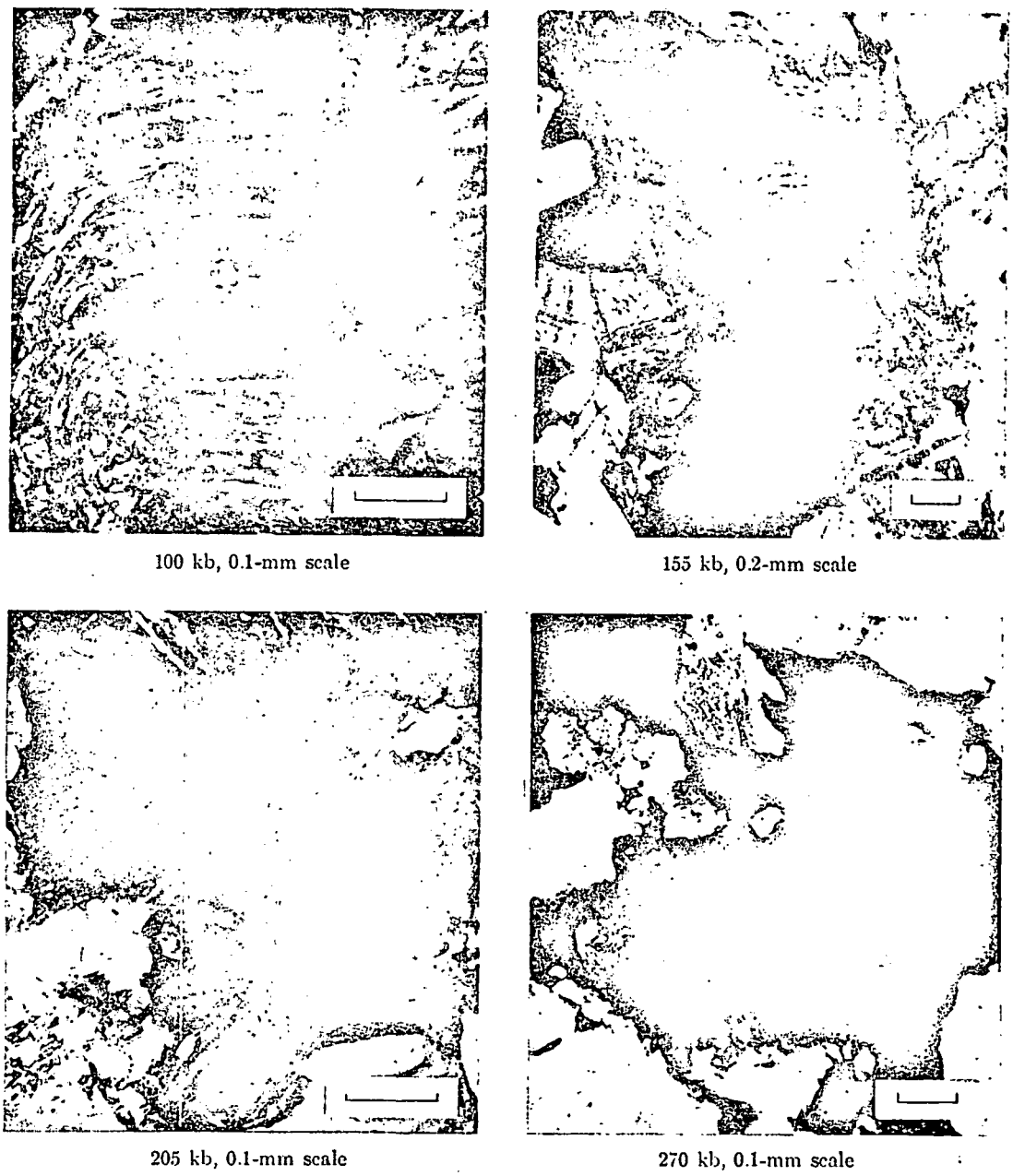

100 kb, 0.1-mm scale

155 kb, 0.2-mm scale

205 kb, 0.1-mm scale

270 kb, 0.1-mm scale

Fig. 11. Progressive development of kinking with increased peak radial stress in biotite.

There is only a slight preferential development of kink bands in grains of particular crystallographic orientations within the granodiorite. However, kink bands within grains at a single thin section do show a moderate preferred orientation. Presumably, the bands tend to be normal to the peak radial stress, although this orientation cannot be tested except in uniquely oriented core. *Cummings* [1965] came to similar conclusions. In regimes above 100 kb, kinking becomes extreme, and the generalizations made above are tenuous. Close-in the stress-time history is particularly complex. The rock has been repeatedly deformed not only by a radiating

18 kb, 0.1-mm scale

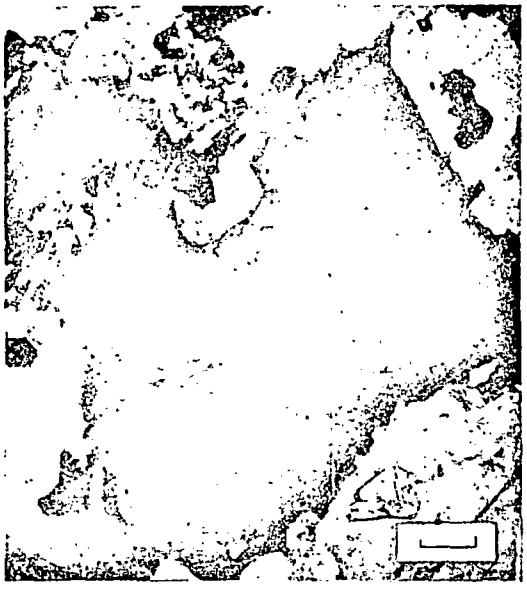

30 kb, 0.2-mm scale

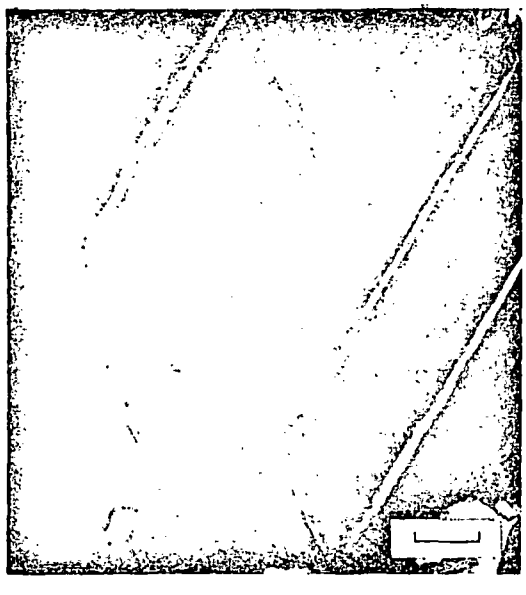

40 kb, 0.1-mm scale

51 kb, 0.2-mm scale

Fig. 11. (continued)

shock pulse but also by strong rarefacted shock waves reflected from pre-existing discontinuities. Locally concentrated and oriented stresses related to the brittle failure of the strong components further complicate the stress picture.

Feldspar. Response of orthoclase and albite-oligoclase to pressures of $\lesssim$270 kb is chiefly by fracture and destruction of the structure on a submicroscopic scale. No shock-induced twinning or planar lamellar structure occurs in either feldspar. As was noted by *Short* [1970], failure of orthoclase is associated with a characteristic fracture network or closely spaced irregular 'tears.' Birefringence of both feldspars is grossly

lowered to 0.003 at 270 kb; however, neither glass, sandine, nor any dense high-pressure phase was detected.

From equation-of-state data on quartz and plagioclase *Stöffler* [1967] deduced that such glasses and high-pressure modifications of the feldspars form at pressures in excess of 250 kb at the Ries meteor crater in Bavaria. With an uncertainty of 10% in both Stöffler's estimate and the shock pressures measured at the Piledriver site, the observations are consistent. On the other hand, plasticity recorded by *Stöffler* [1967] in shocked plagioclase in the 100- to 250-kb range has no counterpart at the Piledriver site.

In view of the intractable nature of acidic plagioclases in static laboratory tests, as contrasted to those whose anorthite content exceeds 30% [*Borg and Heard*, 1970], it is likely that the observed differences in behavior (between laboratory tests cited by Stöffler and the present test) are related to the basic chemical and structural differences of the plagioclases studied. All the nonisotropic planar features in plagioclase described by *Stöffler* [1967] as well as *Robertson et al.* [1968] and *Dworak* [1969] from Canadian craters occur in plagioclase with an anorthite content of >30%, whereas the present observations are restricted to albites and peristerites. Nonetheless, debris recovered from within both the Hardhat and the Piledriver cavity does contain disordered feldspar with localized lamellar and band development accompanied by patches of glass. The pressures associated with these phenomena cannot be accurately specified, and there is a real possibility that they are products of high temperatures associated with the explosion itself and of only moderate stresses rather than of high temperatures associated with high shock pressures.

RÉSUMÉ AND DISCUSSION

The first part of this paper was a review of the parts of the Piledriver experiment that are relevant to the study of shock deformation of granodiorite and its mineral constituents. Satisfactory operation of a large number of stress gages allowed correlation between shock effects and specific shock pressures. The combined error in the measured stress and the location of the core samples at the shot time results in an estimated error of 10–15% in pressure assigned to any sample (C. T. Vincent and J. Rempel, personal communication, 1968). The highest reliable measurement of peak radial pressure measured was 270 kb at a distance of 14.6 meters from the shot point. The remainder of the stress data (Figure 3) suggest that this pressure may be too low by ~25 kb and that a pressure of 270 kb is appropriate to rock located <1 meter farther from the shot point, i.e., rock constituting the present cavity wall. Inasmuch as recovered debris within the cavity has not been considered here, the maximum pressure seen by any core sample is close to 270 kb.

Dissociation of hydrous minerals (e.g., biotite) in the surviving granodiorite indicates that temperatures have reached as high as 600°–700°C locally [*Wones and Eugster*, 1965]. Localization of high-temperature effects in areas adjacent to fractures suggests that mobile hot gases have primarily been responsible. In situ melting of the granodiorite was not recognized, although glasses fill in fractures of recovered core <56 meters from the shot point.

Mechanical phenomena, e.g., slip and twinning, noted in the various mineral constituents have been correlated with particular shock pressures. The stress differential $(\sigma_1 - \sigma_3)$ is more difficult to specify. Calculations of the propagating stress field around an explosive source such as the SOC code indicate that in granodiorite below the Hugoniot elastic limit (~45 kb) the average differential is in the 1–10 kb range [*Cherry and Rapp*, 1968]. However, it is likely that differences in the compressibility of adjacent mineral phases can result in local differentials much greater than these average values. Above the Hugoniot elastic limit, stress differentials can be instantaneously very large, but their magnitudes have not been measured or calculated to date.

Where results of laboratory shock experiments can be compared with results of the present study, e.g., for quartz and biotite, in general, minimum peak shock pressures for the development of lamellas and kinks are lower for the field-shocked samples than for the laboratory-shocked single crystals. The differences may be due to local stress concentrations and locally high stress differentials associated with deformations of heterogeneous materials. They may also reflect the generally lower strain rates in the field test described earlier in this text. *Brace*

and Jones [1971] have shown in room temperature experiments on granite at <10-kb confining pressure that brittle failure is not influenced by strain rates over the 10^{0}–10^{-6} sec^{-1} interval. Nonetheless, it seems likely that the usual strain rate dependence on yielding will hold at higher pressures. Specifically, lower strain rates result in lower yield stresses and lower peak and mean pressures associated with onset of a particular failure mechanism.

Another possible explanation for the differences in the phenomenology observed at given shock pressures in single-crystal shock tests and field shock experiments may lie in a difference in Hugoniot temperatures. The value of T_H is sensitive to void space (pore, fracture, and cleavage porosity), and it is probably locally higher for nuclear explosions and meteoritic impacts than would be indicated by calculations based on equation-of-state measurements of small laboratory samples approaching theoretical density. The effect of increased temperature is to lower the critical resolved shear stress required for the initiation of slip and twinning in mineral components. Thus, owing to higher Hugoniot temperatures, higher local stresses or stress differentials, lower strain rates, or all three factors, it might be anticipated that the initiation of slip and twinning would be associated with lower peak and mean shock pressures for large bodies of shocked rock than for small mineral samples.

APPENDIX: SUMMARY OF PRINCIPAL DATA ON PILEDRIVER EVENT

Shot date: June 2, 1966.

Yield: 61 ± 10 kT, based on determination of the Los Alamos Scientific Laboratory on injected glass encountered in re-entry tunnel 91 meters (300 feet) from the shot point, 14 months after the shot [*Rabb*, 1968; *Boardman*, 1967].

Shot depth: 462.8 meters (1518 feet) below the surface (1089 meters (3572 feet) above msl).

Cavity radius r_c: 40.1 meters (131.5 feet), measured in the drill hole that intersected the cavity wall at a point 10.4 meters (34 feet) below the shot level [*Sterrett*, 1969] (the cavity is a nearly spherical void space formed within seconds of the explosion by the melting and the vaporization of rock and by the thermal expansion of gaseous products).

Chimney height: 277.4 meters (910 feet) above the shot level (the chimney is a vertical column of rubble formed at the collapse of the cavity upon cooling; the void space between the rock debris within the chimney and the cavity is equal to the cavity volume before collapse).

Chimney half-width: 48.8 meters (160 feet) measured in the re-entry tunnel at a point 31.6 meters (103.5 feet) above the shot level.

Chimney volume: 19.0×10^{5} m^3 (6.69×10^{7} ft^3) or $>29.4\ r_c^3$.

Pressure of overburden at shot point: 121 bars (1721 psi), calculated on the basis of the average density of 2.66 g/cm^3.

Apical void: 0.61 meters (2 feet) high (the apical void is the empty space between the top of the chimney fill material and the chimney ceiling [*Boardman*, 1967]).

Time of cavity collapse: within 14 sec after the shot [*Rabb*, 1968].

Maximum vertical extent of increased air permeability: 314.6 ± 11.0 meters (1032 ± 36 feet) above the shot level [*Boardman*, 1967].

Acknowledgments. Discussions with H. Heard, T. Ahrens, and T. Butkovich on various aspects of shock metamorphism were very profitable. D. Larsen contributed substantially to the development of equations used to calculate Hugoniot temperatures. Comments on the text by D. Stöffler and F. Hörz were appreciated.

This work was performed under the auspices of the U.S. Atomic Energy Commission.

UDC 661.728.84:546.57

The sorption of silver from fixing solutions by viscose

I A Korneeva, L L Panina, O P Laletina and K A Malyshevskaya (Siberian Technological Institute)

It is known that during the processing of photographic materials about 30% of the silver remains in the emulsion layer in the form of an image, while the remainder passes into the fixing solution[1]). The recovery of silver from spent fixing solutions is one of the important national-economic tasks. Of interest for this purpose is the use of viscose wastes, i.e., the alkaline solution of cellulose xanthate which is an intermediate product in the production of chemical fibres.

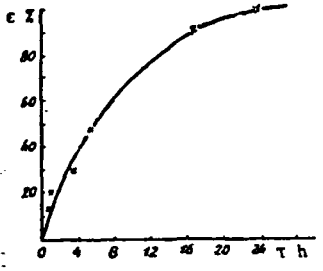

The dependence of the degree of extraction of silver on the length of sorption. Optimum conditions.

For the recovery of silver from spent fixing solutions with a concentration of 2.84 g/l we used the viscose wastes from the Krasnoyarsk chemical fibre plant. Sorption was realised under static conditions. Investigation of the sorption kinetics (fig) showed that full recovery of the silver from the solution is achieved in 24h at room temperature, and the degree of recovery of the silver increases with increase in the amount of viscose added to the solution. A volume ratio of 1:10 between the viscose and fixing solution is optimum.

Change in the degree of esterification of sodium cellulose xanthate from 0.26 to 0.70 does not affect the degree of extraction of silver from the solution. This is explained by the mechanism of sorption. Silver is extracted from the fixing solution by cellulose xanthate with the formation of the stable insoluble silver xanthate and also by the sulphur-containing side products present in the viscose with the formation of insoluble silver sulphides[2]). During the maturing of the viscose the degree of esterification of sodium cellulose xanthate decreases, but on the other hand the content of the side products increases. As a result the degree of extraction of silver remains unchanged.

Experiments on the use of viscoses with various maturities (from 6.3 to 42ml in 1N ammonium chloride) for the sorption of silver showed that the silver is extracted from the solution both by "young" and by "old" viscoses. The maturity of the viscose only affects the degree of dispersion of the precipitate formed during precipitation of the silver. The "older" the viscose, the more disperse is the precipitate obtained on precipitation, i.e., in this case sorption on account of the low-molecular side products which accumulate in the viscose during its maturing predominates.

The spent fixing solutions have a neutral reaction. To investigate the effect of the acidity of the solution on the sorption of the silver the solutions were acidified or made alkaline. Here it was established that difficulty filtered jelly-like precipitates are formed during extraction of the silver from an alkaline fixing solution with pH = 9. If the fixing solution is acidified, the degree of extraction of the silver decreases Change in the pH value from 7 to 6 leads to a decrease in the degree of extraction from 100 to 82.7%. The deterioration of the sorption of silver is explained by the fact that partial decomposition of both the sodium cellulose xanthate and the side products contained in the viscose occurs under the influence of the acid, and this leads to a decrease in the amount of silver-sorbing materials in the viscose. It is mor expedient to extract the silver from the fixing solution witho changing its acidity.

The maximum content of silver in the precipitate during sorption under the optimum conditions (silver concentration 2.64g/l, pH = 7, volume ratio of viscose and fixing solution 1:10, length of process 24h) amounts to 28.4mg for 1ml of viscose or 334mg for 1g of α-cellulose contained in the viscose.

Conclusion

Viscose production wastes with any degree of maturity and with any degree of esterification can be used for the recovery of silver from spent fixing solutions.

References

1) A V Fomin: General course of photography. Legkaya Industriya, Moscow 1974.
2) L I Gratsershtein et alia: Tsvetnye Metally 1975, 25, (1).

UDC 541.135.6:546.94

Alloy formation during the deposition of lithium on a zinc cathode

A I Demidov and N V Temnogorova (Leningrad Polytechnical Institute - Department of Physical Chemistry)

Investigations into the deposition of lithium on various cathodes by electrolysis of molten salts are well known[1])[2]). The present work gives the results from an investigation into the alloy formation process during the deposition of lithium at a molten zinc cathode from the LiCl-KCl eutectic mixture at 450 and 550°C. We used zinc of analytical grade and salts of chemically pure grade. The apparatus, the cell, and the experimental procedure are similar to those described previously[2]).

The polarisation curves for the deposition of lithium at the molten zinc cathode at 450 and 550°C are shown in the figure. At current densities up to $1 \cdot 10^{-2}$ A/cm² the potential of the cathode acquires values of 1.5 (450°C) and 1.56V (550°C) referred to a lithium reference electrode, and this corresponds to the discharge of zinc ions which are present in the electrolyte as a result of its corrosion. At current densities between $1 \cdot 10^{-2}$ and $3 \cdot 10^{-2}$ A/cm² the cathode potential remains unchanged and equal to 1.28 (450°C) and 1.30V (550°C) On the basis of the thermodynamic characteristics of molten alloys in the Li-Zn system[3]) we conclude that depolarisation of more than 1V can hardly be due to an alloy formation process during the deposition of lithium at a molten zinc cathode It is probably due to deposition of lithium at zinc oxide present on the surface of the molten cathode. To confirm this suggestion we undertook a thermodynamic calculation for the reaction of lithium with zinc oxide:

$$\varphi_{expt} = \varphi^{o} + \frac{RT}{nF} \ln \Pi$$

Poehls, K. A. 1974. Seismic refraction on the Mid-Atlantic Ridge at 37°N. *J. Geophys. Res.* 79:3370–73
Raitt, R. W. 1963. See Hill 1963, pp. 85–102 Wiley
Raitt, R. W., Shor, G. G. Jr., Francis, T. J. G., Morris, G. B. 1969. Anisotropy of the Pacific upper mantle. *J. Geophys. Res.* 74:3095–109
Raitt, R. W., Shor, G. G. Jr., Morris, G. B., Kirk, H. K. 1971. Mantle anisotropy in the Pacific Ocean. *Tectonophysics* 12: 173–86
Reid, I., Orcutt, J. A., Prothero, W. A. 1977. Seismic evidence for a narrow intrusive zone of partial melting underlying the East Pacific Rise at 21°N. *Geol. Soc. Am. Bull.* 88:678–82
Rosendahl, B. R., Raitt, R. W., Dorman, L. M., Bibee, L. D. 1976. Evolution of ocean crust. I. A physical model of the East Pacific Rise Crest derived from seismic refraction data. *J. Geophys. Res.* 81: 5294–304
Schreiber, E., Fox, P. J. 1977. Density and p-wave velocity of rocks from the FAMOUS region and their implication to the structure of the oceanic crust. *Geol. Soc. Am. Bull.* 88:600–8
Shor, G. G. Jr. 1963. See Hill 1963, pp. 20–38
Shor, G. G. Jr., Merard, H. W., Raitt, R. W. 1971. Structure of the Pacific Basin. In *The Sea*, ed. M. N. Hill, Vol. 4. New York: Wiley
Shor, G. G. Jr., Raitt, R. W., Henry, M., Bently, L. R., Sutton, G. H. 1973. Anisotropy and crustal structure of the Cocos plate. *Geofis. Int.* 13:337–62
Snydsman, W. E., Lewis, B. T. R., McClain, J. 1975. Upper mantle velocities on the northern Cocos plate. *Earth Planet. Sci. Lett.* 28:46–50
Sutton, G. H., Maynard, G. L., Hussong, D. M. 1971. Widespread occurrence of a high velocity basal layer in the Pacific crust found with repetitive sources and sonobuoys. *Geophys. Monogr. Am. Geophy. Union* 14:193–207
Vine, F. J., Matthews, D. H. 1963. Magnetic anomalies over oceanic ridges. *Nature* 199:947–49
Wenner, D. B., Taylor, H. P. Jr., 1973. Oxygen and hydrogen isotopes studies of the serpentinization of ultramafic rocks in oceanic environments and continental ophiolite complexes. *Am. J. Sci.* 273:207–39
Whitmarsh, R. B. 1973. Median valley refraction line, Mid-Atlantic Ridge at 37°N. *Nature* 246:297–99
Whitmarsh, R. B. 1975. Axial intrusion zone beneath the Median Valley of the Mid-Atlantic Ridge at 37°N detected by explosion seismology. *Geophys. J. R. Astron. Soc.* 42:189–215
Williams, D. L., Von Herzen, R. P., Sclater, J. G., Anderson, R. N. 1974. The Galapagos spreading center: lithosphere cooling and hydrothermal circulation. *Geophys. J. R. Astron. Soc.* 38:587–608
Woollard, G. P. 1975. The interrelationships of crustal and upper mantle parameter values in the Pacific. *Rev. Geophys. Space Phys.* 13:87–137
Wyllie, P. J. 1971. *The Dynamic Earth: Textbook in Geosciences.* New York: Wiley. 416 pp.

Ann. Rev. Earth Planet. Sci. 1978. 6:405–36

STATE OF STRESS IN THE EARTH'S CRUST

A. McGarr[1]
U.S. Geological Survey, Office of Earthquake Studies, Menlo Park, California 94025

N. C. Gay
Bernard Price Institute of Geophysical Research, University of the Witwatersrand, Johannesburg, South Africa

INTRODUCTION

Measurements of the stress field within the crust can provide perhaps the most useful information concerning the forces responsible for various tectonic processes, such as earthquakes. Advances in knowledge of the state of stress at mid-crustal depths are essential if further progress is to be made toward solving a broad class of problems in geodynamics.

Most stress measurements have been, and will continue to be, motivated by engineering needs rather than the needs of geologists engaged in fundamental research. Knowledge of the state of stress is critical to the design of underground excavations for mining and for nuclear waste disposal (e.g. Jaeger & Cook 1969, pp. 435–64). The massive hydraulic fracturing of formations in oil and gas fields to stimulate production is another application for which knowledge of the stress field at depth is very important and, in fact, many of the deeper stress determinations have been by-products of these "hydrofrac" operations (e.g. Howard & Fast 1970). A recent and exciting application of hydraulic fracturing is the Hot-Dry-Rock Geothermal Energy Program (Aamodt 1977). Heat is extracted from the rock by circulating fluid down a pipe into hot rock and then up through a second pipe. A large fracture connecting the two pipes serves as the heat exchanger. Knowing the state of stress is critical in the solution to the problem of creating and maintaining such a crack. There is little argument about the applicability of information on the state of stress to these and many other engineering problems.

The application of stress measurements to the solution of problems in tectonics is not so straightforward as in engineering design. Whereas the engineer is concerned with the stress field affecting the rock, the geologist attempts to deduce the processes that might have caused the stresses. Before the measured stress field can be related

[1] On leave from the Bernard Price Institute of Geophysical Research, University of the Witwatersrand, Johannesburg, South Africa

0084-6597/78/0515-0405$01.00

to tectonic processes it must be correctly interpreted and analyzed, because the total field is influenced by many events in the geologic history of the rock as well as the contemporary tectonic and gravitational forces. Residual stresses are imposed on a rock according to its history of processes such as burial, lithification, denudation, heating, cooling, and past tectonic events. These *residual* stresses persist to some extent after the rock is freed of boundary loads (e.g. Friedman 1972), and their existence complicates the analysis of stress observations considerably.

In spite of these difficulties stress measurements are assuming a steadily increasing role in the solution of geodynamics problems such as the prediction and/or control of earthquakes (e.g. Raleigh, Healy & Bredehoeft 1976), the origin of forces driving plate tectonics (e.g. Sykes & Sbar 1973), and the origin of the forces responsible for regional deformation (e.g. the Rhinegraben in Germany, Greiner & Illies 1977). Almost all of the geodynamics studies to date have involved the analysis of stress directions; stress magnitudes have only been used in a few studies (e.g. Raleigh, Healy & Bredehoeft 1972). This review summarizes all of the data known to us about the *contemporary* state of stress in North America, Southern Africa, central Europe, Australia, and Iceland. We have elected not to discuss indicators of "paleo-stress" such as observations of deformation lamellae, stylolites, grain size, etc, (e.g. Carter & Raleigh 1969, Friedman & Heard 1974).

Because stress measurements are becoming increasingly important in tectonic analyses it is important to identify the significant gaps in our knowledge of the stress field and then to decide on the types of measurements that will contribute the most to our understanding of geodynamic processes. One notable gap in our understanding involves the magnitude of the stresses driving the movement on tectonic faults such as the San Andreas fault in California. Are the shear stresses of the order of 1 or 100 MPa (megapascals)? At present, no one is in a position to answer this question convincingly.

Several review articles have been published recently that summarize many of the stress observations and draw broad conclusions from the data. Ranalli & Chandler (1975) reviewed measurements made all over the world and emphasize observations made using strain relief techniques: Haimson (1977) summarized stresses measured using the hydraulic fracturing technique within the United States. Hast (1969, 1973) reviewed stress measurements throughout much of the world using his stressmeter (Hast 1958). As we shall show, the strain relief methods and the hydrofrac technique have different advantages and drawbacks, so the two sets of observations complement each other. Our primary intent here is to present each type of observation to its maximum advantage and to avoid presenting the least certain components of each data set. We decided not to present comprehensive tables of observations because a monograph is currently in preparation that is intended to be a compilation of these data (K. Hadley, in preparation; Riecker 1977).

Most of the stress magnitudes quoted in this paper are in units of megapascals (MPa). For comparison with other stress units commonly used in the literature $1\,\text{MPa} = 10\,\text{bars} = 145\,\text{psi} = 10.2\,\text{kgf cm}^{-2}$. The Système International (SI) unit of stress is N m^{-2} (Pascal), but this unit is so small that it must be multiplied by 10^6 to be of the order of stresses commonly observed in the crust.

The stress field at a point can be represented as three principal stresses (e.g. Jaeger & Cook 1969, p. 20), which we denote as S_1, S_2, and S_3 for the maximum, intermediate, and minimum stresses, respectively. Because stresses measured in the crust generally are compressive rather than tensile, compressive stresses are taken as positive here. Often one of the principal stresses is oriented in the vertical, or at least a near-vertical, direction. We represent this stress as S_v and the two horizontal principal stresses as $S_{H\min}$ and $S_{H\max}$.

STRESS MEASURING TECHNIQUES

There exist a number of references (e.g. Leeman 1964, Fairhurst 1968, Jaeger & Cook 1969, pp. 363–73) that review the available techniques for measuring in situ stress in rocks. Here we summarize some of these techniques and compare their advantages and disadvantages.

Stress Relief Methods

These methods involve measuring the change in strain that occurs after relieving the ambient stress acting on the rock. The stress relief is achieved by an overcoring or trepanning process. Normally a device capable of monitoring deformation is either inserted into a borehole or attached to a prepared surface. The deformation associated with the stress relief is measured and then can be related to the ambient stress field.

BOREHOLE DEFORMATION CELLS A borehole deformation cell measures changes in the dimensions of one or more diameters of a borehole. Ideally it should be able to measure changes in diameter as small as 0.025 mm. The United States Bureau of Mines (U.S.B.M.) deformation cell (Hooker, Aggson & Bickel 1974) contains three beryllium-copper cantilevers that push with a negligible load against the interior of the borehole. Deflections of the cantilevers during borehole deformation, as a result of overcoring, can be used to calculate the principal stresses acting in a plane perpendicular to the axis of the borehole. Measurements have to be made in three nonparallel boreholes to determine the complete stress tensor.

BOREHOLE STRAIN GAUGE CELLS In these cells, one or more strain rosettes are bonded directly to the surface of the borehole. The most commonly used cell of this type is the C.S.I.R. (Council for Scientific and Industrial Research) "doorstopper" cell (Leeman 1969) consisting of a single-strain rosette that is stuck onto the flat-end surface of a borehole and then overcored. The four gauges making up the rosette record the resultant changes in diameter of the borehole end in various directions. With this cell, it is necessary to make several measurements along three nonparallel boreholes to obtain the complete stress-relief field, which is, in turn, related to the ambient stress field by empirically determined stress-concentration factors (e.g. Crouch 1969, Coates & Yu 1970).

The C.S.I.R. triaxial strain cell (Leeman & Hayes 1966) consists of three four-gauge strain rosettes that are glued to the wall of the borehole at known orientations and

positions. On overcoring, the rosettes record enough changes in the components of strain for the entire stress relief to be calculated at the point of measurement.

DIRECT STRAIN-GAUGE TECHNIQUE This method, used to measure the horizontal components of the stress field at a free surface, consists of simply overcoring foil resistance strain gauges bonded directly to a prepared rock-surface (Swolfs, Handin & Pratt 1974, Engelder & Sbar 1976).

BOREHOLE INCLUSION STRESS METERS Inclusion stressmeters are usually stiff devices with elastic moduli significantly greater than those of rock so that they can measure stresses directly rather than deformations (Abel & Lee 1973, Hast 1958). The instrument used by Hast (1958) consists of a spool of a magnetostrictive nickel alloy around which a solenoid of permalloy is wound. The spool is placed diametrically across the borehole and prestressed against the walls. During overcoring the stress is relieved, resulting in a drop of potential across the solenoid that can be correlated with the change in stress. Four measurements with different orientations are required to calculate the stresses normal and parallel to the borehole, and measurements in two nonparallel, nonperpendicular holes are needed for the determination of the complete state of stress.

The photoelastic stressmeter (Roberts et al 1964) or strain gauge (Hawkes & Moxon 1965) is an inclusion stressmeter that is not rigid but can be used to measure stress directly. The stressmeter consists of a solid cylinder of glass that is preloaded diametrically in a borehole. On overcoring, the change in load in the cylinder is monitored by measuring changes in the photoelastic fringe pattern. Measurements must be made in three nonparallel boreholes for a complete determination of the stress tensor.

DISCUSSION The most serious drawback of strain-relief measurements is that they are operationally limited to distances of 30 to 50 m from a free surface. Furthermore, to obtain reliable results that are not unduly influenced by small-scale inhomogeneities in the rock properties or the stress field, it is necessary to make a series of measurements along each borehole, a time-consuming and costly process.

Probably the most satisfactory tool in terms of cost is the C.S.I.R. triaxial cell (Leeman & Hayes 1966), which allows the complete stress field to be determined at each measuring point. However, this instrument has to be overcored with a relatively large-diameter drilling crown, so it can only be used in very good ground; in broken or highly stressed rock it is impossible to obtain an annulus of rock suitable for the strain-relief measurements. Perhaps the easiest to use is the U.S.B.M. deformation cell, but the necessity to obtain a large diameter core also limits its versatility.

Accurate determinations of the elastic constants of the rock are also required to correlate the strain reliefs with the stresses. Ideally these should be determined under confining pressure and temperature conditions similar to those prevailing at the points of measurement; for this purpose devices such as the C.S.I.R. borehole simulator (Leeman 1969) have been developed. The correct determination of Poisson's ratio is particularly important as this modulus affects the calculation of the stress concentration factors markedly. Stressmeters have an advantage over strain

gauge cells in that they do not depend on accurate determinations of the elastic moduli. However, photoelastic cells are temperature dependent, and difficulty may be experienced in reading the fringe pattern at small stresses (see Kotze 1970).

A potential problem with strain-relief measurements at depth is the influence of the excavation-induced stresses on the observations. Most underground measurements are made from tunnels. If the stress determination is made more than a tunnel diameter into the rock, it should not be influenced significantly by the stresses induced by the tunnel (Herget, Pahl & Oliver 1975). In this review we have tried to present only observations that were not affected by nearby excavations. We note that it is possible to account for the excavation-induced stresses (e.g. Salamon, Ryder & Ortlepp 1964) to recover the ambient stress field but this adds another level of interpretation to the data.

Estimates of the error in measurements have been reported for the various devices as follows: for the doorstopper, 5% (Van Heerden 1971) to 20% (Pallister 1969); for the triaxial strain cell, 5% (Herget 1973b), and for Hast's stressmeter, 2–4% (Hast 1969). We feel that some of these reported estimates of uncertainty are overly optimistic, but we are not in a position to present more realistic figures. Van Heerden & Grant (1967) concluded that both the U.S.B.M. deformation cell and the doorstopper cell were equally reliable. This contrasts with the results of de la Cruz & Raleigh (1972), who measured stresses at surface sites near Rangely, Colorado, using five different methods and found that the U.S.B.M. cell was the most convenient and reliable gauge for determining near-surface, in-situ stresses.

Hydrofrac Technique

Hydraulic fracturing is the only method currently in use that enables measurements to be made at large distances from a free surface. The experimental procedure, discussed in detail by Fairhurst (1968), Haimson & Fairhurst (1970), Haimson 1974, and Zoback et al (1977), consists of isolating a section of a borehole over a known depth interval by means of inflatable packers and then pressurizing this section by pumping in fluid while recording the pressure-time history of the hydraulic fluid.

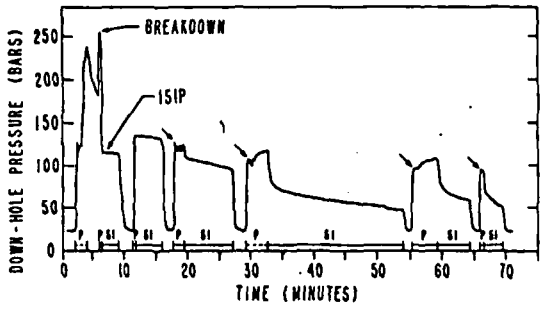

Figure 1 Hydrofrac pressure time history recorded at a site near San Ardo, California at a depth of 240 m (after Zoback, Healy & Roller 1977). *P* and *SI* indicate pumping and shut in, respectively. The inferred stress field was S_1 = 22.5 MPa (N 15 E), S_2 = 11.4 MPa (N 75 W), and S_3 = 5.1 MPa (vertical). (Courtesy of M. D. Zoback).

When the pressure increases to the level at which a tensile fracture occurs, a breakdown pressure P_b (Figure 1) is recorded. If the pump is shut off immediately and the hydraulic circuit is kept closed, an "instantaneous shut-in" pressure (ISIP) is recorded (Figure 1); this is the pressure that is just sufficient to hold the fracture open. The orientation of the tensile fracture is established by inflating an impression sleeve against the borehole wall and determining the orientation of the impression with a downhole compass or by means of a more sophisticated device such as an ultrasonic borehole televiewer (e.g. Bredehoeft et al 1976).

The theory developed by Hubbert & Willis (1957) and Kehle (1964) for fracture around a pressurized borehole is used to relate P_b and the ISIP to the ambient stress field. For a vertical borehole, the tensile fracture should be oriented in a direction perpendicular to $S_{H\min}$, and the magnitude of $S_{H\min}$ is equivalent to the ISIP. $S_{H\max}$ is then determined from

$$P_b = T + 3S_{H\min} - S_{H\max} - P, \tag{1}$$

where T is the tensile strength of the rock and P is the static pore pressure in the rock surrounding the borehole. As T and P can be determined independently, Equation (1) allows $S_{H\max}$ to be determined. Assuming that one of the principal stresses is oriented vertically, the third principal stress can be estimated from $S_v = \rho g H$, where ρ is the average density, g is gravity, and H is the depth to the interval that is isolated by packers.

If the vertical stress is the minimum principal stress, a horizontal tensile fracture might be expected to form (Kehle 1964). However, Zoback et al (1977) argue that the inflatable packers inhibit this and that horizontal fractures form only if fluid penetrates along pre-existing planes of weakness; this contention is supported by laboratory experiments reported by Haimson & Fairhurst (1970). Haimson (1976b) suggested that if $S_v = S_3$ then the induced fractures initiate in a vertical plane and then become horizontal as they propagate.

Quite a number of problems and complications are associated with the interpretation of hydrofrac data, and some of these are illustrated in Figure 1, which shows six pumping cycles of pressure at a depth of 240 m in a borehole near San Ardo, California adjacent to the San Andreas fault (Zoback, Healy & Roller 1977). The pressure drop preceding breakdown was caused by momentarily shutting off the pump. Breakdown, P_b, occurred at 25.2 MPa and the ISIP was 11.4 MPa. On cycle 2 the well was shut in before any breakdown actually occurred. Cycles 3 to 6 show that the shut-in pressure is characterized by a decay that is initially fast and then much slower. The slowly decaying shut-in pressure seems to approach an asymptotic value in the latter cycles that happens to be close to the expected overburden pressure. Zoback, Healy & Roller (1977) suggested that the fracture, initially vertical (oriented N 15° E from an impression sleeve record), was possibly turning into the horizontal plane as it propagated away from the borehole. Thus, the ISIP recorded on the first cycle is $S_{H\min}$ and the asymptotic shut-in pressure (ASIP) is the minimum principal stress of 5.1 MPa, previously established as being oriented vertically.

Another interesting feature of Figure 1 is that the secondary breakdown pressure (with T = 0 in Equation 1) has approached 9.3 MPa by the sixth cycle. The high

"zero-strength" breakdown pressures seen in cycles 3 and 4 are the result of using a fracturing fluid of high viscosity (Zoback & Pollard 1978). The use of high-viscosity fluids was advocated by Zoback et al (1977) as a means of avoiding fluid penetration into pre-existing fractures or into permeable rock before the generation of a tensile fracture; these effects lead to rate-dependent, and thus spurious, estimates of P_b. Zoback & Pollard (1978), however, noted that a drawback of using high-viscosity fluids is that the fracture may initiate significantly in advance of the observed breakdown in the pressure-time history because the fracture propagation is stable until the time at which the fracture attains some critical size. This effect leads to overestimates of P_b, as seen in cycles 3 and 4 of Figure 1.

Another potential ambiguity in the interpretation of hydrofrac data is the possibility that a shear, rather than tensile, fracture may be generated from the borehole if the fluid injection rate is too slow (Lockner & Byerlee 1977); this would lead to a misinterpretation of P_b. This effect might be important in areas where rocks with high permeability are in a state of high tectonic shear stress.

In general there is, at present, considerable controversy over the correct interpretation of P_b, and recent theoretical developments (e.g. Clifton et al 1976, Zoback & Pollard 1978) suggest that a number of existing pressure-time histories from various sites should be re-analyzed.

More positively, there seems to be little argument about the significance of the ISIP among the various practitioners of the hydrofrac technique, and so it appears that the estimates of $S_{H\min}$ are probably on a firm basis. With the amount of attention currently being devoted to the hydrofrac method, it seems reasonable to hope that the other aspects of the data will also be amenable to an unambiguous interpretation in the near future. At this time it seems particularly important to publish the actual pressure-time histories in view of the possibility of re-interpretation at a later date.

Earthquake Source Studies

Analysis of the seismic waves radiated from earthquakes can indicate the *orientations* of the three principal stresses as well as the stress *change* associated with an earthquake.

FAULT PLANE SOLUTIONS The radiation pattern of P (compressional) waves from an earthquake is quadrantal about the source. In two of the quadrants the initial motion of the P waves, as plotted on a stereographic or equal-area projection of the "focal sphere", is toward the source, and in the other two the first motion is away from the source. These quadrants are termed dilational and compressional, respectively, and are separated by nulls in the radiation pattern, termed nodal planes. According to Scheidegger (1964), the directions of S_1 and S_3 are centered in the dilational and compressional quadrants, respectively, and these directions are called the P and T axes. S_2 lies along the intersection of the nodal planes and this direction is the B axis.

It is not clear that the directions of S_1 and S_3 should necessarily coincide with the P and T axes. For example, Sbar & Sykes (1973) chose S_1 to be in a direction 30° from the inferred direction of motion on one of the nodal planes, toward the P axis, on the basis of laboratory experiments of fracture. McKenzie (1969) noted that the

possible presence of pre-existing faults allows the direction of S_1 to be anywhere within the dilational quadrant. So far, however, studies comparing directions of S_1 and S_3 determined from in situ measurements with the directions of the P and T axes have shown good agreement between the results of the two techniques (e.g. Raleigh, Healy & Bredehoeft 1972, de la Cruz & Raleigh 1972, Ahorner 1975).

Perhaps the principal advantage of estimating stress orientations using seismic radiation patterns is that the inferred directions are representative of stresses at substantial depths within the crust over regions comparable in size to the earthquakes. The principal drawback is that only stress directions and not magnitudes are estimated.

STRESS DROPS The source parameters of earthquakes that are commonly determined are the seismic moment, M_0 (Aki 1966), and the source dimension, r_0. If an earthquake is due to an average slip, D, across a fault of area A, then its seismic moment is given by $M_0 = GAD$, where G is the modulus of rigidity. M_0 is the most straightforward measure of the total deformation of an earthquake and its measured value, proportional to the long-period level of the spectrum of the seismic radiation, is quite independent of the choice of earthquake source models.

The source dimension r_0, as estimated from analysis of the seismic radiation, is highly model-dependent. The source model most widely used in recent years has been that of Brune (1970, 1971), who assumed a circular fault of radius r_0. With this model the stress drop is given by

$$\Delta\tau = (7/16)M_0/r_0^3. \qquad (2)$$

Generally Brune's (1970, 1971) model seems to yield source dimensions that are in good agreement with those measured by other means, such as from the distribution of aftershocks (e.g. Hanks & Wyss 1972). It therefore seems unlikely that stress drops estimated from Equation (2) are systematically in error.

Hanks (1977) summarized most of the studies to date of seismic source parameters, and these results are illustrated in Figure 2. We see that over a very broad range in earthquake size nearly all of the points are between the two lines indicating constant stress drops of 1 bar (0.1 MPa) and 100 bars (10.0 MPa), with no apparent dependence of stress drop on M_0 or r_0.

The most controversial aspect of seismic stress drops is the question of how they are related to the absolute state of stress in the seismogenic regions of the crust. If earthquakes release a significant fraction of the ambient stress, then we expect $\Delta\tau$ to be indicative of the strength of the crust (e.g. Chinnery 1964). If this is so, Figure 2 would indicate that the average shear strength of the crust is of the order of several tens of bars (several MPa's). Tucker & Brune (1977) suggested that the peak stress drops of about 300 bars for the San Fernanado aftershocks (Figure 2) might be indicative of the ambient tectonic stress. At the other extreme, Hanks (1977), on the basis of laboratory experiments of rock friction (Brace 1972, Byerlee 1977), has argued that earthquake stress drops are not indicative of ambient tectonic shear stresses which are of the order of kilobars, but rather may be related to the shear stresses applied to the base of the lithosphere.

Measurement of Residual Stress

Most of the measurements of residual stress, the stress present in a rock after removal of the boundary loads, have been by means of strain-relief techniques (e.g. Nichols 1975, Swolfs, Handin & Pratt 1974, Engelder, Sbar & Kranz 1977). Normally, a rock, which has been freed of its boundary loads, is progressively dissected and the

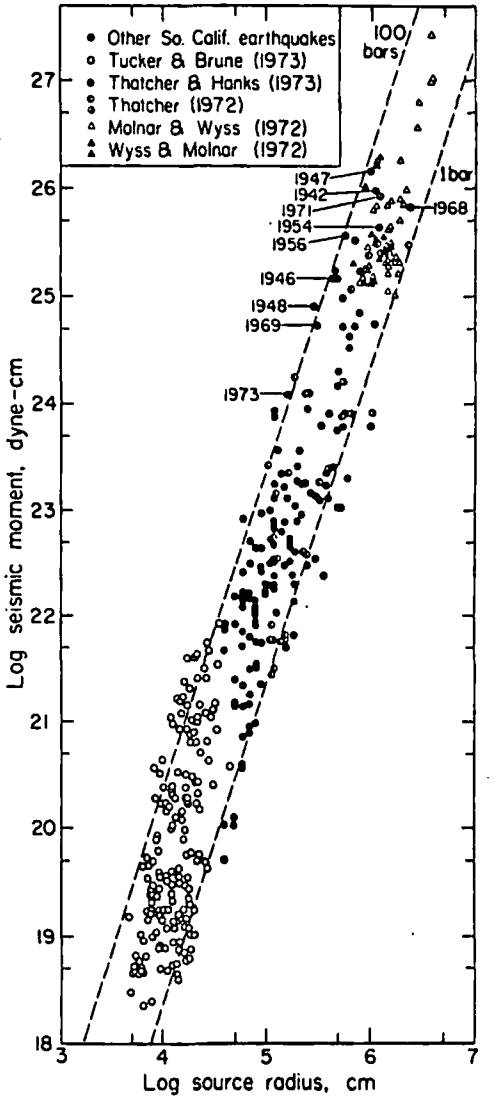

Figure 2 Earthquake moment as a function of source radius. The dashed lines are lines of constant stress drop. (Courtesy of T. C. Hanks).

corresponding strain changes recorded. If the deformation during the strain relief is elastic, then the recorded strain changes can be related to the residual stresses. Tullis (1977a) indicated some problems, based on St. Venant's principle (Love 1934, p. 132), with the interpetation of strain changes observed during the overcoring of isolated blocks. He suggested that some of these strain changes are due to inelastic processes and so it seems that the relationship of these "residual strains" to stresses is, in some cases, questionable.

Friedman's (1967) X-ray diffraction technique involves the measurement of interatomic d-spacings in quartz grains near the polished surface of an oriented sample. Comparison of the measured d spacing to that of strain-free quartz permits the calculation of residual strains and stresses.

Friedman (1972) reviewed the techniques and results of residual stress studies in considerable depth and also suggested some models to explain the existence of residual stresses.

THEORETICAL STRESS FIELDS

At any point in the earth's crust the observed state of stress is generally influenced by many factors such as present topography, present tectonics, man-induced conditions, paleotectonics, paleotopography, and thermal history. To analyze the stress measurements it is desirable to be able to account properly for all of these effects. Here we briefly discuss some of the simpler effects that can be calculated, mostly from the theory of elasticity.

Gravitational Loading

Nearly all theories of the state of stress assume that one of the principal stresses is oriented vertically and of magnitude $S_v = \rho g H$, where ρ is the *average* density of the overburden, g is the acceleration of gravity, about 9.8 m sec^{-1}, and H is the depth. As will be seen (Figure 3), the observations indicate that this is generally a valid assumption.

HEIM'S RULE This theory is based on the assumption that stresses at depth are lithostatic. That is, $S_1 = S_2 = S_3 = \rho g H$ (Jaeger & Cook, 1969, p. 355). Heim's justification for this rule was that rocks tend to creep over long periods of time due to differences in the principal stresses. This state of stress is rarely, if ever, observed in rock, even limestone. In fact, principal stress differences generally increase with depth (e.g. Figure 8), at least in the upper 3–5 km of the crust. The lithostatic state does serve as a convenient reference, however, because departures from this state indicate the stresses available to drive geologic processes, such as folding and faulting.

LATERAL CONSTRAINT If a region of the crust is subject only to the vertical force of gravity and the horizontal displacements are constrained to zero, then (Jaeger & Cook 1969, p. 356) the horizontal stresses are

$$S_H = [\nu/(1-\nu)]S_v = [\nu/(1-\nu)]\rho g H, \tag{3}$$

where ν is Poisson's ratio, typically about 0.25. Thus S_H is only about a third of S_v.

This state of stress has rarely been observed, probably because the assumptions are not realistic. Even in relatively undisturbed sedimentary basins the horizontal stresses tend to be much higher than predicted by Equation (3).

Changes in the Depth of Overburden

A number of workers have appealed to Voight's (1966) denudation effect to explain anomalously high values of the horizontal stresses measured at shallow depths. This hypothesis considers the mechanical effect of removing a layer of overburden of thickness ΔH. The vertical stress is reduced by $\rho g \Delta H$ and from Equation (3) the horizontal stress is reduced by $[\nu/(1-\nu)]\rho g \Delta H$. Thus, after erosion, near-surface values of S_H might be quite high relative to S_v, depending on the state of stress before erosion.

Voight & St. Pierre (1974) considered the thermal, as well as mechanical, effects due to the removal of overburden and found that for normal thermal gradients within the crust, the thermal effect predominates, resulting in a *reduction* in S_H relative to S_v.

Haxby & Turcotte (1976) analyzed stress changes caused by the addition or removal of overburden, taking the effect of isostatic uplift or subsidence into account as well as thermal and mechanical effects. As before, the total change in the vertical stress is $\Delta S_v = \rho g \Delta H$. The effect of uplift or subsidence on S_H is $\Delta S_H^{\sigma} = [Y/(1-\nu)](\rho_s/\rho_m)\Delta H/a$, where Y is Young's modulus, ρ_s is the density of the overburden, ρ_m is the density of the mantle at the depth of compensation, and a is the radius of the earth. Negative ΔH corresponds to a decrease in the depth of overburden (erosion) and a decrease in S_H.

The effect of temperature change, ΔT, on S_H is $S_H^{TH} = \alpha Y \Delta T/(1-\nu)$, where α is the thermal expansivity. ΔT is estimated from the geothermal gradient and a typical value for continents is $\partial T/\partial H = 25°\text{C km}^{-1}$. Thus, removal of 1 km of overburden reduces the temperature by 25°C and reduces S_H because ΔS_H^{TH} is tensional.

Haxby & Turcotte (1976) demonstrated that for a variety of rock types the overall effect of 1 km of erosion on the state of stress is a considerable reduction in S_H relative to S_v due to the effects of uplift and temperature decrease.

Theoretical Models

Price (1966), Seagar (1964), and Price (1974) have presented models, some involving complicated scenarios of geologic events, intended to predict changes in the state of stress in sedimentary basins. These various analyses indicate a broad range of possibilities for the predicted stress field depending on the specific geologic history of the basin.

THE STATE OF STRESS

The following discussion of various aspects of the stress field at depth (Figures 3 to 8) is based largely on the stress measurements listed in Table 1. Because of space limitations we have had to be selective with regard to our regional coverage of the state of stress. We first consider the common assumption that the vertical stress is due to the weight of overburden.

Table 1 Stress determinations in southern Africa, North America and Australia

Locality	Depth m	S_1[a] MPa	Azimuth Degrees	Plunge Degrees	S_2[a] MPa	Azimuth Degrees	Plunge Degrees	S_3[a] MPa	Azimuth Degrees	Plunge Degrees	Reference[b]
Roodepoort, Transvaal, South Africa	2500	88.0	332	18	58.0	112	67	34.0	238	15	1
Boksburg, Transvaal	2400	40.3	024	67	31.5	136	9	19.5	230	21	1
Carletonville, Transvaal	2320	62.5	285	70	40.5	030	5	19.5	120	15	1
Roodepoort, Transvaal	2300	70.0	112	72	52.0	292	18	39.0	203	1	1
Carletonville, Transvaal	1770	55.2	280	70	30.6	126	26	13.0	028	11	1
Evander, Transvaal	1577	49.5	270	88	37.2	081	2	26.4	171	1	1
Virginia, Orange Free State	1500	33.5	176	81	19.3	024	8	13.5	294	4	1
Carletonville, Transvaal	1320	46.0	310	60	19.5	100	25	11.5	200	15	1
Evander, Transvaal	1226	38.6	100	79	31.2	257	10	31.0	345	5	1
Evander, Transvaal	508	16.5	164	2	13.9	284	85	11.0	074	5	1
Copperton, Cape Province	410	13.0	330	6	9.6	098	78	6.4	239	6	29
Copperton, Cape Province	279	22.4	004	22	8.8	123	48	2.5	260	33	29
Drakensberg, Natal	150	12.4	297	13	10.2	206	8	5.9	086	75	2
Drakensberg, Natal	111	8.7	060	3	6.8	150	2	3.0	090	87	2
Ruacana, South West Africa	115	8.8	192	3	6.9	111	7	3.9	308	83	2
Shabani, Rhodesia	350	17.3	279	13	16.1	013	33	8.4	170	57	1
Kafue Gorge, Zambia	160	17.3	291	10	13.7	197	26	7.1	039	62	1
Kafue Gorge, Zambia	400	27.5	275	10	19.4	177	32	12.2	021	55	1
Elliot Lake, Canada	350	21.0	East		18.0	North		11.0	Vertical		3
Elliot Lake	300	37.0	NE		20.0	NW		11.0	Vertical		3
Elliot Lake	700	37.0	East		23.0	North		17.0	Vertical		3
Timmins, Canada	853	61.5	078	13	44.6	170	8	25.7	287	71	4
Timmins	488	33.1	094	6	26.8	186	23	10.7	350	66	5
Timmins	732	72.6	258	19	64.7	358	25	34.4	135	58	5
Timmins	853	53.3	250	10	51.9	342	8.5	19.1	112	77	5
Sudbury Basin, Canada	1219	80.7	243	6	38.6	358	76	36.6	150	22	6
Sudbury Basin	1707	128.8	249	10	100.8	350	52	62.3	152	37	6
Sudbury Basin	2134	79.5	270	20	61.2	013	32	37.4	152	51	6
Sudbury Basin	1219	60.3	250	13	45.7	348	35	34.3	144	52	6
Wawa, Canada	366	21.4	118	12	20.1	027	12	16.1	230	78	7
Wawa	366	42.5	133	33	34.3	229	9	15.1	332	56	7
Wawa	479	30.0	251	11	27.7	343	8	18.7	110	76	7
Wawa	573	47.2	222	17	34.1	315	9	26.7	070	70	7
Wawa	573	31.6	162	11	27.9	070	12	21.5	295	74	7
Wawa	573	19.9	224	4	16.6	315	6	14.6	100	83	7
Wawa	573	38.3	356	22	29.5	090	11	21.4	206	66	7
San Ardo, California, U.S.A.	240.2	22.5	N15E		11.4	N75W		5.1	Vertical		8
Alma, New York	512	22.3	N77E		14.7	N13W		(13.3)	Vertical		9
Nevada Test Site	380	8.8	N35E		7.0	Vertical		3.5	N35W		10[c]
Nevada Test Site	380	8.0	N44E		6.0	Vertical		2.4	N46W		10[d]
Henderson Project, Colorado	624	18.2	Vertical		12.2	308	0	8.1	218	0	11
Henderson Project	785	33.8	338	15	27.7	240	25	22.5	096	60	11
Henderson Project	1131	40.7	321	38	25.0	213	21	22.0	101	44	11
Rangely, Colorado	1914	59.0	N70E		(43.4)	Vertical		31.4	N20W		12, 13
Barberton, Ohio	701	44.8	N90W		24.1	Vertical		23.4	North		14
Falls Township, Ohio	815	28.0	N64E		(21.2)	Vertical		15.0	N26W		15
Fenton Hill Site, GT1, New Mexico	765	(18.0)	Vertical					14.7			16
GT2	1990	(50.4)	Vertical					33.3			16
EE1	2930	(75.3)	Vertical					36.7			16
Michigan Basin	5110	135.0			(127.8)	Vertical		95.0			17
Michigan Basin	3660	(91.5)	Vertical		90.0			67.0			17
Michigan Basin	2806	(70.2)	Vertical		56.0			42.0			17
Michigan Basin	1230	48.0			(30.8)	Vertical		29.5			17
Sierra Nevada Mtns., Calif.	300	9.5	N25E		(8.2)	Vertical		5.4	N65W		18
Oconee County, South Carolina	230	23.0	N60E		16.0	N30W		(6.0)	Vertical		18
Montello, Wisconsin	135	16.0	N63E		7.0	N27W		(3.5)	Vertical		18
Near Charleston, South Carolina	194	4.8	N51E		(4.4)	Vertical		3.0	N39W		19
Silver Summit Mine, Idaho	1670	105.1	N25E		56.8	Vertical		37.5	N65W		20
South of Vernal, Utah	2750	(65.0)	Vertical		56.0	N65W		51.5	N25E		21

Table 1 *continued*

Locality	Depth m	S_1[a] MPa	Azimuth Degrees	Plunge Degrees	S_2[a] MPa	Azimuth Degrees	Plunge Degrees	S_3[a] MPa	Azimuth Degrees	Plunge Degrees	Reference[b]
Southeast of Farmington, N.Mexico	2150	(58.0)	Vertical					32.0	N35W		22
RMA Well, Denver, CO	3671				(83.0)	Vertical		36.2	ENE		23
Marble Falls, Texas	346	28.3	N67W		(8.5)	Vertical		7.6	N23E		24
Lead, South Dakota	1890	(55.2)	Vertical		35.9	N50E		18.0	N40W		25
New Mexico	934				(21.1)	Vertical		14.5			26
Wyoming	2769				(62.6)	Vertical		52.0	N65W		26
Wyoming	4484				(115.1)	Vertical		81.3			26
North of Denver, CO	2303				(52.1)	Vertical		35.4	N70E		26
North of Denver	2322				(52.5)	Vertical		40.4	N75E		26
Piceance Basin, Colorado	453	(10.2)	Vertical		9.5	N87E		7.1	N03W		28[c]
Warrego Mine, Australia	241	12.0	248	3	8.9	339	15	3.5	146	75	27
Warrego Mine	319	24.5	063	17	11.2	315	46	8.3	167	40	27
Mt. Isa Mine	664	21.6	090	45	16.4	000	0	12.4	270	45	27
Mt. Isa Mine	1089	24.8	East		17.7	North		16.3	Vertical		27
Mt. Isa Mine	1000	40.0	095	27	30.0	284	62	20.0	007	4	27
Cobar Mine	366	14.8	086	37	11.2	176	0	4.6	267	55	27
Cobar Mine	588	31.2	108	28	24.6	014	7	10.3	273	61	27
North Broken Hill Mine	1098	42.7	088	25	28.3	180	5	16.5	278	63	27

[a] Parentheses indicate that the stress was calculated from the weight of the overburden.

[b] 1. Gay (1975), 2. Van Heerden (1976), 3. Eisbacher & Bielenstein (1971), 4. Herget (1976), 5. Miles & Herget (1976), 6. Herget, Pahl & Oliver (1975), 7. Herget (1973a), 8. Zoback, Healy & Roller (1977), 9. Haimson (1974), 10. Haimson et al (1974), 11. Hooker, Bickel & Aggson (1972), 12. Raleigh, Healy & Bredehoeft (1972), 13. Haimson (1973), 14. Obert (1962), 15. Haimson & Stahl (1970), 16. Aamodt et al (1977), 17. Haimson (1976c), 18. Haimson (1976b), 19. Zoback & Healy (1977), 20. Chan & Crocker (1972), 21. Brechtel, Abou-Sayed & Jones (1977), 22. Swolfs (1975), 23. Healy et al (1968), 24. Roegiers & Fairhurst (1973), 25. E. Hoskins (unpublished data), 26. H. S. Swolfs (private communication), 27. Denham, Alexander & Worotnicki (1976), 28. Bredehoeft et al (1976), 29. Gay (1977).

[c] Measured using the hydrofrac technique.

[d] Measured using a U.S.B.M. borehole deformation gauge.

[e] This is one of the deepest of 34 measurements reported by these authors.

Vertical Stress at Depth

Figure 3 shows the observed variation of S_v with depth based on the available data from strain-relief measurements. All but one of the observations scatter about the straight line representing the stress gradient due to the overburden with an average density of 2.7 gm cm^{-3}. The high value at 1.7 km was located next to an extensive "sheared zone" (G. Herget, private communication).

The data of Figure 3 are generally consistent with the assumption that the vertical stress corresponds to the weight of the overburden, but localized departures from this assumption are also indicated.

Principal Stress Orientations

We now assess the validity of another common assumption that one of the principal stresses is oriented vertically. To this end we have plotted principal stress directions *for all of the measurements made in Southern Africa* on an equal area projection of the lower hemisphere (Figure 4). If one of the principal stresses were always oriented *vertically we would expect to see a cluster of points about the center of the projection* with the remaining points plotting close to the circumference. As seen in Figure 4 there is a loose cluster of points about the center of the projection and most of the rest of the directions tend to plot near the circumference, but it is clear from these data

Figure 3 Vertical component of stress for depths greater than 100 m. The line corresponding to an average density of overburden of 2.7 gm cm^{-3} is shown for comparison. The sources of data were Gay (1975), Hooker, Bickel & Aggson (1972), Chan & Crocker (1972), Denham, Alexander & Worotnicki (1976), Herget (1973a, 1976), Herget, Pahl & Oliver (1975), Eisbacher & Bielenstein (1971), and Miles & Herget (1976).

that departures from the assumption are common (Table 1). Gay (1972, 1975) showed that over much of the Witwatersrand basin S_1 tends to be oriented closer to the vertical direction than the horizontal, but that over fairly broad areas the direction of S_1 shows a consistent and significant departure from verticality. Most of the maximum principal stresses fall within a circle of radius 30° about the vertical axis, however. Stress measurements made in deep mines in Canada, Australia, and the United States support the conclusion illustrated in Figure 4 that departures from the assumption that one of the principal stress directions is vertical are significant. Most of these data, however, were obtained in mines, often in regions of complex geology, and so it is perhaps not surprising that the observed principal stress directions

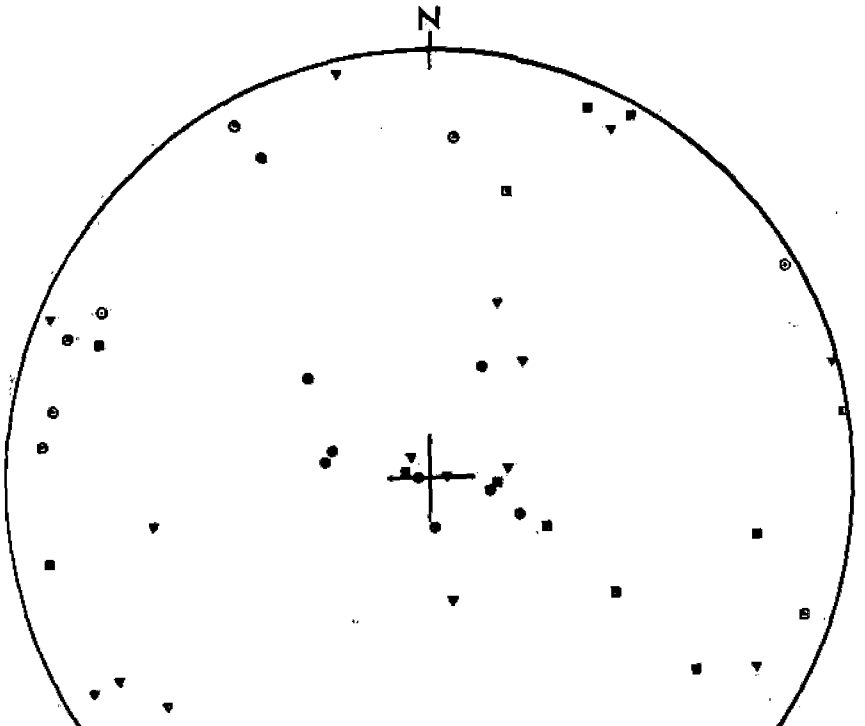

Figure 4 Orientation of principal stresses measured in southern Africa after Gay (1975, 1977) and Van Heerden (1976). Filled symbols refer to sites within the Witwatersrand system and open symbols to sites elsewhere. Circles denote S_1, squares, S_2, triangles, S_3. This is an equal area projection of the lower hemisphere.

show so much scatter. Orientations of stresses measured at depth in sedimentary basins might be expected to conform more closely to the assumption that one of the principal stresses is oriented vertically.

Horizontal Stress Magnitudes

As the vertical stress seems to be fairly predictable from the weight of overburden, measurements of the horizontal components of the stress field are of prime interest because these components could depart substantially from S_v. The extent of departure of $S_{H\min}$ and $S_{H\max}$ is limited only by the strength of the rock and, as mentioned before, very little is known about the strength of the crust. Unlike S_v, the magnitudes $S_{H\min}$ and $S_{H\max}$ are not constrained to 0 at the surface and, in fact, could show very high values at shallow depths.

The question of the relationship between surface measurements of the horizontal stresses and measurements at depth is important because considerable effort continues to be spent on obtaining near-surface data. To address this question we have plotted horizontal stress components as a function of depth for three regions where stress measurements have been made over a range of depths extending to at least 2 km. In the following sections principal stresses oriented within 30° of horizontal are considered to be "horizontal principal stresses," $S_{H\min}$ and $S_{H\max}$. In two of the regions, Southern Africa and Canada, all of the measurements were made using strain-relief techniques, and so the complete state of stress was determined. In the third region, consisting of some sedimentary basins in the United States, most of the measurements were made using the hydrofrac technique.

SOUTHERN AFRICA Figure 5 shows $S_{H\min}$ and $S_{H\max}$ as a function of depth for sites in Southern Africa (Table 1). All of the measurements below 500 m were made at sites in deep gold mines in the Precambrian quartzites of the Witwatersrand basin. These quartzites tend to be strong and brittle, and have a low value of Poisson's ratio, typically about 0.15.

We see that both components of the horizontal stress field generally increase with depth from near surface values of the order of 10 MPa to values centered about 30 MPa at depths between 2 and 2.5 km. Although the data show considerable scatter, all of the points, except one, below 500 m are to the left of the line indicating the stress due to the weight of the overburden. Above 500 m at least one and sometimes both of the horizontal stresses exceed the overburden stress. Between 500 m and 1200 m the stress field changes orientation with S_1 oriented horizontally above 500 m and vertically below 1200 m. Thus, in southern Africa stress measurements in the upper 500 m or so are not indicative of the state of stress at greater depths.

The influence of residual tectonic stresses may explain some of the apparent scatter in the data of Figure 5. For example, Gay (1975) argued that the high horizontal stresses measured by Cahnbley (1970) at the Durban Roodepoort Deep Mine, at depths of 2300 and 2500 m (Table 1), reflect a large component of residual tectonic stress associated with the folding and flattening of the strata.

CANADA The stress determinations in Canada all indicate horizontal components of the stress field in excess of the overburden stress (Table 1). As seen in Figure 6, the

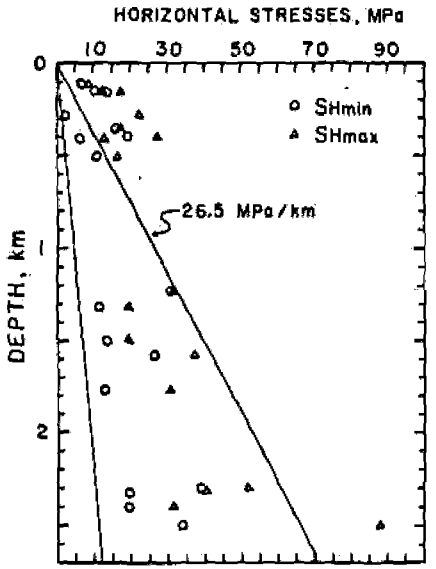

Figure 5 Horizontal stresses measured in southern Africa. For comparison, the line of the expected vertical stress corresponding to a stress gradient of 26.5 MPa km^{-1} is shown. The other line, down the left of the plot, is the horizontal stress predicted from Equation 3. The sources of data were Gay (1975, 1977) and Van Heerden (1976).

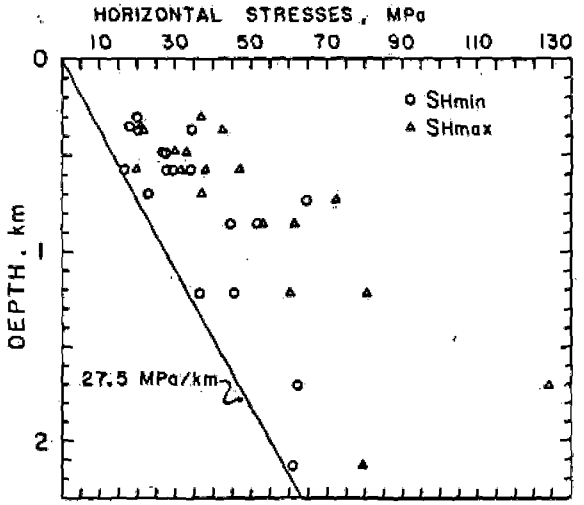

Figure 6 Horizontal stresses measured in Canada. The sources of data were Herget (1973a, 1976), Herget, Pahl & Oliver (1975), Eisbacher & Bielenstein (1971), and Miles & Herget (1976). The very high value of $S_{H\max}$ near the lower right-hand corner of the figure, seems to represent a localized region of high stress on the basis of other measurements in the Creighton mine (Sudbury basin).

horizontal stresses show a general, though irregular, increase with depth to 2.1 km. As with the measurements in southern Africa, part of the spread in the distribution of $S_{H\min}$ and $S_{H\max}$ with depths is probably due to residual tectonic stresses. Eisbacher & Bielenstein (1971) suggested, for instance, that in the Elliot Lake area the high eastward component of the stress field contains a significant remanent component of the tectonic stress field that existed at the time of intense deformation in the area.

Another factor contributing to the apparent scatter in the stress data appears to be variations in rock properties. Herget (1973a) determined the state of stress in tuff, chert, metadiorite and siderite at the G. W. MacLeod Mine, Wawa, Ontario, and showed that the magnitudes of the stresses depend to some extent on the elastic moduli of the rocks; higher elastic moduli correspond generally to greater stresses.

The measurements in the deep Canadian mines, all near the margin of the Canadian shield, indicate a state of stress substantially different from that of Southern Africa (Figure 5). At any given depth the horizontal stresses in the Canadian mines are typically a factor of two or more greater than those within the Witwatersrand mines. This contrast is qualitatively consistent with the tectonics of the two regions in that normal faulting and subsidence were the predominant mode of deformation in the Witwatersrand basin whereas thrust faulting and folding accounted for most of the deformation along the edge of the Canadian shield.

U.S. BASINS A large number of stress measurements using the hydrofrac technique have been made in the oil and gas fields in Colorado, New Mexico, Utah, and Wyoming and in the Michigan basin at depths extending to 5.1 km. This data set is of particular interest because nearly all of the measurements have been made in sandstones and shales in conditions of reasonably homogenous tectonics. The surface measurements, reported by de la Cruz & Raleigh (1972) and H. S. Swolfs, C. E. Brechtel, and H. R. Pratt (in preparation), were made at sites near Rangely, Colorado using the U.S.B.M. borehole deformation gauge and the direct strain gauge technique in the Mesa Verde sandstone. The intense distribution of measurements at depths between 37 and 475 m were made in seven oil-shale test holes in the Piceance Basin of northwest Colorado by Bredehoeft et al (1976). The deeper measurements in shales and sandstones were reported by Haimson (1973), Raleigh, Healy & Bredehoeft (1972), H. S. Swolfs (private communication), Haimson & Stahl (1970), and Haimson (1976c) (Table 1).

Only the measurements of $S_{H\min}$ have been plotted in Figure 7 because at many of the sites $S_{H\max}$ was either not determined or, somewhat uncertain, as discussed previously. We see that in the upper 2.3 km the observations fall remarkably close to the line corresponding to a gradient of 15 MPa km^{-1}, empirically determined from the results of many hydraulic fracturing operations (Howard & Fast 1970). From below 2.3 km to 5.1 km the measurements of $S_{H\min}$ appear to follow a gradient intermediate to the "oilfield" gradient and one corresponding to the average weight of overburden.

As seen in Figure 7, the "soft rock" measurements show much less scatter than those in hard rock (Figures 5 and 6). Part of this reduction in scatter may be attributed to the hydrofrac technique, but the surface measurements made using strain-relief techniques also show very little spread in the magnitudes. This suggests

that the state of stress is inherently more homogeneous in soft rocks, such as shales and sandstones, than in hard rocks, such as granites and quartzites.

Another feature, which deserves more comment (Figure 7), is the departure of the data from the "oilfield" gradient at depths below about 2.3 km. The departure of S_{Hmin} from the average gradient of 15 MPa km^{-1} may be due to the inability of the

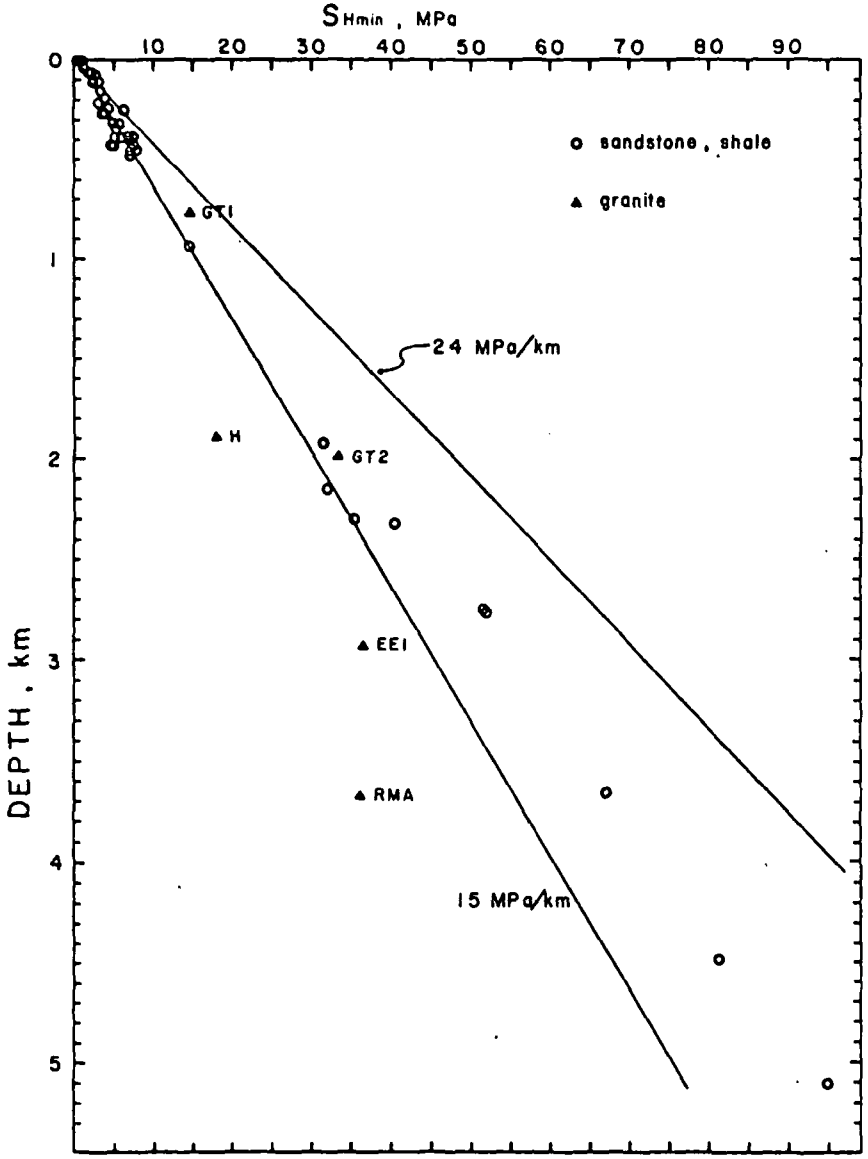

Figure 7 The minimum horizontal stress measured in basins in the U.S.

sandstones and shales to withstand stress differences much in excess of 20–40 MPa. Admittedly, more data below 2.5 km are necessary to confirm this suggestion.

The data in Figure 7 probably provide the best indication of the relationship of magnitudes of stresses measured at the surface to those at depth. The stress magnitudes at the surface fall on the same straight line as the rest of the measurements in the upper 2.3 km. Thus, in this case we can say that the magnitude of the surface stress is consistent with those at depth, although it is close to zero.

For comparison with the "soft rock" stresses we have plotted some estimates of S_{Hmin} in precambrian granite from hydrofrac measurements. GT1 (Geothermal Test 1), GT2, and EE1 (Energy Extraction) (Figure 7) refer to holes drilled in connection with the Hot-Dry-Rock Geothermal Energy Program at the Fenton Hill site, New Mexico (Aamodt et al 1977). RMA represents the Rocky Mountain Arsenal well near Denver, Colorado (Healy et al 1968), and the remaining measurement (*H*) was made in South Dakota by E. Hoskins (unpublished data).

The measurements in granite do not show such a regular increase of stress with depth as the measurements in sandstones and shales. The low value of S_{Hmin} for the point labeled EE1 has immediate engineering significance for the Hot-Dry-Rock Project because a gigantic crack is most easily propagated in conditions of low S_{Hmin}.

Shear Stress

The observed variation of the maximum component of shear stress, $(S_1 - S_3)/2$, is shown in Figure 8, which includes most of the available data from sites below 100 m depth (Table 1). The data have been divided into soft rock measurements—shales, sandstones, limestones, etc.—and hard rock measurements—granites, quartzites, norites, etc. Many of the points for sites in soft rock were determined from hydrofrac measurements and so S_1, as discussed previously, may be uncertain, which makes the maximum shear stress correspondingly uncertain.

The high value of shear stress at 1670 m (Figure 8) was measured in quartzite in the Coeur d'Alene mining district, Idaho (Chan & Crocker 1972) using a U.S.B.M. borehole deformation gauge, and the high value at 1707 m was determined from measurements in the Sudbury basin, Canada (Herget, Pahl & Oliver 1975) using the "doorstopper" method. The high Canadian value of shear stress almost certainly reflects some localized stress concentration because shear stresses measured above and below this site in the same mine are substantially lower, as seen from the points labeled with *S* in Figure 8.

The data of Figure 8 show tremendous scatter but, even so, some conclusions can be drawn. First, the shear stress shows a general increase with depth. The increase appears to be much more rapid in the upper one or two kilometers than at greater depths. The data for the "soft" rocks in Figure 8 indicate that the gradient of the shear stress is substantially less at depths below a kilometer than at shallower levels.

The shear stresses measured in the "hard" rocks (Figure 8) are, for the most part, significantly higher at a given depth than those in "soft" rock. The gradient in shear stress also appears to be diminishing with depth for the hard rock, but this tendency is not very well established because of a lack of data below 3 km.

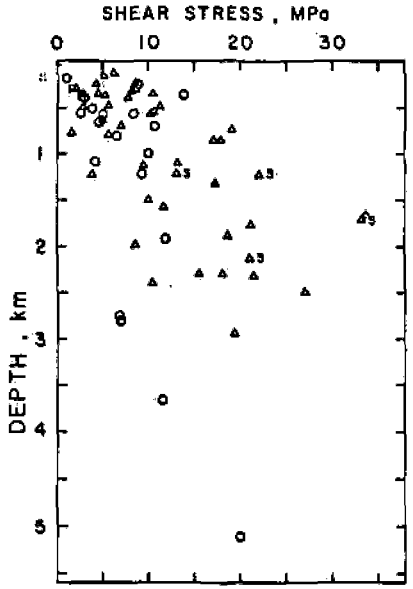

Figure 8 Maximum shear stress, $(S_1 - S_3)/2$. All of these values were derived from observations listed in Table 1. Measurements in soft rock such as shale and sandstone are indicated as circles, and those in granites, quartzites, etc, are shown as triangles. The *P* near the upper-left of the figure denotes the general level of shear stress for the measurements in the Piceance basin (Bredehoeft et al 1976). Symbols marked *S* indicate the same mine in the Sudbury basin, Ontario.

The data of Figure 8 suggest some lower limits for the magnitudes of regional shear stresses at mid-crustal depths (say 20 to 40 MPa), but much more data at depths below 3 km are necessary to check this suggestion. In any case, it is clear that near-surface estimates of the shear stress are not indicative of shear stresses throughout the crustal section.

Horizontal Stress Orientations

Stress orientations are intrinsically much more amenable to analysis than magnitudes because measurements of stress directions at all depths can be meaningfully compared; in addition, measured stress orientations can be compared to directions from earthquake fault-plane solutions and directions inferred from geologic indicators of stress.

Over certain broad regions the horizontal stress orientations appear to be quite homogeneous, although localized anomalies do occur. Over other regions the horizontal stress directions seem to be completely incoherent from site to site. Both of these situations are described in the following discussion of horizontal stress orientations by region.

NORTH AMERICA Sbar & Sykes (1973) presented the results of many in situ stress measurements, earthquake fault-plane studies, and geological observations made in eastern North America and concluded that the maximum compressive stress trends east to northeast from west of the Appalachian Mountain system to the middle of the continent and from southern Illinois to southern Ontario (Figure 9). More recent data, especially from the hydraulic fracturing experiments, tend to support this generalization (e.g. Haimson 1977). Most recently, Sbar & Sykes (1977) specified more exactly the eastern boundary of the "stress domain" for which $S_{H\max}$ trends ENE on the basis of some recent fault-plane solutions, additional in-situ stress measurements, and observations of the orientations of glacial "pop-ups."

Raleigh (1974) commented on possible relationships between the driving forces of plate tectonics and stress orientations observed in the U.S. by means of in-situ measurements, earthquake fault-plane solutions, and some observations of dyke orientations. The stress orientations in the western U.S. are consistent with a state of right-lateral shear along the boundary between the Pacific and North American plates (Figure 9). Essentially all of these orientations were on the basis of fault-plane solutions and indicate that $S_{H\max}$ is generally oriented NNE to NE in California and Nevada becoming NNW to N in orientation from northern California up into Washington. More recent hydrofrac measurements by Haimson (1976a) in the Sierra Nevada Mountains and by Zoback, Healy & Roller (1977) near the San Andreas Fault in central California also indicate a NNE orientation for $S_{H\max}$ in California.

Some Surface Measurements

Here we briefly describe results from selected studies of surface stresses and their bearing on generalizations based on deeper measurements, earthquake fault-plane solutions, and tectonic considerations. Some of the surface measurements have yielded results in good agreement with results from other types of data.

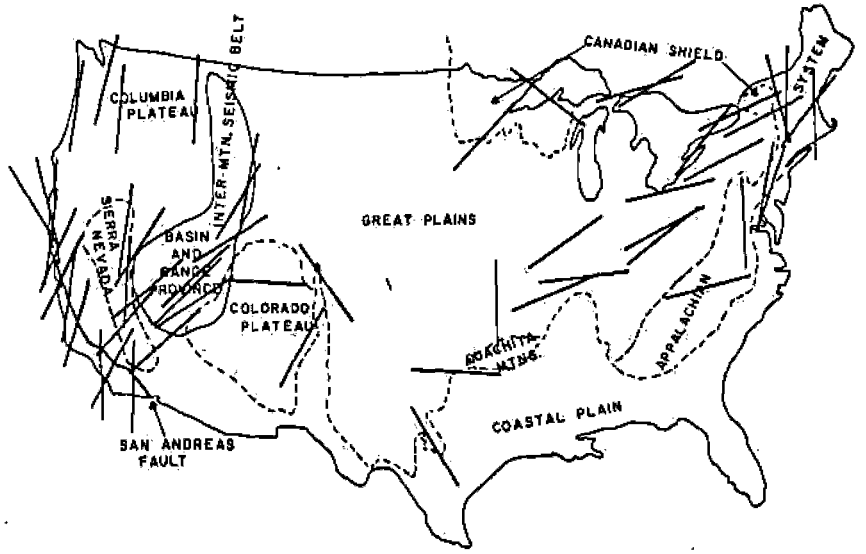

Figure 9 Orientations of $S_{H\max}$ in the U.S. as measured from in situ stress measurements and earthquake fault-plane solutions. [Adapted from Raleigh (1974)].

De la Cruz & Raleigh (1972) found that near-surface stress directions at sites near Rangely, Colorado were consistent with those inferred from earthquake fault-plane solutions (Raleigh, Healy & Bredehoeft 1976) and from existing joint patterns.

Engelder & Sbar (1976) measured stress orientations using the direct strain gauge technique at five sites in the Potsdam sandstone in northern New York and found that the average direction of $S_{H\max}$ at four of the sites is N 78° W and at the fifth the average direction is N 18° E. Over broad areas of the formation, but not the entire formation, the stress seems to be uniformly oriented. They were not able to conclude whether any components of their measured stresses were caused by the broad-scale applied stress trending E to NE hypothesized by Sbar & Sykes (1973) for the eastern U.S.

Newman & Clark (1977) reported near-surface measurements made at three quarries in western Ohio that showed consistent directions for measurements within a particular quarry but inconsistent directions between quarries only a few kilometers apart; at the three quarries $S_{H\max}$ was oriented N 40° E, N 14° W, and N 81° W. They noted that these results do not support the hypothesis of a regional orientation for $S_{H\max}$ in the eastern U.S.

Hooker & Johnson (1969) summarized the results of many near-surface measurements at sites in New England, the Appalachian Piedmont, Missouri, Oklahoma, and Texas. At all but two of these sites they found that $S_{H\max}$ seems to be aligned parallel to the fold axis of the major tectonic structure.

Most recently Tullis (1977b) and Sbar et al (1977) have measured stresses at surface sites adjacent to the San Andreas fault near Palmdale in southern California. Tullis used a U.S.B.M. deformation gauge in shallow holes and Sbar et al used the C.S.I.R. "doorstopper" technique. The two groups made measurements at a number of common sites for comparison of the two methods and found that the measured stress directions were consistent. Interestingly, the direction of $S_{H\max}$ in one area shows considerable, although systematic, changes in orientation through about 90° over distances of the order of 1 km.

CENTRAL EUROPE In-situ stress measurements and earthquake fault-plane solutions indicate that within Switzerland and Germany to the north of the Alps the direction of $S_{H\max}$ is NW. This is a region where shallow stress measurements at many sites have yielded stress directions consistent with those deduced from analyzing a large number of crustal earthquakes. Both the fault-plane solutions (e.g. Ahorner 1975) and the in-situ measurements (e.g. Greiner 1975, Greiner & Illies 1977) show that S_1 and S_3 are horizontal (strike-slip faulting).

Most of the stress measurements were at depths less than 500 m using the "doorstopper" strain-relief technique, but at one site in southwest Germany Rummel & Jung (1975) determined the state of stress at a depth of 25 m using the hydrofrac technique for comparison with the stresses previously determined by Greiner (1975). Both the magnitudes and directions of the stresses measured using the two methods were in good agreement.

Geological evidence taken in conjunction with observations of the present-day stress field has been interpreted by Illies (1975) as indicating a counterclockwise rotation of the direction of $S_{H\max}$ through an angle of 60° beginning in early Miocene times. The Rhinegraben rift system was formed in the pre-existing stress field and the reorientation of the stresses has converted the Rhinegraben into a left-lateral shear zone according to Illies & Greiner (1976), who attribute this change in the stress direction to the development of the Alpine collision front.

AUSTRALIA Earthquake fault-plane solutions (e.g. Fitch, Worthington & Everingham 1973, Mills & Fitch 1977) and in-situ stress measurements (e.g. Stephenson & Murray 1970, Endersbee & Hofto 1963, Denham, Alexander & Worotnicki 1976) show that $S_{H\max}$ is oriented close to E–W throughout much of Australia with the exception of one region extending from the central portion of the continent southward within which $S_{H\max}$ is oriented approximately N–S (e.g. Stewart & Denham 1974).

The stresses were measured using strain relief techniques of various types, most commonly using overcoring methods (Hoskins 1967). Most of the measurements, which were made at depths ranging from near-surface to slightly more than 1 km, and all of the earthquake fault-plane solutions indicate a state of stress in which the minimum principal stress is S_v (thrust faulting).

SOUTHERN AFRICA The directions of $S_{H\min}$ and $S_{H\max}$ in this region (Gay 1977) appear to be broadly distributed as seen in Figure 4 although there may be a slight tendency for these directions to be aligned either N–S or E–W. Even if only the measurements made within the Witwatersrand basin are considered, the horizontal stresses do not show any preferred directions.

ICELAND In-situ stress measurements in Iceland by Hast (1969, 1973) and by Haimson & Voight (1977) have yielded results that are somewhat anomalous in view of the earthquake data and plate-tectonics concepts. From the results of near-surface measurements Hast concluded that the horizontal stresses are high and compressive and not indicative of a spreading ridge. Haimson & Voight (1977) measured stresses using the hydrofrac technique in two boreholes and found that the direction of S_1 changes from horizontal to vertical at a depth of about 250 m in one of the boreholes but not in the other. At all depths the orientation of $S_{H\max}$ is roughly perpendicular to the axis of rifting. This measured state of stress is consistent with neither the earthquake fault-plane solutions nor the geology of the area (Ward, 1971, Klein, Einarsson & Wyss 1977). The re-orientation of S_1 observed in one of the boreholes may indicate that stresses measured in the upper half kilometer or so in Iceland are simply not indicative of the principal stress directions well within the crust. Haimson & Voight (1977) suggested that their results could be explained in terms of a combination of thermoelastic mechanisms associated with the accretion and cooling of spreading lithosphere.

Stress Gradients

Von Schonfeldt, Kehle & Gray (1973) produced maps showing the rate of increase of stress with depth for the oil and gas fields of the United States. They considered data from hydraulic-fracturing treatments of nearly 3000 wells to estimate the regional distribution of stress gradients. They found that the gradient of the minimum

horizontal stress varies from 11.3 to 33.9 MPa km^{-1} and for the maximum horizontal stress from 15.8 to 29.4 MPa km^{-1}.

One of the regions where the gradient, γ, of $S_{H\min}$ is as low as 11.3 MPa km^{-1} is along the Gulf Coast in southern Louisiana and Mississippi where the sediments of the Mississippi embayment are known to be essentially in a state of failure. Normal faulting occurs such that the sediments tend to slump into the Gulf of Mexico. Hubbert & Willis (1957) noted that the observed failure of these sediments can be explained on the basis of the Coulomb (1773) failure criterion if the effect of pore pressure is taken into account.

According to Coulomb (1773), failure occurs at a level of shear stress across the plane of failure given by $|\tau| = \tau_0 + \mu S_n$, where τ_0 is the cohesive strength, μ is the coefficient of friction, and S_n is the compressive stress acting in a direction normal to the plane of failure.

If pore fluid is present at a pressure P, then the failure criterion becomes

$$|\tau| = \tau_0 + (S_n - P)\mu. \tag{4}$$

In general, $\tau = (S_1 - S_3)(\sin 2\theta)/2$ and $S_n = (S_1 + S_3)/2 + (S_1 - S_3)(\cos 2\theta)/2$, where θ is the angle between the normal to the failure plane and the direction of S_1. Along the Gulf coast S_1 is oriented vertically and presumably has magnitude $\rho g H$ at depth H. If we assume that the faults associated with the sediment failure dip 60° then $\theta = 60°$. We also assume that the pore pressure, P, is given by $P = \rho_w g H$, where ρ_w is the fluid density, taken as 1 gm cm^{-3} here. This estimate of P is correct if the water table is near the surface. Finally, if we can neglect the cohesive strength, τ_0, of the poorly consolidated sediments, then we can rewrite Equation (4) in terms of stress gradients since all terms are proportional to H. The critical gradient for failure, γ_c, for $S_{H\min}$ ($S_{H\min} = \gamma H$) is

$$\gamma_c = g[(\rho - 1)(0.43 - 0.25\mu)/(0.43 + 0.75\mu) + 1].$$

Table 2 lists values of γ_c corresponding to various values of ρ and μ. We see that even if μ is as high as 1.0 we still expect the sediments to be in a state of failure along that part of the Gulf Coast where $\gamma \leqq 11.3$ MPa km^{-1}. Probably the most reasonable estimates of ρ and μ, for the Gulf Coast sediments, are 2.2 gm cm^{-3} and 0.6, respectively. In this case we expect normal faulting for $\gamma \leqq 13.6$ MPa km^{-1} (Table 2), and this criterion is met over a fairly broad region of the Gulf Coast (von Schonfeldt, Kehle & Gray 1973).

Table 2 Critical gradients of $S_{H\min}$

γ_c (MPa km^{-1})	ρ (gm cm^{-3})	μ
12.9	2.0	0.6
12.0	2.0	0.8
11.3	2.0	1.0
13.6	2.2	0.6
12.5	2.2	0.8
11.6	2.2	1.0
14.2	2.4	0.6
12.9	2.4	0.8
11.9	2.4	1.0

M. D. Zoback, J. H. Healy, and G. S. Gohn (in preparation) have measured stress at various depths up to 491 m in two wells near Charleston, South Carolina using the hydrofrac technique. They found that in the Coastal Plain sediments the gradient of S_3 is very low, and from an analysis similar to that for the Gulf Coast, these sediments also appear to be in a state of incipient failure.

DISCUSSION AND CONCLUSIONS

High Horizontal Stresses

One of the most common observations emphasized by those who make in-situ stress measurements is the ubiquity of high, horizontal stresses relative to the vertical stress at shallow depths (e.g. Hast 1973). As discussed earlier, none of the usual theories involving gravity, uplift, erosion, or temperature changes can explain the relatively high values of $S_{H\min}$. In particular we wish to emphasize that although the mechanical effect of erosion can lead to relatively high values of the horizontal stresses (Voight 1966), this effect necessarily occurs in conjunction with a reduction in temperature as well as probably some isostatic uplift. The net result is a reduction in the horizontal stresses relative to S_v (Voight & St. Pierre 1974, Haxby & Turcotte 1976).

The data suggest that, at any given depth, if $S_{H\min}$ falls below a certain value, some sort of inelastic process occurs to increase its magnitude. For example, Price (1974) suggested that in the presence of pore pressure, natural hydraulic fracturing would occur in sedimentary basins undergoing erosion and uplift if $S_{H\min}$ fell below the hydrostatic stress minus the tensile strength of the rock. Voight & St. Pierre (1974) suggested that the relaxation of residual stresses during erosion could impose substantial compressive stresses on the rock mass.

Reference State of Stress

Although stress orientations have proved amenable to geologic analysis, magnitudes of stresses have, for the most part, been quite enigmatic. This is because no one knows what magnitudes to expect from the horizontal stress field. A number of workers have considered the horizontal stresses calculated on the basis of lateral constraint (Equation 3) as a reference state, but this seems like a very poor choice because few of the observed horizontal stresses are even close to this predicted state. For example, some of the lowest values of $S_{H\min}$ at depths greater than 1 km have been observed in southern Africa, but we see in Figure 5 that all of the data fall well to the right of the line calculated from Equation 3 for $\nu = 0.15$.

Although the vertical stress at depth is reasonably predictable (Figure 3), it is not possible to generalize about the magnitudes of the horizontal stresses within the crust except to say that they usually increase with depth. In some regions the horizontal components of stress tend to be less than the vertical component (e.g.

Figure 5) and in others the horizontal stresses exceed S_v (e.g. Figure 6). Thus, no reference state of stress exists that actually resembles the stress field in any particular region and yet has world-wide applicability. The lithostatic state of stress (Heim's Rule) serves as a convenient point of departure in discussing stresses at depth, even if it does not actually represent the stress field found in any particular part of the crust.

In this regard it is interesting to note that the stress field as measured in the upper 5 km of the crust does not show any tendency to approach a lithostatic state with increasing depth. In fact, as seen in Figure 8 the shear stress generally increases with depth throughout this range.

Strength of the Crust

Earlier, in the discussion about seismic stress drops (Figure 2), we mentioned some of the conjecture by different workers regarding the shear strength of the crust. From the observed shear stresses (Figure 8) we feel that we can begin to narrow down the limits of the possible range of crustal strengths. Because granite is a very important constituent in continental crustal sections the data for sites in hard rock are probably more indicative of the shear stresses to be found throughout the continental crust than the observations in softer sedimentary rock. These data (Figure 8) suggest a shear strength of at least 20 MPa, and probably much greater, for the continental crust. If so, then the seismic stress drops (Figure 2) represent, in general, only a small fraction of the ambient shear stress.

Acknowledgments

Many of the authors cited in this review generously supplied reprints, preprints and many useful suggestions, for which we are grateful. H. Swolfs was especially helpful in supplying the results of a considerable number of stress measurements, many of which were unpublished. T. Fitch kindly provided much of the Australian data, and J. B. Walsh supplied background material. Extensive discussions with M. Zoback, J. Healy, C. B. Raleigh, H. Pratt, T. Hanks, D. Pollard, and T. Tullis were useful in clarifying some of the issues discussed here. D. Bailey and W. Seiders provided considerable editorial assistance. M. Zoback, D. Pollard, and J. H. Healy reviewed the manuscript. N. C. Gay was supported in part by the Chamber of Mines of South Africa while this review was being prepared.

Literature Cited

Aamodt, R. L. 1977. Hydraulic fracture experiments in GT-1 and GT-2. *Tech. Rep. LA-6712*, Los Alamos Sci. Lab., Los Alamos, N.M.

Aamodt, R. L., Brown, D. W., Lawton, R. G., Murphy, H. D., Potter, R. M., Tester, J. W. 1977. *Ann. Rep. LA-6525-PR*, pp. 60–63, Los Alamos Sci. Lab., Los Alamos, N.M.

Abel, J. F., Lee, F. T. 1973. Stress changes ahead of an advancing tunnel. *Int. J. Rock Mech. Min. Sci. Geomech. Abstr.* 10: 673–97

Ahorner, L. 1975. Present-day stress field and seismotectonic block movements along major fault zones in Central Europe. *Tectonophysics* 29: 233–49

Aki, K. 1966. Generation and propagation of G waves from the earthquake of 16th June 1964. *Bull. Earthquake Res. Inst. Tokyo Univ.* 44: 73–88

Brace, W. F. 1972. Laboratory studies of stick-slip and their application to earthquakes. *Tectonophysics* 14: 189–200

Brechtel, C. E., Abou-Sayed, A. S., Jones, A. 1977. *Terra Tek Rep.*, Terra Tek Inc., Salt Lake City, Utah

Bredehoeft, J. D., Wolff, R. G., Keys, W. S., Shuter, E. 1976. Hydraulic fracturing to determine the regional in situ stress field, Piceance Basin, Colorado. *Geol. Soc. Am. Bull.* 87: 250–58

Brune, J. N. 1970. Tectonic stress and the spectra of seismic shear waves from earthquakes. *J. Geophys. Res.* 75: 4997–5009

Brune, J. N. 1971. Tectonic stress and the spectra of seismic shear waves from earthquakes; correction. *J. Geophys. Res.* 76: 5002

Byerlee, J. D. 1977. Friction of rocks. In *Proc. Conf. II, Experimental Studies of Rock Friction with Application to Earthquake Prediction*, ed. J. F. Evernden, pp. 55–77. Menlo Park, Calif: U.S. Geol. Surv.

Cahnbley, H. 1970. *Grundlagenuntersuchungen über das Entspannungsbohrverfahren wahrend des praktischen Einsatzes in grosser Tiefe.* Dissertation. Tech. Univ. Clausthal, Germany

Carter, N. L., Raleigh, C. B. 1969. Principal stress directions from plastic flow in crystals. *Geol. Soc. Am. Bull.* 80: 1231–64

Chan, S. S. M., Crocker, T. J. 1972. A case study of in situ rock deformation behavior in the Silver Summit Mine, Coeur D'Alene Mining district, *Proc. 7th Can. Rock Mech. Symp., Edmonton, 1971*, pp. 135–60, Mines Branch, Dept. of Energy, Mines and Res., Ottowa

Chinnery, M. A. 1964. The strength of the Earth's crust under horizontal shear stress. *J. Geophys. Res.* 69: 2085–89

Clifton, R. J., Simonson, E. R., Jones, A. H., Green, S. J. 1976. Determination of the critical stress-intensity factor K_{1c} from internally-pressured thick-walled vessels. *Exp. Mech.* 16: 233–38

Coates, D. F., Yu, Y. S. 1970. A note on the stress concentrations at the end of a cylindrical hole. *Int. J. Rock Mech. Min. Sci.* 7: 583–88

Coulomb, C. A. 1773. Sur une application des règles de maximus et minimus à quelques problèmes de statique relatifs à l'architecture. *Acad. R. Sci. Mem. Math. Physique Divers Savans* 7: 343–82

Crouch, S. L. 1969. A note on the stress concentrations at the bottom of a flat-ended borehole. *J. S. Afr. Inst. Min. Metall.* 70: 100–2, 386 k

De la Cruz, R. V., Raleigh, C. B. 1972. Absolute stress measurements at the Rangely anticline, northwestern Colorado. *Int. J. Rock Mech. Min. Sci.* 9: 625–34

Denham, D., Alexander, L. G., Worotnicki, G. 1976. *Stress measurement proposals for Western Australia, Rec. 1976/1*, Dept. Min. and Energy, Bur. Miner. Res., Geol. and Geophys., Australia

Eisbacher, G. H., Bielenstein, H. U. 1971. Elastic strain recovery in Proterozoic rocks near Elliot Lake, Ontario. *J. Geophys. Res.* 76: 2012–21

Endersbee, L. A., Hofto, E. D. 1963. Civil engineering design and studies in rock mechanics for Poatina underground power station, Tasmania. *J. Inst. Eng. Aust.* 35: 187–206

Engelder, J. T., Sbar, M. L. 1976. Evidence for uniform strain orientation in the Potsdam sandstone, northern New York, from in situ measurements. *J. Geophys. Res.* 81: 3013–17

Engelder, J. T., Sbar, M. L., Kranz, R. 1977. A mechanism for strain relaxation of Barre granite: opening of microfractures. *Pure Appl. Geophys.* 115: 27–40

Fairhurst, C. 1968. *Methods of determining in-situ rock stress at great depths, Tech. Rep. No. 1-68*, U.S. Army Corps Eng., Missouri River Div., Omaha, Neb.

Fitch, T. J., Worthington, M. H., Everingham, I. B. 1973. Mechanisms of Australian earthquakes and contemporary stress in the Indian Ocean plate. *Earth Planet. Sci. Lett.* 18: 345–56

Friedman, M. 1967. Measurement of the state of residual elastic strain in quartzose rocks by X-ray diffractometry. *Norelco Rep.* 14: 7–9

Friedman, M. 1972. Residual elastic strain in rocks. *Tectonophysics* 15: 297–330

Friedman, M., Heard, H. C. 1974. Principal stress ratios in Cretaceous limestones from Texas Gulf coast. *Bull. Am. Assoc. Pet. Geol.* 58: 71–78

Gay, N. C. 1972. Virgin rock stresses at Doornfontein Gold Mine, Carletonville, South Africa. *J. Geol.* 80: 61–80

Gay, N. C. 1975. In-situ stress measurements in Southern Africa. *Tectonophysics* 29: 447–59

Gay, N. C. 1977. Principal horizontal stress in Southern Africa. *Pure Appl. Geophys.* 115: 3–10

Greiner, G. 1975. In-situ stress measurements in southwest Germany. *Tectonophysics* 29: 265–74

Greiner, G., Illies, J. H. 1977. Central Europe: active or residual tectonic stresses. *Pure Appl. Geophys.* 115: 11–26

Haimson, B. C. 1973. Earthquake related stresses at Rangely, Colorado. In *New Horizons in Rock Mechanics, Proc. 14th Symp. Rock Mech.*, ed. H. Hardy, R. Stefanko, pp. 689–708. New York: ASCE

Haimson, B. C. 1974. A simple method for estimating in situ stresses at great depths.

In *Field Testing and Instrumentation of Rock, ASTM Spec. Tech. Publ. 554*, pp. 156–82
Haimson, B. C. 1976a. Preexcavation deep-hole stress measurements for design of underground chambers—case histories. In *Proc. 1976 Rapid Excavation and Tunneling Conf.*, ed. R. D. Coulon, R. D. Robbins, pp. 699–714. New York: Soc. Min. Eng. AIME
Haimson, B. C. 1976b. The hydrofracturing stress measuring technique-method and recent field results in the U.S. *Int. Soc. Rock Mech. Symp. Invest. Stress in Rock, Sydney, Australia*
Haimson, B. C. 1976c. Crustal stress measurements through an ultra deep well in the Michigan Basin. *EOS Trans. Am. Geophys. Union* 57:326
Haimson, B. C. 1977. Crustal stress in the continental United States as derived from hydrofracturing tests. *The Earth's Crust, Geophys. Monogr. Am. Geophys. Union*, ed. J. C. Heacock 20:576–92
Haimson, B., Stahl, E. 1970. Hydraulic fracturing and the extraction of minerals through wells. In *Proc. 3rd Symp. on Salt*, pp. 421–32, Northern Ohio Geol. Soc., Cleveland, Ohio
Haimson, B. C., Fairhurst, C. 1970. In situ stress determination at great depth by means of hydraulic fracturing. In *Rock mechanics—Theory and Practice, Proc. 11th Symp. Rock Mech.*, ed. W. Somerton, pp. 559–84. New York: AIME
Haimson, B. C., Lacomb, J., Jones, A. H., Green, S. J. 1974. Deep stress measurements in tuff at the Nevada test site. In *Adv. Rock Mech., Proc. 3rd Congr. Int. Soc. Rock Mech.* II-A:557–62
Haimson, B. C., Voight, B. 1977. Crustal stress in Iceland. *Pure Appl. Geophys.* 115:153–90
Hanks, T. C., Wyss, M. 1972. The use of body wave spectra in the determination of seismic source parameters. *Bull. Seismol. Soc. Am.* 62:561–90
Hanks, T. C. 1977. Earthquake stress drops, ambient tectonic stresses and stresses that drive plate motions. *Pure Appl. Geophys.* 115:441–58
Hast, N. 1958. The measurement of rock pressure in mines. *Sver. Geol. Under. Ser. C.* 52:1–183
Hast, N. 1969. The state of stress in the upper parts of the earth's crust. *Tectonophysics* 8:169–211
Hast, N. 1973. Global measurements of absolute stress. *Phil. Trans. R. Soc. London Ser. A* 274:409–19
Hawkes, I., Moxon, S. 1965. The measurement of in-situ rock stress using the photoelastic biaxial gauge with the core-relief method. *Int. J. Rock Mech. Min. Sci.* 2:405–19
Haxby, W. F., Turcotte, D. L. 1976. Stresses induced by the addition or removal of overburden and associated thermal effects. *Geology* 4:181–84
Healy, J. H., Rubey, W. W., Griggs, D. T., Raleigh, C. B. 1968. The Denver earthquakes. *Science* 161:1301–10
Herget, G. 1973a. Variation of rock stresses with depth at a Canadian iron ore mine. *Int. J. Rock Mech. Min. Sci.* 10:37–51
Herget, G. 1973b. First experiences with the C.S.I.R. triaxial strain cell for stress determinations. *Int. J. Rock Mech. Min. Sci.* 10:509–22
Herget, G. 1976. Field testing of modified triaxial strain cell equipment at Timmins, Ontario. *Rep. MRP/MRL77-2* (IR), Elliot Lake Lab., Canada Cent. Miner. Energy Technol.
Herget, G., Pahl, A., Oliver, P. 1975. Ground stresses below 3000 feet. *Proc. 10th Can. Rock Mech. Symp., Queens Univ., Kingston* 1:281–307
Hooker, V. E., Johnson, C. F. 1969. Near-surface horizontal stresses including the effects of rock anisotropy. *U.S. Bur. Mines Rep. Invest. 7224* 29 pp.
Hooker, V. E., Bickel, D. L., Aggson, J. R. 1972. In situ determination of stresses in mountainous topography. *U.S. Bur. Mines Rep. Invest. 7654* 19 pp.
Hooker, V. E. Aggson, J. R., Bickel, D. L. 1974. Improvements in the three-component borehole deformation gage and overcoring techniques. *U.S. Bur. Mines Rep. Invest. 7894* 29 pp.
Hoskins, E. 1967. *Field and laboratory experiments in rock mechanics.* PhD thesis. Australian National Univ., Canberra.
Howard, G. C., Fast, C. R. 1970. *Hydraulic Fracturing, Monogr. Ser. Soc. Petrol. Eng. of AIME* 2:1–23
Hubbert, M. K., Willis, D. G. 1957. Mechanics of hydraulic fracturing. *AIME Trans.* 210:153–68
Illies, J. H. 1975. Recent and paleo-intraplate tectonics in stable Europe and the Rhinegraben rift system. *Tectonophysics* 29:251–64
Illies, J. H., Greiner, G. 1976. Regionales stress-feld und neotektonik in Mitteleuropa. *Oberrheinische Geol. Abh.* 25:1–40
Jaeger, J. C., Cook, N. G. W. 1969. *Fundamentals of Rock Mechanics.* London: Methuen. 513 pp.
Kehle, R. O. 1964. Determination of tectonic stresses through analysis of hydraulic well fracturing. *J. Geophys. Res.* 69:259–73

Klein, F. W., Einarsson, P., Wyss, M. 1977. The Reykjanes Peninsula, Iceland, earthquake swarm of September 1972 and its tectonic significance. *J. Geophys. Res.* 82:865–88
Kotze, T. J. 1970. Virgin rock stress measurements in the Evander gold field. *C.O.M. Res. Rep. 30/70*, Chamber of Mines of South Africa, Johannesburg. 33 pp.
Leeman, E. R. 1964. The measurement of stress in rock, II. *J. S. Afr. Inst. Min. Metall.* 65:82–114
Leeman, E. R. 1969. The "doorstopper" and triaxial rock stress measuring instruments developed by the C.S.I.R. *J. S. Afr. Inst. Min. Metall.* 69:305–39
Leeman, E. R., Hayes, D. J. 1966. A technique for determining the complete state of stress in rock using a single borehole. *Proc. 1st Congr. Int. Soc. Rock Mech., Lisbon, 1966* 2:17–24
Lockner, D., Byerlee, J. D. 1977. Hydrofracture in Weber sandstone at high confining pressure and differential stress. *J. Geophys. Res.* 82:2018–26
Love, A. E. H. 1934. *A Treatise on the Mathematical Theory of Elasticity.* Cambridge Univ. Press. 643 pp.
McKenzie, D. P. 1969. The relation between fault plane solutions for earthquakes and the directions of the principal stresses. *Bull. Seismol. Soc. Am.* 59:591–601
Miles, P., Herget, G. 1976. Underground stress determinations using the door-stopper method at Timmins, Ontario. *Rep. MRP/MRL76-148 (TR)*, Elliot Lake Lab., Can. Cent. Min. Energy Technol.
Mills, J. M., Fitch, T. J. 1977. Thrust faulting and crust-upper mantle structure in east Australia. *Geophys. J.* 48:351–84
Molnar, P., Wyss, M. 1972. Moments, source dimensions and stress drops of shallow focus earthquakes in the Tonga-Kermadec arc. *Phys. Earth Planet. Inter.* 6:263–78
Newman, D. B., Clark, B. R. 1977. Near-surface in situ stress measurements, Anna, Ohio earthquake zone. *EOS Trans. Am. Geophys. Union.* 58:493
Nichols, T. C. 1975. Deformations associated with relaxation of residual stresses in a sample of Barre granite from Vermont. *U.S. Geol. Surv. Prof. Pap. 875*, 32 pp.
Obert, L. 1962. In situ determination of stress in rock. *Min. Eng.* 14:51–58
Pallister, G. F. 1969. *The measurement of virgin rock stress*, MSc thesis. Univ. Witwatersrand, Johannesburg, South Africa
Price, N. J. 1966. *Fault and Joint Development in Brittle and Semi-brittle Rock.* London: Pergamon. 176 pp.
Price, N. J. 1974. The development of stress systems and fracture patterns in undeformed sediments. In *Advances in Rock Mechanics, Proc. 3rd Congr. Int. Soc. Rock Mech.* IA:487–96
Raleigh, C. B. 1974. Crustal stress and global tectonics. See Price 1974, pp. 593–97
Raleigh, C. B., Healy, J. H., Bredehoeft, J. D. 1972. Faulting and crustal stress at Rangely, Colorado. In *Flow and Fracture of Rocks, Am. Geophys. Union Monogr.* 16:275–84
Raleigh, C. B., Healy, J. H., Bredehoeft, J. D. 1976. An experiment in earthquake control at Rangely, Colorado. *Science* 191:1230–37
Ranalli, G., Chandler, T. E. 1975. The stress field in the upper crust as determined from in situ measurements. *Geol. Rundsch.* 64:653–74
Riecker, R. E. 1977. State of stress in the lithosphere. *EOS Trans. Am. Geophys. Union* 58:597–99
Roberts, A., Hawkes, I., Williams, F. T., Dhir, R. K. 1964. A laboratory study of the photoelastic stressmeter. *Int. J. Rock Mech. Min. Sci.* 1:441–58
Roegiers, J. C., Fairhurst, C. 1973. The deep stress probe—a tool for stress determination. In *New Horizons in Rock Mechanics, Proc. 14th Symp. Rock Mech.*, ed. H. Hardy, R. Stefanko, pp. 755–60. New York: ASCE
Rummel, F., Jung, R. 1975. Hydraulic fracturing stress measurements near the Hohenzollern Graben—structure, S.W. Germany. *Pure Appl. Geophys.* 113:321–30
Salamon, M. D. G., Ryder, J. A., Ortlepp, W. D. 1964. An analogue solution for determining the elastic response of strata surrounding tabular mining excavations. *J. S. Afr. Inst. Min. Metall.* 65:115–37
Sbar, M. L., Marshak, S., Engelder, T., Plumb, R. 1977. Near surface *in situ* stress measurements near the San Andreas fault, Palmdale, California. *EOS Trans. Am. Geophys. Union.* 58:1123
Sbar, M. L., Sykes, L. R. 1973. Contemporary compressive stress and seismicity in eastern North America: an example of intraplate tectonics. *Geol. Soc. Am. Bull.* 84:1861–82
Sbar, M. L., Sykes, L. R. 1977. Seismicity and lithospheric stress in New York and adjacent areas. *J. Geophys. Res.* In press.
Scheidegger, A. E. 1964. The tectonic stress and tectonic motion direction in Europe and western Asia as calculated from earthquake fault-plane solutions. *Bull. Seism. Soc. Am.* 54:1519–28
Seagar, J. S. 1964. Pre-mining lateral

pressures. *Int. J. Rock Mech. Min. Sci.* 1:413–19
Stephenson, B. R., Murray, K. J. 1970. Application of the strain rosette relief method to measure principal stresses throughout a mine. *Int. J. Rock Mech. Min. Sci.* 7:1–22
Stewart, I. C. F., Denham, D. 1974. Simpson Desert earthquake, Central Australia, August, 1972. *Geophys. J.* 39:335–41
Swolfs, H. S. 1975. Determination of *in situ* stress orientation in a deep gas well by strain relief techniques. *Terra Tek Rep. TR* 75–43
Swolfs, H. S., Handin, J., Pratt, H. R. 1974. Field measurements of residual strain in granitic rock masses. See Price 1974, 11A: 563-68
Sykes, L. R., Sbar, M. L. 1973. Intraplate earthquakes, lithospheric stresses and the driving mechanism of plate tectonics. *Nature* 245:298–302
Thatcher, W. 1972. Regional variations of seismic source parameters in the northern Baja California area. *J. Geophys. Res.* 77:1549–65
Thatcher, W., Hanks, T. C. 1973. Source parameters of southern California earthquakes. *J. Geophys. Res.* 78:8547–76
Tucker, B. E., Brune, J. N. 1973. Seismograms, S-wave spectra, and source parameters for aftershocks of San Fernando earthquake. In *San Fernando, California Earthquake of February 9, 1972, Geological and Geophysical Studies*, 3:69–122. U.S. Dept. Commer.
Tucker, B. E., Brune, J. N. 1977. Source mechanism and M_b–M_s analysis of aftershocks of the San Fernando earthquake. *Geophys. J.* 49:371–426
Tullis, T. E. 1977a. Reflections on measurement of residual stress in rock. *Pure Appl. Geophys.* 115:57–68
Tullis, T. E. 1977b. Stress measurements by shallow overcoring on the Palmdale uplift. *EOS Trans. Am. Geophys. Union.* 58:1122
Van Heerden, W. L. 1971. Stress measurements in coal pillars. *Proc. 2nd Congr. Int. Soc. Rock Mech., Belgrade, 1970.* 11:4–16
Van Heerden, W. L. 1976. Practical application of the C.S.I.R. triaxial strain cell for rock stress measurements. In *Exploration for Rock Engineering*, ed. Z. T. Bieniawski. 1:189–94
Van Heerden, W. L., Grant, F. 1967. A comparison of two methods for measuring stress in rock. *Int. J. Rock Mech. Min. Sci.* 4:367–82
Voight, B. 1966. Beziehung zwischen grossen horizontalen Spannungen in Gebirge und der Tektonik und der Abtragung. *Proc. 1st Congr. Int. Soc. Rock Mech., Lisbon, 1966* 11:51–56
Voight, B., St. Pierre, B. H. P. 1974. Stress history and rock stress. See Price 1974, 11A:580–82
Von Schonfeldt, H. A., Kehle, R. O., Gray, K. E. 1973. Mapping of stress field in the upper earth's crust of the U.S. *Final Tech. Rep. USGS (14-08-0001-122278)* 40 pp.
Ward, P. L. 1971. New interpretation of the geology of Iceland. *Geol. Soc. Am. Bull.* 82:2991–3012
Wyss, M., Molnar, P. 1972. Source parameters of intermediate and deep focus earthquakes in the Tonga arc. *Phys. Earth Planet. Int.* 6:279–92
Zoback, M. D., Healy, J. H. 1977. In-situ stress measurements near Charleston, South Carolina. *EOS Trans. Am. Geophys. Union* 58:493
Zoback, M. D., Healy, J. H., Roller, J. C. 1977. Preliminary stress measurements in Central California using the hydraulic fracturing technique. *Pure Appl. Geophys.* 115:135–52
Zoback, M. D., Rummel, F., Jung, R., Raleigh, C. B. 1977. Laboratory hydraulic fracturing experiments in intact and prefractured rock. *Int. J. Rock Mech. Min. Sci. Geomech. Abstr.* 14:49–58
Zoback, M. D, Pollard, D. D. 1978. Hydraulic fracture propagation and the interpretation of pressure-time records for in-situ stress determinations. Submitted to *19th Symp. Rock Mech., Lake Tahoe, Calif., May 1978*

Ann. Rev. Earth Planet. Sci. 1978. 6:437–56

VOLCANIC EVOLUTION OF THE CASCADE RANGE

Alexander R. McBirney
Center for Volcanology, University of Oregon, Eugene, Oregon 97403

INTRODUCTION

Much of the recent interest in andesites has been stimulated by the hope that these rocks, which are so characteristic of regions of plate convergence, may provide a much needed test of the basic concept of subduction. If oceanic lithosphere is being returned to the mantle and continents at rates that balance its formation by seafloor spreading and sedimentation, and if, as many believe, the igneous processes associated with subduction provide the mechanism by which crustal components are returned to the continent, it is obviously essential to evaluate the dynamic aspects of orogenic volcanism in the light of the earth's total geochemical balance.

The Cascade Range of the northwestern United States is an almost ideal place to do this. Although the system lacks some of the features considered typical of convergent plate boundaries, it has a well-preserved record of older rocks and provides a rare perspective of the development of such a system through time. In addition, there are marked variations in the crustal structure along the length of the system that make it possible to examine the effects of differing crustal features on the nature and composition of igneous activity, both in space and time. Numerous detailed geologic and geochemical studies have provided much new information on this system and have opened fresh insights into the magmatic evolution of the continental margin during much of Cenozoic time.

EVOLUTION OF THE CASCADE SYSTEM

The modern volcanic chain that extends from British Columbia to northern California is only the most recent of several igneous belts or zones that have followed the Pacific margin of North America since late Paleozoic time. There is no visible record of Precambrian igneous activity and little evidence for volcanism prior to the last part of the Paleozoic era, but it is clear that there was an important volcanic episode that began during the Permian period and continued well into Early Triassic time. Submarine lavas of this age are exposed in northern California, northeastern Oregon, and northern Washington, and Gilluly (1963) may well be

0084-6597/78/0515-0437$01.00

STRESS STATE, POROSITY, PERMEABILITY AND BREAKDOWN PRESSURE AROUND A BOREHOLE DURING FLUID INJECTION

Nobuo Morita, The Univers
K. E. Gray, The Universi
C. M. Kim, B. J.

Proceedings of the 22nd U.S. Symposium on Rock Mechanics: Rock Mechanics from Research to Application held at Mass. Inst. of Tech., June 28-July 2, 1981 compiled by H.H. Einstein

INTRODUCTION

Generally, boundary value problems with pore fluid pressure have been solved by applying Biot's linear stress-strain theorem. However, his assumptions do not always hold for real rocks. Actual rock consists of various materials such as sand particles, cementing materials, loose materials and pore fluid. If these materials are loaded, the crack opening, the crack propagation and sliding crack interfaces occur together with continuous deformation of constitutive materials. Hence, the stress induced by fluid pressure causes significant microscopic dislocation and in a certain stress state the strain caused by these dislocations is much more significant than the continuous deformation upon which Biot's linear stress-strain theorem is developed.

During fluid injection, various stress states occur ranging from compression to extension. Such boundary value problems require a non-linear stress strain relation reflecting real rock behavior. In a previous report,[1] a non-linear stress-strain relation was developed and used to show what happens around a borehole during fluid injection or hydraulic fracturing operations.

In addition to the non-linearity of stress-strain, changes in porosity and permeability also affect fracture initiation since the rigidity of rock depends upon the stress state induced by fluid flow. These factors are also taken into account in the diffusivity equation.

A simple simulation model was made to predict phenomena occuring during fluid injection; the effect of fluid injection rate and effect of tectonic stress field upon fracture initiation are discussed.

THEORY OF ELASTICITY FOR NON-LINEAR POROUS BODIES WITH FLUID FLOW

In a previous study,[1] the stress-strain behavior of Berea, Ohio, and Pecos sandstones were measured extensively under triaxial loading paths with both compression and extension tests at different pore fluid pressures. These tests showed that four modes can arise in the stress-strain curves up to failure: an initial non-linear portion; a linear portion; a final non-linear portion; and volume change of the rock matrix due to pore fluid pressure. The characteristics of these modes were studied, and the following non-linear model was developed to represent the important characteristics, i. e., the four modes, of the behavior of sandstones by means of a constitutive equation in such a way as to satisfy certain mathematical requirements.

$$\varepsilon_{ij} = \frac{1+\nu}{E}\bar{\sigma}_{ij} - \frac{\nu}{E}\delta_{ij}\bar{\sigma}_{kk} - \frac{1-2\nu_i}{E_i}p\delta_{ij} + \varepsilon^N_{ij} + \varepsilon^P_{ij} \quad (1)$$

where,

ε_{ij}, ε^N_{ij}, ε^P_i = total, initial non-linear and plastic parts of strain tensors, respectively.

E, ν, E_i, ν_i = Young's modulus and Poisson's ratio for rock and interpore materials, respectively.

$\bar{\sigma}_{ij} = \sigma_{ij} + P\delta_{ij}$

σ_{ij}, P = total stress and pore fluid pressure

In the above equation, ε^N_{ij} is the total strain caused by opening and closing of flat pores around pore capillaries and ε^P_{ij} is the strain caused by growth of micro fractures and friction between matrix grains. The initial non-linear part, ε^N_{ij}, of strain is given by:

$$\varepsilon^N_{ij} = a_{ik}\ell_{mk}\ell_{nj}\delta_{mn}(1-e^{\beta\bar{\sigma}'_{mm}})... \quad (2)$$

where $\bar{\sigma}'_{ij}$ and ℓ_{ij} are the principal stresses and the directional cosines, respectively. The coefficient a_{ij} is a tensor of order four and follows transformation rules. Since rock is generally isotropic along the bedding place, the coefficient a_{ij} is simplified as follows.

$$[a_{ij}] = \begin{bmatrix} a_{11} & a_{12} & a_{13} & & & \\ a_{12} & a_{11} & a_{13} & & 0 & \\ a_{13} & a_{13} & a_{33} & & & \\ & & & a_{44} & & \\ & 0 & & & a_{44} & \\ & & & & & 2(a_{11}-a_{12}) \end{bmatrix} \quad (3)$$

where a_{12} and a_{13} are equal to zeros since this non-linear strain occurs in the direction of added stress if the bedding plane coincides with the load.

For the final non-linear part, ε^P_{ij}, an incremental stress-strain relation based upon a kinemetic work-hardening theory is used in this work, that is,

$$d\varepsilon^P_{ij} = \frac{\bar{S}_{kl}d\alpha_{kl}}{2b\bar{J}_2} \quad (4)$$

where

$$J_1 = \bar{\sigma}_{kk} \qquad \bar{J}_2 = 3\bar{S}_{kl}\bar{S}_{kl}$$

$$d\alpha_{ij} = b(\bar{\beta})\ (d\varepsilon_{ij}^{P} - \frac{1}{3}\, d\varepsilon_{kk}^{P}\delta_{ij})$$

$$\bar{\beta} = \alpha_{lm}\alpha_{lm}/(3\sigma_t + J_1)$$

$$\bar{S}_{ij} = \bar{\sigma}_{ij} - \frac{1}{3}\bar{\sigma}_{kk}\delta_{ij} - \alpha_{ij} \qquad (5)$$

σ_t = tensile rock strength

The functions b and g are to be determined empirically from non-linear stress-strain curves.

The equation of equilibrium is

$$\sigma_{ij,\ j} + F_i = 0 \qquad (6)$$

If displacements are small, the strain-displacement relation is

$$\varepsilon_{ij} = \frac{1}{2}(u_{i,\ j} + u_{j,i}) \qquad (7)$$

The equations so far developed in this paper are based upon the assumption that the deformation is infinitesimal. In this case, it is not necessary to distinguish between Lagranian and Eulerian coordinates. From now on, the Lagrangian coordinate system is used to take into account the convection term of fluid flow moving with the rock phase.

The diffusivity equation around a borehole is written as

$$\frac{1}{r}\frac{\partial}{\partial r}\left(\frac{r\rho k_r}{\mu}\frac{\partial P}{\partial r}\right) = \frac{\partial}{\partial t}(\phi\rho) + \frac{1}{r}\frac{\partial}{\partial r}(r\rho\phi\dot{u})$$

where

$$\rho = \rho_0 e^{c\,(P-P_o)} \qquad (8)$$

where the rock phase moves with velocity $\dot{u}$. This equation is applicable to flow of a single phase fluid with small compressibility.

There are various models for porosity vs. pressure based upon elastic deformation between sphere-sphere contact. However, since the non-linear stress-strain relation is given in this paper, it is more accurate to express the porosity change by strain components. The total volume after deformation of a unit cube is

$$V_T = 1 + \varepsilon_{ii} \qquad (9)$$

where ε_{ij} is given by Equation 1. Since the porosity change from linearly elastic behavior is given by

$$\phi - \phi_0 = \left(\frac{1-2\nu}{E} - \frac{1-2\nu_i}{E_i}\right)\bar{\sigma}_{ii} \qquad (10)$$

which can be derived from the strain energy equation, the void space caused by linear part is

$$(1 + \varepsilon_{ii}^{e})\ \left(\frac{1-2\nu}{E} - \frac{1-2\nu_i}{E_i}\right)\bar{\sigma}_{ii} + \phi_0$$

where

$$\varepsilon_{ii}^{e} = \frac{1-2\nu}{E}\bar{\sigma}_{kk} - \frac{3(1-2\nu_i)}{E_i}\,p \qquad (11)$$

Since the initial non-linear strain is caused by pore opening and closing, and the final non-linear strain is caused by growth of micro-fractures, these non-linear strains only increase the void space, but not grain volume. Hence the total void space is

$$V_\phi = (1 + \varepsilon_{ii}^{e})\left[\left(\frac{1-2\nu}{E} - \frac{1-2\nu_i}{E_i}\right)\bar{\sigma}_{ii} + \phi_0\right] + \varepsilon_{ii}^{N} + \varepsilon_{ii}^{P} \qquad (12)$$

Thus the porosity is expressed by

$$\phi = \frac{(1+\varepsilon_{ii}^{e})\left[\left(\frac{1-2\nu}{E} - \frac{1-2\nu_i}{E_i}\right)\bar{\sigma}_{ii} + \phi_0\right] + \varepsilon_{ii}^{N} + \varepsilon_{ii}^{P}}{1 + \varepsilon_{ii}^{e} + \varepsilon_{ii}^{N} + \varepsilon_{ii}^{P}} \qquad (13)$$

For sufficiently small strain, it can be approximated by

$$\phi = \phi_0 + \left(\frac{1-2\nu}{E} - \frac{1-2\nu_i}{E_i}\right)\bar{\sigma}_{ii} + (1-\phi_0)\varepsilon_{ii}^{N} + (1 - \phi_0)\varepsilon_{ii}^{P} \qquad (14)$$

The change in permeability around a hole is anisotropic since all the principal stresses are different. The permeability change under this complicated stress state may be more suitably expressed by strains than stress state since it is more directly related to strains. Consider a rock cube consisting of flat cracks and pores between spherical grains. Since the non-linearity at tensile stress and low compressive stress is mainly due to the opening and closing of these flat cracks, the permeability change at this stress state is significantly affected by the permeability of these flat cracks. On the other hand, the permeability change at higher compressive stress level is mainly due to the change in pore space and specific surface in the pores existing between grains.

In this study, the total permeability is assumed to be a superposition of the permeabilities due to flat cracks and pores existing between spherical grains. The final form of permeability change under triaxial loading path is given by

$$k^{ii} = k_o^{ii}\left[c^i\frac{\phi_{\ell+p}}{\phi^0_{\ell+p}}(1+d_m^i\varepsilon_{mm}^{\ell+p})^2 + c^i\frac{\phi_{Nj}}{\phi^0_{Nj}}(1+h_j^i\varepsilon_{jj}^{N})^2 + c_k^i\frac{\phi_{Nk}}{\phi^0_{Nk}}(1+h_k^i\varepsilon_{kk}^{N})^2\right]$$

$$c^i + c_j^i + c_k^i = 1 \qquad (15)$$

$$\phi^0_{\ell+p} = \phi_0 - (\phi^0_{Ni} + \phi^0_{Nj} + \phi^0_{Nk})$$

$$\phi_{\ell+p} = \phi^0_{\ell+p} + \left(\frac{1-2\nu}{E} - \frac{1-2\nu_i}{E_i}\right)\bar{\sigma}_{ii} + (1-\phi_0)\varepsilon_{ii}^{P} \qquad (16)$$

where k^{ii}, k_o^{ii} = permeabilities in principal directions and their original values at atmospheric pressure.

$\phi_{\ell+p}$, $\phi^0_{\ell+P}$ = porosity between spherical grains and its value at atmospheric pressure, respectively.

$$\phi^0_{Nj} = -a_{jj}(1-\phi_0)$$

$$\phi_{Nj} = \phi^0_{Nj} + (1-\phi_0)\epsilon^N_{jj} \qquad (17)$$

ϕ_{Nj}, ϕ^0_{Nj} = porosity of microfractures whose flat surface is perpendicular to the j-th principal stress direction, and its value at atmospheric pressure, respectively. a_{jj} is given by Equation 3.

c^i, c^i_j, c^i_k, d^i_m, h^i_j, h^i_k = constants to be determined by axial and radial permeability measurements under triaxial loading path.

In the above equation, i denotes one principal direction and j and k denote the other two principal directions.

BOUNDARY CONDITIONS, LOADING HISTORY AND INPUT DATA

Since the stress state depends upon the loading path, the boundary conditions and the initial conditions are specified as follows. Initially the rock which formed near the earth's surface sank to a certain depth. The pore pressure, the overburden pressure, and the horizontal stress linearly changed to the present status, where the present status is

(A) Pore Fluid Pressure = P_i
Overburden Load = σ_{ax}
Horizontal Stress = σ_H

After that, a borehole is drilled. The pressure in the borehole is kept small enough to balance the pore fluid, then

(B) Pore Fluid Pressure = P_i
Overburden Load = σ_{ax}
Horizontal Stress = σ_H
Total Borehole Stress = P_i

After that, when borehole pressure is increased until failure occurs at the borehole, then

(C) Pore Fluid Pressure ($r\to\infty$) = P_i
Borehole Pressure = $P_i + \Delta P(t)$
Horizontal Stress ($r\to\infty$) = σ_H
Total Borehole Stress = $P_i + \Delta P(t)$

Input data are given as follows

k_0^{11} = permeability of Berea, 320 md along the bedding plane

ϕ_0 = porosity of Berea, .207 without load

μ = water viscosity, 1 cp

C = water compressibility, 2×10^{-6} vol/vol/psi

r_w = radius of borehole, .2 ft.

σ_t = tensile strength of Berea, 0.2 kpsi

P_i = .45 psi/ft x 10,000 ft.

Depth = 10,000 ft.

Rate of borehole pressure increment and tectonic stress field were varied. The functions and parameters involved in the constitutive equation 1 were evaluated by least square fitting of extension and compression stress strain curves under triaxial loading paths given in Figures 1, 2 and 3. The coefficients of the permeability equation were determined using the empirical data of horizontal permeability measured under triaxial loading condition.[2]

NUMERICAL RESULTS AND DISCUSSIONS

The Behavior of Non-Linear Material

The rock used to determine non-linear stress-strain coefficients was Berea sandstone. The empirically measured stress-strain relations are shown in Figures 1, 2, and 3. These data were numerically processed and the necessary coefficients in the non-linear stress-strain relation were determined. Figures 4 to 6 show the theoretical non-linear stress-strain curves. The recoverability of original data is satisfactory and reflects the characteristics of the original data.

For the hydrostatic loading path without pore pressure, Figures 7 and 8 show that the porosity initially decreases rapidly and approaches a linear curve. The initial rapid porosity change is due to the closing of pore openings and the linear change of porosity for high confining pressure is due to the linearity of the bulk modulus of rock and inter-pore material in that condition. For hydrostatic loading with pore pressure equal to the confining pressure, the porosity is constant because, under this condition, the pore space shrinks together with the rock frame. For axial loading with confining pressure, the porosity decreases initially but starts increasing rapidly before failure occurs.

For extension stress state under confining pressure, the porosity increases while the axial load is released. The Porosity increases rapidly before it fails.

Figures 9 and 10 show the change in horizontal permeability. For compression load, the permeability changes significantly for small load until the flat cracks around the pore completely close. The change is relatively small for higher load and the permeability starts increasing if failure of the rock starts developing. The change in permeability for extension load is also small for high triaxial stress state but it becomes significantly larger

while micro fracture develops for tensile stress.

Phenomenon Around a Borehole During Fluid Injection up to Fracture Initiation

The numerical model used in this work is a radial model, with incrementally increased load and fluid pressure. Figure 11 shows schematically the feedback loop for fluid injection up to fracture initiation. As the borehole pressure is increased, fluid pressure, stress field, permeability and porosity simultaneously change. The feedback loop is continued until sufficient convergence is obtained. After that, a new cycle starts increasing the borehole pressure. This procedure is continued up to failure of the rock where the empirical failure equation is satisfied.

Figures 12 to 15 show the computation results for stress around a borehole during fluid injection up to failure. It is assumed to be performed for a horizontal bedding plane at 10,000 feet so that the original axial stress, horizontal stress, and the pore pressure are 10 kpsi, 7 kpsi, and 4.5 kpsi, respectively.

The radial stress σ_r is equal to the pore pressure before fracture initiation and its stress concentration is high around the borehole. The radial stress increases with the borehole pressure and the stress concentration disappears.

The tangential stress σ_θ is high on the compression side before fluid injection starts. As fluid injection proceeds, the tangential stress becomes smaller in compression and finally the rock fails when $\sigma_\theta + P = \sigma_t$ is satisfied at 45.5 seconds after fluid injection starts. The tangential stress σ_θ does not change significantly before fracture starts since the stress concentration is relaxed because of the significant non-linearity of the stress-strain curve.

The axial stress σ_{ax} is gradually increasing during the fracture operation mainly because of the increase of pore fluid pressure.

Figure 13 shows the fluid pressure around a borehole. Initially, the pressure distribution around a borehole is logarithmic. As the fluid injection proceeds, it becomes linear around a borehole due to the increase in permeability adjacent to the borehole.

Figure 14 shows the change in porosity. Without any load, the porosity of Berea sandstone is .207. It is compacted to .2028 at 10,000 feet. After a borehole is drilled, the stress in the radial direction is relaxed which causes an increase in porosity around the borehole. As fluid injection proceeds, the stress in the tangential direction is relaxed which results in the growth of micro fracture in this direction and the porosity increases.

Figure 15 shows the change in permeability. The permeability along the bedding plane is 320 md without load. It becomes about 270 md at 10,000 feet due to compaction. After drilling a borehole, the radial permeability becomes around 269 md at the borehole due to the stress concentration of the tangential stress. The permeability increases with fluid injection, and before fracture initiation it becomes more than 317 md at the borehole.

Effect of Fluid Injection Rate upon Fracture Initiation: Table 1 shows the effect of well pressure increment upon fracture initiation. In this table, the original pore pressure is subtracted from the stress state since the effective stress concept approximately holds for both stress-strain and failure of sandstone.

Fracture initiates with lower well pressure for lower pressure increment, because for lower pressure increment, the pore fluid around the borehole sufficiently increases, which decreases the effective stress, and the rigidity of the rock in the tangential direction of the borehole. For sealed boundary, the fracture initiates at the borehole with extremely high pressure. This phenomenon is very similar to the significant difference of the strength between the jacketed and non-jacketed sample for triaxial tension and compression tests.

Effect of Tectonic Force: Table 2 shows that the effect of confining pressure is not proportional to the effective confining stress. The lower the confining stress, the stronger the apparent rock strength due to the non-linearity of the rock for lower stress state.

Effect of the Rigidity of Upper and Lower Layers Bounding the Reservoir: If the upper and lower layers bounding the reservoir are rigid, they don't deform and increase the local axial stress suppressing the reservoir deformation. On the other hand if they are soft, they deform until the axial stress of the reservoir is in equilibrium with the overburden pressure. These two cases correspond to plane strain and plane stress cases.

Table 3 shows a comparison of the fracture initiation under these two conditions. A slightly higher borehole pressure is required for plane strain cases. Actually the state of stress is three dimensional and the actual fracture initiation pressure may be between these two extreme cases.

CONCLUSIONS

1. Sandstones generally exhibit significant non-linearity. The application of non-linear stress-strain behavior, closely approximating real data is important, particularly for boundary value problems in which the stress state varies over a wide range.

2. Porosity and permeability of rock under an arbitrary stress state can be estimated using the strain components. This approach is more accurate than the conventional methods where the change in porosity and permeability are expressed by stress components.

3. For compaction problems, compaction of the rock frame is an important as the change in porosity for estimating pressure distribution around the borehole.

4. Fracture initiation pressure depends upon fluid pressure around the hole. A larger pressure is required for larger fluid pressure gradient.

5. Fracture initiation pressure does not proportionally increase with the confining stress field, as predicted by Biot's linear theorem of stress and strain. It is significantly larger for small confining pressure and tends to be closer to that predicted by Biot's theorem for higher confining pressures.

6. The rigidity of upper and lower layers bounding a reservoir does not significantly change fracture initiation pressure for a vertical fracture, although it may change for a horizontal one.

REFERENCES

1. Morita, N. and Gray, K. E. "A Constitutive Equation for Non-Linear Stress-Strain Curves in Rocks and Its Application to Stress Analysis Around a Borehole During Drilling," SPE 9728, Presented at the 55th Annual Fall Technical Conference and Exhibition, SPE, Dallas, Texas, September 21-24, 1980.

2. Thompson, T. W., Kim, C. M., Kelkar, S., and Gray, K. E. "The Influence of Elevated Pore Pressure on the Mechanical and Flow Behavior of Berea Sandstone and Leuders Limestone," 20th U. S. Symposium on Rock Mechanics, Austin, June 4-6, 1979. PP171-178.

Well Pressure Increment	Effective Fracture Initiation Pressure (P_w-P_o)
.1 Kpsi/sec	4.54 Kpsi
1.0	4.60
10.0	4.70
Sealed	7.38

Data: Effective confining stress (σ_h+P_o)=-2.5Kpsi
Effective axial stress $(\sigma_{ax}+P_o)$=-5.5Kpsi
Other data are given in the text.

TABLE 1 FRACTURE INITIATION VS. WELL PRESSURE INCREMENT

Effective Confining Pressure (σ_H+P_o)	Effective Fracture Initiation Pressure (P_w-P_o)
-1.5 Kpsi	3.08 Kpsi
-2.5	4.60
-3.5	6.10
-4.5	7.60

Data: Effective axial load $(\sigma_{ax}+P_o)$=-5.5Kpsi
Well pressure increment .1 Kpsi/sec
Other data are given in the text.

TABLE 2 FRACTURE INITIATION VS. EFFECTIVE CONFINING PRESSURE

Effective Confining Pressure(σ_H+P_o)	Effective Fracture Initiation Pressure (P_w-P_o)	
	Plane Strain	Plane Stress
-1.5 Kpsi	3.08 Kpsi	2.81 Kpsi
-2.5	4.60	4.38
-4.5	7.60	Horizontal Fracture

Data: Effective axial load $(\sigma_{ax}+P_o)$=-5.5Kpsi
Well pressure increment = .1 Kpsi/sec
Other data are given in the text.

TABLE 3 FRACTURE INITIATION FOR PLANE STRESS AND PLANE STRAIN

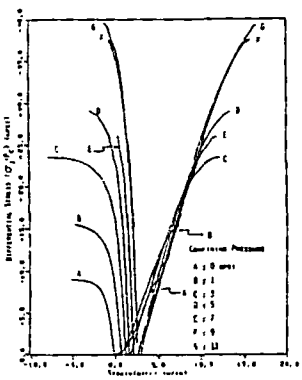

FIG. 1 EXPERIMENTAL STRESS-STRAIN CURVES FOR COMPRESSION TESTS (BEREA SANDSTONE: P_o=0; HORIZONTAL BEDDING PLANE)

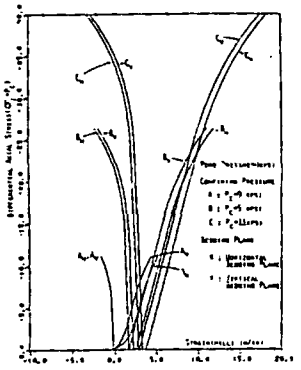

FIG. 4 THEORETICAL STRESS-STRAIN CURVES FOR COMPRESSION LOADING (BEREA SANDSTONE; HORIZONTAL AND VERTICAL BEDDING PLANE: P_o=0)

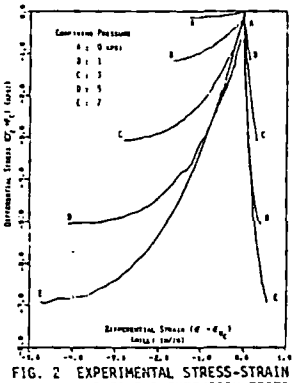

FIG. 2 EXPERIMENTAL STRESS-STRAIN CURVES FOR EXTENSION TESTS (BEREA SANDSTONE: P_o=0; HORIZONTAL BEDDING PLANE)

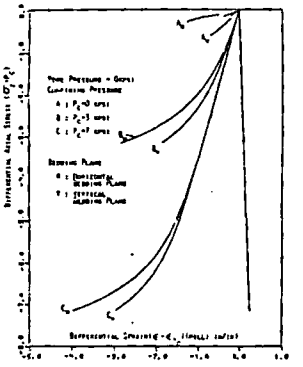

FIG. 5 THEORETICAL STRESS-STRAIN CURVES FOR EXTENSION LOADING (BEREA SANDSTONE: HORIZONTAL AND VERTICAL BEDDING PLANES: P_o=0)

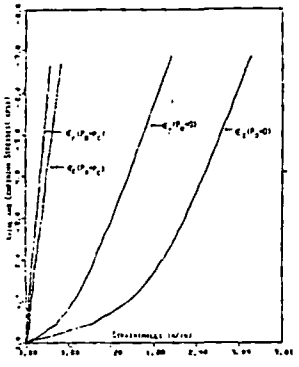

FIG. 3 EXPERIMENTAL STRESS-STRAIN CURVES FOR HYDROSTATIC LOADING (BEREA SANDSTONE; HORIZONTAL BEDDING PLANE)

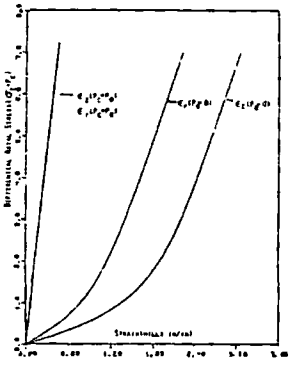

FIG. 6 THEORETICAL STRESS-STRAIN CURVES FOR HYDROSTATIC LOADING (BEREA SANDSTONE; HORIZONTAL BEDDING PLANE)

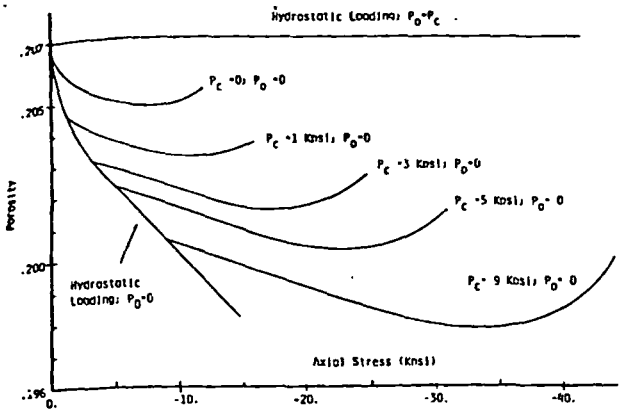

Fig. 7 Porosity vs. Axial Stress for Compression Stress States

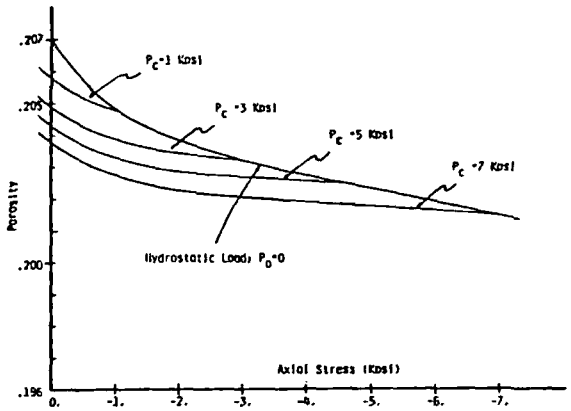

Fig. 8 Porosity vs. Axial Stress for Extension Stress States

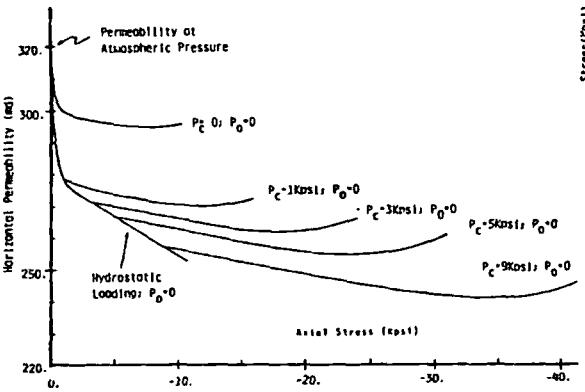

Fig.9 Horizontal Permeability vs. Axial Stress for Compression Stress States

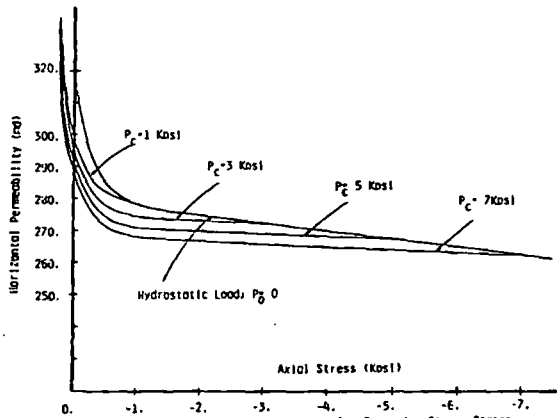

Fig.10 Horizontal Permeability vs. Axial Stress for Extension Stress States

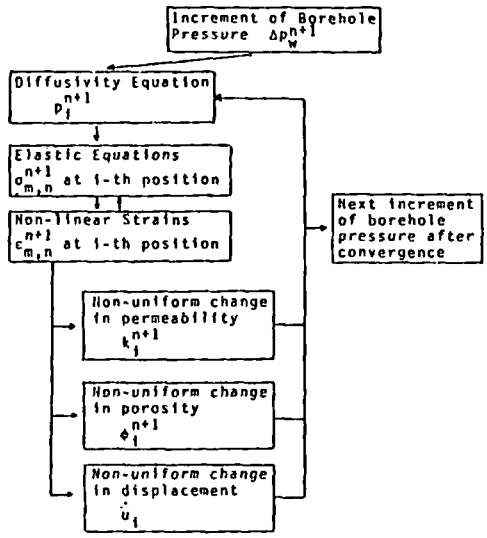

Fig. 11 Feed-back Loop for Fluid Injection up to Fracture Initiation.

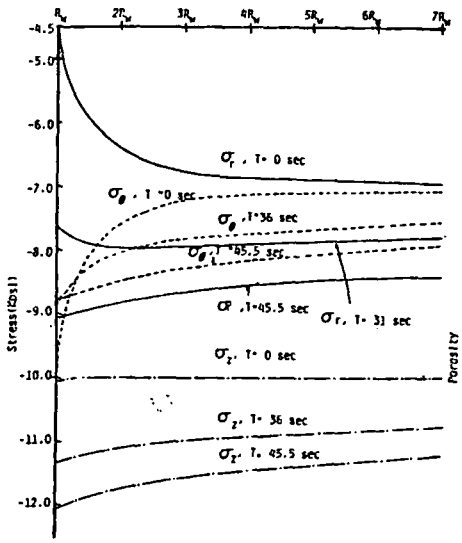

Fig.12 State of Stress around a Borehole during Fracturing Operation(Berea Sandstone)

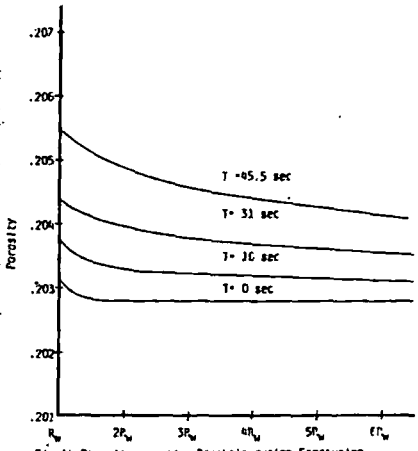

Fig.14 Porosity around a Borehole during Fracturing Operation(Berea Sandstone)

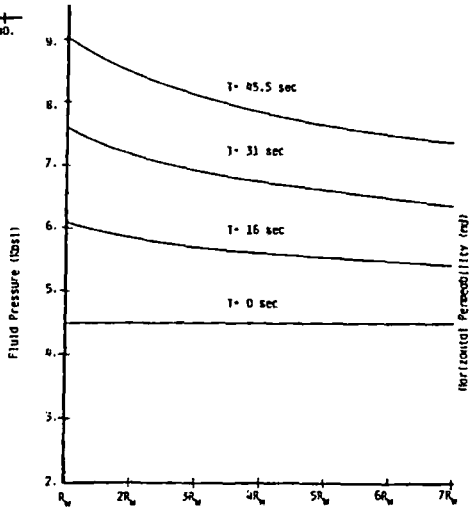

Fig.13 Fluid Pressure Distribution around a Borehole during Fracturing Operation(Berea Sandstone)

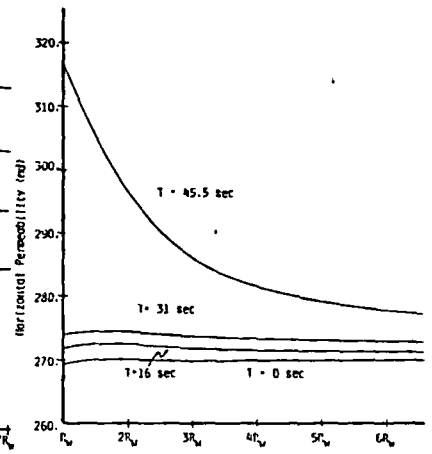

Fig.15 Permeability Distribution around a Borehole during Fracturing Operation(Berea Sandstone)

UDC 669.71.09

Solubility of sodium salts in aluminate solutions and the composition of the equilibrium solid phases

N I Eremin, V F Kocherzhinskaya and A I Timoshenko (Leningrad Mining Institute. Irkutsk Branch, All-Union Aluminium and Magnesium Institute)

During the treatment of aluminium raw materials by the Bayer method compounds of fluorine, sulphur and carbonates are decomposed by the alkaline solution and pass into solution in the form of sodium fluoride, sulphate, sulphide and carbonate. Data on the solubility of these compounds in aluminate solutions are limited[1,2]), but they are of great importance in the selection of a rational technique for their extraction from the process.

The purpose of our investigations was to study the solubility of these compounds in aluminate solutions and the composition of the obtained equilibrium solid phases over a wide range of concentrations and temperatures above 100°C. The investigations were carried out by a thermostatic method on synthetic aluminate solutions with Na_2O_{cu} concentrations of 100, 150, 200, 250, 300 and 350 and with caustic ratios of 1.7 and 3.5 at 125, 150, 200, 250 and 300°C.

Autoclaves with a needle valve, designed at the All-Union Aluminium and Magnesium Institute[3]), were used. A feature of the autoclaves is the reliable airtightness and the complete elimination of packing between the connecting parts. The autoclaves were heated and held at the required temperatures in a salt thermostat, where a eutectic mixture of sodium nitrate and nitrite and potassium nitrate was used as the heating medium. The investigations at 125°C were carried out in an air thermostat.

The holding time for the attainment of equilibrium was established by preliminary tests with solutions at the two extreme concentrations 100 and 350g/l Na_2O_{cu}. At the end of the holding time the liquid phase was filtered into a receiver at the experimental temperature. The autoclaves were then rapidly cooled with water and unloaded. In the liquid phase in the receiver the Al_2O_3, Na_2O_{cu}, Na_2O_{cb}, F and Na_2O_{sulph} contents were determined by volumetric methods. The solid phase was dried between sheets of filter paper, washed with alcohol, and analysed by chemical crystal, optical and X-ray diffraction methods. Chemically pure reagents (sodium carbonate, sodium sulphate and sodium fluoride) were used for the investigation.

Comparison of the solubility curves for Na_2CO_3 (fig. 1) according to our data, with the data of Tsymbal at 125°C [1]) and Bernshtein and Matsenok at 250°C [2]) showed close similarity in the results. The solubility isotherms for sodium carbonate in the range of concentrations which we investigated are given in fig. 2 and show quantitative dependence of the solubility on the concentration of the initial aluminate solution with different caustic ratios at various temperatures. With increase in temperature the solubility of sodium carbonate increases a little, and with increase in the concentration of the solution it decreases substantially.

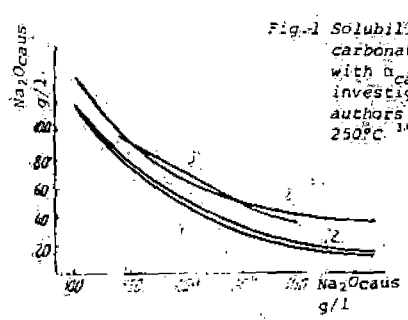

Fig.1 Solubility isotherms for sodium carbonate in aluminate solutions with a_{caus}=1.5 according to our investigations [1,4]), and other authors [2,3]) at 125 [1,2]) and 250°C [3,4]).

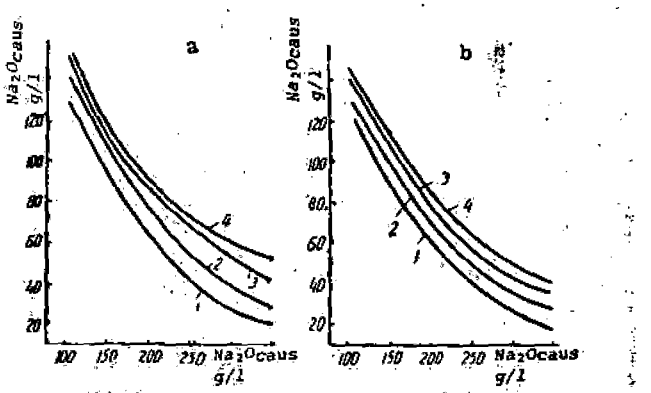

Fig.2 Solubility isotherms for sodium carbonate in aluminate solutions with caustic ratios of 3.5 (a) and 1.7 (b) at 125 (1), 200 (2), 250 (3) and 300°C (4).

By crystal-optical analysis it was established that, irrespective of the experimental conditions, the equilibrium solid phase is represented by thermonatrite in the form of thin plates or tablets with refractive indices N_q = 1.525 and N_p = 1.420[4]). X-ray diffraction analysis confirmed the presence of thermonatrite in the solid phase with clearly defined maxima on the diffractograms (d/n = 5.40, 4.98, 2.78, 2.68, 2.48, 2.38, 2.28, 2. 00 and 1.605kX), characteristic of this compound[5]).

At 125-250°C the solubility of sodium sulphate decreases with increase in the concentration of caustic alkali in the initial solution from 100 to 350g/l (fig. 3). At 300°C the character of the curve changes; the solubility maximum of sodium sulphate corresponds to a concentration of 150g/l Na_2O_{cu}. Further increase in the caustic alkali content leads to a decrease in the solubility of sodium sulphate. The character of the solubility of this salt in aluminate solutions, which we established, is close to the variation of its solubility in alkaline solutions, which we established, is close to the variation of its solubility in alkaline solutions[6]) for the same temperature.

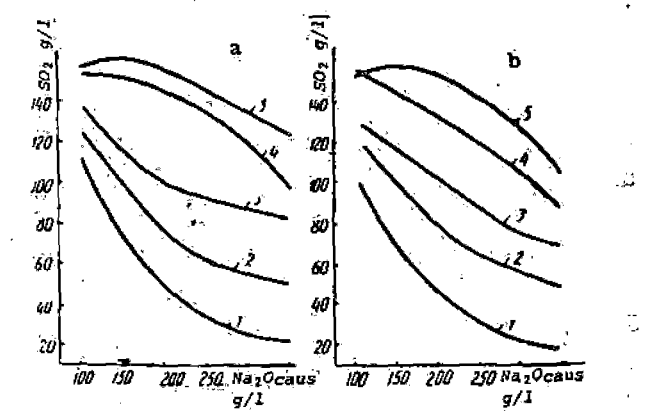

Fig.3 Solubility isotherms of sodium sulphate in aluminate solutions with caustic ratios of 3.5 (a) and 1.7 (b) at 125 (1), 150 (2), 200 (3), 250 (4) and 300°C (5).

Physicochemical investigations of the nature of the solid phase obtained during contact between sodium sulphate and aluminate solutions showed that with initial concentrations of 100 and 150g/l Na_2O_{cu} thenardite is the equilibrium solid phase at all temperatures investigated[4]). It is present in the form of bipyramidal and prismatic

crystals with diffractive indices N_q = 1.481 and N_p = 1.467. The diffractograms of this phase have the following maxima: d/n 4.70, 3.78, 3.14, 3.04, 2.76, 2.62, 2.30, 1.85, 1.675 and 1.550kX, corresponding to thenardite[5]).

In solutions with concentrations of 200g/l Na_2O_{cu} and above and at 200°C the sodium sulphate modification known as form III[4]) is present in the solid part simultaneously with thenardite, and its content increases with increase in the concentration of the solution with respect to caustic alkali. At 300°C the solid phase is fully represented by form III with refractive indices 1.480-1.485. On the diffractograms of sodium sulphate of form III the maxima are as follows: d/n = 4.80, 3.88, 3.72, 3.45, 2.79, 2.62, 2.36 and 1.950 kX.

Consequently, when sodium sulphate is dissolved in aluminate solutions, the transition of Na_2SO_4 from the thenardite modification to form III is observed in the solid phase, depending on the concentration and temperature. The caustic ratio of the aluminate solution within the limits investigated does not affect the transformation of sodium sulphate.

The composition of the equilibrium solid phase in the joint presence of sodium carbonate and sodium sulphate in the aluminate solutions was investigated on mixtures with a weight ratio Na_2CO_3:Na_2SO_4 of 2. By crystal-optical investigations it was established that the equilibrium phases of the solid part of the system under all the investigations it was established that the equilibrium phases of the system under all the investigated conditions are thermonatrite (platelike crystals up to 90μ in size and concretions of fine crystals) and a solid solution of sodium carbonate in berkeyite (thin prismatic crystals and star-like concretions with refractive indices N_q = 1.497 and N_p = 1.455).

Pure berkeyite with the composition $2Na_2SO_4 \cdot Na_2CO_3$ has refractive indices N_q = 1.492 and N_p = 1.450[4]). Soda with Na_{av} = 1.530 was found in the sample in small amounts. The diffractograms of the solid phase, obtained at 300°C with 100g/l Na_2O_{cu}, α_c = 3.5, confirmed the presence of thermonatrite with d/n = 2.77, 2.75, 2.68 and 2.36kX and a solid solution of Na_2CO_3 in berkeyite with maxima d/n = 3.80, 3.75, 3.48, 2.77, 2.62, 2.57, 1.94 and 1.76kX. The following lines are characteristic of pure berkeyite: d/n = 3.83, 3.78, 3.51, 2.78, 2.64, 2.58 and 1.93kX[5]).

increase in the solubility of fluoride with increase in the temperature of the process. For solutions with a caustic ratio of 3.5 it is higher than in solutions with a caustic ratio of 1.7. With increase in the concentration of the solution from 100 to 200g/l Na_2O_{cu} the solubility of fluoride decreases, and with further increase in the concentration it increases. The equilibrium solid phase in all cases is represented by villiomite in the form of round transparent grains and crystals of the cubic system with refractive index N = 1.325. This is confirmed by the diffractograms of the precipitates obtained at 120 and 300°C (d/n = 2.54, 2.32, and 1.42kX).

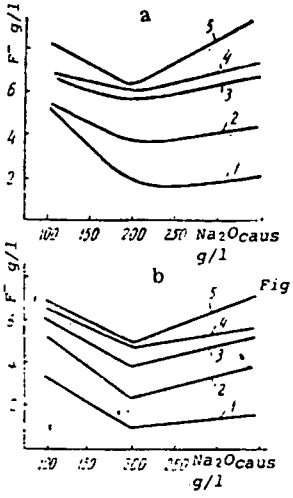

Fig.4 Solubility isotherms of sodium fluoride in aluminate solutions with caustic ratios 3.5 (a) and 1.7 (b) at 125 (1), 150 (2), 200 (3), 250 (4) and 300°C (5).

The composition of the equilibrium solid phase in the joint presence of sodium carbonate, sodium sulphate and sodium fluoride in aluminate solutions was investigated on two mixtures. It was established that during dissolution of a mixture with weight ratios Na_2CO_3:Na_2SO_4:NaF of 2:1:1 the deposits represented thermonatrite, the double salt $Na_2SO_4 \cdot NaF$, and villiomite. The thermonatrite is characterised by plate-like crystals and concretions of fine grains; the double salt is characterised by fine hexagonal tablet crystals with refractive indices N_q = 1.435 and N_p = 1.436. From solutions with a caustic ratio of 1.7 a small amount of cryolite in the form of concretions of fine (up to 5.7μ) octahedral crystals separates out in the deposits.

The diffractogram of the deposit obtained from a solution with a concentration of 100g/l Na_2O_{cu} (α_c = 3.5 at 250°C) contains lines for the double salt $Na_2SO_4 \cdot NaF$ with d/n 4.28, 3.80, 3.50, 2.98, 2.72, 2.57, 2.44, 2.37, 2.28, 2.14, 1.95, 1.74, 1.595 and 1.465; for thermonatrite with d/n 5.24, 2.75, 2.65, 2.44 and 2.37; for villiomite with maxima at 2.31 and 1.635kX. The lines of the double salt are the main lines.

As a result of the reaction of aluminate solutions with

Compositions of solid phases and concentrations of equilibrium aluminate solutions

Components	Concentration of equilibrium solution g/l				Crystal-optical analysis of solid phase
	Na_2O_{carb}	SO_3	Na_2O_{caus}	Al_2O_3	
Na_2CO_3	133.5	-	99.2	45.6	Thermonatrite in form of thin basal plates or crystals (70-80μ) N_q = 1.525, N_p = 1.420
Na_2CO_3:Na_2SO_4 = 2:1	90.7	28.2	98.9	46.2	Thermonatrite and solid solution of soda in berkeyite in form of needle crystals (30-100μ) with N_q = 1.497 and N_p = 1.445. Single grains of Na_2CO_3 with N_{av} = 1.530
Na_2CO_3:Na_2SO_4 = 1:2	36.0	71.3	97.7	45.6	Berkeyite in form of prismatic crystals (100-110μ) with N_q = 1.492 and N_p = 1.450. Rare grains of thenardite with N_q = 1.481 and N_p = 1.467.
Berkeyite	24.6	43.3	99.2	46.5	Berkeyite in form of tablet crystals (130-150μ) with N_q = 1.492 and N_p = 1.450.
Na_2SO_4	-	125.3	100.4	46.9	Thenardite in form of bipyramidal and prismatic crystals (100-110μ).

The compositions of the solid phases and the concentrations of the equilibrium aluminate solutions in the reaction of pure sodium carbonate and sodium sulphate, two mixtures of these components, and berkeyite with an aluminate solution having a concentration of 100g/l Na_2O_{cu} α_c = 3.5, at 150°C are given in the table.

Data on the solubility of sodium fluoride in aluminate solutions are given in fig. 4. They show an appreciable

a mixture having the composition $Na_2CO_3:Na_2SO_4:NaF$ = 2:1:0.5 thermonatrite, the double salt $Na_2SO_4 \cdot NaF$, and a solid solution of soda in berkeyite separate. In the reaction of both mixtures investigated with aluminate solutions the double salt $Na_2SO_4 \cdot NaF$ is formed at a higher rate than berkeyite.

Conclusions

1. The solubility limits of sodium carbonate, sodium sulphate and sodium fluoride in aluminate solutions with concentrations between 100 and 350 g/l Na_2O_{cu} with caustic ratios of 3.5 and 1.7 at 125-300°C were established.
2. It was shown that in the reaction with aluminate solutions the equilibrium solid phase is thermonatrite, sodium fluoride (villiomite) and sodium sulphate (either thenardite or form III).
3. In the joint presence of sodium carbonate and sodium sulphate, in aluminate solutions, depending on their ratio, either berkeyite or solid solutions of a berkeyite phase with variable composition are formed in the solid residue.
4. In the simultaneous reaction of sodium carbonate, sodium sulphate and sodium fluoride with aluminate solutions the formation rate of the double salt $Na_2SO_4 \cdot NaF$ is higher than the formation rate of berkeyite.

References

1) F I Tsymbal: Tr. VAMI 1945, (28), 1.
2) V A Bernshtein et alia: Zh. Prikl. Khim. 1965, 38, 1868.
3) V A Bernshtein et alia: Zh. Prikl. Khim. 1961, 34, 982.
4) A N Vinchell et alia: Optical characteristics of synthetic minerals: (Russian translation) Mir, Moscow 1967, pp. 34, 130, 169, 222, 228.
5) Amer. Soc. Test. Mater. No. 2-0840, 5-0631, 8-448, 8-31, 4-0793, 2-0668.
6) W Schroeder et alia: J. Am. Chem. Soc. 1936, 58, 847.

UDC 661.424.5.011

Removal of hydrogen from molten carnallite

E I Savinkova, A T Podanenko, V A Rudakov and R P Lelekova (Kalush Chemical-Metallurgical Combine. Urals Polytechnical Institute)

Summary

The removal of hydrogen from molten carnallite was investigated under high-temperature conditions, with melts having low magnesium chloride concentrations, and with variable concentrations of chlorine in the chlorinating agent. Treatment of molten carnallite with chlorine has great advantages over thermal dehydrogenation.

The best results were obtained with melts more dilute in $MgCl_2$. Thus, in the treatment of melts containing 43-46% $MgCl_2$ with anodic chlorine at 800°C 0.10 - 0.25% of MgOHCl remains. In the treatment of less concentrated melts (43-44% $MgCl_2$) the same degree of dehydrogenation was achieved by treatment with a chlorine-air mixture at 800°C or by heating the melt at 900°C.

UDC 669.213: 553.411: 549.324

The form of "invisible" gold in arsenopyrite and pyrite

V N Voitsekhovskii, B P Berkovskii, O A Yashchurzhinskaya, L V Chugaev and M V Nikitin (Leningrad Mining Institute. Department of the Metallurgy of Heavy and Noble Metals).

Determination of the form in which "invisible" gold (also called finely dispersed, sub-microscopic gold) is present in sulphide minerals is important for solving the problem of the development of effective methods for the extraction of gold from tenacious gold-containing ores and concentrates. The present work was undertaken with samples from the Bakyrchik deposit (Kazakhstan). The gold content is largely associated with FeAsS, in which the concentration of gold amounts on average to 177 g/t [1]), which is twice its content in FeS_2. The material for the investigation was a sulphide product with a gold content of 210 g/t, isolated on the concentration table from the combined gravity-rotation concentrate. Most attention was paid to arsenopyrite, i.e., the main bearer of gold.

It was not possible by examination of sections, prepared from the sulphide concentrate, under a microscope (up to x 2000) to detect visible gold impregnated in FeAsS or FeS_2, although individual grains of gold in FeAsS have been recorded in the literature. Solution of the problem of the form in which gold is present in sulphides may be assested by investigation of its behaviour when gold-bearing sulphide minerals are heated.

Samples weighing 2.5 g placed in covered glass or quartz test tubes were subjected to heat treatment. Analogous results were obtained by heating in evacuated sealed tubes or in tubes filled with inert gas. From the heated material we prepared sections, mounted them in plastic, and polished them on diamond wheels in order to obtain samples free from relief. We were unable to subject the polished sections to multiple heat treatment, as done by other investigators[2-6]), without destroying them, and a separate sample was therefore heated for each test.

Effects of grain enlargements in the "invisible" gold on heating to 250-300°C are known[2,3]), but our samples heated at 350°C for 4 h and at 450°C for 62 h did not give any grain enlargement of the gold. At 500°C dissociation of FeS_2 in FeAsS occurred (the upper limit of the stability of the FeAsS association is 491 ± 12°C [6]) with the formation of secondary pyrrhotine and the release of sulphur and arsenic. Here, segregations of enlarged gold of several microns in size were easily detected in the secondary pyrrhotine. The size of individual gold particles reached 10-15 μ. Increase in the heat treatment temperature to 550, 600, and 700°C with holding times from 0.5 to 10 h led to enlargement of the gold in the mass of the secondary pyrrhotine. Enlarged visible gold was not detected in the remains of the undecomposed FeAsS.

During microscopic analysis of samples heat treated at 550-700°C no clear relationship was established in the frequency at which gold particles were encountered and the degree of enlargement of the gold as a function of the heating temperature and time. It must be supposed that the only condition for enlargement of the gold is dissociation of the gold-containing sulphides. Intensive processes of the disintegration of the enlarged gold at elevated temperatures (exceeding 500°C for FeAsS), which become stronger with decomposition of the initial sulphides, have been described in the literature[2,3]). The data from microscopic investigations of our samples do not agree with the published description. The following tests were undertaken in order to establish the absence of gold disintegration processes. The

SORBENTS USED TO EXTRACT COPPER FROM SOLUTIONS AND PULPS

UDC669.33:661.183.123

B. N. Laskorin, V. A. Goldobina, N. G. Zhukova, A. N. Bolotov, and Yu. V. Trofimov

In introducing sorption process to hydrometallurgy, a basic step is to find sorbents which meet technology's requirements: the sorbents should have a sufficiently high mechanical and chemical strength, should absorb the extracted metal well, and should be easy to regenerate; this is because the properties of the sorbents being used and its cost occasionally play a decisive role when a particular method is being evaluated.

Table 1
Characteristics of Pilot Batches of Ampholytes

Ionites	Specific swelling, ml/g	Mechanical strength, %	Copper capacity E, mg/g	Ionites	Specific swelling, ml/g	Mechanical strength, %	Copper capacity E, mg/g
SG-1	2,75	98,5	12,7	KU-2A	1,2	87,9	41,0
SG-1A	1,58	96,5	30	AMK	2,7—3,0	98	65
KU-2	2,4	88,7	17,8	VPK	2,5—3,0	90	120

* During concentration, 2 g/l copper, 50 g/l Na_2SO_4, and pH ≈ 4.

Table 2
Comparative Characteristics of Ionites KU-2A, AMK, and VPK During Sorption from Pulp of Flotation Tailings

Ionite	Cu content in starting pulp % (in sol. phase)		Ratio of resin: pulp flows	No. of sorption stages	pH during sorption	Cu content in discharged pulp		Content in commercial regenerate, %		Saturation capacity of resin		Copper extraction from flotation tailings, % (in cake)
	total	oxidized				Solution, g/l	Cake, %	Cu	H_2SO_4	Cu, mg/g	Cu, mg/ml	
SG-1	0,51 0,33	— —	1:3,8 1:4,5	10 10	4,5—3,5 4,5—3,5	0,078 0,032	0,16 0,128	3,3 3,1	5,7 5,10	11,6 10,0	2,6 2,3	68,6 60,6
SG-1A	0,40 0,47	— —	1:3 1:3	10 10	4,5—2,9 4,5—2,8	0,14 0,053	0,12 0,15	2,5 2,5	— —	11,7 17,2	4,15 6,2	70,0 68,0
KU-2	0,60 0,60 0,60	0,54 0,54 0,54	1:5 1:7 1:10	5 5 9	4,3—4,2 4,1—3,8 4,0—3,7	Traces Traces 0,02	0,10 0,12 0,11	26,0 36,0 26,0	45,0 45,0 45,0	25,0 30,0 36,0	25,0 30,0 36,0	83,3 80,0 81,6
AMK	0,5	—	1:15	12	4,0—2,5	0,03	0,16	30,0	60	39,0	19,7	68,0
VPK	0,5 0,5	— —	1:15 1:30	9 9	3,5—2,7 3,4—2,8	0,047 0,03	0,17 0,16	39,0 39,0—43,0	85 85—110	45,0 90	19,0 33,5	66,0 68,0

In order to extract copper from sulfuric acid solutions, one can use ionites of various grades. There is extensive literature on the sorption of copper by anionites from weakly-acid solutions [1, 2]. A pH value of 3.5-4.5 is optimum field of sorption on anionites produced on a base of polyethylenepolyamine. However, because of the low mechanical strength, similar ionites cannot be used for sorption from pulps. Use of high-strength, styrenedivinylbenzene-base, cation-exchange resins is limited by the absence of selectivity with respect to copper ions.

Recently, reports have been published on copper sorption and on the ions of a series of other metals in which ionites have been used which contain complex-forming groups [3, 4]. Studies on copper sorption with aminocarboxy] anionites have shown their superiority to other ionites [5].

The amphoteric ionites SG-1A and KU-2A have higher sorption capacity and selectivity than the original cationites [6]. Due to the high mechanical strength, availability, and low cost these ampholytes can be used for sorption from comparatively low-grade copper solutions and pulps (Table 1).

Very much in prospect for sorption of copper from acid media is the ampholyte VPK which contains pyridinecarboxyl groups and has a high mechanical strength [7].

Recently, researchers have been looking into the possibility of including ampholytes

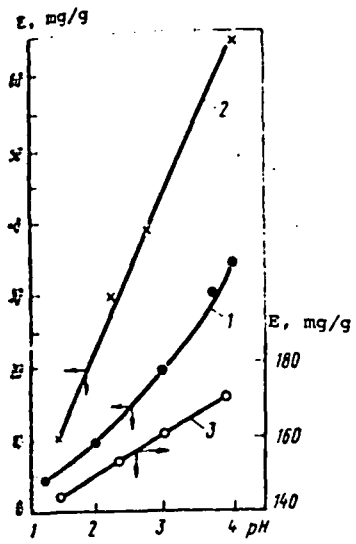

Fig. 1. Relationship of sorption capacity E of ionites to solution pH:
1 - KU-2A; 2 - AMK-1; 3 - VPK.

with iminodiacetate groups. characterized by synthesis simplicity and availability of starting reagents [4, 8]. Among such ampholytes we include ionite AMK-1 -- used in this study.

This work also gives the results of tests on ampholytes SG-1A, KU-2A, and VPK, obtained on a pilot scale.

In the course of the research on the basic rules governing copper sorption from sulfuric-acid solutions it was shown that the sorption capacity of ampholytes KU-2A and AMK depend to a considerable degree on the equilibrium value of the pH (Fig. 1). The optimum effective area for these resins in weakly-acid solutions lies within a pH of 3-4; reducing the pH to 1-1.5 leads to a sharp drop in capacity. For the pyridinecarboxyl ampholyte VPK, an increase in solution acidity to pH = 1 will have no substantial effect on copper sorption.

The relationship of sorption to the equilibrium concentration of copper in a solution was checked on a model solution, containing 50 g/l Na_2SO_4. The nature of the curves (Fig. 2) confirms the fact that these resins operate satisfactorily in the original isotherm region, i.e., in low concentration regions.

An examination of sorption kinetics on ampholyte AMK has shown that an almost complete equilibrium sets in after 5-6 hours of resin contact with the solution, with a content of up to 2 g/l copper. As the copper concentration in the solution drops, the time needed to reach equilibrium is increased (Fig. 3).

Data on copper desorption from resins AMK, KU-2A, and VPK -- saturated from model solutions (Fig. 4) -- show that resins AMK and KU-2A regenerate very well; to completely remove copper from resin, it is sufficient to use 2-3 volumes of desorbed solution for every volume of resin, while the desorption of copper from ionite VPK is difficult even when using concentrated solutions of sulfuric acid (up to 800 g/l) during heating. Moreover, the residual capacity is 30-50% of the original capacity. When regenerating ampholyte types VPK and ANKB-2, satisfactory results are obtained only when employing desorption with cementation [9].

A comparative evaluation was made of ampholytes SG-1A, KU-2A, AMK, and VPK when sorbing copper from the pulps of flotation tailings of "Dzhezkazgan" deposit ores (see Table 2). The ionites can be arranged in the following order of copper sorption capacity per unit of resin weight:

VPK > AMK > KU-2A > SG-1A > SG-1

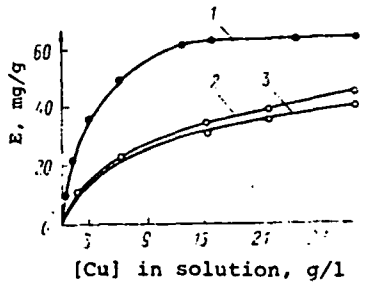

Fig. 2. Isotherm of copper sorption from solutions on resin KU-2A:
1 - pH = 4; 2 - pH = 2; 3 - 20 g/l H_2SO_4.

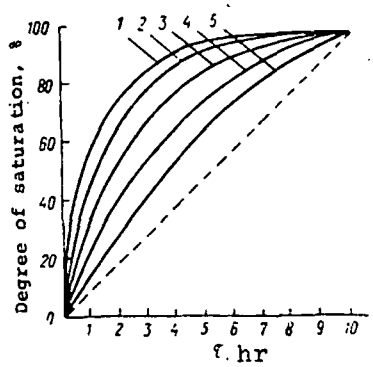

Fig. 3. Kinetics of copper sorption -- on resin AMK -- from solutions, containing copper, g/l:
1 - 1.77; 2 - 1.0; 3 - 0.42; 4 - 0.2; 5 - 0.1.

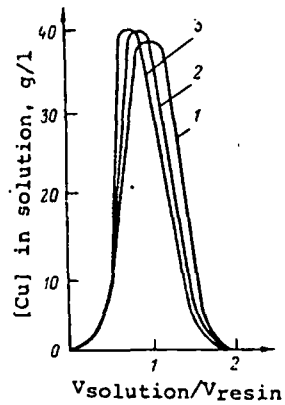

Fig. 4. Desorption of copper from AMK resin in dynamic conditions with H_2SO_4 solutions, g/l:
1 - 300; 2 - 400; 3 - 500

However, in converting to volume units, the capacity of the KU-2A resin becomes comparable to the capacity of resin VPK.

Thus, in order to sorb copper from pulps, one can equally successfully use the type VPL pyridinecarboxyl resins and the resins which have a styroledivinylbenzene base -

the aminosulfate ampholyte KU-2A and the ampholyte type AMK with groups of iminodiacetic acids.

REFERENCES

1. K. M. Saldadze, K. M. Kopylova, V. D. Kopylova, and G. V. Muromtseva. In the book: Ion-Exchange Sorbents in Industry. Moscow, AN SSSR, 1963, pp. 66-70.
2. V. D. Kopylova, K. M. Saldadze, G. D. Asambadze, et al. ZhAKh, 1970, vol. 25, No. 7, pp. 1287-1293.
3. V. G. Sinyavskii. Selective Ionites. Kiev, "Tekhnika," 165 pp., ill.
4. R. Khering. Gelatinous Ion-Exchangers. Moscow, "Mir," 1971, 279 pp., ill.
5. B. N. Laskorin, V. A. Goldobina, N. G. Zhukova, and M. K. Makarov. In the book: Ion-Exchange and Ionites. Moscow, "Nauka," 1970, pp. 212-214.
6. B. N. Laskorin, N. G. Zhukova, V. A. Golobina, et al. USSR Patent No. 317670. Otkr., Izobr., Promyshl. Obraztsy, Tov. Znaki, 1971, No. 31, p. 90.
7. B. N. Laskorin, G. N. Nikul'skaya, G. I. Ostroumova, et al. USSR Patent No. 320503. Otkr., Izobr., Promyshl. Obraztsy, Tov. Znaki, 1971, No. 34, p. 72.
8. E. D. Trostyanskaya and G. Z. Nefedova. "Vysokomolekulyarnye Soedineniya," 1963, vol. 5, No. 1, p. 49-55.
9. L. E. Slobtsov, B. N. Laskorin, V. A. Goldobina, et al. Tsvetnye Metally, 1973, No. 9, pp. 15-16.

Economic Geology
Vol. 74, 1979, pp. 459–461

SULFUR

ALFRED J. BODENLOS AND CARMEN P. NELSON

ABOUT 17 million long tons of sulfur, roughly one-third of the world's annual production, was won in 1977 from elemental deposits in rocks of evaporitic origin. Most such deposits in the United States and Mexico lie in anhydrite cap rocks above salt diapirs, but geographically, widely dispersed deposits also lie in bedded anhydrite or gypsum. The latter include those in the Permian basin of west Texas, those in the evaporite sequence of Sicily, in the Miocene gypsum of the Cis-Carpathian trough of southern Poland and the eastern U. S. S. R., in other evaporite basins in the U. S. S. R., and at least one deposit in the Fars evaporite of Iraq. During the industrial minerals symposium of the Society of Economic Geologists (Denver, February 1978), papers were presented describing the deposits in Poland, Iraq, and west Texas. Two other papers speculated on the origin of elemental sulfur deposits in anhydrite and gypsum and one other paper discussed present and future sulfur supply and demand. Four of the five geologic papers are printed in this volume and the economic paper is summarized in this introduction.

At the symposium the geologic papers described a striking similarity in the composition of all sulfur deposits in evaporites, each consisting mainly of calcite and elemental sulfur, together with small amounts of the sulfate minerals selenite, celestite, and barite. Each paper also emphasized that the location of such deposits is structurally controlled, each one lying either in structural highs of various amplitudes, along faults, or in faulted anticlines. All papers presented the identical thesis that such deposits resulted from the metabolic activity of the anaerobic bacterium *Desulfovibrio desulfuricans,* which in the presence of hydrocarbons oxidized organic material, reduced the sulfate ions of anhydrite or gypsum, and emitted carbon dioxide and hydrogen sulfide as waste products. Hydrated carbon dioxide reacted with available calcium ions, precipitating as calcite to replace anhydrite or gypsum, with the hydrogen sulfide oxidizing to elemental sulfur. However, the authors disagreed and divided into two schools of thought regarding the nature of the reactions leading to the oxidation of hydrogen sulfide. One school advocated the position that a supply of free oxygen had been carried into the mineralized zones by descending meteoric water, the other, that an inorganic reaction between hydrogen sulfide and various ions was produced by the preceding reactions. The authors also disagreed on the hydrologic plumbing system and the movement of ground waters involved in the genesis of the deposits.

History of Sulfur Mining and Recovery

Sulfur is unique among the industrial minerals because it or its acid derivative can be mined or recovered from a wide variety of geologic accumulations: it is mined from elemental deposits in evaporites and in volcanic rocks and it is separated in chemical plants and refineries from sulfur-bearing fossil fuels. Sulfur dioxide resulting from the roasting of pyrite and pyrrhotite or the smelting of base metal sulfide concentrates is directly converted to sulfuric acid or in a few plants to elemental sulfur. The common sulfate minerals, anhydrite and gypsum, can be processed to yield sulfate-bearing fertilizers or, at higher costs, reduced to elemental sulfur.

The Industrial Revolution created increasing demands for sulfur during the 19th century, which were first met by elemental sulfur mined in Sicily and then by production of sulfuric acid from pyrites. Mining of elemental sulfur deposits from cap rocks of the Gulf Coast of the United States became feasible in this century following the development of the Frasch process, in which superheated water melts sulfur within the orebody and pure molten sulfur is brought to the surface. By 1950, Frasch sulfur from the Gulf Coast and sulfuric acid produced at pyrite-roasting plants in Europe were the principal sources of the western world's sulfur supply, although Japan mined elemental sulfur and pyrite from deposits in volcanic vents.

This supply pattern changed rapidly beginning in the 1950s when elemental sulfur deposits were discovered and successively developed in Mexico, Poland, west Texas, and Iraq. Increased use of petroleum and natural gas led to the by-product recovery of hydrogen sulfide contained in sour natural gas and to the generation of hydrogen sulfide in petroleum refineries; this gas is readily converted to elemental sulfur. As a result Canada, France, the United States, and Iraq presently are producing large tonnages of sulfur in sour natural-gas treatment plants and the petroleum refineries throughout the western world are producing by-product elemental sulfur. Sulfur dioxide is being recovered and converted to sulfuric acid from base metal smelters on an increasing scale, both in the United States and in Europe. On a smaller scale, the sulfur contained in

TABLE 1. Present and Forecast Sulfur Supply and Demand in the United States through 1990

	Supply (millions of long tons)			
		Forecast		
	1977	1980	1985	1990
Elemental sulfur (Frasch mines)	5.8	6.2	5.6	4.5
Recovered sulfur				
Oil refineries	2.0	2.8	3.9	5.0
Sour natural gas	1.5	1.8	1.9	1.8
Coal-burning power plants		0.05	0.05	0.3
Coal gasification		0.002	0.04	1.5
Coal liquifaction		0.006	0.03	
Smelter acid, pyrites, H_2S and SO_2 (sulfur content)	1.2	1.6	2.2	2.6
Total	10.5	12.4	13.7	15.7
	Demand (millions of long tons)			
Fertilizer sector	7.1	8.0	9.5	11.0
Industrial sector	4.5	5.3	5.7	6.5
Total	11.6	13.3	15.2	17.5

Canadian tar sands is being recovered and gypsum, primarily in England, is processed to yield the co-products, sulfate-bearing fertilizers and cement. The great tonnages of sulfur contained in coal and oil shale have not yet furnished much of the world's supply of sulfur or sulfuric acid.

Supply

The foregoing indicates that the sulfur supply of the western world during the past 25 years has sustained major shifts both in regard to the sources and types of raw materials being won or recovered and to its geographic distribution. Mexico, Canada, Poland, France, and Iraq have become self-sufficient in the commodity and now export from small to large tonnages throughout the free world. The United States, while still exporting sulfur, also imports Mexican and Canadian sulfur at competitive prices in the vicinity of Tampa, Florida, and in the northwestern states. The oil refineries of Japan have supplanted the costlier mines in volcanic deposits as the main suppliers of sulfur in that country. The symposium accordingly included a paper prepared by Ms. C. P. Nelson containing the forecasts of the Freeport Minerals Company on the United States and western world supply and demand for sulfur through 1990; her paper is summarized in the following section.

The United States

The United States currently produces between 10 and 11 million long tons of sulfur, about one-fifth the global supply of sulfur, and it consumes slightly more than it produces. The United States has been a net importer of sulfur since 1975 and the Freeport analysts forecast that this position will continue through 1990 (Table 1).

Frasch mining of elemental sulfur deposits peaked at 7.7 million long tons in 1974 but has declined since then and will continue to do so as deposits are worked out. Of the 24 cap rock deposits in the Gulf Coast, which since 1903 have produced nearly 240 million long tons of sulfur, only seven are currently operating. Of the dozen deposits found in the Delaware basin of west Texas, only four were developed and three are active. High development costs and increasing fuel costs will discourage the opening of all but the very largest deposits that may be discovered in the future.

Sulfur will be recovered in larger amounts from oil refineries through 1990, assuming that our imports of high-sulfur crudes will increase. The amount of sulfur recovered from domestic sour natural gas will increase slightly and that from pyrites and base-metals smelting probably will double during this period. Future recovery of sulfur from coal-burning thermoelectric plants is written off as negligible by Freeport analysts because such plants will scrub sulfur dioxide in stack gases with lime rather than attempting to produce a saleable product. Should coal liquification and gasification plants be built on a large scale, about 1.5 million long tons might be recovered annually by 1990.

The western world

Freeport analysts predict the western world production of sulfur, including that of the United States, will reach some 47 million long tons by 1990 (Table 2).

Elemental sulfur is mined from two cap rock deposits in Mexico and one deposit in bedded evaporites at Mishraq, Iraq. Mexican production will fluctuate with world demand but probably will decline from 2.0 million long tons in 1980 to 1.5 million long tons in 1990. Iraqi production, largely exported, is limited in part by rail and port capacities and totaled only 0.7 million long tons in 1977; it may rise to about 1.2 million long tons by 1990. Poland and the U. S. S. R. also mine sulfur from elemental deposits. Poland, a major supplier to western Europe, is expected to export about 1.9 million long tons in 1980, probably increasing to 2.5 million long tons in 1990.

Canada, the leading conutry in recovering sulfur from sour natural gas, extracted 6.5 million long tons in 1977. Production is directly related to natural gas production and as gas reserves are being drawn down, production of sulfur will probably decline to

4.5 million long tons by 1990. The gas fields lie in western Canada and sales are limited by slating capacity at recovery plants—rated at 3.5 million long tons in 1977—by railroad capacity, and by loading facilities at Vancouver, British Columbia. Stockpiles have been increasing annually and in 1977 reached 19.5 million long tons, but production and sales should balance after 1980.

France in 1977 recovered 1.8 million long tons from the sour natural gas produced in the Lacq district; there also gas reserves are being depleted and by-product sulfur production will drop to an estimated 0.7 million long tons by 1990. The Middle East contains very large resources of sour natural gas and high-sulfur crude oil; about 0.6 million long tons of sulfur were recovered from natural gas in 1977. Estimates of how well sulfur recovery can be developed in the region are uncertain, but the amount may possibly be increased to as much as 4.7 million long tons by 1990. Sulfur recovered from Middle East and Venezuelan crude oil in the refineries of many countries, excluding those in the United States, totaled about 3.2 million long tons in 1977 and perhaps will reach as much as 6.5 million long tons by 1990.

Roasting of pyrites and recovery of sulfur dioxide in base metal smelters, particularly in western Europe, resulted in a sulfuric acid production containing the sulfur equivalent of about 8.8 million long tons in 1977. Freeport analysts expect production from these sources to increase to more than 13 million long tons by 1990.

Demand

Sulfur is perhaps the most widely used industrial commodity, most of it in the form of sulfuric acid. It is involved in the manufacture of hundreds of products including such diverse items as paper, pigments, synthetic fibers, vulcanized rubber, detergents, and explosives; such uses comprise about 45 percent of the total U. S. demand. The remaining 55 percent is used in the manufacture of fertilizers, mainly in acidulating phosphate rock and converting it either into superphosphate or phosphoric acid. Future sulfur demand depends in part on industrial growth but more critically on fertilizer demand, which fluctuates from year to year. Future fertilizer demand also will depend on the level of exports to developing countries.

In the United States one industrial application that undoubtedly will demand more sulfuric acid is the leaching of copper and uranium oxide ores, concentrates, and old oxide-ore dumps. More sulfur, in one form or another, also will be used as a plant nutrient, particularly because sulfur deficiencies in soils are being discovered in many parts of the world. The physical properties of elemental sulfur, including its high strength, low thermal conductivity, and resistance to chemical attack could lead to its extensive use as an additive to special concretes and construction foam. A mixture of sulfur in asphalt as a paving material has been found to exhibit a significantly higher fatigue life. The ultimate development of these new uses will determine their role in the balance between supply and demand during the next 10 to 15 years.

TABLE 2. Present and Forecast Sulfur Supply and Demand in the Western World through 1990

	Supply (millions of long tons)			
		Forecast		
	1977	1980	1985	1990
Mined elemental sulfur	8.2	9.4	9.1	7.2
Elemental sulfur recovered from fossil fuels	15.6	17.6	20.5	25.2
Smelter acid, pyrites, H_2S and SO_2 (sulfur content)	10.1	11.3	13.4	15.0
Total	33.9	38.3	43.0	47.4
Net imports from Poland	2.2	-1.9	2.3	2.5
	Demand (millions of long tons)			
Smelter acid, pyrites, H_2S and SO_2 (sulfur content)	10.1	11.3	13.4	15.0
Elemental sulfur (mined and recovered)	23.8	28.3	33.4	38.2
Total	33.9	39.6	46.8	53.2

As can be seen in Table 2, demand is forecast to exceed the supply from 1985 through 1990. Ms. Nelson does not anticipate a shortage because prices will rise accordingly and this in turn will lead to greater use of the more costly raw materials. Sulfuric acid plants using pyrite roasters are more expensive to build and operate than plants using elemental sulfur, but massive pyrite deposits contain enormous sulfur resources and are widely distributed on most continents. Even larger resources are contained in the gypsum beds of the world, from which sulfate chemicals and, at a higher price, elemental sulfur can be produced.

A. J. B.
U. S. GEOLOGICAL SURVEY
NATIONAL CENTER, MAIL STOP 956
RESTON, VIRGINIA

C. P. N.
FREEPORT MINERALS COMPANY
200 PARK AVENUE
NEW YORK, NEW YORK 10017
January 19, 1979

Economic Geology
Vol. 74, 1979, pp. 462–468

Bioepigenetic Sulfur Deposits

J. B. DAVIS AND D. W. KIRKLAND

Abstract

Isotope analyses distinguish biogenic sulfur deposits from nonbiogenic deposits but do not distinguish bioepigenetic from biosyngenetic deposits. Sulfur deposits in cap rocks over salt domes and in bedded Permian evaporites of West Texas, however, are clearly bioepigenetic. Anhydrite, introduced by salt diapirs into geologically younger sediments, is converted biogenically to sulfur and calcite in the presence of petroleum in cap rock over the Challenger Knoll, a salt dome at a water depth of 12,000 ft in the Gulf of Mexico. Bedded evaporites of West Texas in association with petroleum show an obvious epigenetic displacement of the anhydrite layers by biogenic sulfur and calcite.

Introduction

THE principal sources of mined elemental sulfur in the free world are the overlying cap rocks of salt domes along the northern margin of the Gulf of Mexico and in Mexico's Isthmus of Tehauntepec, as well as the Permian bedded anhydrite formations of West Texas. The sulfur in such deposits is mined by the Frasch process. The sulfur deposits result from the biogenic, postsedimentary conversion of anhydrite or gypsum to hydrogen sulfide, and its oxidation to sulfur. The geochemistry of hydrogen-sulfide oxidation, particularly in cap rock sulfur deposits, has not been clarified.

Use of stable isotope analysis to determine the biogenic process of sulfur deposition is now a classic example of applying geochemical methods to geology. Geologists for many years had noted and described the epigenetic replacement of anhydrite by calcite and sulfur. Although Hunt (1915) proposed that the elemental sulfur deposits of Sicily were generated by the activity of anaerobic bacteria, early students of the Gulf Coast deposits concluded that anhydrite or gypsum was altered to calcite and elemental sulfur by means of inorganic reactions. Wolf (1926) considered the possibility that the carbon in petroleum was involved in the reduction of the sulfate ion but eliminated bacteria as the active agents on the grounds that they were found only at the surface. Taylor (1938) noted that bacteria had not been found in cap rocks and attributed the reactions to hydrogen sulfide and carbon dioxide carried into cap rocks from exterior sources, the former accompanying petroleum, the latter dissolved in ground water. With the advent of isotope analysis, Thode and his Canadian associates (1954) discovered the basic mechanism which is mediated by the sulfate-reducing bacteria, *Desulfovibrio desulfuricans*, involving the following molar balance:

$$CaSO_4 + \underset{\text{petroleum}}{(C + 4H)} \xrightarrow{\text{sulfate-reducing bacteria}} H_2S + CaCO_3 + H_2O.$$

This group established that the ^{32}S and ^{34}S isotopic ratios in the anhydrite, hydrogen sulfide, and sulfur of the cap rock deposits differ, strong evidence that the reduction of anhydrite is biochemical. Further, the ^{12}C and ^{13}C isotopic ratios in the calcite and in associated petroleum are similar, indicating that petroleum carbon is incorporated into the calcite (Thode et al., 1954; Feely and Kulp, 1957). Oxidation of petroleum hydrocarbons by *Desulfovibrio desulfuricans* was reported by Davis and Yarbrough (1966).

This paper will summarize some of our current knowledge concerning bioepigenetic sulfur deposits in (1) salt-dome cap rocks of the north and south margins of the Gulf of Mexico, (2) a deposit over a salt dome in Challenger Knoll, in the center of the Gulf of Mexico, and (3) sulfur deposits in Permian evaporites of the Delaware basin, West Texas (Fig. 1).

Sulfur Deposits in Cap Rocks over Salt Domes in the North and South Margins of the Gulf of Mexico

Twenty-four of the 329 onshore and offshore salt diapirs in the U. S. coastal area of the Gulf of Mexico and 4 of the 41 salt domes in the Isthmus of Tehuantepec, southeast Mexico, are overlain by cap rocks that contain sulfur ore (Fig. 1). Cap rock begins to form when the apex of a salt diapir penetrates an aquifer or approaches or reaches the sea floor; halite is then dissolved, leaving a concentration of relatively insoluble anhydrite (Taylor, 1938; Bodenlos, 1970). Calcium sulfate is the requisite source rock from which sulfur is derived. Organic matter is another

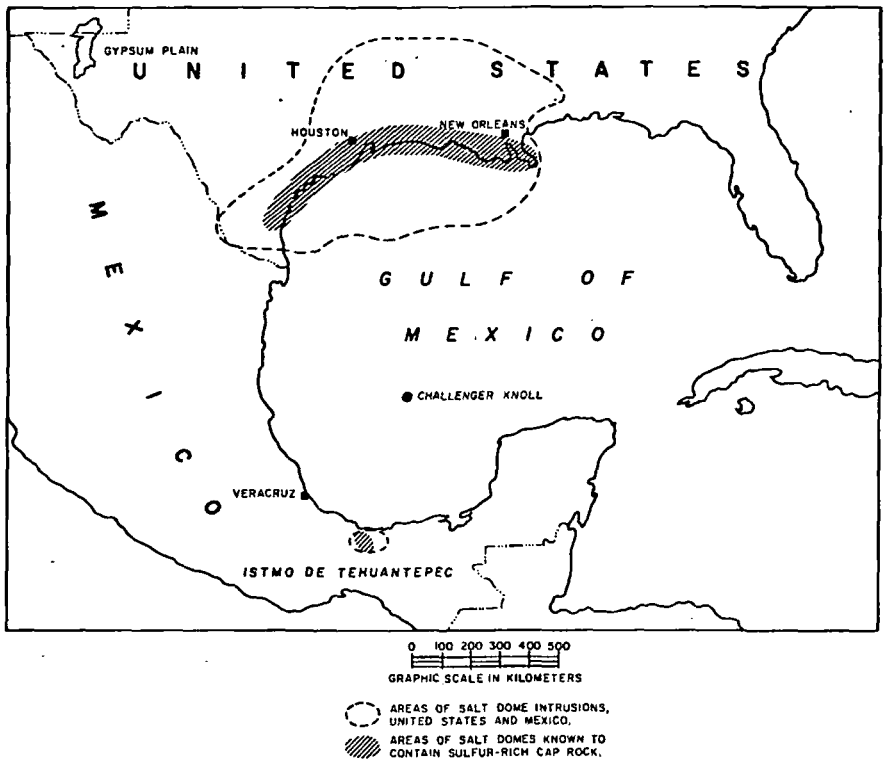

FIG. 1. Area which includes the bioepigenetic sulfur deposits discussed: the sulfur-bearing salt domes of the north and south margins of the Gulf of Mexico, Challenger Knoll, and the bedded evaporites of the Gypsum Plain, West Texas.

requisite, as shown by the common presence of petroleum in sulfur-bearing cap rocks. The final requisite is the action of sulfate-reducing bacteria, which metabolically couple the reduction of the sulfate ion of anhydrite (or gypsum) with the oxidation of petroleum to yield hydrogen sulfide and carbon dioxide (Feely and Kulp, 1957). Alteration of anhydrite or gypsum ensues with the deposition of calcite derived from bacterially produced carbon dioxide, followed by oxidation of the hydrogen sulfide to elemental sulfur (Fig. 2). In essence, there is a post-sedimentary, biochemical conversion of anhydrite into calcite and sulfur.

Sulfur deposits large enough to mine form only through the proper combination of geologic conditions and sequence of events (Bodenlos, 1973). The history of any cap rock sulfur deposit is dynamic, according to Feely and Kulp (1957), and whether more or less sulfur is found depends on the present stage in its history. U. S. Gulf Coast salt diapirs originated from Jurassic salt beds now lying 20,000 to 50,000 ft below the surface. As the salt masses moved upward through the sedimentary sequences, dissolution of halite and consequent concentration of anhydrite at the top of the salt dome could occur within 5,000 ft of the surface. At a depth of about 3,000 ft the temperature over salt domes is about 55° to 60°C and bacterial action could begin, provided a source of organic matter, such as petroleum, was available. Vigorous bacterial action probably did not occur until the cap rock came to within 1,000 to 2,000 ft of the surface. The resulting biochemical calcite became the host rock for sulfur derived from bacterially generated hydrogen sulfide.

Strata penetrated by salt diapirs are dragged upward and those above the masses may be domed and commonly are faulted. The cap rock, therefore, must become stable and effectively sealed, largely by impervious clays, if the sulfur is to be contained and not lost as hydrogen sulfide. The sulfur : calcite ratio averages about 1 : 4 in minable deposits; however, many calcite cap rocks lack sulfur almost completely, indicating a loss of hydrogen sulfide probably due to the lack of an overlying seal. Oxidation of hydrogen sulfide in cap rocks occurs by as yet unclarified reactions. Cap rocks containing minable sulfur deposits characteristically contain a thick mass of porous calcite, and the sulfur content generally increases as the ratio of calcium carbonate to calcium sulfate increases.

The cap rock of one small deposit lies at the surface; the remaining 23 U. S. sulfur-productive cap rocks range in minimum depth from 280 to 1,800 ft and the depth to underlying salt ranges from about

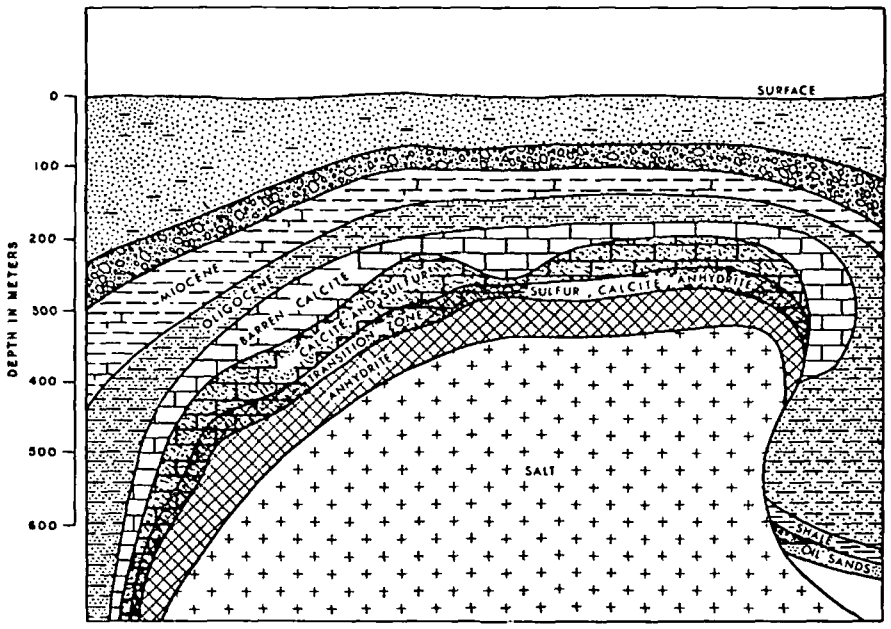

FIG. 2. Schematic cross section of a typical salt dome sulfur deposit, showing anhydrite immediately above the salt plug, with overlying calcitic and sulfurized zones.

370 to 2,300 ft. The maximum thicknesses of cap rock lenses range from several hundred to about 1,200 ft. Most sulfur deposits range from 900 to 2,000 ft in depth, but some extend to 3,200 ft in an overhang on the flank of the Orchard salt dome.

Zobell (1949) isolated sulfate-reducing bacteria from a core of salt-dome cap rock taken at a depth of 1,560 ft by the Freeport Sulfur Company. Butlin (1953) found large numbers of sulfate reducers in water containing hydrogen sulfide issuing from a 4,000-ft well near Tripoli; these bacteria were cultivated readily in the laboratory at a temperature of 55°C.

Most sulfur-bearing cap rocks occur within strata ranging in age from the Oligocene to the Pliocene. The principal factor restricting sulfur formation to this stratigraphic interval apparently has been the availability of petroleum. The area of U. S. sulfur-bearing salt domes is almost identical with the limits of late Tertiary oil in the Gulf coastal province. Within this area more than 90 percent of the salt domes are associated with oil production, outside this area only about 30 percent are. In the interior salt dome provinces of Texas, Louisiana, and Mississippi, the required combination or the sequence of factors did not occur in a manner that promoted cap rock sulfur deposition or preservation.

Salas (1967) notes that the salt structures of southeast Mexico are not piercement domes but are oval-shaped, rather shallow protrusions from salt massifs. Sulfur-bearing cap rock is found only in the southwest and west part of the Mexico saline basin where overlying Oligocene and Miocene strata are thin. Sulfur occurs at depths less than 1,000 ft. The common lithologic sequence is sulfur-bearing calcite cap rock overlying an anhydrite layer that ranges from a few feet to several hundred feet in thickness. Some cap rocks are impregnated with oil. The Saline Basin of southeastern Mexico yields a significant portion of Mexico's oil production.

Salas suggested that calcite in Mexican cap rocks indicates the possible presence of sulfur and that exploration for sulfur should not be attempted below 2,000 to 3,000 ft because deeper cap rocks do not contain calcite. In the U. S. Gulf region, however, it is possible that sulfur-bearing cap rocks may lie deeper than 3,000 ft, the approximate limiting depth of sulfate-reducing bacterial activity. Depth to cap rock depends on the rate of upward movement of salt, the rate of salt solution at the apex of the salt structure, and the rate of deposition or erosion of sediments over the dome. Due to the mechanics of salt diapirism, most salt structures ultimately must have risen into the zone of potential sulfur formation within 3,000 ft of the surface. Parker and McDowell (1955) suggest that many domes may have reached or come close to the surface at one or more stages of their development, and Ellisor (1926) reported ancient coral reefs around several sulfur-bearing cap rocks in the Gulf Coast, including those lying on Boling dome, Damon mound, and Nash dome. If subsequent accumulation of sediments exceeded the rate of dome growth at any given stage, formerly shallow domes could be buried well below 3,000 ft.

Parker and McDowell (1955) also suggest that cap rock formed at one stage in the development of a dome could be sloughed, should upward growth of a dome be resumed. Sulfur-bearing cap rock near a depth of 7,000 ft on the flank of the Grand Isle dome and the remnants of cap rock at depths of 4,000 and 6,000 ft on the flank of Hockley dome, Harris County, Texas, appear to have formed in this manner (Canada, 1953).

Biogenic hydrogen sulfide must be oxidized to elemental sulfur within the cap rock, but geologists do not agree on the nature of the reactions. Oxidation of hydrogen sulfide to sulfur by free oxygen, often with the supplemental aid of hydrogen sulfide-oxidizing bacteria, *Thiobacillus thioparus,* is known to occur in near surface deposits such as the Shor Su in the U.S.S.R. (Ivanov, 1968). This is a straight-forward and readily demonstrable oxidative process. For cap rock sulfur deposits, Feely and Kulp (1957) proposed an anaerobic mechanism involving oxidation of hydrogen sulfide by sulfate ions:

$$SO_4^{-2} + 3H_2S \rightarrow 4S + 2OH^- + 2H_2O.$$

Davis and others (1970) were unable to substantiate this reaction experimentally at salt-dome cap rock temperatures or thermodynamically and doubt its validity as the means by which hydrogen sulfide is oxidized to elemental sulfur in this environment. However, even very slightly oxygenated ground waters can oxidize hydrogen sulfide to sulfur and these may reach and mix with the hydrogen sulfide-saturated waters in the cap rock:

$$2H_2S + O_2 \rightarrow 2S + 2H_2O.$$

Whether the reaction is mediated by *Thiobacillus thioparus* as Ivanov (1968) demonstrated in Russia is unknown. Since the above reaction is known to occur at the earth's surface and is known to extend at least several hundred feet below the surface, the question is, how deep can one expect oxygenated ground waters to penetrate? Certainly the depth of penetration is limited, but it is probably not too unreasonable to consider a limit on the order of 2,000 ft in sediments overlying a typical salt dome.

Feely and Kulp (1957) mentioned oxidation of hydrogen sulfide to sulfur by oxygen as an alternative mechanism but did not subscribe to it. They did point out that deposited sulfur in places has been oxidized and leached out of salt-dome cap rocks, presumably by meteoric ground waters. In fact, bacteria are again implicated, because they are the primary mediators of the oxidation of elemental sulfur to sulfate in nature. *Thiobacillus thiooxidans* is active in the oxidative destruction of shallow sulfur deposits in the Soviet Union (Ivanov, 1968; Sokolova and Karavaiko, 1968). No comparable biochemical studies of sulfur deposits have been made in the United States.

Sulfur Deposit in Challenger Knoll of the Sigsbee Deep, Gulf of Mexico

In 1968, sulfur and oil were discovered in cap rock at a depth of 450 ft in Challenger Knoll, a salt dome in the Sigsbee Deep abyssal plain of the Gulf of Mexico. The discovery was made by Maurice Ewing, together with Lamar Worzel and their associates, with a deep-sea drilling vessel, the Glomar Challenger (Ewing et al., 1969). The water depth was approximately 12,000 ft (3,572 m) and the nearest land more than 200 miles (350 km) distant. The borehole was drilled to a depth of 472 ft (144 m). Five intervals were cored, and the hole was plugged soon after encountering oil and gas. Three feet of calcitic oil-saturated core were recovered, as well as an underlying 1.5 ft of calcitic core containing 19 percent elemental sulfur. Gypsum was found below the sulfur zone. Based on this limited drilling and coring at the apex of the salt dome, which has a diameter of about 5 miles, one cannot adequately judge the extent of the sulfur deposit. However, its analogy with known salt-dome sulfur deposits is unquestionable. The isotopic composition of the sulfur and carbon clearly substantiates the similarity (Table 1).

Due to the geologic setting of the Challenger Knoll sulfur deposit, ground water can be ruled out as the

TABLE 1. Sulfur[1] and Carbon[2] Isotope δ Values for Challenger Knoll Compared with Typical Salt Dome Sulfur Deposits

	$\delta^{34}S_{NBS}$		$\delta^{13}C_{PDB}$	
	Anhydrite	Sulfur	Calcite	Oil
Challenger Knoll	+30.0	+14.2	−21.7 to −25.3	−26.6 to −26.7
Salt domes[3]			−23.8 to −51.1	−24.9 to −27.1
Boling	+12.2 to +39.2	0.0 to +4.0		
Moss Bluff	+14.0 to +52.7	−10.8 to −5.2		
Spindletop	+17.6 to +61.7	+0.9 to +15.3		

[1] Approximate ‰ relative to $^{32}S/^{34}S_{NBS}$ 120 standard.
[2] ‰ relative to $^{12}C/^{13}C_{PDB}$ standard.
[3] Sulfur values from Feely and Kulp (1957); carbon values from Cheney and Jensen (1967).

agent that dissolved and leached the halite of the salt diapir and thus concentrated anhydritic cap rock. There is a consensus that ground water has had this role primarily, if not completely, with respect to the salt-dome cap rocks of the Gulf Coast. The development of sulfur-bearing cap rock in Challenger Knoll suggests that at least some of the Gulf Coast cap rocks may have formed near the sea floor as a result of dissolution of the halite by sea water. Cap rock formed this way may not be as extensive as that formed by ground water, unless the dome is at the surface.

Sulfate-reducing bacteria were cultivated from a specimen of the gypsum recovered from the bottom of the borehole (Davis and Bray, 1969, p. 421). An unsuccessful, limited attempt was made to detect hydrogen sulfide-oxidizing and sulfur-oxidizing bacteria, but this does not rule out their possible presence.

Challenger Knoll is only one of approximately 2,000 diapirs within the Campeche-Sigsbee salt dome province, which extends northward from the Isthmus of Tehauntepec to the center of the Gulf of Mexico.

Sulfur Deposits in Permian Rocks of the Delaware Basin, West Texas

Based on sulfur and carbon isotopes analysis, we judge that sulfur deposits in West Texas were derived by the same bioepigenetic reactions that occurred in salt-dome cap rocks. The geologic setting is quite different, however. In salt-dome sulfur deposits, anhydrite was brought up from depth by salt diapirs and concentrated as cap rock within shallow, much younger strata. Anhydrite in the Permian sequence of West Texas consists of bedded evaporites laid down in a basin restricted from the sea by reefs but subject to an influx of sea water (Adams, 1944).

Sulfur is contained in orebodies within the late Permian (Ochoan) Salado and Castile Formations. Most deposits are small, but the Duval mine in Culberson County, Texas, originally had estimated reserves of 57 million long tons between the depths of 240 and 1,250 ft, within an area of about 1,400 acres (Zimmerman and Thomas, 1969). Several deposits are in the laminated Castile Formation. Alternating anhydrite and carbonate layers can be correlated for tens of kilometers (Anderson and Kirkland, 1966), and some individual laminae extend throughout much of the basin. However, the formation has been brecciated and fractured, the result of uplift of the Delaware Mountains during the Cenozoic. Brecciation also resulted from structural collapse following solution of halite and gypsum (or anhydrite) by meteoric ground waters. This permitted an influx of petroleum-bearing waters from underlying sandstones of the Bell Canyon Formation. The resulting association of petroleum and anhydrite led to the generation of the bioepigenetic sulfur deposits.

TABLE 2. Sulfur and Carbon Isotope δ Values[1] in Sulfur-Calcite Mineralized Section of Core of Castile Formation, Culberson County, Texas

	$\delta^{13}C_{PDB}$	$\delta^{34}S_{NBS}$
Calcite associated with sulfur	−24.1 to −38.0	
Calcite laminae of Castile Formation	+0.5	
Oil	−26.1	
Sulfur		+6.7
Anhydrite		+26.6

[1] Compare with Table 1 data.

Sulfur-calcite mineralization within the Castile Formation, in a 70-ft depth interval between 665 and 735 ft below the surface and 95 ft above the Bell Canyon Formation, was described by Davis and Kirkland (1970). The core we studied was cut from a deposit 20 miles northwest of the Duval mine. Elemental sulfur occurred intermittently in vuggy calcite throughout this 70-ft zone, with sulfur comprising up to 20 percent of the rock. Oil staining occurred intermittently within the mineralized section. The sulfur and carbon isotope data are essentially identical to data reported by Thode and others (1954) and Feely and Kulp (1957) for cap rock sulfur deposits (Table 2), so we conclude that sulfur deposits in the Permian bedded evaporites and in salt-dome cap rocks resulted from the same biogenic reactions. Epigenetic deposition within the laminated Castile Formation is obvious because the anhydrite laminae have been replaced by calcite and sulfur, often leaving as clearly recognizable the original, thin alternating carbonate laminae. The conspicuous buttes ("castiles") in the Castile Formation are exposed calcite masses, bioepigenetically derived during the anhydrite-reduction process (Hinds and Cunningham, 1970; Kirkland and Evans, 1976).

Oxidation of bacterially produced hydrogen sulfide to elemental sulfur in the West Texas anhydrite beds by atmospheric oxygen is less controversial than such oxidation in salt-dome cap rocks. The anhydrite beds, because of numerous sink holes and obvious fractures in the surface of the Gypsum Plain overlying the sulfur deposits, are subject to descending meteoric waters. Ivanov (1968) has presented evidence for the oxidation of hydrogen sulfide to sulfur by atmospheric oxygen in somewhat similar sulfur deposits in the Soviet Union.

Discussion

Whereas the biogenic sulfur deposits in the cap rocks of salt domes and in West Texas are epigenetic, some biogenic deposits are syngenetic. Ivanov (1968)

believes that the Cis-Carpathian sulfur deposits, for example, are biosyngenetic, although Sokolov (1969) does not. A biosyngenetic origin has been ascribed to the Sicilian sulfur deposits (Dessau et al., 1962). According to Ivanov, the principal criterion for identifying biosyngenetic sulfur deposits is their confinement, first, to a definite stratigraphic horizon and, second, to a certain lithologic facies. Moreover, petroleum is not found in biosyngenetic sulfur deposits, implying that the carbon from which the calcite of these deposits was derived was in some other form of organic matter. A high rate of bacterial sulfate reduction can occur in lagoons in which there is a high production of organic matter, leading to extensive generation of biosyngenetic sulfur. Some sediments being currently deposited provide insight into biosyngenetic processes (Ivanov, 1968), i.e., those along the shores of the Bay of Bengal which contain 20 to 30 percent elemental sulfur. These sites of sulfur accumulation are inundated by sea water yearly during the 6 months of the monsoon season. The sulfates of the sea water are reduced by sulfate-reducing bacteria to hydrogen sulfide in the organic-rich soils. When the sea water recedes, the hydrogen sulfide is oxidized to sulfur, probably with the participation of hydrogen sulfide-oxidizing bacteria.

Inland lakes also are sites of biosyngenetic sulfur accumulation. Sulfur in such deposits is cryptocrystalline and is free of calcite. Lake Cyrenaica, in Africa, is subject to an influx of hydrogen sulfide-rich waters; oxidation of the hydrogen sulfide and precipitation of sulfur proceeds with the participation of both the anaerobic, photosynthetic bacteria *Chlorobium* and *Chromatium* spp. and the aerobic *Thiobacillus* sp. (Butlin and Postgate, 1954).

The isotopic composition of biosyngenetic and bioepigenetic sulfur deposits is similar, so their differentiation must be based on reconstruction of the geologic history of their host rocks. The sulfur deposits of salt domes and deposits in West Texas are classified as bioepigenetic through such considerations. The anhydritic cap rocks of salt domes are obviously post-sedimentary accumulations, and the laminated Permian anhydritic evaporites of West Texas obviously formed prior to their postsedimentary fracturing. In both environments the anhydrite was later subjected to petroleum-bearing waters and a large-scale bacterial generation of hydrogen sulfide ensued. This contrasts with the Cis-Carpathian deposits where lenses of calcite and sulfur grade laterally into gypsum.

In West Texas, the oxidation of the hydrogen sulfide to sulfur by oxygenated meteoric waters is highly probable, whereas in Gulf Coast cap rocks oxidation by atmospheric oxygen is less certain. One can assume that the alternative mechanism of the oxidation of hydrogen sulfide by sulfate ions, proposed by Feely and Kulp (1957), if operable, would lead to elemental sulfur wherever both sulfide and sulfate ions are concomitant in the subsurface. However, elemental sulfur does not form in many oil-bearing formations that contain anhydrite and hydrogen sulfide, nor does it form in many subsurface waters rich in sulfate and sulfide ions. The sulfur in salt-dome cap rocks and in West Texas thus would be exceptional instances of this reaction.

Hydrogen sulfide can react inorganically with sulfate ions to form sulfur at high temperature and pressure (Toland, 1960), unrealistic physical conditions for shallow, biogenic sulfur deposits. But at high temperature and pressure any sulfur formed is reduced immediately to hydrogen sulfide by organic matter. Orr (1974) proposed this mechanism to explain the isotopically heavy, ^{34}S-enriched hydrogen sulfide associated with oils in the deeper, hotter reservoirs of the Big Horn basin, Wyoming.

Acknowledgments

We are grateful to A. J. Bodenlos for his careful review of the original manuscript and editorial suggestions. We thank Mobil Research and Development Corporation for permission to publish this review.

MOBIL RESEARCH AND DEVELOPMENT CORPORATION
FIELD RESEARCH LABORATORY
DALLAS, TEXAS 75221
October 6, 1978

REFERENCES

Adams, J. E., 1944, Upper Permian Ochoan series of Delaware Basin, west Texas and southeastern New Mexico: Am. Assoc. Petroleum Geologists Bull., v. 28, p. 1596–1625.

Anderson, R. Y., and Kirkland, D. W., 1966, Intrabasin varve correlation: Geol. Soc. America Bull., v. 77, p. 241–256.

Bodenlos, A. J., 1970, Cap-rock development and salt-stock movement, *in* Geology and technology of Gulf Coast salt—A symposium: Baton Rouge, School of Geoscience, Louisiana State Univ., p. 73–86c.

—— 1973, Sulfur, *in* United States mineral resources: U. S. Geol. Survey Prof. Paper 820, p. 605–617.

Butlin, K. R., 1953, The bacterial sulfur cycle: Research Applied in Industry, v. 6, p. 184–191.

Butlin, K. R., and Postgate, J. R., 1954, The microbiological formation of sulfur in Cyrenaican Lakes, *in* Biology of deserts: London, Symposia Inst. Biology, v. 112.

Canada, W. R., 1953, Hockley Field, Harris County, Texas: Guidebook, Joint Ann. Mtg., Am. Assoc. Petroleum Geologists-Soc. Econ. Paleontology and Mineralogy-Soc. Exploration Geophysicists, 1953, Houston, Texas, p. 125–128.

Cheney, E. S., and Jensen, M. L., 1967, Corrections to carbon isotopic data of Gulf Coast salt dome rock: Geochim. et Cosmochim. Acta, v. 31, p. 1345–1346.

Davis, J. B., and Bray, E. E., 1969, Analyses of oil and cap rock from Challenger (Sigsbee) Knoll, *in* Initial reports of the Deep Sea drilling project, Vol. 1: Washington, U. S. Geovernment Printing Office, p. 415–500.

Davis, J. B., and Kirkland, D. W., 1970, Native sulfur deposition in the Castile Formation, Culberson County, Texas: ECON. GEOL., v. 65, p. 107–121.

Davis, J. B., and Yarbrough, H. F., 1966, Anaerobic oxidation of hydrocarbons by *Desulfovibrio desulfuricans:* Chem. Geology, v. 1, p. 137–144.

Davis, J. B., Stanley, J. P., and Custard, H. C., 1970, Evidence against oxidation of hydrogen sulfide by sulfate ions to produce elemental sulfur in salt domes: Am. Assoc. Petroleum Geologists Bull., v. 54, p. 2444–2447.

Dessau, G., Jensen, M. L., and Nakai, N., 1962, Geology and isotopic studies of Sicilian sulfur deposits: Econ. Geol., v. 57, p. 410–438.

Ellisor, A. C., 1926, Coral reefs in the Oligocene of Texas: Am. Assoc. Petroleum Geologists Bull., v. 10, p. 976–985.

Ewing, M., Worzel, J. L., Beall, A. O., Berggren, W. A., Bukry, D., Burk, C. A., Fischer, A. G., and Pessagno, E. A., 1969, Initial reports of the Deep Sea drilling project, Vol. 1: Washington, U. S. Government Printing Office, p. 84–111.

Feely, H. W., and Kulp, J. L., 1957, Origin of Gulf Coast salt dome sulfur deposits: Am. Assoc. Petroleum Geologists Bull., v. 41, p. 1802–1853.

Hinds, J. S., and Cunningham, R. R., 1970, Elemental sulfur in Eddy County, New Mexico: U. S. Geol. Survey Circ. 628, 13 p.

Hunt, W. F., 1915, The origin of the sulfur deposits of Sicily: Econ. Geol., v. 10, p. 543–579.

Ivanov, M. V., 1968, Microbiological processes in the genesis of native sulfur deposits: Israel program for Scientific Translations, Cat. No. 1850, U. S. Dept. Commerce, 298 p. (English translation from Russian)

Kirkland, D. W., and Evans, R., 1976, Origin of limestone buttes, Gypsum Plain, Culberson County, Texas: Am. Assoc. Petroleum Geologists Bull., v. 60, p. 2005–2018.

Orr, W. L., 1974, Changes in sulfur content and isotopic ratios of sulfur during petroleum maturation—study of Big Horn basin Paleozoic oils: Am. Assoc. Petroleum Geologists Bull., v. 58, p. 2295–2318.

Parker, T. J., and McDowell, A. N., 1955, Model studies of salt-dome tectonics: Am. Assoc. Petroleum Geologists Bull., v. 39, p. 2384–2470.

Salas, G. P., 1967, Sulfur and petroleum in the salt domes of southern Mexico: 7th World Petroleum Congress, Mexico City, v. 1A, p. 65.

Sokolov, A. S., 1969, State and main problems of geologic investigations of native sulfur, *in* Geology of the native sulfur deposits: Moscow, Izdatel'stvo Nedra, p. 5–24. (English translation by D. B. Vitaliano for U.S.G.S.)

Sokolova, G. A., and Karavaiko, G. I., 1968, Physiology and geochemical of *Thiobacilli:* Israel Program for Scientific Translations, Cat. No. 1851, U. S. Dept. of Commerce, 283 p. (English translation from Russian)

Taylor, R. E., 1938, Origin of the caprock of Louisiana salt domes: Louisiana Geol. Survey Bull. 11, 191 p.

Thode, H. G., Wanless, R. K., and Wallough, R., 1954, The origin of native sulfur deposits from isotope fractionation studies: Geochim. et Cosmochim. Acta, v. 5, p. 286–298.

Toland, W. G., 1960, Oxidation of organic compounds with aqueous sulfate: Am. Chem. Soc. Jour., v. 82, p. 1911–1916.

Wolf, A. G., 1926, Big Hill salt dome, Matagorda County, Texas, *in* Geology of salt dome oil fields: Tulsa, Oklahoma, Am. Assoc. Petroleum Geologists, p. 691–717.

Zimmerman, J. B., and Thomas, E., 1969, Sulfur in west Texas: its geology and economics: Austin, Univ. of Texas, Bur. Econ. Geol. Cir. 69-2, 35 p.

Zobell, C. E., 1949, Report of progress. Fundamental research on the occurrence and recovery of petroleum, 1946–1947: New York, New York, Am. Petroleum Inst., p. 105–106.

SEISMIC WAVE ATTENUATION IN ROCKS

Gerald Mavko[1], Einar Kjartansson and Kenneth Winkler

Rock Physics Project, Department of Geophysics

Stanford University, Stanford, CA 94305

[1]Now at U.S. Geological Survey,
Menlo Park, CA 94025

Introduction

A fundamental feature associated with the propagation of stress waves in all solids is absorption of energy, which usually results in a change of the shape of transient waveforms. Despite its importance, the processes by which mechanical wave energy is converted into heat, and its effect on seismic observations, have been poorly understood. Although considerable progress has been made during the past few years, seismic attenuation remains a controversial subject as there is still considerable disagreement between different authors about some of its most fundamental aspects.

In the first section of this paper the progress in arriving at a general phenomenological description of wave propagation and related effects such as the frequency dependence of the elastic moduli and transient creep will be covered. It turns out that for most attenuation mechanisms that are significant in rocks, this can be treated relatively independent of the details of the particular physical mechanisms responsible for the energy dissipation, which are treated in the second section. The third section gives a review of experimental results.

We have chosen not to discuss work on unconsolidated sediments. Recent papers on the subject are by Hamilton (1972), Hampton and Anderson (1974), Stoll (1977) and Pilbeam and Vaisnys (1973). Application to earth models is discussed elsewhere in this report.

Phenomenological Description

Early laboratory work on absorption in rocks showed the loss per cycle or wavelength to be essentially independent of frequency. Since at that time no known linear theory could fit this observation, Born (1941) proposed that the loss was due to rate independent friction of the same kind as observed when two surfaces slide against each other. Kolsky (1956) and Lomnitz (1957) gave linear descriptions of the absorption that could account for the observed frequency independence and that were also consistent with other independent observations of the transient creep in rocks (Lomnitz, 1956; Pandit and Savage, 1973) and with the change in shape of pulses propagating through thin rods. Despite this and the fact that a satisfactory nonlinear friction model for attenuation has never been developed to the point where meaningful predictions could be made about the propagation of waves, nonlinear friction is commonly assumed to be the dominant attenuation mechanism in rocks (McDonal et al., 1958; Knopoff, 1964; White, 1966; Gordon and Davis, 1968; Lockner et al., 1977; Johnston et al., 1979).

A different type of theory for attenuation has been advocated by Ricker (1953, 1977). In his model the absorption is described by adding a single term to the wave equation. This model is often referred to as the Voigt solid (Voigt, 1892). Because of this simplicity, this theory has been further developed for the propagation of transient waves than the other theories. For this reason, wavelets based on the Ricker theory have been commonly used in the computation of synthetic seismograms, although the frequency dependence of Q that is implied by the model contradicts practically all experimental observations.

Perhaps the most noted advance during the quadrannium, was the recognition by Liu et al. (1976), that the dispersion required by anelasticity was a first order effect and sometimes about an order of magnitude greater than the uncertainty in the data, such as in the comparison of body wave travel times and free oscillation periods. Although the presence of this dispersion had often been pointed out previously (i.e. Lomnitz, 1957; Futterman, 1962; Kogan, 1966; Strick, 1967; Azimi et al., 1968), and its importance stressed by Jeffreys (1967), Randall (1976) and Strick (1971), most geophysicists have assumed that the elastic parameters of rocks were independent of frequency. An exception is in computation of synthetic earthquake seismograms where it is common practice to convolve a Futterman "Q operator" with a seismogram computed for a lossless earth. The "Q operator" (Burdick and Helmberger, 1978), refers to the seismogram resulting from an impulse plane wave source in a material with Q approximately independent of frequency and with a phase velocity $c(\omega)$ that over a resticted range of frequencies is given by the relation

$$c(\omega) = c_0\left(1 + \frac{1}{\pi Q} \ln\left(\frac{\omega}{\omega_0}\right)\right) \qquad (1)$$

where c_0 is the phase velocity at the reference frequency ω_0. The reason for the reluctance to recognize the importance of dispersion for surface and free oscillation problems may in part have been that Futterman (1962) arrived at his results by imposing causality on the propagating wave, and did not

Paper number 9R0560.
0034-6853/79/009R-0560$06.00

consider the constitutive stress-strain relations. This was done, however, by Kolsky (1956), Lomnitz (1957), and in some of the work done in the Soviet Union, reviewed by Kogan (1966).

In investigations of the actual physical mechanisms responsible for the energy conversion, it is common to look for an approximation that leads to a first order differential equation that describes the process, whether it is the diffusion of ions, molecules or heat, or the flow of fluids. Such first order differential equations have solutions that are decaying exponentials. Hence this form of solution is sometimes the result of approximations as much as a property of the mechanism itself.

A mechanism that fits a first order differential equation, or a linear superposition of first order differential equations, may be modelled by a network of springs and dashpots. In the theory of viscoelasticity it is customary to cast the behavior of materials in this form. A good summary is given by Gross (1953). Liu et al. (1976) and Kanamori and Anderson (1977) have used viscoelastic distributions to derive four parameter models that feature Q approximately independent of frequency over a restricted range of frequencies. In addition to the two parameters that are constrained by observations, i.e. propagation velocity and Q, the models include two parameters (high and low frequency cutoffs) that cannot be reliably determined from available data. It is assumed in these models that Q approaches infinity for both low and high frequencies, at a rate that is proportional to ω or ω^{-1}. This is a direct contradiction to what is known about the long term behavior of the mantle from such evidence as postglacial rebound, Chandler wobble and plate tectonics (Jeffreys, 1976). Neither is there any evidence for such rapid increase of Q with frequency from laboratory measurements, where the frequency range extends up to the megacycle range (White, 1965). Another problem with the band limited, near constant Q models is that it is assumed in the derivations that Q is large so the results are not internally consistent with low values of Q, such as commonly found in near surface sediments and suggested for parts of the upper mantle, i.e. by Anderson et al. (1977).

Kjartansson (1979) has given a two parameter model that avoids these complications by featuring Q that is exactly independent of frequency. The model is derived by assuming a particular form for the transient creep response while an alternative derivation from a viscoelastic distribution is also shown. Strick (1967) arrived at the same result by imposing causality on the time domain wave pulse. According to the Constant Q model the dependence of phase velocity on frequency is given by

$$c(\omega) = c_0 \omega^{\gamma} \qquad (2)$$

where

$$1/Q = \tan(\pi\gamma) \qquad (3)$$

and c_0 is the phase velocity at a unit frequency. Equation (1) is consistent with these equations within the approximations involved in the derivation of equation (1). While practically all available evidence seems to indicate that the variation of Q with frequency is much slower than the ω or ω^{-1} dependence implied by the simple viscoelastic models, there is no reason to believe that Q for all rocks is exactly constant. The approach used in the derivation of the constant Q model can also be used to derive simple three or four parameter models featuring arbitrarily rapid variations of Q with frequency (Kjartansson, 1979).

Carpenter (1966) used the phase velocity dispersion relations given by Kolsky (1956) and Futterman (1962) to compute a time domain seismogram for an implusive plane wave source. He found that when all terms of second order or higher in 1/Q are dropped, the wave shape depends only on the ratio t/Q, often referred to as t^*, where t is the travel time. The pulse width was approximately proportional to t^*, while the maximum amplitude is approximately inversely proportional to t^*. Gladwin and Stacey (1974) computed wave shapes for most of the published attenuation models, and found that the risetime τ, which they defined as the maximum amplitude divided by maximum slope, gave a reasonable fit to a relation of the form

$$\tau = C\frac{t}{Q} + \tau_0 \qquad (4)$$

Equation (4) also gave a good fit to in situ measurements of pulse shapes where the value of the constant C was found to be 0.53 ± 0.04. The Constant Q model (Kjartansson, 1979) implies that any particular measure of pulse width, such as risetime, would be exactly proportional to travel time, which is not exactly proportional to distance because of the velocity dispersion. The value of the parameter C depends on Q, but approaches a limiting value near 0.485 as Q becomes large. These results indicate that Q may be determined directly from time domain waveforms. This has been attemped by Ramana and Rao (1974) and Reiter and Monfort (1977). Minster (1978a, b) has used asymptotic approximations to compute pulse shapes for the band limited near constant Q models. Since the models used included four parameters, the results were not as simple to characterize as those for the Constant Q model, and some of the features found appear to be quite sensitive to parameters that are poorly constrained.

Mechanisms of Attenuation

In the previous section we have discussed some phenomenological aspects of wave attenuation. These allow us to categorize observations and to describe in detail the propagation of waves in the earth. In contrast, we now discuss mechanisms to explain observed losses in terms of the microstructure of rock.

It is most convenient to consider these mechanisms in two groups: those that involve pore fluids and those that do not. In the last four years the pore fluid mechanisms have by far received the most attention. One reason is the dramatic discovery that even trace amounts of water and volatiles increased attenuation in

lunar samples by an order of magnitude or more (Tittmann et al., 1972). Since rocks in the crust of the earth are almost always saturated (or at least moist), it is possible that fluid-related mechanisms might easily dominate dry rock sources of attenuation. In the mantle and crust a melt phase may play a similar role in lowering Q. There is also the motivation that measurements of attenuation can yield information distinct from that obtained from velocities about in situ conditions.

In the following we discuss separately losses associated with (1) viscous fluid flow, (2) the thermoelastic effect and phase change and (3) anelasticity of the solid rock matrix.

Viscous Fluid Flow. The source of viscous fluid attenuation in rock is relative motion between the solid and pore liquid. This motion causes shearing stresses in the fluid and, consequently, viscous dissipation of mechanical energy. Published models describe various modes of fluid motion that might be induced under the excitation of a passing wave.

The most comprehensive single treatment of wave propagation with dissipative fluid motion is the classical work of Biot (1956a, b). Biot assumes a saturated solid and includes the effects of fluid compressibility and coupled fluid and solid stress. Details of pore shape and local flow are neglected and lumped into parameters which relate only the averaged solid and fluid motions on a scale much larger than the pore size.

Physically, there are two simple sources of induced fluid flow in the Biot model (White, 1965). The first results from relative accelerations of the solid and liquid. Both P and S wave excitation cause acceleration of the solid matrix, while inertia causes the liquid to lag. Viscous stresses couple the solid and liquid, resulting in dissipation. The second mechanism occurs only with P waves. Differential compression along each wave length induces pressure gradients in the fluid. The fluid, in turn, diffuses through the solid according to Darcy's law.

Although the Biot formulation dominated modeling attempts for some time, its importance is restricted to high frequency and high permeability. White (1965) evaluates Biot's expression for P-wave attenuation for a high porosity (19%) and high permeability (200 mD) sandstone and finds it unimportant at frequencies less than 100 hz. Johnston et al. (1979) and Johnston and Cheng (1978) conclude the same thing, but add that Biot flow may be important for sedimentary rocks at ultrasonic frequencies. Stoll and Bryan (1970) and Stoll (1974, 1977) refine Biot's theory by allowing for additional (frequency-independent) losses in the rock matrix. They conclude that in low permeability materials like fine sediments where fluid mobility is low, Biot losses are negligible. The same is true for low porosity igneous rocks.

The last four years have seen an important shift in attention away from Biot flow, toward details of the microscopic flow field. When a section of rock is excited by a passing wave, heterogeneities, i.e., variations in pore shape, saturation and orientation produce large pressure gradients and flow on the scale of individual pores. Considerable dissipation may result. The distribution of heterogeneities produces several modes of flow with a rich relaxation spectrum. Because the average of the local flow over many pores is zero, this mechanism is ignored in the original Biot (1956a, b) model. It should be noted that Biot (1962) later suggested the idea of local flow and dissipation, but it wasn't pursued by other authors until recently. At least three generalized modes of local flow can be imagined, distinguished by the time scales appropriate to each.

The quickest flow is the viscous relaxation of simple shear stress across each pore. This is easiest to visualize in the case of a thin saturated crack. If a shear stress is abruptly applied across the crack the finite viscosity acts to instantaneously glue the opposite faces of the crack together; the faces subsequently slide past each other as simple shear relaxation occurs in the fluid. Walsh (1969) modeled these thin cracks as penny shaped spheroids. For a small concentration of cracks with identical aspect ratio he showed that the shear response of the composite is that of a standard linear solid with maximum attenuation occurring at approximately

$$\omega \approx \frac{\alpha\mu}{\eta} \qquad (5)$$

where α is the crack aspect ratio, μ is the shear modulus and η is the fluid viscosity. Walsh applied the model to high viscosity melts, though the latter values are subject to considerable uncertainty (Yoder, 1976). O'Connell and Budiansky (1977) use the self consistent approximation to extend the Walsh model to greater crack concentrations. Mavko and Nur (1979) treat simple shear relaxation of partially saturated cracks. Much earlier, shear relaxation along flat cracks and grain boundaries was discussed qualitatively by Ke (1948) and Zener (1948). Oldroyd (1956) considered the case of saturated spheres in shear relaxation.

The second mode of local flow involves pressure equalization within individual cracks (Mavko and Nur, 1978). For example, a uniform normal stress (compression) applied across a crack of variable thickness will induce instantaneous high pressures where the crack is thin and lower pressures where the crack is thick. The pressure gradient induces flow and dissipation. The flow differs from shear relaxation and is slower because there is a net transport of liquid along portions of the crack, whereas in shear there is not. The effect does not exist in ellipsoidal pore models where the instantaneous pressure is uniform (Eshelby, 1957). Mavko and Nur (1979) consider in detail the extreme case where individual cracks are partially saturated. In their model a liquid droplet occupies part of the crack length, with a highly compressible gas elsewhere. The much lower induced pressure in the gas produces a large pressure gradient and enhances flow. The predicted dissipation is so great that, ignoring other sources of loss, a few tenths of a percent by volume of water in very thin cracks can lower

Q to ~100. At low frequencies $Q^{-1} \propto \omega$ and at very high frequencies $Q^{-1} \propto \omega^{-3/2}$. Peak attenuation occurs in the range

$$\omega \approx \frac{1}{D}\sqrt{\frac{K_f}{\rho}} \qquad (6)$$

where K_f and ρ are the bulk modulus and density of the liquid and D is the length of the drop.

When the second mode of flow is nearly complete, individual cracks will be internally equilibrated (a condition termed "saturated isolated" by O'Connell and Budiansky, 1977). However, neighboring cracks will generally be at different pressures. With any deviatoric stress, cracks at different orientations will have different pore pressures (Mavko and Nur, 1975; O'Connell and Budiansky, 1977). Also, pores with different aspect ratios even with the same normal stress, will have different induced pore pressures (Korringa and Thompson, 1977). Hence, the third mode of flow consists of flow or local "squirt" (Mavko and Nur, 1975; O'Connell and Budiansky, 1977) from cracks of higher pressure to nearby cracks of lower pressure. The characteristic frequency of squirt has been estimated by O'Connell and Budiansky (1977) as

$$\omega \approx \frac{K}{\eta}\alpha^3 \qquad (7)$$

where K is the bulk modulus of the uncracked rock, η is the liquid viscosity and α is the crack aspect ratio.

The resulting state of locally equilibrated pressure has been called "undrained" (Rice and Cleary, 1976) and "saturated isobaric" (O'Connell and Budiansky, 1977). In the undrained condition only large scale pressure gradients remain, corresponding to the applied stress gradients of the passing seismic wave. This is the condition treated by the theory of Biot (1956a, b).

The values of Q corresponding to the various modes of local flow have been approximated in several ways. Walsh (1969) and O'Connell and Budiansky (1977) start with expressions for a purely elastic composite and assign complex moduli to the fluid inclusions. For shear relaxation of pores this amounts to simply making the shear modulus imaginary. However for flow between cracks (third mode) the complex moduli are only approximate, following from rough intuitive pictures of the way pores are connected. In both cases the resulting effective moduli for the rock are complex and yield frquency dependent velocity and attenuation. For the partially saturated case Mavko and Nur (1979) solve for the frequency dependent flow field in each pore and directly compute the viscous energy dissipation.

Although these various modes of local flow and relaxation have been recognized for some time a comprehensive quantitative analysis of Q and relaxation times was done only recently by O'Connell and Budiansky (1977) and Mavko and Nur (1979). In addition O'Connell and Budiansky (1977) attempt to account for partial crack interaction using the self-consistent approximation, although the validity of the latter has been seriously questioned (Bruner, 1976; Chatterjee et al., 1978). Prior to this the analyses by Walsh (1969) and Biot (1956a, b) dominated interpretation of viscous fluid losses.

O'Connell and Budiansky (1977) convincingly argue that fluid flow between cracks is the most probable interpretation of high frequency laboratory measurements of Q in water saturated rocks and partially molten solids. Shear relaxation may also contribute for high viscosity liquids. At seismic frequencies flow between cracks may be only marginally important, while some non-viscous mechanisms begin to contribute.

An additional model of attenuation for partially saturated rocks that is intermediate between local flow and Biot flow is by White (1975). His treatment resembles Biot's in that lumped parameters describe the material and flow properties on a scale much greater than a pore dimension. Only low frequency viscous flow is considered. White includes undersaturation by considering regions of dry rock containing many pores imbedded in regions of saturated rock also containing many pores. High pressure gradients and flow occur at the contact between wet and dry rock and result in large attenuation. At low frequencies White's expression for Q^{-1} varies as ω while at higher frequencies Q^{-1} varies as $1/\omega$.

Thermoelasticity and Phase Changes

Thermal relaxation is a well known mechanism in solids (Zener, 1948). Savage (1965) and Armstrong (1979) have estimated the seismic attenuation in dry rocks. The results indicate that although this is probably not the dominant mechanism for seismic attenuation in the upper crust, it may be responsible for the background attenuation observed in very dry rocks on the moon and in the laboratory (Tittmann, 1978). Kjartansson and Denlinger (1977) and Kjartansson (1978a) have applied the thermal relaxation mechanisms to porous rocks where the pore space contains fluid or vapor phases. Their results indicate that the attenuation due to thermal relaxation and phase transitions between the pore fluids and the rock matrix, is sensitive to pore pressure, degree of fluid saturation and temperature. The greatest attenuation is predicted for partially saturated rocks at moderate pore pressures and water satured rocks at high temperatures. Vaisnys (1968) and Kjartansson (1978a) treated the attenuation due to phase transitions in rocks containing partial melt. They predict large attenuation especially in pure compression, whenever any partial melt is present in the rock. Combined with observation data for bulk loss in the earth, this mechanism should provide a useful upper bound on the extent of partial melt in the crust and upper mantle.

Solid Phase Losses

Although fluid mechanisms may dominate attenuation in certain portions of the crust and upper mantle, observations have shown that losses do not go to zero in the limit of zero saturation. Instead, a residual level is present which must be attributed to anelasticity

of the individual mineral grains or to the interaction between adjacent grains. Jackson and Anderson (1970) give a comprehensive review of solid mechanisms relevant to high temperatures and pressures. These include damped resonance of pinned dislocation segments, dislocation unpinning, motion of dislocation kinks, atomic diffusion, grain boundary relaxation and vacancy diffusion. In addition, we have already mentioned thermoelasticity and stress-induced phase changes. Comparatively little work in this area has been done in the last four years except for a hand-full of papers concerning frictional sliding and dislocations.

Frictional sliding on crack surfaces and grain boundaries has been the most quoted (Johnston and Cheng, 1978; Lockner et al., 1977; Gordon and Davis, 1968) explanation of attenuation at low pressures. The intuitive attraction is that simple Coulomb friction is independent of frequency, as is commonly observed for Q. In addition, attenuation is greater for polycrystalline rocks than for single crystals (Peselnick and Zietz, 1959) suggesting the importance of grain boundaries. Walsh (1966), in one of the first analyses of frictional attenuation in rocks, approximated sliding surfaces as elliptic cracks. Mindlin and Deresiewicz (1953) considered the case of spherical surfaces in contact. Miller (1978) examines reflection and transmission across an infinite plane which provides frictional coupling between two halfspaces. More recently, Mavko (1979) analyses frictional losses on irregularly shaped nonelliptic cracks. The most important result is that in all cases the models predict an amplitude dependent attenuation. Mavko (1979) points out that friction can explain the amplitude dependence in certain large strain laboratory measurements, but must become negligibly small at wave strains. Also, the net slip on reasonable sized cracks becomes comparable at wave strains to atomic spacing and can probably not be described with macroscopic sliding friction (Savage, 1969). This suggests a transition at small strains to an atomic level mechanism of grain boundary relaxation--perhaps a linear mechanism associated with the motion of lattice dislocations.

Mason et al. (1977, 1978) suggest that solid phase attenuation in rocks can be explained by dislocation motion in the interior of grains and at grain boundaries. At low frequencies energy is lost when dislocation kinks cross Peierls barriers of the second kind. This nonlinear loss is proportional to the number of kink displacements and is independent of frequency. A second linear source of loss is a damping force proportional to dislocation velocity. The combined mechanisms would give a constant Q^{-1} at low frequencies, followed by increasing, then decreasing, values at higher frequencies. Mason et al. (1970) find such a frequency dependence for fine grain Westerly granite over the range $2 \cdot 10^4$ to $2 \cdot 10^6$ Hz.

Laboratory Observations and Their Interpretation

In recent years significant advances have been made in the experimental methods used to study seismic attenuation in the laboratory. Those which we will discuss include:

a. At frequencies from 50 hz to 15 khz, it has been shown that ultra-high vacuum can significantly decrease attenuation in both lunar and terrestrial rocks.
b. Low frequency quasi-static techniques at periods of several hundred seconds have been extended to lower strains, now approaching 10^{-7}.
c. Resonance experiments below 1 khz have been performed on water saturated rocks with independently controlled confining pressure and pore pressure, providing insights into fluid flow energy loss mechanisms.
d. Ultrasonic measurements using resonating rock spheres have been used to separate the energy losses in pure shear and bulk compression.
e. Pulse experiments have shown that rise-time measurements may provide a simpler means of measuring attenuation than conventional Fourier techniques. Field studies have been made using the rise-time methods.

One of the first observations of lunar seismology was that seismic waves propagated with much less attenuation on the moon than is observed in the earth's crust (Latham et al., 1970). A Q of 3000-5000 was observed on the moon, whereas measurements on returned lunar samples at ambient room conditions indicated Q $\sim$100, comparable to terrestrial rocks (Tittmann et al., 1972; Warren and Trice, 1974; Herminghous and Berckhemer, 1974). This initiated efforts to measure attenuation in the lab under lunar conditions of low temperature and high vacuum. Decreasing temperature to -200° C was found to increase Q by a factor of 2-3 in several terrestrial rocks and lunar samples (Tittmann et al., 1972; Herminghous and Berckhemer, 1974), but de-gassing of rocks in a hard vacuum was found to have an even more significant effect. Several investigators made studies in this area (Pandit and Tozor, 1970; Warren, 1973; Warren and Trice, 1974; Herminghous and Berckhemer, 1974), but the most complete series of experiments was performed by Tittmann and his colleagues over a period of several years (Tittmann et al., 1972, 1973, 1974, 1975, 1976; Tittmann, 1977, 1978). Tittmann has shown that in materials ranging from lunar and terrestrial rocks to a ceramic and porous glass, ultra-high vacuum (to 10^{-10} torr) combined with heat treatments to 300° C can increase Q by roughly two orders of magnitude over the values at room conditions. A lunar sample with a Q of 60 has had its Q increased to over 4800, putting it in the range found by lunar seismology. While most of Tittmann's experiments were done at $\sim$10 khz using a free resonance technique, the latest experiments have been done at $\sim$50 hz (with similar results) using a mass-loaded resonance technique. The cause of this behavior has been linked to trace amounts of volatiles found in the samples, particularly water vapor, but the mechanism causing these effects has not yet been identified. An extension of the partial saturation model of Mavko and Nur (1979) to

extremely small degrees of saturation is one possibility, but this is highly speculative.

On a different front, progress has been made towards resolving the apparently contradictory evidence of nonlinear attenuation at strains greater than $\sim 10^{-6}$ with the linear behavior observed at lower strains. Amplitude dependence of Q has been reported by a number of investigators, but Gordon and Davis (1968) showed that Q is nearly constant at strains below 10^{-6} (at 90 khz) whereas it decreases with strain amplitude at larger strains. They also reported cusped (as opposed to elliptical) stress-strain hysteresis loops in high strain ($>10^{-5}$), low frequency (0.014 hz) quasi-static experiments. The interpretation of cusped loops in terms of static hysteresis was made somewhat ambiguous by the use of triangular loading cycles (Stacey et al., 1975) but subsequent experiments with sinusoidal loading cycles confirmed their results. This nonlinear behavior could be explained by a Coulomb friction mechanism, but there was no evidence of nonlinear behavior at the low strains typical of many experiments and most seismic waves (Savage and Hasegawa, 1967; Savage, 1969).

Observations of the amplitude dependence of Q were extended to the millihertz range by Gordon and Rader (1971), again at strains greater than 10^{-5}. Similar experiments by McKavanagh (1973) also showed variation of attenuation with strain amplitude as well as a corresponding variation of Young's modulus. McKavanagh and Stacey (1974) found that cusped loops persisted at strains approaching 10^{-6}, but with further refinements Brennan and Stacey (1977) found that the stress-strain loops did become elliptical at strains of $\sim 10^{-6}$. Brennan and Stacey also observed the velocity dispersion predicted by linear, constant Q theories of attenuation.

The variation of Q with strain amplitude was studied further by Winkler et al. (1979) using a resonant bar technique at $\sim$ 1 khz. They found that the amplitude dependence was a function of effective confining pressure (confining pressure minus pore pressure) and the moderately low confining pressures eliminated the effect. The presence of water was shown to increase the amplitude dependence. Materials not containing microcracks (lucite, porous glass, aluminum) showed no variation of Q with amplitude. Winkler et al. also found that velocity varied with strain amplitude in the same manner as Q, although the effect was an order of magnitude smaller. These observations, together with the cusped stress-strain loops, have been interpreted in terms of a nonlinear frictional energy loss that becomes negligible at low strain amplitudes.

The observations of nonlinear vs. linear attenuation of seismic waves have thus been related to the strain amplitudes at which the measurements were made. Nonlinear effects are observed only at large strains (greater than 10^{-6}) and at low confining pressures. Seismic waves propagate at strains much lower than 10^{-6} and in rock at high confining pressure, so nonlinear effects will be suppressed in situ. Since grain boundary friction is the most likely source of nonlinear, amplitude dependent attenuation, these results strongly suggest that simple friction is not an important energy loss mechanism for seismic waves.

In a series of experiments using composite resonator and pulse reflection techniques over the frequency range from 15 khz to 15 Mhz, Mason and his co-workers (Mason et al., 1970, 1971; Mason, 1971a, b) found that in several rocks a peak attenuation occurred near a frequency of 1 Mhz. Attenuation was found to vary by nearly a factor of ten over a decade of frequency. If this result is found to be general, it will throw serious doubt on the constant Q assumption commonly quoted in the literature. Because of decreasing attenuation at the highest frequencies, this behavior was attributed not to scattering losses but to dislocation damping at cracks and grain boundaries. Mason was able to fit his data to theoretical curves based on combinations of linear and nonlinear dislocation mechanisms.

Separation of energy loss into shear and bulk compressional components is a useful approach for evaluating attenuation mechanisms, but Birch (1975) appears to have been the first to suggest applying this method to laboratory data on rocks. Birch studies resonance modes of spheres of granite, glass and steel, and shows that in steel shear energy losses dominate over compressional losses. Mason et al. (1978) extended these techniques to several other rocks and minerals. Although the relative importance of shear and compressional losses varied among the samples, some of the data was interpreted in terms of dislocation motion on cracks.

Winkler and Nur (1979) have used extensional and torsional data to calculate shear and bulk compressional energy losses in resonating rock bars. For both a sandstone and porous Vycor glass they have found that in dry and fully saturated samples shear attenuation is greater than compressional attenuation, whereas in partially saturated samples, shear loss is less than the compressional loss. These results have been interpreted in terms of fluid flow and thermoelastic mechanisms. In partially saturated rock the mechanisms presented by Mavko and Nur (1979) and Kjartansson and Denlinger (1977) adequately explain the observations, but the data cannot distinguish between them. Although the absolute magnitude of the attenuation cannot be accurately predicted, reasonable estimates of the model parameters do predict attenuation of the observed order of magnitude. In addition, the models predict bulk losses to be roughly twice the loss in shear, and this is very close to what is observed. These mechanisms are suppressed when the rock is totally saturated and the attenuation must then be described either by Biot's flow mechanism or by "squirting" flow (Mavko and Nur, 1975; O'Connell and Budiansky, 1977). Both mechanisms predict more energy loss in shear than in bulk compression, which is in agreement with he observations of Winkler and Nur (1979). However, Biot's mechanism predicts a magnitude of attenuation which is too low by at least an order of magnitude. The model developed by O'Connell and Budiansky apparently can predict the observed magnitude of the attenuation and so is in good agreement with experimental results. All of the data presented by Winkler and Nur can

be explained by local flow mechanisms and a thermal mechanism, and the mechanisms intermesh as the degree of saturation increases to total saturation. These experiments were done at frequencies between 500 and 1000 hz. Although theory is available to describe the data, theoretical extrapolation to lower frequencies is not possible because of the possibility of superposition of relaxation times (Liu, et al., 1977; O'Connell and Budiansky, 1977). O'Connell and Budiansky suggest that "squirting" flow may be important at seismic frequencies, but experiments are needed to decide the issue.

Several other studies in recent years have provided insights into attenuation mechanisms. Pandit and Savage (1973) have used a theory due to Lomnitz (1956) to predict values of Q from creep experiments. The predictions were in good agreement with values measured at sonic frequencies. This work provides strong evidence that attenuation is a linear phenomenon, at least under the conditions of the experiment. Gordon (1974) has presented data taken by V. Clark showing the relaxation spectrum (and associated modulus defect) of Rhode Island granite saturated with glycerine. An attenuation peak occurs at a fluid viscosity of 40 poise at a frequency of 50 khz indicating that if the pore fluid were water (.01 poise) the peak would occur at 20 Mhz. Therefore, this particular relaxation is not likely to be observed in the earth.

Kissel (1972) has measured attenuation in resonating bars of room dry rock as temperature was varied from -200°C to 600°C. The significant effects on attenuation were explained by the effect of temperature on the moisture content of the samples. Stocker and Gordon (1975) used a composite resonator to measure attenuation in partially melted metal alloys. They found that attenuation usually increased with melt fraction, and that the magnitude of the effect was strongly dependent on the dihedral angle between melt and solid.

Lockner et al. (1977) have measured relative attenuation in triaxially stressed rock as dilatancy causes cracks to open prior to fracture. By recording P, SV and SH waves propagating in various directions relative to the stress axis, they have shown the strong effect that cracks and crack orientation have on attenuation. Toksoz et al. (1979), using an ultrasonic spectral ratio technique, have measured attenuation in dry, saturated and frozen samples of sandstone and limestone. Johnston et al. (1979) have modeled these observations theoretically and concluded that frictional losses dominate over fluid loss mechanisms. Attenuation anisotropy has been measured in limestone and taconite by Singh (1976) using an ultrasonic pulse echo technique.

Discussion and Conclusions

Attempts have been made to interpret observations in terms of specific mechanisms, based on frequency dependence. For example, the often observed weak dependence of Q on frequency has in the past been attributed to nonlinear mechanisms. More recently it has been shown that superposition of linear mechanisms may provide a more reasonable explanation for the weak dependence. Superposition of relaxation times points up a difficulty in evaluating attenuation mechanisms. Every linear attenuation mechanism predicts a specific frequency dependence for attenuation. This frequency dependence, along with the relative and absolute magnitudes of bulk and shear energy loss, are the most significant measurable quantities by which to evaluate a particular mechanism. However, since the relaxation times of most mechanisms are determined by heterogeneities in rock, (generally crack sizes and shapes), and these heterogeneities vary in scale, it is expected that the frequency dependence will not be that which is predicted by the simplest form of the mechanism. While superposition of relaxation times may well explain the weak dependence of Q on frequency, it makes it difficult or impossible to use such measurements to evaluate attenuation mechanisms. By the same token it is not at present possible to use specific mechanisms to extrapolate high frequency lab data to in situ frequencies. It has been well documented that velocities measured at ultrasonic frequencies provide a good measure of velocities at seismic frequencies. The same statement cannot be made about attenuation.

A more promising test of specific mechanisms is the predicted ratio of bulk and shear losses (Q_p/Q_s). For most models this ratio is relatively insensitive to specific model parameters. Other potentially useful tests are the dependence of Q on temperature, strain amplitude, degree of saturation, and the correlation between variations in Q and velocity. Precise experimental data are needed to establish these dependences.

The most serious limitation on the quantitative reliability is the uncertainty of parameters describing pore geometry and fluid distribution. In most models these paramters can be adjusted within physically reasonable limits to give plausible predictions. However, several different models can often account for observed attenuation. The paramters are not known well enough to distinguish the relative contributions of the mechanisms.

Acknowledgements. This work was supported by a contract from the Department of Energy EY76-S-03-0326 PA#45. Dr. Gerald Mavko was supported on an National Science Foundation Postdoctoral Fellowship.

References

Anderson, D.L., H. Kanamori, R.S. Hart and H.-P. Liu, The earth as a seismic absorption band, Science, 196, 1104-1106, 1977.

Armstrong, B.H., Background internal friction of heterogeneous solids (abstract), Geophysics, 44, 334, 1979.

Azimi, Sh. A., A.V. Kalinin, and B.L. Pivavarov, Impulse and transient characteristics of media with linear and quadratic absorption laws, Izv., Earth Phys., 2, 42-54, 1968. (English transl.)

Biot, M.A., Theory of propagation of elastic waves in a fluid saturated porous solid. I. Low-

frequency range, J. Acoust. Soc. of Am., 28, 168-178, 1956a.
Biot, M.A., Theory of propagation of elastic waves in a fluid-saturated porous solid. II. Higher frequency range, J. Acoust. Soc. of Am., 28, 179-191, 1956b.
Biot, M.A., Generalized theory of acoustic propagation in porous dissipative media, J. Acoust. Soc. Am., 34, 1254-1264, 1962.
Birch, F., Velocity and attenuation from resonant vibrations of spheres of rock, glass, and steel, J. Geophys. Res., 80, 756-764, 1975.
Born, W.T., The attenuation constant of earth materials, Geophysics, 6, 132-148, 1941.
Brennan, B.J. and F.D. Stacey, Frequency dependence of elasticity of rock-test of seismic velocity dispersion, Nature, 268, 220-222, 1977.
Bruner, W.M., Comment on 'Seismic velocities in dry and saturated cracked solids' by R.J. O'Connell and B. Budiansky, J. Geophys. Res., 81, 2573-2576, 1976.
Burdick, L.J. and D.V. Helmberger, The upper mantle P velocity structure of the western United States, J. Geophys. Res., 83, 1699-1712, 1978.
Carpenter, E.W., Absorption of elastic waves - an operator for a constant Q mechanism, AWRE Report No. O-43/66, H.M. Stationary Office, 1966.
Chatterjee, A.K., A.K. Mal, and L. Knopoff, Elastic moduli of two-component systems, J. Geophys. Res., 81, 1785-1792, 1978.
Eshelby, J.D., The determination of the elastic field of an ellipsoidal inclusion, and related problems, Proc. Roy. Soc. London, A, 241, 376, 1957.
Futterman, W.I., Dispersive body waves, J. Geophys. Res., 67, 5279-5291, 1962.
Gladwin, M.T. and F.D. Stacey, Anelastic degradation of acoustic pulses in rock, Phys. Earth Planet. Int., 8, 332-336, 1974.
Gordon, R.B., Mechanical relaxation spectrum of crystalline rock containing water, J. Geophys. Res., 79, 2129-2131, 1974.
Gordon, R.B. and L.A. Davis, Velocity and attenuation of seismic waves in imperfectly elastic rock, J. Geophys. Res., 73, 3917-3935, 1968.
Gordon, R.B., and D. Rader, Imperfect elasticity of rock: its influence on the velocity of stress waves, in Structure and Physical Properties of the Earth's Crust, Geophys. Monograph Series, v. 14, edited by G. Heacock, pp. 235-242, 1971.
Gross, B., Mathematical Structure of the Theories of Viscoelasticity, 74 pp., Hermann, Paris, 1953.
Hamilton, E.L., Compressional-wave attenuation in marine sediments, Geophysics, 37, 620-646, 1972.
Hampton, L.D., and A.L. Anderson, Acoustics and gas in sediments: applied research laboratories (ARL) experience, in Natural Gases in Marine Sediments, edited by I.R. Kaplan, Plenum Press, New York, 1974.
Hart, R.S., L. Anderson, and H. Kanamori, The effect of attenuation on gross earth models, J. Geophys. Res., 82, 1647-1653, 1977.
Herminghous, C., and H. Berckhemer, Shock induced ultra-sound absorption in lunar anorthosite, Proc. Lunar Sci. Conf. 5th, 2939-2943, 1974.
Jackson, D.D., and D.L. Anderson, Physical mechanisms of seismic-wave attenuation, Rev. of Geophysics and Space Physics, 8, 1-63, 1970.
Jeffreys, H., Radius of the earth's core, Nature, 215, 1365-1366, 1967.
Jeffreys, H., The damping of P waves, Geophys. J. R. astr. Soc., 47, 347-349, 1976.
Johnston, D.H., and C.H. Cheng, The role of fluid flow in attenuation, (abstract) EOS Transactions Am. Geophys. Un., 59, 377, 1978.
Johnston, D.H., and M.N. Toksoz, Attenuation of seismic waves in dry and saturated rocks, (abstract) Geophysics, 42, 1511, 1977.
Johnston, D., N. Toksoz, and A. Timur, Attenuation of seismic waves in dry and saturated rocks, II: Mechanisms, Geophysics, 44, 691-711, 1979.
Kanamori, H., and D.L. Anderson, Importance of physical dispersion in surface wave and free oscillation problems: review, Rev. Geophys. Space Phys., 15, 105-112, 1977.
Ke, T.-S., Experimental evidence of the viscous behavior of grain boundaries in metals, Phys. Rev., 71, 533, 1948.
Kissell, F.N., Effect of temperature variation on internal friction in rocks, J. Geophys. Res., 77, 1420-1423, 1972.
Kjartansson, E., Thermal relaxation, an attenuation mechanism for porous rocks (abstract), EOS Trans. Am. Geophys. Un., 59, 324, 1978a.
Kjartansson, E., Frequency dependence of Q -- a theoretical framework (abstract), EOS Trans. Am. Geophys. Un., 59, , 1978b.
Kjartansson, E., Constant Q -- wave propagation and attenuation, J. Geophys. Res., in press, 1979.
Kjartansson, E. and R. Denlinger, Seismic wave attenuation due to thermal relaxation in porous media (abstract), Geophysics, 42, 1516, 1977.
Knopoff, L., Q, Rev. Geophys. Space Phys., 2, 625-660, 1964.
Kogan, S. Ya., A brief review of seismic wave absorption theories II., Izv. Earth Phys., 11, 17-28, 1966.
Kolsky, H., The propagation of stress pulses in viscoelastic solids, Phyl. Mag., 1, 693-710, 1956.
Korringa, J., and D.D. Thompson, Comment on the self-consistent imbedding approximation in the theory of elasticity in porous media, J. Geophys. Res., 82, 933-934, 1977.
Kuster, G.T., An interaction model for elastic wave propagation in a two-phase media, Geophys. Prospect., 25, 481-495, 1977.
Kuster, G.T., and M.N. Toksoz, Velocity and attenuation of seismic waves in two-phase media. Part I. Theoretical formulations, Geophysics, 39, 587-606, 1974a.
Kuster, G.T., and M.N. Toksoz, Velocity and attenuation of seismic waves in two-phase media: Part II. Experimental results, Geophysics, 39, 607-618, 1974b.
Latham, G.V., M. Ewing, J. Dorman, F. Press, N. Toksoz, G. Sutton, R. Meissner, F. Duennebier, Y. Nakamura, R. Kovach and M. Yates, Seismic data from man-made impacts on the moon, Science, 170, 620-626, 1970.
Liu, H.-P., D.L. Anderson and H. Kanamori, Velocity dispersion due to anelasticity: implications for seismology and mantle composition, Geophys. J. Roy. astr. Soc., 47, 41-58, 1976.

Lockner, D.A., J.B. Walsh, and J.D. Byerlee, Changes in seismic velocity and attenuation during deformation of granite, J. Geophys. Res., 82, 5374-5378, 1977.

Lomnitz, C., Creep measurements in igneous rocks, J. Geol., 64, 473-479, 1956.

Lomnitz, C., Linear dissipation in solids, J. Appl. Phys., 28, 201-205, 1957.

Lomnitz, C., Application of the logarithmic creep law to stress wave attenuation in the solid earth, J. Geophys. Res., 67, 365-368, 1962.

McDonal, F.J., F.A. Angona, R.L. Mills, R.L. Sengbush, R.G. van Nostrand, and J.E. White, Attenuation of shear and compressional waves in Pierre shale, Geophysics, 23, 421-439, 1958.

McKavanagh, B., M.Sc. Thesis, Dept. of Physics, Univ. of Queensland, Australia, 1973.

McKavanagh, B. and F.D. Stacey, Mechanical hysteresis in rocks at low strain amplitudes and seismic frequencies, Phys. Earth. Planet. Int., 8, 246-250, 1974.

Mason, W.P., Internal friction in moon and earth rocks, Nature, 234, 461-463, 1971a.

Mason, W.P., Internal friction at low frequencies due to dislocations: applications to metals and rock mechanics, in Physical Acoustics, edited by W.P. Mason and R.N. Thurston, v. 8, p. 347-371, Academic Press, N.Y., 1971b.

Mason, W.P., D.N. Beshers and J.T. Kuo, Internal friction in Westerly granite: relation to dislocation theory, J. Appl. Phys., 41, 5206-5209. 1970.

Mason, W.P., and J.T. Kuo, Internal friction of Pennsylvania slate, J. Geophys. Res., 76, 2084-2089, 1971.

Mason, W.P., K.J. Marfurt, D.N. Beshers, and J.T. Kuo, Internal friction of metal spheres showing the effect of the anisotropy of the component metals, J. Acoust. Soc. Am., 62, 1206-1212, 1977.

Mason, W.P., K.J. Marfurt, D.N. Beshers, and J.T. Kuo, Internal friction in rocks, J. Acoust. Soc. Am., 63, 1596-1603, 1978.

Mavko, G.M., Frictional attenuation: an inherent amplitude dependence, J. Geophys. Res., in press, 1979.

Mavko, G.M., and A. Nur, Melt squirt in the asthenosphere, J. Geophys. Res., 80, 1444-1447, 1975.

Mavko, G.M. and A. Nur, The effect of nonelliptical cracks on the compressibility of rocks, J. Geophys. Res., 83, 4459-4468, 1978.

Mavko, G.M. and A. Nur, Wave attenuation in partially saturated rocks, Geophysics, 44, 161-178, 1979.

Miller, R.K., The effects of boundary friction on the propagation of elastic waves, Bull. Seism. Soc. Am., 68, 987-998, 1978.

Mindlin, R.D., and H. Deresiewicz, Elastic spheres in contact under varying oblique forces, J. Appl. Mech., 20, 327-344, 1953.

Minster, J.B., Transient and impulse responses of a one-dimensional linearly attenuating medium, 1. Analytical results, Geophys. J. R. astr. Soc., 52, 479-501, 1978a.

Minster, J.B., Transient and impulse responses of a one-dimensional linearly attenuating medium, II. A parametric study, Geophys. J. R. astr. Soc., 52, 503-534, 1978b.

Murase, T., and A.R. McBirney, Properties of some common igneous rocks and their melts at high temperatures, Geol. Soc. Am. Bull., 84, 3563-3592, 1973.

O'Connell, R.J., and B. Budiansky, Reply, J. Geophys. Res., 81, 2577-2578, 1976.

O'Connell, R.J., and B. Budiansky, Viscoelastic properties of fluid-saturated cracked solids, J. Geophys. Res., 82, 5719-5735, 1977.

O'Connell, R.J., and B. Budiansky, Measures of dissipation in viscoelastic media, Geophys. Res. Lett., 5, 5-8, 1978

Oldroyd, J.G., The effect of small viscous inclusions on the mechanical properties of an elastic solid, in Deformation and Flow of Solids, IUTAM Colloquium, Madrid, 1955, edited by Grammel, Springer-Verlag, Berlin, 1956.

Pandit, B.I., and J.C. Savage, An experimental test of Lomnitz's theory of internal friction in rocks, J. Geophys. Res., 78, 6097-6099, 1973.

Pandit, B.I., and D.C. Tozer, Anamalous propagation of elastic energy within the moon, Nature, 226, 335, 1970.

Peselnick, L., and I. Zietz, Internal friction of fine-grained limestones at ultrasonic frequencies, Geophysics, 24, 285-296, 1959.

Pilbeam, C.C., and J.R. Vaisnys, Acoustic velocities and energy losses in granular aggregates, J. Geophys. Res., 78, 810-824, 1973.

Ramana, Y.V., and M.V.M.S. Rao, Q by pulse broadening in rocks under pressure, Phys. Earth Planet. Int., 8, 337-341, 1974.

Randall, M.J., 1976, Attenuative dispersion and frequency shifts of the earth's free oscillations, Phys. Earth Planet. Int., 12, 1-4, 1976.

Reiter, L. and M.E. Monfort, Variations in initial pulse width as a function of anelastic properties and surface geology in central California, Bull. Seism. Soc. Am., 67, 1319-1338, 1977.

Rice, J.R., and M.P. Cleary, Some basic stress diffusion solutions for fluid-saturated elastic porous media with compressible constituents, Rev. of Geophys. and Space Physics, 14, 227-242, 1976.

Ricker, N., The form and laws of propagation of seismic wavelets, Geophysics, 18, 10-40, 1953.

Ricker, N., Transient Waves in Visco-Elastic Media, Elsevier, Amsterdam, 278 pp., 1977.

Savage, J.C., Attenuation of elastic waves in granular mediums, J. Geophys. Res., 70, 3935-3942, 1965.

Savage, J.C., Comments on paper by R.B. Gordon and L.A. Davis, 'Velocity and attenuation of seismic waves in imperfectly elastic rock,' J. Geophys. Res., 74, 726-728, 1969.

Savage, J.C., and H.S. Hasegawa, Evidence for a linear attenuation mechanism, Geophysics, 22, 1003-1014, 1967.

Singh, V.P., Investigations of attenuation and internal friction of rocks by ultrasonics, Int. J. Rock Mech. Min. Sci. & Geomech. Abstr., 13, 69-74, 1976.

Stacey, F.D., M.T. Gladwin, B. McKavanagh, A.T. Linde, and L.M. Hastie, Anelastic damping of acoustic and seismic pulses, Geophys. Surveys, 2, 133-151, 1975.

Stocker, R.L., and R.B. Gordon, Velocity and internal friction in partial melts, J. Geophys. Res., 80, 4828-4836, 1975.

Stoll, R.D., Acoustic waves in saturated sediments, in Physics of Sound in Marine Sediments, edited by L. Hampton, Plenum Press, New York, 1974.

Stoll, R.D., Acoustic waves on ocean sediments, Geophysics, 42, 715-725, 1977.

Stoll, R.D., and G.M. Bryan, Wave attenuation in saturated sediments, J. Acoust. Soc. Am., 47, 1440-1447, 1970.

Strick, E., The determination of Q, dynamic viscosity and creep curves from wave propagation measurements, Geophys. J. Roy. Astr. Soc., 13, 197-218, 1967.

Strick, E., A predicted pedistal effect for pulse propagation in constant Q solids, Geophysics, 35, 387-402, 1970.

Strick, E., An explanation of observed time discrepancies between continuous and conventional well velocity surveys, Geophysics, 35, 285-295, 1971.

Tittmann, B.R., Lunar rock seismic Q in 3000-5000 range achieved in laboratory, Phil. Trans. R. Soc. Lond. A, 285, 475-479, 1977.

Tittman, B.R., Internal friction measurements and their implications in seismic Q structure models of the crust, the earth's crust, Geophys. Monog. Series, Amer. Geophys. Un., 1978.

Tittmann, B.R., M. Abdel-Gawad and R.M. Housley, Elastic velocity and Q measurements on Apollo 12, 14, and 15 rocks, Proc. Lunar Sci. Conf. 3rd, 2565-2575, 1972.

Tittman, B.R., R.M. Housley, and E.H. Cirlin, Internal friction of rocks and volatiles on the moon, Proc. Lunar Sci. Conf. 4th, 2631-2637, 1973.

Tittmann, B.R., R.M. Housley, G.A. Alers, and E.H. Cirlin, Internal friction in rocks and its relationship to volatiles on the moon, Proc. Lunar Sci. Conf. 5th, 2913-2918, 1974.

Tittmann, B.R., J.M. Curnow, and R.M. Housley, Internal friction quality factor Q > 3100 achieved in lunar rock 70215,85, Proc. Lunar Sci. Conf. 6th, 3217-3226, 1975.

Tittmann, B.R., L. Ahlberg, and J. Curnow, Internal friction and velocity measurements, Proc. Lunar Sci. Conf. 7th, 3123-3132, 1976.

Toksoz, M.N., D.H. Johnston and A. Timur, Attenuation of seismic waves in dry and saturated rocks, I. Laboratory measurements, Geophysics, 44, 681-690, 1979.

Vaisnys, J.R., Propagation of acoustic waves through a system undergoing phase transformatons, J. Geophys. Res., 73, 7675-7683, 1968.

Voigt, W., Uber innere Reibund fester Korper, insbesondere der Metalle, Annal. der Physik und Chemie, Neu Floge, 47, 671-693, 1892.

Walsh, J.B., Seismic wave attenuation in rock due to friction, J. Geophys. Res., 71, 2591-2599, 1966.

Walsh, J.B., New analysis of attenuation in partially melted rocks, J. Geophys. Res., 74, 4333, 1969.

Warren, N. and R. Trice, Ultrasonic attenuation: Q measurements on 70215,29, Proc. Lunar Sci. Conf. 5th, 2977-2938, 1974.

White, J.E., Seismic Waves, McGraw-Hill Book Co., Inc., New York, 1965.

White, J.E., Static friction as a source of seismic attenuation, Geophysics, 31, 333-339, 1966.

White, J.E., Computed seismic speeds and attenuation in rocks with partial gas saturation, Geophysics, 40, 224-232, 1975.

Winkler, K., M. Gladwin and A. Nur, The dependence of seismic attenuation on effective stress (abstract), EOS Transactions, Am. Geophys. Un., 58, 1183, 1977.

Winkler, K. and A. Nur, Pore fluids and seismic attenuation in rocks, Geophys. Res. Lett., 6, 1-4, 1979.

Winkler, K., A. Nur and M. Gladwin, Friction and seismic attenuation in rocks, Nature, 277, 528-531, 1979.

Yoder, H.S., Jr., Generation of Basaltic Magma, National Academy of Sciences, Washington D.C., 265 pp., 1976.

Zener, C., Elasticity and Anelasticity of Metals, Univ. of Chicago Press, Chicago, 1948.

SOCIETY OF MINING ENGINEERS of AIME

345 EAST 47TH STREET, NEW YORK, N.Y. 10017

PREPRINT NUMBER

71-AS-36

19P.

SOLUTION MINING WELL COMPLETION SERVICES AND TECHNIQUES

L. D. Boughton
Regional Manager, Mining Services, Eastern Area
Dowell Division of the Dow Chemical Company
Tulsa, Oklahoma

This paper is to be presented at the AIME CENTENNIAL ANNUAL MEETING - New York, New York - February 26 - March 4, 1971.

ABSTRACT

Solution mining projects are conducted through one or more boreholes which penetrate an ore body. Proper drilling, completion and maintenance of the boreholes, therefore, is essential to the success of any solution mining operation. Wells drilled for solution mining encounter problems quite similar to problems encountered by the petroleum industry in drilling, completing and maintaining wells for the production of oil, gas or water. Many of the services developed and much of the experience gained by the petroleum industry is applicable to solution mining wells. As in the petroleum industry, each individual wellbore and ore body in a solution mining project provides its own problems. These vary greatly from well to well, and it is not possible to set down data or outline programs that will apply to all wells. Instead, the design of the drilling, completion, production and maintenance programs should be worked out for each individual well. The purpose of this paper, then, is to generally describe materials, equipment and techniques available for these programs and to discuss the purpose and sequence of their use.

INTRODUCTION

Mineral deposits exist that are either too deep or too lean to recover by conventional mining methods. Many of these deposits may be profitably exploited by in-situ leach mining techniques. Essentially, the leach mining process consists of injecting a reactant into the ore body to dissolve the desired mineral and recovering the saturated reactant. In order to do this, one or more boreholes must be drilled into the ore body from the surface. The drilling, completion and maintenance of these boreholes are processes quite similar to those used for boreholes intended for recovery of petroleum. The services and techniques developed by the petroleum industry, therefore, are applicable to solution mining boreholes. These services consist of drilling, logging, cementing, perforating and stimulation, and maintenance services. This paper will consider only those services applicable after the borehole has been drilled into

the deposit.

LOGGING

Wireline logging refers to continuous recordings of various formation properties obtained by logging tools run into drilled holes at the end of electrically insulated cables.

Logging services have been performed by wireline companies serving the oil industry for many years. Figure 1 shows the interior of a typical logging truck. These same companies now provide logging services to the mining industry. Considerable research efforts are devoted to provide improved logs and log interpretation as required by the mining industry.

Logs are used to determine in-situ properties of drilled formations. These logs are used to supplement information obtained from drillers' logs, cores, seismic surveys and other sources. Logs provide a fast, economical means of obtaining information required to develop well completion programs.

Wireline logs provide information which is used to determine:

(a) The lithology of drilled formations.

(b) The pay or salt thickness.

(c) The stringers of insoluble material interbedded with the salt.

(d) The composition of the soluble salts.

(e) The thickness and composition of formations overlying and underlying the salt formation.

(f) The economic evaluation of a proposed solution mining project.

The information obtained from wireline logs in conjunction with that obtained from other sources is used in determining whether casing should be set through or on top of the salt section, the casing point, the desired fracture initiation point or depth, and the continuity of the salt bed between two wells to be fracture connected.

The wireline logs most commonly

Resistivity Logs. Resistivity the flow of electrical current. Res fication of ohm - m^2/M). Salt beds they are more resistive than surrour mineral content requires additional

Gamma Ray-Neutron Log. The ga a Scintillation detector. The dete coming mostly from three elements: elements are usually found in shale to determine shale content of the

The neutron log is a measurem formations. The response is prima whether from water of hydration or log is used to determine formatio of the matrix mineral as do other identifying the salt through char porosity logs.

Density Logs. The density log records the formation densit proportional to specific gravity use of an apparent density for i ative data for various salts and

Acoustic Logs. The acoust for a sonic compressional wave is known for many minerals.

The required number and ty evaluated. Logging needs also

The wireline logs most commonly used by solution mining operators include:

Resistivity Logs. Resistivity is the property of the formation to oppose the flow of electrical current. Resistivity is expressed in ohm-meters (a simplification of ohm - m^2/M). Salt beds are easily located by resistivity logs since they are more resistive than surrounding sedimentary beds. Definition of the mineral content requires additional logs.

Gamma Ray-Neutron Log. The gamma ray tool utilizes either Geiger-Mueller or a Scintillation detector. The detector measures the number of gamma ray emissions coming mostly from three elements: potassium, thorium, or uranium. Since these elements are usually found in shale, the gamma ray log may be used quantitatively to determine shale content of the formation being evaluated.

The neutron log is a measurement resulting from neutron irradiation of the formations. The response is primarily a function of the hydrogen concentration, whether from water of hydration or from water (or oil) in the pore space. The log is used to determine formation porosity. The log also responds to variations of the matrix mineral as do other porosity logs. Here, the primary interest is identifying the salt through characteristic responses on one or more of the porosity logs.

Density Logs. The density logging tool is a nuclear measuring device. The log records the formation density in gm/cc. The electron density is not quite proportional to specific gravity for some minerals. Such minerals require the use of an apparent density for interpretation. The logging companies have comparative data for various salts and evaporites to obtain the true bulk density.

Acoustic Logs. The acoustic log measures the time in microseconds required for a sonic compressional wave to move one foot in the formation. This parameter is known for many minerals.

The required number and type logs will vary with the particular salt being evaluated. Logging needs also vary as to whether the evaluation is being made in

a new property or in development of an established field. Figure 2 shows a composite log of a salt formation.

WELL SERVICES

"Well Services" as used here are those services required after the well has been drilled and logged. These services include running casing, cementation, and post-cementation operations.

Solution mining projects demand that the casing be hydraulically sealed in the drilled hole. Injected fluids obviously must be confined to the desired point of application, otherwise the project will be a costly failure. The casing size is of prime importance. The bit size used to drill the hole is selected to provide a hole diameter sufficient to handle the optimum size casing. An annular clearance between casing and open hole should be at least 1-1/2 inch or greater on diameters.

The casing must be considered as processing equipment the same as evaporators, boilers, etc. The size, weight, and grade are selected to meet the possible demands to be imposed. Some of the factors to be considered in designing the casing program include: (a) well depth; (b) fracturing pressures to be encountered; (c) friction loss during fracturing and brining operations; (d) will a single well system be employed if fracturing is unsuccessful--if so, what size casing is required; (e) what size casing is required to facilitate remedial operations; (f) is tubing required to dilute production to prevent salting up.

The tendency is to falsely economize and use casing which is too small. Seldom is too large casing used.

The hole and drilling mud must be conditioned prior to and after running casing. Conditioned mud has uniform low viscosity, and density consistent with other hole or formation requirements.

A well service frequently used by solution mining operators is the open hole caliper survey (Figures 3 and 4). It is run in the drilled hole prior to inserting casing. Mechanical feelers o
ant recorded caliper survey provides th
calculating the volume of cement requir
various formations.

Along with well-conditioned, thin
the drilled hole to better assure comp
Pockets or stringers of mud, not displ
or channel in the cemented casing-well
not be confined to the desired point

Auxiliary casing hardware is att
casing string itself. This equipment
The equipment includes cementing shoe
wiper plugs, and special stage cement
hardware, special cementing heads an
company.

All of this hardware is designe
in the drilled wellbore. Many diffe
hardware are available. The cement
that equipment best suited for the

Stage cementing devices (Figur
when the drilled formations will no
full annular column of cement. Th
designed to fill the annulus to a
collar is installed at this depth
the first stage cement has set, th
stage collar which is then closed.

A successful cement job requ
an impermeable, long-lasting seal
vide a hydraulic seal. It must b

inserting casing. Mechanical feelers or legs contact the formation. The resultant recorded caliper survey provides the hole size versus depth. It is used in calculating the volume of cement required and the extent of wash-outs in the various formations.

Along with well-conditioned, thinned mud, the casing must be centralized in the drilled hole to better assure complete mud removal by the sealing material. Pockets or stringers of mud, not displaced by the sealant, can provide a conduit or channel in the cemented casing-wellbore annulus. Fracturing fluids then will not be confined to the desired point of application.

Auxiliary casing hardware is attached to and becomes an integral part of the casing string itself. This equipment is provided by oilfield cementing companies. The equipment includes cementing shoes, float collars, centralizers, cementing wiper plugs, and special stage cementing devices (Fig. 5). Along with this casing hardware, special cementing heads and plugs are furnished by the cementing service company.

All of this hardware is designed to aid in hydraulically sealing the casing in the drilled wellbore. Many different designs and modifications of the casing hardware are available. The cementing service company will recommend and provide that equipment best suited for the particular well in question.

Stage cementing devices (Figure 6), commonly called "stage collars," are used when the drilled formations will not support the hydrostatic pressure exerted by a full annular column of cement. The primary or first stage cementation then is designed to fill the annulus to a height the formations will support. The stage collar is installed at this depth as an integral part of the casing string. After the first stage cement has set, the remainder of the annulus is filled through the stage collar which is then closed.

A successful cement job requires that the annulus be completely filled with an impermeable, long-lasting sealant of adequate strength. The sealant must provide a hydraulic seal. It must be of reasonable cost.

Modified portland cements are used to seal solution mining casing strings. A salt-saturated cement system is used. The salt or salts are those exposed in the wellbore. For example, the cement should be saturated with both NaCl and KCl when cementing a potash well. Service company, customer service personnel formulate the optimum cement system.

The salt-saturated cement system can be either salts dry blended with the cement or saturated brine mix water. In the latter case, a lesser amount of salts are dry blended with the cement to insure a saturated system under bottom-hole conditions of elevated temperature and pressure.

The normal practice is to place a salt-saturated neat cement across and 200 to 500 feet above the salt formation. A less expensive filler cement precedes to fill the annulus to surface.

Smith[4] points out that salt-saturated cements expand after setting. This provides a more effective seal than would a nonexpanding cement. Boughton[5] describes the use of commercially available expanding cement saturated with salt which has provided outstanding success.

Where sulfate-resistant cement is required, API Class C sulfate-resistant cement or Class A-pozzolan blends are used.

Relatively inexpensive, lightweight, lower-strength cement systems rely on extra mix water as an extender. Attapulgite clay hydrates more completely than does bentonite in brines. Therefore, more mix water can be incorporated in the attapulgite cement slurry without free water separation occurring. A sack of cement thus yields a greater volume of cement slurry at a reduced slurry cost. The average mid-continent cost of one cubic foot of salt-saturated Type I cement slurry (materials and mixing charge) is $1.73. The average mid-continent cost of one cubic foot of salt-saturated Type I cement, 4% attapulgite (materials and mixing charge) is $1.49 [1970].

Other cement additives can be used to solve particular well problems such as fluid-loss additives, lost-circulation fillers, dispersants, retarders, etc.

Again, the cementing service company will design

the specific need.

Ladd et al[6] report research and field studi

slurry should be placed in either so-called plug

should not be placed in streamline flow. Solut

ideal candidates for plug flow cementing. Norm

are not deep and hot. Placement rates of less

fill are practical and desirable.

Two other requirements for a successful ce

relationship between cement and drilling mud pr

should be a minimum of one pound per gallon hea

gel strength should exceed the mud gel strength

square feet. Figure 7 presents this informatic

Post cementing considerations include the

internal hydrostatic pressure while the cement

selection of a float collar with a back-pressur

bled from the casing after cementing. When th

sure applied to the casing, the casing is expa

released and the casing is evacuated, there is

bond to fail as the casing contracts.

Cement bond logging service is offered by

This log is designed to indicate whether or no

intact. Some logs are also designed to check

same time (Figure 8).

HYDRAULIC FRACT

Hydraulic fracturing is a process whereby

that is subsequently pressurized by surface pu

achieved at which rocks surrounding the wellbo

Again, the cementing service company will design the optimum cement system to meet the specific need.

Ladd et al[6] report research and field studies have confirmed that cement slurry should be placed in either so-called plug flow or in turbulent flow. It should not be placed in streamline flow. Solution mining projects usually are ideal candidates for plug flow cementing. Normally, the bedded salt formations are not deep and hot. Placement rates of less than 90 feet per minute annular fill are practical and desirable.

Two other requirements for a successful cementing operation involve the relationship between cement and drilling mud properties. The cement slurry should be a minimum of one pound per gallon heavier than the mud. The cement gel strength should exceed the mud gel strength by at least 20 pounds per 100 square feet. Figure 7 presents this information in graphical form.

Post cementing considerations include the casing be subjected to a minimum internal hydrostatic pressure while the cement sets. This requires the proper selection of a float collar with a back-pressure valve incorporated. Pressure is bled from the casing after cementing. When the cement sets with internal pressure applied to the casing, the casing is expanded. When the pressure is released and the casing is evacuated, there is a tendency for the cement-casing bond to fail as the casing contracts.

Cement bond logging service is offered by the wireline logging companies. This log is designed to indicate whether or not the cement bond to the casing is intact. Some logs are also designed to check the cement-formation bond at the same time (Figure 8).

HYDRAULIC FRACTURING

Hydraulic fracturing is a process whereby a wellbore is filled with a fluid that is subsequently pressurized by surface pumps until a state of stress is achieved at which rocks surrounding the wellbore fail by an extension (tension)

fracture. Fracturing creates the necessary flow channel to move the solvent, exposes surface area to facilitate solutioning, and provides conduits to transmit both the solvent and solute to and from the salt formation (Figure 9).

The economics of multiple well solution mining projects are reviewed elsewhere in this section. Hydraulic fracturing provides the fastest and least expensive means of producing multiple well projects.

Fracturing of salt wells is normally considered to be a three-step operation. First is the fracture initiation or formation breakdown. The formation is hydraulically pressured until the formation fails. A sudden reduction in surface pressure is noted when the fracture is initiated. The second step in the process is fracture propagation. As additional fracturing fluid is injected, the fracturing fluid will communicate to the target well and circulate to the surface (Step three). Figure 10 presents a typical pressure, volume versus time chart of a fracture treatment.

Fracturing fluids and auxiliary materials used in solution mining projects differ from oilfield fracturing in some respects. Propping agents (sand, glass beads, nut shells, etc.) are not used to maintain an open fracture. Continuous water circulation is employed to enlarge the fracture in salt formations. Fluid-loss additives are not used as there is little if any fracture fluid leaking from the fracture into the salt formation. Friction-reducing agents are used when economically advantageous.

Special pumps used to fracture the formation are also used to pump water to enlarge the fracture by dissolution. When the injection pressure is lowered sufficiently, the field circulating pumps take over. The majority of fracturing jobs are performed by oilfield service companies. Figure 11 shows a typical frac job in progress. Piper[7] reports the use of high-speed centrifugal pumps for this use. Specially built, high-volume, high-pressure pumps are provided on a service charge basis. The equipment is too diverse and complex to review here. Suffice it to say that the range includes turbine-powered units of 1000 plus hydraulic

horsepower capacity. In addition, service co
which, when added to the frac fluids, reduce
additional hydraulic horsepower required by
expensive. Figure 12 is a typical friction-
versus flow rate in 2-7/8 inch pipe. Many t
agents will produce an overall savings in th
pressure which otherwise would exceed the al

Service companies rent fracturing pumps
horsepower [1970] for the first four hours.
calculated using the formula --

$$Hhp = \frac{\text{pressure (p}}{}$$

(where a barrel = 42 U.S. gallons). The fr
2200 feet of 2-7/8 inch tubing at 15 BPM is
psi/1000 feet. The total loss then is 2.2
horsepower required to overcome the unprod

$$\frac{2200 \text{ (psi)} \times 1}{40.8}$$

The cost of overcoming the friction loss
[1970 pricing].

The predictability of the success of
formations has been reviewed. Here, we w
be horizontally fractured, provided the f
correct formation depth. Various means e
point in open-hole formations following
temperature survey and radioactive surve
Televiewer developed by the Mobil Oil Co
picture of a borehole wall (Figure 13).

horsepower capacity. In addition, service companies sell friction-reducing agents which, when added to the frac fluids, reduce the injection pressure. The additional hydraulic horsepower required by the friction loss is unproductive and expensive. Figure 12 is a typical friction-loss graph and presents friction loss versus flow rate in 2-7/8 inch pipe. Many times, the use of friction-reducing agents will produce an overall savings in the fracturing operation, or reduce the pressure which otherwise would exceed the allowable pressure rating of the casing.

Service companies rent fracturing pumps for approximately $1.16 per hydraulic horsepower [1970] for the first four hours. Delivered hydraulic horsepower is calculated using the formula --

$$\text{Hhp} = \frac{\text{pressure (psi)} \times \text{rate (BPM)}}{40.8}$$

(where a barrel = 42 U.S. gallons). The friction loss when fracturing through 2200 feet of 2-7/8 inch tubing at 15 BPM is determined from Figure 12 to be 1000 psi/1000 feet. The total loss then is 2.2 x 1000 = 2200 psi. The hydraulic horsepower required to overcome the unproductive friction loss is --

$$\frac{2200 \text{ (psi)} \times 15 \text{ BPM}}{40.8} = 812 .$$

The cost of overcoming the friction loss then is 812 Hhp x $1.16/Hhp = $942.00 [1970 pricing].

The predictability of the success of obtaining horizontal fractures in salt formations has been reviewed. Here, we will assume that the formation can be horizontally fractured, provided the fracture is properly initiated at the correct formation depth. Various means are available to determine the fracture point in open-hole formations following a fracture treatment. Bird[3] lists the temperature survey and radioactive survey. A newer logging tool, the Borehole Televiewer developed by the Mobil Oil Company, logs a continuous acoustic picture of a borehole wall (Figure 13).

Solution mining projects employ either open-hole or cased completions. Open-hole completion requires cementing the casing at the top of the salt and then drilling through the salt formation which remains open. The cased completion requires drilling through the salt formation and then cementing casing through the salt.

An industry survey shows the cased completion procedure is preferred although both are used. This is to be expected as each type completion has inherent advantages and disadvantages. Also, geological and operating considerations may dictate a preference for one or the other.

Cased completions provide better control of fracturing fluids. Fracturing fluids contact the salt formation (in properly cemented wells) only at the desired fracture initiation point. The key to fracture placement is to restrict fluid egress to the desired elevation and, if possible, to weaken the formation in the desired direction.[14] Cased completions do not require the use of packers to confine the fracturing fluid to the desired initiation depth. This permits fracturing down the casing which reduces costly, unproductive friction loss while fracturing.

Open-hole completions, on the other hand, permit a more detailed and accurate study of the dissolutioning pattern during brining operations. The logging surveys read a relatively short distance from the wellbore. The Sonar Caliper, Borehole Televiewer and mechanical caliper function in open hole--but not in casing.

The use of chemically removable casing has not been practiced by solution mining operators. The use permits cased completions for fracturing and initial production. The casing through the salt can later be efficiently and economically removed to provide the benefits of an open-hole completion.

A sharp notch in a single horizontal plane best insures the initiation of a horizontal fracture at the wellbore. The notch made at the correct depth at the base of the formation provides a fracture path for the most efficient mining point. The economics of washing upward in the salt as compared to downward has been reviewed.

Only the well to be fractured is normal
prefractured or back-fractured.

The wireline service companies pro
shaped charges in a single plane (Fig.
first run to be sure that the notch is
formation. Mechanical notching tools
single plane. In the latter case, san
through special jetting tools (Fig. 15
by the "sand blasting action." Notchi
completions.

Anticipated friction loss through
tions should create no friction loss
friction loss through perforations du
and Fast[13] state the optimum pump rat
1-1/4 barrels per minute for 3/8" per
1/4" perforations; and 2 to 3 barrels
continuous notch obtained by abrasive
opening through the casing and cement
is negligible. Abrasive jetting doe
thus does not crack or fracture the

Many instances have occurred wh
and communicated with a well hundred
well. Aughenbaugh and Pullen[2] descr
the target well. These stresses car
into the target well.

Most solution mining operators
the target well; pressuring the tar
pressure, in some cases simultaneou
the target well.

Only the well to be fractured is normally notched unless the target well is to be prefractured or back-fractured.

The wireline service companies provide a notching service using multiple shaped charges in a single plane (Fig. 14). An orientation log (gamma ray) is first run to be sure that the notch is made at the exact planned depth in the formation. Mechanical notching tools are available as is abrasive jetting in a single plane. In the latter case, sand-laden fluids are pumped at high pressure through special jetting tools (Fig. 15). The casing, cement and formation are cut by the "sand blasting action." Notching is employed in both open-hole and cased completions.

Anticipated friction loss through the notch must be reviewed. The perforations should create no friction loss during the solutioning operation. The friction loss through perforations during fracturing should be a minimum. Howard and Fast[13] state the optimum pump rate per perforation when fracturing is 1 to 1-1/4 barrels per minute for 3/8" perforations, 1.5 to 2 barrels per minute for 1/4" perforations; and 2 to 3 barrels per minute for 3/4" perforations. The continuous notch obtained by abrasive jetting provides the maximum possible size opening through the casing and cement. The friction loss through this type notch is negligible. Abrasive jetting does not exert a shock load on the cement and thus does not crack or fracture the cement above and below the notch.

Many instances have occurred where the fracture has bypassed the target well and communicated with a well hundreds and even thousands of feet beyond the target well. Aughenbaugh and Pullen[2] describe the stresses in the formation surrounding the target well. These stresses can prevent a fracture from breaking through and into the target well.

Most solution mining operators combat this problem by: back-fracturing from the target well; pressuring the target well to slightly less than fracturing pressure, in some cases simultaneously fracturing both wells, and prefracturing the target well.

A typical fracturing operation is to prefracture the updip well. Approximately 25% of the total estimated required fluid volume is injected to propagate the fracture. After this predetermined volume of fluid is injected, the downdip well is then fractured with approximately 75% of the estimated required volume of frac fluid. Fluid injection is continued until the wells are connected or it is evident that they will not communicate. A pressurized target well serves as an observation well while fracturing. Pressure response indicates the nearness of connection. Communication has been established between two wells 400 feet apart in just a few minutes; in other instances in the same field, it has taken days and even weeks. The volume of frac fluid or duration of pumping cannot be predicted with certainty.

Early fracturing jobs employed saturated brine until communication was established and confirmed to be where desired. Fresh water was then used to enlarge the fracture for normal field production. The thinking is that an unsuccessful fracture will heal and another fracture can be initiated at another point in the formation. The majority of today's solution mining fracturing operations use fresh water throughout.

The optimum injection rate again is subject to debate. However, the majority of operators use rates of 20 to 40 barrels (42 gallons per barrel) per minute. Experience in a given field will determine the most efficient operation. Fracturing service is charged for on a time basis per hydraulic horsepower. A cost analysis then is in order prior to fracturing.

MAINTENANCE SERVICES

Certain remedial services are required to maintain an efficient operation.

The Sonar Caliper Survey Service is used to determine the wash pattern in open-hole completions (Fig. 16). The Sonar Caliper cannot be used in cased-through completions. Myers[8] points out the benefits of open-hole Sonar Caliper Survey findings. The Sonar Caliper determines the leached void in the salt

formation. It also shows the condition of
formations. It locates rubble heaps in rel
basis for deciding whether or not to revers

A mechanical caliper survey will also
wellbore. The mechanical caliper is limite
to four feet, while the Sonar will read dis

Other tools to determine the solution
neutron log, temperature surveys, and acou

One of the major unsolved problems th
lack of a means to accurately define the e
voids. The logging services mentioned are
seeing device which can look through solid
subsurface void in its entirety.

A hydrocarbon blanket can be used to
highest grade section of the salt formati
solution mine a potash section within a s
the water solvent in the fracture, thus p
salt overlying the potash.

Other maintenance services include p
out and replacing damaged wash or product
bedded in salt formations will collapse v
pipe will be broken or mashed, and new p

CONC

Numerous problems can occur in comp
solution mining wells. Most of these ca
already developed by the petroleum indus
scope of this paper to present all data
efficient completion and repair programs
their applications, however, should pro
programs.

formation. It also shows the condition of the roof and interbedded insoluble formations. It locates rubble heaps in relation to wash strings. It provides a basis for deciding whether or not to reverse mine.

A mechanical caliper survey will also provide a profile of the open-hole wellbore. The mechanical caliper is limited to reading hole diameters from three to four feet, while the Sonar will read distances to 1,000 feet.

Other tools to determine the solutioning pattern include the gamma ray-neutron log, temperature surveys, and acoustic logs.

One of the major unsolved problems the solution mining operator faces is the lack of a means to accurately define the exact size and dimension of solutioned voids. The logging services mentioned are beneficial and vital. Industry needs a seeing device which can look through solid material and accurately delineate a subsurface void in its entirety.

A hydrocarbon blanket can be used to confine the washing action to the highest grade section of the salt formation. Shock[9] describes the process used to solution mine a potash section within a salt formation. The hydrocarbon floats on the water solvent in the fracture, thus preventing the leaching of the undesired salt overlying the potash.

Other maintenance services include poisitioning of wash strings, hole clean-out and replacing damaged wash or production strings. Insoluble stringers inter-bedded in salt formations will collapse when sufficiently unsupported. Often, the pipe will be broken or mashed, and new pipe must be installed.

CONCLUSIONS

Numerous problems can occur in completion, operation, and maintenance of solution mining wells. Most of these can be solved by services and techniques already developed by the petroleum industry. It has not been possible within the scope of this paper to present all data required for design of effective and efficient completion and repair programs. The description of the services and their applications, however, should provide a starting point for planning such programs.

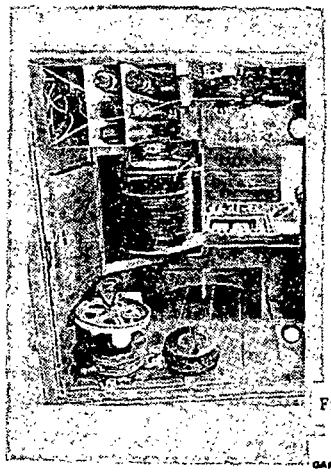

Figure 1 Interior of typical electrical logging service truck

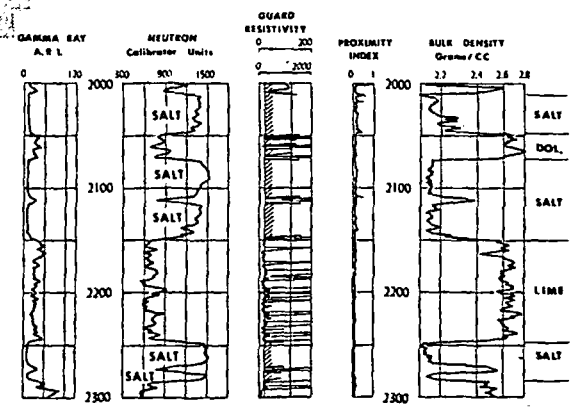

Figure 2 Composite log of typical salt formation

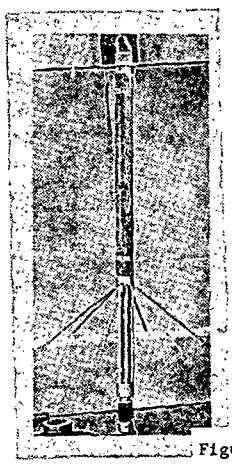

Figure 3 Open hole caliper tool used to measure hole diameter

Figure 4 Calip conjunction with

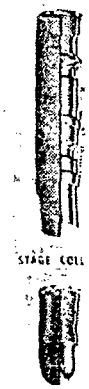

Figure 5 - Casing cementing hardware

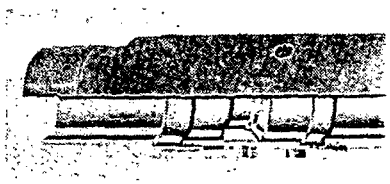

Figure 6 - Cutaway view of cementi

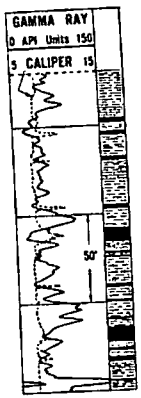

Figure 4 Caliper survey (dotted line) run in conjunction with gamma ray log

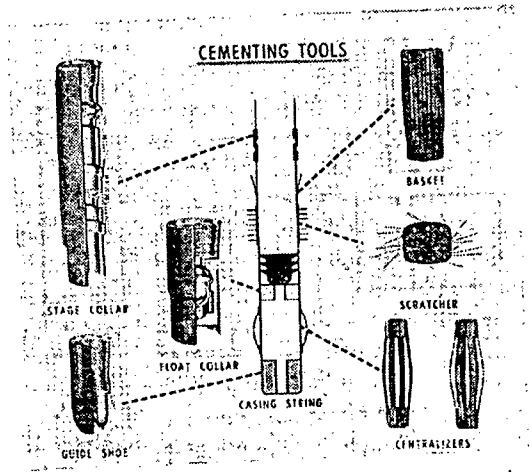

Figure 5- Casing cementing hardware and approximate location in casing string

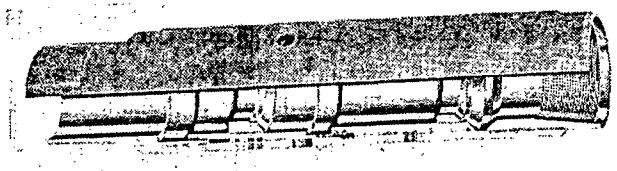

Figure 6 - Cutaway view of cementing "stage collar"

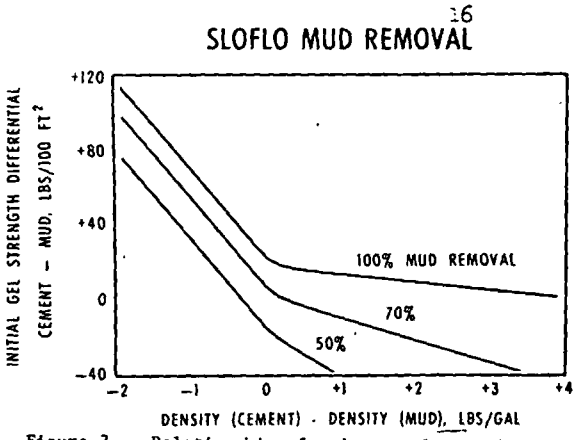

Figure 7 Relationship of mud removal to mud and cement gel strength and mud and cement density differentials

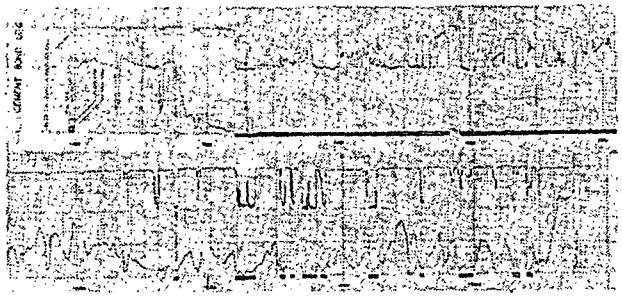

Figure 8 Typical cement bond logs showing poor and good cement bonds

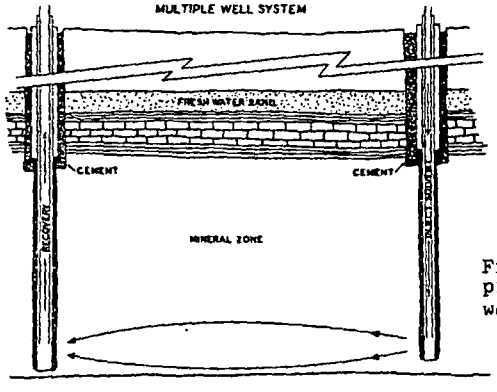

Figure 9 Hydraulic fracturing provides flow channels between wells to facilitate solutioning.

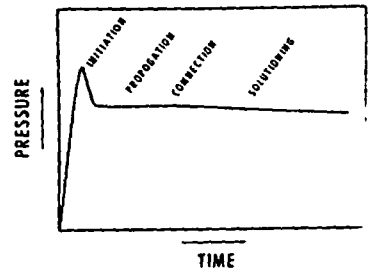

Figure 10 Pressure record of typi fracture treatment

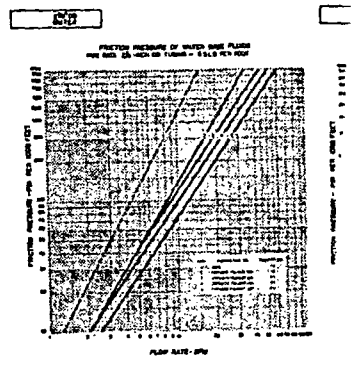

Figure 12 Friction los

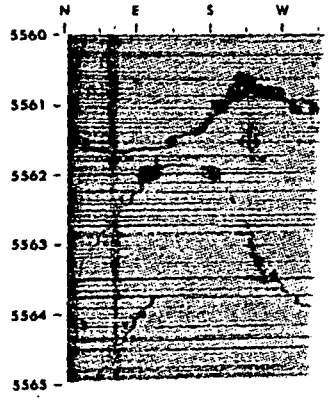

71-AS-36

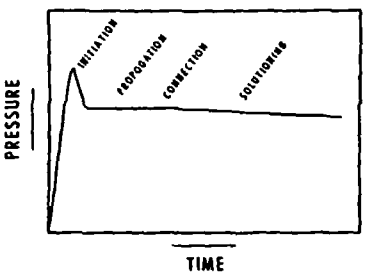

Figure 10 Pressure record of typical fracture treatment

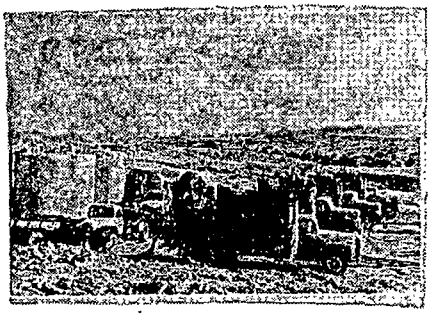

Figure 11 Fracture job in progress

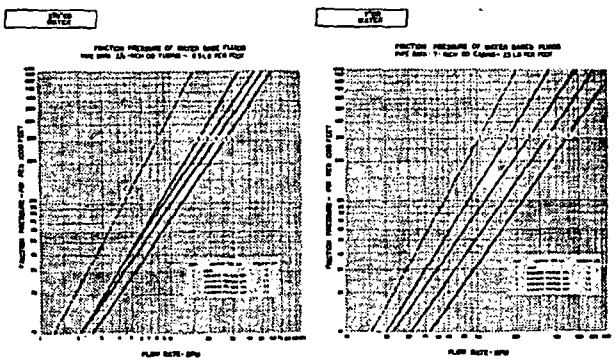

Figure 12 Friction loss curves for water and thickened water

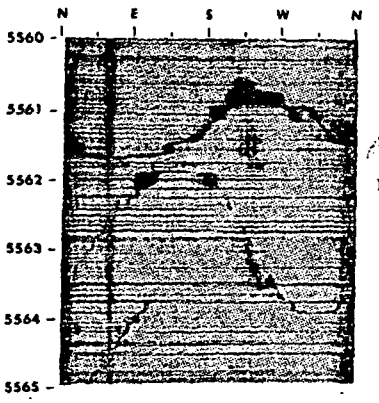

Figure 13 Borehole televiewer log

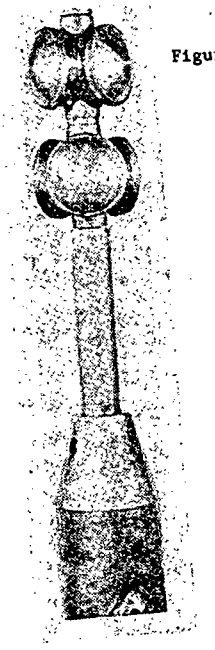

Figure 14 Notching tool provides multiple shaped charges in a single plane

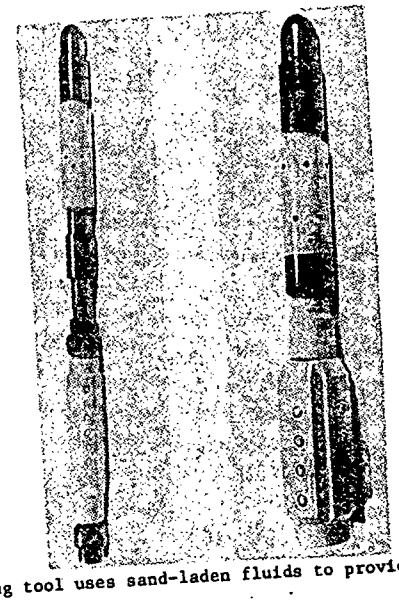

Figure 15 Abrasive jetting tool uses sand-laden fluids to provide cutting action

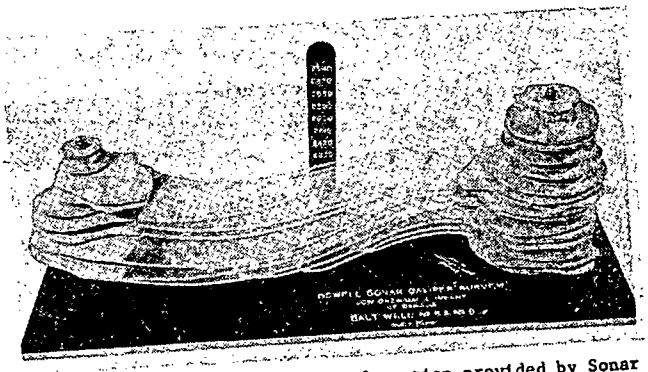

Figure 16 Model made from information provided by Sonar Caliper Survey shows wash patterns in open-hole completions